

THE UNIVERSITY OF CHICAGO

MOLECULAR ELECTROSTATIC EFFECTS FROM ANIONIC BORATE LIGANDS IN
OXIDATIVE REACTIVITY

A DISSERTATION SUBMITTED TO
THE FACULTY OF THE DIVISION OF THE PHYSICAL SCIENCES
IN CANDIDACY FOR THE DEGREE OF
DOCTOR OF PHILOSOPHY

DEPARTMENT OF CHEMISTRY

BY

MARGARET LOUISE KELTY

CHICAGO, ILLINOIS

JUNE 2022

Table of Contents

List of Figures	x
List of Schemes	xxi
List of Tables.....	xxii
List of Abbreviations.....	xxv
Acknowledgments.....	xxvii
Abstract	xxx
Preface.....	xxxiii
Chapter 1: Introduction.....	1
1.1 Externally Applied Electric Field Catalysis.....	1
1.1.1 Introduction to Electric Field Catalysis.....	1
1.1.2 Electric Field Effects in Enzymatic Catalysis	3
1.1.3 Externally Applied Electric Field Catalysis	6
1.2 Electrostatics in Coordination Chemistry	8
1.2.1 Introduction and Motivation.....	8
1.2.2 Charged Crown Ether Complexes	11
1.2.3 Charged Porphyrin Complexes.....	13
1.2.4 Additional Complexes Incorporating Electrostatic Effects.....	16
1.2.5 Conclusions	17
1.3 Approaches to Stabilizing High Valent Intermediates.....	19

1.3.1 Introduction	19
1.3.2 Examples of Electrostatic Effects on Metal Oxygen Based Reactivity.....	21
1.4 References	25
Chapter 2: Isolable Iodosylarene and Iodoxyarene Adducts of Co and Their O-atom Transfer and C-H Activation Reactivity.....	32
2.1 Introduction	32
2.2 Results and Discussion.....	33
2.2.1 Synthesis of Adduct Complexes.....	33
2.2.2 Crystallography	35
2.2.3 Reactivity Studies	37
2.2.4 Discussion of Possible Mechanism	42
2.3 Conclusions	44
2.4 Experimental	45
2.4.1 Materials and Instrumentation	45
2.4.2 Complex Synthesis and Characterization.....	46
2.4.3 Kinetic Experiments	50
2.4.4 X-Ray Crystallography.....	51
2.5 References	53
Chapter 3: Electrostatic vs. Inductive Effects in Phosphine Ligand Donor Properties and Reactivity	58

3.1 Introduction	58
3.2 Results and Discussion.....	62
3.2.1 Synthesis and Characterization of PPh ₂ CH ₂ BF ₃ K (K1).....	62
3.2.2 Tolman Electronic Parameter and J_{P-Se} Determination	63
3.2.3 Analysis of Donor Strength Solvent Dependence	66
3.2.4 Electrostatic Contributions to Donor Strength	71
3.2.5 Extension and Comparison to Other Phosphines	73
3.2.6 C–F Oxidative Addition Reactivity	75
3.2.7 Catalytic Defluoroborylation Reactivity	78
3.3 Conclusions	81
3.4 Experimental	82
3.4.1 General Considerations.....	82
3.4.2 Synthesis of Reported Compounds	84
3.4.3 X-Ray Structure Determination.....	88
3.4.4 Discussion of van der Waals Radii in 2	88
3.4.5 Computational Procedures.....	89
3.4.6 Discussion of the Slopes of J_{P-Se} vs. $1/4\pi\epsilon$	92
3.4.7 Procedure for Oxidative Addition of C ₆ F ₆	93
3.4.8 Procedures for Catalytic C–F Borylation	95
3.5 References	98

Chapter 4: Electrostatic Effects on Bond Vibrations in Ni Nitrosyl Compounds Featuring a Novel Borate Anion	111
4.1 Introduction	111
4.2 Results and Discussion.....	115
4.2.1 Computational Prediction of Donor Strength.....	115
4.2.2 Synthesis and Characterization of Heteroaryl Phosphines with BF ₃ K Substituents ..	117
4.2.3 Synthesis and Characterization of Pyridines with BF ₂ CF ₃ K Substituents	119
4.2.4 Synthesis and Characterization of Ni-NO Complexes	122
4.3 Conclusion.....	123
4.4 Experimental	124
4.4.1 General Procedures.....	124
4.4.2 Syntheses	125
4.4.3 X-Ray Crystallography.....	129
4.4.4 Computational Methods	129
4.5 References	131
Appendix 1: Synthesis and Metalation of Anionic Tetra-pyrazole Lutidine Based Ligands	136
A1.1 Introduction	136
A1.2 Results and Discussion.....	138
A1.2.1 Metalation and Oxidation of pz ₄ lut.....	138
A1.2.2 Test Deprotonations of pz ₄ lut	140

A1.2.3 Sulfonation of pz4lut and Subsequent Metalation	141
A1.2.4 Attempted Installation of a Borate Group on pz4lut	143
A1.3 Experimental	144
A1.3.1 General.....	144
A1.3.2 Preliminary Synthetic Procedures.....	145
A1.4 Supporting data.....	147
A1.4.1 NMR Spectra	147
A1.4.2 Cyclic Voltammetry.....	164
A1.4.3 UV-vis Spectra.....	166
A1.5 References	170
Appendix 2: Supporting Data for Chapter 2	172
A2.1 Characterization Data.....	172
A2.1.1 IR Spectra	172
A2.1.2 UV-vis Spectra.....	176
A2.1.3 NMR Spectra	177
A2.1.4 EPR Spectra.....	191
A2.1.5 Mass Spectra.....	197
A2.1.6 Electrochemistry	201
A2.2 Kinetic Experiments.....	201
A2.2.1 Kinetic Plots.....	201

A2.2.2 Kinetic Isotope Effect	210
A2.3 X-Ray Crystallography.....	215
A2.3.1 Structures	215
A2.3.2 Metrical Parameters	219
A2.3.3 Refinement Details	220
Appendix 3: Supporting Data for Chapter 3	226
A3.1 NMR Characterization Data.....	226
A3.1.1 PPh ₂ CH ₂ BF ₃ K (K1).....	226
A3.1.2 [PPh ₄][Rh(acac)(CO)(PPh ₂ (CH ₂ BF ₃))] (2).....	229
A3.1.3 [PPh ₄][SePPh ₂ (CH ₂ BF ₃)] ([PPh ₄][1 ^{Se})]	232
A3.1.4 [NEt ₄][SePPh ₂ (CH ₂ BF ₃)] ([TEA][1 ^{Se})]	236
A3.1.5 Comparison between [TEA][1 ^{Se}] and [PPh ₄][1 ^{Se}]	238
A3.1.6 [PPh ₄][SePPh ₂ (2-BF ₃ Ph)] ([PPh ₄][3 ^{Se})].....	241
A3.2 Infrared Spectra	244
A3.3 UV-visible spectra.....	248
A3.4 X-Ray Crystallography.....	254
A3.5 Calculations	260
A3.5.1 Matlab Code for Estimating Electric Field Using Coulombs Law.....	260
A3.5.2 Optimized Structures	261
A3.6 Variable Solvent ³¹ P{ ¹ H} NMR.....	276

A3.6.1 [PPh ₄][1 ^{Se}]	276
A3.6.2 [TEA][1 ^{Se}]	279
A3.6.3 [PPh ₄][3 ^{Se}]	280
A3.6.4 Neutral Congeners	281
A3.7 Correlation between J_{P-Se} and TEP	282
A3.8 Analysis of J_{P-Se} Solvent Dependence	284
A3.9 NMR Spectra of C ₆ F ₆ Oxidative Addition	286
A3.9.1 K1 with Ni(COD) ₂	286
A3.9.2 PCy ₃ with Ni(COD) ₂	292
A3.9.3 PEt ₃ with Ni(COD) ₂	296
A3.10 Characterization of Products in Defluoroborylation Reactions	301
A3.10.1 NMR Spectra	301
A3.10.2 GC/MS Characterization	306
A3.11 Catalytic C-F Borylation Trial Reactions	308
Appendix 4: Supporting Data for Chapter 4	316
A4.1 Characterization data	316
A4.1.1 PPh(6-BF ₃ -2-pyH) ₂	316
A4.1.2 P(6-BF ₃ -2-pyH) ₃	319
A4.1.3 [P(2-py) ₃ NiNO][BPh ₄]	322
A4.1.4 K[2-Br-4-BF ₂ CF ₃ -py]	326

A4.1.5 K[2-Br-3-BF ₂ CF ₃ -py]	331
A4.1.6 K[2-Br-5-BF ₂ CF ₃ -py]	333
A4.1.7 K[2-Br-6-BF ₂ CF ₃ -py]	335
A4.2 SXRD Tables.....	337
A4.3 Calculations	338
A4.3.1 Coordinates of Optimized Structures.....	338
A4.3.2 Matlab Code Used to Predict Fz in the 3 Isomer.....	347

List of Figures

Chapter 1

Figure 1.1 Simplified depiction of the active site in ketosteroid isomerase	4
Figure 1.2 Simplified diagram of the parallel plate capacitor.....	7
Figure 1.3 Simplified diagram of the Diels- Alder reaction within an STM set-up	7
Figure 1.4 Complexes described in the “electrostatics in coordination chemistry” section	10
Figure 1.5 Tetra-cationic porphyrin complex	15
Figure 1.6 Metal complexes incorporating charged moieties	22

Chapter 2

Figure 2.1 XRD structures and selected bond lengths for complexes 1 , 2 , and 3	35
Figure 2.2 UV-vis spectral changes during the decay of 1	37
Figure 2.3 Plots of observed rate constants for the reaction of 2 and 3	40
Figure 2.4 Potential reaction pathways for Co-iodosyl- and iodoxyarene adducts 1-3	42

Chapter 3

Figure 3.1 SXRD structures of the anions of K1 , 2 , [PPh ₄][1 ^{Se}], and [PPh ₄][3 ^{Se}].....	63
Figure 3.2 Correlation between the TEP of selected phosphine ligands and the J_{P-Se}	65
Figure 3.3 Solvent dependence of J_{P-Se} for anionic and neutral phosphines.....	68
Figure 3.4 Substrate scope defluoroborylation catalysis	80

Chapter 4

Figure 4.1 Proposed series of complexes.....	114
Figure 4.2 DFT optimized structures of the proposed Ni-NO complexes.....	116
Figure 4.3 The proposed ligands P(6-BF ₃ -2-py) ₃ and PPh(6-BF ₃ -2-pyridine) ₂	118

Figure 4.4 Synthetic routes towards the preparation of a BF ₂ CF ₃ substituted pyridine.	120
Figure 4.5 SXR structure of 2-Br-4-BF ₂ CF ₃ K-pyridine	121
Figure 4.6 SXR structure of [PPy ₃ NiNO][BPh ₄]	122

Appendix 1

Figure A1.1 UV-vis spectra of the reaction between ^s PhIO and [Fe(pz ₄ lut)MeCN][OTf] ₂	140
Figure A1.2 Ball and stick model of SXR structures of the Mn(pz ₄ lut(SO ₃) ₂)(DMF) and Fe(pz ₄ lut(SO ₃) ₂)(MeCN).....	142
Figure A1.3 Ball and stick model depictions of SXR structures of the reaction products generated between pz ₄ lut and B(C ₆ F ₅) ₃ in THF and toluene	144
Figure A1.4 ¹ H and ¹⁹ F NMR of [Fe(pz ₄ lut)MeCN][OTf] ₂ in CD ₃ CN	147
Figure A1.5 ¹ H and ¹⁹ F NMR spectra of [Fe(pz ₄ lut)MeCN][OTf] ₂	148
Figure A1.6 NMR spectra of pz ₄ lut with 2.2 equivalents of nBuLi in <i>d</i> ₈ -THF	149
Figure A1.7 NMR spectrum in <i>d</i> ₈ -THF of the reaction between pz ₄ lut and 2.2 equivalents of nBuLi at -50 °C with tentative assignments for the resonances.....	150
Figure A1.8 ¹ H NMR in DMSO of the reaction between 3 equiv. KO ^t Bu and pz ₄ lut.....	151
Figure A1.9 ¹ H NMR of the methylated pz ₄ lut.....	152
Figure A1.10 ¹ H NMR spectrum of Li ₂ pz ₄ lut(SO ₃) ₂ in CD ₃ CN.....	153
Figure A1.11 ¹ H NMR of the reaction between Li ₂ pz ₄ lut(SO ₃) ₂ and Fe(MeCN) ₂ OTf ₂	154
Figure A1.12 ¹ H NMR of the reaction between Li ₂ pz ₄ lut(SO ₃) ₂ and Mn(MeCN) ₂ OTf ₂	155
Figure A1.13 ¹ H NMR of the reaction between Li ₂ pz ₄ lut(SO ₃) ₂ and Co(MeCN) ₆ (OTf) ₂	156
Figure A1.14 ¹ H NMR spectra of the reaction between pz ₄ lut and BF ₃ •Et ₂ O.....	157
Figure A1.15 ¹ H NMR spectra of K ₂ pz ₄ lut.....	158
Figure A1.16 ¹ H NMR of the reaction between pz ₄ lut and B(C ₆ F ₅) ₃ in THF.....	159

Figure A1.17 ^1H NMR of the reaction between pz4lut and $\text{B}(\text{C}_6\text{F}_5)_3$ in toluene	160
Figure A1.18 ^1H NMR spectrum of the reaction between pz4lut and $\text{ICH}_2\text{B}(\text{O}^i\text{Pr})_2$	161
Figure A1.19 ^1H NMR of the reaction between $\text{pz4lut}(\text{CH}_2\text{B}(\text{O}^i\text{Pr})_2)_2$ and KHF_2	162
Figure A1.20 ^1H , ^{19}F and ^{11}B NMR characterization of the proposed $\text{pz4lut}(\text{CH}_2\text{BF}_3)_2$	163
Figure A1.21 Full cyclic voltammogram of $[\text{Fe}(\text{pz4lut})\text{MeCN}][\text{OTf}]_2$	164
Figure A1.22 Cyclic voltammogram of $\text{Fepz4lut}(\text{SO}_3)_2(\text{MeCN})$	165
Figure A1.23 UV-vis of the decay of $[\text{Fe}(\text{pz4lut})\text{MeCN}][\text{OTf}]_2$ with $^s\text{PhIO}$	166
Figure A1.24 UV-vis spectrum of the reaction between $[\text{Fe}(\text{pz4lut})\text{MeCN}][\text{OTf}]_2$ and $^s\text{PhIO}$. 167	
Figure A1.25 UV-vis spectra of the reaction between $\text{Fepz4lut}(\text{SO}_3)_2(\text{MeCN})$ and $^s\text{PhIO}$	168
Figure A1.26 UV-vis spectra of the reaction between $\text{Fepz4lut}(\text{SO}_3)_2(\text{MeCN})$ and mCPBA ...	169

Appendix 2

Figure A2.1 Vibrational spectrum of 1 as KBr pellet	172
Figure A2.2 Vibrational spectrum of 2 as KBr pellet	173
Figure A2.3 Vibrational spectrum of 3 as KBr pellet	174
Figure A2.4 Vibrational spectrum of 4 as KBr pellet	174
Figure A2.5 Vibrational spectrum of 5 as KBr pellet	175
Figure A2.6 UV-vis spectra for complexes 1 - 5	176
Figure A2.7 The ^1H NMR spectrum of 1	177
Figure A2.8 The ^1H NMR spectrum of 2	178
Figure A2.9 The ^1H NMR spectrum of 3	179
Figure A2.10 The ^1H NMR spectrum of 4	180
Figure A2.11 The ^1H NMR spectrum of 5	181
Figure A2.12 The ^1H NMR spectrum of the decay of 1	182

Figure A2.13 The ^1H NMR spectrum of the decay of 2	183
Figure A2.14 The ^1H NMR spectrum of the reaction of 1 with PMe_3 and OPMe_3	184
Figure A2.15 The ^1H NMR spectrum of 2 and 3 with PPh_3	185
Figure A2.16 The ^1H NMR spectrum of $\text{CoTp}^{\text{tBu}}\text{-OPPh}_3$ adduct	186
Figure A2.17 The ^1H NMR spectrum of the reaction of 2 and 3 with thioanisole	187
Figure A2.18 The ^1H NMR spectrum of $\text{CoTp}^{\text{tBu}}\text{-PhSOMe}$ adduct	188
Figure A2.19 The ^1H NMR spectrum of the reaction of 3 with ^sPhI	189
Figure A2.20 The ^1H NMR spectrum of the crystals of 6	190
Figure A2.21 The X-band EPR spectrum of 1	191
Figure A2.22 The X-band EPR spectrum of 2	192
Figure A2.23 The X-band EPR spectrum of 3	193
Figure A2.24 The X-band EPR spectrum of 4	194
Figure A2.25 The X-band EPR spectrum of 5	195
Figure A2.26 The X-band EPR spectrum of 6	196
Figure A2.27 The MS data for the self-decay of 1	197
Figure A2.28 The MS data for the self-decay of 2	198
Figure A2.29 The MS data for the self-decay of 3	199
Figure A2.30 The MS data for the reaction of 1 with Sc^{3+} ions	200
Figure A2.31 The cyclic voltammograms of 1 and 2	201
Figure A2.32 Kinetic data obtained for complex 1	202
Figure A2.33 Representative plot of the decay of 2	203
Figure A2.34 Kinetic data obtained for complex 2	204
Figure A2.35 Kinetic data obtained for complex 2	205

Figure A2.36 The ^1H NMR spectrum of the decay of 3	206
Figure A2.37 Kinetic data obtained for complex 3	207
Figure A2.38 Kinetic data obtained for complex 3	208
Figure A2.39 Kinetic data obtained for the background reaction of $^s\text{PhIO}$	209
Figure A2.40 A representative MS trace for determination of the KIE for 1	210
Figure A2.41 Structure of 3 showing the secondary interaction of a THF molecule	215
Figure A2.42 Depiction of the molecular structure of 4 determined by X-ray diffraction.....	216
Figure A2.43 Depiction of the molecular structure of 5 determined by X-ray diffraction.....	217
Figure A2.44 Depiction of the molecular structure of 6 determined by X-ray diffraction.....	218

Appendix 3

Figure A3.1 ^1H NMR spectrum of K1 in $\text{DMSO-}d_6$ with inset showing CH_2 peak.	226
Figure A3.2 $^{31}\text{P}\{^1\text{H}\}$ NMR spectrum of K1 in $\text{DMSO-}d_6$	227
Figure A3.3 $^{19}\text{F}\{^1\text{H}\}$ NMR spectrum of K1 in $\text{DMSO-}d_6$	227
Figure A3.4 $^{13}\text{C}\{^1\text{H}\}$ NMR spectrum of K1 collected in $\text{DMSO-}d_6$	228
Figure A3.5 $^{11}\text{B}\{^1\text{H}\}$ NMR spectrum of K1 in $\text{DMSO-}d_6$	228
Figure A3.6 ^1H NMR spectrum of 2 collected in CDCl_3	229
Figure A3.7 $^{31}\text{P}\{^1\text{H}\}$ NMR spectrum of 2 collected in CDCl_3	230
Figure A3.8 $^{19}\text{F}\{^1\text{H}\}$ NMR spectrum of 2 collected in CDCl_3	230
Figure A3.9 $^{13}\text{C}\{^1\text{H}\}$ NMR spectrum of 2 collected in CDCl_3	231
Figure A3.10 $^{11}\text{B}\{^1\text{H}\}$ NMR spectrum of 2 in CDCl_3	231
Figure A3.11 ^1H NMR spectrum of $[\text{PPh}_4][\mathbf{1}^{\text{Se}}]$ in CDCl_3	232
Figure A3.12 $^{31}\text{P}\{^1\text{H}\}$ NMR spectrum of $[\text{PPh}_4][\mathbf{1}^{\text{Se}}]$ in CDCl_3	233
Figure A3.13 $^{19}\text{F}\{^1\text{H}\}$ NMR spectrum of $[\text{PPh}_4][\mathbf{1}^{\text{Se}}]$ in CDCl_3	233

Figure A3.14 $^{13}\text{C}\{^1\text{H}\}$ NMR spectrum of $[\text{PPh}_4][\mathbf{1}^{\text{Se}}]$ in CDCl_3	234
Figure A3.15 $^{11}\text{B}\{^1\text{H}\}$ NMR spectrum of $[\text{PPh}_4][\mathbf{1}^{\text{Se}}]$ in CDCl_3	234
Figure A3.16 DOSY NMR spectrum of $[\text{PPh}_4][\mathbf{1}^{\text{Se}}]$ in CDCl_3	235
Figure A3.17 ^1H NMR spectrum of $[\text{TEA}][\mathbf{1}^{\text{Se}}]$ in CDCl_3	236
Figure A3.18 $^{31}\text{P}\{^1\text{H}\}$ NMR spectrum of $[\text{TEA}][\mathbf{1}^{\text{Se}}]$ in CDCl_3	236
Figure A3.19 $^{19}\text{F}\{^1\text{H}\}$ NMR spectrum of $[\text{TEA}][\mathbf{1}^{\text{Se}}]$ in CDCl_3	237
Figure A3.20 $^{13}\text{C}\{^1\text{H}\}$ NMR spectrum of $[\text{TEA}][\mathbf{1}^{\text{Se}}]$ in CDCl_3	237
Figure A3.21 $^{11}\text{B}\{^1\text{H}\}$ NMR spectrum of $[\text{TEA}][\mathbf{1}^{\text{Se}}]$ collected in CDCl_3	238
Figure A3.22 ^1H NMR spectra of $[\text{TEA}][\mathbf{1}^{\text{Se}}]$ and $[\text{PPh}_4][\mathbf{1}^{\text{Se}}]$ in CD_2Cl_2	238
Figure A3.23 ^1H NMR spectra of $[\text{TEA}][\mathbf{1}^{\text{Se}}]$ and $[\text{PPh}_4][\mathbf{1}^{\text{Se}}]$ in $\text{DMSO-}d_6$	239
Figure A3.24 ^1H NMR spectra showing methylene of $[\text{TEA}][\mathbf{1}^{\text{Se}}]$ and $[\text{PPh}_4][\mathbf{1}^{\text{Se}}]$	239
Figure A3.25 ^{19}F NMR spectra showing the BF_3 of $[\text{TEA}][\mathbf{1}^{\text{Se}}]$ and $[\text{PPh}_4][\mathbf{1}^{\text{Se}}]$	240
Figure A3.26 ^1H NMR spectrum of $[\text{PPh}_4][\mathbf{3}^{\text{Se}}]$ in CD_3CN	241
Figure A3.27 $^{31}\text{P}\{^1\text{H}\}$ NMR spectrum of $[\text{PPh}_4][\mathbf{3}^{\text{Se}}]$ in CD_2Cl_2	242
Figure A3.28 $^{19}\text{F}\{^1\text{H}\}$ NMR spectrum of $[\text{PPh}_4][\mathbf{3}^{\text{Se}}]$ in CD_3CN	242
Figure A3.29 $^{13}\text{C}\{^1\text{H}\}$ NMR spectrum of $[\text{PPh}_4][\mathbf{3}^{\text{Se}}]$ in CD_3CN	243
Figure A3.30 $^{11}\text{B}\{^1\text{H}\}$ NMR spectrum of $[\text{PPh}_4][\mathbf{3}^{\text{Se}}]$ in CD_3CN	243
Figure A3.31 IR spectrum (KBr Pellet) of K1	244
Figure A3.32 IR spectrum (DCM Solution) of 2	244
Figure A3.33 IR spectrum (KBr pellet) of 2	245
Figure A3.34 IR spectrum (CDCl_3 solution) of $[\text{PPh}_4][\mathbf{1}^{\text{Se}}]$	245
Figure A3.35 IR spectrum (KBr pellet) of $[\text{TEA}][\mathbf{1}^{\text{Se}}]$	246
Figure A3.36 IR spectrum (KBr pellet) of $[\text{PPh}_4][\mathbf{3}^{\text{Se}}]$	246

Figure A3.37 IR spectra of 2 in different solvents.....	247
Figure A3.38 IR spectra of Rh(CO) ₂ acac in different solvents.	247
Figure A3.39 UV-vis traces of the reaction between Ni(COD) ₂ , K1 , and C ₆ F ₆	248
Figure A3.40 UV-vis traces of the reaction between Ni(COD) ₂ , K1 , and C ₆ F ₆	249
Figure A3.41 UV-vis traces of the reaction between Ni(COD) ₂ , 3 equiv. K1 , and C ₆ F ₆	250
Figure A3.42 UV-vis traces of the reaction between Ni(COD) ₂ , 4 equiv. K1 , and C ₆ F ₆	251
Figure A3.43 UV-vis traces of the reaction between Ni(COD) ₂ , 8 equiv. K1 , and C ₆ F ₆	252
Figure A3.44 UV-vis traces of the reaction of Ni(COD) ₂ and K1 without C ₆ F ₆	253
Figure A3.45 SXR structure of K1 with K ⁺ counterion shown.	254
Figure A3.46 SXR structure of 2 with PPh ₄ ⁺ counterion shown.	254
Figure A3.47 SXR structure of [PPh ₄][1 ^{Se}] with PPh ₄ ⁺ counterion shown.....	255
Figure A3.48 Space filling model of the SXR structure of [PPh ₄][1 ^{Se}].....	255
Figure A3.49 SXR structure of [TEA][1 ^{Se}] with TEA ⁺ counterion shown.....	256
Figure A3.50 Space filling model of the SXR structure of [TEA][1 ^{Se}] with TEA ⁺	256
Figure A3.51 SXR structure of [PPh ₄][3 ^{Se}] with PPh ₄ ⁺ counterion shown.....	257
Figure A3.52 Calculated structure of 1 ^{Se} (cisoid structure).	261
Figure A3.53 Calculated structure of 1 ^{Se} (transoid structure).	262
Figure A3.54 Optimized structure of SePPh ₂ Et.....	264
Figure A3.55 Optimized structure of 2	265
Figure A3.56 Optimized structure of 1 ^{Se} with explicit MeCN solvation.....	267
Figure A3.57 Optimized structure of 1 ^{Se} with explicit DCM solvation.....	270
Figure A3.58 Optimized structure of 1 ^{Se} with explicit CHCl ₃ solvation.	273
Figure A3.59 ³¹ P { ¹ H} NMR spectra of [PPh ₄][1 ^{Se}] in CD ₃ CN and DMSO- <i>d</i> ₆	276

Figure A3.60 $^{31}\text{P}\{^1\text{H}\}$ NMR spectra of $[\text{PPh}_4][\mathbf{1}^{\text{Se}}]$ in CDCl_3 and CD_2Cl_2	276
Figure A3.61 $^{31}\text{P}\{^1\text{H}\}$ NMR spectrum of $[\text{PPh}_4][\mathbf{1}^{\text{Se}}]$ in $(\text{CD}_3)_2\text{CO}$	277
Figure A3.62 $^{31}\text{P}\{^1\text{H}\}$ NMR spectra of $[\text{PPh}_4][\mathbf{1}^{\text{Se}}]$ in the indicated solvent mixtures.....	277
Figure A3.63 $^{31}\text{P}\{^1\text{H}\}$ NMR spectra of $[\text{PPh}_4][\mathbf{1}^{\text{Se}}]$ in CD_2Cl_2 with addition of PPh_4Br	278
Figure A3.64 $^{31}\text{P}\{^1\text{H}\}$ NMR spectra of $[\text{PPh}_4][\mathbf{1}^{\text{Se}}]$ in CDCl_3 with addition of TBA salts.	278
Figure A3.65 $^{31}\text{P}\{^1\text{H}\}$ NMR spectra of $[\text{PPh}_4][\mathbf{1}^{\text{Se}}]$ in CDCl_3 with TEA and PPN salts.	279
Figure A3.66 $^{31}\text{P}\{^1\text{H}\}$ NMR spectrum of $[\text{TEA}][\mathbf{1}^{\text{Se}}]$ in the indicated solvents.....	279
Figure A3.67 $^{31}\text{P}\{^1\text{H}\}$ NMR spectrum of $[\text{TEA}][\mathbf{1}^{\text{Se}}]$ in the indicated solvents.....	280
Figure A3.68 $^{31}\text{P}\{^1\text{H}\}$ NMR spectra of $[\text{PPh}_4][\mathbf{3}^{\text{Se}}]$ in different solvents.....	280
Figure A3.69 $^{31}\text{P}\{^1\text{H}\}$ NMR spectra of SePPH_2Et in the indicated solvents.	281
Figure A3.70 $^{31}\text{P}\{^1\text{H}\}$ NMR spectra of SePPH_3 in the indicated solvents.	281
Figure A3.71 Plot of experimental $J_{\text{P-Se}}$ vs. TEP	282
Figure A3.72 Plots of $J_{\text{P-Se}}$ as a function of solvent dielectric.....	284
Figure A3.73 $^{31}\text{P}\{^1\text{H}\}$ NMR spectrum of the reaction of K1 and $\text{Ni}(\text{COD})_2$ in THF.	286
Figure A3.74 $^{19}\text{F}\{^1\text{H}\}$ NMR spectrum of the reaction of K1 , $\text{Ni}(\text{COD})_2$, and C_6F_6	287
Figure A3.75 $^{19}\text{F}\{^1\text{H}\}$ NMR spectrum of the reaction of K1 , $\text{Ni}(\text{COD})_2$, and C_6F_6	287
Figure A3.76 ^{19}F NMR spectrum of the reaction between K1 , $\text{Ni}(\text{COD})_2$ and C_6F_6	288
Figure A3.77 Time course monitoring of the ^{19}F NMR spectrum of the reaction between K1 , $\text{Ni}(\text{COD})_2$ and C_6F_6	289
Figure A3.78 $^{31}\text{P}\{^1\text{H}\}$ NMR spectrum of the reaction between K1 , $\text{Ni}(\text{COD})_2$ and C_6F_6	290
Figure A3.79 Time course monitoring of the $^{31}\text{P}\{^1\text{H}\}$ NMR spectrum of the reaction between K1 , $\text{Ni}(\text{COD})_2$ and C_6F_6	291
Figure A3.80 ^{19}F NMR spectrum of the reaction between PCy_3 , $\text{Ni}(\text{COD})_2$ and C_6F_6	292

Figure A3.81 Time course monitoring of the ^{19}F NMR spectrum of the reaction between PCy_3 , $\text{Ni}(\text{COD})_2$ and C_6F_6	293
Figure A3.82 $^{31}\text{P}\{^1\text{H}\}$ NMR spectrum of the reaction between PCy_3 , $\text{Ni}(\text{COD})_2$ and C_6F_6	294
Figure A3.83 Time course monitoring of the $^{31}\text{P}\{^1\text{H}\}$ NMR spectrum of the reaction between PCy_3 , $\text{Ni}(\text{COD})_2$ and C_6F_6	295
Figure A3.84 ^{19}F NMR spectrum of the reaction between PEt_3 , $\text{Ni}(\text{COD})_2$ and C_6F_6	296
Figure A3.85 Time course monitoring of the ^{19}F NMR spectrum of the reaction between PEt_3 , $\text{Ni}(\text{COD})_2$ and C_6F_6 in THF	297
Figure A3.86 $^{31}\text{P}\{^1\text{H}\}$ NMR spectrum of the reaction between PEt_3 , $\text{Ni}(\text{COD})_2$ and C_6F_6	298
Figure A3.87 Time course monitoring of the $^{31}\text{P}\{^1\text{H}\}$ NMR spectrum of the reaction between PEt_3 , $\text{Ni}(\text{COD})_2$ and C_6F_6	299
Figure A3.88 $^{31}\text{P}\{^1\text{H}\}$ NMR spectrum of the reaction of PEt_3 , $\text{Ni}(\text{COD})_2$, and C_6F_6	300
Figure A3.89 $^{19}\text{F}\{^1\text{H}\}$ NMR spectrum of the borylation reaction of 1,2-difluorobenzene	301
Figure A3.90 $^{19}\text{F}\{^1\text{H}\}$ NMR spectrum of the borylation reaction of 1,3-difluorobenzene.	302
Figure A3.91 $^{19}\text{F}\{^1\text{H}\}$ NMR spectrum of the borylation reaction of 1,4-difluorobenzene	303
Figure A3.92 $^{19}\text{F}\{^1\text{H}\}$ NMR spectrum of the borylation reaction of 1,2,4-trifluorobenzene	304
Figure A3.93 $^{19}\text{F}\{^1\text{H}\}$ NMR spectrum of the borylation reaction of 1,3,5-trifluorobenzene	305
Figure A3.94 GC trace of the borylation reaction of $\text{C}_6\text{H}_5\text{F}$	306
Figure A3.95 Mass spectrum of the $\text{C}_6\text{H}_5\text{Bpin}$ peak from the borylation reactions of $\text{C}_6\text{H}_5\text{F}$..	307

Appendix 4

Figure A4.1 ^1H NMR spectrum of $\text{PPh}(\text{6-BF}_3\text{-2-pyH})_2$ in $\text{DMSO-}d_6$	316
Figure A4.2 $^{31}\text{P}\{^1\text{H}\}$ NMR spectrum of $\text{PPh}(\text{6-BF}_3\text{-2-pyH})_2$ in $\text{DMSO-}d_6$	317
Figure A4.3 $^{19}\text{F}\{^1\text{H}\}$ NMR spectrum of $\text{PPh}(\text{6-BF}_3\text{-2-pyH})_2$ in $\text{DMSO-}d_6$	317

Figure A4.4 $^{11}\text{B}\{^1\text{H}\}$ spectrum of $\text{PPh}(6\text{-BF}_3\text{-2-pyH})_2$ in $\text{DMSO-}d_6$	318
Figure A4.5 Negative mode ESI-MS of $\text{PPh}(6\text{-BF}_3\text{-2-pyH})_2$ in MeCN	318
Figure A4.6 ^1H NMR spectrum of $\text{P}(6\text{-BF}_3\text{-2-pyH})_3$ in $\text{DMSO-}d_6$	319
Figure A4.7 $^{31}\text{P}\{^1\text{H}\}$ NMR spectrum of $\text{P}(6\text{-BF}_3\text{-2-pyH})_3$ in $\text{DMSO-}d_6$	319
Figure A4.8 $^{19}\text{F}\{^1\text{H}\}$ NMR spectrum of $\text{P}(6\text{-BF}_3\text{-2-pyH})_3$ in $\text{DMSO-}d_6$	320
Figure A4.9 $^{11}\text{B}\{^1\text{H}\}$ NMR of $\text{P}(6\text{-BF}_3\text{-2-pyH})_3$ in $\text{DMSO-}d_6$	320
Figure A4.10 Negative mode ESI-MS of $\text{P}(6\text{-BF}_3\text{-2-pyH})_3$ in MeCN	321
Figure A4.11 Aromatic region of the ^1H NMR spectrum of $[\text{P}(2\text{-py})_3\text{NiNO}][\text{BPh}_4]$	322
Figure A4.12 $^{31}\text{P}\{^1\text{H}\}$ NMR spectrum of $[\text{P}(2\text{-py})_3\text{NiNO}][\text{BPh}_4]$ in CD_2Cl_2	323
Figure A4.13 $^{11}\text{B}\{^1\text{H}\}$ NMR spectrum of $[\text{P}(2\text{-py})_3\text{NiNO}][\text{BPh}_4]$ in CD_2Cl_2	323
Figure A4.14 Cyclic voltammogram of $[\text{P}(2\text{-py})_3\text{NiNO}][\text{BPh}_4]$	324
Figure A4.15 Cyclic voltammogram of first reduction of $[\text{P}(2\text{-py})_3\text{NiNO}][\text{BPh}_4]$	325
Figure A4.16 IR spectrum of $[\text{P}(2\text{-py})_3\text{NiNO}][\text{BPh}_4]$ collected in a KBr pellet.	325
Figure A4.17 ^1H NMR spectrum of crude $\text{K}[2\text{-Br-4-BF}_2\text{CF}_3\text{-py}]$	326
Figure A4.18 $^{19}\text{F}\{^1\text{H}\}$ NMR spectrum of crude $\text{K}[2\text{-Br-4-BF}_2\text{CF}_3\text{-py}]$	327
Figure A4.19 $^{11}\text{B}\{^1\text{H}\}$ NMR spectrum of crude $\text{K}[2\text{-Br-4-BF}_2\text{CF}_3\text{-py}]$	327
Figure A4.20 ^1H NMR spectrum in CD_3CN of crystalline $\text{K}[2\text{-Br-4-BF}_2\text{CF}_3\text{-py}]$	328
Figure A4.21 $^{19}\text{F}\{^1\text{H}\}$ NMR spectrum in CD_3CN of crystalline $\text{K}[2\text{-Br-4-BF}_2\text{CF}_3\text{-py}]$	329
Figure A4.22 $^{11}\text{B}\{^1\text{H}\}$ NMR spectrum in CD_3CN of crystalline $\text{K}[2\text{-Br-4-BF}_2\text{CF}_3\text{-py}]$	329
Figure A4.23 $^{13}\text{C}\{^1\text{H}\}$ NMR spectrum in CD_3CN of crystalline $\text{K}[2\text{-Br-4-BF}_2\text{CF}_3\text{-py}]$	330
Figure A4.24 ^1H NMR spectrum of crude reaction with $\text{B}(\text{OMe})_2\text{CF}_3$ without dioxane	330
Figure A4.25 ^1H NMR spectrum of the crude $\text{K}[2\text{-Br-3-BF}_2\text{CF}_3\text{-py}]$	331
Figure A4.26 $^{19}\text{F}\{^1\text{H}\}$ NMR spectrum of the crude $\text{K}[2\text{-Br-3-BF}_2\text{CF}_3\text{-py}]$	332

Figure A4.27 $^{11}\text{B}\{^1\text{H}\}$ NMR spectrum of the crude $\text{K}[2\text{-Br-3-BF}_2\text{CF}_3\text{-py}]$	332
Figure A4.28 ^1H NMR spectrum of the crude $\text{K}[2\text{-Br-5-BF}_2\text{CF}_3\text{-py}]$	333
Figure A4.29 $^{19}\text{F}\{^1\text{H}\}$ NMR spectrum of the crude $\text{K}[2\text{-Br-5-BF}_2\text{CF}_3\text{-py}]$	334
Figure A4.30 $^{11}\text{B}\{^1\text{H}\}$ NMR spectrum of the crude $\text{K}[2\text{-Br-5-BF}_2\text{CF}_3\text{-py}]$	334
Figure A4.31 ^1H NMR spectrum of the crude reaction attempting to prepare $\text{K}[2\text{-Br-6-BF}_2\text{CF}_3\text{-py}]$	335
Figure A4.32 $^{19}\text{F}\{^1\text{H}\}$ NMR spectrum of the crude reaction attempting to prepare $\text{K}[2\text{-Br-6-BF}_2\text{CF}_3\text{-py}]$	336
Figure A4.33 $^{11}\text{B}\{^1\text{H}\}$ NMR spectrum of the crude reaction attempting to prepare $\text{K}[2\text{-Br-6-BF}_2\text{CF}_3\text{-py}]$	336
Figure A4.34 Coordinates of optimized geometry for PPy_3NiNO	338
Figure A4.35 Coordinates of optimized geometry for $\text{P}(6\text{-BF}_3\text{-2-py})_3\text{NiNO}$	339
Figure A4.36 Coordinates of optimized geometry for $\text{P}(5\text{-BF}_3\text{-2-py})_3\text{NiNO}$	341
Figure A4.37 Coordinates of optimized geometry for $\text{P}(4\text{-BF}_3\text{-2-py})_3\text{NiNO}$	343
Figure A4.38 Coordinates of optimized geometry for $\text{P}(3\text{-BF}_3\text{-2-py})_3\text{NiNO}$	345

List of Schemes

Chapter 2

Scheme 2.1 Synthetic routes to generate complexes **1-5** starting from the appropriate Tp ligand.
A: Co(MeCN)₆OTf₂, DCM, N₂, r.t., **B:** 1) 1.1 equivalents NaBAr^F₄ 2) 1.1 equivalents ^sPhIO_x, Et₂O,
N₂, r.t..... 34

Chapter 3

Scheme 3.1 Synthesis of **K1** and reactions to form [PPh₄][**1**^{Se}], **2**, and the proposed product of C-F oxidative addition by a Ni complex featuring **1**. 61

Appendix 1

Scheme A1.1 Two limiting resonance structures for metal-oxygen moieties and targeted pz₄lut ligand substitution at methine carbon 137

Scheme A1.2 Summary of the reactivity with deprotonated pz₄lut and electrophiles 138

List of Tables

Chapter 2

Table 2.1 Observed reaction rates and KIEs of 1 , 2 , and 3 ^[a]	38
--	----

Chapter 3

Table 3.1 Experimental (A.) and Computational (B.) J_{P-Se} Coupling Constants	72
---	----

Table 3.2 Selected optimization conditions for defluoroborylation of 1,3-difluorobenzene	79
---	----

Appendix 2

Table A2.1 Raw data and KIE values determined for the reactions of 1 , 2 , 3 , and ^s PhIO with a 250 mM 1:1 mixture of H ₄ -DHA:D ₄ -DHA in DCM.	211
--	-----

Table A2.2 KIE values determined for the reactions of 1 , 2 , 3 , and ^s PhIO with DHA.....	212
---	-----

Table A2.3 Raw GCMS data for the reactions of ^s PhIO in the presence of Lewis acids with DHA for KIE calculations	213
---	-----

Table A2.4 KIE values determined for the reactions of ^s PhIO with DHA in the presence of Lewis acids using a minimum detectable value of D ₂ -anthracene	214
---	-----

Table A2.5 Selected bond distances and angles for the Co complexes reported.	219
--	-----

Table A2.6 Crystal data and structure refinement for 1	220
--	-----

Table A2.7 Crystal data and structure refinement for 2	221
--	-----

Table A2.8 Crystal data and structure refinement for 3	222
--	-----

Table A2.9 Crystal data and structure refinement for 4	223
--	-----

Table A2.10 Crystal data and structure refinement for 5	224
---	-----

Table A2.11 Crystal data and structure refinement for 6	225
---	-----

Appendix 3

Table A3.1 Selected average bond lengths for SXRD structures.	257
Table A3.2 Refinement data for crystal structures of K1, 2, [PPh ₄][1 ^{Se}], [TEA][1 ^{Se}], and [PPh ₄][3 ^{Se}].	259
Table A3.3 Coordinates of optimized structure of 1 ^{Se} (cisoid structure).....	262
Table A3.4 Coordinates of calculated structure of edited 1 ^{Se} (transoid structure).....	263
Table A3.5 Calculated electric field and J_{P-Se} for calculated structures of 1 ^{Se}	263
Table A3.6 Coordinates of calculated structure of SePPh ₂ Et	265
Table A3.7 Coordinates of calculated structure of 2.....	266
Table A3.8 Coordinates of calculated structure of 1 ^{Se} with explicit MeCN solvation.	269
Table A3.9 Coordinates of calculated structure of 1 ^{Se} with explicit DCM solvation	272
Table A3.10 Coordinates of calculated structure of 1 ^{Se} with explicit CHCl ₃ solvation.....	275
Table A3.11 Additional data points added to Figure 3.2	282
Table A3.12 Phosphines used in the J_{P-Se} vs. TEP fit	283
Table A3.13 J_{P-Se} (Hz) for [PPh ₄][1 ^{Se}], [TEA][1 ^{Se}], [PPh ₄][3 ^{Se}], SePPh ₂ Et and SePPh ₃	285
Table A3.14 Fit parameters for the linear fits of J_{P-Se}	285
Table A3.15 J_{P-Se} (Hz) for [PPh ₄][1 ^{Se}] with the addition of various additional salts	286
Table A3.16 Summary of observed rates from NMR monitoring experiments.....	300
Table A3.17 Initial scan of additives for C-F borylation of 1,3 difluorobenzene.....	308
Table A3.18 Variation of reaction conditions with H ₂ O as an additive.....	309
Table A3.19 Variation of reaction conditions with alcohols as additives.....	310
Table A3.20 Variation of reaction conditions with MeOH as an additive.....	311
Table A3.21 Variation of reaction time with MeOH and CsOH additives and controls	312
Table A3.22 Variation of addition order and additives.....	313

Table A3.23 Variation of cations.	314
Table A3.24 Variation of reaction solvent.	315

Appendix 4

Table A4.1 Refinement data for crystal structures of K[2-Br-4-BF ₂ CF ₃ -py] and [P(2-py) ₃ NiNO][BPh ₄].	337
--	-----

List of Abbreviations

acac	Acetylacetonate
B ₂ cat ₂	Bis(catecholato)diboron
B ₂ nep ₂	Bis(neopentylglycolato)diboron
B ₂ pin ₂	Bis(pinacolato)diboron
BAr ^F ₄	Tetrakis(3,5-bis(trifluoromethyl)phenyl)borate
BDFE	Bond dissociation free energy
cm ⁻¹	Wavenumber
COD	1,5 cyclooctadiene
CPET	Concerted proton electron transfer
DCM	Dichloromethane
DFT	Density functional theory
DHA	9,10 dihydroanthracene
DMSO	Dimethylsulfoxide
E _{1/2}	Redox potential
EXAFS	Extended X-ray absorption fine structure
F _z	Electric field along the z axis
GCMS	Gas chromatography mass spectrometry
HAT	Hydrogen atom transfer
HOMO	Highest occupied molecular orbital
J _{P-Se}	Phosphorus selenium coupling constant
k ₂	Second order rate constant
KHMDS	Potassium hexamethyldisilazide
KIE	Kinetic isotope effect
k _{obs}	Observed rate
KSI	Ketosteroid isomerase
LFER	Linear free energy relationship
LUMO	Lowest unoccupied molecular orbital
MV/cm	Megavolt per centimeter
NHC	N-heterocyclic carbene
NMR	Nuclear magnetic resonance
NRVS	Nuclear resonance vibrational spectroscopy
OA	Oxidative addition
ORR	Oxygen reduction reaction
OTf	Trifluoromethanesulfonate
PhIO	Iodosylbenzene
pK _a	Acid strength
PPN	Bis(triphenylphosphine)iminium
PY5	Tetra(2-pyridyl)lutidine

pz ₄ lut	Tetra-pyrazolyl lutidine
^s PhIO	2-(tert-butylsulfonyl)phenyl iodosylbenzene
^s PhIO ₂	2-(tert-butylsulfonyl)phenyl iodoxybenzene
STM	Scanning tunneling microscopy
SXRD	Single crystal X-ray diffraction
TEA	Tetraethylammonium
TEP	Tolman electronic parameter
THF	Tetrahydrofuran
TMA	Trimethylammonium substituent
TMS	Trimethylsilyl
TOF	Turnover frequency
Tp	Tris-pyrazolyl borate
Tp ^{Ad,Me}	Tris-pyrazolyl borate with adamantyl and methyl substituted pyrazoles
Tpm	Tris-pyrazolyl methane
Tp ^{tBu}	Tris-pyrazolyl borate with tert-butyl substituted pyrazoles
TS	Transition state
TSS	Transition state stabilization
ϵ	Molar absorptivity in chapter 2 and dielectric constant in chapter 3
η	Overpotential
μ	Dipole
ν_{CO}	Carbonyl stretching frequency
ν_{NO}	Nitrosyl stretching frequency

Acknowledgments

I'm fortunate to have received a significant amount of academic and personal support and guidance throughout my degree.

First and foremost, I would like to thank my PhD advisor Professor John Anderson for the opportunity to carry out research in his lab and for his mentorship. Throughout numerous discussions over the years I have developed a much deeper understanding of chemistry and my project thanks to his teaching. John is always willing to take the time to discuss anything his students need help with. Ranging from detailed lab results to big picture research directions to professional development opportunities, John always has insightful advice. John truly cares about his students' success, and his mentorship has really helped me grow as a scientist and an individual.

I would like to acknowledge Professors Viresh Rawal and Mark Levin for their time and effort serving on my thesis committee, I really appreciate their detailed questions on my project.

The Anderson lab as a whole has provided me with a great environment to pursue research. I am grateful to all my lab mates who have helped me learn new techniques, made insightful suggestions and comments during group meetings, aided my research through their various group responsibilities, and otherwise supported my education and work. In particular, I would like to thank Professor Ethan Hill for his mentorship early in my degree. I learned a significant amount about air-free chemistry techniques, manuscript preparation and how to think carefully about my experiments and results from him. I would like to thank Dr. McKenna Goetz, who regularly helped me talk through scientific problems and provided me with guidance and friendship throughout the entire process. I would also like to thank Dr. Jorge Martinez for working with me on the electrostatics project over the last few years, our conversations have really helped me structure my

thinking about this field and make progress in synthesizing anionic pyridines. I would like to acknowledge Dr. Andrew McNeece for his initial work on the anionic phosphine described in Chapter 3, which proved to be a very interesting project for me to work on after his graduation. Overall, I have been very fortunate to make numerous strong friendships throughout my time in the Anderson lab, and I'm so happy to have been able to share lunches with McKenna, Ethan, Norman, Noah, Jorge and Pat at various points over the past few years. I always enjoyed our fun conversations, and they brightened my days!

I would like to thank the X-ray diffraction and nuclear magnetic resonance facility managers Dr. Alex Filatov and Dr. Josh Kurutz. The facility resources were crucial for my research, and they were always maintained in optimal condition.

I would like to acknowledge Smarthealth Catalyzer and Aspire Capital and the mentors I found through internships at those organizations. My work there expanded my scientific horizon to include biomedical topics, and the process of learning helped me further refine and build confidence in my scientific capabilities.

Additionally, I'm very fortunate to have many friends who made my time in Chicago enjoyable and helped me relax while away from work. I would like to thank my roommate Melanie, who first made Hyde Park feel like a home. I'm so grateful for my current roommates Hannah, Chris and Lawson, who have become like family over the past few years in Hyde Park. I love spending time with you all and we always have entertaining conversations. I would also like to thank Elizabeth, for being a great friend since our meeting at the first-year picnic. I am so grateful to have been a part of such a wonderful community of friends in the Chemistry department who all made wine and cheese gatherings, holiday parties, and many other events so much fun. Thank you

to my Chicago friends, Misha, Mayank, Rahul, Kim, and Kyle for helping me escape Hyde Park and explore the city from time to time.

I'm also so happy to have met my wonderful partner Tim while at the University. I want to thank Tim for his support over the past few years. You make all the difference by finding ways to make me laugh and helping me recognize my own accomplishments, even if they seem like small steps in the scheme of the long process towards this degree!

I want to thank my parents, Sarita and Lawrence, for encouraging me to study and value education while I was growing up. From them I learned how to tackle intimidating, but rewarding, challenges with courage and Lord of the Rings quotes. Thank you for your love and support throughout my degree, my visits home were always refreshing and your wisdom and advice was always helpful! Thank you also to my parents and brother Gus for your visits to Chicago, sharing the city with you made my home here seem all the more exciting.

Abstract

Metal oxygen multiply bonded intermediates mediate challenging C–H functionalization and O–O coupling reactions in enzymatic systems with impressive rates and selectivity. The preparation of synthetic metal complexes with comparable reactivity is appealing for the functionalization of fine chemicals and catalysis of the water oxidation half reaction in alternative energy schemes. Numerous model complexes featuring metal-oxo moieties have provided insight into the reactivity of these species in biological systems. However, these model systems show significantly attenuated reactivity compared to natural systems, mediating H-atom and O-atom transfer at much slower rates and infrequently resulting in O–O coupling reactivity. One notable distinction between natural systems and the model complexes are the ligand environments of the metal-oxo moieties. While model complexes typically employ strongly donating amide and carbene ligands, enzymes coordinate metal ions using weakly donating pyrrole, imidazole, and carboxylate ligands. In lieu of the wide variety of ligands available to synthetic systems, enzyme active sites are known to exert large electric fields on substrates, altering the energy of transition states and the properties of metalloenzymes. The involvement of electric field catalysis in enzymatic reactivity has motivated the study of electrostatic effects in molecular complexes featuring non-interacting charged functional groups. Inspired by these examples, this thesis details the use of weakly donating and charged ligands to target metal-oxo model complexes with unusual electronic structures. En route to these targeted complexes, the fundamental effects of charged groups on molecular properties, specifically donor strength, were also explored to provide additional context for the design of charged ligands.

In Chapter 2, an unusual series of discrete iodosyl- and iodoxyarene adducts of Co are isolated from the reaction between cobalt metalated tris-pyrazolyl borate complexes and the respective O-

atom transfer reagents. The formation of these adducts was confirmed by a suite of techniques including single crystal X-ray diffraction. These complexes represent the first crystallographically characterized examples of Co iodosylbenzene adducts and the first example of a crystallographically characterized transition metal iodoxybenzene adduct. The reactivity of these adducts with O-atom acceptors and an H-atom donor was investigated with particular focus on elucidating mechanistic details. Reactivity data are consistent with the involvement of a transient oxo complex in one case, while the two other systems appear to react with substrates directly as iodosyl- or iodoxyarene adducts. These results support that reactivity typically ascribed to metal-oxo complexes, such as O-atom transfer and C–H activation, can also be mediated by discrete transition metal iodosyl- or iodoxyarene adducts that are frequent intermediates in the generation of oxo complexes. The observation of adduct complexes suggest that the monoanionic tris-pyrazolyl borate ligand is not sufficiently donating to support high valent intermediates, although transient formation of an oxo may be possible in one case. These results motivated a deeper investigation of the effects of charged moieties on ligand donor strength in an effort to find systems that may better stabilize high-valent intermediates with weak donor ligands.

In Chapter 3, the synthesis of a novel anionic phosphine, $\text{PPh}_2\text{CH}_2\text{BF}_3\text{K}$, the corresponding tetraphenyl phosphonium and tetraethyl ammonium selenides $[\text{PPh}_4][\text{SePPh}_2\text{CH}_2\text{BF}_3]$ and $[\text{TEA}][\text{SePPh}_2\text{CH}_2\text{BF}_3]$, and the Rh carbonyl complex $[\text{PPh}_4][\text{Rh}(\text{acac})(\text{CO})(\text{PPh}_2(\text{CH}_2\text{BF}_3))]$ are reported. Solvent-dependent changes in the phosphorus selenium coupling constants ($J_{\text{P-Se}}$) of the selenides were fit using Coulomb's law. These data support that up to 80% of the increase in donor strength of $[\text{PPh}_4][\text{SePPh}_2\text{CH}_2\text{BF}_3]$ relative to SePPh_2Et is a result of electrostatic contributions from the anionic moiety. This $J_{\text{P-Se}}$ method was extended to $[\text{PPh}_4][\text{SePPh}_2(2\text{-BF}_3\text{Ph})]$ and likewise estimates up to a 70% electrostatic contribution to the increase in donor strength relative

to SePPh_3 despite the presence of an aryl linker. The use of $\text{PPh}_2\text{CH}_2\text{BF}_3\text{K}$ also accelerated C–F oxidative addition reactivity with $\text{Ni}(\text{COD})_2$ by an order of magnitude in comparison to the comparatively donating neutral phosphines PEt_3 and PCy_3 . This enhanced reactivity prompted the investigation of catalytic fluoroarene C–F borylation, with improved yields observed for less fluorinated arenes. These results demonstrated that covalently bound charged functionalities can exert a significant electrostatic influence under common solution phase reaction conditions. This lends support to the idea that electrostatic effects in charged ligands can be leveraged to stabilize high oxidation states with traditionally weakly donating ligands.

In Chapter 4, the synthetic approaches to tri-anionic weakly donating tris-pyridyl ligands are outlined. The overall charge on the ligand is anticipated to provide additional stabilization for a high valent metal in comparison to the tris-pyrazolyl borate system. The multiple carbon positions on the pyridine ring offer the opportunity to vary the location of the charge across a series of ligands. Preliminary work on the preparation of these ligands using the trifluoroborate substituted pyridine result in low yields. The preparation of a novel BF_2CF_3^- anion to increase the solubility is reported. Future studies with these new ligands will initially be directed at characterizing the donor strength through metalation with Ni-NO and measurement of the nitrosyl stretching frequency. The impact of charge location on the nitrosyl stretching frequency is expected to provide insight on the electric field environment at the metal center. Correlations between the location of a charge and the applied electric field will enable the rational synthesis of molecular systems incorporating electrostatic effects and inform the analysis of future studies with metal-oxo compounds using these ligands.

Appendix 1 details the synthesis of pentadentate anionic ligands based on the tetra-pyrazolyl lutidine ligand. The incorporation of trifluoroborate moiety into a distal methine position was

ultimately inhibited by the instability of the carbanion with two adjacent pyrazoles, which are observed to undergo ring opening in one example. The substitution with sulfonate at the methine position is observed, however metalation of the ligand with first row transition metals displays competitive coordination to the sulfonate moiety.

Appendices 2-4 contain supporting data for Chapter 2-4.

Preface

All chapters have an independent compound numbering system. Characterization spectra are provided in the corresponding appendix for each chapter.

Chapter 1: Introduction

1.1 Externally Applied Electric Field Catalysis

1.1.1 Introduction to Electric Field Catalysis

The incorporation of electric fields into catalytic systems is a promising strategy to accelerate reactions and dictate selectivity across multiple fields of catalysis. In these systems, correctly oriented electric fields can lower transition state barriers as well as alter catalyst properties. Originally proposed as a primary contributor to enzymatic catalysis, electric field effects have since been incorporated into various heterogeneous and molecular systems. While the exact method of applying an electric field varies from enzymatic to heterogeneous and molecular systems, the general conceptual rationale for these effects remains relatively consistent. As described by Coulomb's law below, a test charge q_1 will experience a vector force \mathbf{F}_1 as a result of electric fields generated by nearby charges

$$\mathbf{F}_1 = \sum_j \frac{1}{4\pi\epsilon_0} \frac{q_j}{r_{1j}^2} \mathbf{e}_{1j}$$

where $1/4\pi\epsilon_0$ is the electric force constant, q_j is the sum of nearby charges, r_{1j}^2 is the distance and \mathbf{e}_{1j} is the unit vector between the points.^{1,2} This force generates an electrostatic potential energy between the charges, which can be converted into kinetic energy and the movement of q_1 according to the respective charge signs. Analogous behavior is observed in the case of partial charges, such as dipoles (μ) and polar bonds. As the majority of reactions require the movement of electron density and have transition state charge distributions that are distinct from the reactant state, electric fields favoring the transition state dipole will lower the transition state energy and accelerate the reaction.³ The transition state stabilization (TSS) effected by electric fields has also

been described in terms of the re-ordering and mixing of molecular orbitals, as well as in terms of field-induced bond ionicity in valence bond theory and in thermodynamic free energy reaction coordinates.^{1,4,5,6} While different interpretations can be suited to particular systems or computational methods, a general conclusion of electric field catalysis is that an electric field aligned with the change in dipole moment over the course of a reaction will lower the energy of the transition state.^{1,7,8}

$$\Delta\Delta G^\ddagger = F_1\Delta\mu$$

Likewise, selectivity between different reaction pathways can be accessed using electric fields when the dipoles of each transition state are differentially stabilized in the electric field.⁸ In addition to TSS effects, electric fields can change fundamental properties of a catalyst itself, influencing both the thermodynamics and mechanisms of reactions. These properties include the electronic configuration i.e. orbital population and ordering, redox potential ($E_{1/2}$) and bond dissociation free energy (BDFE), among other properties.^{9,10} Given the generality of the explanation above, the first part of this introduction provides specific examples how externally applied electric fields affect catalysis. Following that, the second section provides examples of how the concept of electric field catalysis has been applied to molecular systems via the incorporation of charged moieties. The examples provided in the first and second section are meant to illustrate common themes in electric field catalysis and are not exhaustive. Additionally, multiple sign conventions exist to report electric field strengths.¹ In this introduction, electric fields will be reported as positive values by default unless, within an example, there is an electric field applied in the opposite direction as well, in which case both positive and negative signs will be included. Finally, the third section explores the motivation for studying molecular metal oxo

complexes and how the presence of negatively charged functional groups may alter their electronic structure and reactivity.

1.1.2 Electric Field Effects in Enzymatic Catalysis

Electrostatic TSS within enzyme active sites was first proposed as the dominant contributor to enzymatic catalysis in the 1970's by Warshel and coworkers.^{11,12} Quantitative calculations compared the reaction barriers for hydrolysis reactions in the lysozyme enzyme and in water. The ~7 kcal/mol difference in transition state energies, accounting for a rate difference of 10^6 , was almost entirely accounted for by electrostatic stabilization of the carbocation intermediate by adjacent anionic Glu and Asp residues. The positioning of these charges within a hydrophobic enzyme superstructure was necessary to maximize the electrostatic stabilization, as the analogous configuration in water results in attenuation of the charges by the multiple solvation layers. The enzyme active site is electrostatically pre-organized to support the dipole of the transition state, thereby removing the solvent reorganization energy penalty present in bulk solution. Calculations comparing the free energy of a variety of reactions in water and within enzyme active sites demonstrate that electrostatic catalysis is a generally applicable concept in enzymatic catalysis.⁴

Experimental quantification of enzymatic electric fields was provided by Boxer and coworkers in the early 2000's using the vibrational Stark effect.⁷ IR and Raman spectroscopies probe the energy difference between the ground and first excited vibrational states of molecules. In the case of polar diatoms, the first excited state has a larger dipole moment than the ground state, resulting in a larger response to an applied field.¹³ The change in the frequency of a specific vibration (cm^{-1}) with an applied electric field (MV/cm) relates linearly to the magnitude of the field, giving the Stark tuning rate for that vibration ($\text{cm}^{-1}/(\text{MV}/\text{cm})$). Vibrations which are predominantly decoupled from the rest of a molecule, such as CO or CN, report on the electric field in their

environment by comparison to their Stark tuning rates. This technique was used to measure the electric field within ketosteroid isomerase (KSI), one of the most rapid enzymes known with a k_{cat}/K_m for a C=C isomerization approaching the diffusion limit.¹⁴ The carbonyl stretch (ν_{CO}) of a substrate-like inhibitor within the active site

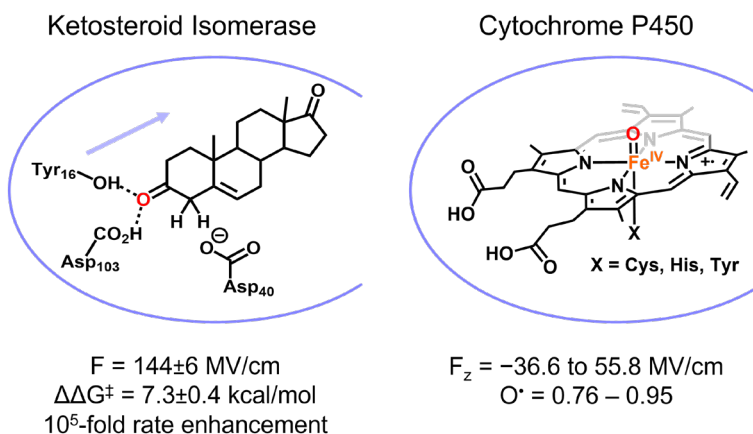


Figure 1.1 Simplified depiction of the active site in ketosteroid isomerase and the electric field effects determined by Boxer and coworkers in reference 13 (left). Simplified depiction of the active oxidant in cytochrome p450 enzymes and the electric fields predicted computationally by Alexandrova and coworkers in reference 10 and the predicted O centered spin density (right).

indicated that KSI applied an extremely large field of 144 MV/cm (Figure 1.1). Mutagenesis experiments demonstrated that reductions in the applied electric field linearly correlate with changes in k_{cat} and the free energy barrier.^{14,15} The electric field contribution to the TSS was estimated at 7.3 kcal/mol, consistent with a rate enhancement of 10^5 and accounting for 70% of the total enhancement relative to the reaction in water. Notably, the ν_{CO} was much narrower than the same stretch observed in water, and nitrile stretches in the areas surrounding the active site indicated a significantly weaker electric field. Together, these highlight the extremely precise nature of the fields applied within enzyme active sites. Analogous Stark effect studies have identified electric fields within enzyme active sites ranging from 20 to 144 MV/cm.¹³

Although less commonly explored, electric field effects have likewise been predicted in metalloenzymes.^{10,16} Recent computational work by the Alexandrova group estimates electric fields ranging from 55.8 MV/cm to -36.6 MV/cm within iron-heme active sites across 200 distinct

cytochrome p450 enzymes (Figure 1.1).¹⁰ These enzymes are responsible for a variety of oxidation reactions involved in metabolism, most notably the hydroxylation of challenging C–H bonds, and proceed through the formation of a high valent Fe^{IV}–oxo intermediates which mediate hydrogen atom transfer (HAT) reactions. The electric fields in the active site were found to be greatest along the Fe–O bond axis (F_z), and the magnitude correlated with protein function. Rather than calculating the dipole of the transition state, the report focused on the changes effected by the electric field on the active oxidant. The largest average electric fields ($F_{z \text{ avg}} = 28.5 \text{ MV/cm}$) were observed in the Cys ligated heme centers responsible for the most challenging C–H oxidations. The average electric fields in the less reactive Tyr and His ligated heme centers were 3.0 MV/cm and -8.7 MV/cm, respectively. Larger positive electric fields are proposed to increase spin density on the oxygen atom, resulting in a more electrophilic oxidant. Additionally, the O–H BDFE of the resulting Fe^{IV}–OH is likewise sensitive to the electric field, ranging from 97 kcal/mol in Cys ligated hemes to 94 kcal/mol and 88 kcal/mol for His and Tyr ligated heme centers, respectively. The rate of HAT in metal oxo systems is frequently determined by the difference in BDFE of the initial C–H bond and the resulting O–H bond, indicating that the electric fields in cytochrome p450 enzymes alter the rate of HAT reactivity.¹⁷ This work demonstrates how catalyst properties such as $E_{1/2}$, pK_a , and spin density are sensitive to externally applied electric fields and can alter the rate and selectivity of enzymatic reactions.

Finally, a key consideration is the origin of electric fields within enzyme active sites. Generally, the electric field can be separated into contributions from the immediate coordination sphere of the active site and contributions from the remaining protein structure.^{18,19} Originally, Warshel and Boxer both considered the sum of a wide range of interactions to be electrostatic in origin, including carboxylate anions directly adjacent to the substrate and H-bonding interactions.^{4,13}

Typical contributors also include charged and polar residues and occasionally charged ions such as Ca^{2+} or Zn^{2+} .^{4,9} The relative contributions of the immediate coordination sphere in comparison to the overall protein structure is challenging to quantify. Stark effect studies with KSI demonstrated that up to 60 MV/cm of applied field remained even upon mutation of prominent residues in the active site.¹⁴ Likewise, calculations from the Head-Gordon group predict a 28% contribution from the protein scaffold to the total electric field within the KSI active site.^{19,20} In modeling cytochrome p450 enzymes, Alexandrova and coworkers only considered contributions to the electric field from the overall protein structure, excluding any active site contributions.¹⁰ While synthetic chemists may hesitate to consider H-bonding interactions in the active site as electrostatic in nature, the contributions to the electric field from the overall protein structure unequivocally highlight that electric fields contribute to rate acceleration within active sites and warrant further exploration in synthetic systems.

1.1.3 Externally Applied Electric Field Catalysis

In addition to the substantial work identifying electric fields in enzymatic systems, electric field catalysis has also been observed in a wide range of synthetic systems.⁶ Heterogeneous reaction set-ups involving capacitors are conducive to exploring electric field effects as a potential can be applied at the surface without competing electron transfer reactivity.²¹ The Kanan group has explored the influence of electric fields on selectivity in epoxide rearrangement⁸ and cyclopropanation reactions in parallel plate capacitors.²² In the former, Al_2O_3 deposited on silica electrodes catalyzed the rearrangement of *cis*-stilbene oxide to a mixture of two products (Figure 1.2). Application of an electric field altered the selectivity from a 1:3.7 product ratio in CH_2Cl_2 with no applied field to a ratio of 16.9:1 at 5 V and a ratio of 11.3:1 at -4.5 V. The selectivity difference between 0 V and 5 V corresponds to a 2.5 kcal/mol change in the transition state

energies, likely favoring the transition state with a larger dipole. Notably, the selectivity change was approximately the same with both positive and negative applied fields, as the substrate in solution was free to reorient within the field.

This experiment highlights the utility of electric fields in altering selectivity between different reaction pathways. However, it also demonstrates how control over selectivity will be limited unless the orientation of the electric field is fixed relative to the substrates.

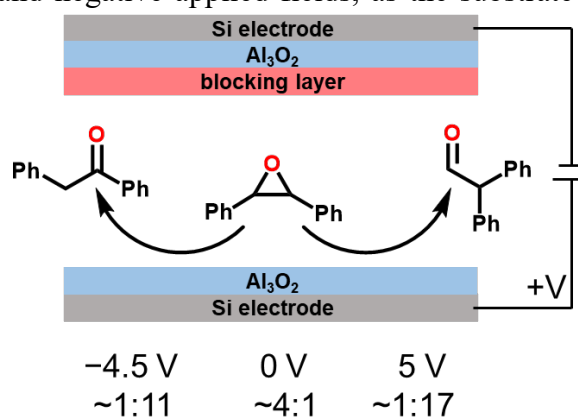


Figure 1.2 Simplified diagram of the parallel plate capacitor and product selectivity changes with applied field reported by the Kanan group.

Another elegant approach to demonstrating electric field effects on molecular reactivity is the use of scanning tunneling microscopy (STM) techniques to apply precise fields.^{3,23-25} In experiments by Coote and coworkers, a Diels-Alder reaction was accelerated in the presence of an

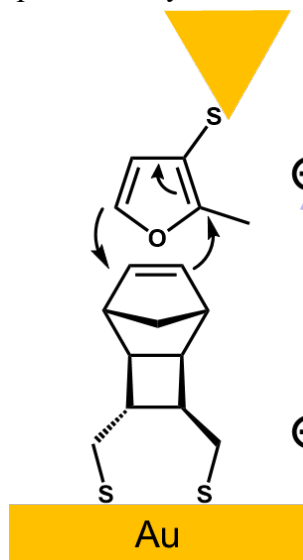


Figure 1.3 Simplified diagram of the Diels-Alder reaction within an STM set-up reported by the Coote group.

electric field applied using the STM set up (Figure 1.3).³ To carry out these break-junction experiments, the diene was first attached to the gold tip via sulfur linkages and the dienophile was attached to the gold surface. The gold tip was moved across the gold surface at a distance allowing for reactivity but inhibiting electron transfer (~1 nm). When a Diels-Alder reaction occurred between the two substrates, a temporary increase in conductance was observed between the tip and surface due to the molecular linkage. When the tip continued across the surface, the junction was broken and the current returned to zero, with the overall change in current referred to as a blinking event. Changing the applied field from -0.05 V to -0.75

V resulted in a 5x increase in the blinking frequency, consistent with acceleration of the Diels-Alder reaction. Notably, minimal change in the blinking frequency was observed when a field was applied in the opposite direction, reiterating the determining role of orientation in electric field catalysis.

1.2 Electrostatics in Coordination Chemistry

1.2.1 Introduction and Motivation

The examples surveyed above demonstrate how electric fields can significantly influence catalytic rates and selectivity through stabilization of the transition state dipole and modification of the catalyst electronic properties. As the majority of chemical reactions include a change in dipole, electric field catalysis should in principle be widely applicable. Despite the versatility of this technique, there remain significant challenges to rationally incorporating these effects into catalytic systems. A primary challenge is synthetic, as methods for rationally controlling the orientation and magnitude of electric fields are limited. The scalability of the STM and parallel plate systems in the previous section likewise presents an obstacle. Finally, predicting the effects of electric fields is challenging, particularly in reactions with multiple steps or unknown/complicated mechanisms. Given these considerations, the exploration of electric field effects in molecular systems is an area of current interest, as molecular catalysts are both scalable and tunable. Regarding control over the electric field, charged functional groups within a rigid molecular catalyst should exert an electric field on their surroundings, ensuring that every catalytic center experiences a similar electric field within the limit of molecular motions. Repositioning the functional group(s) should also afford the opportunity to invert selectivity, unlike the Kanan example, or effect opposite changes on catalyst structure, such as the oxyl intermediates in p450

detailed by Alexandrova.^{8,10} In addition, significant work over the past few decades on the synthesis of zwitterionic complexes has provided the groundwork for the synthesis of charged complexes.^{26,27}

While there are many potential advantages to applying the concepts of electric field catalysis to molecular systems, there remains much to be determined regarding the exact implementation and interpretation of these effects. For example, the accuracy of interpreting electrostatic effects from *intramolecular* charges analogously to an *externally applied* electric fields such as those in a parallel plate capacitor has not been clearly established. Accordingly, the stabilization of transition states via a stable oriented intramolecular electric field has not been clearly demonstrated in molecular systems, although transition state stabilization by an adjacent charge has been proposed in a few examples.^{28,29} Assuming an orientation dependence can be observed in synthetic systems, the synthesis of molecules with correctly aligned electric fields resulting from correctly positioned charges will likely require the development of new synthetic design principles. Additionally, assigning changes in electronic structure and reactivity in charged molecular systems to electrostatic rather than inductive contributions is challenging as the charges are covalently bound to the complex of interest. The terminology in this field is fairly ambiguous as the differences, if any, between electric field, electrostatic, and charge effects have not been defined. Likewise, the units of applied electric field tend to vary between different applications, with MV/cm favored in enzymatic systems and mV or mV/Å favored in molecular systems. While there remain open questions and certain concepts in the field remain ill-defined, many recent examples of complexes incorporating distally charged functional groups have begun to address these gaps in knowledge.

In the following sections, progress towards characterizing the contribution of electrostatic effects on reactivity and catalyst properties in molecular complexes will be summarized. While there are multiple insightful reports of electrostatic effects in organic reactions and compounds, this introduction will focus on studies carried out with inorganic complexes of greater relevance to this thesis.^{30,31,32} Electrostatic interactions between a charged catalyst and an oppositely charged substrate have also been used to direct selectivity through positioning enforced by ion pairing.^{33,34} These examples have not been included below as the influence of the charges on the electronic aspects of the reaction

coordinate and catalyst are not described, and instead the selectivity determination is more akin to steric arguments.

Additionally, while there are multiple studies on the redox potentials, basicity and reactivity of charged porphyrins in

aqueous media, they have not been included due to the anticipated quenching of

electrostatic effects in aqueous solution.^{35,36} The examples described below describe systems in which the electrostatic effects of distally charged moieties in the ligand on the electronic structure and reactivity of a metal center were explicitly analyzed. Examples of metal complexes with charged ligands in which electrostatic effects were not addressed have not been included for

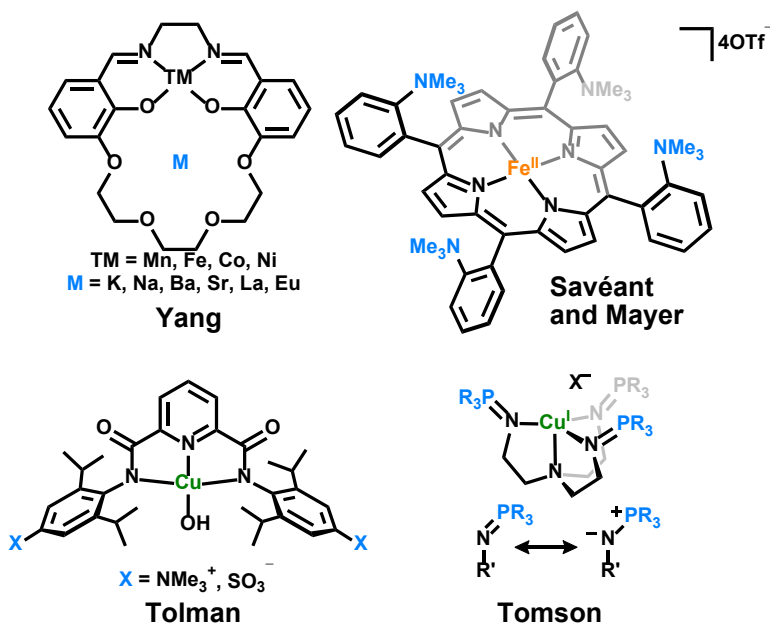


Figure 1.4 Complexes described in the “electrostatics in coordination chemistry” section with the charged moieties depicted in blue, and the research groups investigating each compound listed underneath.

simplicity, although they may still offer insight. Finally, the included examples are all experimental, and exclusively computational work has not been described although it is relevant to the field.^{37,38}

1.2.2 Charged Crown Ether Complexes

Metal complexes containing alkali metal encapsulating crown ether moieties have been studied by multiple groups over the past 4 decades.³⁹ Recently, the Yang group has developed a series of complexes with a crown ether substituted salen ligand and investigated how the alkali metal charge affects the reactivity and electronic structure from an electrostatic perspective (Figure 1.4). The salen has been metalated with Fe^{III}, Mn^V, Co^{II} and Ni^{II} with a varying series of alkali metals in the crown ether, including Na⁺, K⁺, Ca²⁺, Ba²⁺, Sr²⁺, La³⁺ and Eu³⁺ ions.⁴⁰⁻⁴⁴ Coulomb's law predicts electric fields in the Co series from the adjacent cations of 110 and 120 mV for K⁺ and Na⁺, and twice that with the dications Ba²⁺, Sr²⁺, and Ca²⁺ (210, 220 and 230 mV).⁴⁰ With all transition metals a large dependence is found between the redox potential and the charge of the adjacent cation, with typical changes on the order of 100-200 of mV/change in unit charge (Co^{II/I}, Mn^{VI/V}, Ni^{II/I}). The observed change is slightly larger for the Fe^{II/III} couple, which increases by 440 mV with K⁺ and 640 with Ba²⁺ relative to the neutral salen.⁴¹ Surprisingly, a related compound with a methylene linker between the Na⁺ crown ether and a pyridine di-imine core results in a much smaller influence on the redox potential (~50 mV).⁴⁵ The incorporation of alkali metal cations into the crown ethers appears to minimally alter the electronic absorption spectra across the series of transition metal compounds. In the case of Ni^{II}, DFT calculations predicted that the adjacent cation uniformly lowers the valence orbitals without prompting any reordering.⁴³

The reactivity of the Mn^V nitride (Mn^VN) and the Fe^{III}Cl crown ether substituted salen compounds is of particular interest as the trends are distinct from those observed with inductive

ligand modification.^{41,42} In the case of Fe^{III}Cl, both the K⁺ and Ba⁺ compounds catalyze the oxidation of cyclohexene to cyclohexanol and cyclohexanone with turnover numbers of ~17 and 46, respectively.⁴¹ Previously reported studies with neutral salen ligands demonstrated a strong correlation between the Fe^{III/II} redox potential with catalytic activity. However, in the crown ether examples oxidation reactivity is observed even though the redox potentials are 300-400 mV lower than those needed in neutral salen systems. Additionally, the repulsion between the cations inhibits the formation of a μ -oxo decomposition product. In the case of the Mn^VN with Na⁺, K⁺, Ba²⁺ and Sr²⁺ in the crown ether, the rate of bimolecular coupling upon oxidation to form N₂ was found to vary inversely with redox potential.⁴² Specifically, the more oxidizing nitrides (Ba²⁺ and Sr²⁺) reacted more slowly, counter to the expected linear free energy relationship, as a result of electrostatic repulsion between the complexes. These observed reactivity trends demonstrate how charged moieties can enhance reactivity in comparison to traditional electron withdrawing and donating functional groups.

Recently, the influence of alkali metals on HAT reactivity was explored with the Mn^{VI}N complex by examining the range in the E_{1/2} and pK_a, which can be used to determine the N-H BDFE of the resulting Mn^VNH complex.⁴⁴ The redox potentials for the Mn^{V/VI}N couple with the neutral salen and with Na⁺, K⁺, Ba²⁺, Sr²⁺, La³⁺, and Eu³⁺ in the crown ether varied across ~700 mV, with higher potentials required to oxidize the complexes with greater positive charge. The pK_a of the corresponding protonated [Mn^VNH]⁺ nitride was estimated to range by 9 units across the series, with higher alkali metal charges leading to less basic amides. Despite the dramatic changes in redox potential and pK_a, relatively similar BDFE values for the resulting HAT product were determined, suggesting the changes approximately balance out. Although the spread in BDFE spans ~8 kcal/mol, the error on the values is ~3 kcal/mol and they are mostly all within similar

ranges. This result implies that charged moieties may alter the transition state structure for the HAT reactions more than the thermodynamics, consistent with the asynchronous reactivity trends recently demonstrated in Co-oxo mediated HAT reactions, suggesting alternative means of determining selectivity may be accessible using electrostatic effects.⁴⁶

1.2.3 Charged Porphyrin Complexes

Cationic porphyrin complexes are among the best molecular electrocatalysts for small molecule reduction reactions. Savéant et al. investigated CO₂ reduction by Fe⁰ in a tetraphenyl porphyrin ligand with trimethylammonium moieties at either the ortho (*o*-TMA) or para (*p*-TMA) phenyl positions, as well as a version with para sulfonate groups (*p*-SO₃) (Figure 1.4).⁴⁷ The CO₂ reduction overpotential (η) and turnover frequency (TOF) with the charged porphyrins deviated from the expected linear free energy relationship (LFER) determined using a series of porphyrins modified inductively through fluorination of the phenyls.⁴⁸ In particular, the cationic complexes exhibited higher rates of CO₂ reduction than would be predicted by the LFER given the onset potential, and the *o*-TMA has a significantly lower overpotential and higher rates than the *p*-TMA. In contrast, the anionic complexes exhibited lower rates than would be expected from the LFER. Initially, the observation that less reducing cationic compounds show enhanced reductive reactivity is counterintuitive. However, the Nocera group observed a similar trend between charge and reactivity in a hangman porphyrin with anionic carboxylates in the primary coordination sphere.⁴⁹ The Fe metalated anionic porphyrin likewise displayed reduced reactivity in comparison to neutral ligands. Additionally, there are multiple other examples of enhanced electrocatalytic CO₂ reduction reactivity through the incorporation of positively charged functional groups in the ligand framework.^{50,51,52} These results suggest that the reduction potential is not the most important factor for accelerating CO₂ reduction reaction. Instead, the cationic TMA moieties were proposed by

Savéant to favor the formation of the reduced Fe-CO₂^{•-} intermediate *via* electrostatic stabilization. Computational investigations by Mayer and coworkers suggest that the Fe-CO₂^{•-} adduct develops significant negative charge on the oxygen, which then is stabilized by the adjacent cations.⁵³ Importantly, they also identified that four distinct atropisomers of the *o*-TMA porphyrin were present in the electrochemical studies by Savéant.⁵⁴ The distinct atropisomers enabled them to investigate the orientation dependence of electrostatic effects in molecular systems, as in each case the exact arrangement of *o*-TMA moieties is distinct. Overall, the difference in the Fe^{II/I} and Fe^{I/0} redox potentials between the distinct atropisomers varies by less than 50 mV, while the difference from neutral porphyrin is on the order of 400 mV.⁵⁴ Additionally, the TOF for CO₂ reduction mediated by the different atropisomers showed very little variation ($\log(\text{TOF}_{\text{max}}/\text{s}^{-1}) = 4.6\text{-}5.3$) despite the distinct field orientations at Fe.⁵⁵ These studies demonstrated again that charged moieties can lead to useful reactivity trends outside the bounds set by inductive LFER. However, they also challenged the assumption that electric fields generated by intramolecular charges lead to similar orientation dependent field effects as those observed in heterogeneous and enzymatic systems. Instead, the charge density is proposed as a more significant factor in determining reactivity than the exact location of the charge above or below the Fe plane. These extremely interesting set of studies underscore several of the challenges associated with interpreting electrostatic effects in solution, and motivate well-defined studies aimed at disentangling these effects.

An additional complication with interpreting electrostatic effects in molecular systems is the propensity for multi-step reactions, in which case each step will be differentially affected by an

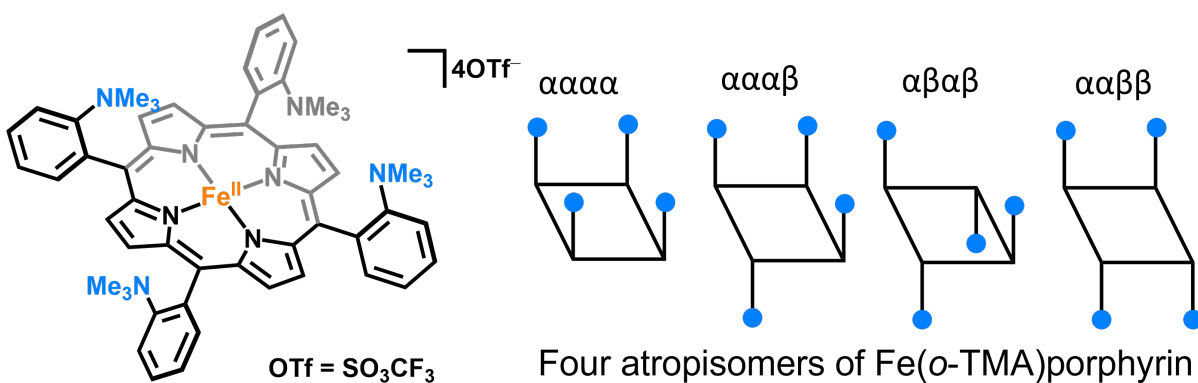


Figure 1.5 Tetra-cationic porphyrin complex explored in the electrocatalytic reduction of CO₂ and O₂ and simplified representations of the distinct atropisomers resulting from restricted rotation around the Ph-C_{por} bond (por = porphyrin). The blue circles correspond to the tri-methylammonium groups.

adjacent charge. In the case of CO₂ reduction, the prediction that electrostatic effects will stabilize the reduced CO₂^{•-} was supported computationally. However, since then, additional investigations into the mechanism by Mayer and coworkers suggest that the mechanism is more complicated than initially thought, involving an electron transfer and chemical step prior to the true catalytic onset.⁵⁵ The tetra-cationic *o*-TMA substituted iron porphyrin complex is also among the best O₂ reduction reaction (ORR) molecular electrocatalysts, although for distinct mechanistic reasons. Although conceptually the reduction of O₂ by Fe^{III} to generate an Fe^{II}-OO^{•-} is similar to the initial CO₂ reduction step, the accumulation of negative charge on the oxygen is 10x less than in CO₂, and the resulting electrostatic interaction is much weaker.⁵³ Instead, the cationic groups facilitate acetate coordination, which shifts the Fe^{III} reduction potential cathodically and results in a more reducing compound. The acetate bound compound reacts with O₂, while the initial complex without acetate shows no reactivity towards O₂. The rate of acetate binding was found to be sensitive to the concentration of electrolyte in solution, supporting that the enhanced binding is electrostatic in nature and can be quenched with additional ion pairing interactions. The disparate means of

electrostatic catalysis between the two reduction reactions demonstrates that care must be taken in assigning the origin of catalysis to electrostatic interactions.

1.2.4 Additional Complexes Incorporating Electrostatic Effects

The electronic structure and reactivity of a series of $[\text{Cu}^{\text{II}}\text{-OH}]$ complexes with negatively (SO_3^- , SO_3^-L) or positively (NMe_3^+ , NMe_3^+L) substituted pyridine carboxamide ligands was evaluated by the Tolman lab and compared to a neutral ligand congener (L) (Figure 1.4).⁵⁶ The distal charges had little effect on the electronic structure of the $[\text{Cu}^{\text{II}}\text{-OH}]$ core, as UV-vis and EPR spectra of the complexes were similar. However, the charges significantly altered the $\text{Cu}^{\text{II/III}}$ oxidation potential, with the $E_{1/2}$ increasing anodically with the overall charge of the complex in the order $\text{SO}_3^-\text{L} < \text{L} < \text{NMe}_3^+\text{L}$, spanning approximately 300 mV in applied potential. The increase in oxidation potential to more positive values with increasing cationic charge on the molecule is consistent with observations in the crown ether examples from the Yang group, and supports that the effect of anionic charges on redox potential is consistent with this trend.⁴² In the presence of additional alkali metal salts the oxidation potential of the $[\text{Cu}^{\text{II}}\text{-OH}]$ with SO_3^-L shifted to more positive potentials, consistent with increased shielding of the charge and quenching of the electrostatic effects. The O-H BDFE in the products resulting from HAT reactions, $[\text{Cu}^{\text{II}}\text{-OH}_2]^+$, was found to vary only slightly between SO_3^-L and NMe_3^+L (91 vs. 91.5 kcal/mol), suggesting a change in the $\text{p}K_a$ compensates for the change in redox potential. A similar compensation between redox potential and $\text{p}K_a$ was observed with the N-H BDFE of $\text{Mn}^{\text{V}}\text{N}$ complexes in the crown ether appended salen complexes with alkali metals of different charges from the Yang group.⁴⁴ Despite similar O-H BDFE values, the $[\text{Cu}^{\text{II}}\text{-OH}]$ with SO_3^-L ligand was found to react up to 150x more rapidly with dihydroanthracene than the NMe_3^+L complex, although steric hinderance with the counterions likely contributes to the distinct reactivity. While this example demonstrates that anionic charges can

also exert electrostatic influences on $E_{1/2}$ and reaction rates, the sulfonate anion is not ideal for such studies as it can coordinate to Cu and is more easily quenched in the presence of excess ions than TMA. The development of a more a more rigorously non-coordinating anion would be beneficial for expanding the study of anion effects. Additionally, this example demonstrates how electrostatic effects on mechanism can be difficult to separate from other influences, such as the presence of bulky counterions.

A few additional examples of electrostatic effects in molecular systems will be described briefly. The Tompson group demonstrated in a Cu^{I} metalated phosphinimine tren complex (Figure 1.4) that partial positive charge on the phosphines preferentially stabilizes the a_1 frontier molecular orbital in comparison to complexes with neutral tren ligands, altering the identity of the highest occupied molecular orbital (HOMO).⁵⁷ The Lavallo group determined that the use of an anionic carborane substituted phosphine leads to enhanced Pd mediated oxidative addition of aryl chlorides relative to a neutral carborane containing analogue.⁵⁸ The increased reactivity is attributed to dissociation of the ligand due to electrostatic repulsion in the resting bis-ligated complex, furnishing a more reactive mono-ligated Pd complex. The Kanan group demonstrated that electrostatic interactions between ion pairs can stabilize polar transition states during Au(I) catalyzed reactions.^{28,29} In these examples, counterions with higher charge density in low polarity solvent most effectively stabilize polar transition states to afford selectivity between two distinct products. Examples of electrostatic effects relating to metal-oxygen chemistry will be discussed in the next section.

1.2.5 Conclusions

While the field of molecular electrostatics is relatively young and most studies thus far have only examined the influence of adjacent cations, general conclusions regarding the impact of charged

functional groups are beginning to form. In every example considered, the redox potential is sensitive to the presence of adjacent charges. Specifically, more positive charges result in anodic shifts of a given redox couple in comparison to congeners with neutral ligands.⁹ The influence of electrostatic effects on molecular orbitals remains more unclear. In certain cases the presence of charged moieties uniformly lowers the energy of the orbitals,⁴³ while in others the charges exert a more selective impact on specific orbitals and cause reordering.⁵⁷ In systems with HAT reactivity, the presence of variably charged moieties has been observed to minimally alter the resulting E-H (E=N,O) BDFE.^{44,56} This is despite significant changes in redox potential and pK_a , implying there may be significant differences in the transition state of these complexes, as is suggested in the asynchronous concerted proton-electron transfer (CPET) literature.⁴⁶ Additionally, in multiple examples the incorporation of charged functional groups leads to reactivity that is not well-described by LFER's determined using neutral ligands.^{42,47,56} The incorporation of charged functional groups can therefore serve as an orthogonal approach to modifying reactivity in conjunction with neutral modification. Despite these general trends, there remain many open questions. For example, separating electrostatic contributions from inductive effects is challenging in molecular systems where the charge is incorporated directly into the ligand. In general, properties that can be described by equations such as Coulomb's law or the Debye length have been considered electrostatic in origin.^{40,53} The dependence of an experimental property, such as $E_{1/2}$ or the rate of association, on the ionic strength or dielectric constant of the solvent is also considered to indicate an electrostatic origin.^{53,56} Overall, the actual similarities between externally applied electric fields and intramolecular electric fields generated by charged functional groups remain unclear. While the reactivity of the Diels-Alder reaction in the STM system described above was dependent on the orientation of the externally applied field,³ a similar correlation

between field direction and electronic structure/reactivity has not been demonstrated in the molecular electrostatic literature. Instead, the density of charge has been proposed to be more influential than the orientation of the field.^{53,55} Studies examining the influence of charge positioning are very limited at this point,^{47,55} in part due to the lack of synthetic means to vary the electric field at a given metal center. Regardless of whether charge orientation or density proves more influential, the rational positioning of the charges within the secondary coordination sphere will require the development of new ligand systems and potentially new charged functional groups. Detailed studies investigating the influence of electrostatics on discrete reaction steps will be required to inform the design of these systems, as electrostatic effects will vary between differing mechanistic steps.

1.3 Approaches to Stabilizing High Valent Intermediates

1.3.1 Introduction

High valent metal oxygen multiply bonded species are frequently the active oxidants in challenging oxidation reactions mediated in nature.^{59,60-62} The hydroxylation of alkanes is mediated by Fe^{IV}-oxo porphyrin radical cations in cytochrome p450 enzymes, and Fe^{IV}-oxo intermediates in alpha ketoglutarate dependent enzymes have been observed to mediate hydroxylation as well as chlorination, desaturation, and epoxidation.^{60,61} The formation of high valent Mn^{IV}-oxo intermediates is thought to proceed the formation of an O₂ bond in the oxygen evolving complex in photosystem II, generating oxygen from water during photosynthesis.⁶² Additionally, Cu^{III}-oxo intermediates in Cu monooxygenase enzymes are likewise proposed to mediate C-H hydroxylation reactions.^{59,63} The selective functionalization of C-H bonds is a key

challenge in the synthesis of fine chemicals and has also been investigated in the upcycling of polymers.^{64,65} Likewise, the oxygen formation step of water oxidation is considered the more challenging half reaction of water splitting and limits the use of water as a hydrogen source in the preparation of solar fuels.⁶⁶ Given the impact of these reactions, studies on metal-oxo intermediates have been pursued to gain insight on how these reactions are mediated in natural systems and how they could be applied in synthetic systems.

One approach towards the study of metal-oxo intermediates is the synthesis of model complexes.^{63,67-69} Indeed, numerous examples of metal-oxo complexes have been prepared by designing strongly donating ligands and stabilizing secondary interactions such as hydrogen bonds.^{63,67-69} These studies have elucidated many fundamental aspects of metal-oxo reactivity, such as the typical correlation between the rate of HAT and the thermodynamics of the reaction, as described in the Bell-Evans-Polanyi principle.⁴⁶ However, these model complexes typically display muted C-H activation reactivity in comparison to natural systems.^{63,67-69} One possible reason for the difference is the ligand field, which in natural systems is composed of fairly weak imidazole and carboxylate donors. In contrast, the coordination environments in synthetic systems typically involve strongly donating ligands such as amides or carbenes as well as higher coordination numbers. Additionally, many enzymatic metal-oxo intermediates have alternatively been described with a metal-oxyl resonance structure, wherein the metal is reduced by 1 electron and the oxygen is in the 1⁻ rather than a 2⁻ oxidation state.^{59,70,71} This electronic structure has been proposed to be more reactive than complexes with predominantly metal-oxo resonance structures.⁶⁹ However, the model complexes prepared to date are predominantly metal-oxos and provide minimal insight on the reactivity of putative metal-oxyl species. The incorporation of electric field effects into model complexes may allow for access to metal-oxos with unusual

electronic structures because weaker ligand fields can be used, and the orientation of negative charge near an O ligand may favor O-centered oxidation.

Electric fields in protein active sites have been proposed to alter the spin density on the oxygen in Fe^{IV}-oxo intermediates in cytochrome p450 enzymes.¹⁰ Additionally, the redox potential of metal ions within enzyme active sites are proposed to be modified by the presence of alkali metal cations.⁷² It has recently been established that electric fields within enzyme active sites can likely also alter the donor strength of ligands as a correlation between Hammett parameter and applied potential.⁷³ Given these observations, electric fields in enzymes may aid in the formation of high valent intermediates despite the weakly donating ligand fields. This electric field strategy may analogously be useful for preparing high-valent metal-oxo model compounds with more weakly donating and biologically relevant ligand fields. The combination of weaker ligand fields and electrostatic effects may lead to unusual electronic structures and reactivity for the model complexes. This hypothesis is supported by the observed orbital reordering due to electrostatics in a Cu phosphinimine tren ligand and by the unusual HAT reactivity observed in the cases of a Mn^VN and [Cu^{II}-OH] complexes supported by charged ligands.^{44,56,57} Indeed, examples of oxygen-based reactivity in metal systems with charged ligands have begun to be investigated over the past few years. Although preliminary, these studies indicate (1) that the presence of alkali metals near the metal-oxo bond decreases the bond strength, (2) that O-atom transfer reactivity will also be influenced by the charge of the complex, and (3) that high valent oxidation states may be supported by weakly donating anionic ligands.

1.3.2 Examples of Electrostatic Effects on Metal Oxygen Based Reactivity

A recent study from the Borovik group assessed the influence of alkali earth metal cations on the electronic structure of an Fe^{IV}-oxo supported by a phosphinic amide substituted tren ligand

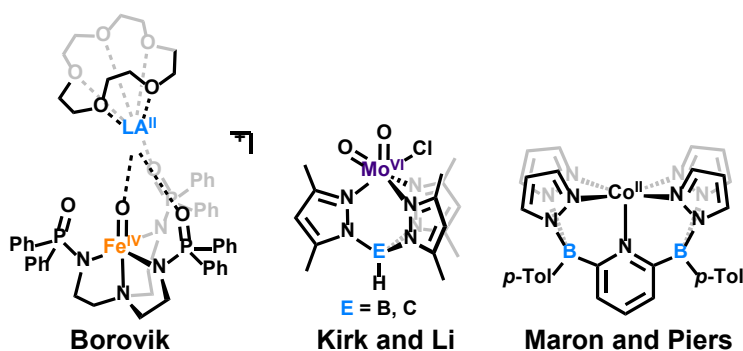


Figure 1.6 Metal complexes incorporating charged moieties (depicted in blue) which have been investigated in the context of metal-oxo chemistry.

(Figure 1.6).⁷⁴ The alkali earth metals are proposed to coordinate to two of the phosphine oxides and the Fe^{IV}-oxo. Coordination of the M²⁺ alters the extent of electron donation from the oxo ligand to the metal center, resulting in a $\sim 18\text{ cm}^{-1}$ reduction

in the $\nu_{\text{Fe-O}}$ stretch as reported by nuclear resonance vibrational spectroscopy (NRVS). However, the change in the bond distance upon coordination of an alkali earth metal is too small to observe in extended X-ray absorption fine structure (EXAFS) spectra of the complexes ($\Delta 0.02\text{ \AA}$). The E[xz,yz] orbitals in the alkali earth metal coordinated Fe^{IV}-oxo complexes move lower in energy, resulting in a shifted d-d transition in the UV-vis spectra. The shift in the energy of the d-d transition was found to correlate with the acidity of the alkali earth metal cations. Overall, the coordination of an alkali earth metal cation weakens the Fe^{IV}-O bond to a similar extent as the weakening observed upon the introduction of H-bonding interactions in the related urea substituted tren ligand. The similarities between H-bonding interactions and alkali earth metal coordination are reminiscent of Boxer's treatment of H-bonding interactions in protein active sites as contributors to the applied electric field.¹³ However, the relative influence of covalent contributions from the coordination of the alkali earth metal to the oxo and the electrostatic effects from the charge of the cation remain convoluted in this system.

The effect of overall charge on the electronic structure and O-atom transfer reactivity of a tris-pyrazolylmethane (Tpm) and tris-pyrazolyl borate (Tp) supported Mo^{VI}O₂Cl core was investigated

by the Li and Kirk groups (Figure 1.6).⁷⁵ The difference in the $\nu_{\text{Mo-O}}$ stretching frequencies between the two compounds was relatively small at 7 cm^{-1} . Additionally, the $\text{Mo}^{\text{VI/V}}$ redox potential was shifted anodically by 350 mV in the Tpm complex relative to the Tp complex. This shift is consistent with the calculated decrease in the energy of the HOMO in the cationic Tpm complex relative to the neutral Tp complex, resulting in a more electrophilic oxo complex. The lowering of the HOMO results in a 500-fold increase in the rate of O-atom transfer to PPh_3 in the Tpm complex relative to the Tp complex. The smaller HOMO-LUMO gap between the Tpm complex and PPh_3 is proposed to lead to enhanced orbital mixing and a computed lowering of the transition state by 36.6 kcal/mol. The experimental Eyring analysis suggests that both complexes proceed through an associative mechanism for the O-atom transfer step. In contrast to the examples discussed in the previous section, the $E_{1/2}$ and K_{OAT} of the Tpm complex correlates well with a previously determined semi-linear relationship between these values in neutral compounds. The computed Löwdin atomic charges suggest that 50% of the difference between the Tpm and Tp complexes is localized at the central C or B atom, while the remaining 50% is delocalized, complicating separation of the inductive and electrostatic contributions to the experimental differences in $E_{1/2}$ and K_{OAT} .

The cobalt mediated activation of O_2 was studied in a novel dianionic ligand prepared by the Maron and Piers groups (Figure 1.6).⁷⁶ The ligand is reminiscent of the pentapyridine PY5 ligand explored previously in metal-oxo chemistry,^{77,78} although the bridgehead carbon atom has been replaced with boron and the heterocycles in the plane are pyrazoles rather than pyridines. The $\text{Co}^{\text{II/III}}$ couple in the dianionic ligand is shifted cathodically by 90 mV relative to the couple in the PY5 ligand set despite the use of more weakly donating heterocycles. Oxygen activation has been observed previously with Co in related pentadentate heterocyclic ligand environments and is

proposed to proceed via the formation of $\text{Co}^{\text{IV}}\text{-oxo} \leftrightarrow \text{Co}^{\text{III}}\text{-oxyl}$ intermediates, without definite assignment of the oxo or oxyl resonance structure.⁷⁹ In the case of the dianionic ligand, the oxygen activation is proposed to proceed through the formation of a $\text{Co}^{\text{V}}\text{-oxo} \leftrightarrow \text{Co}^{\text{IV}}\text{-oxyl}$ intermediate, consistent with anionic charges supporting the formation of highly oxidized intermediates. While reactivity studies and DFT in this report support the formation of a high valent intermediate, the exact assignment of a $\text{Co}^{\text{IV}}\text{-oxyl}$ resonance structure is only supported by a computational spin density analysis.

1.4 References

1. Shaik, S.; Ramanan, R.; Danovich, D.; Mandal, D. Structure and Reactivity/Selectivity Control by Oriented-External Electric Fields. *Chem. Soc. Rev.* **2018**, *47* (14), 5125–5145.
2. Feynman, R.P.; Leighton, R. B.; Sands, M. L. Chapter 4: Electrostatics. In *The Feynman Lectures on Physics: Mainly Electromagnetism and Matter* [Online]; Gottlieb, M. A., Pfeiffer, R., Eds.; Basic Books, USA, **2011**. <https://www.feynmanlectures.caltech.edu/info/> (accessed March 2022).
3. Aragonès, A. C.; Haworth, N. L.; Darwish, N.; Ciampi, S.; Bloomfield, N. J.; Wallace, G. G.; Diez-Perez, I.; Coote, M. L. Electrostatic Catalysis of a Diels-Alder Reaction. *Nature* **2016**, *531*, 88–91.
4. Warshel, A.; Sharma, P. K.; Kato, M.; Xiang, Y.; Liu, H.; Olsson, M. H. M. Electrostatic Basis for Enzyme Catalysis. *Chem. Rev.* **2006**, *106* (8), 3210–3235.
5. Schopf, P.; Mills, M. J. L.; Warshel, A. The Entropic Contributions in Vitamin B12 Enzymes Still Reflect the Electrostatic Paradigm. *Proc. Natl. Acad. Sci.* **2015**, *112* (14), 4328–4333.
6. Che, F.; Gray, J. T.; Ha, S.; Kruse, N.; Scott, S. L.; McEwen, J.-S. Elucidating the Roles of Electric Fields in Catalysis: A Perspective. *ACS Catal.* **2018**, *8* (6), 5153–5174.
7. Fried, S. D.; Boxer, S. G. Electric Fields and Enzyme Catalysis. *Annu. Rev. Biochem.* **2017**, 387–415.
8. Gorin, C. F.; Beh, E. S.; Kanan, M. W. An Electric Field-Induced Change in the Selectivity of a Metal Oxide-Catalyzed Epoxide Rearrangement. *J. Am. Chem. Soc.* **2012**, *134* (1), 186–189.
9. Léonard, N. G.; Dhaoui, R.; Chantarojsiri, T.; Yang, J. Y. Electric Fields in Catalysis: From Enzymes to Molecular Catalysts. *ACS Catalysis.* **2021**, 10923–10932.
10. Bím, D.; Alexandrova, A. N. Local Electric Fields as a Natural Switch of Heme-Iron Protein Reactivity. *ACS Catal.* **2021**, *11* (11), 6534–6546.
11. Warshel, A.; Levitt, M. Theoretical Studies of Enzymic Reactions: Dielectric, Electrostatic and Steric Stabilization of the Carbonium Ion in the Reaction of Lysozyme. *J. Mol. Biol.* **1976**, *103* (2), 227–249.
12. Warshel, A. Energetics of Enzyme Catalysis. *Proc. Natl. Acad. Sci.* **1978**, *75* (11), 5250–5254.
13. Fried, S. D.; Boxer, S. G. Measuring Electric Fields and Noncovalent Interactions Using the Vibrational Stark Effect. *Acc. Chem. Res.* **2015**, *48* (4), 998–1006.

14. Fried, S. D.; Bagchi, S.; Boxer, S. G. Extreme Electric Fields Power Catalysis in the Active Site of Ketosteroid Isomerase. *Science* **2014**, *346* (6216), 1510–1514.
15. Wu, Y.; Boxer, S. G. A Critical Test of the Electrostatic Contribution to Catalysis with Noncanonical Amino Acids in Ketosteroid Isomerase. *J. Am. Chem. Soc.* **2016**, *138* (36), 11890–11895.
16. Bím, D.; Alexandrova, A. N. Electrostatic Regulation of Blue Copper Sites. *Chem. Sci.* **2021**, *12* (34), 11406–11413.
17. Mayer, J. M. Understanding Hydrogen Atom Transfer: From Bond Strengths to Marcus Theory. *Acc. Chem. Res.* **2011**, *44* (1), 36–46.
18. Hennefarth, M. R.; Alexandrova, A. N. Direct Look at the Electric Field in Ketosteroid Isomerase and Its Variants. *ACS Catal.* **2020**, *10* (17), 9915–9924.
19. Bhowmick, A.; Sharma, S. C.; Head-Gordon, T. The Importance of the Scaffold for de Novo Enzymes: A Case Study with Kemp Eliminase. *J. Am. Chem. Soc.* **2017**, *139* (16), 5793–5800.
20. Welborn, V. V.; Ruiz Pestana, L.; Head-Gordon, T. Computational Optimization of Electric Fields for Better Catalysis Design. *Nat. Catal.* **2018**, *1* (9), 649–655.
21. Ciampi, S.; Darwish, N.; Aitken, H. M.; Díez-Pérez, I.; Coote, M. L. Harnessing Electrostatic Catalysis in Single Molecule, Electrochemical and Chemical Systems: A Rapidly Growing Experimental Tool Box. *Chem. Soc. Rev.* **2018**, *47* (14), 5146–5164.
22. Gorin, C. F.; Beh, E. S.; Bui, Q. M.; Dick, G. R.; Kanan, M. W. Interfacial Electric Field Effects on a Carbene Reaction Catalyzed by Rh Porphyrins. *J. Am. Chem. Soc.* **2013**, *135* (30), 11257–11265.
23. Zhang, L.; Laborda, E.; Darwish, N.; Noble, B. B.; Tyrell, J. H.; Pluczyk, S.; Le Brun, A. P.; Wallace, G. G.; Gonzalez, J.; Coote, M. L.; Ciampi, S. Electrochemical and Electrostatic Cleavage of Alkoxyamines. *J. Am. Chem. Soc.* **2018**, *140* (2), 766–774.
24. Huang, X.; Tang, C.; Li, J.; Chen, L. C.; Zheng, J.; Zhang, P.; Le, J.; Li, R.; Li, X.; Liu, J.; Yang, Y.; Shi, J.; Chen, Z.; Bai, M.; Zhang, H. L.; Xia, H.; Cheng, J.; Tian, Z. Q.; Hong, W. Electric Field-Induced Selective Catalysis of Single-Molecule Reaction. *Sci. Adv.* **2019**, *5* (6), 3072–3093.
25. Alemani, M.; Peters, M. V.; Hecht, S.; Rieder, K. H.; Moresco, F.; Grill, L. Electric Field-Induced Isomerization of Azobenzene by STM. *J. Am. Chem. Soc.* **2006**, *128* (45), 14446–14447.
26. Chauvin, R. Zwitterionic Organometallates. *Eur. J. Inorg. Chem.* **2000**, 577–591.
27. Stradiotto, M.; Hesp, K. D.; Lundgren, R. J. Zwitterionic Relatives of Cationic Platinum Group Metal Complexes: Applications in Stoichiometric and Catalytic σ -Bond Activation. *Angew. Chem., Int. Ed.* **2010**, *49* (3), 494–512..

28. Lau, V. M.; Gorin, C. F.; Kanan, M. W. Electrostatic Control of Regioselectivity via Ion Pairing in a Au(I)-Catalyzed Rearrangement. *Chem. Sci.* **2014**, *5*, 4975–4979.
29. Lau, V. M.; Pfalzgraff, W. C.; Markland, T. E.; Kanan, M. W. Electrostatic Control of Regioselectivity in Au(I)-Catalyzed Hydroarylation. *J. Am. Chem. Soc.* **2017**, *139* (11), 4035–4041.
30. Ye, J.; Kalvet, I.; Schoenebeck, F.; Rovis, T. Direct α -Alkylation of Primary Aliphatic Amines Enabled by CO₂ and Electrostatics. *Nat. Chem.* **2018**, *10* (10), 1037–1041.
31. Klinska, M.; Smith, L. M.; Gryn'ova, G.; Banwell, M. G.; Coote, M. L. Experimental Demonstration of pH-Dependent Electrostatic Catalysis of Radical Reactions. *Chem. Sci.* **2015**, *6* (10), 5623–5627.
32. Lee, K.; Silverio, D. L.; Torker, S.; Robbins, D. W.; Haeffner, F.; van der Mei, F. W.; Hoveyda, A. H. Catalytic Enantioselective Addition of Organoboron Reagents to Fluoroketones Controlled by Electrostatic Interactions. *Nat. Chem.* **2016**, *8*, 768–777.
33. Montero Bastidas, J. R.; Oleskey, T. J.; Miller, S. L.; Smith, M. R.; Maleczka, R. E. Para-Selective, Iridium-Catalyzed C-H Borylations of Sulfated Phenols, Benzyl Alcohols, and Anilines Directed by Ion-Pair Electrostatic Interactions. *J. Am. Chem. Soc.* **2019**, *141* (39), 15483–15487.
34. Yi, J.; Zhan, S.; Chen, L.; Tian, Q.; Wang, N.; Li, J.; Xu, W.; Zhang, B.; Ahlquist, M. S. G. Electrostatic Interactions Accelerating Water Oxidation Catalysis via Intercatalyst O-O Coupling. *J. Am. Chem. Soc.* **2021**, *143* (6), 2484–2490..
35. Boaz, N. C.; Bell, S. R.; Groves, J. T. Ferryl Protonation in Oxoiron(IV) Porphyrins and Its Role in Oxygen Transfer. *J. Am. Chem. Soc.* **2015**, *137*, 2875–2885.
36. Wang, D.; Groves, J. T. Efficient Water Oxidation Catalyzed by Homogeneous Cationic Cobalt Porphyrins with Critical Roles for the Buffer Base. *Proc. Natl. Acad. Sci.* **2013**, *110* (39), 15579–15584.
37. Shaik, S.; Mandal, D.; Ramanan, R. Oriented Electric Fields as Future Smart Reagents in Chemistry. *Nat. Chem.* **2016**, *8*, 1091–1098.
38. Shaik, S.; Danovich, D.; Joy, J.; Wang, Z.; Stuyver, T. Electric-Field Mediated Chemistry: Uncovering and Exploiting the Potential of (Oriented) Electric Fields to Exert Chemical Catalysis and Reaction Control. *J. Am. Chem. Soc.* **2020**, 12551–12562.
39. Yoo, C.; Dodge, H. M.; Miller, A. J. M. Cation-Controlled Catalysis with Crown Ether-Containing Transition Metal Complexes. *Chem. Commun.* **2019**, *55* (35), 5047–5059.
40. Reath, A. H.; Ziller, J. W.; Tsay, C.; Ryan, A. J.; Yang, J. Y. Redox Potential and Electronic Structure Effects of Proximal Nonredox Active Cations in Cobalt Schiff Base Complexes. *Inorg. Chem.* **2017**, *56* (6), 3713–3718.

41. Chantarojsiri, T.; Ziller, J. W.; Yang, J. Y. Incorporation of Redox-Inactive Cations Promotes Iron Catalyzed Aerobic C–H Oxidation at Mild Potentials. *Chem. Sci.* **2018**, *9* (9), 2567–2574.
42. Chantarojsiri, T.; Reath, A. H.; Yang, J. Y. Cationic Charges Leading to an Inverse Free-Energy Relationship for N–N Bond Formation by MnVI Nitrides. *Angew. Chem., Int. Ed.* **2018**, *57* (43), 14037–14042.
43. Kang, K.; Fuller, J.; Reath, A. H.; Ziller, J. W.; Alexandrova, A. N.; Yang, J. Y. Installation of Internal Electric Fields by Non-Redox Active Cations in Transition Metal Complexes. *Chem. Sci.* **2019**, *10* (43), 10135–10142.
44. Léonard, N. G.; Chantarojsiri, T.; Ziller, J. W.; Yang, J. Y. Cationic Effects on the Net Hydrogen Atom Bond Dissociation Free Energy of High-Valent Manganese Imido Complexes. *J. Am. Chem. Soc.* **2022**, *144* (4), 1503–1508..
45. Delgado, M.; Ziegler, J. M.; Seda, T.; Zakharov, L. N.; Gilbertson, J. D. Pyridinediimine Iron Complexes with Pendant Redox-Inactive Metals Located in the Secondary Coordination Sphere. *Inorg. Chem.* **2016**, *55* (2), 555–557.
46. Goetz, M. K.; Anderson, J. S. Experimental Evidence for pK_a -Driven Asynchronicity in C-H Activation by a Terminal Co(III)-Oxo Complex. *J. Am. Chem. Soc.* **2019**, *141* (9), 4051–4062.
47. Azcarate, I.; Costentin, C.; Robert, M.; Savéant, J.-M. Through-Space Charge Interaction Substituent Effects in Molecular Catalysis Leading to the Design of the Most Efficient Catalyst of CO₂-to-CO Electrochemical Conversion. *J. Am. Chem. Soc.* **2016**, *138* (51), 16639–16644.
48. Azcarate, I.; Costentin, C.; Robert, M.; Savéant, J.-M. Dissection of Electronic Substituent Effects in Multielectron– Multistep Molecular Catalysis. Electrochemical CO₂-to-CO Conversion Catalyzed by Iron Porphyrins. *J. Phys. Chem. C* **2016**, *120*, 45.
49. Margarit, C. G.; Asimow, N. G.; Gonzalez, M. I.; Nocera, D. G. Double Hangman Iron Porphyrin and the Effect of Electrostatic Nonbonding Interactions on Carbon Dioxide Reduction. *J. Phys. Chem. Lett.* **2020**, *11* (5), 1890–1895.
50. Sung, S.; Kumar, D.; Gil-Sepulcre, M.; Nippe, M. Electrocatalytic CO₂ Reduction by Imidazolium-Functionalized Molecular Catalysts. *J. Am. Chem. Soc.* **2017**, *139* (40), 13993–13996.
51. Sung, S.; Li, X.; Wolf, L. M.; Meeder, J. R.; Bhuvanesh, N. S.; Grice, K. A.; Panetier, J. A.; Nippe, M. Synergistic Effects of Imidazolium-Functionalization on Fac-Mn(CO)₃ Bipyridine Catalyst Platforms for Electrocatalytic Carbon Dioxide Reduction. *J. Am. Chem. Soc.* **2019**, *141* (16), 6569–6582.
52. Deluca, E. E.; Xu, Z.; Lam, J.; Wolf, M. O. Improved Electrocatalytic CO₂ Reduction with Palladium Bis(NHC) Pincer Complexes Bearing Cationic Side Chains. *Organometallics* **2019**, *38* (6), 1330–1343..

53. Martin, D. J.; Johnson, S. I.; Mercado, B. Q.; Raugei, S.; Mayer, J. M. Intramolecular Electrostatic Effects on O₂, CO₂, and Acetate Binding to a Cationic Iron Porphyrin. *Inorg. Chem.* **2020**, *59* (23), 17402–17414.
54. Martin, D. J.; Mercado, B. Q.; Mayer, J. M. All Four Atropisomers of Iron Tetra(o- N, N, N-Trimethylanilinium)Porphyrin in Both the Ferric and Ferrous States. *Inorg. Chem.* **2021**, *60* (7), 5240–5251.
55. Martin, D. J.; Mayer, J. M. Oriented Electrostatic Effects on O₂ and CO₂ Reduction by a Polycationic Iron Porphyrin. *J. Am. Chem. Soc.* **2021**, *143* (30), 11423–11434.
56. Dhar, D.; Yee, G. M.; Tolman, W. B. Effects of Charged Ligand Substituents on the Properties of the Formally Copper(III)-Hydroxide ([CuOH]²⁺) Unit. *Inorg. Chem.* **2018**, *57* (16), 9794–9806.
57. Weberg, A. B.; McCollom, S. P.; Thierer, L. M.; Gau, M. R.; Carroll, P. J.; Tomson, N. C. Using Internal Electrostatic Fields to Manipulate the Valence Manifolds of Copper Complexes. *Chem. Sci.* **2021**, *12* (12), 4395–4404..
58. Chan, A. L.; Estrada, J.; Kefalidis, C. E.; Lavallo, V. Changing the Charge: Electrostatic Effects in Pd-Catalyzed Cross-Coupling. *Organometallics* **2016**, *35* (19), 3257–3260..
59. Decker, A.; Solomon, E. I. Dioxygen Activation by Copper, Heme and Non-Heme Iron Enzymes: Comparison of Electronic Structures and Reactivities. *Curr. Opin. Chem. Biol.* **2005**, *9* (2), 152–163.
60. Poulos, T. L. Heme Enzyme Structure and Function. *Chem. Rev.* **2014**, *114* (7), 3919–3962.
61. Kal, S.; Que, L. Dioxygen Activation by Nonheme Iron Enzymes with the 2-His-1-Carboxylate Facial Triad That Generate High-Valent Oxoiron Oxidants. *Journal of Biological Inorganic Chemistry*. 2017, pp 339–365..
62. Suga, M.; Akita, F.; Yamashita, K.; Nakajima, Y.; Ueno, G.; Li, H.; Yamane, T.; Hirata, K.; Umena, Y.; Yonekura, S.; Yu, L. J.; Murakami, H.; Nomura, T.; Kimura, T.; Kubo, M.; Baba, S.; Kumasaka, T.; Tono, K.; Yabashi, M.; Isobe, H.; Yamaguchi, K.; Yamamoto, M.; Ago, H.; Shen, J. R. An Oxyl/Oxo Mechanism for Oxygen-Oxygen Coupling in PSII Revealed by an X-Ray Free-Electron Laser. *Science* **2019**, *366* (6463), 334–338.
63. Quist, D. A.; Diaz, D. E.; Liu, J. J.; Karlin, K. D. Activation of Dioxygen by Copper Metalloproteins and Insights from Model Complexes. *J Biol Inorg Chem* **2017**, *22*, 253–288..
64. Hartwig, J. F. Catalyst-Controlled Site-Selective Bond Activation. *Acc. Chem. Res.* **2017**, *50* (3), 549–555.
65. Williamson, J. B.; Lewis, S. E.; Johnson, R. R.; Manning, I. M.; Leibfarth, F. A. C–H Functionalization of Commodity Polymers. *Angew. Chem.- Int. Ed.* **2019**, 8654–8668.
66. Nocera, D. G. Solar Fuels and Solar Chemicals Industry. *Acc. Chem. Res.* **2017**, 616–619.

67. Gupta, R.; Taguchi, T.; Lassalle-Kaiser, B.; Bominaar, E. L.; Yano, J.; Hendrich, M. P.; Borovik, A. S. High-Spin Mn-Oxo Complexes and Their Relevance to the Oxygen-Evolving Complex within Photosystem II. *Proc. Natl. Acad. Sci.* **2015**, *112* (17), 5319–5324.
68. McDonald, A. R.; Que, L. High-Valent Nonheme Iron-Oxo Complexes: Synthesis, Structure, and Spectroscopy. *Coord. Chem. Rev.* **2013**, 414–428.
69. Larson, V. A.; Battistella, B.; Ray, K.; Lehnert, N.; Nam, W. Iron and Manganese Oxo Complexes, Oxo Wall and Beyond. *Nature Reviews Chemistry.* **2020**, 404–419.
70. Ye, S.; Neese, F. Nonheme Oxo-Iron(IV) Intermediates Form an Oxyl Radical upon Approaching the C-H Bond Activation Transition State. *Proc. Natl. Acad. Sci.* **2011**, *108* (4), 1228–1233.
71. Srnec, M.; Wong, S. D.; Matthews, M. L.; Krebs, C.; Bollinger, J. M.; Solomon, E. I. Electronic Structure of the Ferryl Intermediate in the Alpha-Ketoglutarate Dependent Non-Heme Iron Halogenase SyrB2: Contributions to H Atom Abstraction Reactivity. *J. Am. Chem. Soc.* **2016**, *138*, 5110–5122.
72. Tsui, E. Y.; Kanady, J. S.; Agapie, T. Synthetic Cluster Models of Biological and Heterogeneous Manganese Catalysts for O₂ Evolution. *Inorg. Chem.* **2013**, *52* (24), 13833–13848.
73. Sarkar, S.; Patrow, J. G.; Voegtle, M. J.; Pennathur, A. K.; Dawlaty, J. M. Electrodes as Polarizing Functional Groups: Correlation between Hammett Parameters and Electrochemical Polarization. *J. Phys. Chem. C* **2019**, *123* (8), 4926–4937.
74. Oswald, V. F.; Lee, J. L.; Biswas, S.; Weitz, A. C.; Mitra, K.; Fan, R.; Li, J.; Zhao, J.; Hu, M. Y.; Alp, E. E.; Bominaar, E. L.; Guo, Y.; Green, M. T.; Hendrich, M. P.; Borovik, A. S. Effects of Noncovalent Interactions on High-Spin Fe(IV)-Oxido Complexes. *J. Am. Chem. Soc.* **2020**, *142* (27), 11804–11817.
75. Paudel, J.; Pokhrel, A.; Kirk, M. L.; Li, F. Remote Charge Effects on the Oxygen-Atom-Transfer Reactivity and Their Relationship to Molybdenum Enzymes. *Inorg. Chem.* **2019**, *58* (3), 2054–2068.
76. Nurdin, L.; Spasyuk, D. M.; Fairburn, L.; Piers, W. E.; Maron, L. Oxygen-Oxygen Bond Cleavage and Formation in Co(II)-Mediated Stoichiometric O₂ Reduction via the Potential Intermediacy of a Co(IV) Oxyl Radical. *J. Am. Chem. Soc.* **2018**, *140* (47), 16094–16105.
77. Chantarojsiri, T.; Sun, Y.; Long, J. R.; Chang, C. J. Water-Soluble Iron(IV)-Oxo Complexes Supported by Pentapyridine Ligands: Axial Ligand Effects on Hydrogen Atom and Oxygen Atom Transfer Reactivity. *Inorg. Chem.* **2015**, *54* (12), 5879–5887.
78. Wasylenko, D. J.; Palmer, R. D.; Schott, E.; Berlinguette, C. P. Interrogation of Electrocatalytic Water Oxidation Mediated by a Cobalt Complex. *Chem. Commun.* **2012**, *48* (15), 2107–2109..

79. Fukuzumi, S.; Mandal, S.; Mase, K.; Ohkubo, K.; Park, H.; Benet-Buchholz, J.; Nam, W.; Llobet, A. Catalytic Four-Electron Reduction of O₂ via Rate-Determining Proton-Coupled Electron Transfer to a Dinuclear Cobalt- μ -1,2-Peroxo Complex. *J. Am. Chem. Soc.* **2012**, *134* (24), 9906–9909.

Chapter 2: Isolable Iodosylarene and Iodoxyarene Adducts of Co and Their O-atom Transfer and C–H Activation Reactivity

This chapter has been adapted from the following source with permission from the Royal Society of Chemistry: Hill, E. A.; Kelty, M. L.; Filatov, A. S.; Anderson, J. S. *Chem. Sci.* 2018, 9, 4493-4499.

2.1 Introduction

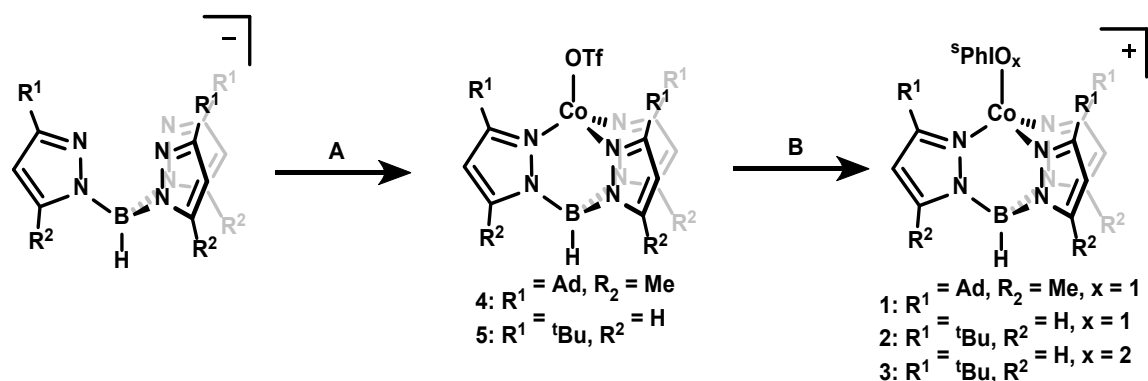
Iodosylbenzene (PhIO) and its derivative iodosylarenes have been widely used as O-atom donor reagents in transition metal mediated oxidation reactions including C–H hydroxylation and O-atom transfer to substrates.¹⁻⁴ The mechanisms of these reactions are proposed to proceed via the formation of a metal iodosylarene adduct followed by transfer of an oxygen atom with concomitant oxidation of the metal center to form iodoxyarene and a high-valent metal-oxo complex as the active oxidant.⁵⁻¹¹ Concurrent to the development of this mechanistic paradigm have been studies suggesting that hypervalent iodine adducts themselves are likewise capable of performing atom transfer reactions to substrates.¹²⁻²⁴ This alternative mode of activity has motivated efforts at isolating discrete transition metal iodosylarene adducts and studying their reactivity. While rare, there are some examples of well characterized transition metal iodosylarene adducts, including several that have been structurally characterized.²⁵⁻³¹ Much of the focus thus far has been on Fe and Mn adducts, as these metals are most frequently featured in oxidation catalysis. More recently, iodosylarenes have been used to generate high-valent Co complexes as well.³²⁻³⁴ Iodosylarene adducts have been cited in these studies as intermediates but have not yet been isolated or thoroughly characterized to examine their reactivity.

Herein, we report the first isolable examples of Co iodosyl and iodoxyarene adducts $[\text{Co}^{\text{II}}\text{Tp}^{\text{Ad,Me}}(\text{sPhIO})]^+$ (**1**), $[\text{Co}^{\text{II}}\text{Tp}^{\text{tBu}}(\text{sPhIO})]^+$ (**2**), and $[\text{Co}^{\text{II}}\text{Tp}^{\text{tBu}}(\text{sPhIO}_2)]^+$ (**3**) (Tp = hydrotris(pyrazolyl)borate and $\text{sPh} = 2\text{-(tert-butylsulfonyl)phenyl}$; Scheme 2.1). Complexes **1**, **2**, and **3** have been crystallographically characterized and detailed kinetic studies reveal a range of reactivity for these three adducts. Complex **1** shows unique behavior that may be consistent with transient oxo formation, but complexes **2** and **3** appear to react as adducts. The observed C–H activation kinetic isotope effect (KIE) is large in all cases, potentially consistent with proton tunnelling transition states.³⁵⁻³⁸ These observations, in addition to controls with redox-innocent Lewis acids, suggest that Lewis acid activation of iodosylarenes leads to H-atom abstraction with large KIEs. While transient oxo formation may occur in complex **1**, the adduct reactivity observed in complexes **2** and **3** indicate that tris-pyrazolyl borate ligands are not sufficiently donating to support high-valent oxidation states despite their anionic charge.

2.2 Results and Discussion

2.2.1 Synthesis of Adduct Complexes

Starting materials and ligands were synthesized according to previously reported procedures with slight modifications in some cases (see Experimental).³⁹⁻⁴⁵ Treatment of the previously reported $\text{NaTp}^{\text{Ad,Me}}$ or KTp^{tBu} ligands with $\text{Co}(\text{MeCN})_6(\text{OTf})_2$ in dichloromethane (DCM) yielded complexes $[\text{Co}^{\text{II}}\text{Tp}^{\text{Ad,Me}}(\text{OTf})]$ (**4**) and $[\text{Co}^{\text{II}}\text{Tp}^{\text{tBu}}(\text{OTf})]$ (**5**) (OTf = trifluoromethanesulfonate) in 76% and 64% yield as bright blue crystalline solids. The ^1H NMR spectra of these complexes confirm overall C_3 -symmetry in solution with shifted resonances characteristic of paramagnetic species. The ^{19}F NMR spectra of **4** and **5** support the coordination of OTf in solution as



Scheme 2.1 Synthetic routes to generate complexes **1-5** starting from the appropriate Tp ligand. **A:** $\text{Co}(\text{MeCN})_6(\text{OTf})_2$, DCM, N_2 , r.t., **B:** 1) 1.1 equivalents $\text{NaBAR}_4^{\text{F}}$ 2) 1.1 equivalents ${}^5\text{PhIO}_x$, Et_2O , N_2 , r.t

demonstrated by a shift of the $-\text{CF}_3$ resonance to -8.7 and -30.0 ppm, respectively (the signal from free OTf appears at -78 ppm). Additionally, the EPR spectra of **4** and **5** are consistent with an expected $S = 3/2$ spin state for high-spin Co^{II} centers (Appendix 2.1.4). Both **4** and **5** display similar electrochemistry, with irreversible oxidations at 2 V vs. $[\text{FeCp}_2]^{0/+}$ (see Appendix 2.1.6).

Synthesis of the cobalt iodosylarene adducts was carried out by treatment of **4** and **5** with 1.1 equivalents of ${}^5\text{PhIO}$ and $\text{NaBAR}_4^{\text{F}}$ (BAR_4^{F} = tetrakis(3,5-bis(trifluoromethyl)phenyl)borate) in diethyl ether (Et_2O). This procedure resulted in the clean formation of new paramagnetic species that maintain C_3 -symmetry in solution as judged by ${}^1\text{H}$ NMR. A new set of paramagnetically shifted signals consistent with a bound ${}^5\text{PhIO}$ ligand are also observed, which suggests the formation of a stable adduct in solution (Appendix 2.1.3). These species were assigned as the cationic iodosylarene adducts **1** and **2** that can be isolated as blue powders in 76% and 83% yield, respectively (Scheme 2.1). Complex **3** was first observed as a by-product in ${}^1\text{H}$ NMR spectra from the synthesis of **2**. The identity of **3** as an ${}^5\text{PhIO}_2$ adduct was suspected due to literature reports that upon standing in solution, ${}^5\text{PhIO}$ will disproportionate into ${}^5\text{PhI}$ and ${}^5\text{PhIO}_2$.⁴¹ Treatment of **5** with independently prepared ${}^5\text{PhIO}_2$ in the presence of $\text{NaBAR}_4^{\text{F}}$ in Et_2O led to the isolation of the

targeted $^s\text{PhIO}_2$ adduct **3** in 67% yield as a light blue powder. Solution ^1H NMR spectra showed that complex **3** retains overall C_3 -symmetry with paramagnetically shifted resonances. The X-band EPR spectra of complexes **1-3** are consistent with $S = 3/2$ Co^{II} centers.

2.2.2 Crystallography

Single crystals of **4** and **5** were grown from concentrated solutions in Et_2O layered with petroleum ether and stored at -35 °C for a few days. The X-ray diffraction (XRD) structures of **4** and **5** confirm coordination of the Tp ligand and OTf counter-ion to the Co center (Appendix 2.3.1). The Co centers of these complexes adopt the expected pseudo-tetrahedral geometry observed for other reported $[\text{CoTpX}]$ complexes.⁴⁶⁻⁵¹ One metric to note is the deviation of the B-Co-O angle from nearly linear in **5** ($175.59(4)^\circ$) to $161.11(5)^\circ$ in **4**. This distortion is attributed to the steric clashing of the $-\text{CF}_3$ group with the adamantyl substituents that is not present for the *t*-butyl substituted Tp ligand.

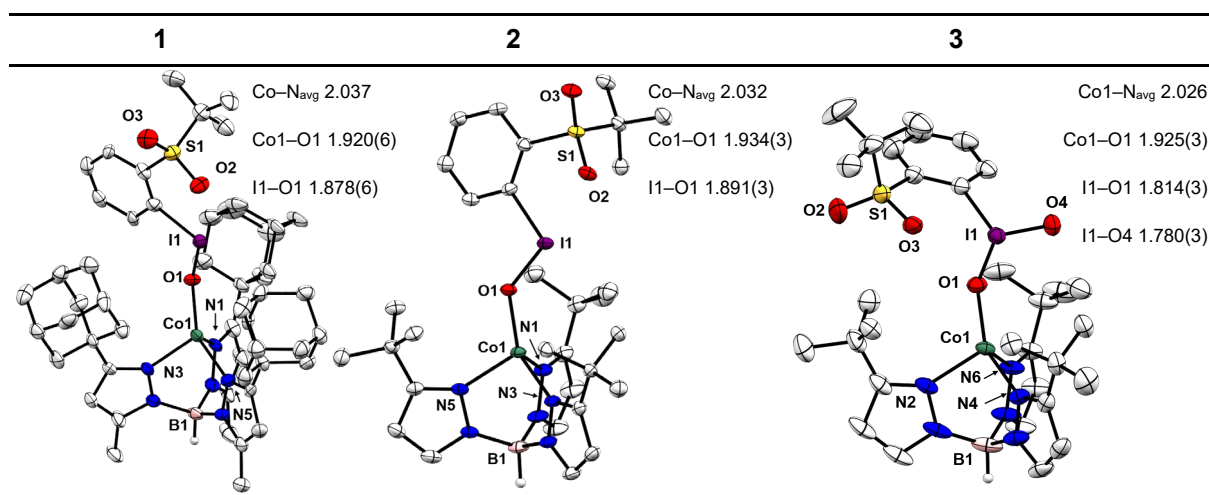


Figure 2.1 XRD structures and selected bond lengths for complexes **1**, **2**, and **3** (Å). Structures depicted as ellipsoids at 50% probability. Hydrogen atoms (other than B-H), BAr^{F_4} counter ions, and solvent molecules omitted for clarity.

Crystals of **1** were grown under the same conditions to those of **4** and **5**, while crystals of **2** were grown from a concentrated solution of Et₂O layered with hexamethyldisiloxane and stored at -35 °C for 7 days. The XRD structures of **1** and **2** confirm the expected pseudo-tetrahedral geometry at Co and furthermore confirm coordination of the ^sPhIO ligand in the solid state (Figure 2.1). The average Co–N bond distances are nearly identical to those in **4** and **5**, suggesting the oxidation and spin state of Co is unchanged, which is also corroborated by the aforementioned spectroscopic data. The I–O bond lengths in **1** and **2** are 1.878(6) and 1.891(3) Å. When compared to the I–O distance of 1.848(5) Å for free ^sPhIO there appears to be minimal activation of the iodosylarene by the Co center in these complexes.³⁹ The Co–O bond lengths are 1.920(6) and 1.934(3) Å, which are comparable with other Co^{II}–O bonds as well as the OTf starting complexes **4** and **5**.⁵² Complex **3** has also been structurally characterized with crystals grown from a layered Et₂O/ petroleum ether solution stored at -35 °C. The average Co–N bond lengths of **3** are nearly identical to those of the starting Co–OTf complex **5** and the I–O bond lengths of 1.814(3) and 1.780(3) Å are also similar to those in the structure of free ^sPhIO₂ at 1.822(3) and 1.796(2) Å.⁴¹ Isolable iodoxyarene adducts are quite rare, and to our knowledge **3** represents the first structurally characterized example with a transition metal.³⁰ While the I–O bond lengths in this series of complexes are all similar to those reported in the free hypervalent iodine reagents, suggestive of minimal activation, the S=O⋯I interactions show more sensitivity to Co coordination. The S=O⋯I distances are in fact shorter than those found in the structures of the free oxidants, suggesting some effect of binding the Lewis acidic Co^{II} center. For **1** and **2** the distances have substantially shortened to 2.481(6) and 2.520(3) Å compared to 2.707(5) Å for free ^sPhIO.³⁹ For **3**, an analogous but smaller contraction from 2.693(2) Å to 2.662(3) Å is observed.⁴¹ In the case of **3**, there is an unusual close interaction

between a solvent THF molecule and the iodine center which may also speak to a more electron deficient adduct (Figure A2.41).³⁰

The structural data for **1**, **2**, and **3** support the formation of well-defined adducts with no substantial change in the Co oxidation state, spin state, or activation of the hypervalent iodine unit. This series of complexes represents an unusual family of isolable, well-characterized hypervalent iodine adducts. These species are generally rare and, as mentioned in the introduction, there have been no examples to date of isolated Co adducts despite the use of iodosylarene reagents in Co-mediated oxidation reactivity.³²⁻³⁴

2.2.3 Reactivity Studies

The isolability of this series of iodosyl- and iodoxyarene adducts prompted us to investigate their oxidative activity. We were particularly interested in examining the O-atom transfer and C-H activation reactivity of these complexes with a focus on developing an understanding of the mechanism of these transformations. More specifically, we wanted to determine whether high-

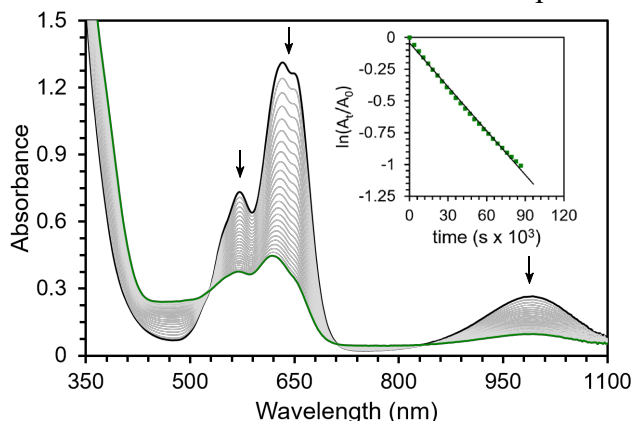


Figure 2.2 UV-vis spectral changes during the decay of **1** (black, 2.5 mM) in Et₂O at 23 °C over 24 h. Inset shows plot of the natural log of the change in concentration of **1** (monitored at 995 nm) vs time with linear fit ($R^2 = 0.98$).

valent oxo complexes were generated over the course of these reactions or whether the adducts themselves could mediate oxidative reactivity.

While complexes **1**, **2**, and **3** were stable enough to allow for their isolation, they do slowly decompose in solution at room temperature. Complex **1** decays with a rate constant of $k_{\text{obs}} = 1.4(\pm 0.4) \times$

10^{-5} s^{-1} at room temperature in Et₂O (Figure 2.2, Table 2.1). Analysis of the resulting reaction mixture by ¹H NMR spectroscopy indicated a complex array of peaks that were not easily assigned (Figure A2.12). Analysis by ESI-MS shows evidence of incorporation of oxygen into the

ligand backbone suggesting ligand-based oxidation as a mode of decay for complex **1** (Figure A2.27). Attempts to react **1** with external substrates were carried out by addition of either 10 equivalents of thioanisole or up to 100 equivalents of 9,10-dihydroanthracene (DHA). In both cases no increase in the rate of decay was observed by UV-vis spectroscopy (Figure A2.32). Complex **1** does react rapidly with PMe₃ in ~120 s to generate what is assigned as an OPMe₃ adduct. The assignment of the phosphine oxide adduct is supported by independent synthesis from OPMe₃ (Figures A2.14).

Complexes **2** and **3** were similarly unstable in solution and decayed with markedly slower rate constants than **1**. The decay of **2** was monitored via UV-vis spectroscopy to obtain a rate of decay with $k_{\text{obs}} = 6.3(\pm 0.8) \times 10^{-7} \text{ s}^{-1}$ at room temperature in Et₂O. Complex **3** decayed with $k_{\text{obs}} = 6.3(\pm 0.4) \times 10^{-6} \text{ s}^{-1}$ as monitored with ¹H NMR spectroscopy at room temperature in CDCl₃. In addition, the decay profiles of both complexes are much less complicated than that observed for **1**; complex **2** decays to a single paramagnetic product and **3** decays to this same product while also

Substrate	1 ^[b]	2 ^[b]	3 ^[c]	producing some amount of 2
self-decay	14(4)	0.63(8)	6.3(4)	(Figures A2.13 and A2.36).
thioanisole	no change	1.12(9)	16(8)	Similar to 1 , these species
9,10-DHA	no change	1.2(3)	10.3(2)	show rapid reactivity with
9,10-DHA KIE ^[d]	>12	14(5)	9(1)	phosphines to generate

[a] Reported rates are 10^{-6} s^{-1} . Reaction conditions: 2.5 mM cobalt complex, 23 °C, 25 mM substrate (250 mM for DHA). [b] Monitored via UV-vis spectroscopy in Et₂O. [c] Monitored via ¹H NMR spectroscopy in CDCl₃. [d] 1:1 mixture of 125 mM each H₄-DHA and D₄-DHA in DCM.

Table 2.1 Observed reaction rates and KIEs of **1**, **2**, and **3** ^[a]

putative phosphine-oxide adducts (also supported by

independent syntheses, Figures A2.15 and A2.16). Unlike **1**, both **2** and **3** show distinct reactivity with other substrates. In the presence of 10 equivalents of thioanisole, the rate of disappearance of **2** or **3** increased by roughly two-fold. In the reactions of **2** and **3** with thioanisole, the adduct of the corresponding oxidized substrate, phenylmethanesulfoxide, was observed by ^1H NMR spectroscopy. This assignment was again confirmed by independent synthesis of the adduct (Figures A2.17 and A2.18). Smaller, concentration dependent rate enhancements were observed for **2** and **3** treated with excess DHA ($k_2 = 2.4 \times 10^{-6}$ and $1.4 \times 10^{-5} \text{ M}^{-1} \text{ s}^{-1}$, Figures A2.33, A2.35 and A2.38). In this case, anthracene was detected by GCMS analysis of the reaction mixtures (Tables A2.1 and A2.2).

Control reactions were also performed to assess the relative reactivity of **1** and **2** compared to free $^s\text{PhIO}$. The complementary study to compare **3** with $^s\text{PhIO}_2$ was hindered by the extremely poor solubility of $^s\text{PhIO}_2$ in organic solvents. The rate of decay of $^s\text{PhIO}$ monitored via ^1H NMR spectroscopy with either 50 equivalents of DHA or 10 equivalents of thioanisole gave rates of $1.7(\pm 0.2) \times 10^{-5}$ and $4.3(\pm 0.1) \times 10^{-4} \text{ s}^{-1}$, respectively (Figure A2.39). The reaction of $^s\text{PhIO}$ with 10 equivalents of PPh_3 was too rapid to monitor by this method; it was complete within 3 minutes of mixing. These data show that the rate of decay of $^s\text{PhIO}$ with thioanisole is at least an order of magnitude faster than for **1** and **2** under the same conditions and the rate with DHA is on the same order of magnitude as **1** and an order of magnitude faster than for **2** under similar conditions.

It has been previously shown for metal–porphyrin complexes that an equilibrium exists between metal iodosylarene adducts and the corresponding metal–oxo complexes.^{13,17} This equilibrium can be shifted towards the metal iodosylarene adduct by addition of a sufficient excess of the iodoarene. In order to test whether the Co complexes presented here may reversibly form high-valent Co–oxo species, we tested the effect of added iodoarene on reaction rates. For complex **1**,

an excess of ^sPhI (10 equivalents) was added and the self-decay monitored. Under these conditions, no change of the rate of self-decay was observed (Figure A2.32). The reactions of **2** and **3** with thioanisole or DHA were also investigated with the addition of excess iodoarene. In both cases, no inhibition was observed with additional ^sPhI . However, in the case of **2**, increased rates were observed and for **3**, a complex reaction occurred which produced unknown paramagnetic products in addition to the formation of **2** (Figures A2.34 and A2.19). While we do not have a concrete explanation for these observations, these experiments still oppose a simple reversible oxo formation pathway (see below).

Given a lack of reactivity studies that have been performed with discrete metal iodosyl- and iodoxyarene adducts, we sought to examine more carefully their C–H activation reactivity. As a mechanistic probe of C–H activation, KIEs for the reaction of **1–3** with DHA were measured. Due to the sluggish rates of reaction, we turned to a method reported in the literature for estimating KIE values using GCMS data from the relative ratio of the mass peaks of the H_2 - and D_2 -anthracene produced from the competition reaction of the oxidant with a 1 : 1 mixture of H_4 - and D_4 -DHA.⁵³ In these experiments, relatively large KIEs were observed for complexes **1**, **2**, and **3** (Table 2.1).

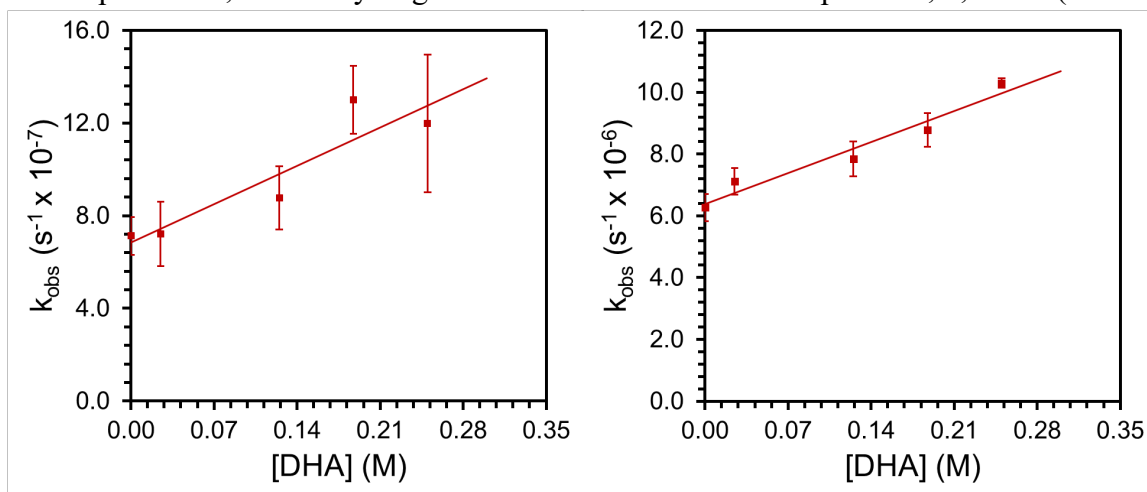


Figure 2.3 Plots of observed rate constants for the reaction of **2** (left) and **3** (right) with varying concentrations of DHA to determine second order rate constants, k_2

With this method, it was difficult to precisely determine the KIE value for **1** because there was no increase in the amount of D₂-anthracene detected and instead a value is estimated with a lower bound of 12 using the variability in the instrument response for D₂-anthracene in the control mixture (see Experimental and Table A2.2). The KIE values for **2** and **3** could be determined more precisely at 14 and 9, respectively. The KIE for free ^sPhIO was also determined using this method and was found to have a lower bound of 3, which is consistent with the value reported for PhIO.⁵³ Additionally, controls were performed involving redox-innocent, diamagnetic Lewis acids to determine whether the higher KIE values for complexes **1–3** could be due to the influence of the paramagnetic Co ion. Oxidation reactions under the conditions described using ^sPhIO in the presence of either Sc(OTf)₃ or NaBAR^F₄ display a high selectivity for H₄-DHA to give KIE values of >66 and >11, respectively. These results suggest that a paramagnetic Lewis acid is not essential for the observation of large KIE values under these conditions. Furthermore, all of the observed KIEs are larger than that measured for free ^sPhIO, supporting the agency of metal-based intermediates in the observed reactivity as opposed to simple dissociation of ^sPhIO.

As a final set of experiments to explore the reactivity of the Co iodosyl- and iodoxyarene complexes, we examined the effect of a Lewis acid on their stability and reactivity. Recently, there have been several reports suggesting that in the oxidation of a Co complex with ^sPhIO, strong Lewis acids such as Sc³⁺ can stabilize high valent, [Co–O–Sc]⁵⁺ moieties.^{33,34} However, there has been some debate about the nature of these species,⁵⁴ prompting us to investigate the reactivity of our discrete adducts with Lewis acids. When complexes **2** and **3** were treated with excess Sc(OTf)₃, the only observed reaction was slow conversion to complex **5**, presumably from the coordination of OTf. When complex **1** was treated with excess Sc(OTf)₃ under the same conditions a mixture of products was obtained. We have been unable to purify a single species from this mixture, but

we have crystallographically characterized a new asymmetric Co^{II} complex which appears to be the major product by ^1H NMR analysis (**6**, Figure A2.20). Complex **6** shows a single Co center coordinated to two pyrazole arms from the Tp ligand, a free Ad,Me-pyrazole, and OTf with an outer sphere BAr^{F_4} ion. Notably, the mass spectrum of this solution did not show evidence of ligand oxidation that is typically observed in the self-decay of **1** (Figure A2.30). While there was no incorporation of Sc^{3+} or oxygen into the complex and we do not know the mechanism leading to ligand degradation, this new reaction product demonstrates an alternative pathway is operative for **1** when Sc^{3+} ions are added. These data do not allow us to definitively support or exclude the formation of transient, high-valent $[\text{Co}-\text{O}-\text{Sc}]^{5+}$ species.

2.2.4 Discussion of Possible Mechanism

The key question that remains is the mode of oxidative activity for these complexes. As mentioned

in the introduction, the most common paradigm in the literature is a pathway involving adduct decomposition to form a high-valent oxo complex. In our case, we have considered three potential reaction pathways summarized in Fig. 2.4: (A) irreversible, rate-determining I-O bond scission to form a reactive, transient high-valent Co-oxo complex, (B) reversible I-O bond scission to form a transient Co-oxo complex or (C) direct oxidation of substrate by the Co iododisyl- or iodoxyarene adducts. We have ruled out a

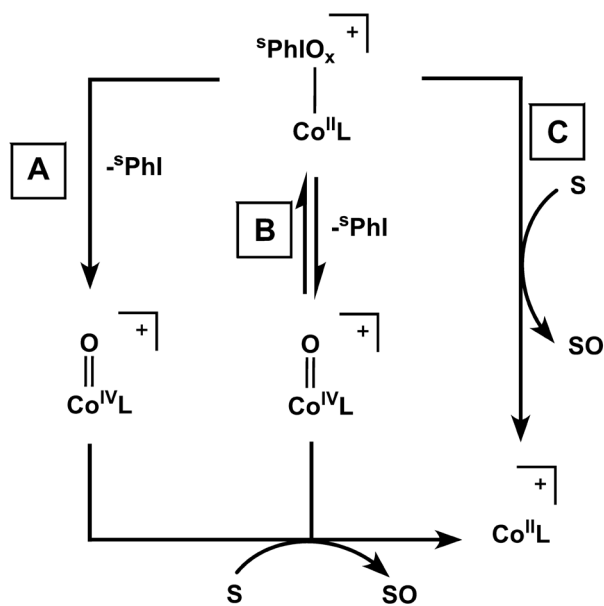


Figure 2.4 Potential reaction pathways for Co-iodosyl- and iodoxyarene adducts **1-3** involving A) irreversible Co-oxo formation, B) reversible Co-oxo formation, or C) direct substrate oxidation. Where L = Tp ligand, S = generic substrate molecule, and SO = oxidized substrate molecule.

mechanism involving dissociation of the hypervalent iodine oxidants on the basis of the observed differences in rates of reactions and KIEs of free $^s\text{PhIO}$ and the Co adducts (see Appendix 2.2).

The data for complex **1** are consistent with a rate-determining, irreversible Co-oxo forming step (Fig. 2.4, pathway A). To be clear, we have no spectroscopic evidence for a Co-oxo species, but its potential involvement is proposed based on the observed reactivity and cannot be ruled out. The rate of decay of complex **1** was not inhibited by addition of excess ^sPhI , which argues against any equilibrium between **1** and a Co-oxo species as shown in pathway B of Fig. 2.4. If **1** were to follow pathway C, it is expected that the rate of decay would be dependent on substrate concentration. Instead, the rate of decay of **1** was not accelerated by external substrates, with the exception of phosphines. Furthermore, the decay of **1** results in a complicated mixture of paramagnetic products and some degree of ligand oxidation in the mixture can be inferred from the ESI-MS data. Finally, the large calculated KIE for **1** is comparable to other reported metal-oxo complexes.⁵⁵⁻⁵⁷ These data taken together are consistent with the involvement of a Co-oxo intermediate in the case of **1**, but are certainly not conclusive on their own. At minimum the data support a distinct reactivity pathway for **1** compared with complexes **2** and **3**.

For **2**, there is an observed substrate dependence on the rate of decay, suggesting I-O bond scission is not rate-limiting; this observation argues against pathway A. Furthermore, the reactivity of **2** is not inhibited by the addition of excess ^sPhI , which argues against a reversible oxo formation mechanism as would be observed in pathway B. These combined data support the direct agency of adduct **2** in the observed oxidative activity rather than decomposition into a Co-oxo complex (Fig. 2.4, pathway C). The observed large KIE for **2** also suggests that this adduct is directly involved in reactivity, as opposed to a dissociative pathway where free $^s\text{PhIO}$ acts as the active

oxidant. Given that the electrochemistry for both the Ad and the ^tBu systems shows similar electronic properties in both cases, the observed differences in reactivity between **1** and **2** are likely due to the differing steric profiles of these two systems.

The self-decay and observed substrate reactivity for **3** are similar to that of **2**, suggesting that a related mechanism may be operative. However, because formation of **2** is frequently observed in the reactivity of **3**, it is difficult to deconvolute relative contributions from these two species in certain experiments such as the KIE analysis and the inhibition of reactivity by added ^sPhI. These factors make it difficult to distinguish between pathways B and C, but the observed rate dependence on substrate concentration for **3** suggests that pathway A can be excluded.

2.3 Conclusions

Complexes **1** and **2** represent the first examples of isolable Co iodosylarene complexes and **3** represents the only example of a transition metal iodoxyarene complex to be thoroughly characterized. The studies herein demonstrate that these adducts display O-atom transfer reactivity and C-H bond activation with appropriate substrates. While the data are consistent with complex **1** reacting *via* transient oxo formation, complexes **2** and **3** appear to react directly as adducts. This series of complexes represents an unusual family of transition metal hypervalent iodine adducts and the detailed reactivity studies reported here further support the diverse reactivity that these species can exhibit. Notably, it must be underscored that these adduct species - which are frequently invoked only as intermediates - can be competent oxidants themselves in oxidative reactions. Although complex **1** may proceed through an oxo intermediate, our inability to isolate an oxo intermediate combined with the adduct reactivity observed with complexes **2** and **3** suggest

that additional optimization of the ligand scaffold is necessary to stabilize high valent metals with weakly donating ligands. These observations motivated further studies into how charged functional groups alter ligand donor strength to inform the design of weakly donating ligands that can support metal oxo species.

2.4 Experimental

2.4.1 Materials and Instrumentation

All manipulations were carried out under a dry N₂ atmosphere using either standard Schlenk technique or in an mBraun Unilab Pro glove box. All chemicals were obtained from commercial sources and used as received unless otherwise stated. Solvents were dried on a solvent purification system from Pure Process Technologies before storing over 4Å molecular sieves under N₂. Tetrahydrofuran (THF) was stirred over NaK alloy and passed through a column of activated alumina prior to storing over 4Å sieves under N₂. Iodosylbenzene, Na[Tp^{Ad,Me}], NaBAr^F₄, Co(MeCN)₆OTf₂, and d₄-DHA were prepared following literature procedures.^{39,40,42-44} Synthesis of K[Tp^{tBu}] followed a literature procedure for the synthesis of Li[Tp^{tBu}] substituting KBH₄ for LiBH₄, all other synthetic procedures were followed as reported.⁴⁵

The iodoxyarene, ^sPhIO₂, was prepared by allowing a concentrated solution of ^sPhIO (300 mg, 0.88 mmol) in 10 mL of DCM to stir until the yellow color had dissipated, approximately three days. The resulting white precipitate was collected by filtration and washed several times with cold DCM and Et₂O before drying under vacuum to yield a white powder (212 mg, 67%). The spectroscopic features of this material matched a previous literature report.⁴¹

UV-vis spectra were recorded on either a Thermo Scientific Evolution 300 spectrometer with the VISIONpro software suite or a Cary 5000 UV/Vis/IR UMA spectrophotometer located in the UChicago MRSEC Materials Preparation and Measurement Laboratory. IR spectra were recorded on a Bruker Tensor II spectrometer with the OPUS software suite. All IR samples were prepared as KBr pellets in a homemade press. EPR spectra were recorded on a Bruker Elexsys E500 spectrometer with an Oxford ESR 900 X-band cryostat and a Bruker Cold-Edge Stinger. NMR spectra for ^1H , $^{19}\text{F}\{^1\text{H}\}$, and $^{31}\text{P}\{^1\text{H}\}$ were recorded on either Bruker DRX-400 or AVANCE-500 spectrometers. Integrations of paramagnetic species are relative only to paramagnetic peaks, therefore in reported spectra below, resonances from diamagnetic protons, such as BAr^{F_4} counterions, were not given integral values. Combustion analysis was performed by Midwest Microlab. Mass spectra were recorded on an Agilent 6130 ESI LC-MS by direct injection. Organic products identified by GC-MS using an Agilent 7890B GC equipped with an Agilent HP-5MS column coupled to an Agilent 5977A EI-MS. Isotope patterns compared to the NIST library to confirm assignments.

2.4.2 Complex Synthesis and Characterization

$[\text{CoTp}^{\text{Ad,Me}}(^s\text{PhIO})][\text{BAr}^{\text{F}_4}]$ (1). To a solution of **4** (50 mg, 0.058 mmol) in 6 mL of Et_2O was added $\text{NaBAr}^{\text{F}_4}$ (54 mg, 0.061 mmol) followed by $^s\text{PhIO}$ (21 mg, 0.060 mmol). This mixture was allowed to stir for ~15 min before filtering through Celite. The resulting blue solution was then layered under petroleum ether in several portions before placing in a $-35\text{ }^\circ\text{C}$ freezer for several days to afford blue clumps of crystalline material (78 mg, 76%). Single crystals were grown by slow diffusion of petroleum ether into a concentrated solution in DCM at $-35\text{ }^\circ\text{C}$ over several days. UV-vis, nm in Et_2O $25\text{ }^\circ\text{C}$ (ϵ , $\text{M}^{-1}\text{cm}^{-1}$): 572 (330), 634 (610), 652 (580), and 995 (120). IR (cm^{-1}): 2909 (s), 2855 (m), 2564 (m, $\nu_{\text{B-H}}$), 1875 (w), 1835 (w), 1781 (w), 1656 (m), 1544 (s), 1479

(m), 1452 (m), 1425 (m), 1355 (m), 1280 (m), 1182 (m), 1130 (m), 939 (m), 887 (m), 840 (m), 792 (m), 748 (m), 715 (w), 680 (m), 667 (m), 642 (m). ^1H NMR (CDCl_3 , 400 MHz): δ 78.00 (s, 3H), 18.86 (d, 1H), 18.37 (s, 9H), 14.61 (s, 1H), 10.06 (s, 1H), 7.75 (s, BAr^{F_4}), 7.57 (s, BAr^{F_4}), 6.09 (br, 18H), 2.77 (s, 9H), 2.44 (s, 9H), 1.51 (s, 9H), 0.80 (s, 9H). ^{19}F NMR (CDCl_3 , 470 MHz): δ -62.6. Anal. Calc. for $\text{C}_{84}\text{H}_{83}\text{N}_6\text{O}_3\text{SB}_2\text{F}_{24}\text{ICo}$: C 52.55, H 4.36, N 4.38, Found: C 52.37, H 4.43, N 4.08.

[CoTp^{tBu}(^sPhIO)][BAr^F₄] (2). To a solution of **5** (40 mg, 0.068 mmol) in 6 mL of Et₂O was added NaBAr^F₄ (66.2 mg, 0.075 mmol) and ^sPhIO (25.4 mg, 0.075 mmol). After 20 minutes of stirring the blue solution was filtered through Celite and dried under vacuum. The resulting blue solid was redissolved in DCM before filtering through Celite to remove insoluble material and dried under vacuum once more. Finally, the blue residue was washed three times with petroleum ether and dried under vacuum to yield a blue powder (93 mg, 83%) which could be used without further purification. Single crystals suitable for X-ray diffraction were grown from a concentrated Et₂O solution layered with hexamethyldisiloxane and stored at -35 °C for 7 days. UV-vis, nm in Et₂O, 25 °C (ϵ , $\text{M}^{-1}\text{cm}^{-1}$): 576 (350), 634 (700), 652 (680), 946 (96). IR (cm^{-1}): 3156 (m), 2970 (s), 2876 (w), 2498 (w, $\nu_{\text{B-H}}$), 1660 (w), 1611 (m), 1503 (m), 1398 (m), 1355 (s), 1279 (s), 1127 (s), 932 (m), 887 (m), 714 (m). ^1H NMR (CDCl_3 , 500 MHz): δ 77.53 (s, 3H), 31.03 (s, 3H), 16.61 (s, 1H), 7.89 (br, 1H), 7.67 (s, BAr^{F_4}), 7.47 (s, BAr^{F_4}), 6.50 (br, 1H), 6.00 (br, 27H), 0.77 (s, 9H), -6.45 (br, 1H), -10.01 (br, 1H). ^{19}F NMR (CDCl_3 , 470 MHz): δ -62.6. Anal. Calc. for $\text{C}_{63}\text{H}_{59}\text{B}_2\text{CoF}_{24}\text{IN}_6\text{O}_3\text{S}$: C 46.04, H 3.62, N 5.11. Found: C 46.06, H 3.74, N 4.93.

[CoTp^{tBu}(^sPhIO₂)] [BAr^F₄] (3). To a solution of **5** (73 mg, 0.12 mmol) in 6 mL of Et₂O was added NaBAr^F₄ (116 mg, 0.13 mmol) and ^sPhIO₂ (47 mg, 0.13 mmol). After 20 minutes of stirring, the blue solution was filtered through Celite and dried under vacuum. The resulting blue residue was

redissolved in minimal DCM and filtered once more through Celite to remove insoluble material before drying under vacuum to yield a blue powder (138 mg, 67%) which could be used without further purification. Single crystals of **3** were grown from a concentrated solution of diethyl ether layered beneath petroleum ether at $-35\text{ }^{\circ}\text{C}$ over several days. UV-vis, nm in Et₂O, 25 $^{\circ}\text{C}$ (ϵ , $\text{M}^{-1}\text{cm}^{-1}$): 580 (sh, 530), 635 (820), 950 (140). IR data (cm^{-1}): 3159 (m), 2972 (m), 2500 (w, $\nu_{\text{B-H}}$), 1661 (w), 1612 (w), 1504 (m), 1399 (m), 1355 (s), 1279 (s), 1127 (s), 1029 (m), 713 (m). ¹H NMR (CDCl₃, 500 MHz): δ 82.85 (s, 3H), 20.38 (s, 3H) 10.89 (s, 1H), 9.81 (br, 27H), 7.48 (s, BAr^F₄), 7.31 (s, BAr^F₄), 6.41 (s, 1H), 3.74 (s, 1H), -5.11 (s, 1H), -23.69 (br, 1H). ¹⁹F NMR (CDCl₃, 470 MHz): δ -62.6 . Anal. Calc. for C₆₃H₅₉B₂CoF₂₄IN₆O₄S C 45.59, H 3.58, N 5.06, Found: C 45.57, H 3.59, N 5.04.

[CoTp^{Ad,Me}(OTf)] (4). To a solution of [NaTp^{Ad,Me}] (500 mg, 0.73 mmol) in 20 mL of DCM was added Co(MeCN)₆(OTf)₂ (445 mg, 0.74 mmol). The mixture was allowed to stir for 24 h before filtering through a fine fritted glass funnel to remove insoluble materials and yield a deep blue solution. The volatiles were removed *in vacuo* and the resulting blue residue was taken up in boiling petroleum ether with minimal THF (~5 mL, 9:1 ratio of petroleum ether to THF) before filtering hot through Celite. The resulting solution was cooled to room temperature whereupon dark blue crystals began to form. After cooling, crystallization was driven to near completion by storing in a $-35\text{ }^{\circ}\text{C}$ freezer overnight. The supernatant was then decanted away from the crop of blue crystals which were rinsed with cold petroleum ether before drying *in vacuo* to obtain dark blue crystalline material (480 mg, 76%). Single crystals suitable for X-ray diffraction were grown from slow diffusion of petroleum ether into a concentrated THF solution at $-35\text{ }^{\circ}\text{C}$ over the course of several days. UV-vis, nm in DCM 25 $^{\circ}\text{C}$ (ϵ , $\text{M}^{-1}\text{cm}^{-1}$): 512 (sh, 90), 546 (260), 556 (270), 620 (420), 630 (400), and 1030 (70). IR (cm^{-1}): 2910 (s), 2850 (m), 2564 (m, $\nu_{\text{B-H}}$), 1653 (m), 1546 (s),

1427 (m), 1342 (m), 1230 (m), 1200 (m), 1098 (m), 1067 (m), 1014 (m), 862 (m), 791 (m), 750 (m), 682 (m), 631 (m). ^1H NMR (CDCl_3 , 400 MHz): δ 79.0 (3H), 15.9 (9H), 8.2 (18H), 2.9 (9H), 2.2 (9H), 0.0 (9H), -4.5 (1H). ^{19}F NMR (CDCl_3 , 470 MHz): δ -7.4. Anal. Calc. for $\text{C}_{43}\text{H}_{58}\text{N}_6\text{O}_3\text{F}_3\text{BSCo}$: C 59.65, H 6.75, N 9.71, Found: C 59.92, H 6.74, N 9.03. Anal. Calc. for $\text{C}_{47}\text{H}_{66}\text{N}_6\text{O}_4\text{F}_3\text{BSCo}$ (one additional molecule of THF included): C 60.19, H 7.09, N 8.96, Found: C 59.90, H 6.77, N 8.58. Elemental analysis for **4** is slightly but consistently off from the predicted value for the molecular formula. We believe that this variability may be due to solvent inclusion from crystallization. As can be seen, the experimental values match well with those predicted for a mono-THF solvate.

[CoTp^{tBu}OTf] (5). To a solution of $\text{K}[\text{Tp}^{\text{tBu}}]$ (400 mg, 0.95 mmol) in 18 mL DCM was added $\text{Co}(\text{MeCN})_6\text{OTf}_2$ (574 mg, 0.95 mmol). After stirring for 24 hours, the reaction was filtered through a medium fritted glass funnel and the resulting blue filtrate was dried under vacuum. The residue was dissolved in boiling petroleum ether and THF mixture and filtered hot before being cooled to room temperature and stored at $-35\text{ }^\circ\text{C}$ for one day to yield microcrystalline product (357 mg, 64%). Single crystals suitable for X-ray diffraction were grown from a concentrated Et_2O solution layered with petroleum ether and stored at $-35\text{ }^\circ\text{C}$ for two days. UV-vis, nm in Et_2O $25\text{ }^\circ\text{C}$ (ϵ , $\text{M}^{-1}\text{cm}^{-1}$): 574 (330), 616 (580), 956 (70). IR (cm^{-1}): 3137 (m), 2967 (s), 2869 (m), 2516 (w, $\nu_{\text{B-H}}$), 1636 (w), 1503 (s), 1396 (s), 1258 (s), 1194 (s), 1170 (m), 1058 (m), 1033 (m), 788 (m), 735 (m), 639 (m). ^1H NMR (CDCl_3 , 500 MHz): δ 79.91 (s, 3H), 23.64 (s, 3H), 9.79 (br, 27H), -21.07 (br, 1H). ^{19}F NMR (CDCl_3 , 470 MHz): δ -30.0 (s). Anal. Calc. for $\text{C}_{22}\text{H}_{34}\text{BCoF}_3\text{N}_6\text{O}_3\text{S}$: C 44.84, H 5.82, N 14.26. Found: C 44.79, H 5.73, N 14.27.

[CoTp^{Ad,Me}H(pyr^{Ad,Me})OTf][BAR^F₄] (6). To a solution of **1** (25 mg, 0.013 mmol) in 3 mL of Et_2O was added ScOTf_3 (64 mg, 0.13 mmol). The suspension was stirred overnight during which time

a purple solution formed which was filtered through Celite and layered under petroleum ether at $-35\text{ }^{\circ}\text{C}$. Single crystals formed from this solution over the course of several days which were suitable for X-ray diffraction studies (17 mg). Due to the complicated ^1H NMR spectrum, peaks were not assigned and relative integrations were reported only for well isolated peaks. UV-vis, nm, $25\text{ }^{\circ}\text{C}$ in Et_2O : 542, 596, ~ 1090 . ^1H NMR (CDCl_3 , 400 MHz): δ 48.11 (s, 2H), 38.69 (s, 1H), 36.91 (s, 6H), 12.53 (d, 2H), 8.65 (s, 6H), 7.90 (s, BAr^{F_4}), 7.61 (s, BAr^{F_4}), 6.58 (d, 9H), 6.17 (s, 1H), 5.07, 4.77, 4.58, 2.38 (s, 3H), 2.09 (s), 1.89 (s), 0.22 (s), -0.43 (s br), -0.46 (s), -2.89 (s, 6H), -9.52 (br), -11.67 (br).

2.4.3 Kinetic Experiments

Data for rate determination were collected in triplicate unless otherwise noted. In a typical experiment, a solution of Co complex was prepared in the appropriate solvent (Et_2O , DCM, or CDCl_3). Substrates were then either added as solids, liquids, or concentrated solutions in the same solvent to the Co complex solution to yield a final Co concentration of 2.5 mM. Reaction mixtures were then transferred to either air-free cuvettes fitted with Teflon plugs to be monitored by UV-vis spectroscopy or to J. Young NMR tubes to be monitored by ^1H NMR spectroscopy over the course of 24-36 hours. UV-vis spectral data were analyzed by plotting the natural log of the absorbance at a given wavelength at time t (A_t) divided by initial absorbance (A_0) vs time in seconds to give the observed rate k_{obs} as the slope of the linear fit of the data. Experiments monitored by ^1H NMR spectroscopy were processed and analyzed using the MestReNova software package v 12.0.0-20080 by plotting the integral graph of a given resonance. The data were plotted as the natural log of the integration at time t (A_t) divided by initial integration (A_0) vs time in seconds to yield the observed rate k_{obs} as the slope of the linear fit of the data. Plotting the k_{obs} vs

concentration of DHA yielded second order rate constants k_2 as the slope of the linear fit of the data.

Kinetic isotope effects (KIEs) were determined using GC-MS data. In a typical experiment, a solution of Co complex (2.5 mM) was prepared using a mixture of 50 equiv. each of H₄-DHA and D₄-DHA in a 1:1 molar ratio (for a total of 100 equiv. of DHA) dissolved in DCM. The solutions were allowed to stand for 62 hours before being filtered through a column of silica and then subjected to GC-MS analysis. The amount of anthracene present was calculated using a standard calibration curve. Using the relative ratios of the peak intensity at 178.1 and 180.1 m/z for H₂-anthracene and D₂-anthracene, respectively, the concentrations of proteo- and deuterio-anthracene were calculated for the starting 1:1 mixture and reaction solutions. After subtracting the quantity of anthracene and d₂-anthracene present in the original mixture from the amount detected in the reaction solutions, the amount of each produced over the course of the reaction could be calculated. The ratio of H₂-anthracene to D₂-anthracene formed during the reaction gave the KIE value. In the case of **1**, ^sPhIO, ^sPhIO with Sc³⁺, and ^sPhIO with Na⁺, the amount of D₂-anthracene produced gave unreasonable values within the error of the measurement. Instead of using the raw data, the standard deviation of the 1:1 mix was used to as a representative amount of D₂-anthracene that may have been produced below a reasonable detection limit. This maximum amount of potential D₂-anthracene provided estimates for the lower bounds of the KIE in these cases. The raw data is provided in Tables A2.1 and A2.3, and the substituted data is provided in Tables A2.2 and A2.4.

2.4.4 X-Ray Crystallography

The diffraction data for **3** were measured at 100 K on a Bruker D8 fixed-chi with PILATUS1M (CdTe) pixel array detector (synchrotron radiation, $\lambda = 0.41328 \text{ \AA}$ (30 KeV)) at the ChemMatCARS 15-ID-B beamline at the Advanced Photon Source (Argonne National Laboratory). The

diffraction data for **1**, **2**, **4**, **5**, and **6** were measured at 100 K on a Bruker D8 VENTURE diffractometer equipped with a microfocus Mo-target X-ray tube ($\lambda = 0.71073 \text{ \AA}$) and PHOTON 100 CMOS detector. Data reduction and integration were performed with the Bruker APEX3 software package (Bruker AXS, version 2017.3-0, 2018). Data were scaled and corrected for absorption effects using the multi-scan procedure as implemented in SADABS (Bruker AXS, version 2014/5).⁵⁸ The structures was solved by SHELXT (Version 2014/5)⁵⁹ and refined by a full-matrix least-squares procedure using OLEX2 (XL refinement program version 2018/1).^{60,61}

2.5 References

1. Stang, P. J.; Zhdankin, V. V. Organic Polyvalent Iodine Compounds. *Chem. Rev.* **1996**, *96*, 1123-1178.
2. Zhdankin, V. V.; Stang, P. J. Recent Developments in the Chemistry of Polyvalent Iodine Compounds. *Chem. Rev.* **2002**, *102*, 2523-2584.
3. Zhdankin, V. V.; Stang, P. J. Chemistry of Polyvalent Iodine. *Chem. Rev.* **2008**, *108*, 5299-5358.
4. Yoshimura, A.; Zhdankin, V. V. Advances in Synthetic Applications of Hypervalent Iodine Compounds. *Chem. Rev.* **2016**, *116*, 3328-3435.
5. Groves, J. T.; Nemo, T. E.; Myers, R. S. Hydroxylation and Epoxidation Catalyzed by Iron-Porphine Complexes. Oxygen Transfer from Iodosylbenzene. *J. Am. Chem. Soc.* **1979**, *101* (4), 1032-1033.
6. Groves, J. T.; Kruper, W. J.; Haushalter, R. C. Hydrocarbon Oxidations with Oxometalloporphines. Isolation and Reactions of a (Porphinato)Manganese(V) Complex. *J. Am. Chem. Soc.* **1980**, *102* (20), 6375-6377.
7. Song, W. J.; Seo, M. S.; George, S. D.; Ohta, T.; Song, R.; Kang, M.-J. Tosha, T.; Kitagawa, T.; Solomon, E. I.; Nam, W. Synthesis, Characterization, and Reactivities of Manganese(V)-Oxo Porphyrin Complexes. *J. Am. Chem. Soc.* **2007**, *129* (5), 1268-1277.
8. England, J.; Martinho, M.; Farquhar, E. R.; Frisch, J. R.; Bominaar, E. L. Münck, E.; Que, L. A Synthetic High-Spin Oxoiron(IV) Complex: Generation, Spectroscopic Characterization, and Reactivity. *Angew. Chem., Int. Ed.* **2009**, *48* 3622-3626.
9. Nguyen, A. I.; Hadt, R. G.; Solomon E. I.; Tilley, T. D. Efficient C-H bond activations *via* O₂ cleavage by a dianionic cobalt(II) complex. *Chem. Sci.* **2014**, *5*, 2874-2878.
10. Koola J. D.; Kochi, J. K. Cobalt-catalyzed epoxidation of olefins. Dual pathways for oxygen-atom transfer. *J. Org. Chem.* **1987**, *52* (20), 4545-4553.
11. McDonald A. R.; Que, L. High-valent nonheme iron-oxo complexes: Synthesis, structure, and spectroscopy. *Coord. Chem. Rev.* **2013**, *257* (2), 414-428.
12. Collman, J. P.; Chien, A. S.; Eberspacher, T. A.; Brauman, J. I. Multiple Active Oxidants in Cytochrome P-450 Model Oxidations. *J. Am. Chem. Soc.* **2000**, *122*, 11098-11100.
13. Nam, W.; Choi, S. K.; Lim, M. H.; Rohde, J.-U.; Kim, I.; Kim, J.; Kim C.; Que, L. Reversible Formation of Iodosylbenzene-Iron Porphyrin Intermediates in the Reaction of Oxoiron(IV) Porphyrin π -Cation Radicals and Iodobenzene. *Angew. Chem., Int. Ed.* **2003**, *42*, 109-111.
14. Collman, J. P.; Zeng, A. L.; Brauman, J. I. Donor Ligand Effect on the Nature of the Oxygenating Species in Mn^{III}(salen)-Catalyzed Epoxidation of Olefins: Experimental Evidence for Multiple Active Oxidants. *Inorg. Chem.* **2004**, *43*, 2672-2679.
15. Wang, S. H.; Mandimutsira, B. S.; Todd, R.; Ramdhanie, B.; Fox J. P.; Goldberg, D. P. Catalytic Sulfoxidation and Epoxidation with a Mn(III) Triazacorrole: Evidence for A "Third Oxidant" in High Valent Porphyrinoid Oxidations. *J. Am. Chem. Soc.* **2004**, *126*, 18-19.

16. Bryliakov K. P.; Talsi, E. P. Evidence for the Formation of an Iodosylbenzene(salen)iron Active Intermediate in a (Salen)iron(III)-Catalyzed Asymmetric Sulfide Oxidation. *Angew. Chem., Int. Ed.* **2004**, *43*, 5228–5230.
17. Song, W. J.; Sun, Y. J.; Choi, S. K.; Nam, W. Mechanistic Insights into the Reversible Formation of Iodosylarene-Iron Porphyrin Complexes in the Reactions of Oxoiron(IV) Porphyrin π -Cation Radicals and Iodoarenes: Equilibrium, Epoxidizing Intermediate, and Oxygen Exchange. *Chem. Eur. J.*, **2006**, *12*, 130–137.
18. Leeladee P.; Goldberg, D. P. Epoxidations Catalyzed by Manganese(V) Oxo and Imido Complexes: Role of the Oxidant-Mn-Oxo (Imido) Intermediate. *Inorg. Chem.* **2010**, *49*, 3083–3085.
19. Hong, S.; Wang, B.; Seo, M. S.; Lee, Y.-M.; Kim, M. J.; Kim, H. R.; Ogura, T.; Garcia-Serres, R.; Clémancey, M.; Latour J.-M.; Nam, W. Highly Reactive Nonheme Iron(III) Iodosylarene Complexes in Alkane Hydroxylation and Sulfoxidation Reactions. *Angew. Chem., Int. Ed.* **2014**, *53* (25), 6388–6392.
20. Wang, B.; Lee, Y.-M.; Seo, M. S.; Nam, W. Mononuclear Nonheme Iron(III)-Iodosylarene and High-Valent Iron-Oxo Complexes in Olefin Epoxidation Reactions. *Angew. Chem., Int. Ed.* **2015**, *127* (40), 11906–11910.
21. Protasiewicz, J. D. Organoiodine(III) Reagents as Active Participants and Ligands in Transition Metal-Catalyzed Reactions: Iodosylarenes and (Imino)iodoarenes. In *Hypervalent Iodine Chemistry*, Springer International Publishing, 2015; pp 263–288.
22. Kang, Y.; Li, X.-X.; Cho, K.-B.; Sun, W.; Xia, C.; Nam, W.; Wang, Y. Mutable Properties of Nonheme Iron(III)-Iodosylarene Complexes Result in the Elusive Multiple-Oxidant Mechanism. *J. Am. Chem. Soc.* **2017**, *139* (22), 7444–7447.
23. Zdilla M. J.; Abu-Omar, M. M. Mechanism of Catalytic Aziridination with Manganese Corrole: The Often Postulated High-Valent Mn(V) Imido Is Not the Group Transfer Reagent. *J. Am. Chem. Soc.* **2006**, *128* (51), 16971–16979.
24. Abu-Omar, M. M. High-valent iron and manganese complexes of corrole and porphyrin in atom transfer and dioxygen evolving catalysis. *Dalton Trans.* **2011**, *40*, 3435–3444.
25. Lennartson A.; McKenzie, C. J. An Iron(III) Iodosylbenzene Complex: A Masked Non-Heme Fe^VO. *Angew. Chem., Int. Ed.* **2012**, *51* (27), 6767–6770.
26. de Sousa, D. P.; Wegeberg, C.; Vad, M. S.; Mørup, S.; Frandsen, C.; Donald, W. A.; McKenzie, C. J. Halogen-Bonding -Assisted Iodosylbenzene Activation by a Homogeneous Iron Catalyst. *Chem. Eur. J.* **2016**, *22* (11), 3810–3820.
27. Wang, C.; Kurahashi, T.; Fujii, H. Structure and reactivity of an iodosylarene adduct of a manganese(IV)-salen complex. *Angew. Chem., Int. Ed.* **2012**, *51* (31), 7809–7811.
28. Wang, C.; Kurahashi, T.; Inomata, K.; Hada, M.; Fujii, H. Oxygen-Atom Transfer from Iodosylarene Adducts of a Manganese(IV) Salen Complex: Effect of Arenes and Anions on I(III) of the Coordinated Iodosylarene. *Inorg. Chem.* **2013**, *52* (16), 9557–9566.
29. Turlington, C. R.; Morris, J.; White, P. S.; Brennessel, W. W.; Jones, W. D.; Brookhart M.; Templeton, J. L. Exploring Oxidation of Half-Sandwich Rhodium Complexes: Ozygen Atom

Insertion into the Rhodium-Carbon Bond of κ^2 -Coordinated 2-Phenylpyridine. *Organometallics* **2014**, *33* (17), 4442–4448.

30. Au-Yeung, K.-C.; So, Y.-M.; Wang, G.-C.; Sung, H. H.-Y.; Williams, I. D.; Leung, W.-H. Iodosylbenzene and iodylbenzene adducts of cerium(IV) complexes bearing chelating oxygen ligands. *Dalton Trans.* **2016**, *45*, 5434–5438.

31. de Ruiter, G.; Carsch, K. M.; Gul, S.; Chatterjee, R.; Thompson, N. B.; Takase, M. K.; Yano, J.; Agapie, T. Accelerated Oxygen Atom Transfer and C-H Bond Oxygenation by Remote Redox Changes in Fe₃Mn-Iodosobenzene Adducts. *Angew. Chem., Int. Ed.* **2017**, *56* (17), 4772–4776.

32. Wang, B.; Lee, Y.-M.; Tcho, W.-Y.; Tussupbayev, S.; Kim, S.-T.; Kim, Y.; Seo, M. S.; Cho, K.-B.; Dede, Y.; Keegan, B. C.; Ogura, T.; Kim, S. H.; Ohta, T.; Baik, M.-H.; Ray, K.; Shearer, J.; Nam, W. Synthesis and reactivity of a mononuclear non-haem cobalt(IV)-oxo complex. *Nat. Commun.* **2017**, *8*, 14839.

33. Hong, S.; Pfaff, F. F.; Kwon, E.; Wang, Y.; Seo, M.-S.; Bill, E.; Ray, K.; Nam, W. Spectroscopic Capture and Reactivity of a Low-Spin Cobalt(IV)-Oxo Complex Stabilized by Binding Redox-Inactive Metal Ions. *Angew. Chem., Int. Ed.* **2014**, *53* (39), 10403–10407.

34. Pfaff, F. F.; Kundu, S.; Risch, M.; Pandian, S.; Heims, F.; Pryjomska-Ray, I.; Haack, P.; Metzinger, R.; Bill, E.; Dau, H.; Comba, P.; Ray, K. An Oxocobalt(IV) Complex Stabilized by Lewis Acid Interactions with Scandium(III) Ions. *Angew. Chem., Int. Ed.* **2011**, *50* (7), 1711–1715.

35. Caldin, E. F. Tunneling in Proton-Transfer Reactions in Solution. *Chem. Rev.* **1969**, *69*, 135–156.

36. Cong, Z.; Kinemuchi, H.; Kurahashi, T.; Fujii, H. Factors Affecting Hydrogen-Tunneling Contribution in Hydroxylation Reactions Promoted by Oxoiron(IV) Porphyrin π -Cation Radical Complexes. *Inorg. Chem.* **2014**, *53* (19), 10632–10641.

37. Mandal, D.; Mallick, D.; Shaik, S. Kinetic Isotope Effect Determination Probes the Spin of the Transition State, Its Stereochemistry, and Its Ligand Sphere in Hydrogen Abstraction Reactions of Oxoiron(IV) Complexes. *Acc. Chem. Res.* **2018**, *51* (1), 107–117.

38. Mayer, J. M. Understanding Hydrogen Atom Transfer: From Bond Strengths to Marcus Theory. *Acc. Chem. Res.* **2011**, *44* (1), 36–46.

39. Macikenas, D.; Skrzypczak-Jankun, E.; Protasiewicz, J. D. A New Class of Iodonium Ylides Engineered as Soluble Primary Oxo and Nitrene Sources. *J. Am. Chem. Soc.* **1999**, *121* (30), 7164–7165.

40. Song, F.; Wang, C.; Falkowski, J. M.; Ma, L.; Lin, W. Isorecticular Chiral Metal-Organic Frameworks for Asymmetric Alkene Epoxidation: Tuning Catalytic Activity by Controlling Framework Catenation and Varying Open Channel Sizes. *J. Am. Chem. Soc.* **2010**, *132* (43), 15390–15398.

41. Macikenas, D.; Skrzypczak-Jankun, E.; Protasiewicz, J. D. Redirecting Secondary Bonds to Control Molecular and Crystal Properties of an Iodosyl- and an Iodylbenzene. *Angew. Chem., Int. Ed.* **2000**, *39* (11), 2007–2010.

42. Mckimming, A.; Harman, W. H. A Terminal N₂ Complex of High-Spin Iron(I) in a Weak, Trigonal Ligand Field. *J. Am. Chem. Soc.* **2015**, *137* (28), 8940–8943.

43. *Inorganic Syntheses*; Angelici, R. J., Ed.; Inorganic Syntheses; John Wiley & Sons, Inc.: Hoboken, NJ, USA, 1990; Vol. 28.
44. Goldsmith, C. R.; Jonas, R. T.; Stack, T. D. P. C-H Bond Activation by a Ferric Methoxide Complex: Modeling the Rate-Determining Step in the Mechanism of Lipoyxygenase. *J. Am. Chem. Soc.* **2002**, *124* (1), 83–96.
45. Chakrabarti, N.; Sattler, W.; Parkin, G. Structural Characterization of *Tris*(Pyrazolyl)Hydroborato and *Tris*(2-Pyridylthio)Methyl Lithium Compounds: Lithium in Uncommon Trigonal Pyramidal and Trigonal Monopyramidal Coordination Environments. *Polyhedron* **2013**, *58*, 235–246.
46. Gorrell, I. B.; Parkin, G. (*Tris*(3-Tert-Butylpyrazolyl)Hydroborato)Manganese(II), -Iron(II), -Cobalt(II), and -Nickel(II) Halide Derivatives: Facile Abstraction of Fluoride from [BF₄]⁻. *Inorg. Chem.* **1990**, *29* (13), 2452–2456.
47. Thyagarajan, S.; Incarvito, C. D.; Rheingold, A. L.; Theopold, K. H. In Pursuit of a Stable Peroxynitrite Complex - NO_x (X=1-3) Derivatives of Tp^{t-Bu,Me}Co. *Inorganica Chim. Acta* **2003**, *345*, 333–339.
48. Jewson, J. D.; Liable-Sands, L. M.; Yap, G. P. A.; Rheingold, A. L.; Theopold, K. H. Paramagnetic Alkyl, Hydride, and Alkene Complexes of the Tp^{t-Bu,Me}Co Moiety. *Organometallics* **1999**, *18* (3), 300–305.
49. Detrich, J. L.; Konečný, R.; Vetter, W. M.; Doren, D.; Rheingold, A. L.; Theopold, K. H. Structural Distortion of the TpCo-L Fragment (Tp = *Tris*(Pyrazolyl)Borate). Analysis by X-Ray Diffraction and Density Functional Theory. *J. Am. Chem. Soc.* **1996**, *118* (7), 1703–1712.
50. Thyagarajan, S.; Incarvito, C. D.; Rheingold, A. L.; Theopold, K. H. Formation and Reactivity of a Cobalt(II) Hydroperoxide Intermediate. *Chem. Commun.* **2001**, *1* (21), 2198–2199.
51. Egan, J. W.; Haggerty, B. S.; Rheingold, A. L.; Sendlinger, S. C.; Theopold, K. H. Crystal Structure of a Side-on Superoxo Complex of Cobalt and Hydrogen Abstraction by a Reactive Terminal Oxo Ligand. *J. Am. Chem. Soc.* **1990**, *112* (6), 2445–2446.
52. Groom, C. R.; Bruno, I. J.; Lightfoot, M. P.; Ward, S. C. The Cambridge Structural Database. *Acta Crystallogr. Sect. B Struct. Sci. Cryst. Eng. Mater.* **2016**, *72* (2), 171–179.
53. Kim, S. J.; Latifi, R.; Kang, H. Y.; Nam, W.; De Visser, S. P. Activation of Hydrocarbon C-H Bonds by Iodosylbenzene: How Does It Compare with Iron(IV)-Oxo Oxidants? *Chem. Commun.* **2009**, *13* (12), 1562–1564.
54. Lacy, D. C.; Park, Y. J.; Ziller, J. W.; Yano, J.; Borovik, A. S. Assembly and Properties of Heterobimetallic Co^{II/III}/Ca^{II} Complexes with Aquo and Hydroxo Ligands. *J. Am. Chem. Soc.* **2012**, *134* (42), 17526–17535.
55. Gunay, A.; Theopold, K. H. C-H Bond Activations by Metal Oxo Compounds. *Chem. Rev.* **2010**, *110* (2), 1060–1081.
56. Shen, L. Q.; Kundu, S.; Collins, T. J.; Bominaar, E. L. Analysis of Hydrogen Atom Abstraction from Ethylbenzene by an Fe^VO(TAML) Complex. *Inorg. Chem.* **2017**, *56* (8), 4347–4356.

57. Dhuri, S. N.; Cho, K. Bin; Lee, Y. M.; Shin, S. Y.; Kim, J. H.; Mandal, D.; Shaik, S.; Nam, W. Interplay of Experiment and Theory in Elucidating Mechanisms of Oxidation Reactions by a Nonheme Ru^{IV}O Complex. *J. Am. Chem. Soc.* **2015**, *137* (26), 8623–8632.
58. Krause, L.; Herbst-Irmer, R.; Sheldrick, G. M.; Stalke, D. Comparison of Silver and Molybdenum Microfocus X-Ray Sources for Single-Crystal Structure Determination. *J. Appl. Cryst.* **2015**, *48* (1), 3–10.
59. Sheldrick, G. M. SHELXT - Integrated Space-Group and Crystal-Structure Determination. *Acta Cryst.* **2015**, *A71* (1), 3–8.
60. Dolomanov, O. V.; Bourhis, L. J.; Gildea, R. J.; Howard, J. A. K.; Puschmann, H. OLEX2 : A Complete Structure Solution, Refinement and Analysis Program. *J. Appl. Cryst.* **2009**, *42* (2), 339–341.
61. Sheldrick, G. M. Crystal Structure Refinement with SHELXL. *Acta Cryst.* **2015**, *C71* (1), 3–8.

Chapter 3: Electrostatic vs. Inductive Effects in Phosphine

Ligand Donor Properties and Reactivity

This chapter has been adapted from the following source with permission from the Royal Society of Chemistry: Kelty, M. L.; McNeece, A. J.; Kurutz, J. W.; Filatov, A. S.; Anderson, J. S. *Chem. Sci.* **2022**, *13*, 4377-4387.

3.1 Introduction

Spectroscopic and computational studies have cited oriented electric fields in active sites as key contributors to enzymatic reactivity.^{1- 7} Enzymes maintain and orient electric fields using polar and charged functional groups in the protein scaffold around the active site, a strategy that is appealing for synthetic molecular systems but difficult to mimic.^{8- 12} Multiple approaches have been proposed for incorporating similar electric fields into systems that lack an enzymatic superstructure. Electric fields can be directly applied to synthetic compounds through attachment to electrode surfaces or STM tips and these approaches have been shown to increase catalytic rates.^{13- 22} Another approach is to rationally append charged functional groups onto molecular scaffolds to offer control over the orientation and magnitude of electrostatic effects. Indeed, there has been enormous interest in modeling or leveraging electrostatic interactions in organic and inorganic molecules.^{23- 46} Computations predict that electrostatic effects can have a large impact on reactivity and catalysis.^{47- 61}

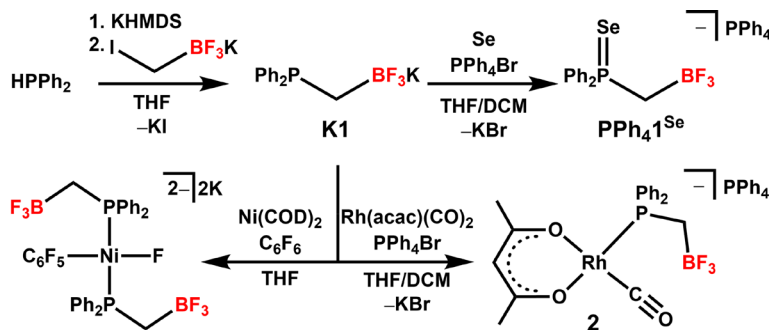
In particular, we are interested in designing weakly donating ligands in which pendant anionic charges sufficiently alter the donor strength and redox potential of the ligand and

resulting metal complex so that high valent metal-oxo species can be isolated and studied. A detailed understanding of the relative magnitudes of inductive and electrostatic charged substituent effects would be valuable in rationally tuning molecular reactivity through ligand design. In this context, *inductive* represents through bond polarization of the molecule, similar to effects observed with electron donating or withdrawing groups, while *electrostatic* indicates through space polarization of a bond consistent with Coulomb's law. Experimentally parsing out the relative inductive and electrostatic contributions to reactivity and electronic structure from charged functional groups is challenging even in simple systems. A prime example of this is in classic Hammett literature where inductive through-bond and electrostatic through-space influences from substituents were predominantly treated as one lump effect, sometimes referred to as σ_i .⁶² However, in a subset of this literature, there has been considerable debate on whether electrostatics or through-bond electron density factors are dominant in σ_i . Hammett originally considered the influence of substituents to be entirely electrostatic in nature, a view supported by Ri, Eyring, and Westheimer.^{63,64} Conversely, Jaffe considered substituent effects primarily through electron density, foreshadowing modern computational analyses.^{65,66} The efficacy of both methods in rationalizing reactivity trends supports that both electrostatic and inductive interactions are active, and methods to distinguish between them are still being pursued to this day.⁶⁷⁻⁶⁹ A more thorough understanding of the inductive and electrostatic factors influencing the electronic structure and reactivity of distally charged ligands and complexes would be instructive, particularly as leveraging through-space interactions can serve as a strategy to break free-energy relationships.⁷⁰⁻⁷⁶

Phosphines are ideal scaffolds for quantifying the influence of electrostatics as these ligands feature prominently in catalysis and have well defined parameters for rationalizing reactivity trends, such as the Tolman Electronic Parameter (TEP) and cone angle.⁷⁷ Indeed, cationic and anionic moieties have previously been incorporated into phosphines, frequently leading to distinct properties or reactivity in comparison to neutral analogues.⁷⁸⁻

⁸³ Phosphine borate ligands specifically have been prepared through the incorporation of triaryl- and trifluoroborate and carborane functional groups, and have shown enhanced reactivity in polymerization,^{84- 93} cross coupling,⁹⁴⁻⁹⁶ and hydrofunctionalization^{97,98} reactions. These anionic phosphines are uniformly considered to be stronger donors than their neutral isostructural analogues. However, the origin of this increase (electrostatic or inductive) has remained elusive, and has largely been considered inductive by default.^{68,69,94-96,98- 101} The ambiguity regarding through space effects of covalently bound distal anions limits the rational design of ligand scaffolds that leverage electric fields to enhance reactivity. For instance, a recent computational study predicts accelerated oxidative addition (OA) reactivity at a PMe_3 supported Pd complex in the presence of either an externally applied electric field or a correctly positioned chloride ion.⁵³ This study suggests that similar effects may be replicated using distally charged anionic phosphines if a suitably thorough understanding of electrostatic effects in covalently bound anions can be obtained.

Herein we report a method to assign the electrostatic and inductive contributions of anionic functional groups to phosphine donor strength using the solvent dependence of phosphorus selenium coupling values ($J_{\text{P-Se}}$). This method is initially developed using the novel phosphine $\text{PPh}_2\text{CH}_2\text{BF}_3^-$ (**1**) (Scheme 3.1). The R-BF_3^- functional group is ideal for



Scheme 3.1 Synthesis of **K1** and reactions to form $[PPh_4][1^{Se}]$, **2**, and the proposed product of C–F oxidative addition by a Ni complex featuring **1**.

this analysis as it provides a more compact charge in comparison to commonly used aryl borates.⁹⁶ Additionally, trifluoroborate groups are relatively inert in comparison to aryl borates, which can engage in aryl-group transfer decomposition pathways⁸⁷ and intramolecular C–H oxidative addition reactivity.⁹⁹ The methylene linker to the phosphine precludes convoluting resonance influences that may be present in aryl linkers. We report the synthesis of the potassium salt of this phosphine, **K1**, and assess the electrostatic impact of the R–BF₃[–] moiety via both the solvent dependent NMR coupling constants of its phosphine selenide SePPh₂CH₂BF₃[–] (**1^{Se}**) and its complexation to Rh carbonyls to give [PPh₄][Rh(acac)(CO)(PPh₂(CH₂BF₃))] (**2**). The possibility of competing contributions to J_{P-Se} from ion pairing is excluded through controls with two different counteranions, [PPh₄][**1^{Se}**] and [TEA][**1^{Se}**]. The solvent dependence of [PPh₄][**1^{Se}**] shows a $1/4\pi\epsilon$ dependence, consistent with Coulomb’s law, and fits suggest that up to 80% of the increase in donor strength relative to SePPh₂Et is attributable to electrostatic effects, a conclusion which we replicate using calculations. This study is then extended to an additional anionic phosphine selenide with a longer and more rigid aryl linker, SePPh₂(2-BF₃Ph)[–] (**3^{Se}**),^{90,91}

and the $1/4\pi\epsilon$ fit similarly suggests that up to 70% of the increase in donor strength relative to PPh_3 results from electrostatic contributions.

Finally, an order of magnitude acceleration in the OA of aryl fluorides mediated by **K1** and $\text{Ni}(\text{COD})_2$ is observed relative to neutral phosphines of comparable donor strengths, PEt_3 and PCy_3 . This finding suggests a unique impact of electrostatic effects beyond that expected from increased donor strength. This accelerated reactivity is applied to the catalytic defluoroborylation of fluoroarenes, with improved reactivity observed with comparatively unactivated substrates. In summary, this work illustrates how electrostatic interactions from charged functional groups are a substantial contributor to phosphine donor strength in common organic solvents and that these electrostatic effects can be leveraged for increased reactivity and catalysis.

3.2 Results and Discussion

3.2.1 Synthesis and Characterization of $\text{PPh}_2\text{CH}_2\text{BF}_3\text{K}$ (**K1**)

Synthesis of the phosphine proceeds readily via deprotonation of Ph_2PH with KHMDs (KHMDs = potassium hexamethyldisilazide), followed by dropwise addition to a stirring THF solution of potassium iodomethyltrifluoroborate, and yields **K1** as a white powder following workup (Scheme 3.1). We note that a related zwitterionic triphenyl phosphonium methyl trifluoroborate has been previously synthesized.¹⁰²⁻¹⁰⁴ The ^1H NMR of **K1** shows the expected aromatic signals for the phenyl groups, and a doublet of quartets at 0.8 ppm from coupling of the CH_2 linker to phosphorus, boron, and fluorine (Figure A3.1). The $^{31}\text{P}\{^1\text{H}\}$ NMR spectrum shows a quartet at -15 ppm due to fluorine coupling with an identical chemical shift to that observed for PPh_2Et (Figure A3.2). This observation is consistent with previous reports that charged phosphines have similar shifts as

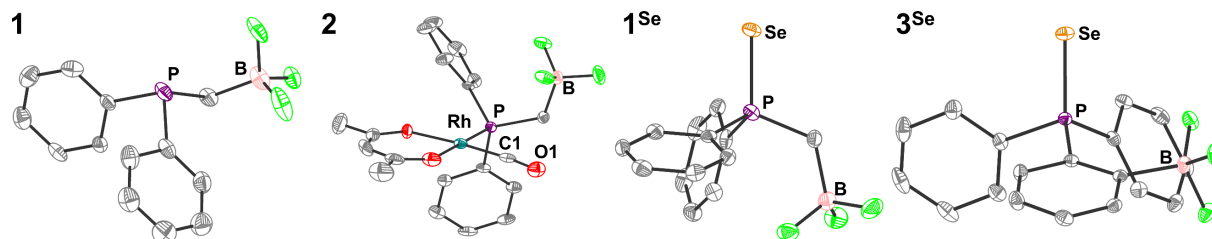


Figure 3.1 SXRDR structures of the anions of **K1**, **2**, [PPh₄][**1**^{Se}], and [PPh₄][**3**^{Se}] with ellipsoids at 50% and H-atoms and counterions omitted for clarity. C is shown in grey, O in red, F in bright green, and other atom types are labelled. Selected bond lengths and angles (averaged where appropriate): (A) B⋯P 2.858(3) Å (B) Rh–C1 1.797(3) Å, Rh–P 2.2408(6) Å, C1–O1 1.152(3) Å, C1–Rh–P 89.5(1)°, Rh–C1–O1 175.1(3)° Rh⋯B 4.150(4) Å, B⋯C 3.719(5) Å, B⋯O 3.955(4) Å (C) P–Se 2.129(1) Å, P⋯B 3.029(6) Å. (D) P–Se 2.112(5) Å, P⋯B 3.562(2) Å.

their neutral analogues.^{90,91,101} Analysis by ¹⁹F{¹H} and ¹¹B{¹H} NMR indicates the expected shifts and coupling for a R–BF₃[–] group, supporting the presence of this anionic unit (Figures A3.3 and A3.5).¹⁰⁵ Compound **K1** was structurally characterized via single-crystal X-ray diffraction (SXRDR, Figure 3.1). The SXRDR structure shows the expected connectivity with an average B⋯P distance of 2.858(3) Å and a close association between K and B (~3 Å, Figure A3.45). While it is unclear if this association is preserved in solution, larger cations were chosen to limit ion pairing in further analyses (see below).

3.2.2 Tolman Electronic Parameter and *J*_{P–Se} Determination

To assay the donor strength of phosphine **1**, its Tolman Electronic Parameter (TEP) was determined using a Rh carbonyl complex of the form Rh(acac)(CO)L, (L=phosphine). While the limitations of TEP in reflecting M–L bond strengths has been noted previously,¹⁰⁶ it remains a standard in the literature for the comparison of phosphine donor strength.¹⁰⁷ The TEP is a measure of the donation of electron density from a phosphine to a metal complex through the combined effects of σ donation (P→M) and π back-bonding (M→P) interactions.^{83,107} TEP is traditionally determined from the A₁-symmetrical ν_{CO} stretching frequency in Ni(CO)₃L complexes, where a higher ν_{CO} indicates a less electron rich metal

center resulting from weaker phosphine donors. However, the toxicity of the $\text{Ni}(\text{CO})_4$ starting material has motivated the development of other model complexes to determine TEP. One such complex which displays a robust linear correlation between ν_{CO} and TEP is $\text{Rh}(\text{acac})(\text{CO})\text{L}$, (see Figure A3.32 for equation), and accordingly the complex with $\text{L} = \mathbf{1}$ was synthesized.¹⁰⁸

Addition of **K1** to $\text{Rh}(\text{acac})(\text{CO})_2$ with PPh_4Br affords $[\text{PPh}_4][\text{Rh}(\text{acac})(\text{CO})(\text{PPh}_2(\text{CH}_2\text{BF}_3))]$ (**2**) as a yellow solid. The SXRD structure of **2** shows a square planar geometry at Rh (Figure 3.1). The BF_3^- unit is located significantly above the Rh square plane and close contacts ($\sim 2.3 \text{ \AA}$) are observed between the BF_3^- and protons on PPh_4^+ , consistent with H-bonding interactions (Figure A3.46). No secondary interactions between PPh_4^+ and CO are observed. The $\text{B}\cdots\text{C}$ and $\text{B}\cdots\text{O}$ distances are 3.719(5) and 3.955(4) \AA , notably shorter than the $\text{B}\cdots\text{Rh}$ distance of 4.150(4) \AA , although the difference diminishes upon normalizing to van der Waals radii (see Experimental). Compound **2** is readily identified in solution by the appearance of a doublet of quartets in the $^{31}\text{P}\{^1\text{H}\}$ NMR spectrum arising from coupling of the phosphorus nucleus to ^{103}Rh ($J_{\text{P-Rh}} = 166 \text{ Hz}$) and ^{19}F ($J_{\text{P-F}} = 10 \text{ Hz}$), consistent with the solid-state structure (Figure A3.7). The solution IR spectrum of **2** in CH_2Cl_2 shows a ν_{CO} of 1965 cm^{-1} , which correlates to a TEP of 2061.7 cm^{-1} (Figure A3.32). This TEP is identical to that of PEt_3 (2061.7 cm^{-1}), and is significantly more donating than the related alkyldiaryl phosphine PPh_2Et (2066.7 cm^{-1}) (Figure 3.2).⁷⁷ This result is consistent with the enhanced donation previously observed for phosphines with anionic borates.^{68,83,86,90-92,95,96,100,101,109-112}

In addition to metal carbonyl adducts, phosphine selenide compounds have also been used to quantify the donor strength and basicity of phosphines via their P–Se coupling

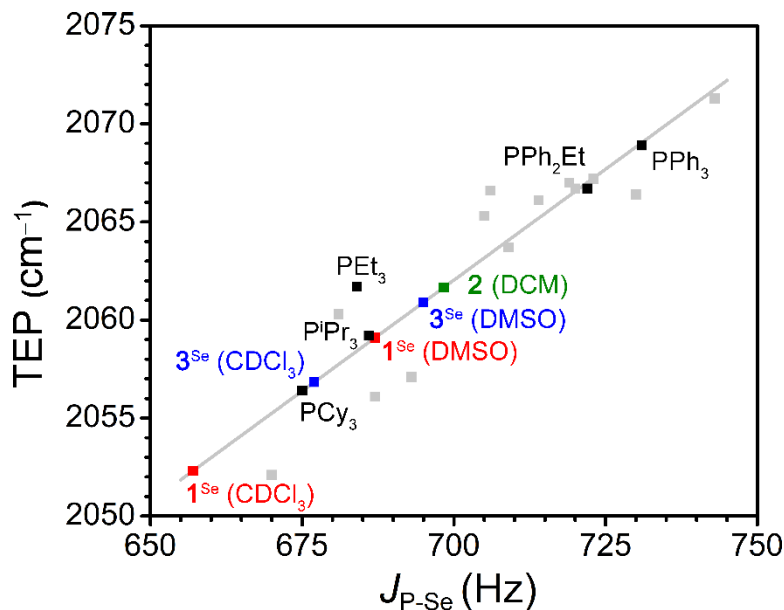


Figure 3.2 Correlation between the TEP of selected phosphine ligands and the J_{P-Se} in $CDCl_3$ of their respective phosphine selenides (black and grey squares, grey line is the linear fit).^{77,108,122} The green square is the experimental TEP for **1** determined using compound **2** and the calculated J_{P-Se} . The squares in red and blue are the experimental J_{P-Se} for $[PPh_4][1^{Se}]$ and $[PPh_4][3^{Se}]$ in $DMSO-d_6$ and $CDCl_3$ and the calculated TEP. The linear fit was used to determine calculated values. (See SI for the fit parameters and a comprehensive list of phosphines included).

constants (J_{P-Se}).^{113,114} The use of NMR coupling constants is advantageous due to greater instrumental resolution and sensitivity in the coupling value as compared to vibrational spectroscopy.¹¹⁵ Changes in J_{P-Se} report on changes in the s character of the P-Se bond.^{116,117} The electron donating/withdrawing character of the substituents on P influences this s character through hybridization changes as predicted by Bent's rule.^{118,119} Electron withdrawing R groups on PR_3 increase the s character and J_{P-Se} , while electron donating R groups effect the opposite.¹¹³

The phosphine selenide, $[PPh_4][SePPh_2CH_2BF_3]$ ($[PPh_4][1^{Se}]$), was prepared by stirring **K1** overnight in THF with an excess of elemental Se and PPh_4Br . The facile oxidation is consistent with the increased donor strength of **1**, as most preparations require heating of elemental Se or the use of soluble red selenium.^{118,120} The SXRD structure confirms the

geometry of $[\text{PPh}_4][\mathbf{1}^{\text{Se}}]$ and shows close contacts ($\leq 2.7 \text{ \AA}$) between the protons on PPh_4^+ and the BF_3^- (Figure 3.1 and Figure A3.47). The $^{31}\text{P}\{^1\text{H}\}$ NMR spectrum of $[\text{PPh}_4][\mathbf{1}^{\text{Se}}]$ shows full conversion to the selenide with a quartet peak at ~ 33 ppm and satellite quartets at ~ 31 and ~ 35 ppm from coupling to the ^{77}Se nucleus (Figure A3.12). In $\text{DMSO-}d_6$ the $J_{\text{P-Se}}$ of 687 Hz is nearly identical to the $J_{\text{P-Se}}$ of SeP^iPr_3 (686 Hz, CDCl_3) and indicates an increase in donor strength relative to the neutral congener SePPh_2Et (722 Hz, CDCl_3) (Figure A3.59).¹⁰¹

We then sought to compare our two experimental assays of phosphine donor strength. While the use of $J_{\text{P-Se}}$ to measure phosphine donor strength is well established, specific correlations between $J_{\text{P-Se}}$ and TEP have not been clearly defined.^{118,121} Fitting of the reported $J_{\text{P-Se}}$ and TEP values for a series of 18 alkyl and aryl phosphines resulted in a reasonable linear correlation ($R^2 = 0.84$, see section A3.7).^{77,108,122} Using this analysis to extrapolate a value of $J_{\text{P-Se}}$ from the experimentally determined TEP of **2** provides $J_{\text{P-Se}} = 698$ Hz, which is significantly larger than the experimentally determined value of 687 Hz for $[\text{PPh}_4][\mathbf{1}^{\text{Se}}]$ in $\text{DMSO-}d_6$. Surprisingly, measuring the $J_{\text{P-Se}}$ of $[\text{PPh}_4][\mathbf{1}^{\text{Se}}]$ in CDCl_3 results in a significant decrease in $J_{\text{P-Se}}$ to 657 Hz ($\Delta = 30$ Hz), suggesting that phosphine **1** is a stronger donor in CDCl_3 than DMSO . Overall, the TEP and $J_{\text{P-Se}}$ values clearly indicate that the anionic charge promotes a large increase in the donor strength of phosphine **1**. However, we wanted to further understand the origin of the large solvent dependence of this donor strength.

3.2.3 Analysis of Donor Strength Solvent Dependence

The presence of the charged borate in phosphine **1** and the discrepancy between TEP values determined via different methods prompted us to investigate how electrostatic effects contribute to these measurements. “Through-space“ interactions have been suggested

previously to explain anomalous J_{P-Se} behavior in phosphines with 2-furyl and *o*-methoxyphenyl substituents, but a thorough analysis of this effect has not been undertaken.¹²³ A dependence on solvent ionic strength was proposed as a means of separating electrostatic and inductive contributions of a R-NMe₃⁺ substituent on the rate of acetate binding in iron porphyrins.³⁸ We reasoned that a similar solvent variation approach would be useful for separating inductive and electrostatic contributions to the donor strength of **1**. Specifically, the through-space electrostatic influence of the charged group should be modified by the solvent dielectric (ϵ), a measure of a medium's ability to shield a charge,¹²⁴ while the through-bond interactions should remain constant.

IR spectra of **2** and the parent Rh(CO)₂(acac) were initially acquired in MeCN, THF, and DCM. However, no variation of ν_{CO} outside of instrumental error is observed (Figures A3.37 and A3.38). This is perhaps not surprising as the expected change in stretching frequency of $\sim 10\text{ cm}^{-1}$ is not large compared to the instrumental resolution (4 cm^{-1}). Resolving dielectric induced shifts is further limited by spectral convolution or broadening, likely from Rh–P rotational isomers of **2** with different stretching frequencies as has been observed in other carbonyl systems.¹²⁵ This manifests as substantially broader spectra for **2** than for Rh(CO)₂(acac). These competing factors complicate the interpretation of donor strength in **2** and suggest that the higher sensitivity and resolution of J_{P-Se} may make it a more conducive method for examining electrostatic effects.

While the inductive donor effects in [PPh₄][**1**^{Se}] should be insensitive to ϵ , the electrostatic stabilization of the formally cationic phosphonium in the dominant resonance structure Se[–]–P⁺R₃ by the adjacent BF₃[–] anion should increase as ϵ decreases.^{101,126} Lower ϵ solvents will less effectively screen the anion, resulting in greater stabilization of the

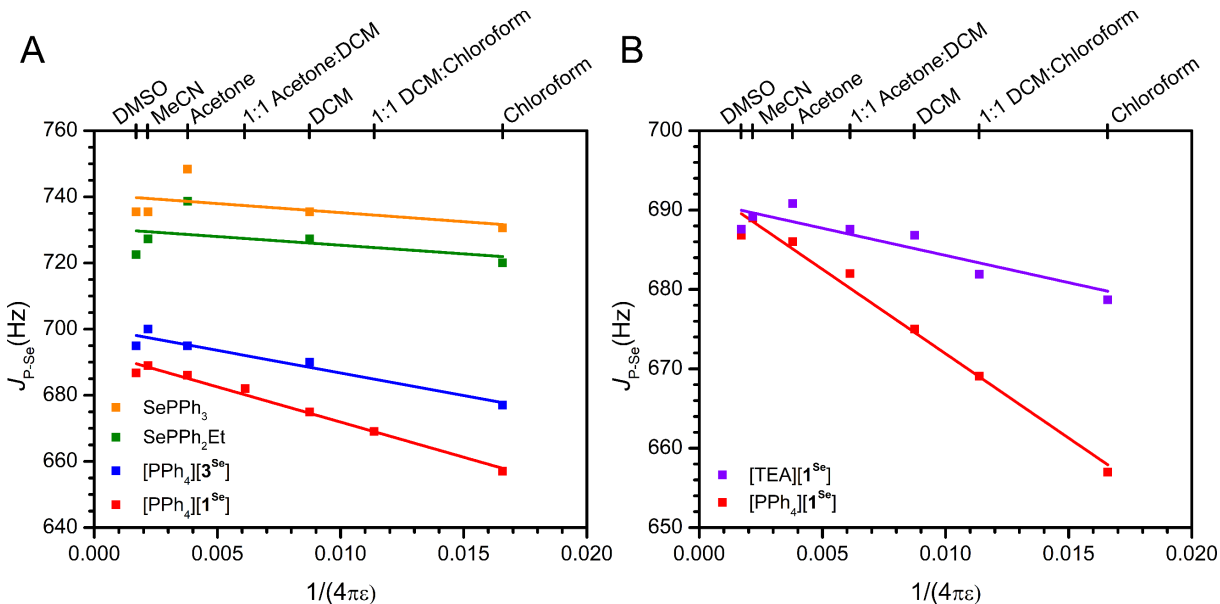


Figure 3.3 (A) Solvent dependence of J_{P-Se} for anionic and neutral phosphines. The fit data for $[PPh_4][1^{Se}]$ is provided in the text, and the fit data for $[PPh_4][3^{Se}]$ is $R^2 = 0.92$, $J_{P-Se} = 700(2) - 1.4(2) \cdot 10^3 \cdot (1/4\pi\epsilon)$. (B) Solvent dependence of $[TEA][1^{Se}]$ in comparison to $[PPh_4][1^{Se}]$ (repeated from A for comparison), the fit data for $[TEA][1^{Se}]$ is $R^2 = 0.77$, $J_{P-Se} = 691(2) - 7(2) \cdot 10^2 \cdot (1/4\pi\epsilon)$. Linear fits are shown as lines. Further discussion of the fits is provided in appendix 3. Different dielectrics (ϵ) were generated with $CDCl_3$ ($\epsilon = 4.8$), CD_2Cl_2 ($\epsilon = 9.1$), acetone- d_6 ($\epsilon = 21$), CD_3CN ($\epsilon = 36.6$), DMSO- d_6 ($\epsilon = 46.7$), or mixtures thereof (Table A3.13).

positive formal charge and a lower J_{P-Se} . Although it is difficult to predict solution structures, SXRD and DFT analysis (see below) of all phosphine selenides considered in this report show shorter distances between P and B than Se and B, supporting the feasibility of the anion stabilizing a formal positive charge on P (Table A3.1). We note that previous literature studies demonstrate some solvent dependence to J_{P-Se} , with one report suggesting variation between 2-3%.^{127,128} In our analysis, comparison of J_{P-Se} in the anionic phosphine to a neutral analogue and restricting solvent choice to aprotic solvents serve as controls for any incidental trends.

As mentioned, an overall decrease of 30 Hz in the J_{P-Se} of $[PPh_4][1^{Se}]$ is observed upon moving from $CDCl_3$ ($\epsilon = 4.8$) to DMSO- d_6 ($\epsilon = 46.7$). Expanding the solvent selection to

include CD₃CN, acetone-*d*₆, CD₂Cl₂, and mixtures thereof shows a consistent decrease in J_{P-Se} as ϵ decreases (Figure 3.3, Figures A3.59-A3.62, Table A3.13). In comparison, only a slight change of 7 Hz is observed across the same ϵ range for the neutral congener SePPh₂Et (Figure 3.3, Figure A3.69, Table A3.13). Coulomb's law suggests that a linear dependence on $1/4\pi\epsilon$ should be expected for a primarily electrostatic effect. Indeed, the observed solvent dependence of J_{P-Se} for [PPh₄][**1**^{Se}] follows this trend. The variable solvent coupling data for [PPh₄][**1**^{Se}] was fit to the linear relationship $J_{P-Se} = 693(1) - 2.12(12) \cdot 10^3 \cdot (1/4\pi\epsilon)$ ($R^2 = 0.98$). The neutral congener was also fit and shows a shallower slope of $-5(6) \cdot 10^2$ and a worse $R^2 = 0.06$ value (Table A3.14).

While this solvent trend for [PPh₄][**1**^{Se}] is well modeled by an electrostatic effect, we also wanted to account for any ion pairing interactions. Ion pairing can range from separated free ions to close contact ion pairs, with varying degrees of ion solvation and association in between. These solvent separated ion pairs may also exist in an equilibrium, and generally it is difficult to precisely characterize the speciation of an ion pair in solution.¹²⁹ Increased ion pairing in low ϵ solvents may influence the observed solvent dependence in the J_{P-Se} of [PPh₄][**1**^{Se}]. To exclude this possibility, [TEA][**1**^{Se}] (TEA⁺ = NEt₄⁺) was prepared as a control with comparatively stronger ion pairing due to the higher charge density of the TEA⁺ cation. As H-bonding interactions between the cation and the BF₃⁻ are observed in the crystal structures of [TEA][**1**^{Se}] and [PPh₄][**1**^{Se}], the CH₂ and BF₃⁻ ¹H and ¹⁹F resonances are used as reporters on ion pairing in solution (Figures A3.47 and A3.49). In DMSO-*d*₆, the methylene and fluorine resonances in [TEA][**1**^{Se}] and [PPh₄][**1**^{Se}] are superimposable, consistent with identical **1**^{Se} environments. In CD₂Cl₂ ($\epsilon = 9.1$), the methylene resonance in [TEA][**1**^{Se}] is shifted downfield by 0.4 ppm relative to [PPh₄][**1**^{Se}]

and the F resonance is shifted downfield by 1.0 ppm (Figures A3.22-A3.25). The downfield shift is consistent with stronger H-bonding interactions in solution deshielding the methylene protons and fluorines of [TEA][**1**^{Se}] to a greater extent than in [PPh₄][**1**^{Se}]. Some degree of ion pairing in [PPh₄][**1**^{Se}] is likely present, as DOSY of [PPh₄][**1**^{Se}] in CDCl₃ shows that the cation and anion diffuse at the same speed (Figure A3.16). However, the NMR experiments demonstrate that the extent of contact-ion pairing in solution appears to be greater in [TEA][**1**^{Se}] than in [PPh₄][**1**^{Se}], as is expected based on the differing size of the cations.

Once it was established that TEA⁺ ion pairs more strongly than PPh₄⁺, the impact of cation identity on J_{P-Se} was investigated. The J_{P-Se} of [TEA][**1**^{Se}] in high ϵ solvents shows nearly identical J_{P-Se} values to that of [PPh₄][**1**^{Se}], consistent with isolated free ions. However, moving to lower ϵ solvents only results in a decrease of 9 Hz in the J_{P-Se} for [TEA][**1**^{Se}] (Figures 3.3, A3.66 and A3.67, Table A3.13). The magnitude of this change and the slope of the linear fit ($-7(2)*10^2$, $R^2 = 0.77$) resembles those of the neutral analogues (Table A3.14). Intuitively, these results suggest that the enhanced ion pairing between TEA⁺ and **1**^{Se} results in shielding of the BF₃⁻ charge, thus limiting the detection of electrostatic effects on J_{P-Se} in low ϵ solvents. In contrast, the large size and diffuse charge of PPh₄⁺ less effectively shields the BF₃⁻ and allows for the observation of solvent dependent through space effects. Similar effects have been observed in ion-pair catalysis, where a small compact SbF₆⁻ anion stabilizes polar transition states and affords greater product selectivity in lower ϵ solvents, while a larger and more diffuse B(3,5-CF₃Ph)₄⁻ anion shows no improvement.²⁷ The effect of alternative cations on the J_{P-Se} of [PPh₄][**1**^{Se}] in CDCl₃ was also explored. The addition of 20 equivalents of PPh₄Br or PPNCl (PPN⁺ =

bis(triphenylphosphine)iminium⁺) results in minimal deviation (<4 Hz), while 20 equivalents of NBu₄Cl or TEABr result in significant increases in the coupling, as expected for the formation of tighter ion pairs and enhanced anion shielding (Table A3.15). Overall, these controls with [TEA][1^{Se}] support the assignment of electrostatic effects instead of ion pairing in rationalizing the observed solvent dependence.

3.2.4 Electrostatic Contributions to Donor Strength

Assigning the solvent dependence of J_{P-Se} as electrostatic in origin enables the separation of electrostatic and inductive contributions to donor strength (Table 1). The difference in J_{P-Se} between [PPh₄][1^{Se}] and the SePPh₂Et in high ϵ solvents, where the charge is effectively shielded, provides an estimate of the inductive contributions of the BF₃⁻ group. The change in J_{P-Se} for [PPh₄][1^{Se}] upon moving to less shielding environments represents the introduction of electrostatic contributions, with the maximum contribution at the hypothetical vacuum limit. The high ϵ and vacuum limits of J_{P-Se} obtained from the linear fits to [PPh₄][1^{Se}] and SePPh₂Et therefore provide the relative electrostatic and inductive contributions to donor strength. Simply shifting from the high ϵ limit (693 Hz) to the vacuum limit (524 Hz) of [PPh₄][1^{Se}] yields an overall change in J_{P-Se} of 169 Hz.

Comparison of this electrostatic shift with the 207 Hz difference in coupling between the vacuum limit of [PPh₄][1^{Se}] (524 Hz) and the high ϵ limit of SePPh₂Et (731 Hz) provides an estimated electrostatic contribution of 82% to the total increase in donor strength (Table 3.1A). While this analysis uses the extrapolated limits, the experimental data from the accessible range of ϵ suggest that the electrostatic contribution is ~50% (Table A3.13). These analyses show that electrostatic factors have a major, and even dominant, impact on the donor properties in these systems.

Table 3.1 Experimental (A.) and Computational (B.) J_{P-Se} Coupling Constants as a Function of Charge and Dielectric. All values in Hz except the relative contribution ratios.

A. Experimental	R = Et X = 1	R = Ph X = 3	B. DFT	
SePPh ₂ R ($\epsilon = \infty, J_{neutral}$)	731	741	SePPh ₂ Et ($\epsilon = 1, J_{neutral}$)	872
[PPh ₄][X ^{Se}] ($\epsilon = \infty, J_{\infty}$)	693	700	SePPh ₂ Et (point charge, $\epsilon = 1, J_{point}$)	809
[PPh ₄][X ^{Se}] ($\epsilon = 1, J_{vac}$)	524	591	[PPh ₄][1 ^{Se}] ($\epsilon = 1, J_{anion}$)	792
$\Delta J_{covalent} = J_{\infty} - J_{neutral}$	- 38	- 41	$\Delta J_{covalent} = J_{anion\infty} - J_{point}$	- 17
$\Delta J_{electrostatic} = J_{vac} - J_{\infty}$	- 169	- 109	$\Delta J_{electrostatic} = J_{point} - J_{neutral}$	- 63
$\Delta J_{tot} = J_{vac} - J_{neutral}$	- 207	- 150	$\Delta J_{tot} = J_{anion} - J_{neutral}$	- 80
Relative contributions to ΔJ			Relative contributions to ΔJ	
$\Delta J_{electrostatic}/\Delta J_{tot}$	0.82	0.73	$\Delta J_{electrostatic}/\Delta J_{tot}$	0.79
$\Delta J_{covalent}/\Delta J_{tot}$	0.18	0.27	$\Delta J_{covalent}/\Delta J_{tot}$	0.21

To further investigate the relative contribution of through-space and through-bond effects, Density Functional Theory (DFT) calculations were performed to estimate J_{P-Se} and compare with experimentally determined values (Table 3.1B). For simplicity, two local geometries of the phosphine 1^{Se} were considered to capture limiting rotamers that may be present in solution: one transoid rotamer with a Se–P–C–B dihedral of 158° and one cis rotamer with a Se–P–C–B dihedral of 74° (Figures A3.52 and A3.53). A Boltzmann weighted average of these two extremes predicts a nearly 100% population of the transoid isomer at room temperature, with a calculated gas phase J_{P-Se} of 792 Hz. We then performed optimizations of the transoid rotamer with explicit solvation to see if the observed experimental trends were reproduced computationally. Optimizations in CHCl₃, DCM, and MeCN predict $|J_{P-Se}|$ values of 648, 675, and 684 Hz respectively (Figures A3.56-A3.58, Table A3.13). These values are in remarkably good agreement with both the experimentally determined J_{P-Se} as well as the observed trend with solvent dielectric.

To computationally deconvolute electrostatic contributions to $J_{\text{P-Se}}$, we analyzed the effect of including point charges in the gas phase. Coulomb's law was used to estimate the electric field at P generated by a negative point charge located at B in the transoid rotamer of $\mathbf{1}^{\text{Se}}$. This analysis gives an electric field parallel to the P–Se bond (defined as the z-axis) of ~ -1.07 V/Å (Table A3.5). The electrostatic contribution to $J_{\text{P-Se}}$ was then determined by calculating the $J_{\text{P-Se}}$ for SePPh₂Et with a negative point charge at ~ 3.7 Å from P in the z direction, resulting in an applied field of comparable magnitude. The inclusion of this point charge lowers $J_{\text{P-Se}}$ to 809 Hz from 872 Hz in the neutral analogue, suggesting that the purely electrostatic contribution to $J_{\text{P-Se}}$ is 63 Hz. This electrostatic contribution is 79% of the total computed difference in $J_{\text{P-Se}}$ between $\mathbf{1}^{\text{Se}}$ and SePPh₂Et (80 Hz, Table 3.1), which is identical within error to that determined experimentally. Thus, DFT calculations support the experimental data demonstrating that electrostatic effects play a significant role in the donor properties of $\mathbf{1}$.

3.2.5 Extension and Comparison to Other Phosphines

The selenide of an anionic phosphine previously investigated for Pd catalyzed olefin polymerization/oligomerization, [PPh₄][SePPh₂(2-BF₃Ph)] ([PPh₄][$\mathbf{3}^{\text{Se}}$]), was synthesized analogously to [PPh₄][$\mathbf{1}^{\text{Se}}$]. This phosphine was targeted to test the generality of this solvent-dependence analysis of electrostatic contributions to donor properties, particularly in the presence of increased rigidity and possible convoluting resonance effects from an aryl linker.^{90,91} The SXRD structure of [PPh₄][$\mathbf{3}^{\text{Se}}$] confirms the expected connectivity and also shows that the B of the BF₃[−] group is farther from the phosphine than in [PPh₄][$\mathbf{1}^{\text{Se}}$] (Figure 3.1, 3.562(2) and 3.029(6) Å respectively). The P of the PPh₄⁺ cation is located at 5.895(2) Å from the B, however H-bonding interactions between the PPh₄⁺ aryl protons and the BF₃[−] fluorines are observed (Figure A3.51).

The solvent dependence of J_{P-Se} for $[PPh_4][3^{Se}]$ was measured with the related assumption that inductive and resonance contributions along the covalent linkage would be predominantly independent of solvent ϵ screening. The J_{P-Se} of $[PPh_4][3^{Se}]$ decreases by 18 Hz upon moving from DMSO- d_6 to $CDCl_3$, a smaller change than the 30 Hz shift observed for $[PPh_4][1^{Se}]$ (Figures 3.3 and A3.68, Table A3.13). Furthermore, the magnitude of the slope of the linear fit to the solvent dependence for $[PPh_4][3^{Se}]$ is $\sim 70\%$ of that for $[PPh_4][1^{Se}]$. This is consistent with the ratio predicted from a $1/(r^2)$ dependence from Coulomb's law based on the relative B \cdots P distances in the anionic fragments of $[PPh_4][3^{Se}]$ and $[PPh_4][1^{Se}]$ from SXRD (3.562(2) and 3.029(6) Å respectively, 72%, see Experimental).

The neutral congener of $[PPh_4][3^{Se}]$, $SePPh_3$, was also prepared and the J_{P-Se} changes by 5 Hz upon switching from $CDCl_3$ to DMSO- d_6 (Figures 3.3 and A3.70, Table A3.13). Using the J_{P-Se} values from the high ϵ and vacuum limits determined from the linear fit of $[PPh_4][3^{Se}]$ and an identical comparison method to that described above suggests an electrostatic contribution to the overall shift of 73%, which is slightly smaller than that for $[PPh_4][1^{Se}]$ (82%). In sum, all the experimental data acquired on both $[PPh_4][1^{Se}]$ and $[PPh_4][3^{Se}]$ support a significant and potentially major role that through-space electrostatic interactions have in the donor properties of these phosphines, and furthermore illustrate that J_{P-Se} is a useful probe for deconvoluting electrostatic from inductive or resonance effects.

Comparing the overall shifts in J_{P-Se} from $[PPh_4][1^{Se}]$ and $[PPh_4][3^{Se}]$ from their respective neutral congeners to other anionic phosphine systems is instructive, even in the absence of comparable solvent dependence studies. In one example a triptycene borate phosphine with a P \cdots B distance of 3.03 Å was compared to a silicon based neutral analogue.^{96,111} The shift in J_{P-Se}

observed in CDCl₃ upon switching from the neutral to anionic version approached 90 Hz. The magnitude of this shift is larger than the 63 Hz shift between [PPh₄][**1**^{Se}] and SePPh₂Et and the 54 Hz difference between [PPh₄][**3**^{Se}] and SePPh₃ in CDCl₃. The greater magnitude of the shift can be rationalized by the orientation of the anionic functional group, which is constrained to align with the P–Se bond in the triptycene case. The significant change in J_{P-Se} coupling observed in the triptycene case contrasts with another example featuring an anionic BPh₃[−] group, SePPh₂(*p*-BPh₃Ph)[−].¹⁰¹ The difference in coupling between this compound and the neutral congener SePPh₃ is only 30 Hz in CDCl₃, likely due to the larger distance between the charged group and the phosphine (6.49 Å from DFT) and delocalization of the anionic charge into the aryl rings on boron.^{96,99,101} These examples illustrate that the distance, orientation, and anion structure influence the magnitude of the impact on phosphine donor properties.

3.2.6 C–F Oxidative Addition Reactivity

The comparatively strong donor properties of phosphine **1** prompted us to consider its application in challenging oxidative addition (OA) reactions. Indeed, anionic phosphines have previously shown enhanced coupling reactivity with aryl chlorides in comparison to neutral isostructural congeners.⁹⁴⁻⁹⁶ Uniquely, the J_{P-Se} analysis carried out above with [PPh₄][**1**^{Se}] allows for comparison between the reactivity of **K1** and phosphines of quantitatively similar donor strengths. Comparison with PEt₃ is instructive as the J_{P-Se} (684 Hz) closely matches that of [PPh₄][**1**^{Se}] in DMSO (687 Hz) and the cone angles are similar (132° and 140° for PEt₃ and PPh₂Et).⁷⁷ The reactivity of PCy₃ was also investigated as the J_{P-Se} (675 Hz) closely matches that predicted for [PPh₄][**1**^{Se}] in THF using the $1/4\pi\epsilon$ linear fit ($\epsilon = 7.6$, 671 Hz). While these comparisons do not perfectly account for enhanced ion

pairing from K^+ or imperfect matching of cone angles, they are nonetheless useful to reveal trends in reactivity as a function of electrostatic contributions to donor strength.

The OA of aryl fluoride bonds was chosen for this comparison due to a recent computational report suggesting that this reaction is accelerated in the presence of an electric field.⁵³ Additionally, the OA of C_6F_6 by $Ni(COD)_2$ (COD = 1,5-cyclooctadiene) with PEt_3 has been previously reported to proceed very slowly, taking ~4 weeks in hexane for completion.¹³⁰ Therefore, the rates of C_6F_6 OA by $Ni(COD)_2$ with **K1**, PEt_3 and PCy_3 in THF were determined along with the overall conversion.

The combination of $Ni(COD)_2$ and 2 equivalents of **K1** in THF generates a red solution with an absorbance in the UV-vis spectrum at 464 nm (Figure A3.44). The $^{31}P\{^1H\}$ NMR spectrum of the reaction shows the appearance of three new resonances with some unreacted **K1**, indicating a mixture of differentially ligated species (Figure A3.73). Addition of 10 equivalents of C_6F_6 , as well as CF_3Ph and $OPPh_3$ as internal standards, results in the disappearance of these resonances and the formation of a new doublet at 9.6 ppm consistent with coupling to a Ni-F (Figure A3.78). Similarly, the ^{19}F NMR spectrum shows the appearance of resonances consistent with Ni- C_6F_5 (-117.5, -166.4, and -167.1 ppm) and Ni-F (-383.6 ppm) moieties (Figures A3.74-A3.76). The product resonances grow in with an average observed rate of $1.6(2)E-4\ s^{-1}$, and level off after ~7 hours with an average yield of 25(3)% (Figures A3.77 and A3.79, Table A3.16). The reaction between $Ni(COD)_2$, 2 equivalents of **K1** and 21 equivalents of C_6F_6 was also examined by monitoring the decay of the absorbance at 464 nm using UV-vis spectroscopy (Figure A3.40). The observed rate of decay is on the same order of magnitude as the rate of formation determined by NMR methods ($5.6(4)E-4\ s^{-1}$). Reducing the amount of added

K1 to 1 equivalent decreases the observed rate ($2.8\text{E}-4\text{ s}^{-1}$), which is inconsistent with a mechanism involving the dissociation of a ligand prior to OA (Figure A3.39). The rate is also reduced with the addition of 3, 4, or 8 equivalents of **K1**, with the appearance of a new absorbance at 375 nm suggesting additional coordination of **K1** to Ni may be possible (Figures A3.41-A3.43). As a control, the absorbance at 464 nm was monitored in the absence of substrate and indicated minimal decay over the same time frame (Figure A3.44).

Carrying out the same reaction with PEt_3 and PCy_3 results in the growth of similar NMR signals as those observed with **K1**, but with significantly slower rates of product formation ($3.7(7)\text{E}-6\text{ s}^{-1}$ and $2.0(1)\text{E}-5\text{ s}^{-1}$, respectively) (Figures S80-S87, Table A3.16). In contrast to **K1**, the OA product growth continues throughout the time the reaction was monitored, reaching 24(2)% at 114 h for PEt_3 and 66(15)% at 53 h for PCy_3 . The enhanced rate observed with **K1** not only supports previous observations that anionic groups enhance rates of OA reactions,⁹⁴⁻⁹⁶ but also demonstrates that the rate enhancement is greater than would be predicted on the basis of donor strength. This is perhaps most clearly illustrated by the one order of magnitude rate acceleration with **K1** over PCy_3 , despite the nearly identical donor strengths predicted by our analysis. A distinct mechanism for electrostatic rate enhancement beyond an increase in donor strength has been suggested previously with an anionic carborane phosphine, wherein accelerated OA reactivity was attributed to ligand dissociation and transition state (TS) stabilization.⁹⁵ The exact nature of the rate acceleration with **K1** is not yet clear. It is possible that the TS is lowered by the presence of an electric field generated by the BF_3^- , as is predicted computationally,⁵³ but other factors, such as ion pairing with K^+ , may also be determinative. Regardless, these results

emphasize that anionic charges enhance reactivity through mechanisms beyond simply increasing donor strength.

3.2.7 Catalytic Defluoroborylation Reactivity

The significant rate acceleration observed in stoichiometric reactivity led us to investigate catalytic C–F borylation with **K1** and Ni(COD)₂. Defluoroborylation of fluorinated arenes with Ni has been reported previously with N-heterocyclic carbene (NHC) and PCy₃ ligands.¹³¹⁻¹³³ The use of strongly donating ligands is consistent with the difficulty of the OA step, as C–F bonds have the highest BDE among carbon-halogen bonds.¹³¹ Likewise, high catalyst loadings (10%), reaction temperatures (110 °C), and long reaction times (≥12 h) highlight the difficulty of these transformations.

Optimization reactions were carried out using **K1** and Ni(COD)₂ for the defluoroborylation of 1,3-difluorobenzene using B₂pin₂ (bis(pinacolato)diboron) as the test substrate. Ultimately, a 50% yield of 1-Bpin-3-C₆FH₄ was realized with the following conditions: 9% catalyst loading with 1.8 equivalents of B₂pin₂, 0.72-0.75 equivalents of CsOH•xH₂O (15-20% H₂O), and 1.9 equivalents of methanol in THF heated at 50 °C for 4 hours (Tables 3.2 and A3.17-A3.24 contain information on optimization trials). Notably, substituting **K1** for PEt₃, PCy₃, or PPh₂Et under identical reaction conditions results in no conversion to the borylated product (Tables 3.2 and A3.21). NMR monitoring over time indicates that the reaction is complete after 2 hours (Tables 3.2 and A3.21). Increasing the temperature to 100 °C for 2 hours or stirring at room temperature for 22 hours only slightly affects the yield (48% and 44%, respectively, Tables 3.2 and A3.22). Switching B₂pin₂ for B₂nep₂ (bis(neopentylglycolato)diboron) or B₂cat₂ (bis(catecholato)diboron) to test alternative transmetallating agents significantly reduces the yield (32% and 0%, Tables 3.2

and A3.22), in contrast to previous studies with PCy₃.¹³⁴ Both MeOH and CsOH are required for catalysis, with alternative alcohols or metal salts reducing the yield. Exchanging the K⁺ counterion on **1** for more solubilizing counterions does not improve the

Defluoroborylation conditions explored with 1,3 difluorobenzene		
Variation	Time (h)	Yield borylated product
None	1	47%
None	2	55%
None	4	54%
None	6	55%
PEt ₃ (2 equiv.) no K1	4	0%
PPh ₂ Et (2 equiv.) no K1	4	0%
PCy ₃ (2 equiv.), no K1	4	0%
B ₂ neop ₂ (20 equiv.), no B ₂ pin ₂	4	32
B ₂ cat ₂ (20 equiv.), no B ₂ pin ₂	2	0
LiOMe (10 equiv.), no CsOH·xH ₂ O	4	29
LiOMe (10 equiv.), no CsOH·xH ₂ O, no MeOH	4	10
No CsOH·xH ₂ O	2	8
No CsOH·xH ₂ O, no MeOH	2	6
RT	22	44
100 °C	2	48

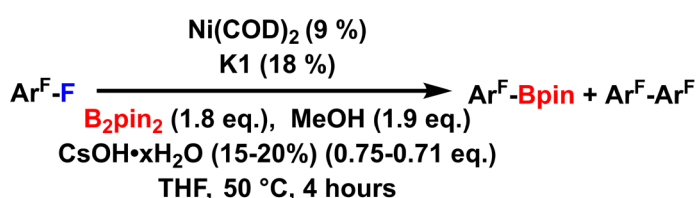
Reaction conditions unless otherwise stated – 1,3 C₆F₂H₄ (40 μL, 0.4 mmol, 11 equiv.), Ni(COD)₂ (10 mg, 0.036 mmol), K1 (22 mg, 0.072 mmol), B₂pin₂ (184 mg, 0.72 mmol, 20 equiv.), CsOH·xH₂O (15-20% H₂O) (54 mg, 0.29-0.31 mmol, 8-8.5 equiv.), CF₃Ph (20 μL, 0.16 mmol, 4.5 equiv.) and MeOH (30 μL, 0.72 mmol, 20 equiv.) were dissolved in 1 mL of THF and heated with stirring at 50 °C for the specified time. Yields determined by integration of ¹⁹F NMR peak of 1-Bpin-3-C₆FH₄ and comparison to the internal standard CF₃Ph. Yields are relative to the theoretical yield (0.4 mmol) determined using 1,3 C₆F₂H₄.

*Standard order of addition: combine Ni(COD)₂, K1, and B₂pin₂ in 1 mL THF. Add CF₃Ph, then 1,3 C₆F₂H₄, then CsOH·xH₂O (15-20% H₂O) and finally MeOH before placing on hot plate.

Table 3.2 Selected optimization conditions varied from the final conditions developed for defluoroborylation of 1,3-difluorobenzene. See SI for additional optimizations.

yield (Table A3.23), and no trend is observed with solvent ϵ across a limited series of ethereal solvents (Table A3.24).

This method was extended to other fluoroarenes to examine the scope of reactivity (Figure 3.4). The highest yield observed is for 1,3 difluorobenzene (50%), followed by fluorobenzene (42%), with lower yields for more highly fluorinated substrates. The trend of decreasing yields with higher levels of fluorination contrasts with the trend observed with an NHC, where more highly fluorinated substrates are more easily defluoroborylated.¹³³ Additionally, homocoupling is competitive in substrates with adjacent fluorine atoms in our system. The fluorobenzene borylation with K1 is higher than



Substrate	Yield borylated product		Yield coupled product	
C ₆ H ₅ F	C ₆ H ₅ Bpin	42(3)% ^a	n/a	
1,2-C ₆ F ₂ H ₄	1-Bpin-2-C ₆ FH ₄	14(1)%	2,2'-F ₂ -1,1'-Ph ₂	56(2)%
1,3-C ₆ F ₂ H ₄	1-Bpin-3-C ₆ FH ₄	50(1)%	n/a	
1,4-C ₆ F ₂ H ₄	1-Bpin-4-C ₆ FH ₄	21(1)%	n/a	
1,2,4-C ₆ F ₃ H ₃	n/a		2,2',5,5'-F ₄ -1,1'-Ph ₂	29(5)%
1,3,5-C ₆ F ₃ H ₃	1-Bpin-3,5-C ₆ F ₂ H ₃	20(1)%	n/a	
	1,3-Bpin-5-C ₆ FH ₃	18(3)%		

Figure 3.4 Substrate scope defluoroborylation catalysis. Unless otherwise specified, all reactions were carried out in 1 mL of THF with Ni(COD)₂ (10 mg, 0.036 mmol), K1 (22 mg, 0.072 mmol), B₂pin₂ (184 mg, 0.72 mmol), CsOH·xH₂O (15-20%) (54 mg, 0.29-0.31 mmol), MeOH (30 μ L, 0.72 mmol), CF₃Ph (20 μ L, 0.16 mmol) and substrate (0.4 mmol) and were heated with stirring for 4 hours at 50 °C. All yields unless otherwise specified were determined in triplicate by comparison to an internal CF₃Ph integral standard. (a) Yield determined using GCMS, no CF₃Ph added to the reaction. For more details see SI.

that with an NHC ligand (20%),¹³³ but in general other systems perform defluoroborylation of more diverse fluoroarenes with higher yields than the current system.^{131,132}

Based on the observed formation of a C-F OA product with C₆F₆, it is likely that defluoroborylation proceeds through a traditional OA, transmetalation, and reductive elimination

mechanism. The differing reactivity trend with arene fluorination implies that the enhanced OA rate in the present system makes transmetalation the turnover limiting step. This hypothesis is consistent with increased yields with an excess of B₂pin₂ as well as the need for more nucleophilic hydroxide or alkoxide additives over fluoride sources. We speculate that in-situ generated methoxide may facilitate transmetalation of B₂pin₂ by exchanging with Ni-F intermediates, as a similar σ -bond metathesis of B₂pin₂ with Ni alkoxide complexes has been reported.¹³⁵ However, the specific role played by Cs⁺ and MeOH remains unclear. Faster rates and unique reaction conditions for this system (ie. lower temperature, base, water and alcohol) suggest that it may offer complementary reactivity to the established neutral phosphine systems and motivates further investigation. Regardless of specific methodological applications, the fact that the inclusion of a BF₃⁻ group enables a diarylalkyl phosphine to perform comparably with an NHC in C-F borylation highlights how electrostatic effects can both dramatically enhance stoichiometric OA reactivity as well as catalytic processes.

3.3 Conclusions

In conclusion, a new anionic phosphine ligand has been synthesized and demonstrates that the inclusion of an anionic trifluoroborate group dramatically increases the donor properties relative to neutral analogues. Furthermore, a series of experiments and calculations have demonstrated that a significant portion of the increase in donor strength arises from electrostatic as opposed to inductive effects. The electrostatic interactions in this ligand accelerate OA rates by an order of magnitude compared to ligands of similar donor strength, consistent with theoretical predictions. This enhanced OA reactivity can be leveraged for

the catalytic defluoroborylation of C–F bonds with reactivity trends that differ from previously reported examples. While there are several reports on the influence of appended anionic groups on mono- or polydentate phosphine ligands, this work is the first case where the relative contributions from inductive versus electrostatic donation have been disentangled. The ability of charged groups to stabilize specific resonance structures, such as the zwitterionic $\text{Se}^--\text{P}^+\text{R}_3$ structure, offers tremendous potential in tuning catalytic systems as we demonstrate here. The fact that a major portion of the increase in donor strength arises from electrostatic effects in common organic solvents with charge-diffuse counterions has important implications for ligand design as the directionality of electric fields provides a unique variable for influencing reactivity and breaking classic free-energy relationships. Given that charged functional groups exert a significant through space influence on donor properties and reactivity, the location of a charge in space relative to the ligand donor atom and the metal center is expected to likewise have a significant effect.

3.4 Experimental

3.4.1 General Considerations

All reagents were purchased from commercial suppliers and used without further purification unless otherwise specified. $\text{K}[\text{ICH}_2\text{BF}_3]$,¹³⁶ $\text{K}[\text{PPh}_2(o\text{-BF}_3\text{Ph})]$,^{90,91,137} SePPh_3 and SePPh_2Et ^{113,122} were synthesized according to literature procedures. All manipulations were carried out under an atmosphere of N_2 using standard Schlenk and glovebox techniques. Glassware was dried at 180 °C for a minimum of two hours and cooled under vacuum prior to use. All reactions were carried out in 20 mL scintillation vials unless otherwise specified. Catalytic reactions were carried out in 4 mL screw thread borosilicate glass vials. All volumes below 1 mL were measured using

Hamilton 100 or 250 μL syringes. Solvents were dried on a solvent purification system from Pure Process Technology and stored over 4 \AA molecular sieves under N_2 . Tetrahydrofuran was stirred over NaK alloy and run through an additional activated alumina plug prior to use to ensure dryness. Solvents were tested for H_2O and O_2 using a standard solution of sodium-benzophenone ketyl radical anion. C_6D_6 , CDCl_3 , acetone- d_6 , CD_3CN , and $\text{DMSO-}d_6$ were dried by passage over a column of activated alumina and stored over 4 \AA molecular sieves in the glovebox. ^1H , $^{13}\text{C}\{^1\text{H}\}$, $^{19}\text{F}\{^1\text{H}\}$, $^{11}\text{B}\{^1\text{H}\}$, and $^{31}\text{P}\{^1\text{H}\}$ data were acquired on a combination of three spectrometers: a 400 MHz Bruker DRX spectrometer equipped with a BBO probe; a 500 MHz Bruker Avance-II+ spectrometer equipped with a $^1\text{H}\{^{19}\text{F},^{13}\text{C},^{31}\text{P}\}$ QNP probe; and a 500 MHz Bruker Avance III HD spectrometer equipped with a Bruker BBFO “Smart” probe. All spectrometers use Topspin. Chemical shifts are reported in ppm units referenced to residual solvent resonances for ^1H and $^{13}\text{C}\{^1\text{H}\}$ spectra, and external standards for ^{31}P , ^{11}B , and ^{19}F . Assignments for ^{13}C NMR resonances were made based on previously reported (PPh_4) and related compounds ($\text{Rh}(\text{acac})(\text{CO})\text{PPh}_3$, PPh_2Et , $\text{PPh}_2(2\text{-BF}_3\text{-Ph})$).^{90,91,138-141} Unless otherwise indicated, multipoint baseline corrections were applied to ^{19}F NMR spectra in Mnova to remove broad peaks in the baseline around 150 – 220 ppm resulting from Teflon within the probe. NMR samples were prepared by dissolving approximately 10-20 mg of the sample in about 0.5 mL of the appropriate deuterated solvent. No change in signal position or coupling was observed as a function of concentration. IR spectra were recorded on a Bruker Tensor II. Solution IR were recorded in a solution cell using CaF_2 windows, and then the solvent signal was subtracted out. Solid IR were recorded using a KBr pellet. Elemental analysis was performed by Midwest Microlabs.

3.4.2 Synthesis of Reported Compounds

Synthesis of Ph₂PCH₂BF₃K (K1). To a stirring solution of PPh₂ (0.368 g, 1.97 mmol) in THF (5 mL) was added a solution of KHMDS (0.398 g, 1.99 mmol, 1 eq) in THF (5 mL), resulting in a bright red homogeneous solution. This was added dropwise over 20 minutes to a stirring slurry of K[ICH₂BF₃] (0.541 g, 2.18 mmol, 1.1 eq) in THF (5 mL). After addition, the resulting slurry was stirred for 1 hour, placed in the freezer at -40 °C to settle for 1 hour and then filtered through Celite. The filtrate was dried under vacuum, and the resulting sticky white solid was washed with Et₂O (2 x 10 mL), leaving behind Ph₂PCH₂BF₃K as a white powder (0.301 g, 0.98 mmol, 50%). ¹H NMR (400 MHz, 25 °C, DMSO-*d*₆) δ = 7.33 (t, *J* = 8 Hz, 4H, *o*-Ph-H), 7.24-7.14 (m, 6H, *m*- and *p*-Ph-H), 0.8 (dq, *J*_{P-H} = 14 Hz, *J*_{F-H} = 4 Hz, 2H, CH₂BF₃). ³¹P{¹H} NMR (162 MHz, 25 °C, DMSO-*d*₆) δ = -15.9 (q, *J*_{P-F} = 13 Hz, PPh₂(CH₂BF₃)). ¹⁹F{¹H} NMR (376 MHz, 25 °C, DMSO-*d*₆) δ = -133.9 (broad s, 3F, BF₃). ¹³C{¹H} NMR (126 MHz, 25 °C, DMSO-*d*₆) δ = 144.4 (d, *J*_{C-P} = 25 Hz, *C*_{ipso}), 132.0 (d, *J*_{C-P} = 50 Hz, *C*_{ortho}), 127.6 (s, *C*_{para}), 126.9 (s, *C*_{meta}), 17.0 (broad s, CH₂BF₃). ¹¹B{¹H} NMR (160 MHz, 25 °C, DMSO-*d*₆) δ = 4.0 (broad s). IR (KBr pellet): 3419 (w), 3053 (m), 2916 (w), 2885 (w), 1954 (w), 1881 (w), 1807 (w), 1584 (m), 1480 (m), 1433 (s), 1386 (m), 1168 (s), 1093 (m), 1046 (s), 931 (s), 742 (s), 697 (s). K1 was too air sensitive for reliable elemental analysis, and instead was consistent with full oxidation of the phosphine sample despite multiple attempts. Elem. Anal: Calc'd (Ph₂PCH₂BF₃K+O): C 48.5 H 3.8 N 0 Found: C 48.1 H 4.0 N 0.

Synthesis of [PPh₄][Rh(acac)(CO)(PPh₂(CH₂BF₃))] (2). To a stirring THF solution (3 mL) of Rh(acac)(CO)₂ (67 mg, 0.26 mmol) was added a THF solution (5 mL) of K1 (80 mg, 0.26 mmol, 1 eq) and a DCM solution (4 mL) of PPh₄Br (109 mg, 0.26 mmol, 1 eq), resulting in a color change from light yellow to brown. The reaction was stirred at room temperature for 1 hour, then filtered,

evacuated to dryness, and washed with petroleum ether leaving $[\text{PPh}_4][\text{Rh}(\text{acac})(\text{CO})(\text{PPh}_2(\text{CH}_2\text{BF}_3))]$ as a brown oil, which was crystallized by vapor diffusion of Et₂O into a CHCl₃ or DCM solution at room temperature to yield yellow crystals (146 mg, 0.17 mmol, 67%). ¹H NMR (400 MHz, 25 °C, CDCl₃) δ = 7.85 (m, 8H, Ph and PPh₄) 7.73 (m, 8H, PPh₄), 7.57 (m, 8H, PPh₄) 7.19 (m, 6H, Ph) 5.30 (s, 1 H, CH_{acac}), 1.92 (s, 3H, CH_{3acac}), 1.62 (m, 2H, CH₂BF₃), 1.56 (s, 3H, CH_{3acac}). ³¹P {¹H} NMR (162 MHz, 25 °C, CDCl₃) δ = 40.4 (dq, *J*_{P-Rh} = 166 Hz, *J*_{P-F} = 10 Hz, 1P, PPh₂(CH₂BF₃)), 25.6 (s, 1P, PPh₄). ¹⁹F {¹H} NMR (376 MHz, 25 °C, CDCl₃) δ = -131.6 (broad s, 3F, BF₃). ¹³C {¹H} NMR (126 MHz, 25 °C, CDCl₃) δ = 190.5 (dd, *J*_{C-Rh} = 79 Hz, *J*_{C-P} = 25 Hz, Rh-CO), 186.6 (s, CO_{acac}), 185.6 (s, CO_{acac}), 137.7 (d, *J*_{C-P} = 49 Hz, C_{ipso}), 135.9 (d, *J*_{C-P} = 4 Hz, PPh₄ C_{para}), 134.5 (d, *J*_{C-P} = 10 Hz, PPh₄ C_{meta}), 134.0 (d, *J*_{C-P} = 11 Hz, C_{ortho}), 130.9 (d, *J*_{C-P} = 13 Hz, PPh₄ C_{ortho}), 128.5 (d, *J*_{C-P} = 3 Hz, C_{para}), 127.0 (d, *J*_{C-P} = 10 Hz, C_{meta}), 117.6 (d, *J*_{C-P} = 89 Hz, PPh₄ C_{ipso}), 100.3 (s, CH_{acac}), 27.7 (d, *J*_{C-P} = 5 Hz, CH_{3acac}), 27.0 (s, CH_{3acac}), 19.1 (br s, CH₂BF₃). ¹¹B {¹H} NMR (160 MHz, 25 °C, CDCl₃) δ = 3.6 (broad s). IR (DCM solution, CaF₂ windows, cm⁻¹): 3068 (m), 2969 (s), 2859 (m), 1962 (s, Rh-C≡O), 1574 (s, acac C=O), 1514 (s), 1487 (m), 1434 (m), 1383 (m), 1167 (m), 1104 (s). Elem. Anal: Calc'd ([PPh₄][Rh(acac)(CO)(PPh₂(CH₂BF₃))] C 61.8 H 4.7 N 0. Found: C 61.5 H 4.9 N 0.

Synthesis of [PPh₄][SePPh₂(CH₂BF₃)] ([PPh₄][¹Se]). To a stirring solution of K1 (50 mg, 0.16 mmol) in THF (5 mL) was added a 10-fold excess of elemental selenium powder (129 mg, 1.6 mmol, 10 eq), followed by PPh₄Br (75 mg, 0.17 mmol, 1.1 eq) in DCM (3 mL). This mixture was stirred overnight, then filtered through Celite and all volatiles were removed in vacuo. Crystallization by vapor diffusion of Et₂O into a CDCl₃ or DCM solution of [PPh₄][¹Se] gave the product as clear crystals (60 mg, 0.087 mmol, 55%). Analytically pure samples were obtained by crystallizing [PPh₄][¹Se] from a mixture of hot MeCN and THF. ¹H NMR (400 MHz, 25 °C,

CDCl_3) $\delta = 7.98\text{-}7.92$ (m, 4H, Ph-H), 7.88-7.82 (m, 4H, *p*-Ph-H PPh₄), 7.77-7.70 (m, 8H, PPh₄), 7.65-7.57 (m, 8H, PPh₄), 7.30-7.24 (m, 6H, Ph-H) 1.89 (dq, $J_{\text{P-H}} = 10$ Hz, $J_{\text{F-H}} = 4$ Hz, 2H, CH_2BF_3). $^{31}\text{P}\{^1\text{H}\}$ NMR (162 MHz, 25 °C, CDCl_3) $\delta = 33.59$ (q, $J_{\text{P-F}} = 10$ Hz, $J_{\text{P-Se}} = 656$ Hz, 1P, $\text{SePPh}_2(\text{CH}_2\text{BF}_3)$), 22.08 (s, 1P, PPh₄). $^{19}\text{F}\{^1\text{H}\}$ NMR (376 MHz, 25 °C, CDCl_3) $\delta = -132.93$ (broad s, 3F, BF_3). $^{13}\text{C}\{^1\text{H}\}$ NMR (126 MHz, 25 °C, CDCl_3) $\delta = 135.9$ (d, $J_{\text{C-P}} = 88.2$ Hz, C_{ipso}), 135.9 (s, PPh₄ C_{para}), 134.4 (d, $J_{\text{C-P}} = 12.6$ Hz, PPh₄ C_{meta}), 132.3 (d, $J_{\text{C-P}} = 12.6$ Hz, C_{ortho}), 130.9 (d, $J_{\text{C-P}} = 25.2$ Hz, PPh₄ C_{ortho}), 129.8 (s, C_{para}), 127.5 (d, $J_{\text{C-P}} = 25.2$ Hz, C_{meta}), 117.5 (d, $J_{\text{C-P}} = 113.4$ Hz, PPh₄ C_{ipso}), 26.7 (broad s, CH_2BF_3). $^{11}\text{B}\{^1\text{H}\}$ NMR (160 MHz, 25 °C, CDCl_3) $\delta = 3.1$ (broad s). IR (CDCl_3 solution): 3058 (m), 1978 (w), 1907 (w), 1814 (w), 1590 (m), 1487 (m), 1438 (s), 1310 (w), 1144 (m), 1103 (s), 1023 (s). Elem. Anal: Calc'd ([PPh₄][SePPh₂(CH₂BF₃)] C 64.8 H 4.7 N 0. Found: C 65.0 H 4.7 N 0.3.

Synthesis of [TEA][SePPh₂(CH₂BF₃)] ([TEA][¹Se]). To a stirring solution of K1 (50 mg, 0.16 mmol) in THF (5 mL) was added a 10-fold excess of elemental selenium powder (129 mg, 1.6 mmol, 10 eq), followed by TEABr (36 mg, 0.17 mmol, 1.05 eq) in DCM (3 mL). This mixture was stirred overnight, then filtered through Celite and all volatiles were removed in vacuo. Crystallization by vapor diffusion or layering of Et₂O into a DCM solution of [TEA][¹Se] at -35 °C gave the product as clear colorless needle shaped crystals (49 mg, 0.103 mmol, 63%). ^1H NMR (400 MHz, 25 °C, CDCl_3) $\delta = 7.93\text{-}7.84$ (m, 4H, Ph-H), 7.36-7.3 (m, 6H, Ph-H), 3.18 (q, $J_{\text{H-H}} = 5$ Hz, 8 H, $\text{N}(\text{CH}_2\text{CH}_3)_4$), 1.94 (dq, $J_{\text{P-H}} = 16$ Hz, $J_{\text{F-H}} = 4$ Hz, 2H, CH_2BF_3), 1.20 (t, $J_{\text{H-H}} = 4$ Hz, 12 H, $\text{N}(\text{CH}_2\text{CH}_3)_4$). $^{31}\text{P}\{^1\text{H}\}$ NMR (162 MHz, 25 °C, CDCl_3) $\delta = 32.2$ (q, $J_{\text{P-F}} = 10$ Hz, $J_{\text{P-Se}} = 678$ Hz, 1P, $\text{SePPh}_2(\text{CH}_2\text{BF}_3)$). $^{19}\text{F}\{^1\text{H}\}$ NMR (376 MHz, 25 °C, CDCl_3) $\delta = -131.4$ (broad s, 3F, BF_3). $^{13}\text{C}\{^1\text{H}\}$ NMR (101 MHz, 25 °C, CDCl_3) $\delta = 136.4$ (d, $J_{\text{C-P}} = 70$ Hz, C_{ipso}), 131.5 (d, $J_{\text{C-P}} = 11$ Hz, C_{ortho}), 130.0 (d, $J_{\text{C-P}} = 2$, C_{para}), 127.8 (d, $J_{\text{C-P}} = 12$ Hz, C_{meta}), 52.5 (t, $J_{\text{C-N}} = 2$ Hz, $\text{N}(\text{CH}_2\text{CH}_3)_4$),

23.3 (broad s, CH₂BF₃), 7.6 (s, N(CH₂CH₃)₄). ¹¹B {¹H} NMR (160 MHz, 25 °C, CDCl₃) δ = 2.9 (broad s). IR (KBr pellet): 2981 (w), 2948(w), 1486, (m), 1436 (m), 1393 (w), 1370(w), 1310 (w), 1262 (w), 1139 (s), 1099 (s), 1023 (s), 969 (s), 953 (s), 808 (m), 762 (m), 732 (m), 698 (s). Elem. Anal: Calc'd ([TEA][SePPh₂(CH₂BF₃)] C 53.0 H 6.8 N 2.9. Found: C 52.8 H 7.0 N 3.1.

Synthesis of [PPh₄][SePPh₂(2-BF₃Ph)] ([PPh₄][³Se]). To a stirring acetonitrile solution (10 mL) of K[PPh₂(2-BF₃Ph)] (50 mg, 0.14 mmol) was added an excess of elemental selenium powder (109 mg, 1.4 mmol, 10 eq) and this mixture was stirred for 6 hours at room temperature. The solution was filtered, and PPh₄Br (62 mg, 0.14 mmol, 1 eq) was added as a solid, the resulting slurry was stirred for 10 min, then all volatiles were removed under vacuum. The white powder was washed with 2 mL CHCl₃ to remove excess PPh₄Br, and then extracted into MeCN. Crystallization by diffusion of Et₂O into the filtered MeCN solution afforded [PPh₄][SePPh₂(2-BF₃Ph)] as clear crystals (Yield: 10 mg, 0.014 mmol, 10%). ¹H NMR (400 MHz, 25 °C, CD₃CN) δ = 8.04 (dd, 1H, *J*_{F-H} = 16 Hz, *J*_{H-H} = 8 Hz) 7.91 (t, 4H, *J* = 8 Hz), 7.76-7.65 (m, 20H), 7.4-7.2 (m, 9H). ³¹P {¹H} NMR (162 MHz, 25 °C, CD₃CN) δ = 40.3 (s, *J*_{P-Se} = 700 Hz, 1P, SePPh₂(2-BF₃Ph)), 22.9 (s, 1P, PPh₄). ¹⁹F {¹H} NMR (376 MHz, 25 °C, CD₃CN) δ = -132.6 (m, 3F, BF₃). ¹³C {¹H} NMR (126 MHz, 25 °C, CD₃CN) δ = 136.9 (d, *J*_{C-P} = 97 Hz, C_{ipso}), 136.4 (s, PPh₄ C_{para}), 135.9 (s), 135.8 (d, *J*_{C-P} = 16 Hz, C³-Ar), 135.7 (d, *J*_{C-P} = 13 Hz, PPh₄ C_{meta}), 133.4 (d, *J*_{C-P} = 13 Hz, C_{ortho}), 132.0 (s), 131.3 (d, *J*_{C-P} = 13 Hz, PPh₄ C_{ortho}), 130.9 (s, C_{para}), 128.3 (d, *J*_{C-P} = 13 Hz, C_{meta}), 126.4 (d, *J*_{C-P} = 25 Hz, C⁶-Ar), 119.0 (d, *J*_{C-P} = 113 Hz, PPh₄ C_{ipso}). ¹¹B {¹H} NMR (160 MHz, 25 °C, CDCl₃) δ = 2.4 (broad q, *J*_{B-F} = 51 Hz). IR (KBr pellet): 3048 (m) 1586 (m) 1482 (m) 1434 (s) 1315 (w) 1260 (w) 1181 (m) 1162 (m) 1109 (s) 1052 (w) 978 (m) 955 (m) 935 (s) 759 (m) 725 (s) 691 (s) 610 (m). Elem. Anal: Calc'd ([PPh₄][SePPh₂(2-BF₃Ph)]) C 67.5 H 4.6 N 0. Found: C 67.7 H 4.9 N 0.

3.4.3 X-Ray Structure Determination

The diffraction data were measured at 100 K on a Bruker D8 VENTURE with PHOTON 100 CMOS detector system equipped with a Mo-target micro-focus X-ray tube ($\lambda = 0.71073 \text{ \AA}$). Data reduction and integration were performed with the Bruker APEX3 software package (Bruker AXS, version 2015.5-2, 2015). Data were scaled and corrected for absorption effects using the multi-scan procedure as implemented in SADABS (Bruker AXS, version 2014/5, 2015, part of Bruker APEX3 software package). The structure was solved by the dual method implemented in SHELXT¹⁴² and refined by a full-matrix least-squares procedure using OLEX23¹⁴³ software package (XL refinement program version 2014/7¹⁴⁴). Suitable crystals were mounted on a cryo-loop and transferred into the cold nitrogen stream of the Bruker D8 Venture diffractometer. Most of the hydrogen atoms were generated by geometrical considerations and constrained to idealized geometries and allowed to ride on their carrier atoms with an isotropic displacement parameter related to the equivalent displacement parameter of their carrier atoms. The co-crystallized THF and phenyl rings of the phosphine were modeled for disorder in K1. For [PPh₄][1^{Se}], after fully solving and refining the structure, a relatively large residual peak was observed suggesting a possible co-crystallized submixture. The peak was located close to the CH₂-BF₃ bond, and the distance correlated well with a P-I bond length. Thus, this component was refined as a (Ph₂)P-I (refined occupancy about 4%). While it is hard to concretely assign the identity of such a small submixture, we note that several examples of (R₂)P-I molecules have been previously reported with P-I bond lengths between 2.45-2.55 Å).¹⁴⁵

3.4.4 Discussion of van der Waals Radii in **2**

Given that the van der Waals radii of B, C, O and Rh are 205, 196, 171, and 232 pm, the sum of the covalent radii for B···C, B···O, and B···Rh are 401, 376, and 437 respectively.¹⁴⁶ The

interatomic distances for B···C, B···O, and B···Rh in the crystal structure of **2** are 371.9(4), 395.5(4) and 415.0(4) pm. Dividing the interatomic distances by the sum of the covalent radii gives 0.93, 1.05, and 0.95 for B···C, B···O, and B···Rh, respectively. Although the interatomic distances between B···C and B···O are significantly shorter than that between B···Rh, the lengths normalized for the sum of covalent radii are similar.

3.4.5 Computational Procedures

General

The structure of **1**^{Se}, SePPh₂Et, and **2** were optimized in Orca version 4.0¹⁴⁷ using the B3P Functional, with the def2-TZVP¹⁴⁸ basis set on C, H, B, and F, and def2-TZVPP¹⁴⁸ basis set on Rh, Se, and P. Rh also had an ECP applied. Different local minima geometries of the BF₃ group were found by changing the input geometry, which resulted in optimization to two local minima in the two extremes of the BF₃ positioning. The “transoid” geometry (with a larger Se-P-C-B dihedral) was the global minimum based on comparison of energy by 3.4 kcal, but both geometries were confirmed as local minima with frequency calculations.

NMR couplings were calculated in Gaussian16¹⁴⁹ with the “Mixed” method using mPW1PW91 functional and 6-311++G(2d,2p) basis set, similar to methods used in the literature to calculate Se chemical shifts.¹⁵⁰ The average coupling was weighted for a Boltzmann population of the cisoid and transoid isomers based on the calculated energy difference which predicts a nearly 100% population of the ground state transoid isomer at room temperature.

We also considered several solvation models to understand to rationalize the trends we observed. While implicit solvation failed to reproduce our observed trends, explicit solvation did match our observations. For these calculations, the starting geometries of **1**^{Se} were used with 10 randomly arranged solvent molecules of either MeCN, DCM, or CHCl₃. The geometry of this model was

then optimized with ORCA 5.0¹⁵¹ with the BP86 functional, with def2-QZVP basis sets on all atoms as well as the D3BJ dispersion correction. Local minima were found, but we did not perform frequency calculations both due to the size of the system, and the high likelihood of multiple minima of similar energy due to minor changes in solvent coordinates. NMR couplings were then calculated in ORCA 5.0 using the EPR/NMR module with the same basis sets but with the O3LYP functional.

Use of Coulomb's Law to Estimate the Electric Field

The electric field exerted at phosphorus in **1^{Se}** as a result of the anionic BF₃ moiety was estimated using a variation of Coulomb's law. The electric field equation was obtained by dividing coulombs law by q_1 and explicitly separating the vector connecting the points into x, y and z components.¹⁵² Doing this results in three equations describing the x, y and z components of the electric field where the z-axis vector is defined as the P-Se bond vector. The equation for the z component is shown below.

$$E_z(x_1, y_1, z_1) = \frac{q_2}{4\pi\epsilon_0} \frac{z_1 - z_2}{[(x_1 - x_2)^2 + (y_1 - y_2)^2 + (z_1 - z_2)^2]^{3/2}}$$

The charge of q_2 is in Coulombs, the constant of proportionality is in V/mC (or equivalently Nm²/C²), and the x,y,z coordinates are in meters. The resulting electric field is in units of V/m.

Two separate optimized geometries for **1^{Se}** were considered, the transoid and cisoid rotamers (Figures A3.52 and A3.53). Both geometries were considered in order to estimate the range of accessible geometries in solution. Starting with optimized geometries, the z-axis was aligned along the P-Se bond in Avogadro.¹⁵³ The x,y,z coordinates for the B were used as the location of a negative charge, point 2, and the coordinates for phosphorus were used as point 1. An example of

the code put into Matlab to calculate the electric field in the transoid geometry (coordinates included in code) is shown below. The electric field calculated at P for this geometry in $\text{V}/\text{\AA}$ was $E(x, y, z) = (0.5145, 0.9015, -1.0672)$. The electric field was analogously calculated at Se(x,y,z) = (0, 0, 2.14028) in $\text{V}/\text{\AA}$ and was (0.1334, 0.2338, -0.5423). The coordinates for boron and selenium in the cisoid geometry were $B(x, y, z) = (0.52958, 2.85487, -0.94860)$ and $Se(x,y,z) = (0, 0, 2.11743)$. The electric field calculated at P in the cisoid geometry in $\text{V}/\text{\AA}$ is $E(x, y, z) = (0.2679, 1.4444, -0.4799)$. The electric field at Se in the cisoid geometry in $\text{V}/\text{\AA}$ was (0.1014, 0.5467, -0.5872). The same code was used to estimate the location for a point charge on the z axis below the phosphine to replicate the electric field. The x and y coordinates were set to 0 and values were entered into the z coordinate until a similar field was predicted. In this case, placing a negative point charge at (0, 0, -3.7) resulted in a predicted field at P of (0, 0, -1.0533). This negative point charge was included via the “charge” input in Gaussian.

NBO Analysis

We have considered **1**, **1^{Se}**, and **2** with an NBO/NPA analysis to look for any donor-acceptor interactions between non-adjacent atoms. Using the second-order perturbation analysis we have been unable to find any donor-acceptor interactions >2 kcal/mol between B/F and P/Se/Rh in any of the structures we have examined.

We have also used NBO analysis to examine our simplified assumption of a “point charge” centered at B. We have used NBO analysis to look at the sum of the charges on B and the 4 atoms directly bound to it. This sum is -1.62. In the neutral congener Ph_2PEt this analogous sum is -0.69. Comparing these two net values shows that there is almost perfectly an additional -1 charge on the BF_3 substituted phosphine. Furthermore, comparison of the individual charges on each atom shows that this negative charge is fairly symmetrically distributed, albeit with a slightly larger

change going from H to F (more negative) and from C to B (more positive) than is observed in the change of charge on the common methylene carbon. As the electric field at P or Se will be an average of all the charge density, the effects from each individual atom will be averaged. Overall, while there are some subtleties as to the arrangement of the charge, the NBO analysis does support that the estimation of a point charge localized at B is reasonable. This demonstrates that simple electrostatic relationships (Coulomb's Law) and charge assumptions (approximating a BF₃ as a point charge) provide a good model for solution phase electrostatic effects.

3.4.6 Discussion of the Slopes of J_{P-Se} vs. $1/4\pi\epsilon$

The linear fits of J_{P-Se} versus $1/(4\pi\epsilon)$ for [PPh₄][1^{Se}] and [PPh₄][3^{Se}] show that Coulomb's law provides a reasonable approximation for how the donor properties of these phosphine selenides vary with different solvents:

$$F = \frac{q_1 q_2}{4\pi\epsilon r^2}$$

Coulomb's law also has dependences on the charges involved in the electrostatic interaction (q_1 and q_2) as well as the distances between those charges. If we make the assumption that the charges in [PPh₄][1^{Se}] and [PPh₄][3^{Se}] should be identical (or at least similar), then the ratio of the slopes to the linear fits of J_{P-Se} versus $1/(4\pi\epsilon)$ should be proportional to the difference in the square of the point charge-to-test charge distances in the two phosphine selenides. If we use the B...P distance for this value, the distances are 3.029 and 3.562 Å. The ratio of the squares of these distances is 0.72. This suggests that, simplistically, we might expect that the ratio of the slopes of J_{P-Se} versus $1/(4\pi\epsilon)$ for [PPh₄][1^{Se}] and [PPh₄][3^{Se}] should be ~1.4. The ratio from the linear fits to the data is 1.5, in good agreement to the predicted ratio from the difference charge-to-charge distance.

3.4.7 Procedure for Oxidative Addition of C₆F₆

UV-visible Spectroscopic Monitoring

To a stirring THF solution (1 mL) of Ni(COD)₂ (14 mg, 0.051 mmol) was added a THF solution (1 mL) of K1 (30 mg, 0.099 mmol, 1.9 eq) and an excess of C₆F₆ (200 mg, 1.07 mmol, 21 eq), resulting in a deep red solution. After stirring for one hour, the solution had become brown-yellow, and NMR indicated oxidative addition of the C–F bond via the appearance of characteristic ¹⁹F NMR peaks at –383 (Ni–F) and –117 (*o*-C–F) ppm and the disappearance of ³¹P peaks associated with K1 (Figures A3.74–A3.79). Further characterization of the oxidative addition product could not be obtained due to the instability of the resulting species. Samples for UV-vis were prepared by dissolving Ni(COD)₂ (10 mg, 0.035 mmol), K1 (22 mg, 0.072 mmol, 2 equiv.), and C₆F₆ (89 μL, 0.76 mmol, 21 equiv.) in 2.9 mL THF, resulting in a 12 mM solution. Diluting 75 μL of this solution in 2.5 mL resulted in a 0.36 mM solution which was used to monitor the decay of the Ni complex by UV-vis. The decay of the absorbance at 464 nm was monitored to determine the rate of decay of the in situ formed Ni complex (Figure A3.40). Monitoring the decay under identical conditions in the absence of C₆D₆ indicates minimal decay (Figure A3.44).

NMR Spectroscopic Measurement of Reaction Kinetics

K1

A THF stock solution was prepared by adding 66 μL of CF₃Ph (0.54 mmol) and 125 μL of C₆F₆ (1.08 mmol) to 9 mL of THF. In a 20 mL scintillation vial Ni(COD)₂ (10 mg, 0.036 mmol), K1 (22 mg, 0.072 mmol, 2 equiv.) and PPh₃O (10 mg, 0.036, 1 equiv.) were dissolved in 3 mL of the stock solution (delivering 0.18 mmol of CF₃Ph, 5 equiv., and 0.36 mmol C₆F₆, 10 equiv.). Approximately 500 μL of this solution was pipetted into an NMR tube, which was then covered

with a small piece of tubing connected to a plastic adapter, removed from the glovebox, frozen in LN₂, placed under vacuum on the Schlenk line and sealed under vacuum. The sample was kept frozen until the time of the first scan.

PCy₃

A THF stock solution was prepared by adding 66 μL of CF₃Ph (0.54 mmol) and 125 μL of C₆F₆ (1.08 mmol) to 9 mL of THF. In a 20 mL scintillation vial Ni(COD)₂ (10 mg, 0.036 mmol), PCy₃ (20 mg, 0.072 mmol, 2 equiv.) and PPh₃O (10 mg, 0.036, 1 equiv.) were dissolved in 3 mL of the stock solution (delivering 0.18 mmol of CF₃Ph (5 equiv.) and 0.36 mmol C₆F₆ (10 equiv.)). Approximately 500 μL of this solution was pipetted into an NMR tube, which was then covered with a small piece of tubing connected to a plastic adapter, removed from the glovebox, frozen in LN₂, placed under vacuum on the Schlenk line and sealed under vacuum. The sample was kept frozen until the time of the first scan. NMR spectra were collected every 3 hours for 18 hours, then every 5 hours for 35 more hours, for 53 hours of monitoring total.

PEt₃

A THF stock solution was prepared by adding 32 μL of PEt₃ (0.216 mmol), 66 μL of CF₃Ph (0.54 mmol) and 125 μL of C₆F₆ (1.08 mmol) to 9 mL of THF. In a 20 mL scintillation vial Ni(COD)₂ (10 mg, 0.036 mmol) and PPh₃O (10 mg, 0.036, 1 equiv.) were dissolved in 3 mL of the stock solution (delivering 0.072 mmol of PEt₃ (2 equiv.), 0.18 mmol of CF₃Ph (5 equiv.), and 0.36 mmol C₆F₆ (10 equiv.)). Approximately 500 μL of this solution was pipetted into an NMR tube, which was then covered with a small piece of tubing connected to a plastic adapter, removed from the glovebox, frozen in LN₂, placed under vacuum on the Schlenk line and sealed under vacuum. The sample was kept frozen until the time of the first scan. Spectra of the reaction were collected every

3 hours for 18 hours, then every 5 hours for 36 more hours, then every 12 hours for 60 more hours, for a total of 114 hours. Previous reports suggest the reaction reaches completion after 4 weeks, and the partial conversion observed here is consistent with that time frame.¹⁵⁴

NMR Spectroscopy Methods

T_1 measurements of the reaction mixtures were used to decide collection parameters for monitoring the course of the reaction. Fluorine NMR was collected without decoupling with the following parameters: NS = 16, O1P = -113 ppm, SW = 140 ppm, D1 = 25 s and AQ = 2s. $^{31}\text{P}\{^1\text{H}\}$ was collected using the following parameters: NS = 31, O1P = 35 ppm, SW = 429 ppm, D1=35 s, and AQ = 2s. The spectra were collected using an automated Bruker Avance III HD nanobay 400 MHz. The rate of formation was determined using Mnova by generating a concentration graph, and fitting the concentration data to a three parameter exponential fit to the equation $y = B + F \cdot \exp(-x \cdot G)$, with G the observed rate.

3.4.8 Procedures for Catalytic C-F Borylation

Trial reactions – A 4 mL screw thread cap vial was charged with solid $\text{Ni}(\text{COD})_2$ (10 mg, 0.036 mmol), K1 (22 mg, 0.072 mmol, 2 equiv.) and B_2pin_2 (amount specified in reaction tables). The solid mixture was then dissolved in 1 mL THF to give dark red solutions. Next, 1,3-difluorobenzene (40 μL , 0.4 mmol, 11 equiv.), CF_3Ph (20 μL , 0.16 mmol, 4.5 equiv.) and any additives were added to the reactions. Solutions were heated at 50 °C for the specified amounts of time. To work up the reactions, the 1 mL reaction was diluted to 5 mL in a scintillation vial. From that solution, 50 μL were diluted to 400 μL within an NMR tube, giving a 4 mM solution of CF_3Ph and what would be a 10 mM solution of product if there were 100% conversion of the fluoroarene. All yields are reported relative to added 1,3-difluorobenzene, consistent with the yields reported

in Figure 3.4. See Tables A3.17-A3.24 for the yields from trial runs. Some of the yields are a slight underestimate because an excess of 1,3-difluorobenzene was added relative to B₂pin₂ (11 equiv. arene vs 10 equiv. B₂pin₂ relative to Ni(COD)₂). Yield was determined by comparing the integration of the CF₃Ph peak to the product peak using the following equation-¹⁵⁵

$$\text{Moles of product} = \frac{\text{Integration of product}}{\text{\# of fluorines in product}} \times \frac{\text{\# of fluorines in CF}_3\text{Ph}}{\text{Integration of CF}_3\text{Ph}} \times \text{moles of CF}_3\text{Ph}$$

Yield = moles of product/theoretical yield * 100

Theoretical yield for borylated products is 0.4 mmol, theoretical yield for coupled products is 0.2 mmol.

Catalytic reactions – Stock solutions were prepared for three reactions at a time by dissolving Ni(COD)₂ (30 mg, 0.108 mmol, 3 equiv.), K1 (66 mg, 0.216 mmol, 6 equiv.), and B₂pin₂ (552 mg, 2.16 mmol, 60 equiv.) in 3 mL THF. Next the substrate (1.2 mmol, 33 equiv.), CF₃Ph (60 μL, 0.48 mmol, 13.5 equiv.), and MeOH (90 μL, 2.16 mmol, 60 equiv.) was added. The solution was divided into three vials which each already contained CsOH (54 mg, 0.36 mmol, 1 equiv.). The reactions were then heated at 50 °C for 4 hours. See Figure 3.4 for the yields from these reactions. To characterize the yield of the C₆FH₅ reaction, the 1 mL reaction was diluted to 5 mL in a scintillation vial. From this solution, 45 μL was subsequently diluted to 3 mL, giving what would be a 1.2 mM solution if there were 100% conversion. This solution was filtered through a short silica plug in a pipette. The integration of the C₆H₅-Bpin was compared to an integral calibration curve prepared with stock solutions of C₆H₅-Bpin. The methods for workup and yield determination by NMR for the remaining catalytic reactions are identical to those for the trial reactions. Literature sources were used to assign the NMR shifts and MS of substrates and products:

Compound	Reference
1,2-difluorobenzene 1-Bpin-2-C ₆ FH ₄ 1,3-difluorobenzene 1-Bpin-3-C ₆ FH ₄ 1,2,4-trifluorobenzene 1,3,5-trifluorobenzene 1-Bpin-3,5-C ₆ F ₂ H ₄ 1,3-Bpin-5-C ₆ FH ₃ MS of C ₆ F ₅ -Bpin	133
2,2'-F ₂ -1,1'-Ph ₂	156
1,4-difluorobenzene	157
1-Bpin-4-C ₆ FH ₄	158
2,2',5,5'-F ₄ -1,1'-Ph ₂	159

3.5 References

1. Warshel, A. Electrostatic Origin of the Catalytic Power of Enzymes and the Role of Preorganized Active Sites. *J. Biol. Chem.* **1998**, *273* (42), 27035–27038.
2. Warshel, A.; Sharma, P. K.; Kato, M.; Xiang, Y.; Liu, H.; Olsson, M. H. M. Electrostatic Basis for Enzyme Catalysis. *Chem. Rev.* **2006**, *106* (8), 3210–3235.
3. Schyman, P.; Lai, W.; Chen, H.; Wang, Y.; Shaik, S. The Directive of the Protein: How Does Cytochrome P450 Select the Mechanism of Dopamine Formation? *J. Am. Chem. Soc.* **2011**, *133* (20), 7977–7984.
4. Fried, S. D.; Boxer, S. G. Measuring Electric Fields and Noncovalent Interactions Using the Vibrational Stark Effect. *Acc. Chem. Res.* **2015**, *48* (4), 998–1006.
5. Fried, S. D.; Boxer, S. G. Electric Fields and Enzyme Catalysis. *Annu. Rev. Biochem.* **2017**, *86*, 387–415.
6. Morgenstern, A.; Jaszai, M.; Eberhart, M. E.; Alexandrova, A. N. Quantified Electrostatic Preorganization in Enzymes Using the Geometry of the Electron Charge Density. *Chem. Sci.* **2017**, *8* (7), 5010–5018.
7. Bím, D.; Alexandrova, A. N. Local Electric Fields as a Natural Switch of Heme-Iron Protein Reactivity. *ACS Catal.* **2021**, *11* (11), 6534–6546.
8. Shaik, S.; Mandal, D.; Ramanan, R. Oriented Electric Fields as Future Smart Reagents in Chemistry. *Nat. Chem.* **2016**, *8*, 1091–1098.
9. Shaik, S.; Ramanan, R.; Danovich, D.; Mandal, D. Structure and Reactivity/Selectivity Control by Oriented-External Electric Fields. *Chem. Soc. Rev.* **2018**, *47* (14), 5125–5145.
10. Ciampi, S.; Darwish, N.; Aitken, H. M.; Díez-Pérez, I.; Coote, M. L. Harnessing Electrostatic Catalysis in Single Molecule, Electrochemical and Chemical Systems: A Rapidly Growing Experimental Tool Box. *Chem. Soc. Rev.* **2018**, *47* (14), 5146–5164.
11. Che, F.; Gray, J. T.; Ha, S.; Kruse, N.; Scott, S. L.; McEwen, J.-S. Elucidating the Roles of Electric Fields in Catalysis: A Perspective. *ACS Catal.* **2018**, *8* (6), 5153–5174.
12. Ye, S.; Riplinger, C.; Hansen, A.; Krebs, C.; Bollinger, J. M.; Neese, F. Electronic Structure Analysis of the Oxygen-Activation Mechanism by Fe^{II}- and α -Ketoglutarate (α KG)-Dependent Dioxygenases. *Chem. Eur. J.* **2012**, *18* (21), 6555–6567.
13. Alemani, M.; Peters, M. V; Hecht, S.; Rieder, K. H.; Moresco, F.; Grill, L. Electric Field-Induced Isomerization of Azobenzene by STM. *J. Am. Chem. Soc.* **2006**, *128* (45), 14446–14447.

14. Gorin, C. F.; Beh, E. S.; Kanan, M. W. An Electric Field-Induced Change in the Selectivity of a Metal Oxide-Catalyzed Epoxide Rearrangement. *J. Am. Chem. Soc.* **2012**, *134* (1), 186–189.
15. Zang, Y.; Zou, Q.; Fu, T.; Ng, F.; Fowler, B.; Yang, J.; Li, H.; Steigerwald, M. L.; Nuckolls, C.; Venkataraman, L. Directing Isomerization Reactions of Cumulenes with Electric Fields. *Nat. Commun.* **2019**, *10*, 1–7.
16. Gorin, C. F.; Beh, E. S.; Bui, Q. M.; Dick, G. R.; Kanan, M. W. Interfacial Electric Field Effects on a Carbene Reaction Catalyzed by Rh Porphyrins. *J. Am. Chem. Soc.* **2013**, *135* (30), 11257–11265.
17. Aragonès, A. C.; Haworth, N. L.; Darwish, N.; Ciampi, S.; Bloomfield, N. J.; Wallace, G. G.; Diez-Perez, I.; Coote, M. L. Electrostatic Catalysis of a Diels-Alder Reaction. *Nature* **2016**, *531*, 88–91.
18. Liu, M.; Pang, Y.; Zhang, B.; De Luna, P.; Voznyy, O.; Xu, J.; Zheng, X.; Dinh, C. T.; Fan, F.; Cao, C.; De Arquer, F. P. G.; Safaei, T. S.; Mepham, A.; Klinkova, A.; Kumacheva, E.; Filleter, T.; Sinton, D.; Kelley, S. O.; Sargent, E. H. Enhanced Electrocatalytic CO₂ Reduction via Field-Induced Reagent Concentration. *Nature* **2016**, *537*, 382–386.
19. Zhang, L.; Laborda, E.; Darwish, N.; Noble, B. B.; Tyrell, J. H.; Pluczyk, S.; Le Brun, A. P.; Wallace, G. G.; Gonzalez, J.; Coote, M. L.; Ciampi, S. Electrochemical and Electrostatic Cleavage of Alkoxyamines. *J. Am. Chem. Soc.* **2018**, *140* (2), 766–774.
20. Ryu, J.; Surendranath, Y. Tracking Electrical Fields at the Pt/H₂O Interface during Hydrogen Catalysis. *J. Am. Chem. Soc.* **2019**, *141* (39), 15524–15531.
21. Heo, J.; Ahn, H.; Won, J.; Son, J. G.; Shon, H. K.; Lee, T. G.; Han, S. W.; Baik, M.-H. Electro-Inductive Effect: Electrodes as Functional Groups with Tunable Electronic Properties. *Science* **2020**, *370*, 214–219.
22. Shetty, M.; Ardagh, M. A.; Pang, Y.; Abdelrahman, O. A.; Dauenhauer, P. J. Electric-Field-Assisted Modulation of Surface Thermochemistry. *ACS Catal.* **2020**, *10* (21), 12867–12880.
23. Warburton, R. E.; Hutchison, P.; Jackson, M. N.; Pegis, M. L.; Surendranath, Y.; Hammes-Schiffer, S. Interfacial Field-Driven Proton-Coupled Electron Transfer at Graphite-Conjugated Organic Acids. *J. Am. Chem. Soc.* **2020**, *142* (49), 20855–20864.
24. DiRocco, D. A.; Noey, E. L.; Houk, K. N.; Rovis, T. Catalytic Asymmetric Intermolecular Stetter Reactions of Enolizable Aldehydes with Nitrostyrenes: Computational Study Provides Insight into the Success of the Catalyst. *Angew. Chem., Int. Ed.* **2012**, *51* (10), 2391–2394.
25. Holland, M. C.; Paul, S.; Schweizer, W. B.; Bergander, K.; Mück-Lichtenfeld, C.; Lakhdar, S.; Mayr, H.; Gilmour, R. Noncovalent Interactions in Organocatalysis: Modulating Conformational Diversity and Reactivity in the MacMillan Catalyst. *Angew. Chem., Int. Ed.* **2013**, *52* (31), 7967–7971.

26. Chattopadhyay, B.; Dannatt, J. E.; Andujar-De Sanctis, I. L.; Gore, K. A.; Maleczka, R. E.; Singleton, D. A.; Smith III, M. R. Ir-Catalyzed Ortho-Borylation of Phenols Directed by Substrate–Ligand Electrostatic Interactions: A Combined Experimental/in Silico Strategy for Optimizing Weak Interactions. *J. Am. Chem. Soc.* **2017**, *139* (23), 7864–7871.
27. Lau, V. M.; Pfalzgraff, W. C.; Markland, T. E.; Kanan, M. W. Electrostatic Control of Regioselectivity in Au(I)-Catalyzed Hydroarylation. *J. Am. Chem. Soc.* **2017**, *139* (11), 4035–4041.
28. Chantarojsiri, T.; Ziller, J. W.; Yang, J. Y. Incorporation of Redox-Inactive Cations Promotes Iron Catalyzed Aerobic C–H Oxidation at Mild Potentials. *Chem. Sci.* **2018**, *9* (9), 2567–2574.
29. Dhar, D.; Yee, G. M.; Tolman, W. B. Effects of Charged Ligand Substituents on the Properties of the Formally Copper(III)-Hydroxide ($[\text{CuOH}]^{2+}$) Unit. *Inorg. Chem.* **2018**, *57* (16), 9794–9806.
30. Kang, K.; Fuller, J.; Reath, A. H.; Ziller, J. W.; Alexandrova, A. N.; Yang, J. Y. Installation of Internal Electric Fields by Non-Redox Active Cations in Transition Metal Complexes. *Chem. Sci.* **2019**, *10* (43), 10135–10142.
31. Erickson, J. D.; Preston, A. Z.; Linehan, J. C.; Wiedner, E. S. Enhanced Hydrogenation of Carbon Dioxide to Methanol by a Ruthenium Complex with a Charged Outer-Coordination Sphere. *ACS Catal.* **2020**, *10* (13), 7419–7423.
32. Deacy, A. C.; Moreby, E.; Phanopoulos, A.; Williams, C. K. Co(III)/Alkali-Metal(I) Heterodinuclear Catalysts for the Ring-Opening Copolymerization of CO₂ and Propylene Oxide. *J. Am. Chem. Soc.* **2020**, *142* (45), 19150–19160.
33. Oswald, V. F.; Lee, J. L.; Biswas, S.; Weitz, A. C.; Mitra, K.; Fan, R.; Li, J.; Zhao, J.; Hu, M. Y.; Alp, E. E.; Bominaar, E. L.; Guo, Y.; Green, M. T.; Hendrich, M. P.; Borovik, A. S. Effects of Noncovalent Interactions on High-Spin Fe(IV)-Oxido Complexes. *J. Am. Chem. Soc.* **2020**, *142* (27), 11804–11817.
34. Martin, D. J.; Johnson, S. I.; Mercado, B. Q.; Raugei, S.; Mayer, J. M. Intramolecular Electrostatic Effects on O₂, CO₂, and Acetate Binding to a Cationic Iron Porphyrin. *Inorg. Chem.* **2020**, *59* (23), 17402–17414.
35. Weberg, A. B.; McCollom, S. P.; Thierer, L. M.; Gau, M. R.; Carroll, P. J.; Tomson, N. C. Using Internal Electrostatic Fields to Manipulate the Valence Manifolds of Copper Complexes. *Chem. Sci.* **2021**, *12* (12), 4395–4404.
36. Klinska, M.; Smith, L. M.; Gryn'ova, G.; Banwell, M. G.; Coote, M. L. Experimental Demonstration of pH-Dependent Electrostatic Catalysis of Radical Reactions. *Chem. Sci.* **2015**, *6* (10), 5623–5627.

37. Martin, D. J.; Mercado, B. Q.; Mayer, J. M. All Four Atropisomers of Iron Tetra(o-N,N,N-Trimethylanilinium)Porphyrin in Both the Ferric and Ferrous States. *Inorg. Chem.* **2021**, *60* (7), 5240–5251.
38. Martin, D. J.; Mayer, J. M. Oriented Electrostatic Effects on O₂ and CO₂ Reduction by a Polycationic Iron Porphyrin. *J. Am. Chem. Soc.* **2021**, *143* (30), 11423–11434.
39. Léonard, N. G.; Chantarojsiri, T.; Ziller, J. W.; Yang, J. Y. Cationic Effects on the Net Hydrogen Atom Bond Dissociation Free Energy of High-Valent Manganese Imido Complexes. *J. Am. Chem. Soc.* **2022**, *144* (4), 1503–1508.
40. Lee, K.; Silverio, D. L.; Torker, S.; Robbins, D. W.; Haeffner, F.; van der Mei, F. W.; Hoveyda, A. H. Catalytic Enantioselective Addition of Organoboron Reagents to Fluoroketones Controlled by Electrostatic Interactions. *Nat. Chem.* **2016**, *8*, 768–777.
41. Kennedy, C. R.; Guidera, J. A.; Jacobsen, E. N. Synergistic Ion-Binding Catalysis Demonstrated via an Enantioselective, Catalytic [2,3]-Wittig Rearrangement. *ACS Cent. Sci.* **2016**, *2* (6), 416–423.
42. Xiao, G.; Cintron-Rosado, G. A.; Glazier, D. A.; Xi, B.-M.; Liu, C.; Liu, P.; Tang, W. Catalytic Site-Selective Acylation of Carbohydrates Directed by Cation- π Interaction. *J. Am. Chem. Soc.* **2017**, *139* (12), 4346–4349.
43. Yamada, S. Cation- π Interactions in Organic Synthesis. *Chem. Rev.* **2018**, *118* (23), 11353–11432.
44. Dhayalan, V.; Gadekar, S. C.; Alassad, Z.; Milo, A. Unravelling Mechanistic Features of Organocatalysis with in Situ Modifications at the Secondary Sphere. *Nat. Chem.* **2019**, *11*, 543–551.
45. Grajeda, J.; Kita, M. R.; Gregor, L. C.; White, P. S.; Miller, A. J. M. M. Diverse Cation-Promoted Reactivity of Iridium Carbonyl Pincer-Crown Ether Complexes. *Organometallics* **2016**, *35* (3), 306–316.
46. Reath, A. H.; Ziller, J. W.; Tsay, C.; Ryan, A. J.; Yang, J. Y. Redox Potential and Electronic Structure Effects of Proximal Nonredox Active Cations in Cobalt Schiff Base Complexes. *Inorg. Chem.* **2017**, *56* (6), 3713–3718.
47. Um, J. M.; Dirocco, D. A.; Noey, E. L.; Rovis, T.; Houk, K. N. Quantum Mechanical Investigation of the Effect of Catalyst Fluorination in the Intermolecular Asymmetric Stetter Reaction. *J. Am. Chem. Soc.* **2011**, *133* (29), 11249–11254.
48. Lyngvi, E.; Bode, J. W.; Schoenebeck, F. A Computational Study of the Origin of Stereoinduction in NHC-Catalyzed Annulation Reactions of α,β -Unsaturated Acyl Azoliums. *Chem. Sci.* **2012**, *3* (7), 2346–2350.

49. Stuyver, T.; Ramanan, R.; Mallick, D.; Shaik, S. Oriented (Local) Electric Fields Drive the Millionfold Enhancement of the H-Abstraction Catalysis Observed for Synthetic Metalloenzyme Analogues. *Angew. Chem., Int. Ed.* **2020**, *59* (20), 7915–7920.
50. Xu, L.; Izgorodina, E. I.; Coote, M. L. Ordered Solvents and Ionic Liquids Can Be Harnessed for Electrostatic Catalysis. *J. Am. Chem. Soc.* **2020**, *142* (29), 12826–12833.
51. Doan, V.; Noble, B. B.; Coote, M. L. Electrostatic Activation of Tetrazoles. *J. Org. Chem.* **2020**, *85* (15), 10091–10097.
52. Welborn, V. V.; Ruiz Pestana, L.; Head-Gordon, T. Computational Optimization of Electric Fields for Better Catalysis Design. *Nat. Catal.* **2018**, *1* (9), 649–655.
53. Joy, J.; Stuyver, T.; Shaik, S. Oriented External Electric Fields and Ionic Additives Elicit Catalysis and Mechanistic Crossover in Oxidative Addition Reactions. *J. Am. Chem. Soc.* **2020**, *142* (8), 3836–3850.
54. Yang, H.; Wong, M. W. Oxyanion Hole Stabilization by C-H···O Interaction in a Transition State -a Three-Point Interaction Model for Cinchona Alkaloid-Catalyzed Asymmetric Methanolysis of Meso-Cyclic Anhydrides. *J. Am. Chem. Soc.* **2013**, *135* (15), 5808–5818.
55. Nguyen, Q. N. N.; Lodewyk, M. W.; Bezer, S.; Gagné, M. R.; Waters, M. L.; Tantillo, D. J. Effects of Helix Macrodipole and Local Interactions on Catalysis of Acyl Transfer by α -Helical Peptides. *ACS Catal.* **2015**, *5* (3), 1617–1622.
56. Seguin, T. J.; Wheeler, S. E. Electrostatic Basis for Enantioselective Brønsted-Acid-Catalyzed Asymmetric Ring Openings of Meso-Epoxydes. *ACS Catal.* **2016**, *6* (4), 2681–2688.
57. Seguin, T. J.; Wheeler, S. E. Stacking and Electrostatic Interactions Drive the Stereoselectivity of Silylium-Ion Asymmetric Counteranion-Directed Catalysis. *Angew. Chem., Int. Ed.* **2016**, *55* (51), 15889–15893.
58. Maji, R.; Wheeler, S. E. Importance of Electrostatic Effects in the Stereoselectivity of NHC-Catalyzed Kinetic Resolutions. *J. Am. Chem. Soc.* **2017**, *139* (36), 12441–12449.
59. Hill, N. S.; Coote, M. L. Strategies for Red-Shifting Type I Photoinitiators: Internal Electric Fields versus Lewis Acids versus Increasing Conjugation. *Aust. J. Chem.* **2019**, *72*, 627–632.
60. Blyth, M. T.; Coote, M. L. A pH-Switchable Electrostatic Catalyst for the Diels-Alder Reaction: Progress toward Synthetically Viable Electrostatic Catalysis. *J. Org. Chem.* **2019**, *84* (3), 1517–1522.
61. Blyth, M. T.; Noble, B. B.; Russell, I. C.; Coote, M. L. Oriented Internal Electrostatic Fields Cooperatively Promote Ground- And Excited-State Reactivity: A Case Study in Photochemical CO₂ Capture. *J. Am. Chem. Soc.* **2020**, *142* (1), 606–613.

62. Hansch, C.; Leo, A.; Taft, R. W. A Survey of Hammett Substituent Constants and Resonance and Field Parameters. *Chem. Rev.* **1991**, *91* (2), 165–195.
63. Ri, T.; Eyring, H. Calculation of Dipole Moments from Rates of Nitration of Substituted Benzenes and Its Significance for Organic Chemistry. *J. Chem. Phys.* **1940**, *8* (6), 433–443.
64. Westheimer, F. H. The Electrostatic Effect of Substituents on the Dissociation Constants of Organic Acids. IV. Aromatic Acids. *J. Am. Chem. Soc.* **1939**, *61* (8), 1977–1980.
65. Jaffé, H. H. Correlation of Hammett's σ -Values with Electron Densities Calculated by Molecular Orbital Theory. *J. Chem. Phys.* **1952**, *20* (2), 279–284.
66. Jaffé, H. H. A Reëxamination of the Hammett Equation. *Chem. Rev.* **1953**, *53* (2), 191–261.
67. Burns, R. J.; Mati, I. K.; Muchowska, K. B.; Adam, C.; Cockroft, S. L. Quantifying Through-Space Substituent Effects. *Angew. Chem., Int. Ed.* **2020**, *59* (38), 2–10.
68. Fischer, P. J.; Senthil, S.; Stephan, J. T.; Swift, M. L.; Storlie, M. D.; Chan, E. T.; Vollmer, M. V.; Young, V. G. Inductive Modulation of Tris(Phosphinomethyl)Phenylborate Donation at Group VI Metals via Borate Phenyl Substituent Modification. *Dalton Trans.* **2018**, *47* (17), 6166–6176.
69. Estrada, J.; Lugo, C. A.; McArthur, S. G.; Lavallo, V. Inductive Effects of 10 and 12-Vertex Closo-Carborane Anions: Cluster Size and Charge Make a Difference. *Chem. Commun.* **2016**, *52* (9), 1824–1826.
70. Azcarate, I.; Costentin, C.; Robert, M.; Savéant, J.-M. Through-Space Charge Interaction Substituent Effects in Molecular Catalysis Leading to the Design of the Most Efficient Catalyst of CO₂-to-CO Electrochemical Conversion. *J. Am. Chem. Soc.* **2016**, *138* (51), 16639–16644.
71. Pegis, M. L.; Wise, C. F.; Koronkiewicz, B.; Mayer, J. M. Identifying and Breaking Scaling Relations in Molecular Catalysis of Electrochemical Reactions. *J. Am. Chem. Soc.* **2017**, *139* (32), 11000–11003.
72. Sung, S.; Kumar, D.; Gil-Sepulcre, M.; Nippe, M. Electrocatalytic CO₂ Reduction by Imidazolium-Functionalized Molecular Catalysts. *J. Am. Chem. Soc.* **2017**, *139* (40), 13993–13996.
73. Yuan, Z.; Yang, H.; Malik, N.; Čolović, M.; Weber, D. S.; Wilson, D.; Bénard, F.; Martin, R. E.; Warren, J. J.; Schaffer, P.; Britton, R. Electrostatic Effects Accelerate Decatungstate-Catalyzed C-H Fluorination Using [¹⁸F]⁻ And [¹⁹F]NFSI in Small Molecules and Peptide Mimics. *ACS Catal.* **2019**, *9* (9), 8276–8284.
74. Sung, S.; Li, X.; Wolf, L. M.; Meeder, J. R.; Bhuvanesh, N. S.; Grice, K. A.; Panetier, J. A.; Nippe, M. Synergistic Effects of Imidazolium-Functionalization on Fac-Mn(CO)₃ Bipyridine Catalyst Platforms for Electrocatalytic Carbon Dioxide Reduction. *J. Am. Chem. Soc.* **2019**, *141* (16), 6569–6582.

75. Zhang, R.; Warren, J. J. Controlling the Oxygen Reduction Selectivity of Asymmetric Cobalt Porphyrins by Using Local Electrostatic Interactions. *J. Am. Chem. Soc.* **2020**, *142* (31), 13426–13434.
76. Margarit, C. G.; Asimow, N. G.; Gonzalez, M. I.; Nocera, D. G. Double Hangman Iron Porphyrin and the Effect of Electrostatic Nonbonding Interactions on Carbon Dioxide Reduction. *J. Phys. Chem. Lett.* **2020**, *11*, 1890–1895.
77. Tolman, C. A. Steric Effects of Phosphorus Ligands in Organometallic Chemistry and Homogeneous Catalysis. *Chem. Rev.* **1977**, *77* (3), 313–348.
78. Stradiotto, M.; Hesp, K. D.; Lundgren, R. J. Zwitterionic Relatives of Cationic Platinum Group Metal Complexes: Applications in Stoichiometric and Catalytic σ -Bond Activation. *Angew. Chem., Int. Ed.* **2010**, *49* (3), 494–512.
79. Puerta-Oteo, R.; Ojeda-Amador, A. I.; Jiménez, M. V.; Pérez-Torrente, J. J. Catalytic Applications of Zwitterionic Transition Metal Compounds. *Dalton Trans.* **2022**, *51* (3), 817–830.
80. Miller, A. J. M.; Labinger, J. A.; Bercaw, J. E. Homogeneous CO Hydrogenation: Dihydrogen Activation Involves a Frustrated Lewis Pair Instead of a Platinum Complex. *J. Am. Chem. Soc.* **2010**, *132* (10), 3301–3303.
81. Nichols, B. R.; Akhmedov, N. G.; Petersen, J. L.; Popp, B. V. Access to a Pair of Ambiphilic Phosphine-Borane Regioisomers by Rhodium-Catalyzed Hydroboration. *Dalton Trans.* **2018**, *47* (25), 8456–8465.
82. Miller, A. J. M.; Labinger, J. A.; Bercaw, J. E. Trialkylborane-Assisted CO₂ Reduction by Late Transition Metal Hydrides. *Organometallics* **2011**, *30* (16), 4308–4314.
83. Alcarazo, M. Synthesis, Structure, and Applications of α -Cationic Phosphines. *Acc. Chem. Res.* **2016**, *49* (9), 1797–1805.
84. Jia, X.; Zhang, M.; Pan, F.; Babahan, I.; Ding, K.; Jia, L.; Crandall, L. A.; Ziegler, C. J. Zwitterionic Nickel(II) Catalyst for CO-Ethylene Alternating Copolymerization. *Organometallics* **2015**, *34* (20), 4798–4801.
85. Zhu, L.; Dai, Y.; Schrage, B. R.; Ziegler, C. J.; Jia, L. Ligand and Solvent Effects on the Catalytic Activity and Lifetime of Zwitterionic Nickel(II) Catalysts for Alternating CO-Ethylene Copolymerization. *J. Organomet. Chem.* **2021**, *952*, 122045.
86. Lu, C. C.; Peters, J. C. Catalytic Copolymerization of CO and Ethylene with a Charge Neutral Palladium(II) Zwitterion. *J. Am. Chem. Soc.* **2002**, *124* (19), 5272–5273.
87. Jia, X.; Zhang, M.; Li, M.; Pan, F.; Ding, K.; Jia, L.; Crandall, L. A.; Engle, J. T.; Ziegler, C. J. Zwitterionic Nickel(II) Catalysts for CO-Ethylene Alternating Copolymerization. *Organometallics* **2017**, *36* (6), 1122–1132.

88. Schmidt, B. M.; Engle, J. T.; Zhang, M.; Babahan, I.; Ziegler, C. J.; Jia, L. Zwitterionic Nickel(II) Complexes: Synthesis, Characterization, Decomposition, and Stoichiometric and Catalytic Reactivities. *J. Organomet. Chem.* **2016**, *805*, 94–99.
89. Gutsulyak, D. V.; Gott, A. L.; Piers, W. E.; Parvez, M. Dimerization of Ethylene by Nickel Phosphino-Borate Complexes. *Organometallics* **2013**, *32* (11), 3363–3370.
90. Gott, A. L.; Piers, W. E.; Dutton, J. L.; McDonald, R.; Parvez, M. Dimerization of Ethylene by Palladium Complexes Containing Bidentate Trifluoroborate-Functionalized Phosphine Ligands. *Organometallics* **2011**, *30* (16), 4236–4249.
91. Kim, Y.; Jordan, R. F. Synthesis, Structures, and Ethylene Dimerization Reactivity of Palladium Alkyl Complexes That Contain a Chelating Phosphine-Trifluoroborate Ligand. *Organometallics* **2011**, *30* (16), 4250–4256.
92. Dai, Y.; He, S.; Peng, B.; Crandall, L. A.; Schrage, B. R.; Ziegler, C. J.; Jia, L. Zwitterionic Design Principle of Nickel(II) Catalysts for Carbonylative Polymerization of Cyclic Ethers. *Angew. Chem., Int. Ed.* **2018**, *57* (43), 14111–14115.
93. Estrada, J.; Woen, D. H.; Tham, F. S.; Miyake, G. M.; Lavallo, V. Synthesis and Reactivity of a Zwitterionic Palladium Allyl Complex Supported by a Perchlorinated Carboranyl Phosphine. *Inorg. Chem.* **2015**, *54* (11), 5142–5144.
94. Thomas, C. M.; Peters, J. C. Coordinating Anions: (Phosphino)Tetraphenylborate Ligands as New Reagents for Synthesis. *Inorg. Chem.* **2004**, *43* (1), 8–10.
95. Chan, A. L.; Estrada, J.; Kefalidis, C. E.; Lavallo, V. Changing the Charge: Electrostatic Effects in Pd-Catalyzed Cross-Coupling. *Organometallics* **2016**, *35* (19), 3257–3260.
96. Konishi, S.; Iwai, T.; Sawamura, M. Synthesis, Properties, and Catalytic Application of a Triptycene-Type Borate-Phosphine Ligand. *Organometallics* **2018**, *37* (12), 1876–1883.
97. Lavallo, V.; Wright, J. H.; Tham, F. S.; Quinlivan, S. Perhalogenated Carba-Closo-Dodecaborate Anions as Ligand Substituents: Applications in Gold Catalysis. *Angew. Chem., Int. Ed.* **2013**, *52* (11), 3172–3176.
98. Betley, T. A.; Peters, J. C. Zwitterionic Relatives to the Classic [(P-P)-Rh(Solv)₂]⁺ Ions: Neutral Catalysts Active for H-E Bond Additions to Olefins (E = C, Si, B). *Angew. Chem., Int. Ed.* **2003**, *42*, 2385–2389.
99. Thomas, J. C.; Peters, J. C. Zwitterionic and Cationic Bis(Phosphine) Platinum(II) Complexes: Structural, Electronic, and Mechanistic Comparisons Relevant to Ligand Exchange and Benzene C-H Activation Processes. *J. Am. Chem. Soc.* **2003**, *125* (29), 8870–8888.
100. Thomas, J. C.; Peters, J. C. Bis(Phosphino)Borates: A New Family of Monoanionic Chelating Phosphine Ligands. *Inorg. Chem.* **2003**, *42* (17), 5055–5073.

101. Tassone, J. P.; Mawhinney, R. C.; Spivak, G. J. An Examination of the Effects of Borate Group Proximity on Phosphine Donor Power in Anionic(Phosphino)Tetraphenylborate Ligands. *J. Organomet. Chem.* **2015**, *776*, 153–156.
102. Seyferth, D.; Grim, S. O. Studies in Phosphinemethylene Chemistry. I. Nucleophilic Displacement of Halide Ion in Metal Halides by Triphenylphosphinemethylene. A New Synthesis of Organometallic-Substituted Phosphonium Salts. *J. Am. Chem. Soc.* **1961**, *83* (7), 1610–1613.
103. Seyferth, D.; Grim, S. O. Studies in Phosphinemethylene Chemistry. II. Adducts of Triphenylphosphinemethylene with Boron Compounds. *J. Am. Chem. Soc.* **1961**, *83* (7), 1613–1616.
104. Bateman, C. M.; Zakharov, L. N.; Abbey, E. R. Crystal Structure of Triphenylphosphoniummethylenetrifluoroborate. *Acta Cryst.* **2017**, *E73* (8), 1140–1142.
105. Oliveira, R. A.; Silva, R. O.; Molander, G. A.; Menezes, P. H. ^1H , ^{13}C , ^{19}F and ^{11}B NMR Spectral Reference Data of Some Potassium Organotrifluoroborates. *Magn. Reson. Chem.* **2009**, *47* (10), 873–878.
106. Setiawan, D.; Kalescky, R.; Kraka, E.; Cremer, D. Direct Measure of Metal-Ligand Bonding Replacing the Tolman Electronic Parameter. *Inorg. Chem.* **2016**, *55* (5), 2332–2344.
107. Gillespie, J. A.; Zuidema, E.; van Leeuwen, P. W. N. M.; Kamer, P. C. J. Phosphorus Ligand Effects in Homogeneous Catalysis and Rational Catalyst Design. In *Phosphorus(III) Ligands in Homogeneous Catalysis: Design and Synthesis*; Kamer, P. C. J., Leeuwen, P. W. N. M. van, Eds.; John Wiley & Sons, Ltd: Chichester, UK, 2012; pp 1–26.
108. Chen, L.; Ren, P.; Carrow, B. P. Tri(1-Adamantyl)Phosphine: Expanding the Boundary of Electron-Releasing Character Available to Organophosphorus Compounds. *J. Am. Chem. Soc.* **2016**, *138* (20), 6392–6395.
109. Thomas, J. C.; Peters, J. C. Benzene C-H Activation at a Charge Neutral Zwitterionic Platinum(II) Complex. *J. Am. Chem. Soc.* **2001**, *123*, 5100–5101.
110. Granville, S. L.; Welch, G. C.; Stephan, D. W. Ni, Pd, Pt, and Ru Complexes of Phosphine-Borate Ligands. *Inorg. Chem.* **2012**, *51* (8), 4711–4721.
111. Drover, M. W.; Nagata, K.; Peters, J. C. Fusing Triphenylphosphine with Tetraphenylborate: Introducing the 9-Phosphatriptycene-10-Phenylborate (PTB) Anion. *Chem. Commun.* **2018**, *54* (57), 7916–7919.
112. Qiao, S.; Hoic, D. A.; Fu, G. C. Nucleophilic Aromatic Substitution Reactions of Borabenzene-Trimethylphosphine: A Versatile Route to 1-Substituted Boratabenzenes. *J. Am. Chem. Soc.* **1996**, *118* (26), 6329–6330.

113. Allen, D. W.; Taylor, B. F. The Chemistry of Heteroarylphosphorus Compounds. Part 15. Phosphorus-31 Nuclear Magnetic Resonance Studies of the Donor Properties of Heteroarylphosphines towards Selenium and Platinum(II). *J. Chem. Soc. Dalt. Trans.* **1982**, 51–54.
114. Beckmann, U.; Süslüyan, D.; Kunz, P. C. Is the $^1J_{\text{PSe}}$ Coupling Constant a Reliable Probe for the Basicity of Phosphines? A ^{31}P NMR Study. *Phosphorus Sulfur Silicon Relat. Elem.* **2011**, 186 (10), 2061–2070.
115. Huynh, H. V. Electronic Properties of N-Heterocyclic Carbenes and Their Experimental Determination. *Chem. Rev.* **2018**, 118 (19), 9457–9492.
116. Verlinden, K.; Buhl, H.; Frank, W.; Ganter, C. Determining the Ligand Properties of N-Heterocyclic Carbenes from ^{77}Se NMR Parameters. *Eur. J. Inorg. Chem.* **2015**, 2015 (14), 2416–2425.
117. Autschbach, J.; Le Guennic, B. Analyzing and Interpreting NMR Spin-Spin Coupling Constants Using Molecular Orbital Calculations. *J. Chem. Educ.* **2007**, 84 (1), 156–171.
118. Muller, A.; Otto, S.; Roodt, A. Rapid Phosphorus(III) Ligand Evaluation Utilising Potassium Selenocyanate. *Dalton Trans.* **2008**, No. 5, 650–657.
119. Levin, C. C. A Qualitative Molecular Orbital Picture of Electronegativity Effects on XH_3 Inversion Barriers. *J. Am. Chem. Soc.* **1975**, 97 (20), 5649–5655.
120. Wossidlo, F.; Frost, D. S.; Lin, J.; Coles, N. T.; Klimov, K.; Weber, M.; Böttcher, T.; Müller, C. Making Aromatic Phosphorus Heterocycles More Basic and Nucleophilic: Synthesis, Characterization and Reactivity of the First Phosphinine Selenide. *Chem. Eur. J.* **2021**, 27 (50), 12788–12795.
121. Ejgandi, A. M. Measuring the Electronic and Steric Effect of Some Phosphine Ligands, Masters Thesis, University of Manchester, 2010.
122. Niemeyer, Z. L.; Milo, A.; Hickey, D. P.; Sigman, M. S. Parameterization of Phosphine Ligands Reveals Mechanistic Pathways and Predicts Reaction Outcomes. *Nat. Chem.* **2016**, 8 (6), 610–617.
123. Allen, D. W.; Nowell, I. W.; Taylor, B. F. The Chemistry of Heteroarylphosphorus Compounds. Part 16. Unusual Substituent Effects on Selenium-77 Nuclear Magnetic Resonance Chemical Shifts of Heteroaryl- and Aryl-Phosphine Selenides. X-Ray Crystal Structure of Tri(2-Furyl)Phosphine Selenide. *J. Chem. Soc. Dalt. Trans.* **1985**, 834 (12), 2505–2508.
124. Anslyn, E. V.; Dougherty, D. A. *Modern Physical Organic Chemistry*, 5th ed.; University Science: Herndon, VA, 2005.

125. Grevels, F.; Jacke, J.; Klotzbücher, W. E.; Krüger, C.; Seevogel, K.; Tsay, Y. Dynamic Processes on the IR Time Scale: Coalescence of CO Stretching Vibrational Bands in [(H₄-Diene)Fe(CO)₃] Complexes. *Angew. Chem., Int. Ed.* **1987**, *26* (9), 885–887.
126. McFarlane, W.; Rycroft, D. S. Studies of Organophosphorus Selenides by Heteronuclear Magnetic Triple Resonance. *J. Chem. Soc. Dalt. Trans.* **1973**, No. 20, 2162–2166.
127. Carr, S. W.; Colton, R. Hydrogen-1, Carbon-13, Phosphorus-31 and Selenium-77 N.M.R. Studies on Organophosphorus Selenides. *Aust. J. Chem.* **1981**, *34* (1), 35–44.
128. Hrib, C. G.; Ruthe, F.; Seppälä, E.; Bätcher, M.; Druckenbrodt, C.; Wismach, C.; Jones, P. G.; du Mont, W. W.; Lippolis, V.; Devillanova, F. A.; Bühl, M. The Bromination of Bulky Trialkylphosphane Selenides R₂R' PSe (R, R' = IPr or TBu) Studied by Physical and Computational Methods. *Eur. J. Inorg. Chem.* **2006**, *2006* (1), 88–100.
129. Marcus, Y.; Hefter, G. Ion Pairing. *Chem. Rev.* **2006**, *106* (11), 4585–4621.
130. Cronin, L.; Higgitt, C. L.; Karch, R.; Perutz, R. N. Rapid Intermolecular Carbon-Fluorine Bond Activation of Pentafluoropyridine at Nickel(0): Comparative Reactivity of Fluorinated Arene and Fluorinated Pyridine Derivatives. *Organometallics* **1997**, *16* (22), 4920–4928.
131. Liu, X. W.; Echavarren, J.; Zarate, C.; Martin, R. Ni-Catalyzed Borylation of Aryl Fluorides via C-F Cleavage. *J. Am. Chem. Soc.* **2015**, *137* (39), 12470–12473.
132. Niwa, T.; Ochiai, H.; Watanabe, Y.; Hosoya, T. Ni/Cu-Catalyzed Defluoroborylation of Fluoroarenes for Diverse C-F Bond Functionalizations. *J. Am. Chem. Soc.* **2015**, *137* (45), 14313–14318.
133. Zhou, J.; Kuntze-Fechner, M. W.; Bertermann, R.; Paul, U. S. D.; Berthel, J. H. J.; Friedrich, A.; Du, Z.; Marder, T. B.; Radius, U. Preparing (Multi)Fluoroarenes as Building Blocks for Synthesis: Nickel-Catalyzed Borylation of Polyfluoroarenes via C-F Bond Cleavage. *J. Am. Chem. Soc.* **2016**, *138* (16), 5250–5253.
134. Malapit, C. A.; Bour, J. R.; Laursen, S. R.; Sanford, M. S. Mechanism and Scope of Nickel-Catalyzed Decarbonylative Borylation of Carboxylic Acid Fluorides. *J. Am. Chem. Soc.* **2019**, *141* (43), 17322–17330.
135. Tran, B. L.; Adhikari, D.; Fan, H.; Pink, M.; Mindiola, D. J. Facile Entry to 3d Late Transition Metal Boryl Complexes. *Dalton Trans.* **2010**, *39* (2), 358–360.
136. Molander, G. A.; Ham, J. Synthesis of Functionalized Organotrifluoroborates via Halomethyltrifluoroborates. *Org. Lett.* **2006**, *8* (10), 2031–2034.
137. J-W.; Wang, L-N.; Li, M.; Tang, P-T.; Luo, X-P.; Jurmoo, M.; Liu, Y-J.; Zeng, M-H. Ruthenium-Catalyzed Gram-Scale Preferential C-H Arylation of Tertiary Phosphine. *Org. Lett.* **2019**, *21* (8), 2885–2889.

138. Shen, Y.; Pan, Y.; Liu, J.; Sattasathuchana, T.; Baldrige, K. K.; Duttwyler, S. Synthesis and full characterization of an iridium B-H activation intermediate of the monocarba-closo-dodecaborate anion. *Chem. Commun.* **2017**, *53*, 176-179.
139. Chen, S.; Manoury, E.; Poli, R. Slow Exchange of Bidentate Ligands between Rhodium(I) Complexes: Evidence of Both Neutral and Anionic Ligand Exchange. *Eur. J. Inorg. Chem.* **2014**, *34*, 5820-5826.
140. Bresler, L. S.; Buzina, N. A.; Varshavsky, Y. S.; Kiseleva, N. V.; Cherkasova, T. G. Carbon-13 nuclear magnetic resonance spectra of rhodium carbonyl complexes. *J. Organomet. Chem.*, **1979**, *171*, 229-235.
141. Bootle-Wilbraham, A.; Head, S.; Longstaff, J.; Wyatt, P. Alane – A chemoselective way to reduce phosphine oxides. *Tetrahedron Lett.*, **1999**, *40*, 5267-5270.
142. Sheldrick, G. M. SHELXT- Integrated space-group and crystal-structure determination. *Acta Cryst.* **2015**, *A71*, 3-9.
143. Dolomanov, O.V.; Bourhis, L. J.; Gildea, R. J.; Howard, A. K.; and Puschmann, H. Olex2, a complete structure solution, refinement, and analysis program. *J. Appl. Cryst.* **2009**, *42*, 339
144. (a) Sheldrick, G. M. A Short History of SHELX. *Acta Cryst.* **2008**, *A64*, 112-122. (b) Sheldrick, G. M. Crystal structure refinement with SHELX. *Acta Cryst.* **2015**, *C71*, 3-8.
145. (a) Diaz, A. A.; Buster, B.; Schomish, D.; Khan, M. A.; Baum, C. J.; Wehmschulte, R. J. Size Matters: Room Temperature P-C Bond Formation Through C-F Activation in *m*-Terphenyldiiodophosphine. *Inorg. Chem.*, **2008**, *47* (7), 2858-2863. (b) Kreienbrink, A.; Sarosi, M. B.; Rys, E. G.; Lonneck, P.; Hey-Hawkins, E. Carborane-substituted 1,2-Diphosphetanes. *Angew. Chem. Int. Ed.* **2011**, *50* (20), 4701-4703.
146. Batsanov, S. S. Van der Waals Radii of Elements *Inorganic Materials* **2001**, *37*, 871-885.
147. Neese, F. The ORCA program system *Wiley interdisciplinary Reviews - Computational Molecular Science*, **2012**, *2*, 73-78.
148. Weigend F.; Ahlrichs, R. Balanced basis sets of split valence, triple zeta valence and quadruple zeta valence quality for H to Rn: Design and assessment of accuracy. *Phys. Chem. Chem. Phys.* **2005**, *7*, 3297.
149. Gaussian 16, Revision C.01, Frisch, M. J.; Trucks, G. W.; Schlegel, H. B.; Scuseria, G. E.; Robb, M. A.; Cheeseman, J. R.; Scalmani, G.; Barone, V.; Petersson, G. A.; Nakatsuji, H.; Li, X.; Caricato, M.; Marenich, A. V.; Bloino, J.; Janesko, B. G.; Gomperts, R.; Mennucci, B.; Hratchian, H. P.; Ortiz, J. V.; Izmaylov, A. F.; Sonnenberg, J. L.; Williams-Young, D.; Ding, F.; Lipparini, F.; Egidi, F.; Goings, J.; Peng, B.; Petrone, A.; Henderson, T.; Ranasinghe, D.; Zakrzewski, V. G.; Gao, J.; Rega, N.; Zheng, G.; Liang, W.; Hada, M.; Ehara, M.; Toyota, K.; Fukuda, R.; Hasegawa, J.; Ishida, M.; Nakajima, T.; Honda, Y.; Kitao, O.; Nakai, H.; Vreven, T.; Throssell, K.;

Montgomery, J. A., Jr.; Peralta, J. E.; Ogliaro, F.; Bearpark, M. J.; Heyd, J. J.; Brothers, E. N.; Kudin, K. N.; Staroverov, V. N.; Keith, T. A.; Kobayashi, R.; Normand, J.; Raghavachari, K.; Rendell, A. P.; Burant, J. C.; Iyengar, S. S.; Tomasi, J.; Cossi, M.; Millam, J. M.; Klene, M.; Adamo, C.; Cammi, R.; Ochterski, J. W.; Martin, R. L.; Morokuma, K.; Farkas, O.; Foresman, J. B.; Fox, D. J. Gaussian, Inc., Wallingford CT, **2016**.

150. Struppe, J.; Zhang, Y.; Rozovsky, S. ^{77}Se Chemical Shift Tensor of L-selenocystine: Experimental NMR Measurements and Quantum Chemical Investigations of Structural Effects. *J. Phys. Chem. B* **2015**, *119* (9), 3643-3650.

151. Neese, F.; Wennmohs, F.; Becker, U.; Riplinger, C., The ORCA quantum chemistry program package. *J. Chem. Phys.* **2020**, *152* (22).

152. Feynman, R.P.; Leighton, R. B.; Sands, M. L. Chapter 4: Electrostatics. In *The Feynman Lectures on Physics: Mainly Electromagnetism and Matter* [Online]; Gottlieb, M. A., Pfeiffer, R., Eds.; Basic Books, USA, **2011**. <https://www.feynmanlectures.caltech.edu/info/> (accessed October 2020).

153. Avogadro: an open-source molecular builder and visualization tool. Version 1.2.0 <http://avogadro.cc/>, Marcus D Hanwell, Donald E Curtis, David C Lonie, Tim Vandermeersch, Eva Zurek and Geoffrey R Hutchison; "Avogadro: An advanced semantic chemical editor, visualization, and analysis platform" *Journal of Cheminformatics* **2012**, *4*, 17.

154. Cronin, L.; Higgitt, C. L.; Karch, R.; Perutz, R. N. Rapid Intermolecular Carbon-Fluorine Bond Activation of Pentafluoropyridine at Ni(0): Comparative Reactivity of Fluorinated Arenes and Fluorinated Pyridine Derivatives. *Organometallics* **1997**, *16*(22), 4920-4928.

155. Amin, N.; Claridge, T. Quantitative NMR Spectroscopy. 2017. <http://nmrweb.chem.ox.ac.uk/Data/Sites/70/userfiles/pdfs/quantitative-nmr.pdf>

156. Bao, F.; Liu, Z.; Bai, H.; Zhang, H.; Liu, P.; Zhang, Q.; Chai, G. Palladium/Sensory Component-Catalyzed Homocoupling Reactions of Aryl Halides. *Synlett*. **2020**, *31*, 1501-1506.

157. Zick, M. E.; Lee, J.-H.; Gonzalez, M. I.; Velasquez, E. O.; Uliana, A. A.; Kim, J.; Long, J. R.; Milner, P. J. Fluoroarene Separations in Metal-Organic Frameworks with Two Proximal Mg^{2+} Coordination Sites. *J. Am. Chem. Soc.* **2021**, *143*, 1948-1958.

158. Firth, J. D.; Hammarback, L. A.; Burden, T. J.; Eastwood, J. B.; Donald, J. R.; Horbaczewskyj, C. S.; McRobie, M. T.; Tramaseur, A.; Clark, I. P.; Towrie, M.; Robinson, R.; Krieger, J.-P.; Lynam, J. M.; Fairlamb, I. J. S. Light- and Manganese-Initiated Borylation of Aryl Diazonium Salts: Mechanistic Insight on the Ultrafast Time-Scale Revealed by Time-Resolved Spectroscopic Analysis. *Chem.-Eur. J.* **2021**, *27*, 3979-3985.

159. Feofanov, M.; Akhmetov, V.; Takayama, R.; Amsharov, K. Catalyst-Free Synthesis of O-Heteroarenes by Ladderization of Fluorinated Oligophenylenes. *Angew. Chem. Int. Ed.* **2020**, *60*, 5199-5203.

Chapter 4: Electrostatic Effects on Bond Vibrations in Ni Nitrosyl Compounds Featuring a Novel Borate Anion

Manuscript in preparation: Kelty, M. L.; Martinez, J. L.; Anderson, J. S.

4.1 Introduction

The incorporation of electric field effects into catalytic systems has emerged as a promising avenue to control reactivity.¹⁻³ Large oriented electric fields have been reported within enzyme active sites and are proposed to be the predominant contributor to enzyme catalysis in certain cases.^{4,5} The most frequently proposed method of electric field mediated transition state stabilization is through alignment of the electric field within the active site to mimic the transition state dipole.⁴⁻⁷ Recently, electric fields within metalloenzymes have also been proposed to alter fundamental properties of the metal active site such as redox potential, basicity, and the localization of spin density.⁸ Externally applied electric fields have also been applied to accelerate reactions and alter selectivity in heterogeneous systems such as capacitor reactors, probe-bed-probe reactors, and integrated circuit reactors.³ Organic reactions can likewise be accelerated by the presence of an externally applied field, as demonstrated using scanning tunneling microscopy experiments.^{9,10}

Electric fields within enzymatic active sites are generated by the presence of alkali metal cations and charged or polar residues throughout the protein structure.^{2,5} A similar strategy for incorporating electric field effects into molecular reactivity can be envisioned through the incorporation of charged functional groups.² Indeed, multiple studies examining the electrostatic influence of cationic alkali and alkaline earth metals,¹¹⁻¹³ cationic trimethylammonium groups,¹⁴⁻¹⁶ and anionic sulfonates,^{14,16,17} borates^{18,19} and carboxylates^{20,21} in transition metal complexes

have been reported in the past few years. Charged moieties can exert a range of different effects on transition metal electronic structure and reaction mechanism. Most commonly, the redox potential of the transition metal is significantly shifted as a function of the charge.² Other electronic features that have been influenced include TM=E basicity (E=O, N)^{11,13,16} and the energy of molecular orbitals.²² Reactivity trends in H-atom transfer,^{11,16} O-atom transfer¹⁸ and O₂ and CO₂ reduction reactivity^{14,15,23} have also been observed to differ from those observed with neutral ligands.

Despite these recent examples, the assignment and interpretation of electrostatic effects remains challenging in molecular systems. One complication involves deconvoluting electrostatic effects from inductive contributions from the charged functional groups. To date, this challenge has been addressed in a few examples by varying the ionic strength or dielectric constant of the surrounding media, which variably quenches the electrostatic contribution to allow assignment.^{16,24} In the previous chapter, we demonstrated that in experimentally accessible conditions up to 46% of the increase in donor strength in an anionic phosphine relative to the neutral congener resulted from electrostatic contributions. The electrostatic influence would increase even more if the compound were soluble in non-polar solvents, given an estimated 82% contribution in a vacuum environment. The significant contribution from through space effects suggests that the location of the charge in space will likewise exert a substantial influence. Given this, an additional challenge in characterizing molecular electrostatic effects regards the anticipated directionality of these effects based on precedent from enzymatic and heterogeneous examples.⁵⁻⁷ However, an orientation dependence to field effects in molecular systems has not been clearly demonstrated. One reason for the dearth of examples is the synthetic challenge of moving charges around a molecule such that the orientation of a field can be varied, and examples of suitable systems are extremely

limited.¹⁴ A recent report from the Mayer group examined the dependence of redox potential and electrocatalytic CO₂ and O₂ reduction reactivity between four different atropisomers of iron metalated *ortho*-trimethylammonium substituted tetraphenyl porphyrin complexes.^{15,24,25} In these atropisomers, the charges are fixed either above or below the porphyrin plane, and result in distinct electric field environments at the iron center. The iron based redox couples, as well as the overpotential and TOF for O₂ and CO₂ reduction was found to vary minimally across the series despite the different electric field environments. Given the lack of variation between the different atropisomers, it was proposed that the density of charge surrounding the iron center plays a larger role in determining the redox potential and reactivity than the exact orientation of the generated field. Considering that the alignment of an applied field with the transition state dipole is a key method of rate acceleration in heterogeneous and enzymatic systems, the lack of orientation dependence in molecular systems suggests that similar effects may not be accessible. To address this question, additional studies on molecular systems in which the field orientation can be altered are necessary.

Measuring the effect of charged ligand scaffolds on the stretching frequency of coordinated small molecules should provide insight on the electric field environment at metal coordination site. Diatomic bond vibrations are known to be sensitive to the magnitude of the field along the bond axis. Specifically, the dipole of the first excited state in a polar diatom is larger than the dipole in the ground state, resulting in a greater sensitivity of the energy of the first excited state to an applied field.^{5,26} As the energies of the two states are differentially affected, the transition energy measured by vibrational spectroscopy shifts accordingly. This effect is known as the vibrational Stark effect and has been used by the Boxer group to measure electric fields in enzymatic and solution

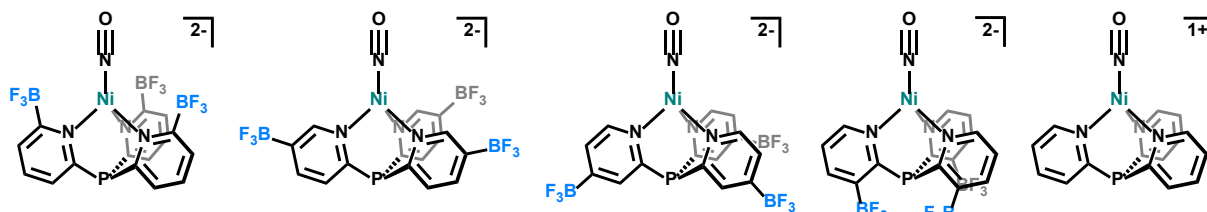


Figure 4.1 Proposed series of complexes with varying electric fields due to differential positioning of the anionic moiety.

environments.^{5,26} Given the response of bond vibrations to external electric fields, analyzing the effect of charged functional groups on a bond vibration in molecular systems may provide insight on the relevance of a field interpretation in these systems. Additionally, bond activation at transition metal centers is a key step in small molecule activation and may provide insight on how to leverage electrostatic effects in similar reactions.

To address the impact of field orientation in molecular systems, this work proposes the synthesis of a series of tridentate pyridine-based ligands with anionic functional groups appended to different positions on the pyridine ring. The large charge on the tri-anionic ligand should lead to significant electrostatic effects, and the variation of the position should lead to distinct field strengths at the metal center. To measure the anion effects on donor strength and the electric field at the metal center, I have targeted metalation with a nickel nitrosyl fragment, a metal diatomic oscillator combination commonly used to measure the donor strength of tri-dentate ligands (Figure 4.1).²⁷ Previous studies have reported a nitrosyl stretching (ν_{NO}) frequency of $\sim 1740 \text{ cm}^{-1}$ in the case of weakly donating ligands such as tris-pyrazolyl borate and decreasing stretching frequencies with the use of more strongly donating ligands such as tris carbene borates ($\sim 1700 \text{ cm}^{-1}$).²⁷ The nitrosyl stretching frequency obtained with the proposed anionic ligands will also be compared to the Ni nitrosyl metalated neutral tris-pyridine ligand (Figure 4.1).

Initially, the synthesis of anionic tripodal pyridine-based ligands was pursued with anionic trifluoroborate (BF_3^-) moieties. DFT calculations on the proposed Ni-NO series indicate that the ν_{NO} is sensitive to the location of the anion. However, the BF_3^- anions reduced the solubility of the starting 2-bromopyridine arms in organic solvents, inhibiting the reliable synthesis of tridentate ligands with a central phosphine atom. To address solubility concerns, the synthesis of the novel anion $\text{R-BF}_2\text{CF}_3^-$ incorporating a trifluoromethyl group was pursued. The incorporation of the $\text{R-BF}_2\text{CF}_3^-$ anion has been preliminarily observed at the 3, 4 and 5 positions of 2-bromo-pyridine, although the work-up procedure remains under development. Upon isolation of pure BF_2CF_3^- substituted 2-bromopyridine, the reagent can be reacted with phosphine electrophiles to generate multi-dentate pyridine-based ligands, analogous to the procedures developed with the BF_3^- substituted 2-bromopyridine.

4.2 Results and Discussion

4.2.1 Computational Prediction of Donor Strength

The influence of anion positioning on the donor strength of tridentate pyridine ligands was assessed computationally across a series of Ni nitrosyl complexes (see experimental section for computational details). In total five distinct ligands were investigated, a neutral tris-pyridyl phosphine (PPy_3) ligand and the series of proposed anionic pyridine ligands $\text{P}(6\text{-BF}_3\text{-2-py})_3$, $\text{P}(5\text{-BF}_3\text{-2-py})_3$, $\text{P}(4\text{-BF}_3\text{-2-py})_3$, and $\text{P}(3\text{-BF}_3\text{-2-py})_3$. The distinct positions of the anions in each ligand is expected to result in a different electrostatic environment, as Coulomb's law predicts a $1/r^2$ dependence of the electric field on distance.²⁸ The ligands were optimized with Ni-NO, as the nitrosyl vibration (ν_{NO}) is a commonly used metric of donor strength for tri-dentate ligands.²⁷ Specifically, ν_{NO} decreases in energy with more strongly donating ligands due to an increase in

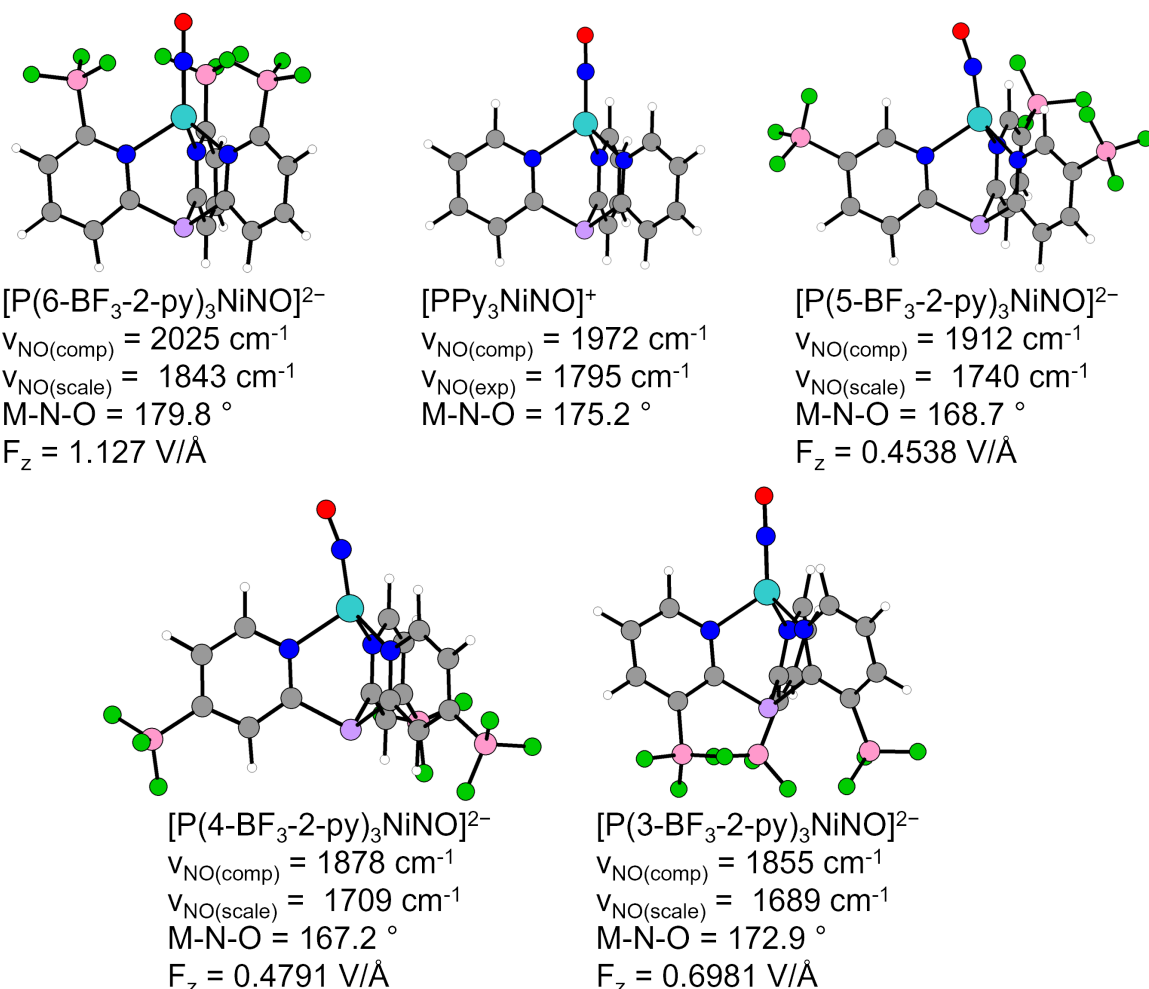


Figure 4.2 DFT optimized structures of the proposed Ni-NO complexes with the calculated stretching frequency ($\nu_{\text{NO}(\text{comp})}$), the experimental ($\nu_{\text{NO}(\text{exp})}$) or scaled ($\nu_{\text{NO}(\text{scale})}$) stretching frequency, M-N-O bond angle, and electric field predicted along the z axis using Coulomb's law and the optimized structures (see experimental section for details).

back bonding from Ni. For example, the ν_{NO} for the tris carbene borate complex $\text{PhB}(\text{tBuIm})_3\text{NiNO}$ is 1701 cm^{-1} , while for the tris-pyrazolyl borate ligand $\text{HB}(\text{pzMe}_2)_3\text{NiNO}$ ν_{NO} is 1746 cm^{-1} .²⁷ Additionally, ν_{NO} is expected to be informative in this case as bond vibrations can report on the electric field in their environment via the vibrational stark effect.⁵ Geometry optimizations of the nitrosyl complexes using the O3LYP functional shows tridentate coordination of the ligand to Ni in all cases and Ni-N-O angles varying between 167.2 and 179.8° (Figures A4.31-A4.35). Nickel nitrosyls can assume two distinct resonance structures, either a linear $\text{Ni-N}\equiv\text{O}$ with a formally

cationic nitrogen and oxygen, or a bent Ni-N=O with a formally anionic nitrogen.^{29,30,31} The angles of the optimized structures are consistent with linear nitrosyl complexes but suggest that the anion position may influence the contributions of each resonance structure. Frequency calculations indicate that the nitrosyl stretch $\nu_{\text{NO}(\text{comp})}$ varies with anion position, with the highest energy stretch predicted for $[\text{P}(6\text{-BF}_3\text{-2-py})_3\text{NiNO}]^{2-}$ (Figure 4.2). The experimentally determined ν_{NO} frequency determined for the neutral ligand PPy₃ nitrosyl complex (see below) can be used to scale the calculated frequencies, a common correction applied to predicted vibrations.³² Surprisingly, the experimental $\nu_{\text{NO}(\text{exp})}$ for $[\text{PPy}_3\text{NiNO}]^+$ is lower in energy than the predicted $\nu_{\text{NO}(\text{scale})}$ for $[\text{P}(6\text{-BF}_3\text{-2-py})_3\text{NiNO}]^{2-}$, suggesting that the neutral ligand is a stronger donor than the tri-anionic ligand. This trend is contrary to what would be expected given the observed increase in phosphine donor strength upon inclusion of a BF₃⁻ moiety in Chapter 3. The remaining anionic ligands are predicted to have lower energy $\nu_{\text{NO}(\text{scale})}$ stretches than $[\text{PPy}_3\text{NiNO}]^+$. Notably, the $\nu_{\text{NO}(\text{scale})}$ stretch in the two examples of meta substitution, $[\text{P}(5\text{-BF}_3\text{-2-py})_3\text{NiNO}]^{2-}$ and $[\text{P}(3\text{-BF}_3\text{-2-py})_3\text{NiNO}]^{2-}$ are predicted to vary by 51 cm⁻¹ despite what are likely similar inductive and resonance contributions, highlighting the potential involvement of through space electrostatic contributions. While the values of the $\nu_{\text{NO}(\text{scale})}$ stretches vary outside of the experimentally established frequency range, they do suggest that substantial variation in the nitrosyl vibration may be observed simply due to modification of anion location.

4.2.2 Synthesis and Characterization of Heteroaryl Phosphines with BF₃K Substituents

The synthesis of bi- and tri-dentate ligands with anionic pyridines was initially pursued with 6-trifluoroborate (BF₃) substituted 2-bromopyridine (2-Br-6-BF₃K-py), the synthesis of which was previously reported in the literature.³³ Given the challenge of selective lithiation in unsymmetric dibromo pyridines, the synthesis of 2-bromopyridines with BF₃ moieties in the 3, 4 and 5 positions

was not initially pursued, although literature reports suggest that selective lithiation and subsequent functionalization is possible.³⁴⁻³⁶ A bromine at the 2 position was included to enable subsequent substitution onto a central tethering atom such as phosphine and furnish the desired multi-dentate ligands. It was found that the lithium-halogen exchange of 2-Br-6-BF₃K-py with nBuLi in THF at -78 °C was aided by the inclusion of stoichiometric LiCl to increase the solubility of the pyridine. Initially, the bi-dentate ligand was targeted as the double substitution was

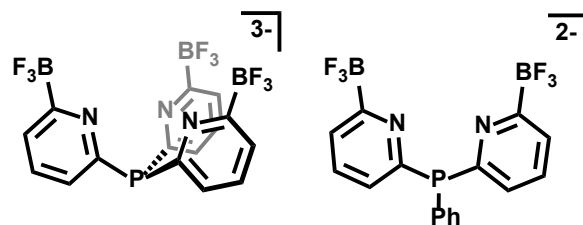


Figure 4.3 The proposed tri- and bi-dentate ligands P(6-BF₃-2-py)₃ and PPh(6-BF₃-2-pyridine)₂.

anticipated to proceed more cleanly (Figure 4.3, right). Indeed, reaction of the lithiated pyridine with pre-cooled PPhCl₂ resulted in the formation of PPh(6-BF₃K-2-pyridine)₂, which was isolated at the protonated zwitterion in 34% yield after stirring with 2 equivalents of HCl_(aq) and extracting into ethyl acetate (Figures A4.1-A4.5). The preparation of a tridentate ligand was subsequently pursued with PCl₃, which proved to be a more challenging electrophile (Figure 4.3, left). Addition of pre-cooled PCl₃ to the pyridine anion usually resulted in the formation of P(6-BF₃K-2-py)₃, which was also isolated as a protonated zwitterion in 11% yield after precipitation from an HCl_(aq)/methanol solution (Figures A4.6-A4.10). Although the syntheses for these multi-dentate phosphine-based ligands have been replicated, they do not reliably result in the desired product and are low yielding. One potential reason for this variability is the minimal solubility of 2-Br-6-BF₃K-py in THF at -78 °C, which may preclude stoichiometric reactivity. In order to address this challenge, the synthesis of more soluble anionic 2-bromopyridines was pursued.

4.2.3 Synthesis and Characterization of Pyridines with $\text{BF}_2\text{CF}_3\text{K}$ Substituents

Anionic 2-bromopyridines with more solubilizing anions were pursued to increase the reliability of the phosphine multi-dentate ligand synthesis. A more soluble anion is also anticipated to benefit the study of electrostatic effects, as non-polar solvents less effectively shield unpaired charges and allow for electrostatic effects over longer length scales.^{7,24,37} Ideally, the selected anion would be solubilizing, non-coordinating to prevent convoluting covalent interactions, inert to common decomposition pathways, and compact to ensure a high charge density. The commonly used sulfonate and carboxylate anions do not fulfill these requirements, as they can coordinate metals and engage in proton-shuttling reactivity.^{16,38,39} Alky and alkoxy borates have been reported to engage in group transfer reactivity,^{40,41} and aryl borates have been observed to engage in redox reactivity and have more charge delocalization into the aryl rings.⁴²⁻⁴⁴ The synthesis of a novel anion to meet these requirements was pursued as no viable options existed to date. The substitution of a fluorine on BF_3 with a CF_3 group was predicted to increase the solubility of the anion while maintaining a compact and chemically and redox inert anion. However, there are extremely limited examples of CF_3 substituted fluoroborates, with $\text{BF}_3\text{CF}_3\text{K}$ being the predominant example.^{45,46} The substitution of R- BF_3 moieties has been reported with TMSCl in the presence of KF , and accordingly the initial attempts at generating the new anion involved the use of TMSCl , KF , and TMSCF_3 with 2-Br-6- BF_3K -py (Figure 4.4).^{47,48} However, no substitution was observed under these conditions. Alternatively, the substitution of boranes with CF_3 has been reported previously with TMSCF_3 and KF and could potentially be implemented with boronic acid substituted 2-bromopyridines (Figure 4.4).^{41,46} However, the synthesis of boronic acid substituted pyridines on large scales is complicated by competing protodeboronation decomposition pathways.^{55,49} Finally, the borane $\text{B}(\text{OMe})_2\text{CF}_3$ has been reported from the reaction between $\text{B}(\text{OMe})_3\text{CF}_3$ and super-

stoichiometric MeSO_2Cl .⁴⁶ In theory the borane could be substituted for the $\text{B}(\text{O}^i\text{Pr})_3$ electrophile used in the reported synthesis of 2-Br-6- BF_3K -pyridine (Figure 4.4). The borane $\text{B}(\text{OMe})_2\text{CF}_3$ is reported to be isolated via distillation, however in our hands the product was very challenging to separate from excess MeSO_2Cl . Alternatively, the abstraction of methoxide from $\text{B}(\text{OMe})_2\text{ArCF}_3$ has been reported with stoichiometric TMSCl .⁴¹ Consistent with this report, the in-situ generation of $\text{B}(\text{OMe})_2\text{CF}_3$ from $\text{B}(\text{OMe})_3\text{CF}_3$ and TMSCl proved to be a synthetically viable route to install a BF_2CF_3 anion (*vide infra*).

While pursuing the design of a novel anion, the method of carbon-halogen exchange to install the anion on 2-bromopyridine was also re-evaluated. It has been reported previously that the use of $i\text{PrMgCl}\cdot\text{LiCl}$, also known as turbo Grignard, can be used to substitute aryl iodides with pinacol boranes.⁵⁰ As this procedure is simpler than lithium halogen exchange at low temperatures, the use of 2-bromo- x -iodo-pyridines ($x = 2, 3, 4$ and 5) was selected for the initial investigations with novel anions. The viability of this method of substitution with the in-situ prepared $\text{B}(\text{OMe})_2\text{CF}_3$ was first investigated with 2-Br-4-I-pyridine. A stoichiometric amount of turbo Grignard was combined with 2-Br-4-I-pyridine in THF at $-10\text{ }^\circ\text{C}$ and then stirred at room temperature for 2

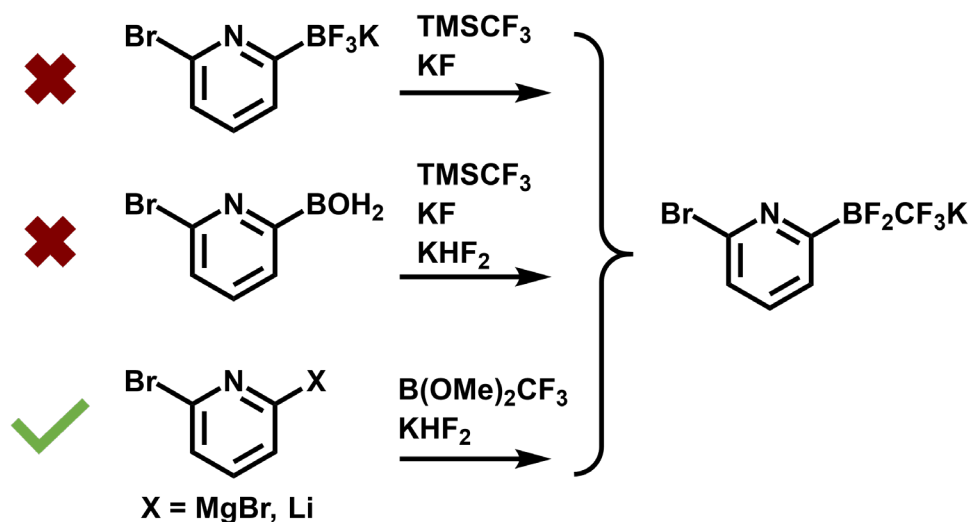


Figure 4.4 Synthetic routes towards the preparation of a BF_2CF_3 substituted pyridine.

hours. The pyridine Grignard was then cooled to $-78\text{ }^{\circ}\text{C}$ and a solution of the borane generated in-situ via the reaction of stoichiometric $\text{KB}(\text{OMe})_3\text{CF}_3$ with 1 equivalent of TMSCl was filtered into the solution. The reaction was warmed to room temperature overnight, and the next morning dioxane was added to precipitate the Mg salts. Without this step, the reaction does not proceed cleanly as Mg can act as a fluoride abstractor (Figure A4.24).⁵¹ Subsequently, the reaction is

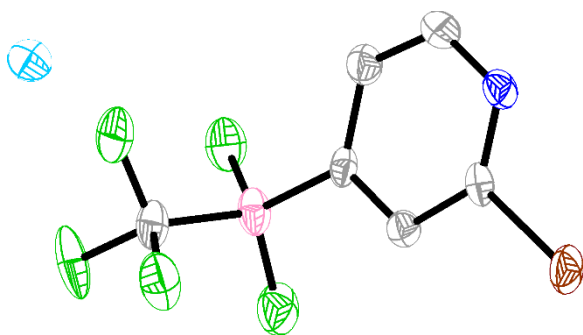


Figure 4.5 SXR structure of 2-Br-4-BF₂CF₃K-pyridine. C is in grey, N is in blue, Br is in brown, B is in pink, F is in green and K is in cyan. H-atoms are omitted for clarity.

filtered and the filtrate is combined with 3 equivalents of $\text{KHF}_2(\text{aq})$ for 30 minutes. Drying of the organic fraction then yields a brown oil which was characterized by NMR spectroscopy. The ^1H NMR spectrum indicates approximately 80% purity as three major resonances with the appropriate splitting patterns are observed (Figure A4.17). Additionally, two resonances consistent with CF_3 and BF_2 resonance are observed in the ^{19}F NMR spectrum (Figure A4.18), and a peak consistent with an anionic boron is observed around 0 ppm in the ^{11}B NMR spectrum (Figure A4.19). Notably, the BF_2 resonance around -170 ppm in the ^{19}F NMR spectrum is significantly shifted in comparison to the BF_3 resonance in 2-Br-6-BF₃K-pyridine, which appears around ~ 140 ppm. Although significant coupling between the fluorine and boron atoms is anticipated, the coupling in these spectra is mostly not resolved. Test scale reactions with 2-Br-3-I-pyridine and 2-Br-5-I-pyridine also suggest the formation of the desired product in $\sim 80\%$ initial purity, while the reaction with 2-Br-6-I-pyridine does not yield the desired product (Figures A4.25-A4.30). Scaling up the synthesis to 3g of 2-Br-4-I-pyridine resulted again in the desired 2-Br-4-BF₂CF₃K-pyridine as the major crude product, although the development of a purification procedure is ongoing. Crystals of this product were obtained from a

concentrated solution of the pyridine in DCM/THF, and the structure determined by single crystal x-ray diffraction (SXR) confirms the presence of the BF_2CF_3 anion on the pyridine (Figure 4.5). The solubility properties of this new anion appear improved relative to the BF_3 pyridine congener, as the brown oil readily dissolves in minimal MeCN, THF, acetone and ethyl acetate. The relatively high purity of the crude products from these reactions are promising, and bulk purification methods are currently being pursued.

4.2.4 Synthesis and Characterization of Ni-NO Complexes

Following large scale synthesis of the BF_2CF_3 substituted bromopyridines, they will be incorporated into tridentate ligands using a synthetic prep analogous to the one developed for the 2-Br-6- BF_3K -pyridine. The next step will be to react them with $n\text{BuLi}$ at -78°C and quench the carbanion with PCl_3 , and it is anticipated that LiCl will not be required given the improved solubility in THF. In order to compare the ν_{NO} stretches of Ni-NO complexes supported by anionic and neutral pyridine ligands, the neutral ligand congener was also prepared. The ligand PPy_3 was synthesized according to literature procedure⁵² and metalated with $\text{NiNOBr}(\text{PPh}_3)_2$ ⁵³ in the presence of NaBPh_4 to furnish $[\text{PPy}_3\text{NiNO}][[\text{BPh}_4]]$. SXR of crystals grown from DCM/benzene confirm coordination of the pyridines to nickel (Figure 4.6). Four

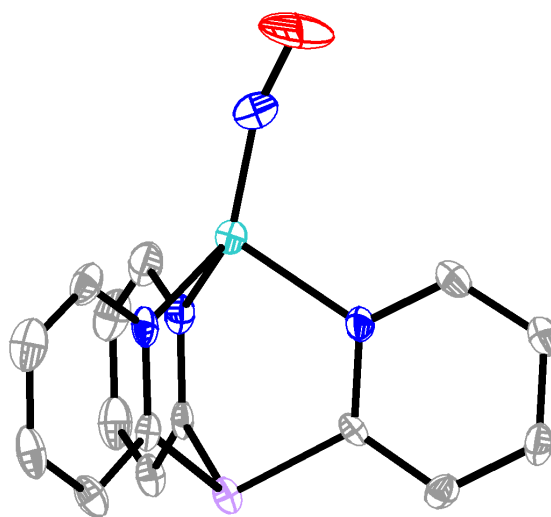


Figure 4.6 SXR structure of $[\text{PPy}_3\text{NiNO}][[\text{BPh}_4]]$. C is in grey, N in blue, O in red, P in purple, and Ni in teal. H atoms and BPh_4 omitted for clarity.

different Ni-NO complexes are present in the asymmetric unit with Ni-N-O bond angles varying from $164.4(5)$ to $172.3(4)^\circ$, suggesting the angle may be impacted by crystal packing. NMR

spectra likewise support the assignment of a symmetric complex in solution (Figures A4.11-A4.13). The IR spectrum of this compound contains the nitrosyl stretch at 1795 cm^{-1} , indicating that the ligand is very weakly donating (Figure A4.16). Cyclic voltammetry of the compound in THF shows two irreversible reductions at -2.05 and -2.81 V vs Fc/Fc^+ (Figures A4.14 and A4.15). The first reduction may be consistent with nitrosyl coupling, which has previously been observed with pyridine ligands.⁵⁴

4.3 Conclusion

The syntheses of novel phosphine linked bidentate and tridentate pyridine ligands with BF_3 substituents at the 6 position on pyridine are reported. However, the syntheses are low yielding and unreliable, possibly due to the limited solubility of the BF_3^- anion in organic solvents. The limited solubility of the BF_3^- anion will also be problematic for the observation of electrostatic effects, which are most prominent in non-polar solvents. Given these considerations, the design of a novel BF_2CF_3^- anion for incorporation into the series of proposed pyridine-based ligands is pursued. Preliminary results towards the synthesis of anionic 2-bromopyridines with BF_2CF_3^- at the 3, 4 or 5 positions on the pyridine are presented. In these procedures, the $\text{B}(\text{OMe})_2\text{CF}_3$ borane is prepared in-situ and reacted with the 2-Br-X-MgBr-pyridine (X = 3, 4, or 5) Grignard and subsequently fluorinated to yield the crude desired 2-Br-X- BF_2CF_3 -pyridine (X = 3, 4, or 5) product in approximately 80% purity as determined by ^1H NMR. A single crystal structure of the 2-Br-4- BF_2CF_3 -pyridine confirms the connectivity of the proposed anionic pyridine and the assignment of NMR resonances. The purification of these novel pyridines will be optimized and their incorporation into tridentate ligands will be pursued. Metalation of these compounds with

NiNO will allow for comparison of the donor strength with other tri-dentate ligands and provide insight into electrostatic effects on bond vibrations.

4.4 Experimental

4.4.1 General Procedures

All reagents were purchased from commercial suppliers and used without further purification unless otherwise specified. The reagents $P(Py)_3$,⁵² $NiNOBr(PPh_3)_2$,⁵³ 2-Br-6-BF₃K-pyridine,^{33,55} and $KB(OMe)_3CF_3$ ⁴⁶ were synthesized according to literature procedures. All manipulations were carried out under an atmosphere of N₂ using standard Schlenk and glovebox techniques. Glassware was dried at 180 °C for a minimum of two hours and cooled under vacuum prior to use. All reactions were carried out in 20 mL scintillation vials unless otherwise specified. All volumes below 0.5 mL were measured using Hamilton 100 or 250 µL syringes. Solvents were dried on a solvent purification system from Pure Process Technology and stored over 4 Å molecular sieves under N₂. Tetrahydrofuran was stirred over NaK alloy and run through an additional activated alumina plug prior to use to ensure dryness. Solvents were tested for H₂O and O₂ using a standard solution of sodium-benzophenone ketyl radical anion. C₆D₆, CDCl₃, acetone-*d*₆, CD₃CN, and DMSO-*d*₆ were dried by passage over a column of activated alumina and stored over 4 Å molecular sieves in the glovebox. ¹H, ¹³C{¹H}, ¹⁹F{¹H}, ¹¹B{¹H}, and ³¹P{¹H} data were acquired on a combination of three spectrometers: a 400 MHz Bruker DRX spectrometer equipped with a BBO probe; a 500 MHz Bruker Avance-II+ spectrometer equipped with a ¹H{¹⁹F, ¹³C, ³¹P} QNP probe; and a 500 MHz Bruker Avance III HD spectrometer equipped with a Bruker BBFO “Smart” probe. All spectrometers use Topspin. Chemical shifts are reported in ppm units referenced to residual

solvent resonances for ^1H and $^{13}\text{C}\{^1\text{H}\}$ spectra, and external standards for $^{31}\text{P}\{^1\text{H}\}$, $^{11}\text{B}\{^1\text{H}\}$, and $^{19}\text{F}\{^1\text{H}\}$. NMR samples were prepared by dissolving approximately 5-10 mg of the sample in about 0.5 mL of the appropriate deuterated solvent. IR spectra were recorded on a Bruker Tensor II using a KBr pellet.

4.4.2 Syntheses

PPh(6-BF₃-2-pyH)₂. A 8 mL THF solution of 2-Br-6-BF₃K-pyridine (300 mg, 1.14 mmol) and LiCl (48 mg, 1.14 mmol, 1 equiv.) was cooled to $-78\text{ }^\circ\text{C}$. To the solution was added nBuLi (454 μL , 1.14 mmol) and the reaction was stirred for 20 minutes. To the reaction was added 1.542 mL of a 2 mL THF stock solution with 100 μL of PPhCl₂ ($\sim 77\text{ }\mu\text{L}$ delivered, 0.56 mmol, 0.5 equiv.) and the reaction was left stirring to warm to room temperature overnight. The reaction was pumped down and then the reaction was suspended in 10 mL MeOH and 12 mL of a 0.1 M HCl_(aq) solution was added. The mixture was extracted with ethyl acetate and the organic fraction was dried under vacuum to yield the desired product as a crude solid (159.6 mg, 0.39 mmol, 34%). ^1H NMR (400 MHz, 25 $^\circ\text{C}$, DMSO-*d*₆) δ = 15.27 (br s, 2H), 8.31 (t, J = 8 Hz, 2H), 7.95 (d, J = 8 Hz, 2 H), 7.60 (m, 3H), 7.47 (m, 2H), 7.19 (d, J = 8 Hz, 2H). $^{31}\text{P}\{^1\text{H}\}$ NMR (162 MHz, 25 $^\circ\text{C}$, DMSO-*d*₆) δ = -13.6 (s). $^{19}\text{F}\{^1\text{H}\}$ NMR (376 MHz, 25 $^\circ\text{C}$, DMSO-*d*₆) δ = -142.0 (br s). $^{11}\text{B}\{^1\text{H}\}$ NMR (160 MHz, 25 $^\circ\text{C}$, DMSO-*d*₆) δ = 0.9 (br s). ESI-MS (negative mode, MeCN) 399.1 (HPPPh(2-BF₃-6-py)₂⁻).

P(6-BF₃-2-pyH)₃. A 40 mL solution of 2-Br-6-BF₃K-pyridine (1.09 g, 4.13 mmol) and LiCl (219 mg, 5.16 mmol, 1.25 equiv.) in THF was cooled to $-78\text{ }^\circ\text{C}$, yielding a sheer white solution. To the solution nBuLi (1.651 mL, 4.13 mmol, 1 equiv.) was added dropwise, resulting in an orange solution. The reaction was stirred for 10 minutes and neat PCl₃ (139 μL , 1.38 mmol, 0.33 equiv) pre-cooled to $-78\text{ }^\circ\text{C}$ was added dropwise using a micro-syringe, and the reaction was allowed to

warm to room temperature overnight with stirring. The next day the brown heterogeneous solution was dried under vacuum. The solid was removed from the glovebox and was suspended in methanol and 41 mL of 0.1 M HCl_(aq) was added. After 1 hour the white precipitate was collected by filtration and dried under vacuum. The solid was pumped into the glovebox and dissolved in minimal DMF and layered under THF at room temperature. After a few days small white crystals were isolated of the product (73.6 mg, 0.16 mmol, 11%). ¹H NMR (400 MHz, 25 °C, DMSO-*d*₆) δ = 15.18 (br s, 3H), 8.37 (t, *J* = 8Hz, 3H), 8.08 (d, *J* = 8Hz, 3H), 7.34 (d, *J* = 8 Hz, 3H). ³¹P{¹H} NMR (162 MHz, 25 °C, DMSO-*d*₆) δ = -19.2 (s). ¹⁹F{¹H} NMR (376 MHz, 25 °C, DMSO-*d*₆) δ = 142.5 (br s). ¹¹B{¹H} NMR (160 MHz, 25 °C, DMSO-*d*₆) δ = 0.7 ppm (br s). ESI-MS (negative mode, MeCN) 747.1 (HLiP(2-BF₃-6py)₃⁻).

[P(2-py)₃NiNO][BPh₄]. In 10 mL of DCM was combined PPy₃ (12.2 mg, 0.04 mmol), NiNOBr(PPh₃)₂ (32 mg, 0.046 mmol, 1.15 equiv.) and NaBPh₄ (15.8 mg, 0.046 mmol, 1.15 equiv.) and the heterogeneous mixture was stirred for 12 hours. Filtration of the heterogeneous solution affords purple solid, which was washed with C₆H₆ to remove excess PPh₃ and PPy₃. The crude material was isolated in quantitative yield and was crystallized from a layering of DCM/C₆H₆ to obtain crystals suitable for diffraction. ¹H NMR (400 MHz, 25 °C, CD₂Cl₂) δ = 10.04 (d, *J* = 4 Hz, 3 H), 7.96 (m, 6H), 7.67 (t, *J* = 4 Hz, 3H), 7.31 (br s, 8H, BPh₄), 6.99 (t, *J* = 8 Hz, 8H), 6.84 (t, *J* = 8 Hz, 4H). ³¹P{¹H} NMR (162 MHz, 25 °C, CD₂Cl₂) δ = -27.9 (s). ¹¹B{¹H} NMR (160 MHz, 25 °C, CD₂Cl₂) δ = -6.6 (s). Cyclic voltammetry (0.1 NaBPh₄ in THF) -2.05 V and -2.81 V vs Fc/Fc⁺. IR (KBr pellet): 1795 cm⁻¹ (ν_{NO}).

Potassium 2-bromopyridin-4-yltrifluoromethyldifluoroborate (K[2-Br-4-BF₂CF₃-py]). A 40 mL THF solution of 2-Br-4-I-pyridine (3g, 0.01 mol) was cooled to -10 °C in the cold well and

$i\text{PrMgCl}\cdot\text{LiCl}$ (8.54 mL, 1.3M in THF, 0.011 mol, 1.05 equiv.) was added dropwise. The reaction was stirred at $-10\text{ }^{\circ}\text{C}$ for 1 hour and at room temperature for 2 hours. The brown homogenous solution was cooled in the cold well to $-78\text{ }^{\circ}\text{C}$. Concurrently, $\text{KB}(\text{OMe})_3\text{CF}_3$ (2.35 g, 0.011 mol, 1.05 equiv.) was dissolved in 40 mL THF and neat TMSCl (1.475 mL, 0.012 mmol, 1.1 equiv.) was added. The reaction was stirred for 1 hour and then filtered through a celite pad. The borane filtrate was added dropwise over the course of an hour to the cooled pyridine solution. The reaction was left to warm to room temperature overnight. Dioxane (20 mL) was added and the reaction was stirred for 1 hour, over which time a precipitate formed. The reaction was filtered through celite and removed from the box. $\text{KHF}_2(\text{aq})$ (2.476 g, 0.032 mmol, 3 equiv.) in 10 mL of water was added and the reaction was stirred for 30 minutes. The organic phase was decanted and dried with K_2CO_3 and then pumped down to a brown oil. The brown oil was transferred back into the glovebox and stirred with 15 mL of 50:50 DCM/hexane at $-78\text{ }^{\circ}\text{C}$ for 30 minutes. Decanting the solution and drying the solid under vacuum yielded 1.7g of brown crude solid, which was $\sim 80\%$ pure by NMR. The oil was dissolved in 5 mL THF and 5 mL DCM was added. The solution was decanted and concentrated by half under vacuum. After a few days at room temperature crystals suitable for diffraction formed at the bottom of the vial. ^1H NMR (400 MHz, $25\text{ }^{\circ}\text{C}$, CD_3CN) $\delta = 8.09$ (d, $J = 8\text{ Hz}$, 1H), 7.57 (s, 1H), 7.41 (d, $J = 4\text{ Hz}$, 1H). $^{19}\text{F}\{^1\text{H}\}$ NMR (376 MHz, $25\text{ }^{\circ}\text{C}$, CD_3CN) $\delta = -74.3$ (d, $J = 38\text{ Hz}$, 3F), -174.0 (q, $J = 76\text{ Hz}$, 2F). $^{13}\text{C}\{^1\text{H}\}$ NMR (126 MHz, $25\text{ }^{\circ}\text{C}$, CD_3CN) $\delta = 166.5$ (br s, 1C, $\text{CF}_3\text{F}_2\text{BC}$), 149.0 (s, 1C), 142.3 (s, 1C, BrC), 132.2 (s, 1C), 127.7 (s, 1C). $^{11}\text{B}\{^1\text{H}\}$ NMR (160 MHz, $25\text{ }^{\circ}\text{C}$, CD_3CN) $\delta = 0.2$ (s, $J = 48\text{ Hz}$, 1B).

Potassium 2-bromopyridin-3-yltrifluoromethyldifluoroborate ($\text{K}[2\text{-Br-3-BF}_2\text{CF}_3\text{-py}]$). An 8 mL solution of 2-Br-3-I-pyridine (300 mg, 1.06 mmol) was cooled in the $-40\text{ }^{\circ}\text{C}$ freezer in the glovebox. The vial was removed and placed on a stir plate, and $i\text{PrMgCl}\cdot\text{LiCl}$ (854 μL , 1.3 M in

THF, 1.1 mmol, 1.05 equiv.) was added dropwise at room temperature. The reaction was left to stir for 3 hours, then cooled to $-78\text{ }^{\circ}\text{C}$ in the cold well. Concurrently, TMSCl (148 μL , 1.16 mmol, 1.1 equiv.) was added to a solution of $\text{KB}(\text{OMe})_3\text{CF}_3$ (235 mg, 1.1 mmol, 1.05 equiv.) in 8 mL of THF and stirred for 1 hour. The borane solution was filtered dropwise into the cooled pyridine solution, and the reaction was left to stir overnight. The next day 2 mL of dioxane was added and the reaction was filtered. A 1 mL solution of $\text{KHF}_{2(\text{aq})}$ (248 mg, 3.2 mmol, 3 equiv.) was added and the reaction was stirred for 30 minutes. The organic fraction was decanted and dried with K_2CO_3 and pumped down to a brown oil under vacuum. The resulting oil was characterized by NMR and was not worked up further. The preliminary assignments for the desired product, observed in $\sim 80\%$ purity by NMR, are as follows. ^1H NMR (400 MHz, $25\text{ }^{\circ}\text{C}$, CD_3CN) $\delta = 8.55$ (d, $J = 8$ Hz, 1H), 8.33 (d, $J = 4$ Hz, 1H), 7.72 (dd, $J = 4$ Hz, 8Hz, 1H). $^{19}\text{F}\{^1\text{H}\}$ NMR (376 MHz, $25\text{ }^{\circ}\text{C}$, CD_3CN) $\delta = -73.0$ (d, $J = 38$ Hz, 3F), -171.0 (d, $J = 76$ Hz, 2F). $^{11}\text{B}\{^1\text{H}\}$ NMR (160 MHz, $25\text{ }^{\circ}\text{C}$, CD_3CN) $\delta = 0.6$ (br s).

Potassium 2-bromopyridin-5-yltrifluoromethyldifluoroborate (K[2-Br-5-BF₂CF₃-py]). An 8 mL solution of 2-Br-5-I-pyridine (300 mg, 1.06 mmol) was cooled in the $-40\text{ }^{\circ}\text{C}$ freezer in the glovebox. The vial was removed and placed on a stir plate, and $i\text{PrMgCl}\cdot\text{LiCl}$ (854 μL , 1.3 M in THF, 1.1 mmol, 1.05 equiv.) was added dropwise at room temperature. The reaction was left to stir for 3 hours, then cooled to $-78\text{ }^{\circ}\text{C}$ in the cold well. Concurrently, TMSCl (148 μL , 1.16 mmol, 1.1 equiv.) was added to a solution of $\text{KB}(\text{OMe})_3\text{CF}_3$ (235 mg, 1.1 mmol, 1.05 equiv.) in 8 mL of THF and stirred for 1 hour. The borane solution was filtered dropwise into the cooled pyridine solution, and the reaction was left to stir overnight. The next day 2 mL of dioxane was added and the reaction was filtered. A 1 mL solution of $\text{KHF}_{2(\text{aq})}$ (248 mg, 3.2 mmol, 3 equiv.) was added and the reaction was stirred for 30 minutes. The organic fraction was decanted and dried with K_2CO_3

and pumped down to a brown oil under vacuum. The resulting oil was characterized by NMR and was not worked up further. The preliminary assignments for the desired product, observed in ~80% purity by NMR, are as follows. ^1H NMR (400 MHz, 25 °C, CD_3CN) δ = 8.38 (s), 7.85 (d, J = 8 Hz, 1H), 7.46 (d, J = 8 Hz, 1H). $^{19}\text{F}\{^1\text{H}\}$ NMR (376 MHz, 25 °C, CD_3CN) δ = -74.7 (s, 3F), -175.4 (d, J = 76 Hz, 2F). $^{11}\text{B}\{^1\text{H}\}$ NMR (160 MHz, 25 °C, CD_3CN) δ = 0.9 (br s).

4.4.3 X-Ray Crystallography

The diffraction data were measured at 100 K on a Bruker D8 VENTURE with PHOTON 100 CMOS detector system equipped with a Mo-target micro-focus X-ray tube (λ = 0.71073 Å). Data reduction and integration were performed with the Bruker APEX3 software package (Bruker AXS, version 2015.5-2, 2015). Data were scaled and corrected for absorption effects using the multi-scan procedure as implemented in SADABS (Bruker AXS, version 2014/5, 2015, part of Bruker APEX3 software package). The structure was solved by the dual method implemented in SHELXT⁵⁶ and refined by a full-matrix least-squares procedure using OLEX23⁵⁷ software package (XL refinement program version 2014/7⁵⁸). Suitable crystals were mounted on a cryo-loop and transferred into the cold nitrogen stream of the Bruker D8 Venture diffractometer. Most of the hydrogen atoms were generated by geometrical considerations and constrained to idealized geometries and allowed to ride on their carrier atoms with an isotropic displacement parameter related to the equivalent displacement parameter of their carrier atoms. The co-crystallized benzene molecule in $[\text{PPy}_3\text{NiNO}][\text{BPh}_4]$ was modeled for disorder.

4.4.4 Computational Methods

Geometry optimizations and subsequent frequency calculations for $[\text{PPy}_3\text{NiNO}]^+$, $[\text{P}(6\text{-BF}_3\text{-2-py})_3\text{NiNO}]^{2-}$, $[\text{P}(5\text{-BF}_3\text{-2-py})_3\text{NiNO}]^{2-}$, $[\text{P}(4\text{-BF}_3\text{-2-py})_3\text{NiNO}]^{2-}$, and $[\text{P}(3\text{-BF}_3\text{-2-py})_3\text{NiNO}]^{2-}$ were carried out using Orca version 4.0⁵⁹ with the O3LYP functional and the def2-SVP⁶⁰ basis set

on C, H, B, and F, and def2-TZVPP⁶⁰ basis set on N, O and Ni. The spin state and charge were set to a triplet and +1 for PPy₃NiNO and a triplet and -2 for the anionic ligands. The frequency results were checked to ensure no negative vibrations were predicted. The frequency values were scaled by multiplying the predicted frequencies $\nu_{\text{NO}(\text{comp})}$ by 0.91, which is the ratio of $\nu_{\text{NO}(\text{exp})}/\nu_{\text{NO}(\text{comp})}$ for [P(2-py)₃NiNO].

4.5 References

1. Shaik, S.; Mandal, D.; Ramanan, R. Oriented Electric Fields as Future Smart Reagents in Chemistry. *Nat. Chem.* **2016**, *8*, 1091–1098.
2. Léonard, N. G.; Dhaoui, R.; Chantarojsiri, T.; Yang, J. Y. Electric Fields in Catalysis: From Enzymes to Molecular Catalysts. *ACS Catal.* **2021**, *11* (17), 10923–10932.
3. Che, F.; Gray, J. T.; Ha, S.; Kruse, N.; Scott, S. L.; McEwen, J.-S. Elucidating the Roles of Electric Fields in Catalysis: A Perspective. *ACS Catal.* **2018**, *8* (6), 5153–5174.
4. Warshel, A.; Sharma, P. K.; Kato, M.; Xiang, Y.; Liu, H.; Olsson, M. H. M. Electrostatic Basis for Enzyme Catalysis. *Chem. Rev.* **2006**, *106* (8), 3210–3235.
5. Fried, S. D.; Boxer, S. G. Electric Fields and Enzyme Catalysis. *Annu. Rev. Biochem.* **2017**, *86*, 387–415.
6. Shaik, S.; Ramanan, R.; Danovich, D.; Mandal, D. Structure and Reactivity/Selectivity Control by Oriented-External Electric Fields. *Chem. Soc. Rev.* **2018**, *47* (14), 5125–5145.
7. Ciampi, S.; Darwish, N.; Aitken, H. M.; Díez-Pérez, I.; Coote, M. L. Harnessing Electrostatic Catalysis in Single Molecule, Electrochemical and Chemical Systems: A Rapidly Growing Experimental Tool Box. *Chem. Soc. Rev.* **2018**, *47* (14), 5146–5164.
8. Bím, D.; Alexandrova, A. N. Local Electric Fields as a Natural Switch of Heme-Iron Protein Reactivity. *ACS Catal.* **2021**, *11* (11), 6534–6546.
9. Zhang, L.; Laborda, E.; Darwish, N.; Noble, B. B.; Tyrell, J. H.; Pluczyk, S.; Le Brun, A. P.; Wallace, G. G.; Gonzalez, J.; Coote, M. L.; Ciampi, S. Electrochemical and Electrostatic Cleavage of Alkoxyamines. *J. Am. Chem. Soc.* **2018**, *140* (2), 766–774.
10. Huang, X.; Tang, C.; Li, J.; Chen, L. C.; Zheng, J.; Zhang, P.; Le, J.; Li, R.; Li, X.; Liu, J.; Yang, Y.; Shi, J.; Chen, Z.; Bai, M.; Zhang, H. L.; Xia, H.; Cheng, J.; Tian, Z. Q.; Hong, W. Electric Field-Induced Selective Catalysis of Single-Molecule Reaction. *Sci. Adv.* **2019**, *5* (6), 3072–3093.
11. Léonard, N. G.; Chantarojsiri, T.; Ziller, J. W.; Yang, J. Y. Cationic Effects on the Net Hydrogen Atom Bond Dissociation Free Energy of High-Valent Manganese Imido Complexes. *J. Am. Chem. Soc.* **2022**, *144* (4), 1503–1508.
12. Chantarojsiri, T.; Ziller, J. W.; Yang, J. Y. Incorporation of Redox-Inactive Cations Promotes Iron Catalyzed Aerobic C–H Oxidation at Mild Potentials. *Chem. Sci.* **2018**, *9* (9), 2567–2574.
13. Oswald, V. F.; Lee, J. L.; Biswas, S.; Weitz, A. C.; Mitra, K.; Fan, R.; Li, J.; Zhao, J.; Hu, M. Y.; Alp, E. E.; Bominaar, E. L.; Guo, Y.; Green, M. T.; Hendrich, M. P.; Borovik, A. S. Effects of

Noncovalent Interactions on High-Spin Fe(IV)-Oxido Complexes. *J. Am. Chem. Soc.* **2020**, *142* (27), 11804–11817.

14. Azcarate, I.; Costentin, C.; Robert, M.; Savéant, J.-M. Through-Space Charge Interaction Substituent Effects in Molecular Catalysis Leading to the Design of the Most Efficient Catalyst of CO₂-to-CO Electrochemical Conversion. *J. Am. Chem. Soc.* **2016**, *138* (51), 16639–16644.

15. Martin, D. J.; Mayer, J. M. Oriented Electrostatic Effects on O₂ and CO₂ Reduction by a Polycationic Iron Porphyrin. *J. Am. Chem. Soc.* **2021**, *143* (30), 11423–11434.

16. Dhar, D.; Yee, G. M.; Tolman, W. B. Effects of Charged Ligand Substituents on the Properties of the Formally Copper(III)-Hydroxide ([CuOH]²⁺) Unit. *Inorg. Chem.* **2018**, *57* (16), 9794–9806.

17. Yi, J.; Zhan, S.; Chen, L.; Tian, Q.; Wang, N.; Li, J.; Xu, W.; Zhang, B.; Ahlquist, M. S. G. Electrostatic Interactions Accelerating Water Oxidation Catalysis via Intercatalyst O-O coupling. *J. Am. Chem. Soc.* **2021**, *143*, 2484-2490.

18. Paudel, J.; Pokhrel, A.; Kirk, M. L.; Li, F. Remote Charge Effects on the Oxygen-Atom-Transfer Reactivity and Their Relationship to Molybdenum Enzymes. *Inorg. Chem.* **2019**, *58* (3), 2054–2068.

19. Schmidt, B. M.; Engle, J. T.; Zhang, M.; Babahan, I.; Ziegler, C. J.; Jia, L. Zwitterionic Nickel(II) Complexes: Synthesis, Characterization, Decomposition, and Stoichiometric and Catalytic Reactivities. *J. Organomet. Chem.* **2016**, *805*, 94–99.

20. Margarit, C. G.; Asimow, N. G.; Gonzalez, M. I.; Nocera, D. G. Double Hangman Iron Porphyrin and the Effect of Electrostatic Nonbonding Interactions on Carbon Dioxide Reduction. *J. Phys. Chem. Lett.* **2020**, *11* (5), 1890–1895.

21. Puerta-Oteo, R.; Jiménez, M. V.; Pérez-Torrente, J. J. Molecular Water Oxidation Catalysis by Zwitterionic Carboxylate Bridge-Functionalized Bis-NHC Iridium Complexes. *Catal. Sci. Technol.* **2019**, *9* (6), 1437–1450.

22. Weberg, A. B.; McCollom, S. P.; Thierer, L. M.; Gau, M. R.; Carroll, P. J.; Tomson, N. C. Using Internal Electrostatic Fields to Manipulate the Valence Manifolds of Copper Complexes. *Chem. Sci.* **2021**, *12* (12), 4395–4404.

23. Martin, D. J.; Mercado, B. Q.; Mayer, J. M. Combining Scaling Relationships Overcomes Rate versus Overpotential Trade-Offs in O₂ Molecular Electrocatalysis. *Sci. Adv.* **2020**, *6* (11), 3318–3331.

24. Martin, D. J.; Johnson, S. I.; Mercado, B. Q.; Raugei, S.; Mayer, J. M. Intramolecular Electrostatic Effects on O₂, CO₂, and Acetate Binding to a Cationic Iron Porphyrin. *Inorg. Chem.* **2020**, *59* (23), 17402–17414.

25. Martin, D. J.; Mercado, B. Q.; Mayer, J. M. All Four Atropisomers of Iron Tetra(o- N, N, N-Trimethylanilinium)Porphyrin in Both the Ferric and Ferrous States. *Inorg. Chem.* **2021**, *60* (7), 5240–5251.

26. Fried, S. D.; Boxer, S. G. Measuring Electric Fields and Noncovalent Interactions Using the Vibrational Stark Effect. *Acc. Chem. Res.* **2015**, *48* (4), 998–1006.
27. Muñoz, S. B.; Foster, W. K.; Lin, H. J.; Margarit, C. G.; Dickie, D. A.; Smith, J. M. Tris(Carbene)Borate Ligands Featuring Imidazole-2-Ylidene, Benzimidazol-2-Ylidene, and 1,3,4-Triazol-2-Ylidene Donors. Evaluation of Donor Properties in Four-Coordinate $\{\text{NiNO}\}^{10}$ Complexes. *Inorg. Chem.* **2012**, *51* (23), 12660–12668.
28. Feynman, R.P.; Leighton, R. B.; Sands, M. L. Chapter 4: Electrostatics. In *The Feynman Lectures on Physics: Mainly Electromagnetism and Matter* [Online]; Gottlieb, M. A., Pfeiffer, R., Eds.; Basic Books, USA, **2011**. <https://www.feynmanlectures.caltech.edu/info/> (accessed March 2022).
29. Enemark, J. H.; Feltham, R. D. Principles of Structure, Bonding, and Reactivity for Metal Nitrosyl Complexes. *Coord. Chem. Rev.* **1974**, *13* (4), 339–406.
30. Tomson, N. C.; Crimmin, M. R.; Petrenko, T.; Rosebrugh, L. E.; Sproules, S.; Christopher Boyd, W.; Bergman, R. G.; Debeer, S.; Dean Toste, F.; Wieghardt, K. A Step beyond the Feltham-Enemark Notation: Spectroscopic and Correlated Ab Initio Computational Support for an Antiferromagnetically Coupled M(II)-(NO)- Description of $\text{Tp}^*\text{M}(\text{NO})$ (M = Co, Ni). *J. Am. Chem. Soc.* **2011**, *133* (46), 18785–18801.
31. Spessard, G. O.; Miessler, G. L. *Organometallic Chemistry*, Second.; Oxford University Press: New York, 2010.
32. <https://cccbdb.nist.gov/vibscalejust.asp> accessed on April 26th 2022.
33. Cho, Y. A.; Kim, D. S.; Ahn, H. R.; Canturk, B.; Molander, G. A.; Ham, J. Preparation of Potassium Azidoaryltrifluoroborates and Their Cross-Coupling with Aryl Halides. *Org. Lett.* **2009**, *11* (19), 4330–4333.
34. Bouillon, A.; Lancelot, J. C.; Collot, V.; Bovy, P. R.; Rault, S. Synthesis of Novel Halopyridinylboronic Acids and Esters. Part 1: 6-Halopyridin-3-yl-Boronic Acids and Esters. *Tetrahedron* **2002**, *58* (14), 2885–2890.
35. Bouillon, A.; Lancelot, J. C.; Collot, V.; Bovy, P. R.; Rault, S. Synthesis of Novel Halopyridinylboronic Acids and Esters. Part 2: 2,4, or 5-Halopyridin-3-yl-Boronic Acids and Esters. *Tetrahedron* **2002**, *58* (17), 3323–3328.
36. Bouillon, A.; Lancelot, J. C.; Collot, V.; Bovy, P. R.; Rault, S. Synthesis of Novel Halopyridinylboronic Acids and Esters. Part 3: 2, or 3-Halopyridin-4-yl-Boronic Acids and Esters. *Tetrahedron* **2002**, *58* (22), 4369–4373.
37. Lau, V. M.; Pfalzgraff, W. C.; Markland, T. E.; Kanan, M. W. Electrostatic Control of Regioselectivity in Au(I)-Catalyzed Hydroarylation. *J. Am. Chem. Soc.* **2017**, *139* (11), 4035–4041.

38. Lee, D.; Hung, P. L.; Spingler, B.; Lippard, S. J. Sterically Hindered Carboxylate Ligands Support Water-Bridged Dimetallic Centers That Model Features of Metallohydrolase Active Sites. *Inorg. Chem.* **2002**, *41* (3), 521–531.
39. Matheu, R.; Ertem, M. Z.; Benet-Buchholz, J.; Coronado, E.; Batista, V. S.; Sala, X.; Llobet, A. Intramolecular Proton Transfer Boosts Water Oxidation Catalyzed by a Ru Complex. *J. Am. Chem. Soc.* **2015**, *137* (33), 10786–10795.
40. Thomas, J. C.; Peters, J. C. Bis(Phosphino)Borates: A New Family of Monoanionic Chelating Phosphine Ligands. *Inorg. Chem.* **2003**, *42* (17), 5055–5073..
41. Elkin, P. K.; Levin, V. V.; Dilman, A. D.; Struchkova, M. I.; Belyakov, P. A.; Arkhipov, D. E.; Korlyukov, A. A.; Tartakovsky, V. A. Reactions of CF₃-Substituted Boranes with α -Diazocarbonyl Compounds. *Tetrahedron Lett.* **2011**, *52* (41), 5259–5263.
42. Connelly, N. G.; Geiger, W. E. Chemical Redox Agents for Organometallic Chemistry. *Chem. Rev.* **1996**, *96* (2), 877–910.
43. Konishi, S.; Iwai, T.; Sawamura, M. Synthesis, Properties, and Catalytic Application of a Triptycene-Type Borate-Phosphine Ligand. *Organometallics* **2018**, *37* (12), 1876–1883.
44. Thomas, J. C.; Peters, J. C. Zwitterionic and Cationic Bis(Phosphine) Platinum(II) Complexes: Structural, Electronic, and Mechanistic Comparisons Relevant to Ligand Exchange and Benzene C-H Activation Processes. *J. Am. Chem. Soc.* **2003**, *125* (29), 8870–8888.
45. Molander, G. A.; Hoag, B. P. Improved Synthesis of Potassium (Trifluoromethyl)Trifluoroborate [K(CF₃BF₃)]. *Organometallics* **2003**, *22* (16), 3313–3315.
46. Kolomeitsev, A. A.; Kadyrov, A. A.; Szczepkowska-Sztolcman, J.; Milewska, M.; Koroniak, H.; Bissky, G.; Barten, J. A.; Rösenthaller, G. V. Perfluoroalkyl Borates and Boronic Esters: New Promising Partners for Suzuki and Petasis Reactions. *Tetrahedron Lett.* **2003**, *44* (45), 8273–8277.
47. Vedejs, E.; Chapman, R. W.; Fields, S. C.; Lin, S.; Schrimpf, M. R.; Conversion of Arylboronic Acids into Potassium Aryltrifluoroborates: Convenient Precursors of Arylboron Difluoride Lewis Acids. *Organometal. Chem.* **1995**, *60* (5), 62.
48. Churches, Q. I.; Hooper, J. F.; Hutton, C. A. A General Method for Interconversion of Boronic Acid Protecting Groups: Trifluoroborates as Common Intermediates. *J. Org. Chem.* **2015**, *80* (11), 5428–5435.
49. Lennox, A. J. J.; Lloyd-Jones, G. C. Selection of Boron Reagents for Suzuki-Miyaura Coupling. *Chem. Soc. Rev.* **2014**, *43* (1), 412–443.
50. Li-Yuan Bao, R.; Zhao, R.; Shi, L. Progress and Developments in the Turbo Grignard Reagent *i*-PrMgCl·LiCl: A Ten-Year Journey. *Chem. Commun.* **2015**, *51* (32), 6884–6900.

51. Dankert, F.; Deubner, H. L.; Müller, M.; Buchner, M. R.; Kraus, F.; von Hänisch, C. C–F Bond Cleavage Reactions with Beryllium, Magnesium, Gallium, Hafnium, and Thorium Halides. *Zeitschrift für Anorg. und Allg. Chemie* **2020**, *646* (18), 1501–1507..
52. Hanf, S.; García-Rodríguez, R.; Bond, A. D.; Hey-Hawkins, E.; Wright, D. S. Sterically-Constrained Tripodal Phosphorus-Bridged Tris-Pyridyl Ligands. *Dalton Trans.* **2016**, *45* (1), 276–283.
53. Feltham, R. D. Metal Nitrosyls. I. Triphenylphosphine Nitrosyl Nickel Complexes. *Inorg. Chem.* **1964**, *3* (1), 116–119.
54. Wright, A. M.; Wu, G.; Hayton, T. W. Formation of N₂O from a Nickel Nitrosyl: Isolation of the *cis*-[N₂O₂]²⁻ Intermediate. *J. Am. Chem. Soc.* **2012**, *134* (24), 9930–9933.
55. Bouillon, A.; Lancelot, J. C.; Santos, J. S. D. O.; Collot, V.; Bovy, P. R.; Rault, S. Synthesis of Novel Halopyridinylboronic Acids and Esters. Part 4: Halopyridin-2-yl-Boronic Acids and Esters Are Stable, Crystalline Partners for Classical Suzuki Cross-Coupling. *Tetrahedron* **2003**, *59* (50), 10043–10049.
56. Sheldrick, G. M. SHELXT- Integrated space-group and crystal-structure determination. *Acta Cryst.* **2015**, *A71*, 3- 9.
57. Dolomanov, O.V.; Bourhis, L. J.; Gildea, R. J.; Howard, A. K.; and Puschmann, H., Olex2, a complete structure solution, refinement, and analysis program. *J. Appl. Cryst.* **2009**, *42*, 339
58. (a) Sheldrick, G. M. A Short History of SHELX. *Acta Cryst.* **2008**, *A64*, 112-122. (b) Sheldrick, G. M. Crystal structure refinement with SHELX. *Acta Cryst.* **2015**, *C71*, 3-8.
59. Neese, F. “The ORCA program system” *Wiley interdisciplinary Reviews - Computational Molecular Science*, **2012**, *2*, 73–78.
60. Weigend F.; Ahlrichs, R. Balanced basis sets of split valence, triple zeta valence and quadruple zeta valence quality for H to Rn: Design and assessment of accuracy. *Phys. Chem. Chem. Phys.* **2005**, *7*, 3297.

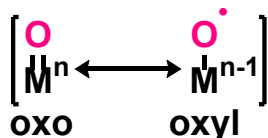
Appendix 1: Synthesis and Metalation of Anionic Tetra-pyrazole Lutidine Based Ligands

A1.1 Introduction

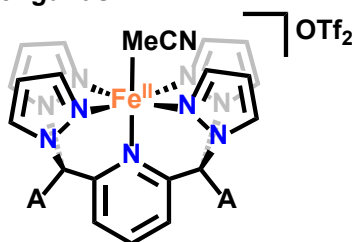
High valent metal oxygen multiply bonded intermediates ($M^n=O$) selectively mediate challenging oxidation reactions in enzymatic catalysis, such as C–H activation and water oxidation.¹ Interest in studying these intermediates is motivated by a desire to replicate the observed enzymatic rates and selectivity in synthetic systems. Advances in synthetically mediated C–H functionalization and water oxidation would be enabling for the design of fine chemicals, such as pharmaceuticals, and the production of renewable fuels, respectively. One means of studying these intermediates is the synthesis of model metal complexes wherein the metal-oxygen moiety may be studied without complications from the protein scaffold. Numerous studies have mapped out the significant influence of d-electron count, metal geometry, H-bonding interactions, and O–H BDFE (among other characteristics) on the resulting electronic structure and reactivity.^{2–4} Computational studies have also provided insight into the active mechanisms for enzymatic oxidation reactions. Recently, the assignment of oxo intermediates with a predominant $M^n=O$ resonance structure has been challenged, with instead metal-oxyl ($M^{n-1}-O^\bullet$) resonance structures being proposed as important for oxidative reactivity (Scheme A1.1).⁵ For instance, in C–H activation the active oxidants in iron-based enzymes such as syringomycin halogenase and taurine/TauD and Cu-based enzymes such as dopamine β -monooxygenase and lytic polysaccharide monooxygenases are respectively proposed to be $Fe^{III}-O^\bullet$ and $Cu^{II}-O^\bullet$ rather than the typical oxo resonance structures.⁵ Likewise, water oxidation mediated by photosystem II and by synthetic cobalt oxide materials have been proposed to proceed via $Mn^{IV}-O^\bullet$ and $Co^{III}-O^\bullet$ intermediates, respectively, rather than $Mn^V=O$

and $\text{Co}^{\text{IV}}=\text{O}$ species.^{6,7} Despite the prevalence of this proposed resonance structure in first-row metal mediated oxidation reactions, there remain only two characterized synthetic examples of $\text{M}^{\text{n}-1}-\text{O}^\bullet$ complexes, a $\text{Zn}^{\text{II}}-\text{O}^\bullet$ isolated within a zeolite and a bimetallic $\text{Ru}^{\text{II}}-\text{O}^\bullet$ complex.⁵

Resonance Structures



Target ligands

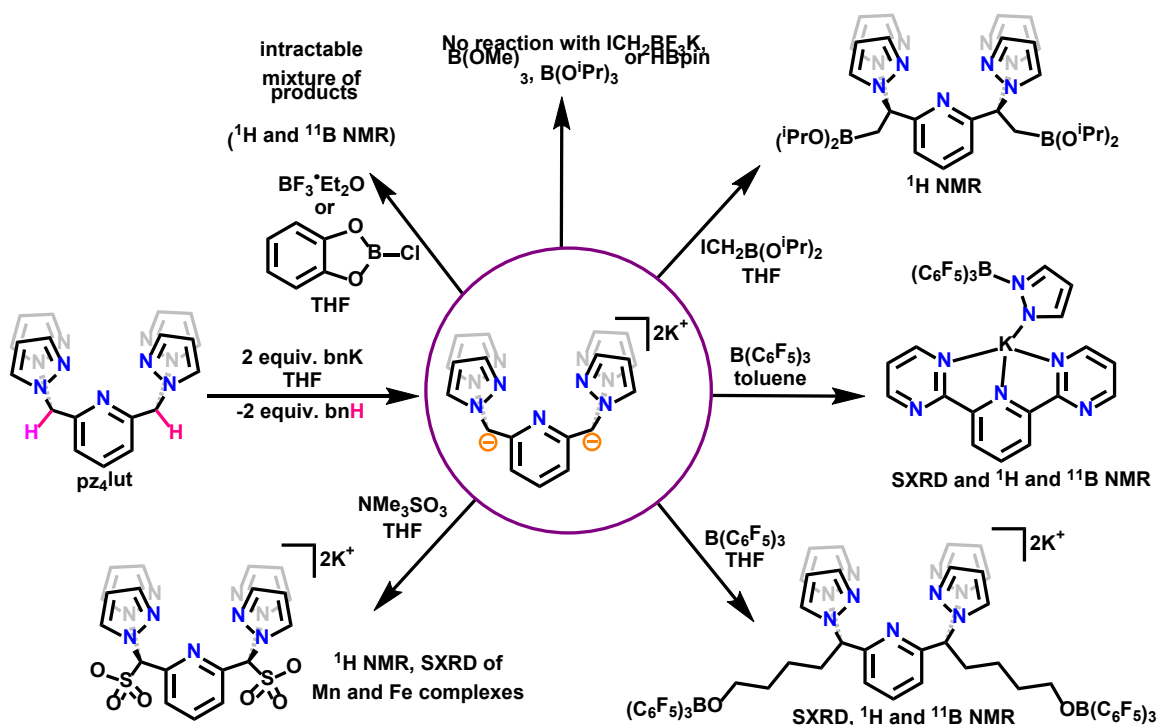


A = H (pz₄lut) or anion (SO₃, BF₃, CH₂BF₃)

Scheme A1.1 (Top) Two limiting resonance structures for metal-oxygen moieties, $\text{M}^{\text{n}}=(\text{O}^{2-})$ on left and $\text{M}^{\text{n}-1}-(\text{O}^{\bullet-})$ on right. (Bottom) Targeted pz₄lut ligand (A = H) and substitution at methine carbon with anionic functional groups.

Notably, very little is known regarding strategies to stabilize a $\text{M}^{\text{n}-1}-\text{O}^\bullet$ resonance structure over the equivalent $\text{M}^{\text{n}}=\text{O}$ metal oxo resonance structure, which hampers the exploration of metal-oxyl reactivity. It has been proposed that the use of π -accepting ligands with strongly donating ligands axial to the metal-oxygen bond should favor oxyl formation,⁵ but additional methods remain to be explored. We hypothesize that the use of weakly donating ligands may encourage oxidation at the O rather than M, while incorporating distal anionic functional groups should allow for accessible redox potentials despite the weak donors due

to the lower overall charge. Additionally, the electric fields generated by the anionic moieties, if correctly aligned, may direct the location of oxidation. To test this hypothesis, we endeavored to generate an anionic congener of the previously reported pentadentate tetra-pyrazole lutidine ligand (pz₄lut).⁸ This choice was inspired by the numerous examples of octahedral metal-oxo complexes generated using heterocycle based ligands⁹ and the proposed intermediacy of a $\text{Co}^{\text{IV}}-\text{O}^\bullet$ intermediate with a dianionic penta-pyridine ligand.¹⁰ Additionally, we anticipated facile functionalization of pz₄lut via deprotonation of the methine backbone carbon and reaction with electrophiles to install distal anionic functional groups (Scheme A1.1).



Scheme A1.2 Summary of the reactivity observed with the deprotonated pz4lut and electrophiles.

In this appendix we report progress towards the synthesis of dianionic congeners (Scheme A1.2) of pz4lut and the comparison of iron-oxygen species in both systems. While preliminary evidence supports the formation of an $\text{Fe}^{\text{IV}}=\text{O}$ with $[\text{Fe}(\text{pz4lut})\text{MeCN}][\text{OTf}]_2$, the challenges associated with the synthesis and metalation of a dianionic congener with non-coordinating anions precluded any comparisons. Preliminary results on the synthesis and metalation of a SO_3^- functionalized pz4lut ligand and the reaction products from borylation attempts are also reported.

A1.2 Results and Discussion

A1.2.1 Metalation and Oxidation of pz4lut

The synthesis of $\alpha,\alpha,\alpha',\alpha'$ -tetra(pyrazolyl)lutidine (pz4lut) was carried out according to the previously reported synthesis.⁸ Multiple coordination geometries have been reported for metalated

pz₄lut complexes. A pentadentate coordination mode is reported for the first row Mn, Fe, Co, Ni and Cu complexes in which the sixth coordination site of the octahedral metal is occupied by a chloride ligand.^{8,11} Alternatively, bidentate coordination has been observed with Ru and Pd complexes, where each set of adjacent pyrazoles coordinates to a metal center and result in bimetallic complexes.^{12,13} Finally, a related bidentate coordination is observed with Ag, which is coordinated by two adjacent pyrazoles from two separate pz₄lut molecules.¹⁴

The ligand pz₄lut was metalated with Fe(OTf)₂(MeCN)₂ in DCM to give [Fe(pz₄lut)MeCN][OTf]₂ as an orange solid after crystallization from MeCN/Ether (OTf = trifluoromethanesulfonate). The observed symmetric diamagnetic ¹H NMR in CD₃CN is consistent with pentadentate coordination to a low spin Fe center (Figure A1.4). Collecting ¹H NMR in CD₂Cl₂ results in a paramagnetic spectrum (Figure A1.5), suggesting that the spin state is sensitive to the axially coordinated ligand. Cyclic voltammetry in a 0.1 M TBAPF₆ propionitrile solution shows a reversible oxidation at 0.96 V vs Fc^{0/+} and an irreversible reduction at -2.11 V vs Fc^{0/+} (Figure A1.21). The reaction between [Fe(pz₄lut)MeCN][OTf]₂ and the O-atom transfer reagent ^sPhIO (Ph = 2-(*tert*-butylsulfonyl)phenyl) in MeCN was monitored by UV-vis at -40 °C. Collecting spectra with 1-minute intervals showed that the addition of quarter equivalents of ^sPhIO resulted in the decay of the absorbance at 424 nm and the appearance of new absorbances at 756 and 890 nm over the course of a few minutes (Figure A1.1). These two absorbances at 756 and 890 nm are consistent with the previously reported absorption spectra of Fe^{IV}=O complexes.¹⁵ The product decays slowly at -40 °C, with a ¼ of the intensity lost after 1 hour (Figure A1.23). In propionitrile at -65 °C a similar species grows in more slowly over the course of 25 minutes (Figure A1.24). While this new species is so far consistent with an Fe^{IV}=O, this assignment is tentative as no further characterization was pursued. With this data suggesting that an oxo complex

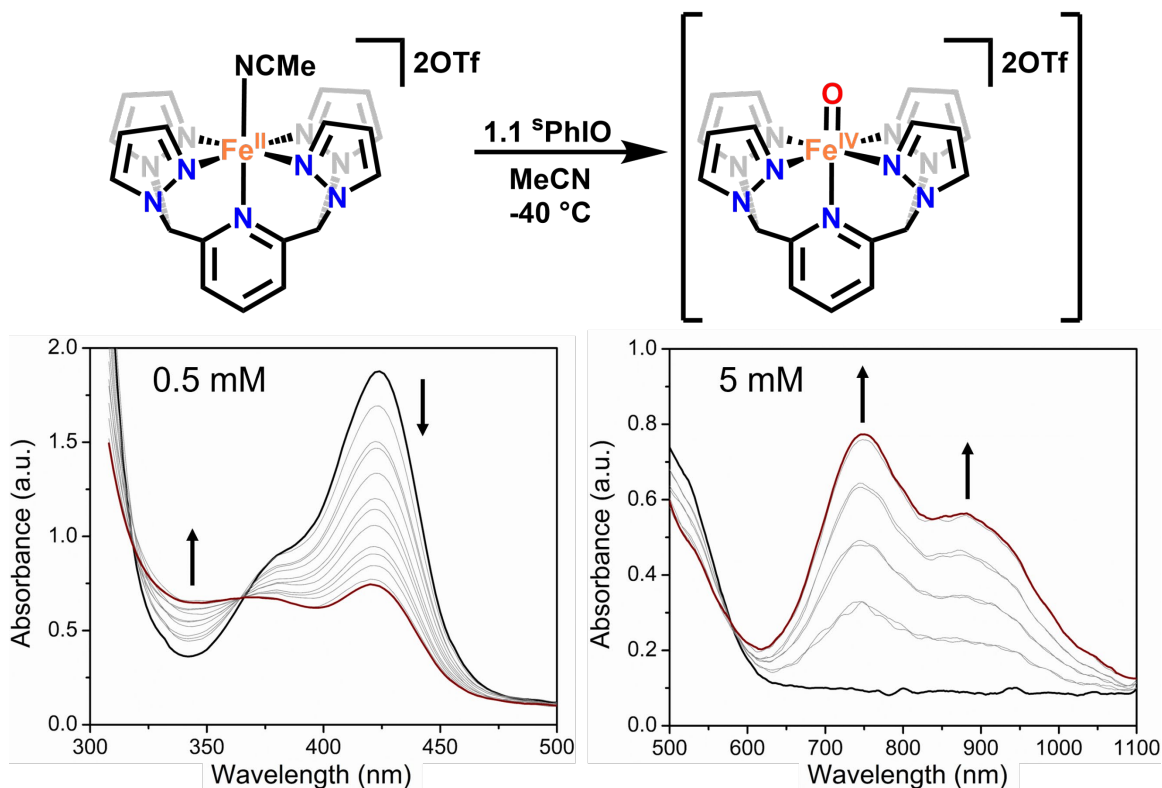


Figure A1.1 UV-vis spectra of the reaction between ${}^5\text{PhIO}$ and $[\text{Fe}(\text{pz4lut})\text{MeCN}][\text{OTf}]_2$ in MeCN at $-40\text{ }^\circ\text{C}$ with scans collected in 1-minute intervals. Two concentrations are shown to emphasize changes with peaks of different intensities. The initial scan is shown in black, and ${}^5\text{PhIO}$ was added in quarter equivalents every 3 (left) or 2 (right) minutes to give the red spectrum.

could be generated using the neutral pz4lut ligand, the synthesis of a dianionic ligand congener was subsequently pursued.

A1.2.2 Test Deprotonations of pz4lut

Methylation at the methine carbon of pz4lut has been previously reported using nBuLi or KO^tBu to deprotonate followed by reaction with MeI as an electrophile.¹⁶ Monitoring the deprotonation with nBuLi in d_8 -THF by variable temperature NMR shows that the deprotonation proceeds at $-78\text{ }^\circ\text{C}$ to generate an asymmetric product (Figure A1.7). Warming to $-50\text{ }^\circ\text{C}$ and $-25\text{ }^\circ\text{C}$ results in slight broadening but overall minimal changes in the spectrum. At $0\text{ }^\circ\text{C}$ the resonances for the asymmetric product disappear and are replaced by broad lumps, suggesting the deprotonated

product is not stable above 0 °C (Figure A1.6). Deprotonation of pz4lut with KO^tBu in THF likewise results in an asymmetric product observed by NMR spectroscopy in DMSO (Figure A1.8). Benzyl potassium (BnK) was also effective at deprotonating pz4lut and produces a yellow precipitate in THF. Reaction of the deprotonated intermediate generated using benzyl potassium with MeI at -40 °C likewise yields the methylated product (Figure A1.9). Given their effectiveness in methylation reactions, these three bases were used in the following attempts to install anionic functional groups.

A1.2.3 Sulfonation of pz4lut and Subsequent Metalation

The sulfonate anion (R-SO₃⁻) can be installed on the backbone of pz4lut by deprotonation and reaction with SO₃NMe₃ as the electrophile at room temperature in THF (Figure A1.10). Either nBuLi at -78 °C or benzyl potassium at room temperature can be used to deprotonate in this reaction, however the use of KO^tBu leads to regeneration of pz4lut. Metalation of Li₂pz4lut(SO₃)₂ with Mn(MeCN)₂OTf₂ in MeCN yielded an asymmetric octahedral Mn complex with coordination of two pyrazoles, the pyridine and two sulfonates (Figure A1.2). This structure was confirmed by SXRD of yellow crystals grown from DMF/ether. The ¹H NMR spectrum of Mn(pz4lut(SO₃)₂)(L) (L=solvent) in DMSO contains broad features in the aromatic region, although it is unknown whether these correspond to the product or other Mn impurities (Figure A1.12). The coordination geometry of the Co(MeCN)₆OTf₂ metalated ligand likewise appears to involve both sulfonates as the ¹H NMR shows 6 inequivalent pyrazole resonances, consistent with two bound and two free pyrazoles (Figure A1.13). However, the structure has not been confirmed by SXRD. Conversely, metalation of Li₂pz4lut(SO₃)₂ with Fe(MeCN)₂OTf₂ in MeCN yields a symmetric complex by NMR spectroscopy and the structure determined by SXRD of orange crystals shows coordination to the metal center through the four pyrazoles and pyridine (Figures A1.2 and A1.11). Cyclic

voltammetry of the $\text{Fe}(\text{pz}_4\text{lut}(\text{SO}_3)_2)(\text{MeCN})$ in DMF shows an irreversible oxidation at 423 mV vs $\text{Fc}^{0/+}$ (Figure A1.22). The irreversible oxidation may be due to structural rearrangement upon oxidation to Fe^{III} . We hypothesize that the ligand coordination mode is determined by hard/soft acid/base interactions, as the softer low spin Fe^{II} favors coordination through the pyrazoles while

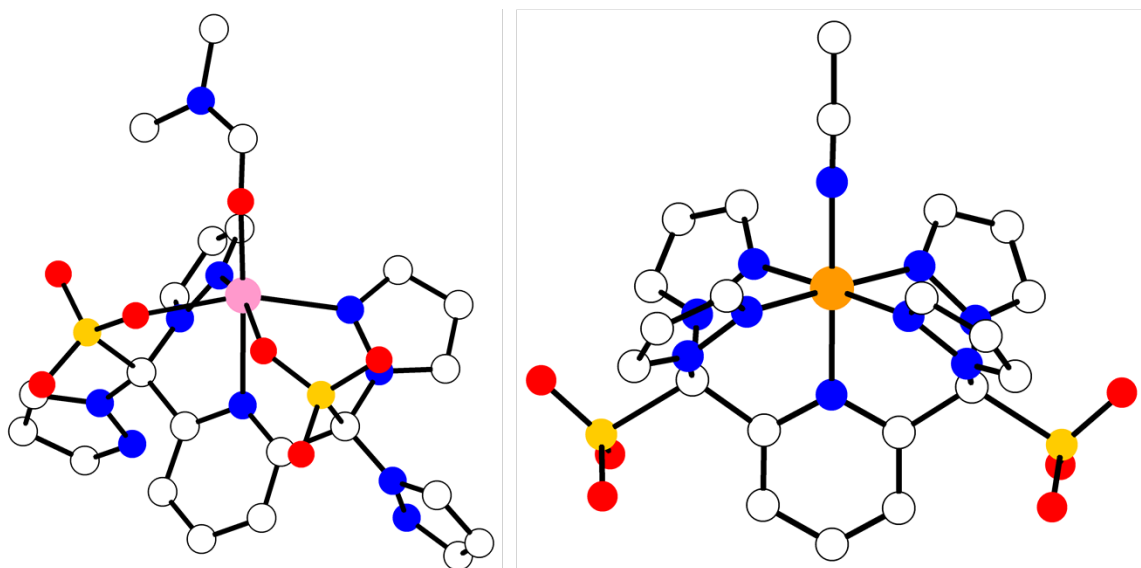


Figure A1.2 Ball and stick model of SXR structures of the $\text{Mn}(\text{pz}_4\text{lut}(\text{SO}_3)_2)(\text{DMF})$ (left) and $\text{Fe}(\text{pz}_4\text{lut}(\text{SO}_3)_2)(\text{MeCN})$ (right) demonstrating the two available coordination geometries. Manganese is shown in pink, iron in orange, carbon in grey, nitrogen in blue, oxygen in red, sulfur in yellow, and H atoms have been omitted for clarity.

the high spin Mn^{II} and Co^{II} prefer oxygen coordination. Oxidation reactions between $\text{Fe}(\text{pz}_4\text{lut}(\text{SO}_3)_2)(\text{MeCN})$ and $^s\text{PhIO}$ (Figure A1.25) or meta-chloroperoxybenzoic acid (Figure A1.26) in MeCN/DCM mixtures were monitored by UV-vis. Minimal changes to the original spectrum were observed upon the addition of the oxidants, suggesting that they were not sufficiently oxidizing to generate an $\text{Fe}^{\text{IV}}=\text{O}$ species. The multiple coordination modes available to the sulfonate substituted pz_4lut motivated the exploration of more rigorously non-coordinating distal anions, such as tetra-valent borates.

A1.2.4 Attempted Installation of a Borate Group on pz4lut

To install a non-coordinating anion on the methine position of pz4lut, multiple borane electrophiles were reacted with the deprotonated pz4lut. Reaction of the pz4lut anion generated using *n*BuLi (-78 °C) or BnK (-40 °C) with BF₃•Et₂O results in a complicated mixture of products (Figure A1.14). Multiple attempts to promote a cleaner reaction were unsuccessful, suggesting the BF₃ is too electrophilic for clean reactivity. The anion generated using KO^tBu or BnK was found to be unreactive with the less electrophilic trialkyl borates B(OMe)₃ or B(OiPr)₃ at room temperature, yielding NMR spectra of either the deprotonated pz4lut in DMSO or deuterated pz4lut in CD₃CN (Figure A1.15). Deprotonation of pz4lut with BnK at room temperature and reaction with B(C₆F₅)₃ in THF yielded a THF activated product, in which the methine position of pz4lut was substituted with C₄H₈OB(C₆F₅)₃⁻ as a result of ring-opening a THF molecule coordinated to the borane. This product was confirmed by the presence of four aliphatic resonances with appropriate integrations in the ¹H NMR spectrum and a low-quality crystal structure confirming the connectivity (Figures A1.3 and A1.16). The major product of the reaction between pz4lut deprotonated using BnK and B(C₆F₆)₃ in toluene is a distinct decomposition product resulting from the loss of a pyrazole on each side of the molecule and ring-opening and closing of the remaining pyrazole to generate a 2,6-pyrimidine-pyridine based product. The assignment of this product is supported by the ¹H NMR spectrum and a low-quality crystal structure (Figures A1.3 and A1.17). The reactivity with the borane substituted iodomethyl electrophile ICH₂B(OⁱPr)₂, prepared according to literature procedure,¹⁷ was also investigated. Reaction of pz4lut with BnK in THF and subsequent addition of ICH₂B(OⁱPr)₂ at room temperature resulted in substitution of the iodine for the pz4lut carbanion to generate pz4lut(CH₂B(OⁱPr)₂)₂, as determined by ¹H NMR spectroscopy (Figure A1.18). Reaction of this product with KHF₂ and water in THF resulted in the formation of an unknown

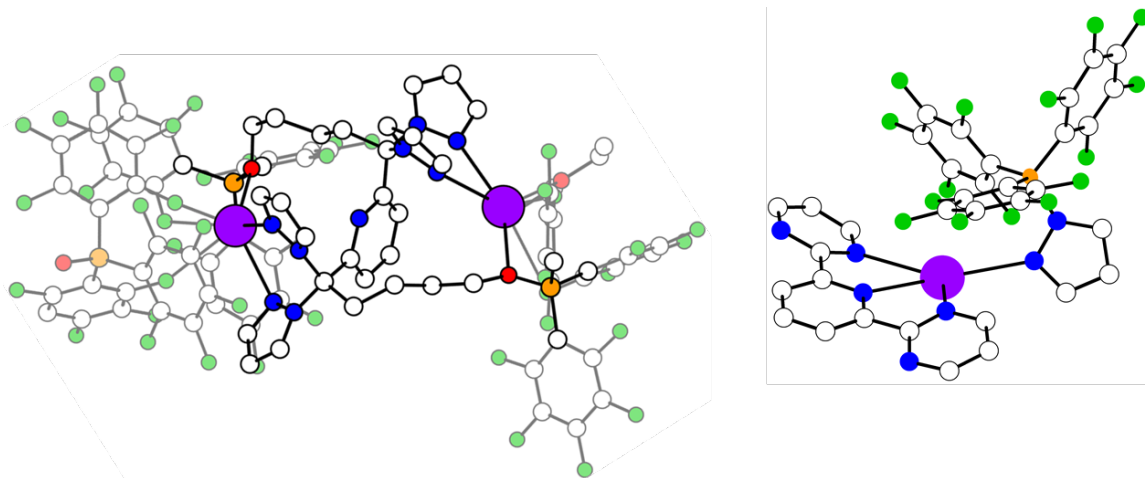


Figure A1.3 Ball and stick model depictions of SXRD structures of the reaction products generated between pz4lut deprotonated with BnK and B(C₆F₅)₃ in THF (left) and toluene (right) suitable to determine connectivity. Carbon is depicted in white, nitrogen is blue, potassium is purple, oxygen is red, boron is orange, and fluorine is green. Hydrogen atoms are omitted for clarity.

product with spectral features inconsistent with pz4lut(CH₂BF₃)₂. Specifically, the pyrazole and pyridine resonances do not integrate correctly, and no appropriate CH₂ peak is identifiable (Figure A1.19). Ultimately, generation of the pz4lut(CH₂BF₃)₂ with KHF₂ and D₂O is proposed to proceed in dilute DMSO with gentle heating (Figure A1.20). While apparently effective, these conditions were not amenable to scale-up and were not pursued further.

A1.3 Experimental

A1.3.1 General

Pz4lut was synthesized according to the previously published synthesis.⁸ The 2,6 pyridine dicarboxaldehyde was prepared by oxidizing 2,6 pyridine dimethanol with selenium dioxide with slight modification to a literature report;¹⁸ the reaction was refluxed for 2 hours and after passing through a silica plug the product was recrystallized by dissolving in hot acetone/hexane and storing at 0 °C. The synthesis of pz4lut was often challenging as the ligand would remain protonated in

the aqueous layer during the extraction step. The crude oil was typically crystallized from a concentrated boiling THF solution cooled to $-40\text{ }^{\circ}\text{C}$ rather than through chromatography. $\text{Fe}(\text{MeCN})_2(\text{OTf})_2$ and $\text{Mn}(\text{MeCN})_2(\text{OTf})_2$ were prepared analogously to $\text{Co}(\text{MeCN})_6(\text{OTf})_2$ (see syntheses). The reagent $\text{ICH}_2\text{B}(\text{O}^i\text{Pr}_3)_2$ was prepared according to literature procedure.¹⁷ All other reagents were purchased from commercial sources. All reactions were performed under nitrogen except the ones which involve water. UV-vis spectra were collected using a dip probe and solvent baths to cool the air free glassware. Spectra were smoothed in origin to remove noise resulting from the set-up.

A1.3.2 Preliminary Synthetic Procedures

$\text{Co}(\text{MeCN})_6(\text{OTf})_2$. In a 500 mL round bottom flask in the glovebox was added 150 mL of MeCN and 6 g of anhydrous CoCl_2 (0.0462 mol) and the mixture stirred until dissolved, adding more MeCN if necessary. Then, TMSOTf (21.57 g, 0.097 mol, 2.1 equiv., 17.56 mL) was slowly injected and the reaction was stirred overnight. The volume was reduced under vacuum until precipitate was observed, and then 200 mL of ether was added and the resulting orange solid was collected via filtration. The solid was transferred back into the flask and stirred with 200 mL of ether for 1 hour. Then mixture was filtered again and washed with more ether. The solid was collected dried under vacuum to yield 18.65 g of pink solid (67% yield).

$[\text{Fe}(\text{pz}_4\text{lut})\text{MeCN}][\text{OTf}]_2$. A scintillation vial was charged with 400 mg of pz_4lut (1.08 mmol) and 470 mg of $\text{Fe}(\text{OTf})_2\text{MeCN}_2$ (1.08 mmol, 1 equiv.) and stirred in 10 mL of DCM for 4 days, over which time orange solid precipitated. The reaction was dried under vacuum and the orange solid was dissolved in 5 mL MeCN and layered under ether. After storing at $-45\text{ }^{\circ}\text{C}$ for 4 days orange crystals and powder were separated from the yellow mother liquor (247 mg, 30% yield). ^1H NMR (400 MHz, $25\text{ }^{\circ}\text{C}$, CD_3CN) $\delta = 8.48$ (s, 4H), 8.45 (s, 4H), 8.33 (s, 2H), 8.24 (m, 3H), 6,70 (s, 3H).

Li₂pz₄lut(SO₃)₂. A vial with pz₄lut (183 mg, 0.5 mmol) dissolved in 10 mL THF was cooled to -78 °C in the cold well of the glovebox. To the solution was added nBuLi (452 μL of 2.5 M solution, 1.13 mmol, 2.3 equiv.) dropwise and the reaction turned orange. The reaction was stirred for 1 hour, and subsequently SO₃NMe₃ was added as a solid and the reaction was allowed to warm to room temperature while stirring overnight, resulting in a green solution. The solution was pumped down to a green solid, which was used without further purification. ¹H NMR (400 MHz, 25 °C, CD₃CN) δ = 7.71 (t, 1H, *J*_{H-H} = 8 Hz), 7.66 (d, 4H, *J*_{H-H} = 4 Hz), 7.55 (d, 4H, *J*_{H-H} = 4 Hz), 6.96 (d, 2H, *J*_{H-H} = 8 Hz), 6.35 (dd, 4H, *J*_{H-H} = 4 Hz).

Fe(pz₄lut(SO₃)₂)(MeCN). A scintillation vial was charged with Li₂pz₄lut(SO₃)₂ (179 mg, 0.33 mmol) and Fe(MeCN)₂(OTf)₂ (144 mg, 0.33 mmol, 1 equiv.) and 5 mL of MeCN was added. The reaction turned green and then orange and was stirred overnight, giving an orange heterogeneous mixture. The reaction was pumped down to an orange solid which was washed with ether. Crystals suitable for SXRD were grown from an MeCN/ether layering stored at -35 °C. Although the collected ¹H NMR spectra frequently contained paramagnetic peaks, the Fe product is tentatively assigned as corresponding to the diamagnetic resonances. ¹H NMR (400 MHz, 25 °C, CD₃CN) δ = 9.06 (d, 4H, *J*_{H-H} = 4 Hz), 8.98 (d, 2H, *J*_{H-H} = 12 Hz), 8.47 (d, 4H, *J*_{H-H} = 4 Hz), 8.13 (t, 1H, *J*_{H-H} = 12 Hz), 6.57 (t, 4H, *J*_{H-H} = 4Hz), 2.34 (s, 3H).

Mn(pz₄lut(SO₃)₂)(MeCN). Combination of Li₂pz₄lut(SO₃)₂ (50 mg, 0.09 mmol) in MeCN with Mn(MeCN)₂OTf₂ (40 mg, 0.09 mmol, 1 equiv.) in 5 mL MeCN resulted in a light green solution with white precipitate. The reaction was dried under vacuum and crystallization from a DMF/ether layering yielded yellow crystals suitable for XRD.

Co(pz₄lut(SO₃)₂)(MeCN). In a scintillation vial Li₂pz₄lut(SO₃)₂ (10 mg, 0.02 mmol) dissolved in MeOD and Co(MeCN)₆OTf₂ (11 mg, 0.02 mmol, 1 equiv.) dissolved in MeOD were combined.

The solution turned green and over 1 hour pink solid precipitated. NMR of the resulting pink solid in DMSO is consistent with the asymmetric coordination of the sulfonate ligand to Co. ^1H NMR (400 MHz, 25 °C, DMSO- d_6) δ = 71.37 (s, 2H), 69.43 (s, 2H), 41.58 (s, 2H), 24.06 (s, 2H), 14.15 (s, 2H), 12.81 (s, 2H), 4.06 (s, 3H), -26.55 (s, 2H).

A1.4 Supporting data

A1.4.1 NMR Spectra

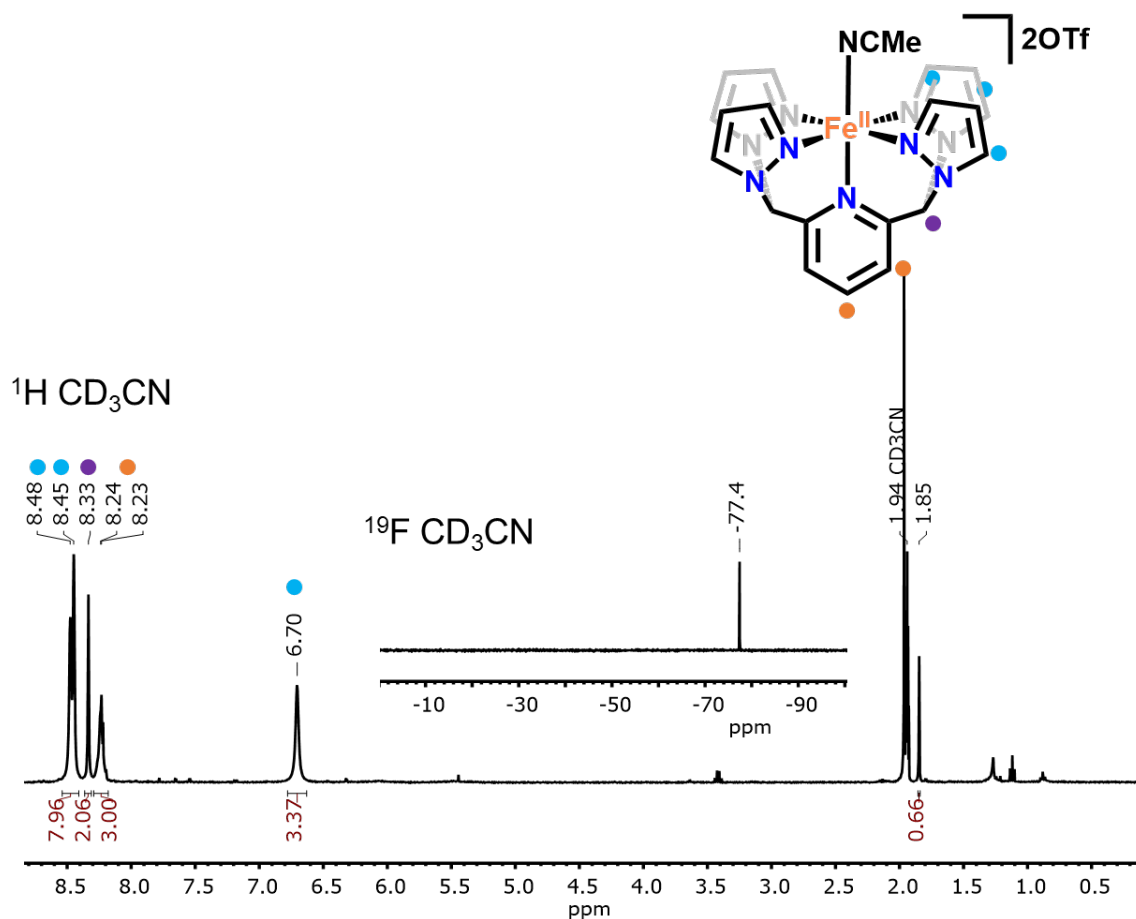


Figure A1.4 ^1H and ^{19}F NMR of $[\text{Fe}(\text{pz}_4\text{lut})\text{MeCN}][\text{OTf}]_2$ in CD_3CN , colored circles peak indicate assignments.

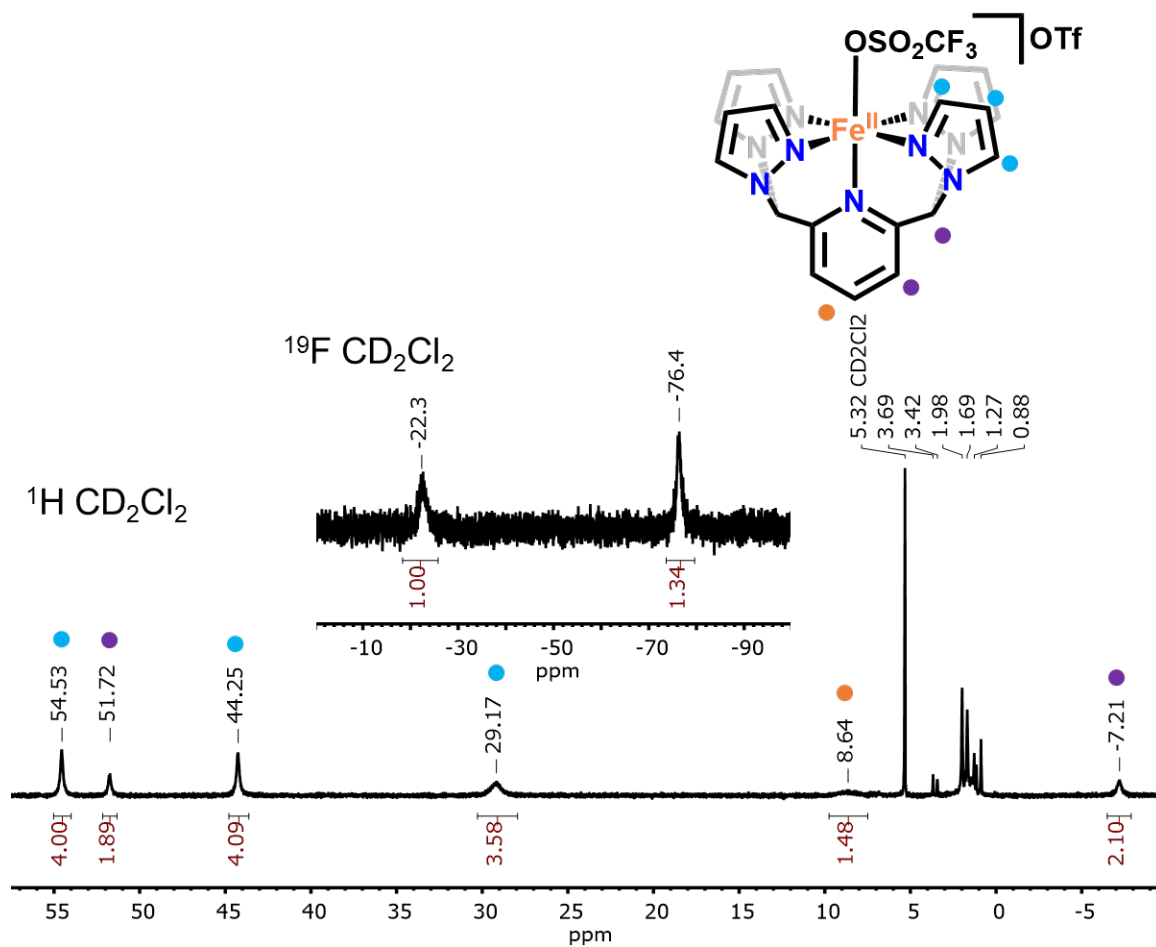


Figure A1.5 ^1H and ^{19}F NMR spectra of $[\text{Fe}(\text{pz}_4\text{lut})\text{MeCN}][\text{OTf}]_2$ in CD_2Cl_2 . The MeCN is likely replaced by OTf given the two ^{19}F signals and the observed spin state change.

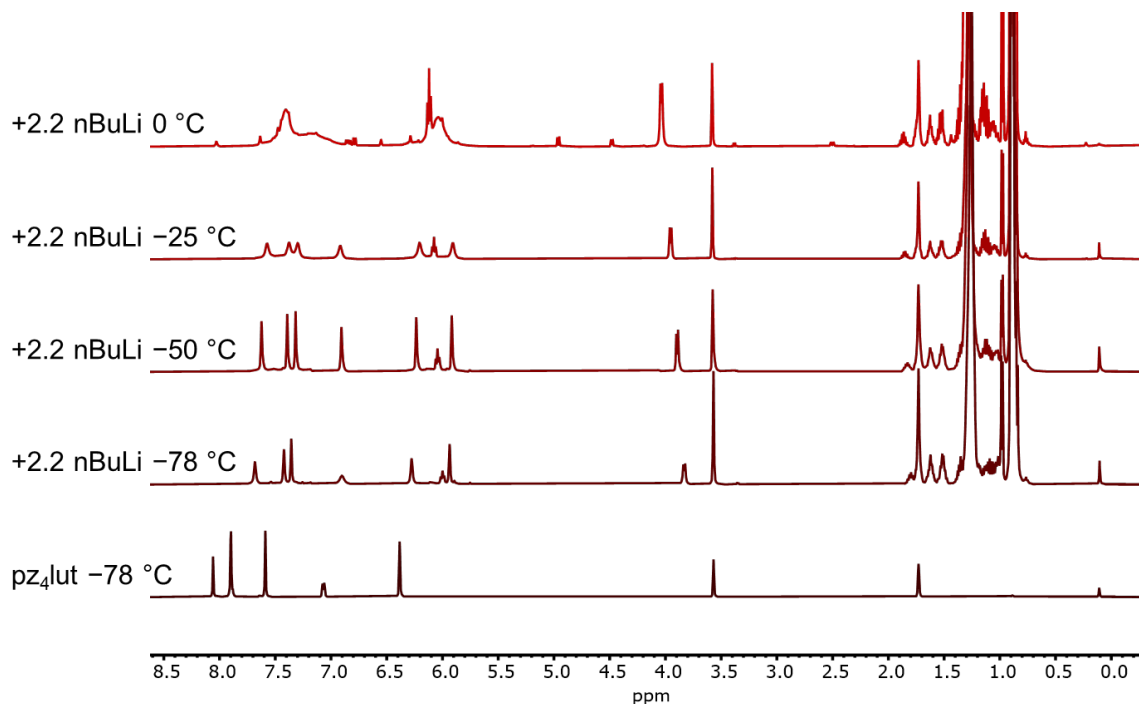


Figure A1.6 NMR spectra of pz₄lut with 2.2 equivalents of nBuLi in *d*₈-THF at the indicated temperatures. Proteo THF peaks observed at ~3.6 and 1.7 ppm. Procedure: A solution of pz₄lut (5mM) was prepared by dissolving 10 mg of pz₄lut (0.027 mmol) in 538 μL *d*₈-THF, and diluting 50 μL of that solution to 500 μL in an NMR tube. The tube was cooled in a dry ice/IPA bath, and nBuLi (24 μL, 2.2 equiv.) was syringed in. The NMR tube was loaded into the pre-cooled spectrometer.

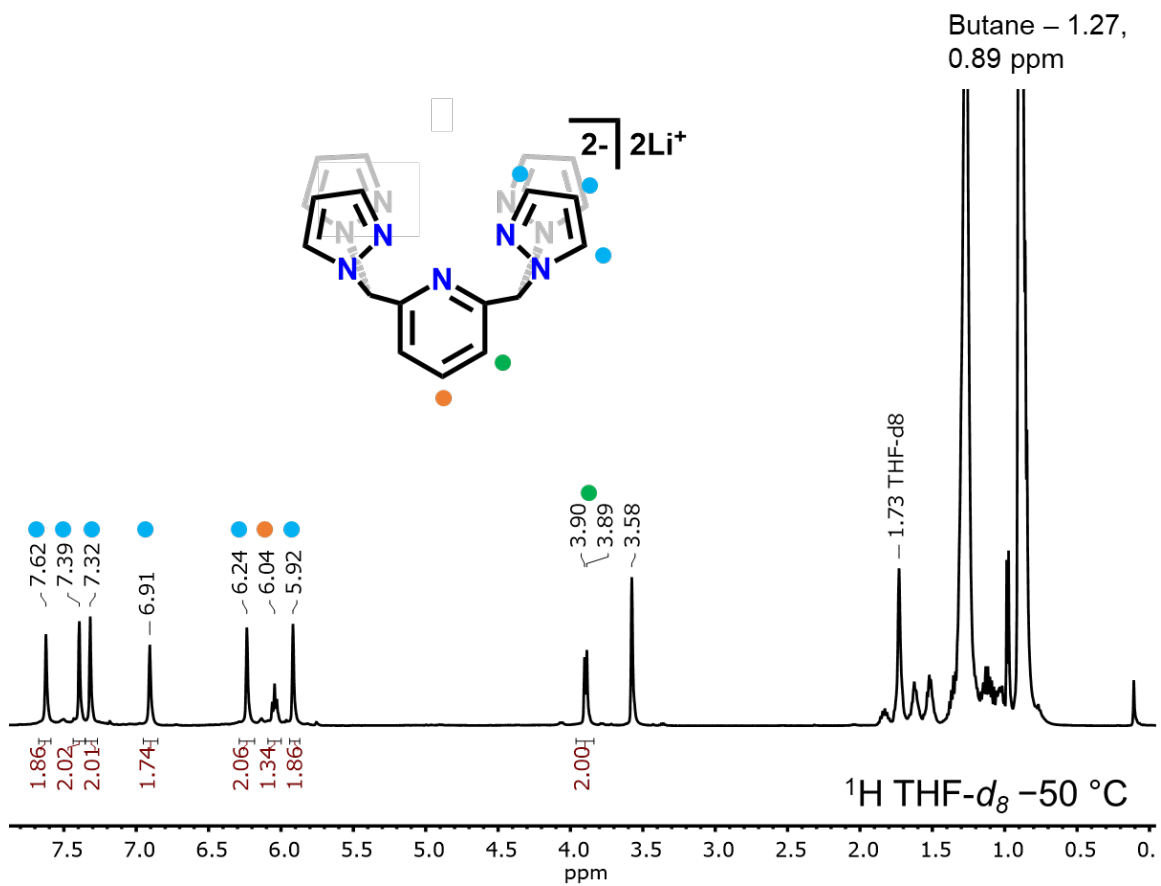


Figure A1.7 NMR spectrum in d_8 -THF of the reaction between pz₄lut and 2.2 equivalents of nBuLi at $-50\text{ }^\circ\text{C}$ with tentative assignments for the resonances. Six resonances are observed for the pyrazole protons rather than the three observed in the spectrum of pz₄lut, suggesting an asymmetric product.

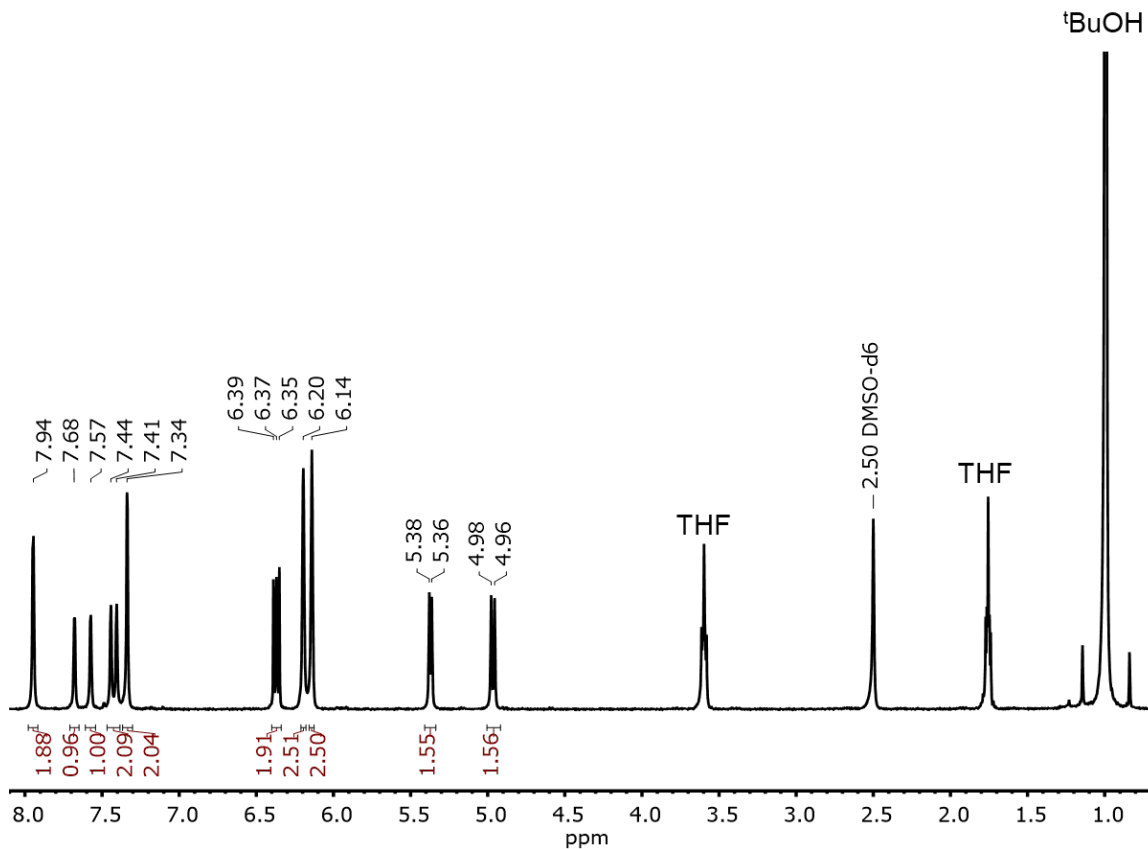


Figure A1.8 ^1H NMR in DMSO of the reaction between 3 equiv. KO^tBu and pz_4lut . The reagents were combined in THF, giving an orange homogeneous solution, and pumped down under vacuum and then dissolved in DMSO.

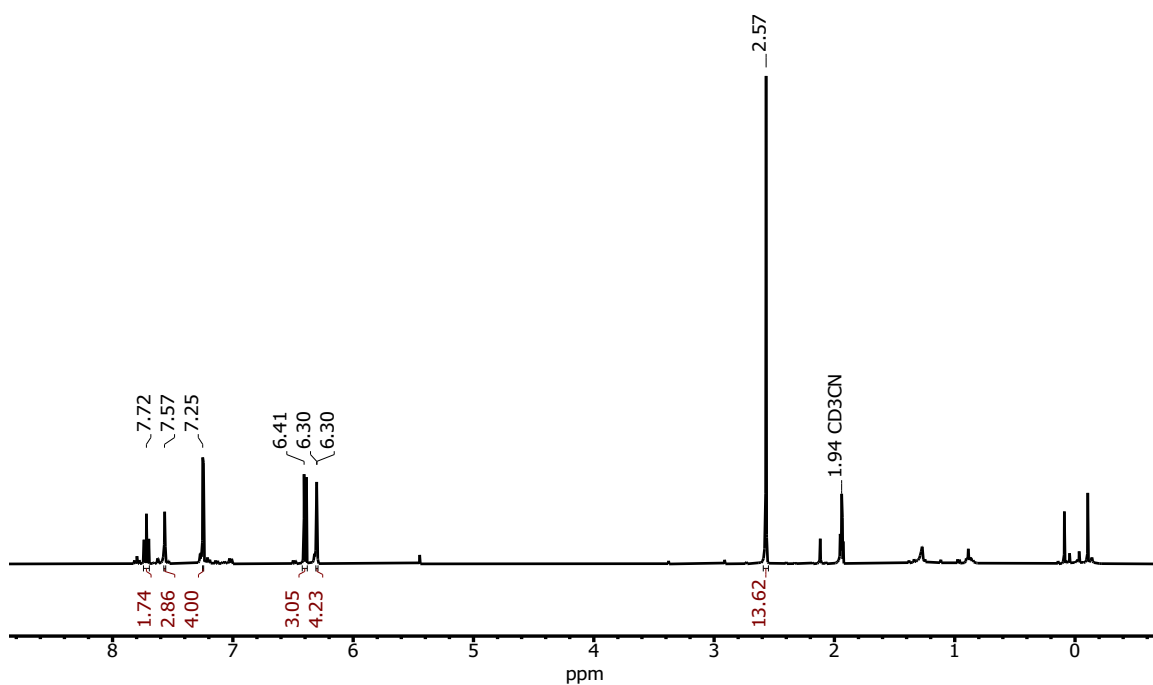


Figure A1.9 ^1H NMR of the methylated pz₄lut generated using benzyl potassium to deprotonate and MeI as the electrophile in THF at $-40\text{ }^\circ\text{C}$. The spectrum was collected in CD_3CN at room temperature. The integrations do not exactly match the expected product, likely due to impurity peaks in the aromatic region and excess MeI, however the peak positions and splitting are consistent with the reported methylated pz₄lut spectrum.

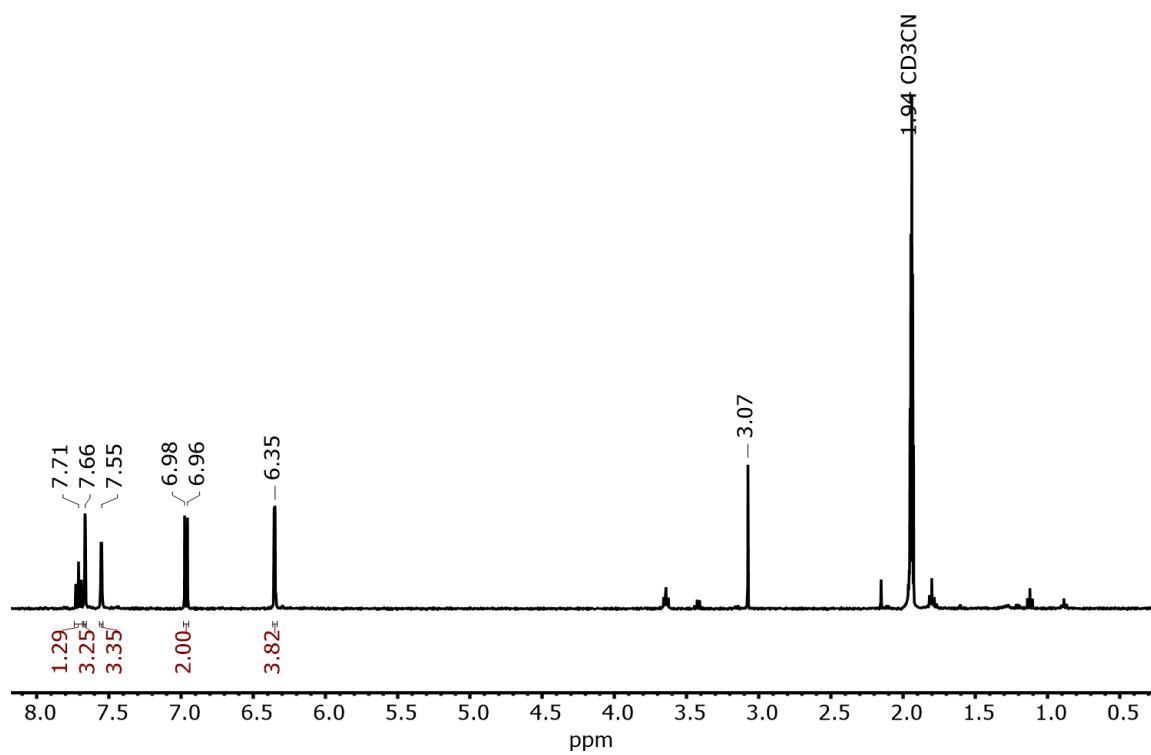


Figure A1.10 ^1H NMR spectrum of $\text{Li}_2\text{pz}_4\text{lut}(\text{SO}_3)_2$ in CD_3CN .

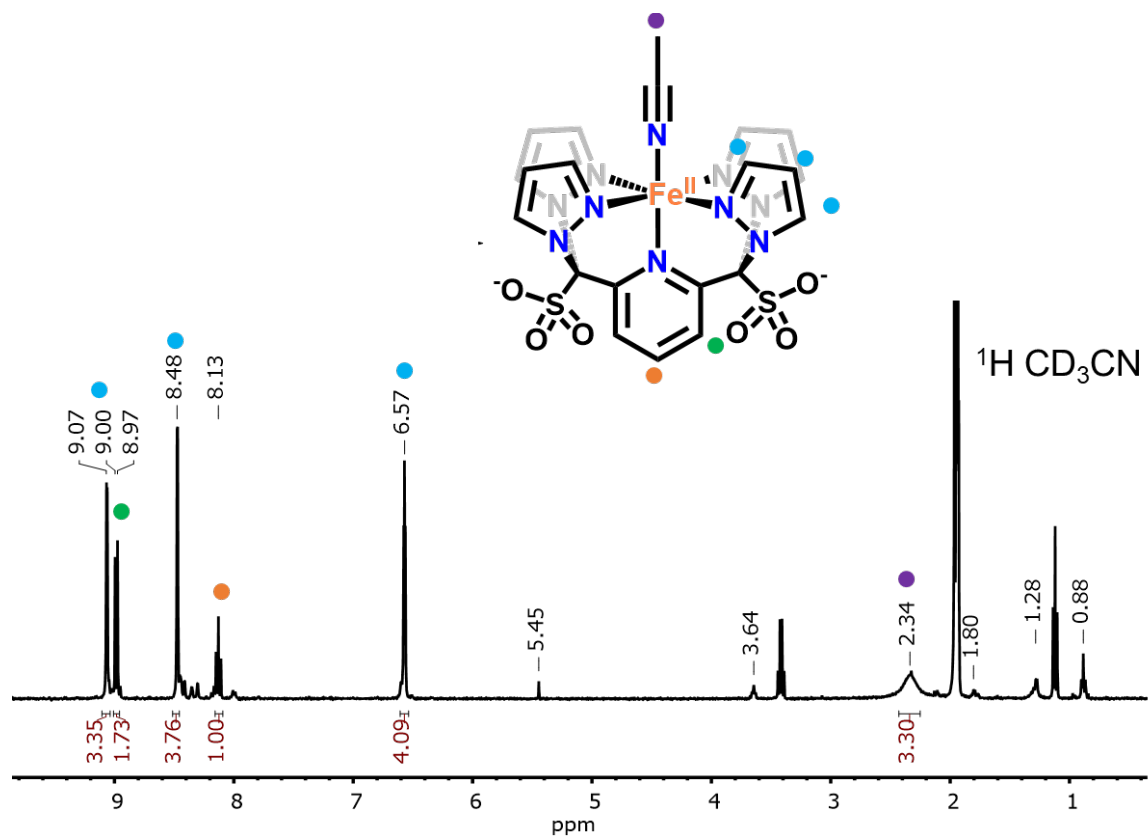


Figure A1.11 ^1H NMR of the reaction product between $\text{Li}_2\text{pz}_4\text{lut}(\text{SO}_3)_2$ and $\text{Fe}(\text{MeCN})_2\text{OTf}_2$ collected in CD_3CN . Tentative assignments are indicated by colored circles.

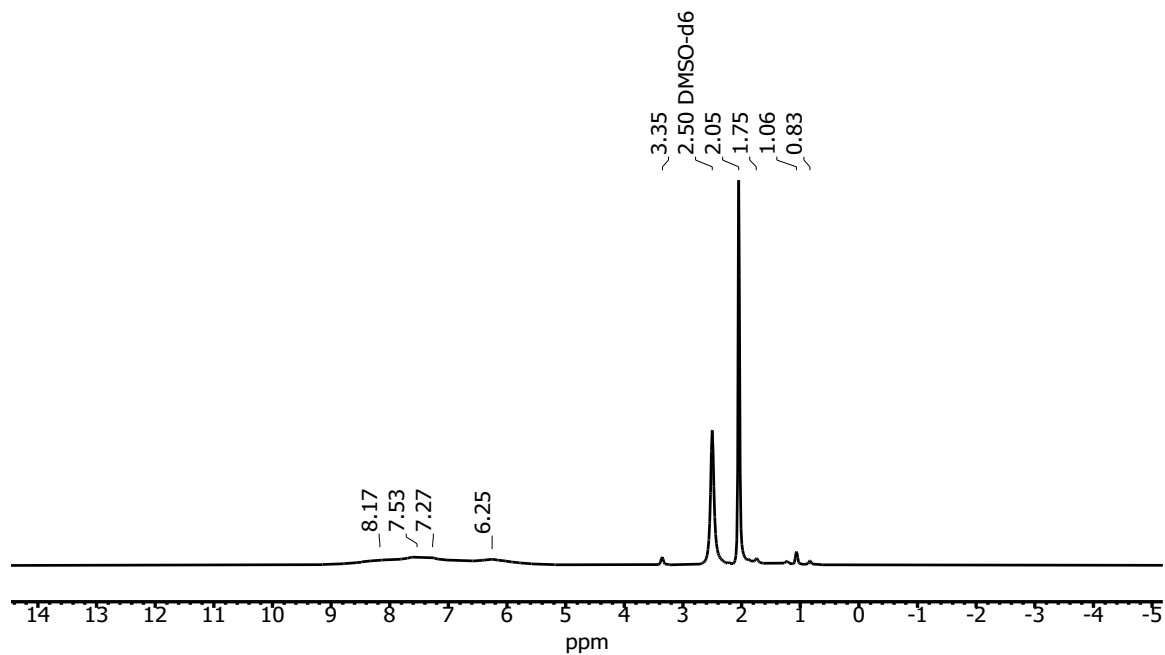


Figure A1.12 ^1H NMR of the reaction between $\text{Li}_2\text{pz}_4\text{lut}(\text{SO}_3)_2$ and $\text{Mn}(\text{MeCN})_2\text{OTf}_2$ collected in $\text{DMSO-}d_6$.

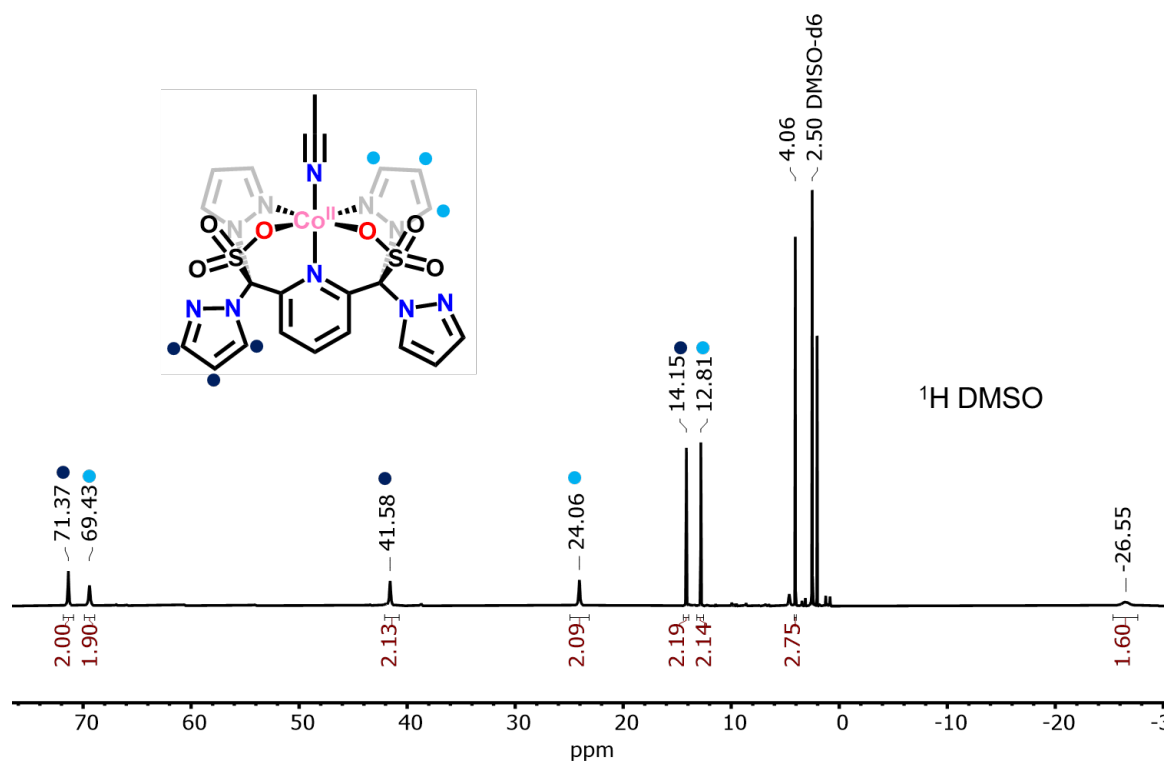


Figure A1.13 ^1H NMR spectrum of the reaction product from $\text{Li}_2\text{pz}_4\text{lut}(\text{SO}_3)_2$ and $\text{Co}(\text{MeCN})_6(\text{OTf})_2$ collected in $\text{DMSO-}d_6$.

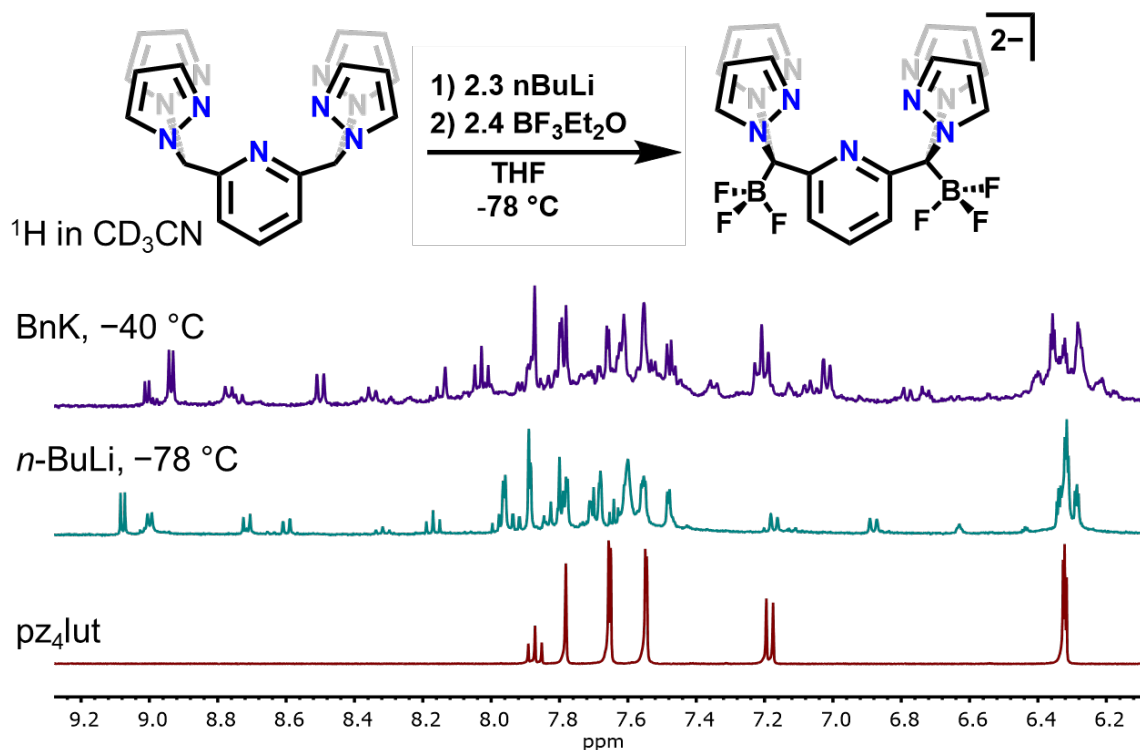


Figure A1.14 ^1H NMR spectra of the crude reaction products in CD_3CN for the following reactions and comparison to pz₄lut. Deprotonation of pz₄lut was carried out in THF with nBuLi at -78 °C or benzyl potassium at -40 °C and was subsequently reacted with $\text{BF}_3\cdot\text{Et}_2\text{O}$ and left to stir and warm to room temperature overnight. After drying, NMR of the crude reactions were collected.

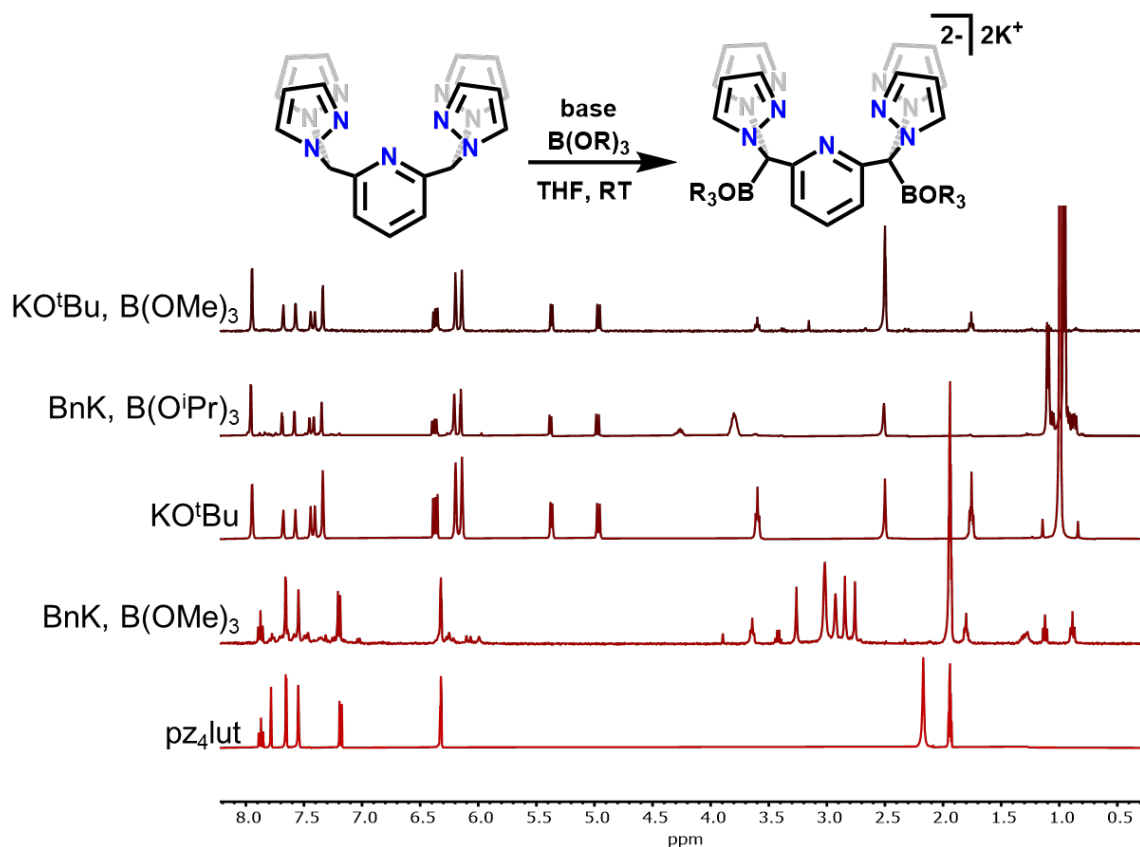


Figure A1.15 ^1H NMR spectra of the crude reaction products from the following reactions in $\text{DMSO-}d_6$ (top three) and CD_3CN (bottom two) and comparisons to separately generated $\text{K}_2\text{pz}_4\text{lut}$ and pz_4lut . General reaction scheme shown above.

(Top, first) 60 mg of pz_4lut (0.16 mmol) was dissolved in THF at RT and KO^tBu (54.4 mg, 0.48 mmol, 3 equiv.) was added as a solid and stirred for 30 minutes. $\text{B}(\text{OMe})_3$ (56 μL , 0.5 mmol, 3.1 equiv.) was dissolved in 2 mL THF and added, yielding a yellow homogeneous solution after stirring for two days. Addition of ether yielded a yellow precipitate, and ^1H NMR in DMSO of both precipitate (shown) and filtrate contain resonances consistent with a potassium salt of deprotonated pz_4lut .

(Second) 60 mg of pz_4lut (0.16 mmol) was dissolved in THF and a solution of benzyl potassium (BnK, 42 mg, 0.32 mmol, 2 equiv.) in THF was added, yielding a yellow heterogeneous solution. $\text{B}(\text{O}i\text{Pr})_3$ in THF (150 μL , 0.646 mmol, 4 equiv.) was added and no change was observed. After stirring overnight the reaction became orange and homogeneous. The reaction was dried under vacuum and ^1H NMR was collected in DMSO (shown).

(Third) 25 mg of pz_4lut was stirred with 23 mg of KO^tBu in THF. The reaction was dried under vacuum, and NMR of the product was collected in DMSO (shown).

(Fourth) 60 mg of pz_4lut (0.16 mmol) was dissolved in THF and BnK (43.1 mg, 0.331 mmol, 2.05 equiv.) in THF was added, yielding a brown heterogeneous solution. A THF solution of $\text{B}(\text{OMe})_3$

(30 μL , 0.27 mmol, 2.1 equiv.) was added. The reaction was filtered and the filtrate dried after stirring for a few hours, and ^1H NMR was collected of the solid (shown).

(Bottom, fifth) ^1H NMR spectrum of pz4lut collected in CD_3CN . Methine proton resonance located at 7.78 ppm.

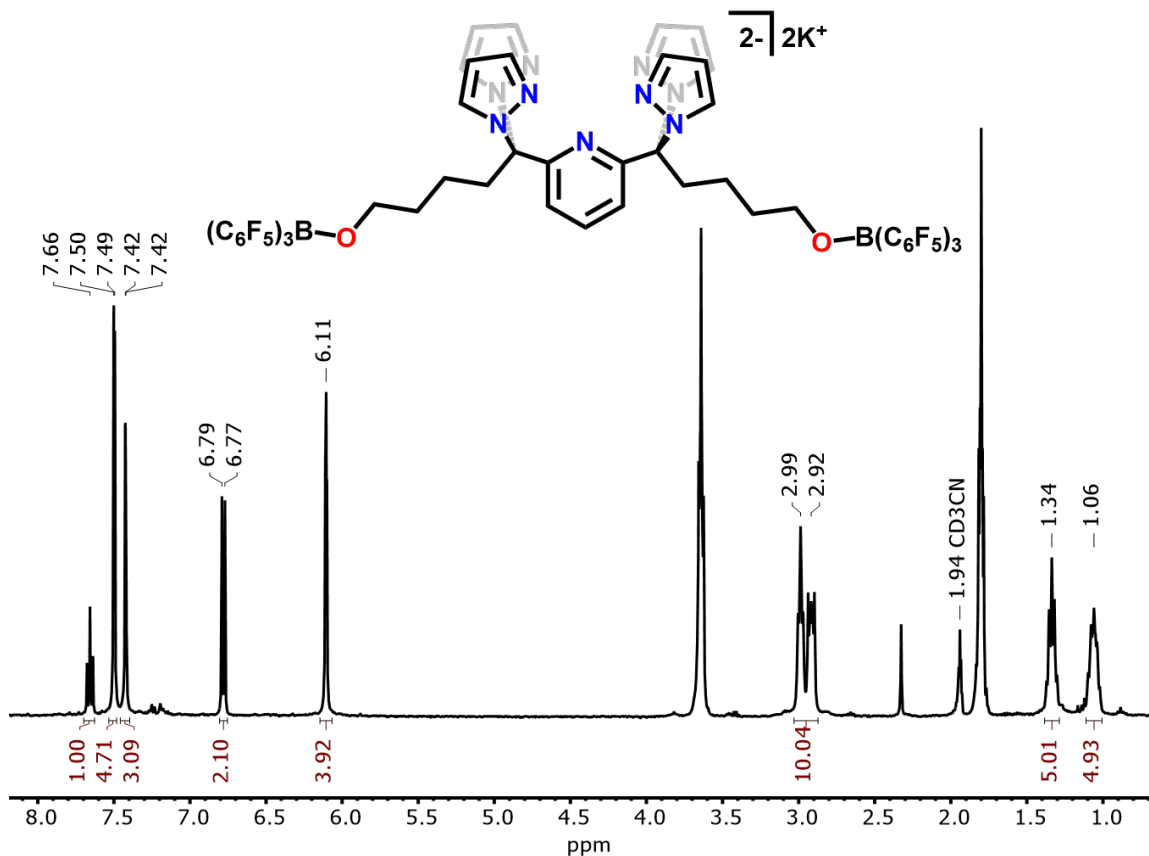


Figure A1.16 ^1H NMR in CD_3CN of the following reaction: pz4lut (138 mg, 0.37 mmol) was dissolved in THF and BnK (101 mg, 0.78 mmol, 2.1 equiv.) was added as a THF solution. The reaction was stirred for 30 minutes, and then a solution of $\text{B}(\text{C}_6\text{F}_5)_3$ in THF was added. After stirring for 1 hour the reaction was dried under vacuum to a brown gel and ^1H NMR was collected in CD_3CN (shown above).

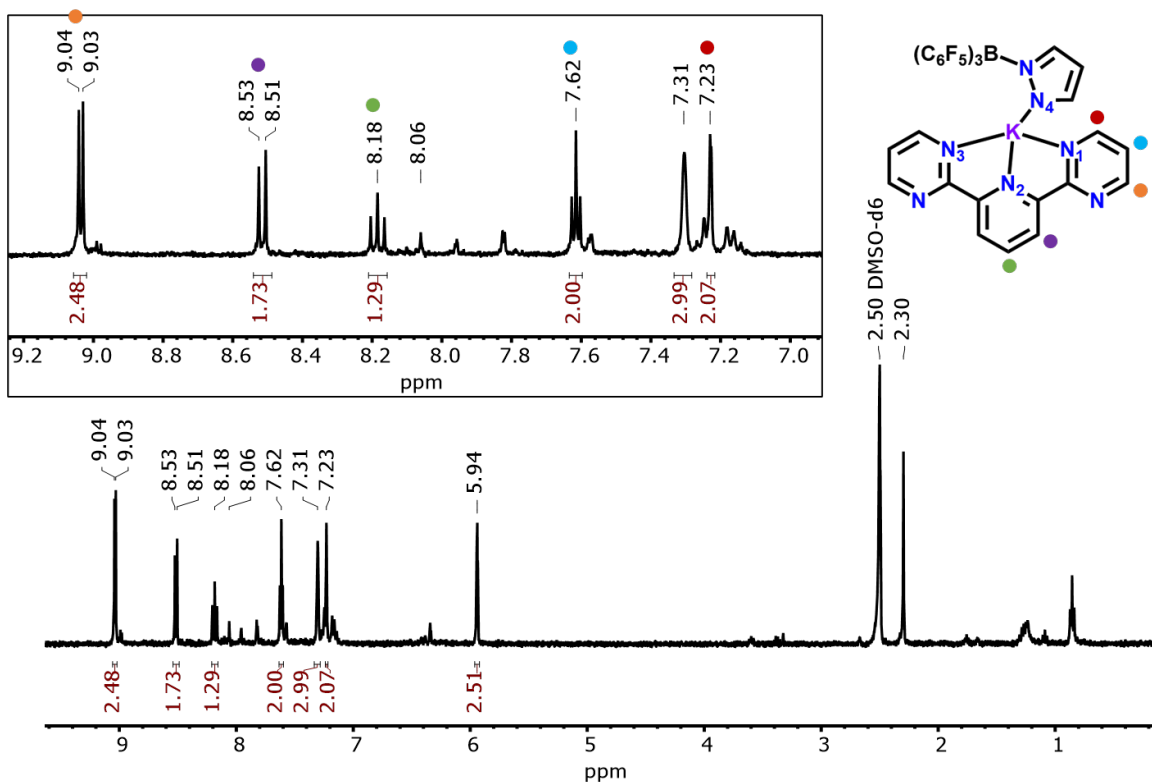


Figure A1.17 ¹H NMR in DMSO-*d*₆ of the reaction mixture generated by reacting pz4lut (100 mg, 0.27 mmol) with BnK (70 mg, 0.54 mmol, 2 equiv.) in THF, drying the solution to collect a yellow solid, and combining the yellow solid suspended in toluene with a solution of B(C₆F₅)₃ in toluene. The reaction was filtered and NMR was collected of the dried filtrate (shown). No further purification was carried out, the NMR is consistent with the pyrimidine structure observed by SXRD of a crystal grown from an ether/hexane layering of this reaction mixture, and tentative assignments for the pyrimidine resonances are indicated with colored circles. The remaining resonances may belong to additional pyrazole-based compounds in solution, but overall they have not been assigned. The resonance at 2.3 ppm is likely the methyl on toluene.

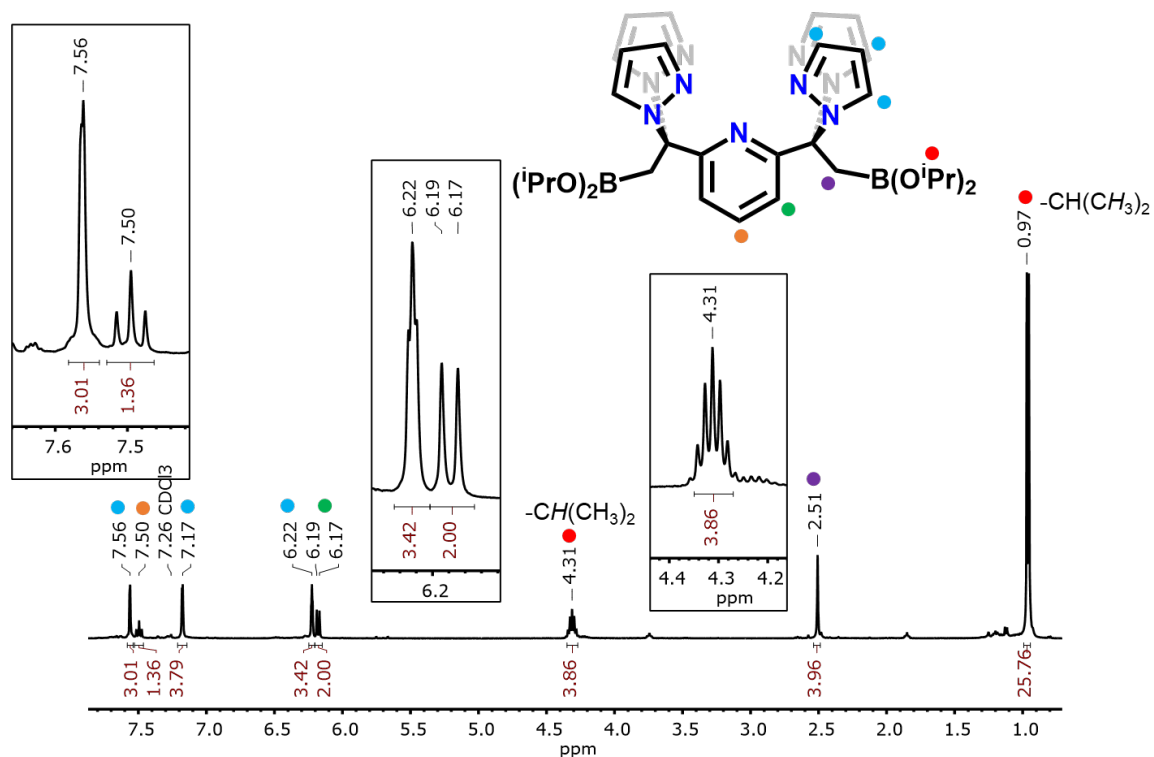


Figure A1.18 ^1H NMR spectrum collected in CDCl_3 of the following reaction: pz4lut (50 mg, 0.13 mmol) and BnK (35 mg, 0.27 mmol, 2 equiv.) were combined in THF at room temperature, resulting in a brown cloudy solution. A solution of $\text{ICH}_2\text{B}(\text{O}^i\text{Pr})_2$ in THF was added and the reaction turned green and remained heterogeneous. The reaction was stirred overnight and filtered, the yellow filtrate was collected and dried under vacuum. ^1H NMR was collected of the CDCl_3 soluble fraction (shown). Colored circles indicate peak assignments.

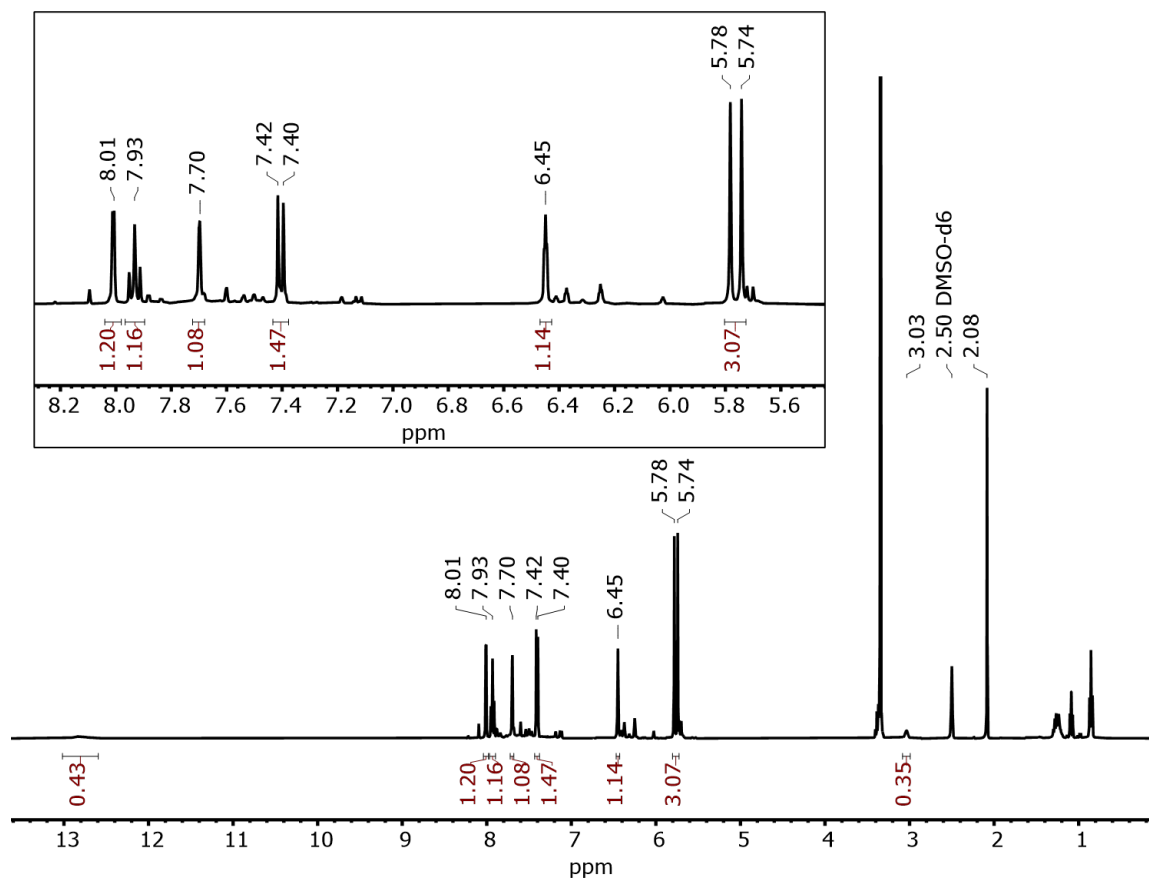


Figure A1.19 ^1H NMR in $\text{DMSO-}d_6$ of the unknown reaction product typically observed upon attempted fluorination of $\text{pz}_4\text{lut}(\text{CH}_2\text{B}(\text{O}^i\text{Pr})_2)_2$ using KHF_2 . In this particular procedure, 75 mg of $\text{pz}_4\text{lut}(\text{CH}_2\text{B}(\text{O}^i\text{Pr})_2)_2$ (0.11 mmol) was dissolved in THF and 54 mg of KHF_2 (0.68 mmol, 6 equiv.) was added along with 140 μL of water. The reaction was stirred overnight and dried under vacuum and triturated with ether. The solid was extracted with acetone, dried under vacuum to a yellow oil, and ^1H NMR was collected in $\text{DMSO-}d_6$ (shown).

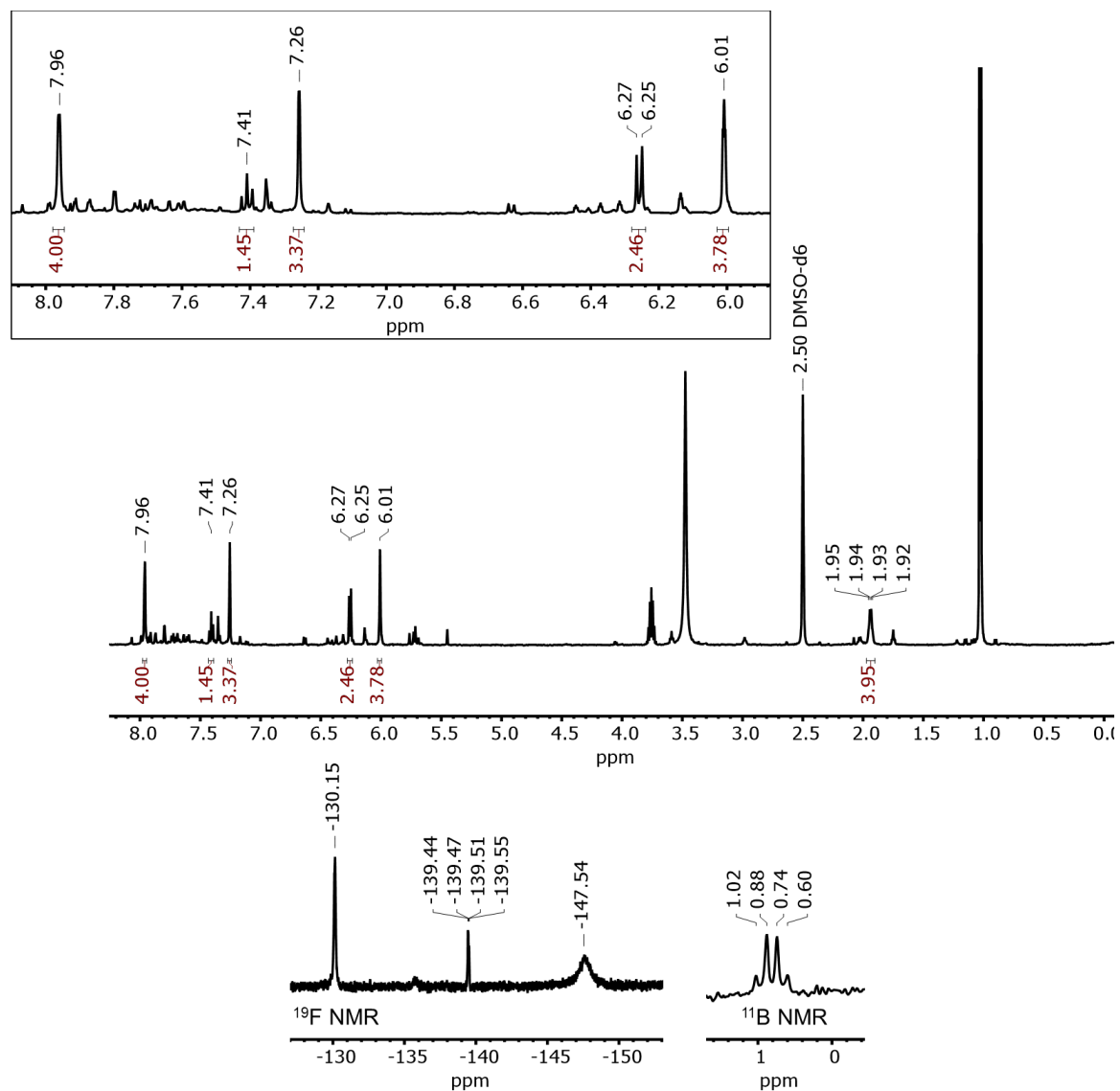


Figure A1.20 ^1H , ^{19}F and ^{11}B NMR characterization of the proposed $\text{pz4lut}(\text{CH}_2\text{BF}_3)_2$ (with impurities) collected in $\text{DMSO-}d_6$. To generate this product, 10 mg of $\text{pz4lut}(\text{CH}_2\text{B}(\text{O}^i\text{Pr})_2)_2$ (0.015 mmol) was dissolved in 3 mL of $\text{DMSO-}d_6$ and 0.5 mL was added to a nmr tube. D_2O (50 μL) and KHF_2 (10 mg, 48 equiv.) were added and the reaction was heated with stirring at 65 $^\circ\text{C}$ for two hours, after which time the stir bar was removed and NMR was collected. Separate experiments increasing the concentration of this reaction results in formation of the product shown in the previous NMR.

A1.4.2 Cyclic Voltammetry

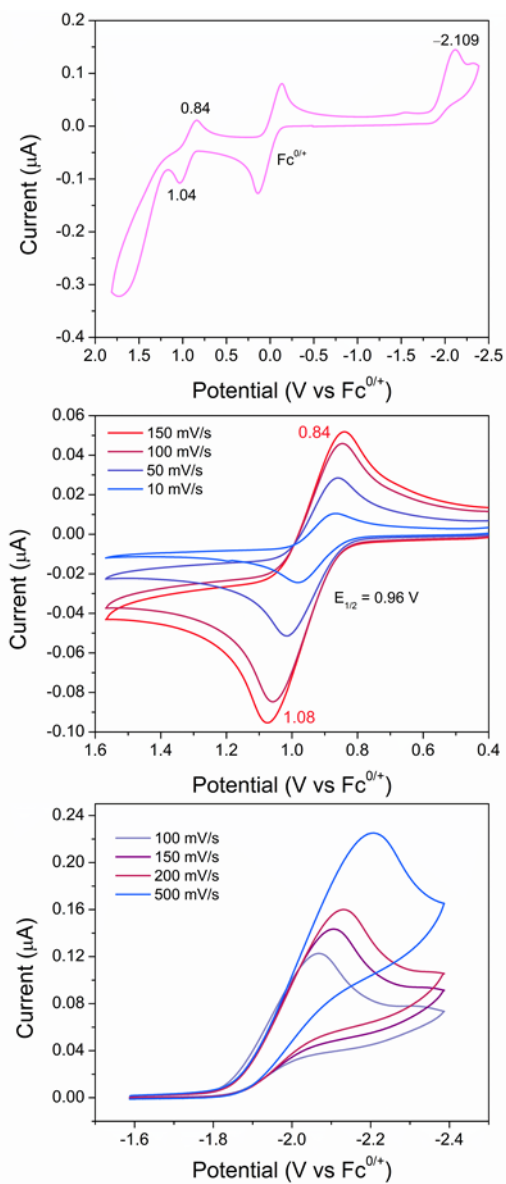


Figure A1.21 (Top) Full cyclic voltammogram of $[\text{Fe}(\text{pz4lut})\text{MeCN}][\text{OTf}]_2$ (5 mM) in a 0.1 M solution of TBAPF₆ in propionitrile with internal ferrocene at room temperature collected at 100 mV/s. (Middle) Cyclic voltammogram of isolated oxidation at differing scan rates. (Bottom) cyclic voltammogram of isolated irreversible reduction at differing scan rates.

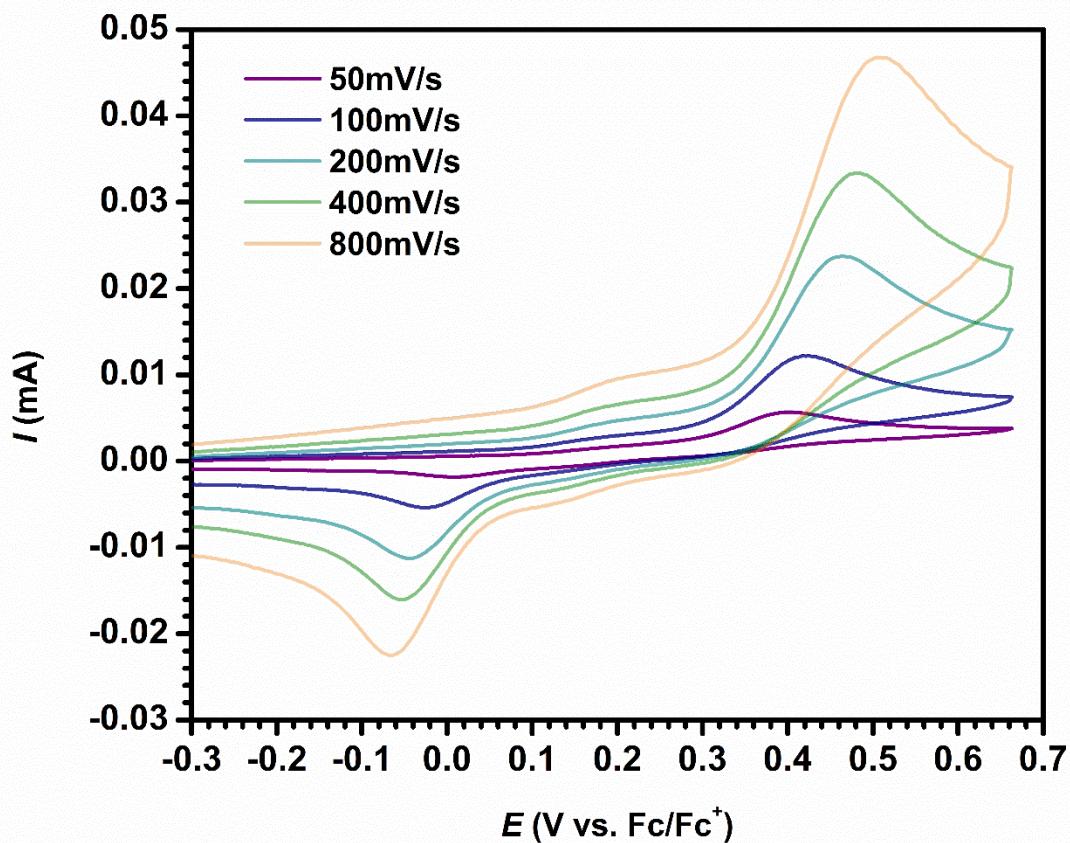


Figure A1.22 Cyclic voltammogram of 3 mM $\text{Fepz}_4\text{lut}(\text{SO}_3)_2(\text{MeCN})$ collected in a 0.1 M TBAPF_6 DMF electrolyte.

A1.4.3 UV-vis Spectra

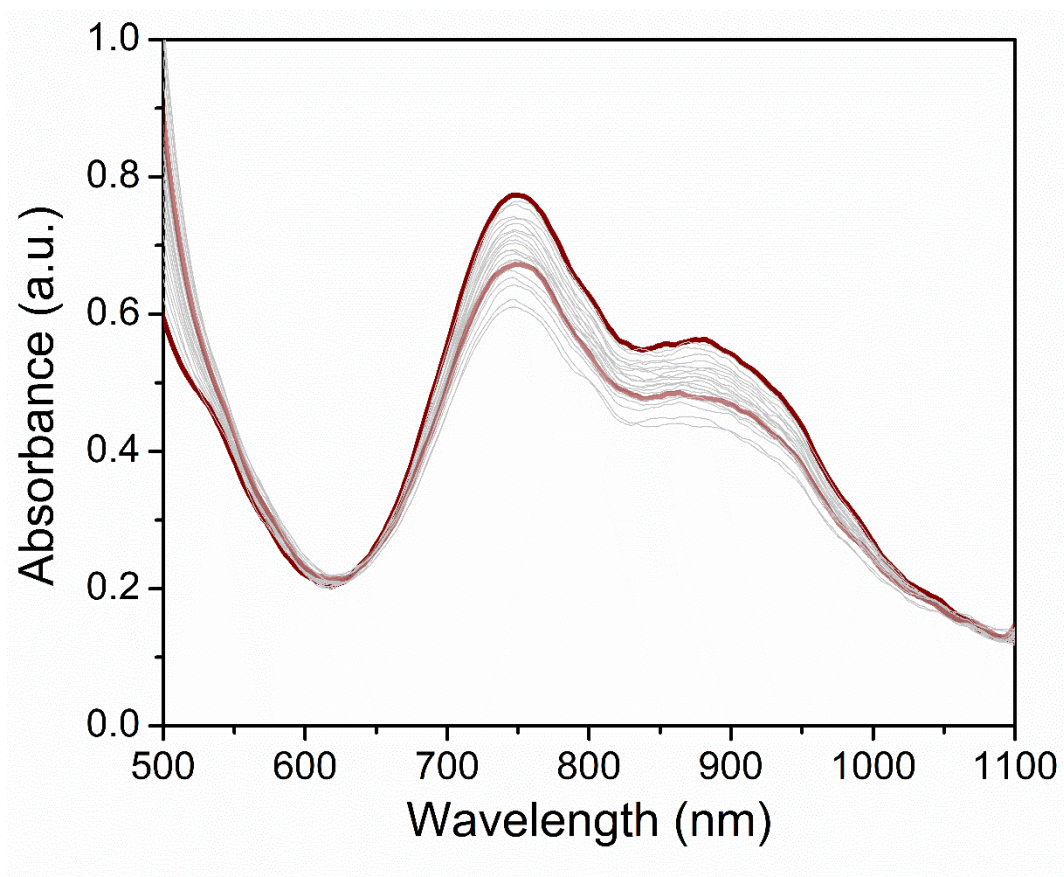


Figure A1.23 UV-vis of the decay of the intermediate formed upon reaction of the 5 mM solution of $[\text{Fe}(\text{pz}_4\text{lut})\text{MeCN}][\text{OTf}]_2$ in MeCN at -40°C with 1.1 equiv. of $^s\text{PhIO}$ added as a DCM solution (Figure A1.1). Scans from the initial spectrum (top, dark red) to the middle spectrum (dark red, 50% transparent) were collected every minute. Scans thereafter were collected every 5 minutes, for a total collection time of 41 minutes.

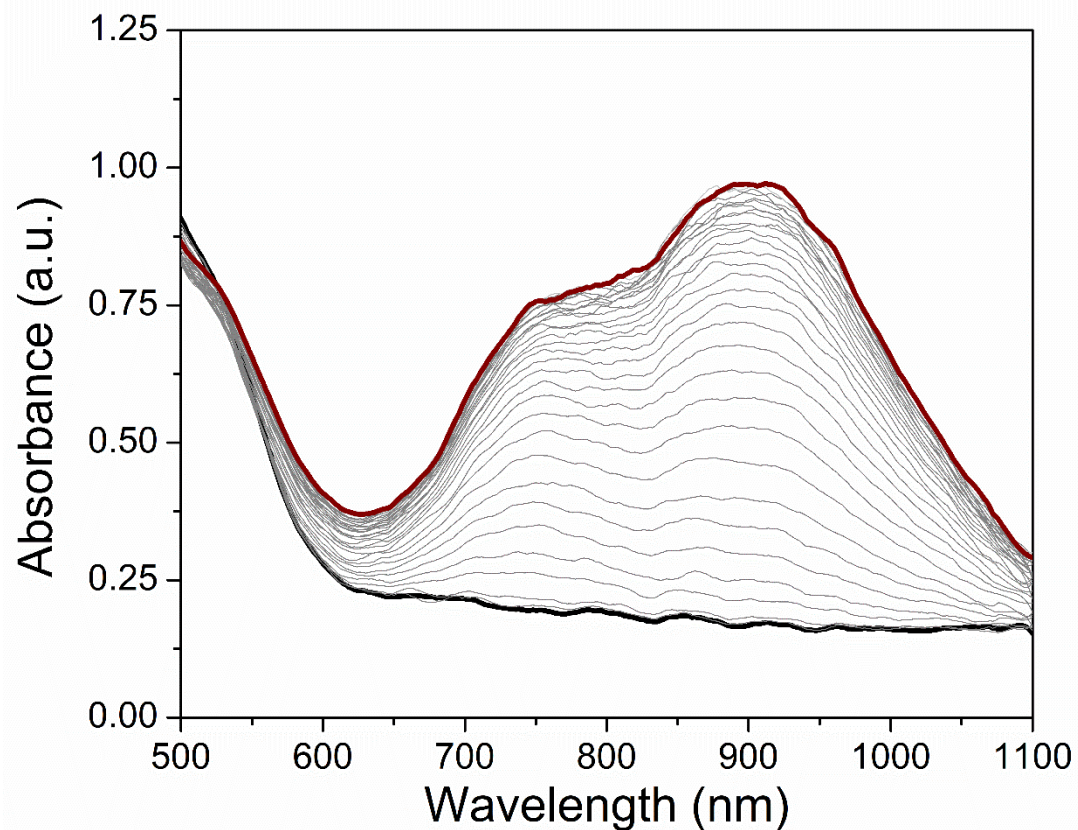


Figure A1.24 UV-vis spectrum of the reaction between a 5 mM solution of $[\text{Fe}(\text{pz}_4\text{lut})\text{MeCN}][\text{OTf}]_2$ in EtCN and 1.1 equiv. $^s\text{PhIO}$ as a DCM solution at $-65\text{ }^\circ\text{C}$ (IPA/dry ice). Scans were collected in 1 minute intervals for approximately 30 minutes before the maximum intensity was reached. The initial spectrum is in black and the final spectrum is in dark red.

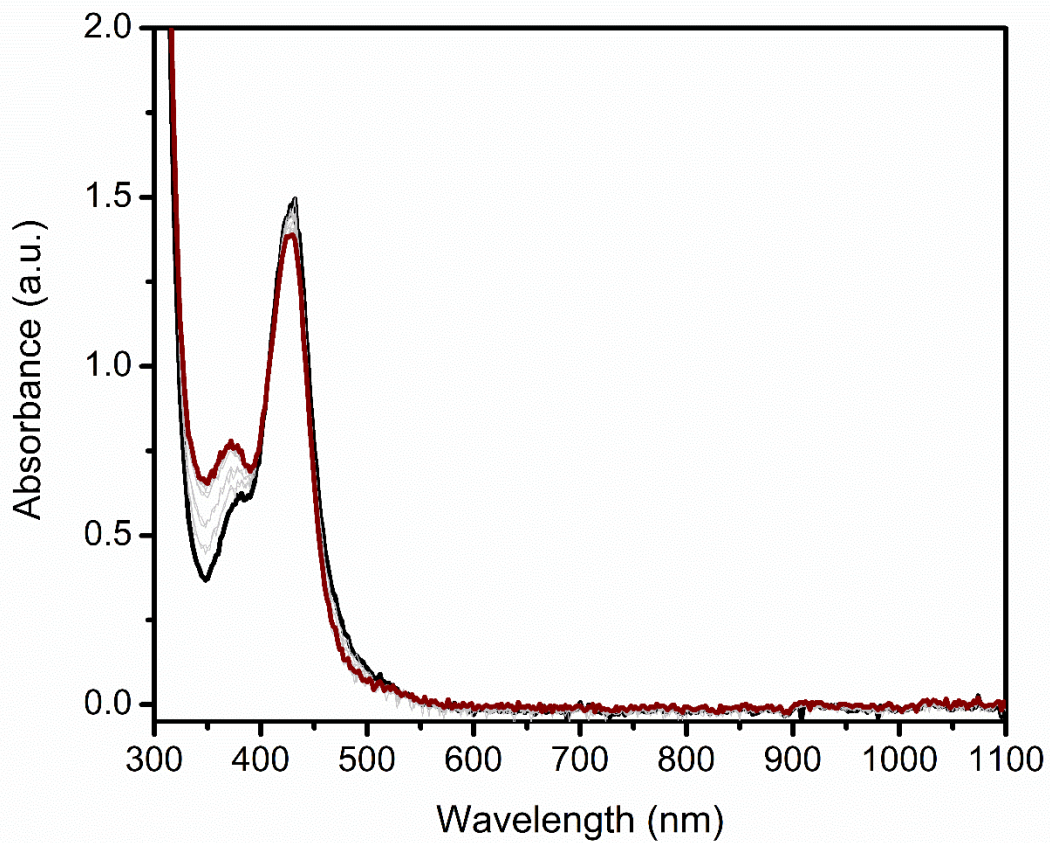


Figure A1.25 UV-vis spectra collected in 1 minute intervals monitoring the reaction between 0.5 mM solution of $\text{Fe}(\text{pz})_4\text{lut}(\text{SO}_3)_2(\text{MeCN})$ in MeCN and 1.1 equiv. of $^s\text{PhIO}$ as a DCM solution at $-40\text{ }^\circ\text{C}$. The initial spectrum is in black and the final spectrum is in red after 16 minutes. No further changes were observed at $-40\text{ }^\circ\text{C}$ nor upon warming.

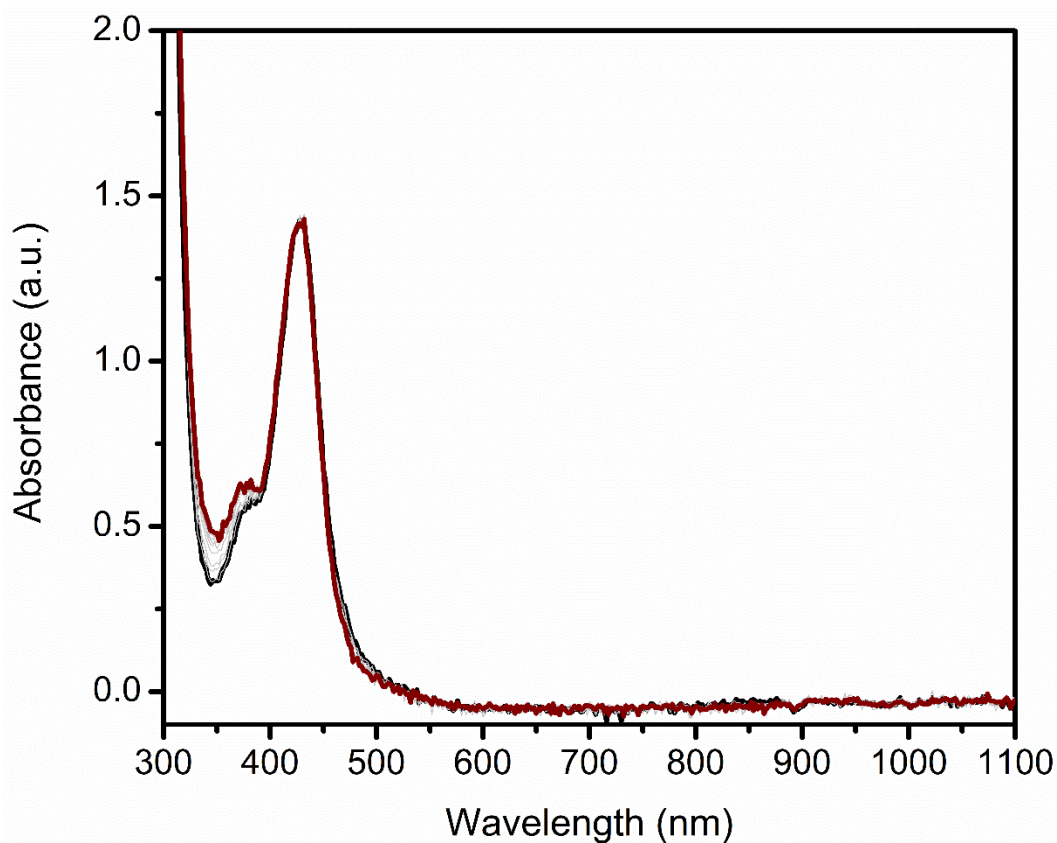


Figure A1.26 UV-vis spectra collected in 1 minute intervals monitoring the reaction between 0.5 mM solution of $\text{Fepz}_4\text{lut}(\text{SO}_3)_2(\text{MeCN})$ in 1:1 DCM/MeCN and 1.1 equiv. of mCPBA as a DCM solution at $-40\text{ }^\circ\text{C}$. The initial spectrum is in black and the final spectrum is in red after 10 minutes. No further changes were observed upon warming and re-cooling aside from a decrease and subsequent increase in intensity of the peak at 430 nm.

A1.5 References

1. Larson, V. A.; Battistella, B.; Ray, K.; Lehnert, N.; Nam, W. Iron and Manganese Oxo Complexes, Oxo Wall and Beyond. *Nature Reviews Chemistry*. 2020, pp 404–419.
2. Borovik, A. S. Role of Metal–Oxo Complexes in the Cleavage of C–H Bonds. *Chem. Soc. Rev.* **2011**, *40* (4), 1870–1874.
3. Saouma, C. T.; Peters, J. C. M≡E and M=E Complexes of Iron and Cobalt That Emphasize Three-Fold Symmetry (E = O, N, NR). *Coord. Chem. Rev.* **2011**, *255* (7–8), 920–937.
4. Chen, Z.; Yin, G. The Reactivity of the Active Metal Oxo and Hydroxo Intermediates and Their Implications in Oxidations. *Chem. Soc. Rev.* **2015**, *44* (5), 1083–1100.
5. Shimoyama, Y.; Kojima, T. Metal-Oxyl Species and Their Possible Roles in Chemical Oxidations. *Inorg. Chem.* **2019**, *58* (15), 9517–9542.
6. Li, X.; Siegbahn, P. E. M. Alternative Mechanisms for O₂ Release and O–O Bond Formation in the Oxygen Evolving Complex of Photosystem II. *Phys. Chem. Chem. Phys.* **2015**, *17* (18), 12168–12174.
7. Ullman, A. M.; Brodsky, C. N.; Li, N.; Zheng, S. L.; Nocera, D. G. Probing Edge Site Reactivity of Oxidic Cobalt Water Oxidation Catalysts. *J. Am. Chem. Soc.* **2016**, *138*, 4229–4236.
8. Morin, T. J.; Bennett, B.; Lindeman, S. V.; Gardinier, J. R. First-Row Transition-Metal Complexes of a New Pentadentate Ligand, $\alpha,\alpha,\alpha',\alpha'$ -Tetra(Pyrazolyl)Lutidine. *Inorg. Chem.* **2008**, *47* (17), 7468–7470.
9. Engelmann, X.; Monte-Pérez, I.; Ray, K. Oxidation Reactions with Bioinspired Mononuclear Non-Heme Metal-Oxo Complexes. *Angew. Chem., Int. Ed.* **2016**, *55* (27), 7632–7649.
10. Nurdin, L.; Spasyuk, D. M.; Fairburn, L.; Piers, W. E.; Maron, L. Oxygen-Oxygen Bond Cleavage and Formation in Co(II)-Mediated Stoichiometric O₂ Reduction via the Potential Intermediacy of a Co(IV) Oxyl Radical. *J. Am. Chem. Soc.* **2018**, *140* (47), 16094–16105.
11. Morin, T. J.; Wanniarachchi, S.; Gwengo, C.; Makura, V.; Tatlock, H. M.; Lindeman, S. V.; Bennett, B.; Long, G. J.; Grandjean, F.; Gardinier, J. R. Pyrazolyl Methyls Prescribe the Electronic Properties of Iron(II) Tetra(Pyrazolyl)Lutidine Chloride Complexes. **2011**, *40*, 8024.
12. Dehury, N.; Tripathy, S. K.; Sahoo, A.; Maity, N.; Patra, S. Facile Tandem Suzuki Coupling/Transfer Hydrogenation Reaction with a Bis-Heteroscorpionate Pd-Ru Complex. *Dalton Trans.* **2014**, *43* (44), 16597–16600.
13. Tripathy, S. K.; Surada, R. K.; Manne, R. K.; Mobin, S. M.; Santra, M. K.; Patra, S. Synthesis, Characterisation and Biological Activities of [(p-cym)RuX(pz4lut)]ⁿ⁺ and [{(p-cym)RuX}₂(μ -

pz4lut)]ⁿ⁺ (X = Cl, H₂O and pz4lut = $\alpha,\alpha,\alpha',\alpha'$ -tetra(pyrazol-1-yl)-2,6-Lutidine). *Dalton Trans.* **2013**, 42 (39), 14081–14091.

14. Morin, T. J.; Merkel, A.; Lindeman, S. V; Gardinier, J. R. Breaking the Cycle: Impact of Sterically-Tailored Tetra(Pyrazolyl)Lutidines on the Self-Assembly of Silver(I) Complexes. *Inorg. Chem.* **2010**, 49, 7992–8002.

15. Que, L. The Road to Non-Heme Oxoferryls and Beyond. *Acc. Chem. Res.* **2007**, 40, 493–500.

16. Wasylenko, D. J.; Tatlock, H. M.; Bhandari, L. S.; Gardinier, J. R.; Berlinguette, C. P. Proton-Coupled Electron Transfer at a [Co-OH_x]^z Unit in Aqueous Media: Evidence for a Concerted Mechanism. *Chem. Sci.* **2013**, 4 (2), 734–738.

17. Roy, C. D.; Soundararajan, R.; Brown, H. C. An Improved Synthesis Route to Functionalized 2-Alkyn-1-Ylboronates: Useful Intermediates for the Preparation of α -Allenic Alcohols. *Monatsh. Chem.* **2008**, 139 (3), 241–249.

18. Abeyayehu, A.; Dutta, R.; Lee, C. H. Synthesis, Characterization and Properties of Expanded Porphyrins: A New Family of Alkylidenyl Porphyrin Homologues Bearing Meso-Exocyclic Double Bonds. *Chem. – A Eur. J.* **2016**, 22 (39), 13850–13856.

Appendix 2: Supporting Data for Chapter 2

A2.1 Characterization Data

A2.1.1 IR Spectra

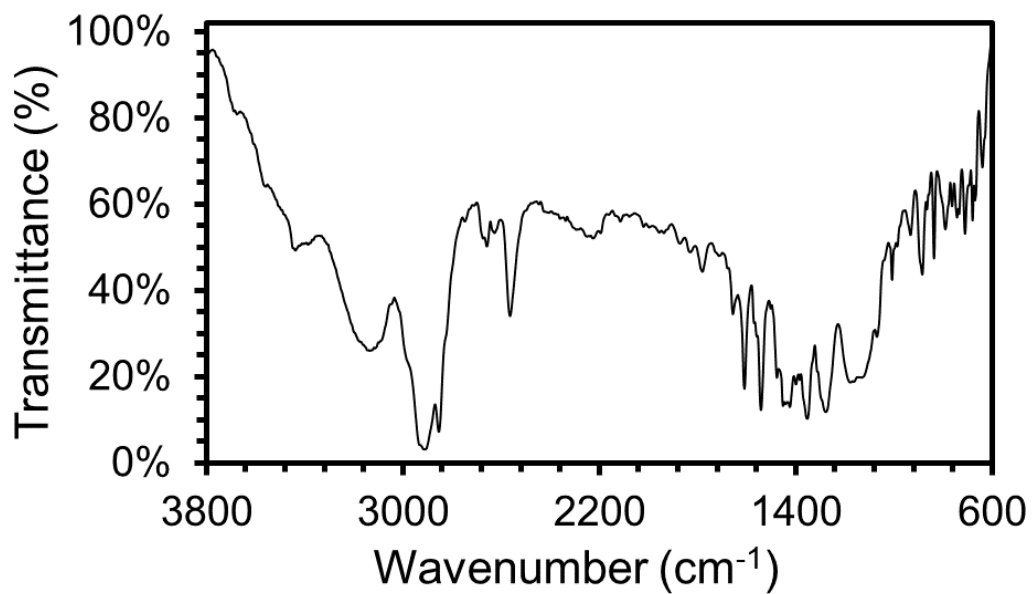


Figure A2.1 Vibrational spectrum of **1** as KBr pellet (see experimental section above for specific peak values).

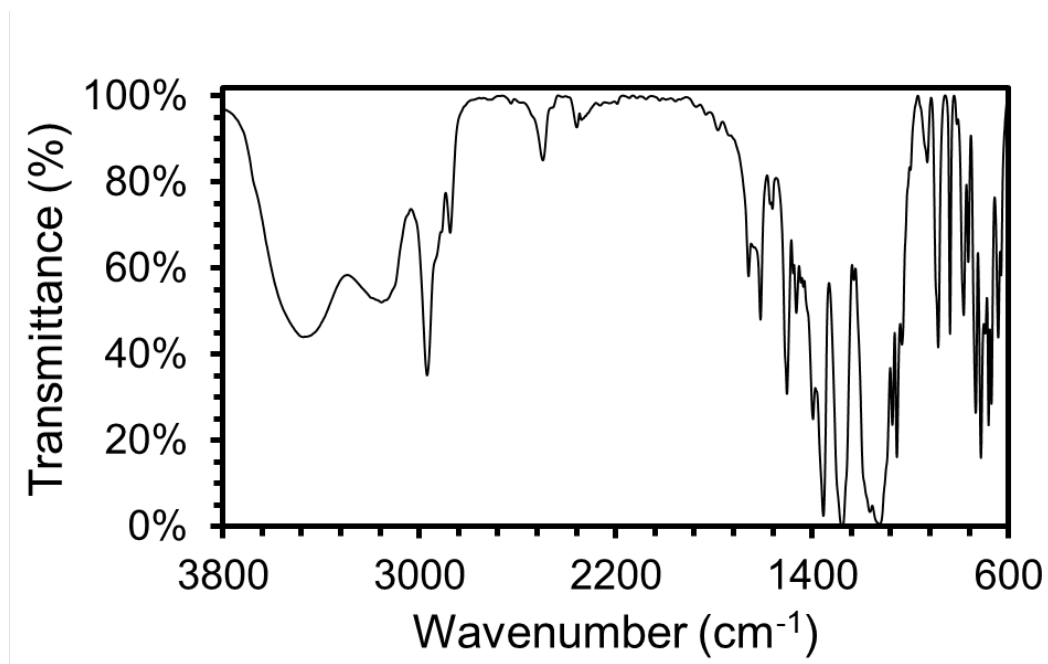


Figure A2.2 Vibrational spectrum of **2** as KBr pellet (see experimental section above for specific peak values).

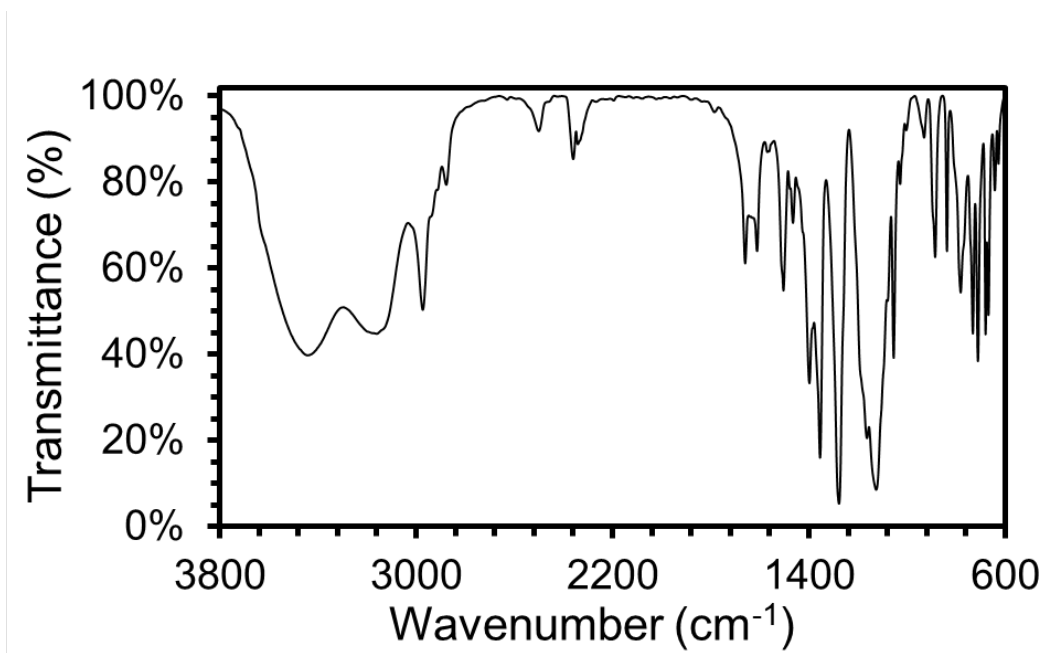


Figure A2.3 Vibrational spectrum of **3** as KBr pellet (see experimental section above for specific peak values).

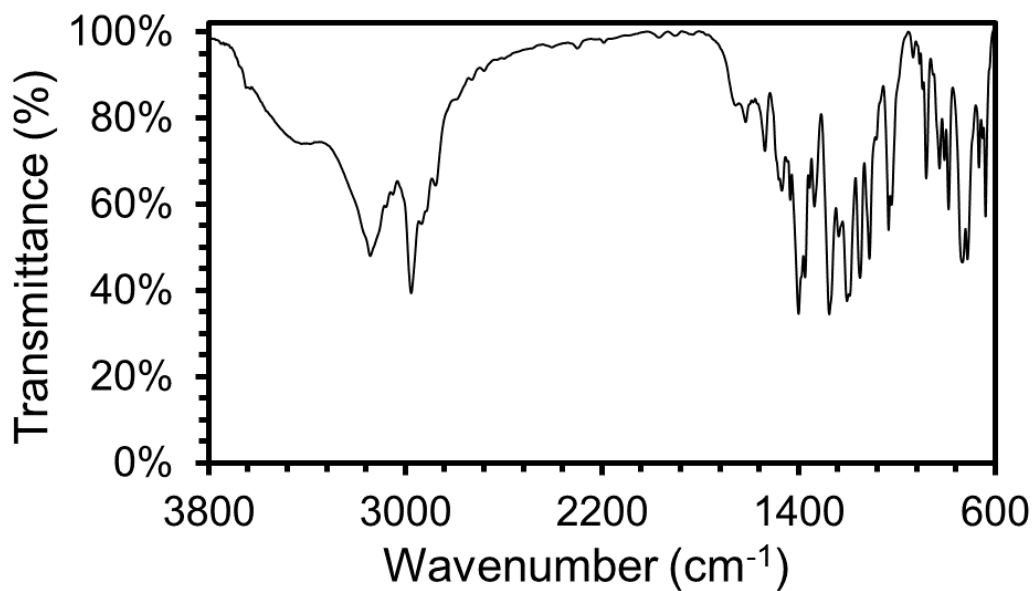


Figure A2.4 Vibrational spectrum of **4** as KBr pellet (see experimental section above for specific peak values).

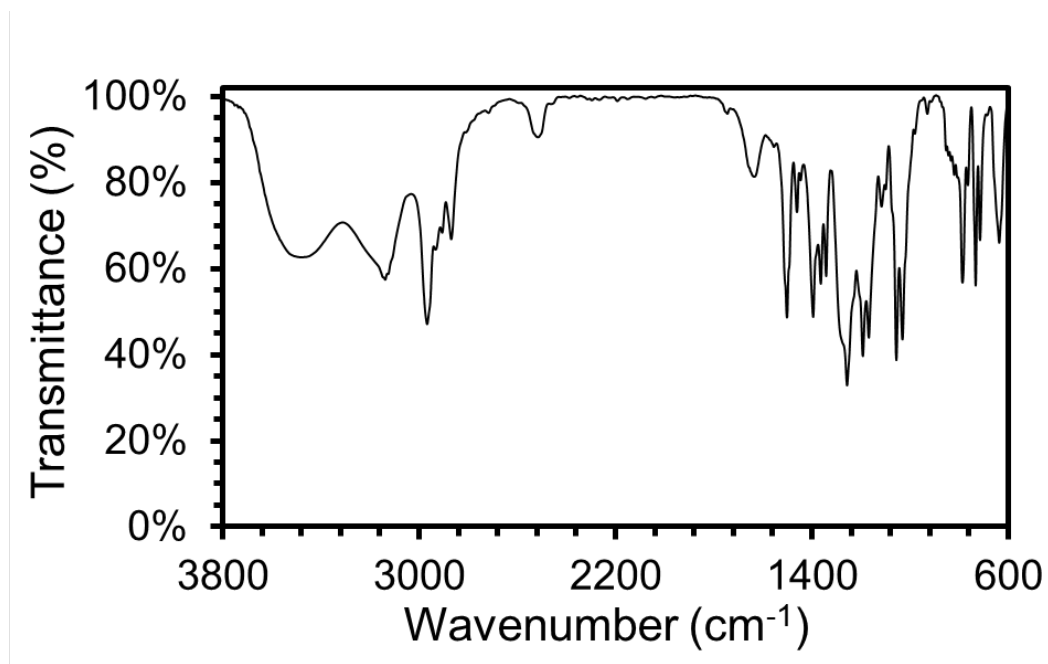


Figure A2.5 Vibrational spectrum of **5** as KBr pellet (see experimental section above for specific peak values).

A2.1.2 UV-vis Spectra

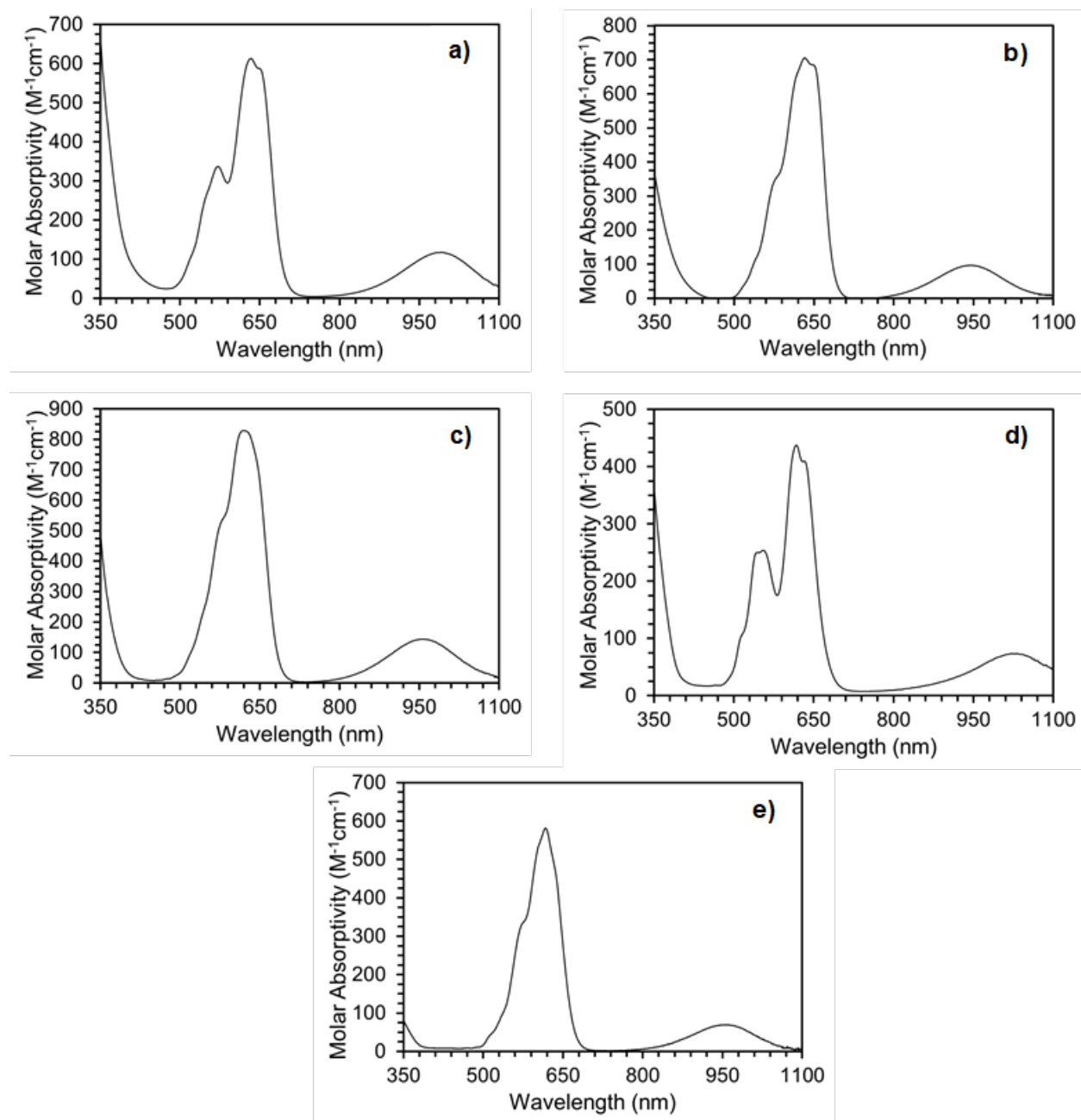


Figure A2.6 UV-vis spectra for complexes **1** (a), **2** (b), **3** (c), **4** (d), and **5** (e). Complexes **1-3** and **5** are solutions in Et₂O while **4** is a solution in DCM, all recorded at room temperature. See text above for detailed peak positions and absorptivity values.

A2.1.3 NMR Spectra

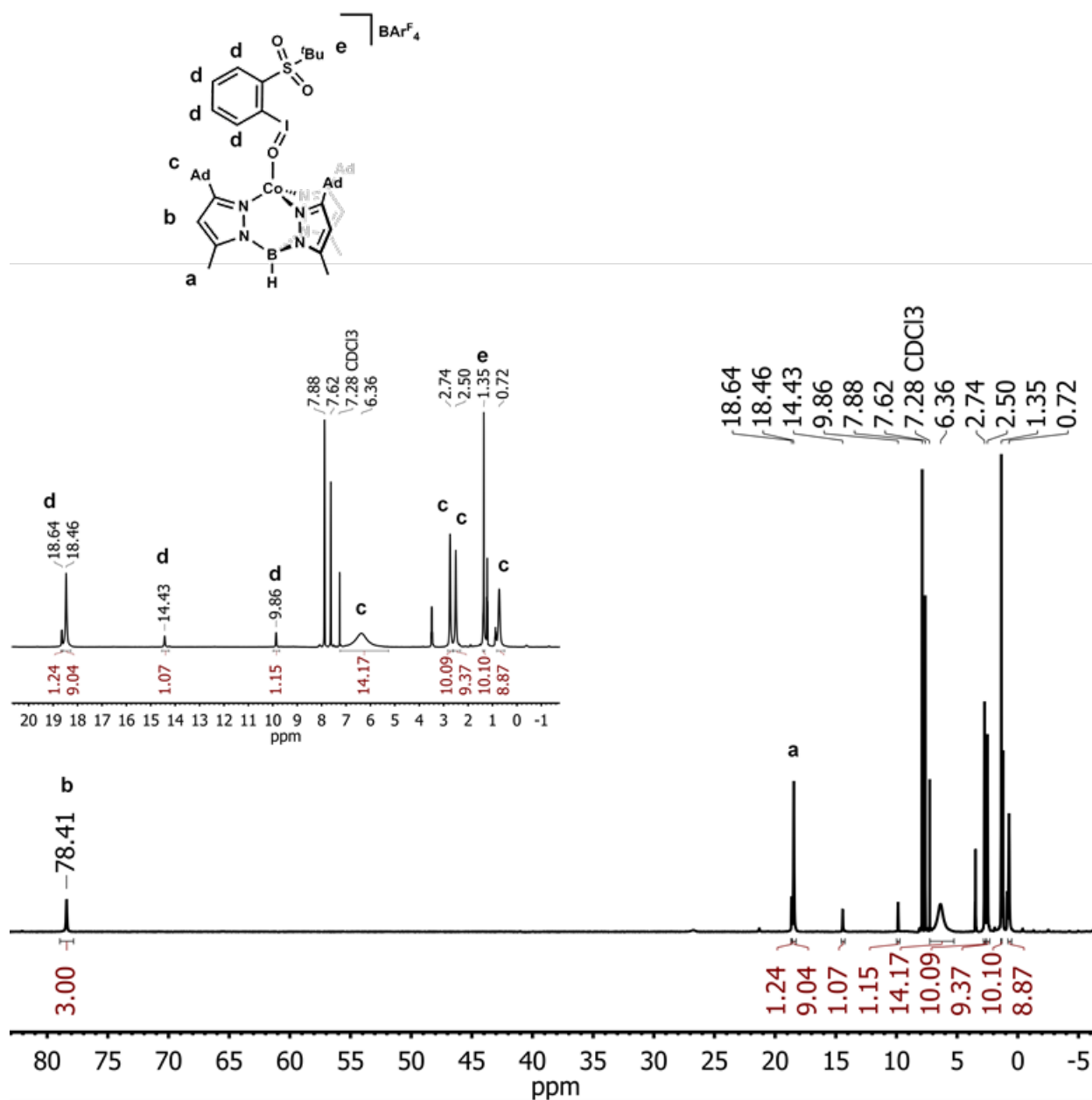


Figure A2.7 The ^1H NMR spectrum of **1** in CDCl_3 . Inset is expanded near the diamagnetic region to show details. Note: Residual solvent and BAr^{F}_4 resonances not labeled.

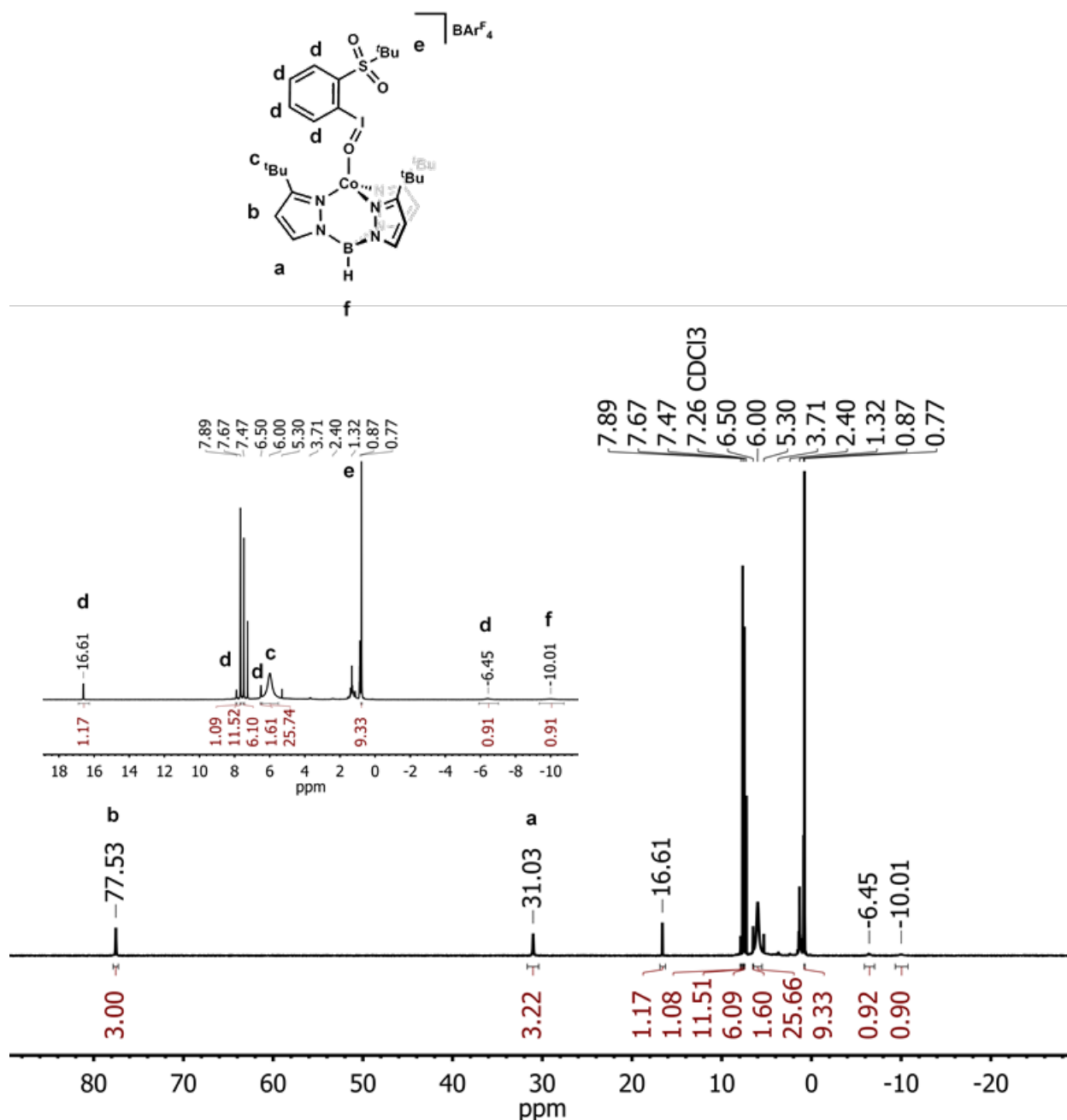


Figure A2.8 The ^1H NMR spectrum of **2** in CDCl_3 . Inset is expanded near the diamagnetic region to show details. Note: Residual solvent and BAr^{F_4} resonances not labeled.

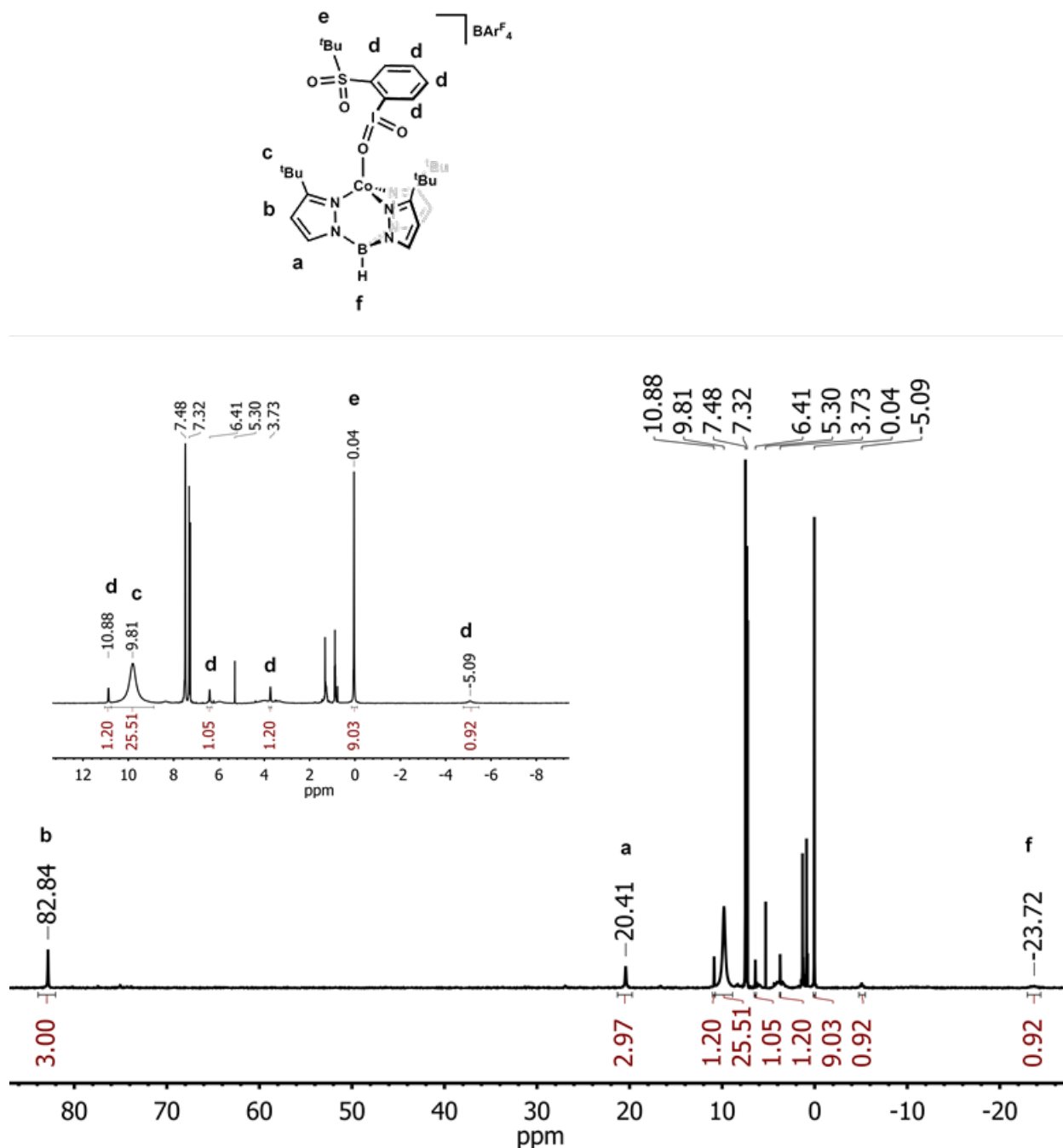


Figure A2.9 The ^1H NMR spectrum of **3** in CDCl_3 . Inset is expanded near the diamagnetic region to show details. Note: Residual solvent and BAr_4^- resonances not labeled.

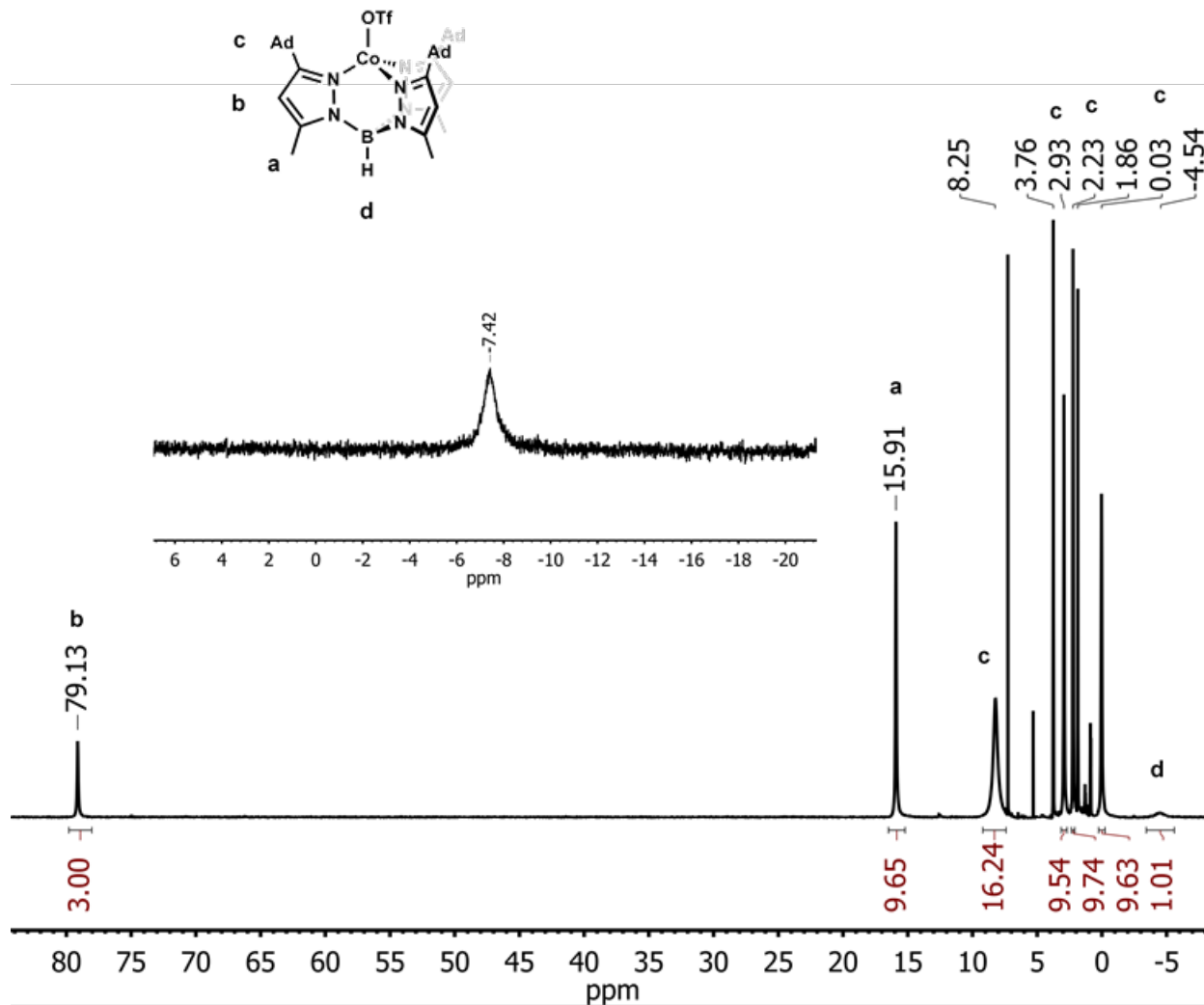


Figure A2.10 The ^1H NMR spectrum of **4** in CDCl_3 . Inset: ^{19}F NMR spectrum of the same solution. Note: Residual solvent resonances not labeled.

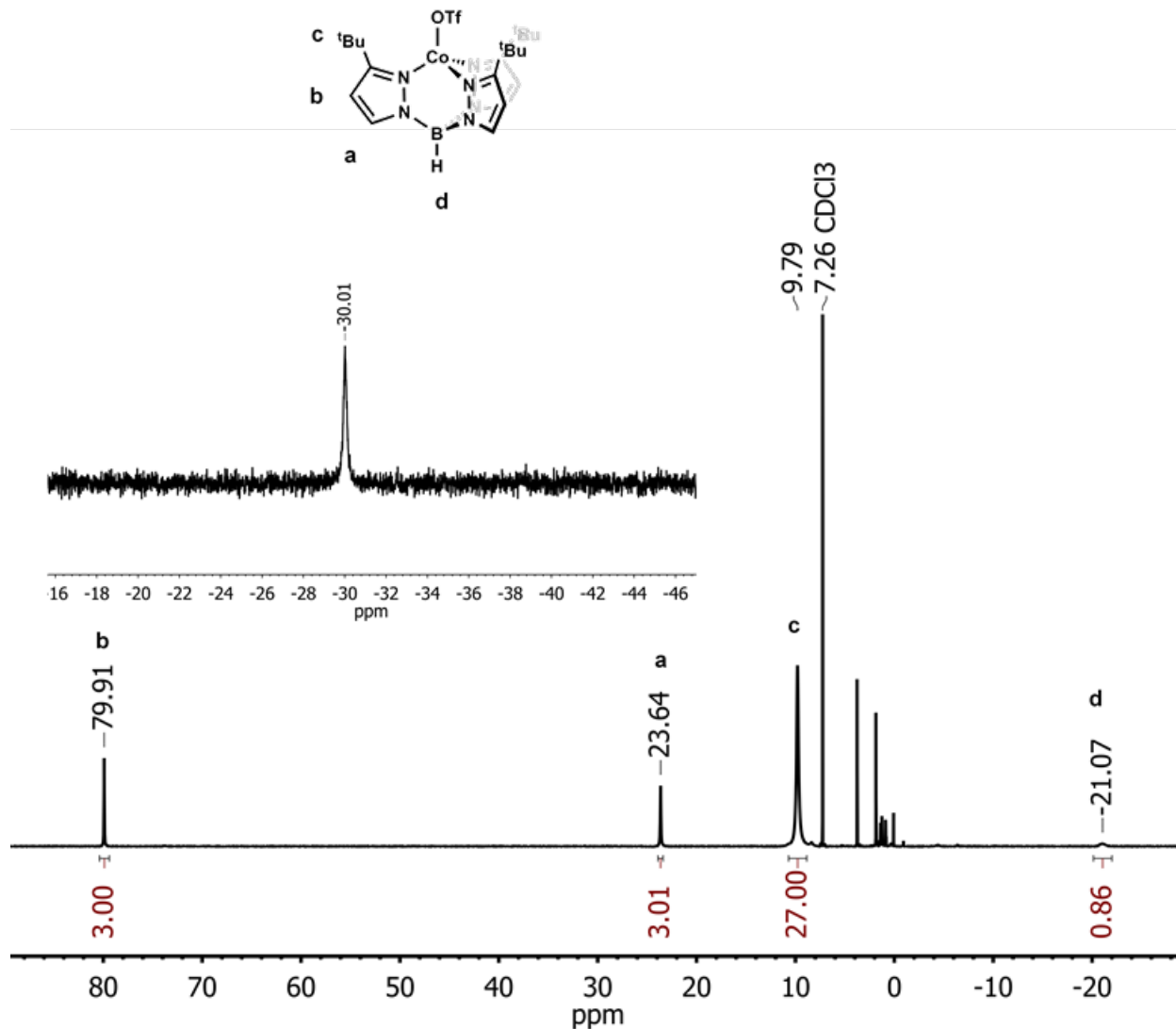


Figure A2.11 The ^1H NMR spectrum of **5** in CDCl_3 . Inset: ^{19}F NMR spectrum of the same solution. Note: Residual solvent resonances not labeled.

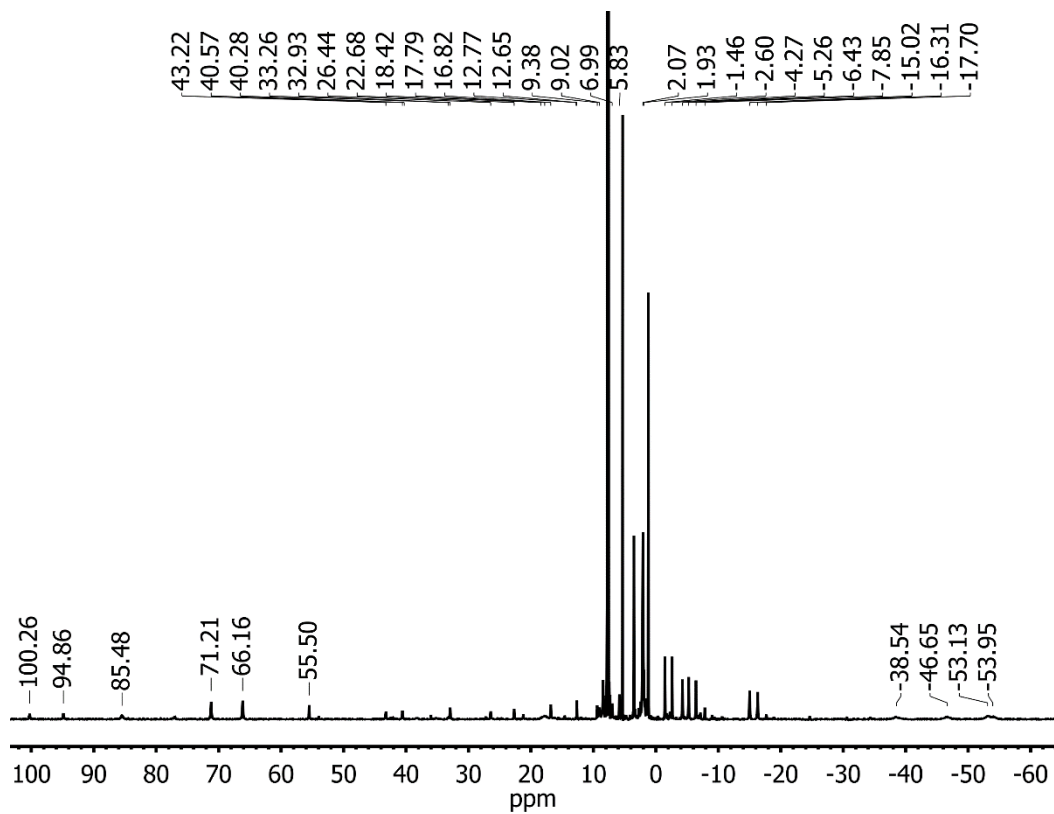


Figure A2.12 The ^1H NMR spectrum of the decay of **1** (2.5 mM in CD_2Cl_2) after 24 h. Note: the top of residual solvent and BAr^{F_4} anion peaks have been clipped to better show paramagnetic peaks.

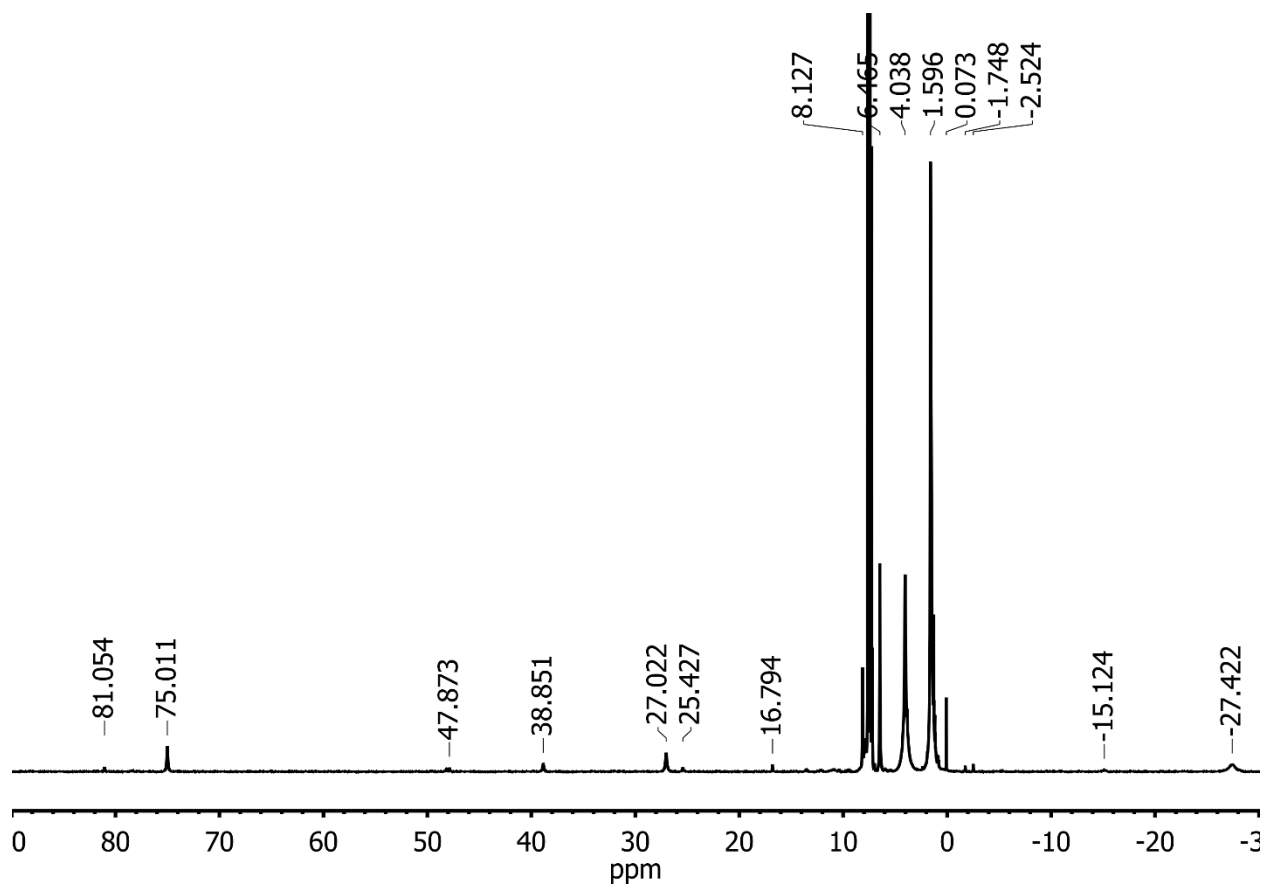


Figure A2.13 The ^1H NMR spectrum of the decay of **2** (in CDCl_3) after standing for 14 d in Et_2O . Note: the top of residual solvent and BAr^{F_4} anion peaks have been clipped to better show paramagnetic peaks.

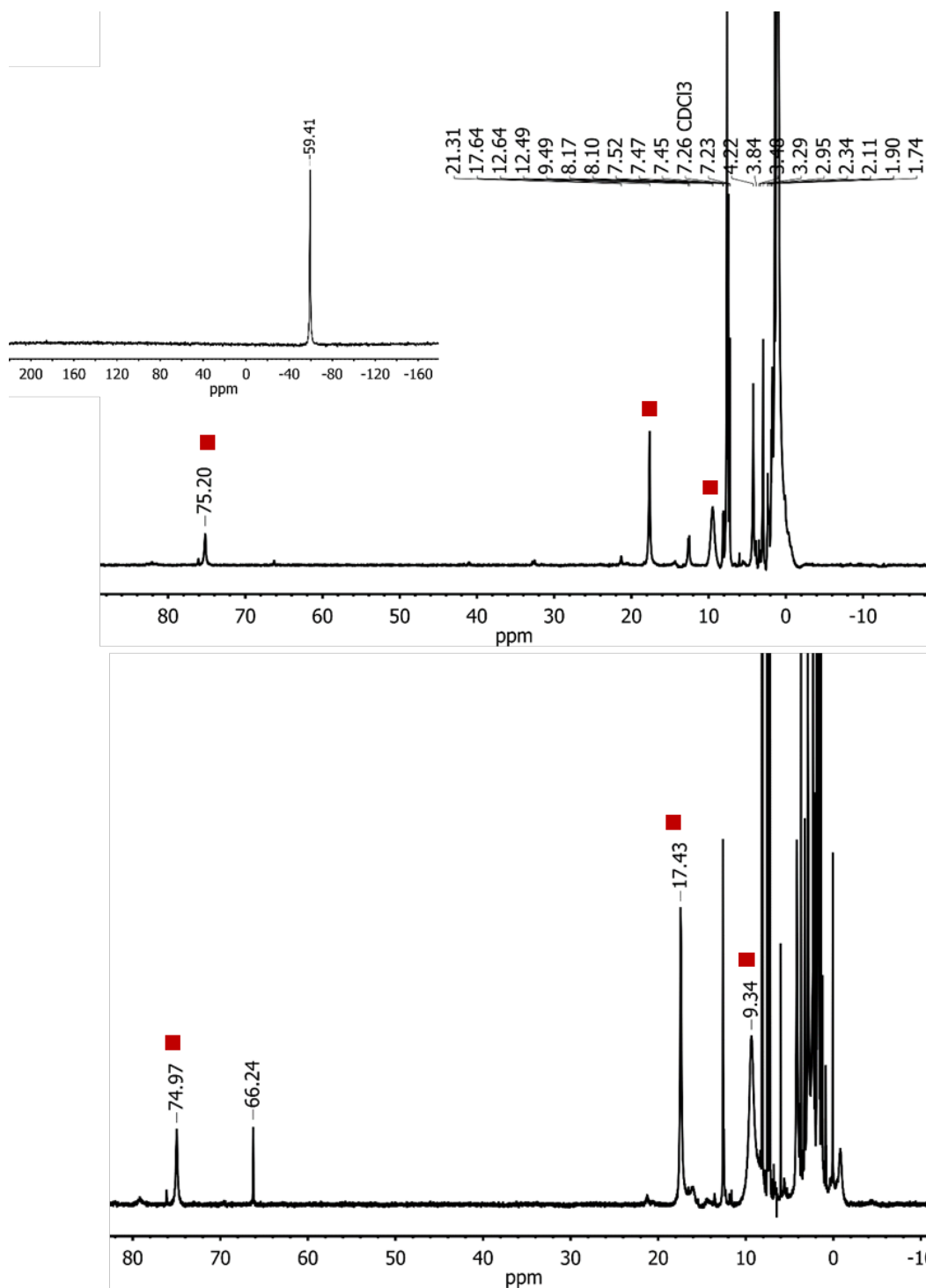


Figure A2.14 The ^1H NMR spectrum of the reaction of **1** (2.5 mM in CDCl_3) with (top) 10 equiv of PMe_3 and (bottom) independently prepared OPMe_3 (OPMe_3 prepared by treating $^8\text{PhIO}$ with 1.1 equiv of PMe_3 in CDCl_3 and stirring for 1 h). Red squares indicate the putative OPMe_3 adduct. Note: the top of the residual solvent peaks and excess PMe_3 have been clipped to better show paramagnetic features. Inset: ^{31}P NMR spectrum of reaction mixture, consistent with free PMe_3 .

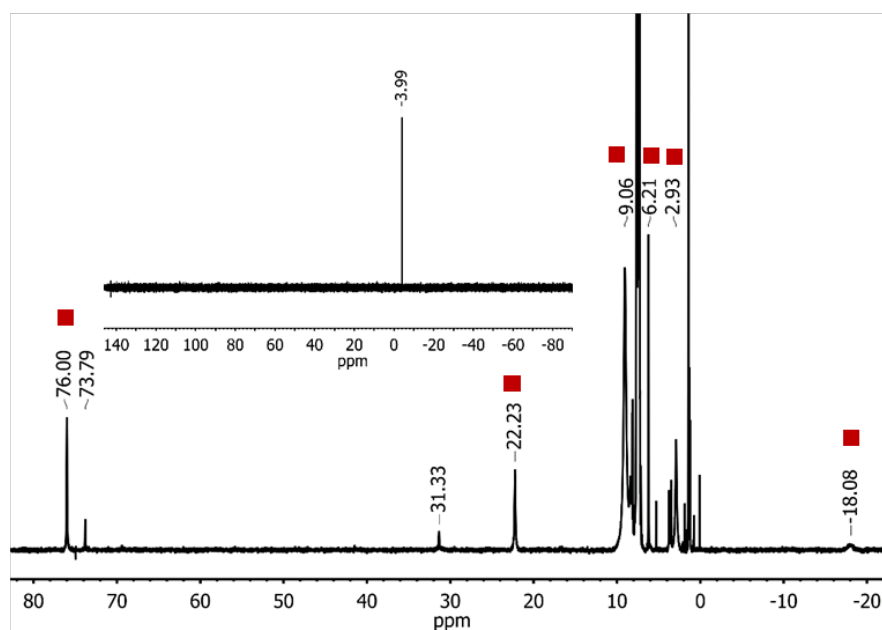
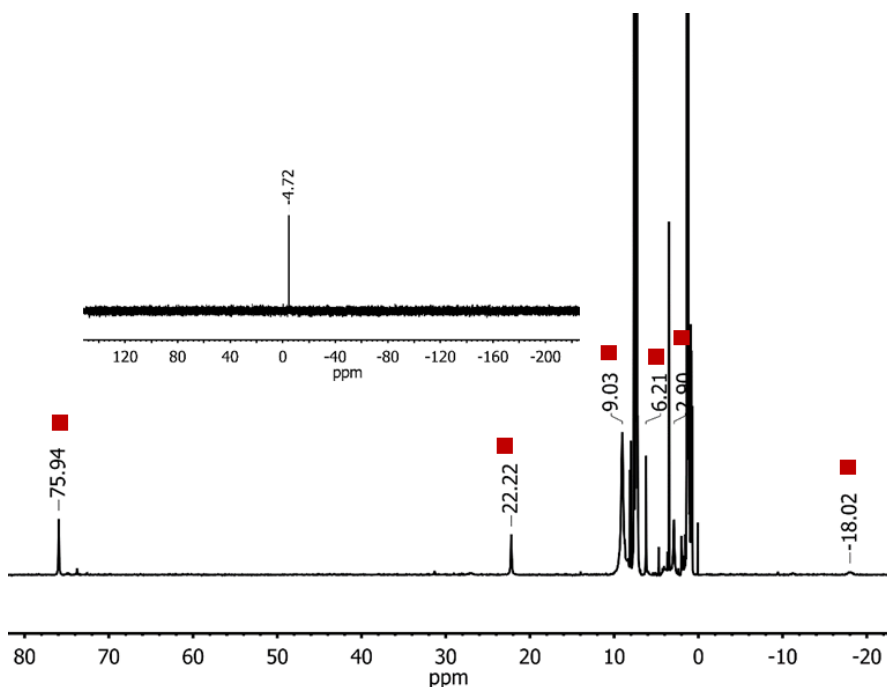


Figure A2.15 The ^1H NMR spectrum (CDCl_3) of the 2.5 mM reaction of **2** (top) and **3** (bottom) with 10 equiv of PPh_3 . Red squares are assigned to resonances for the OPPh_3 adduct, other paramagnetic peaks arise from an unknown impurity. Note: the top of the residual solvent, BAr^{F_4} , and excess PPh_3 resonances have been clipped to better show paramagnetic peaks. Inset: ^{31}P NMR spectrum of the respective reaction mixtures consistent with free PPh_3 .

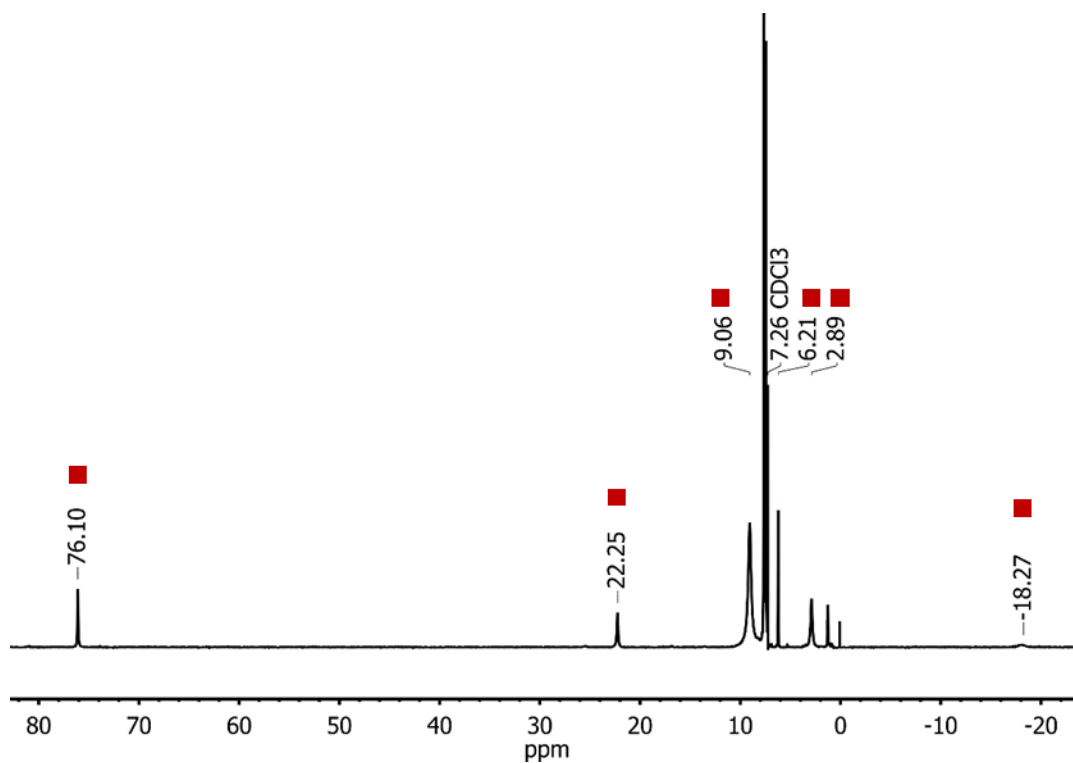


Figure A2.16 The ^1H NMR spectrum of independently synthesized OPPh_3 adduct prepared by treatment of a solution of **5** with 1.1 equiv of OPPh_3 in the presence of 1.1 equiv $\text{NaBAr}^{\text{F}_4}$. Note: Peaks for residual solvent and BAr^{F_4} anion have been clipped off to show detail of paramagnetic features.

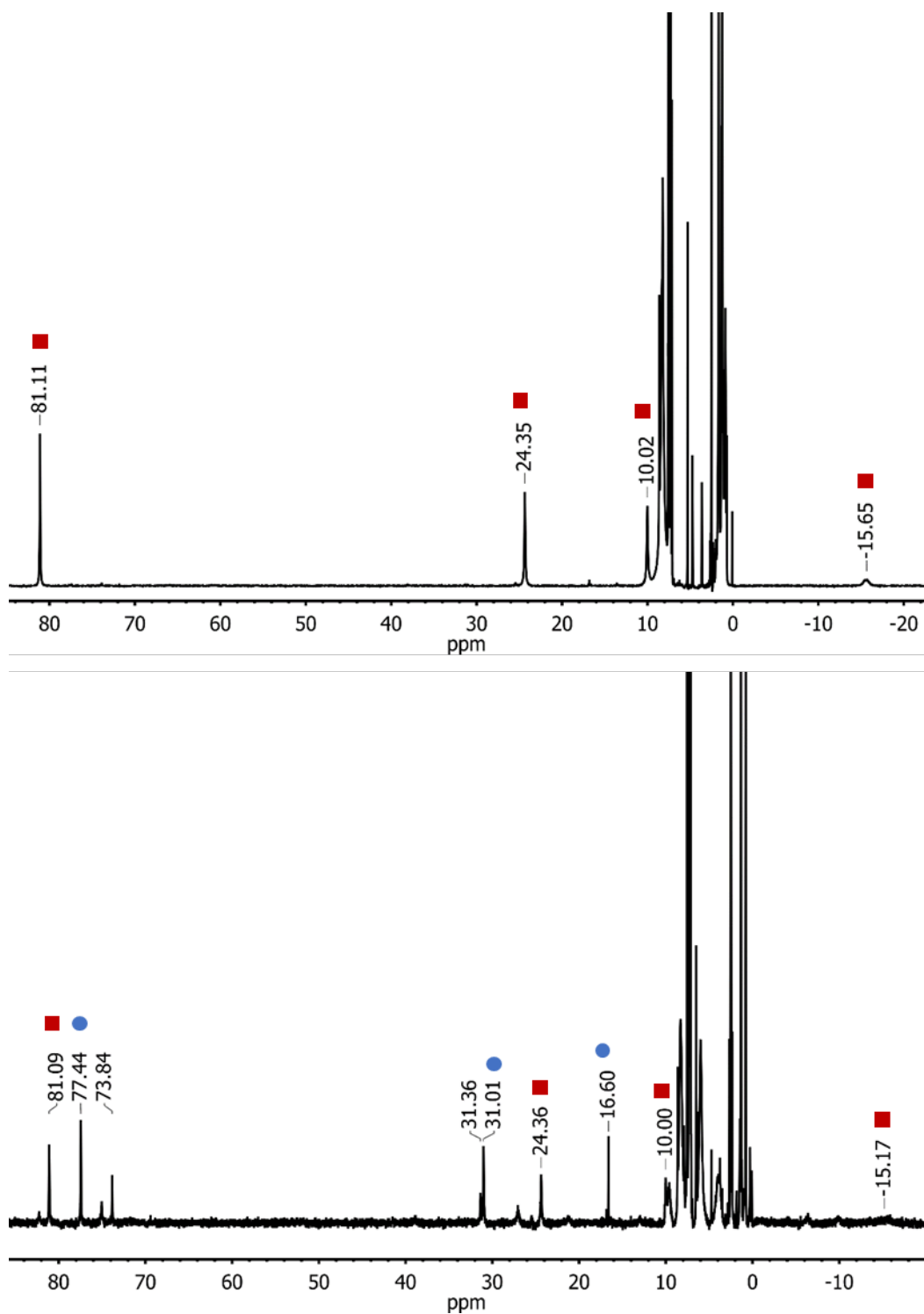


Figure A2.17 The ^1H NMR spectrum of the reaction of **2** (top, CDCl_3) and **3** (bottom, 2.5 mM in CDCl_3) with 10 equiv. thioanisole after 52 and 32 h. Red squares mark resonances for the PhSOME adduct (see below), blue circles are for **2** formed as the immediate decay product of **3**, and other paramagnetically shifted peaks are from an unknown impurity. Note: The top of the residual solvent peaks and BAr^{F}_4 resonances have been clipped off to better show paramagnetic features.

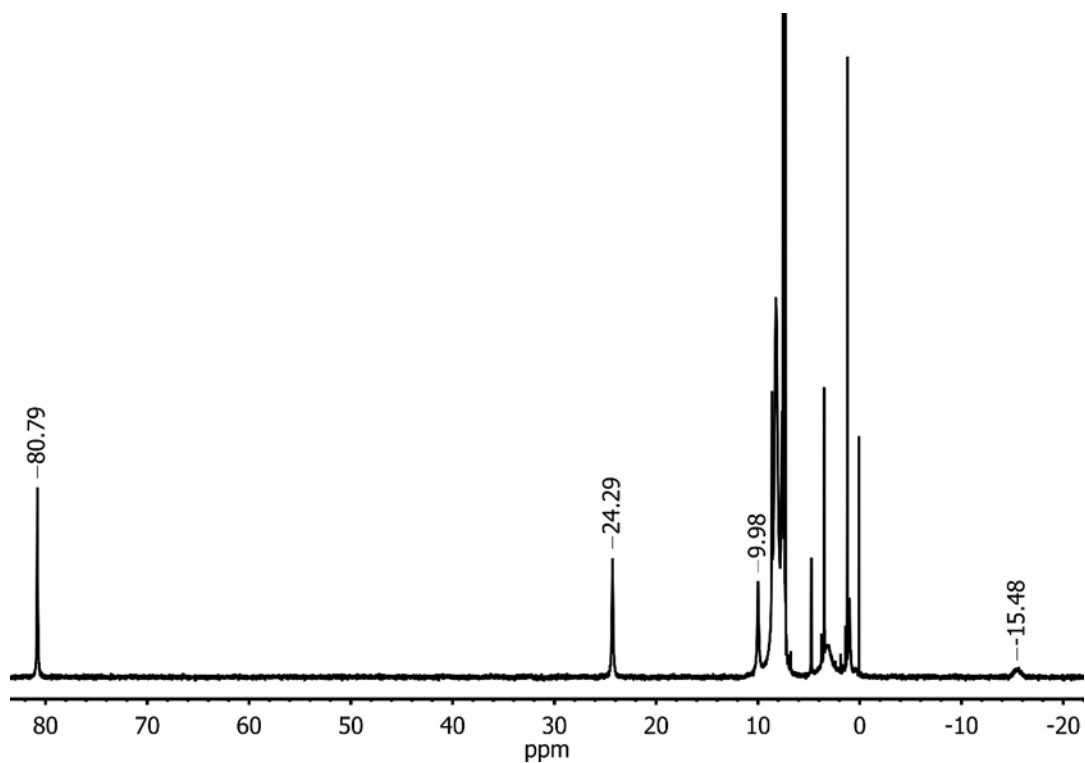


Figure A2.18 The ^1H NMR spectrum of independently prepared $\text{CoTp}^{\text{tBu}}\text{-PhSOMe}$ adduct (CDCl_3) generated by the addition of 1.1 equiv of PhSOMe to **2** in the presence of 1.1 equiv $\text{NaBAR}^{\text{F}_4}$. Note: residual solvent peaks have been clipped at the top to better show paramagnetic peaks.

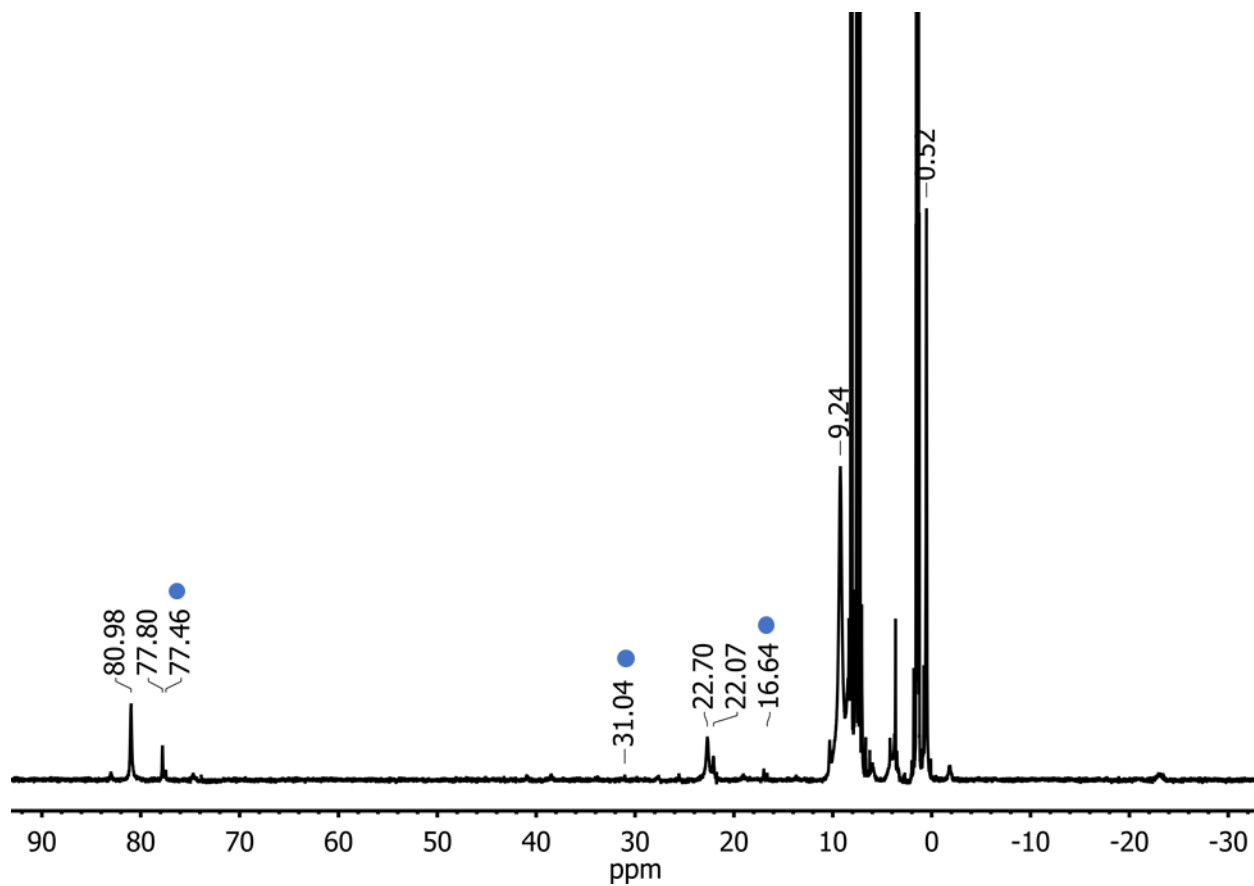


Figure A2.19 The ^1H NMR spectrum of the reaction of **3** with 20 equivalents of ^5PhI in CDCl_3 . Peaks labeled with blue circles correspond to some of complex **2** produced while other labeled resonances belong to unknown paramagnetic products. Note: residual solvent, ^5PhI , and BAr^{F_4} resonances have been clipped at the top to better show paramagnetic peaks.

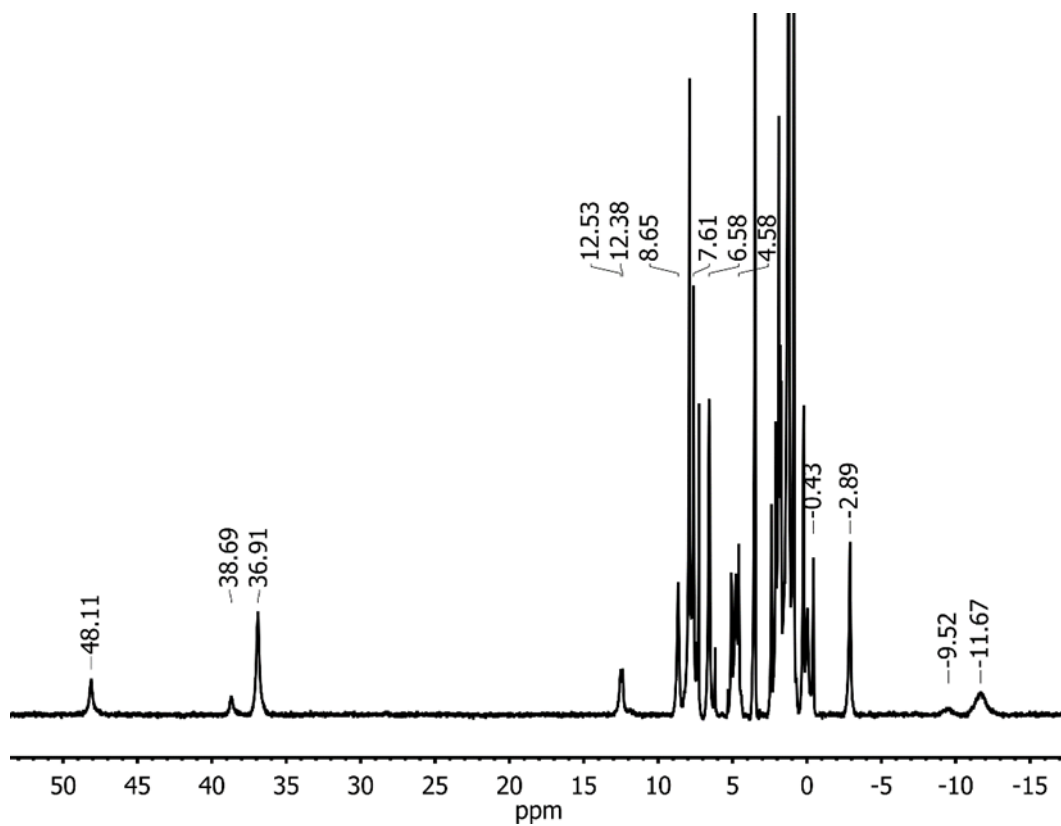


Figure A2.20 The ¹H NMR spectrum of the crystals of **6** obtained from the reaction of **1** with 10 equiv of ScOTf₃. Note: the top of residual solvent peaks has been clipped off to better show the paramagnetic features.

A2.1.4 EPR Spectra

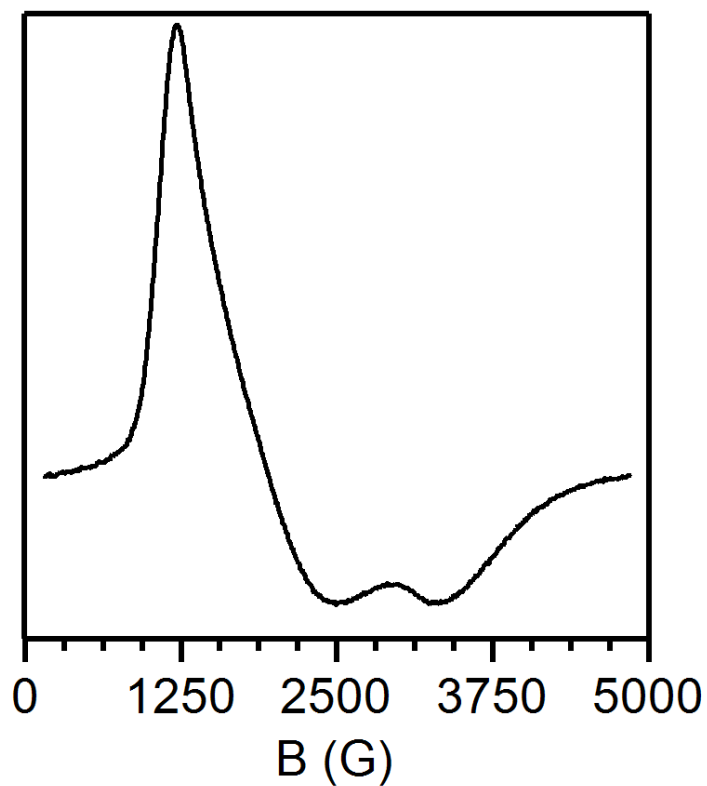


Figure A2.21 The X-band EPR spectrum of **1** collected on a 15 mM solution in Et₂O at 15 K. Microwave frequency: 9.63 GHz, microwave power: 0.2 mW, and $g_{\text{eff}} = 5.55, 3.58, \text{ and } 2.05$.

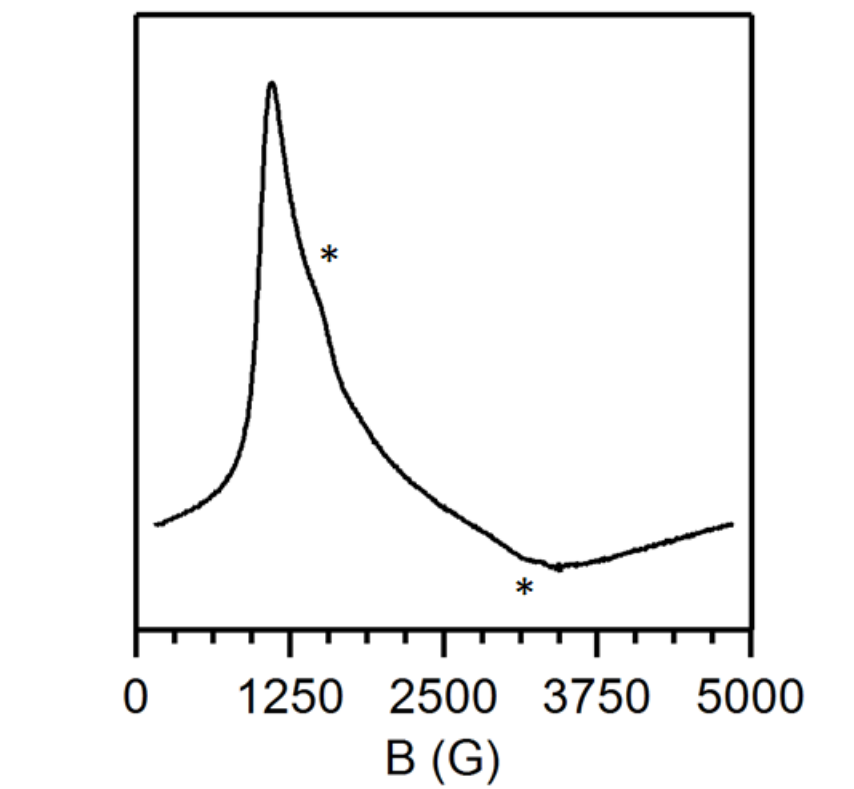


Figure A2.22 The X-band EPR spectrum of **2** collected on a 15 mM solution in Et₂O at 15 K. Microwave frequency: 9.63 GHz, microwave power: 2.0 mW, and $g_{\text{eff}} = 6.25, 3.49,$ and 2.05. Asterisks indicate what is consistent with a small amount of **5**.

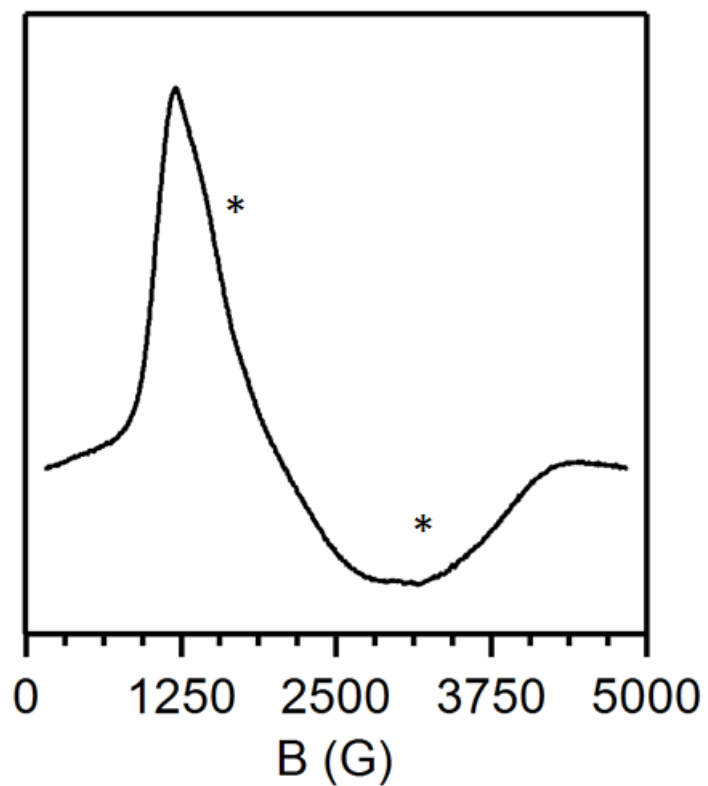


Figure A2.23 The X-band EPR spectrum of **3** collected on a 15 mM solution in Et₂O at 15 K. Microwave frequency: 9.63 GHz, microwave power: 0.6 mW, and $g_{\text{eff}} = 5.66, 3.44,$ and 2.29. Asterisks indicate what is consistent with a small amount of **5**.

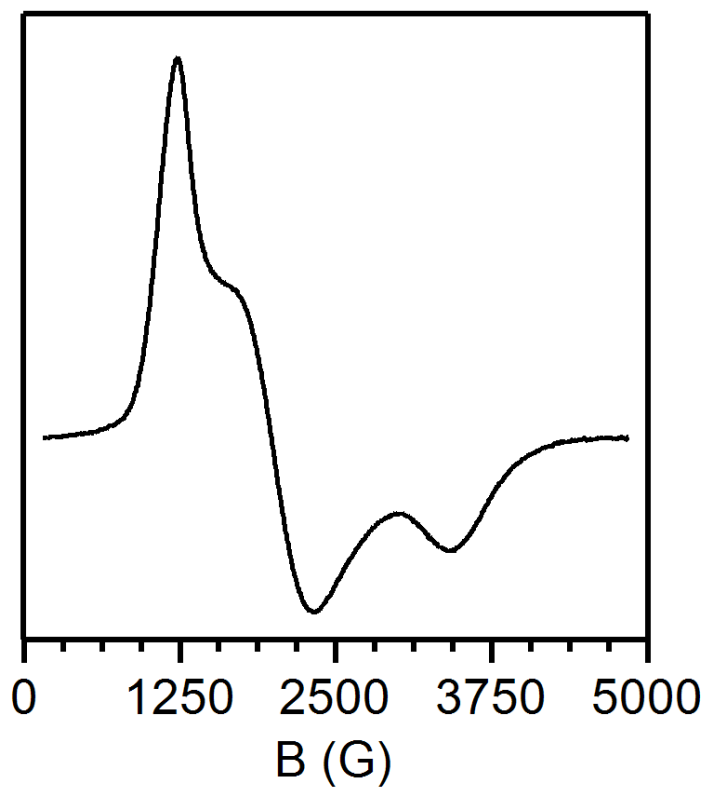


Figure A2.24 The X-band EPR spectrum of **4** collected on a 15 mM solution in THF at 15 K. Microwave frequency: 9.63 GHz, microwave power: 0.2 mW, and $g_{\text{eff}} = 5.51, 3.40, \text{ and } 2.01$.

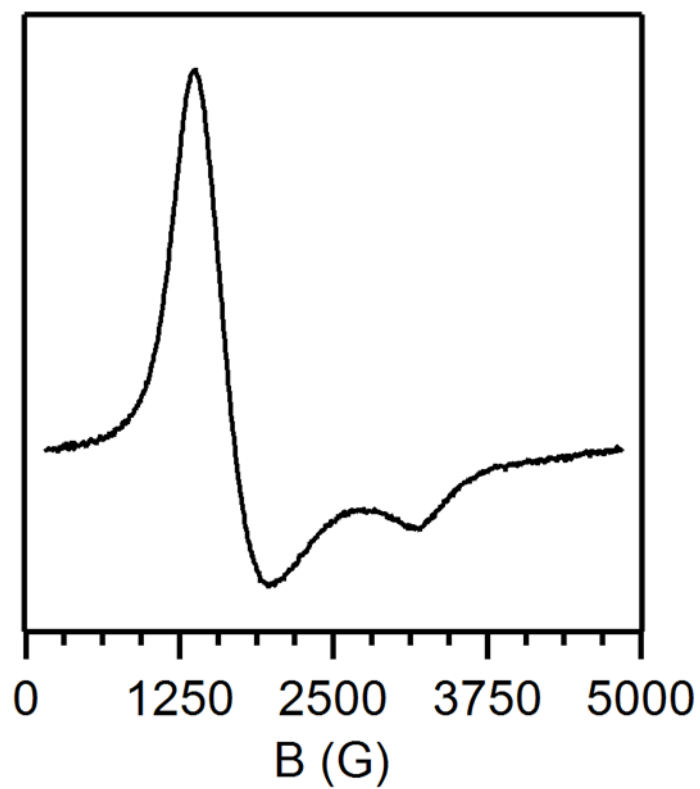


Figure A2.25 The X-band EPR spectrum of **5** collected on a 15 mM solution in Et₂O at 15 K. Microwave frequency: 9.63 GHz, microwave power: 0.2 mW, and $g_{\text{eff}} = 5.02, 4.05, \text{ and } 2.17$.

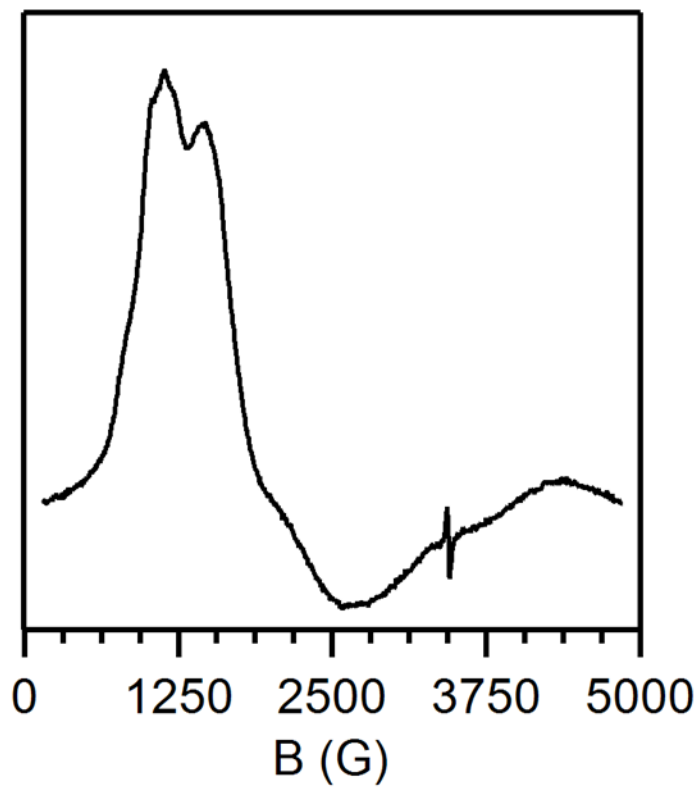


Figure A2.26 The X-band EPR spectrum of **6** collected on a 9 mM solution in CDCl₃ at 15 K. Microwave frequency: 9.63 GHz, microwave power: 4.0 mW, and $g_{\text{eff}} = 5.66, 3.28,$ and 2.15. Asterisk indicates an unknown $S = \frac{1}{2}$ impurity.

A2.1.5 Mass Spectra

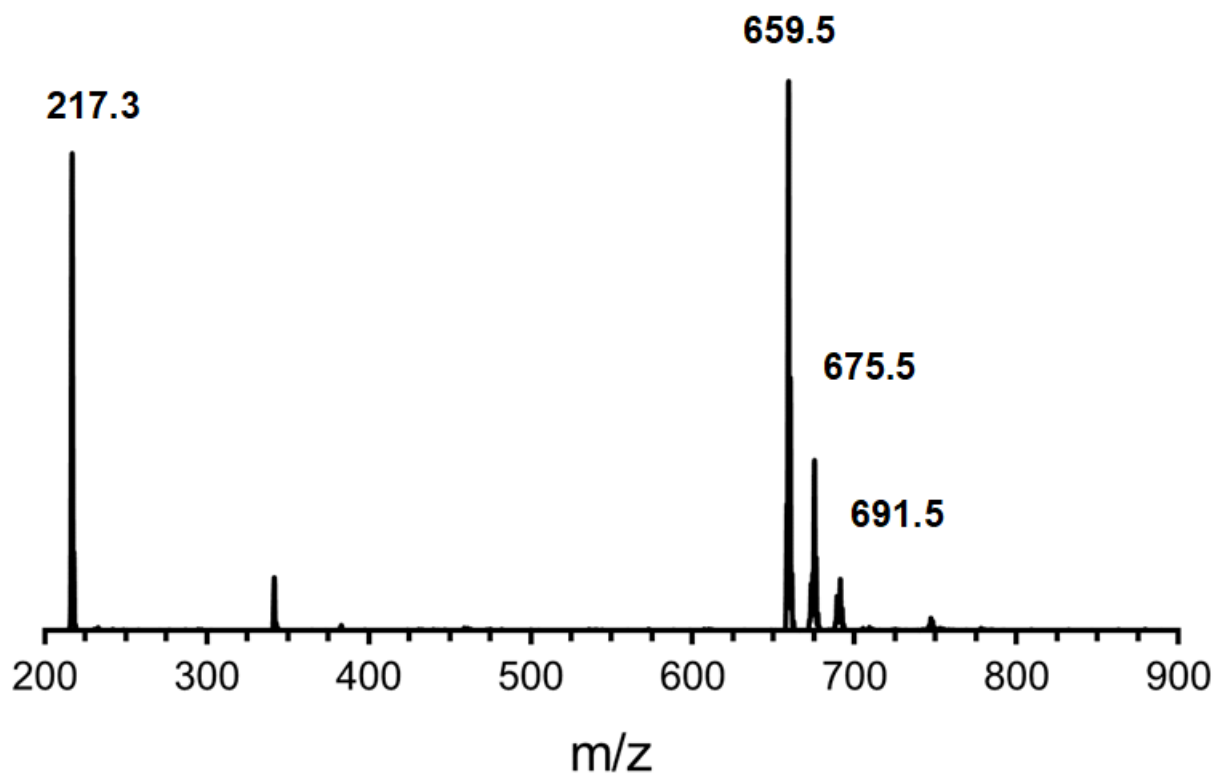


Figure A2.27 The MS data for the self-decay of **1** (2.5 mM in Et₂O) after 24 h showing free pyrazole (m/z 217.3, [pz^{Ad,Me}H]⁺), ligand (m/z 659.5, [H₂Tp^{Ad,Me}]⁺), single oxygen atom incorporation (m/z = 675.5, [H₂OTp^{Ad,Me}]⁺), and double oxygen atom incorporation (m/z = 691.5 [H₂O₂Tp^{Ad,Me}]⁺).

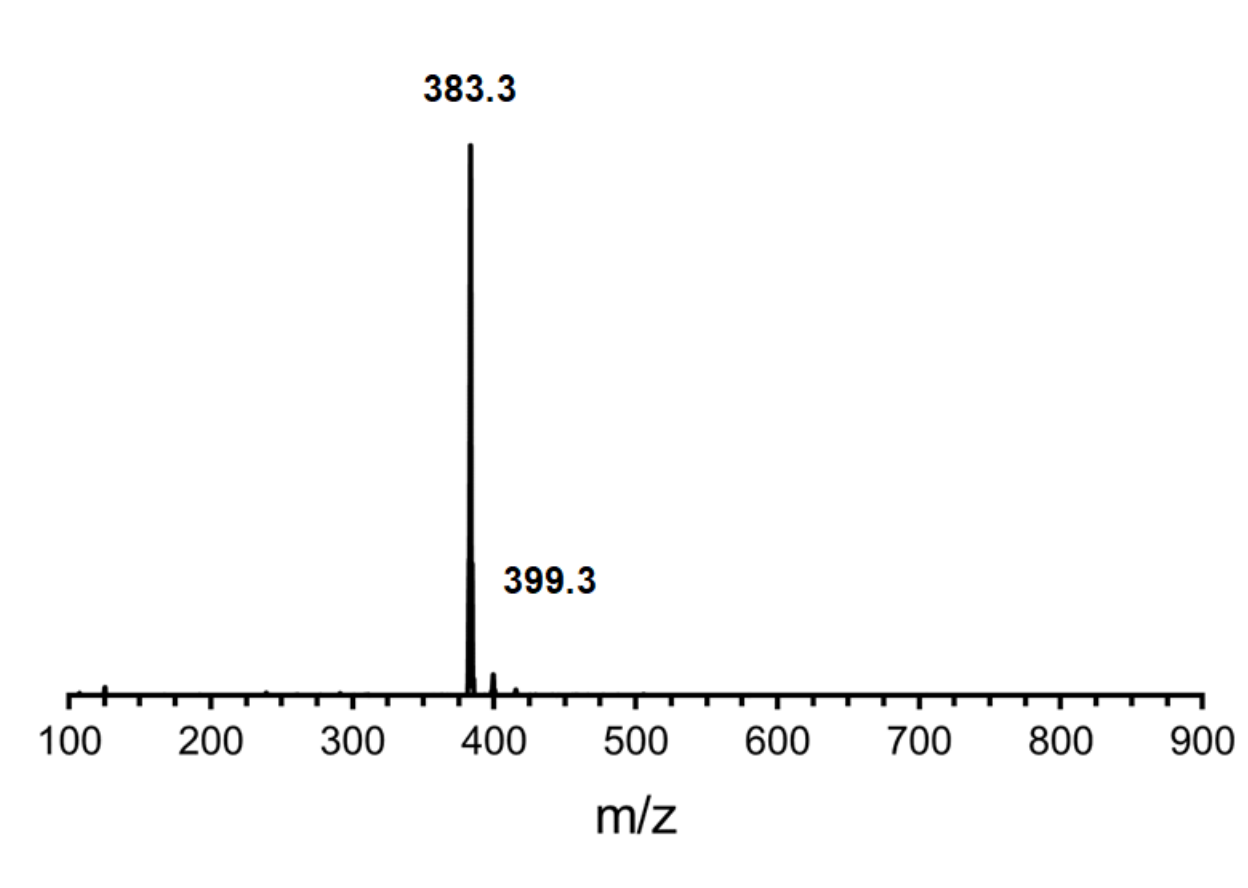


Figure A2.28 The MS data for the self-decay of **2** (isolated from the decay reaction in Et₂O, after a 1 M HCl_{aq} wash) after 24 h showing free ligand (m/z 383.3, [H₂Tp^{tBu}]⁺) and single oxygen-atom incorporation (m/z = 399.3, [H₂OTp^{tBu}]⁺).

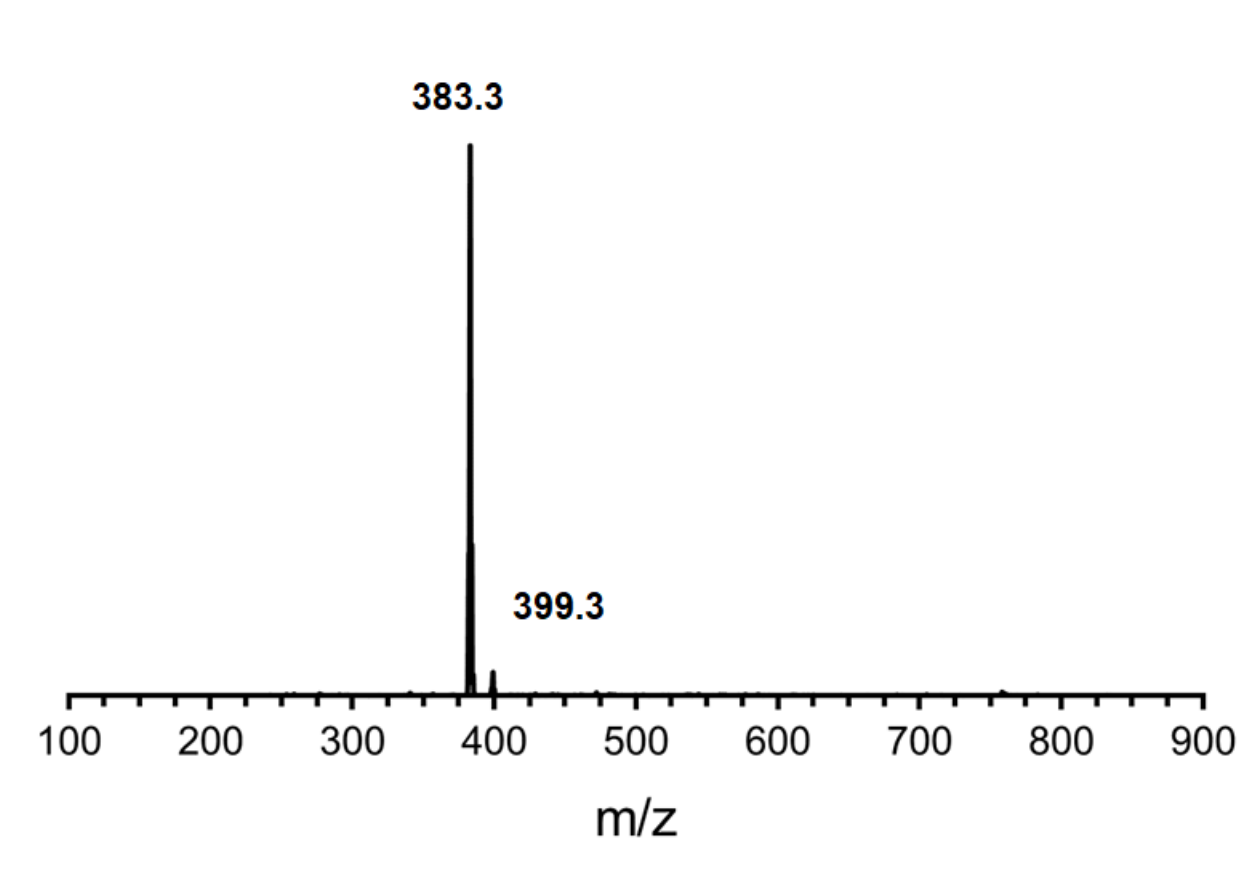


Figure A2.29 The MS data for the self-decay of **3** (2.5 mM in Et₂O) after 24 h showing free ligand (m/z 383.3, [H₂Tp^{tBu}]⁺) and single oxygen atom incorporation (m/z = 399.3, [H₂OTp^{tBu}]⁺).

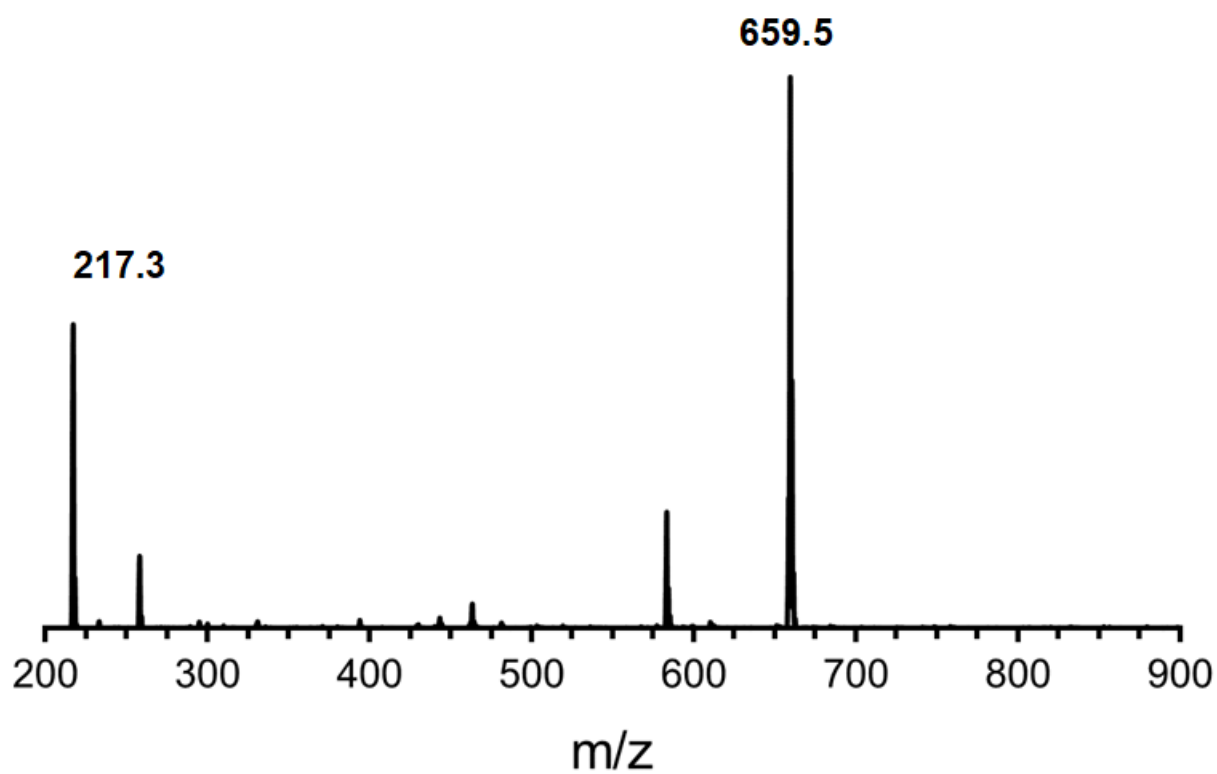


Figure A2.30 The MS data for the reaction of **1** with 10 equiv of Sc^{3+} ions showing free pyrazole (m/z 217.3 [$\text{pz}^{\text{Ad,Me}}]^+$) and ligand ($m/z = 659.5$, [$\text{H}_2\text{Tp}^{\text{Ad,Me}}]^+$).

A2.1.6 Electrochemistry

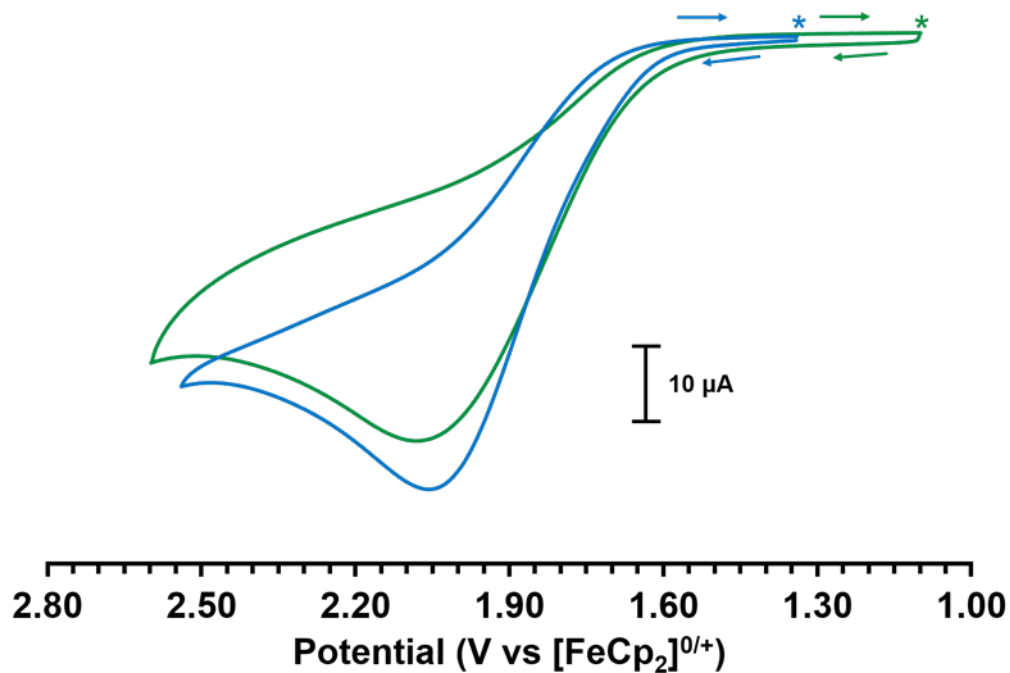


Figure A2.31 The cyclic voltammograms of **1** (green) and **2** (blue) showing irreversible oxidations at 2.07 and 2.05 V vs. [FeCp₂]^{0/+}. Conditions: 5 mM complex with 0.1 M [Bu₄N][PF₆] in DCM, scan rate 100 mV/s, glassy carbon working electrode with platinum wire counter electrode and silver wire as a pseudo-reference. Potentials referenced externally to the [FeCp₂]^{0/+}. Asterisks indicate starting potential and arrows indicate direction of sweep.

A2.2 Kinetic Experiments

A2.2.1 Kinetic Plots

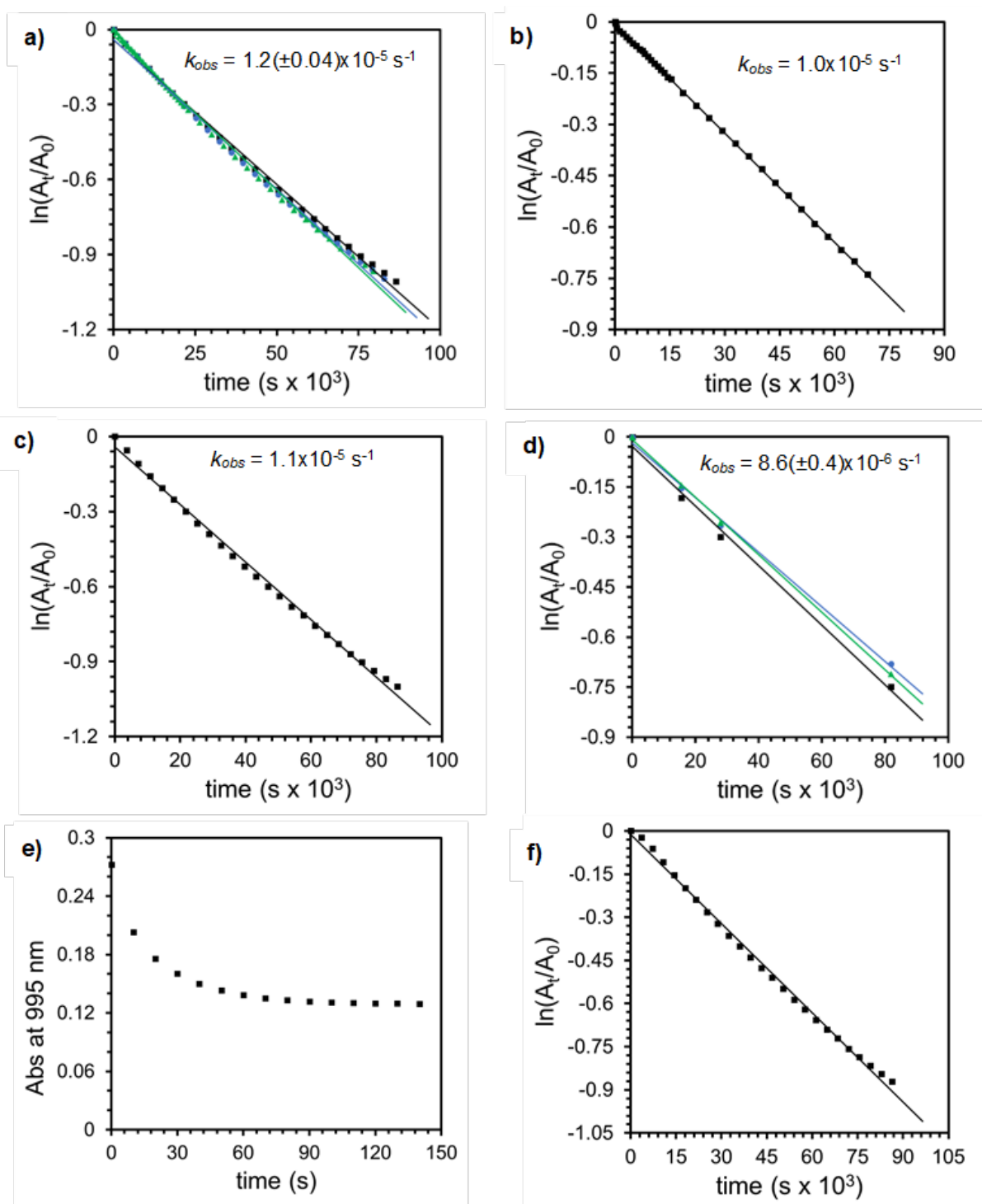


Figure A2.32 Kinetic data obtained for complex **1** (2.5 mM in Et₂O) a) of the self-decay, b) with 10 equiv of DHA, c) with 10 equiv thioanisole, d) 100 equiv of DHA, e) with 10 equiv PMe₃, and f) with 10 equiv ^sPhI. Experiments without errors were not collected in triplicate. Plot for the reaction of **1** with 10 equiv PMe₃ plotted as absorbance vs time as it did not follow pseudo-first order kinetics.

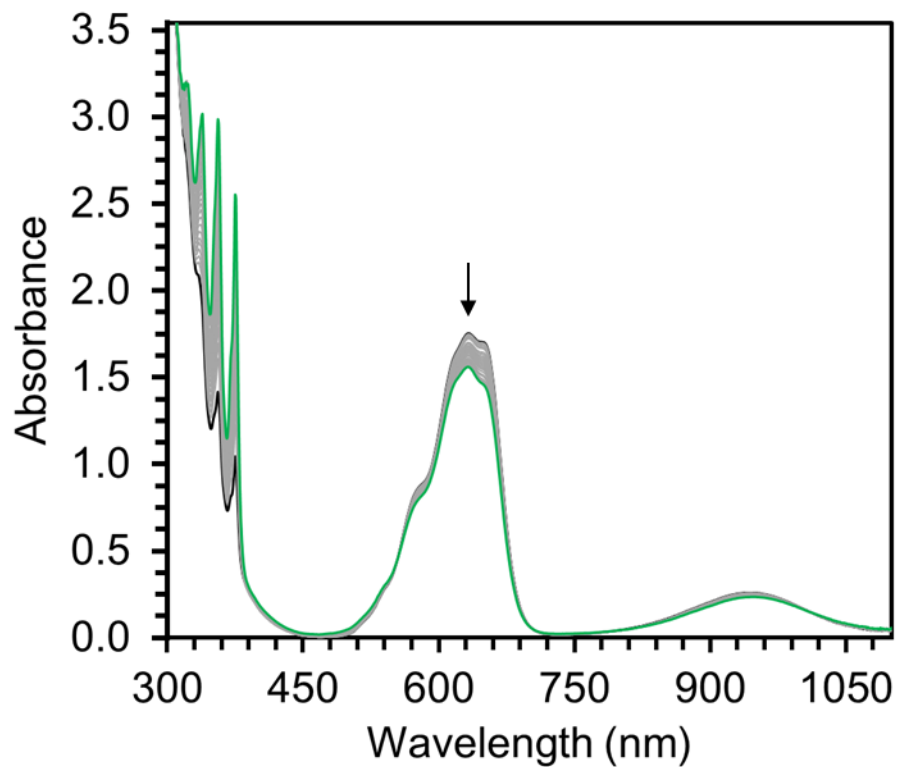


Figure A2.33 Representative plot of the decay of **2** (2.5 mM in Et₂O) in the presence of 100 equiv. of DHA showing both loss of **2** and growth of peaks corresponding to anthracene. Arrow indicates position of wavelength monitored for kinetics, asterisks indicate peaks for anthracene.

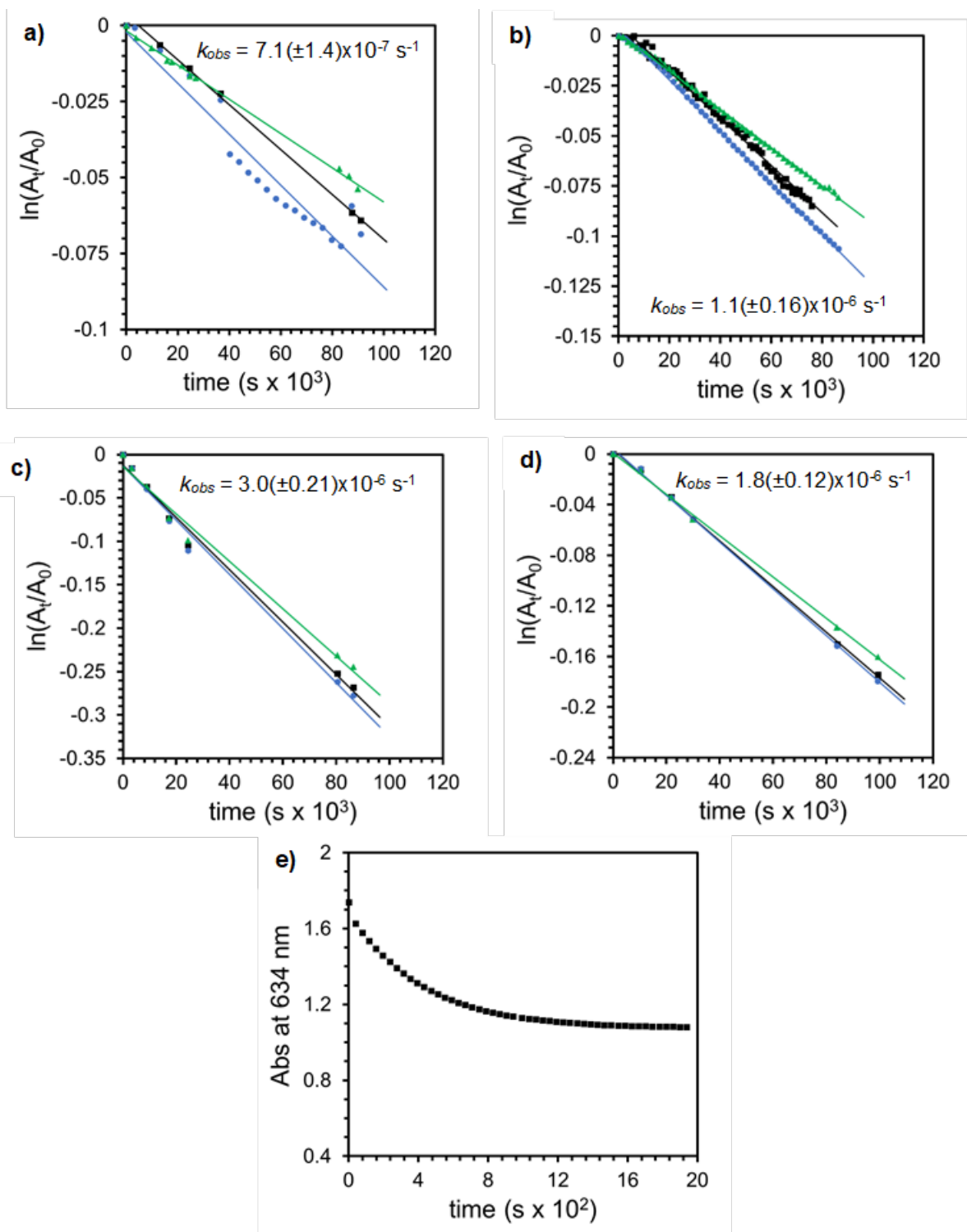


Figure A2.34 Kinetic data obtained for complex **2** (2.5 mM in Et₂O) a) of the self-decay, b) with 10 equiv of thioanisole, c) with 10 equiv thioanisole and 20 equiv of ⁵PhI, d) with 20 equiv ⁵PhI, and e) with 10 equiv PPh₃. Reaction of **2** with 10 equiv PPh₃ plotted as absorbance vs time as it did not follow pseudo-first order kinetics.

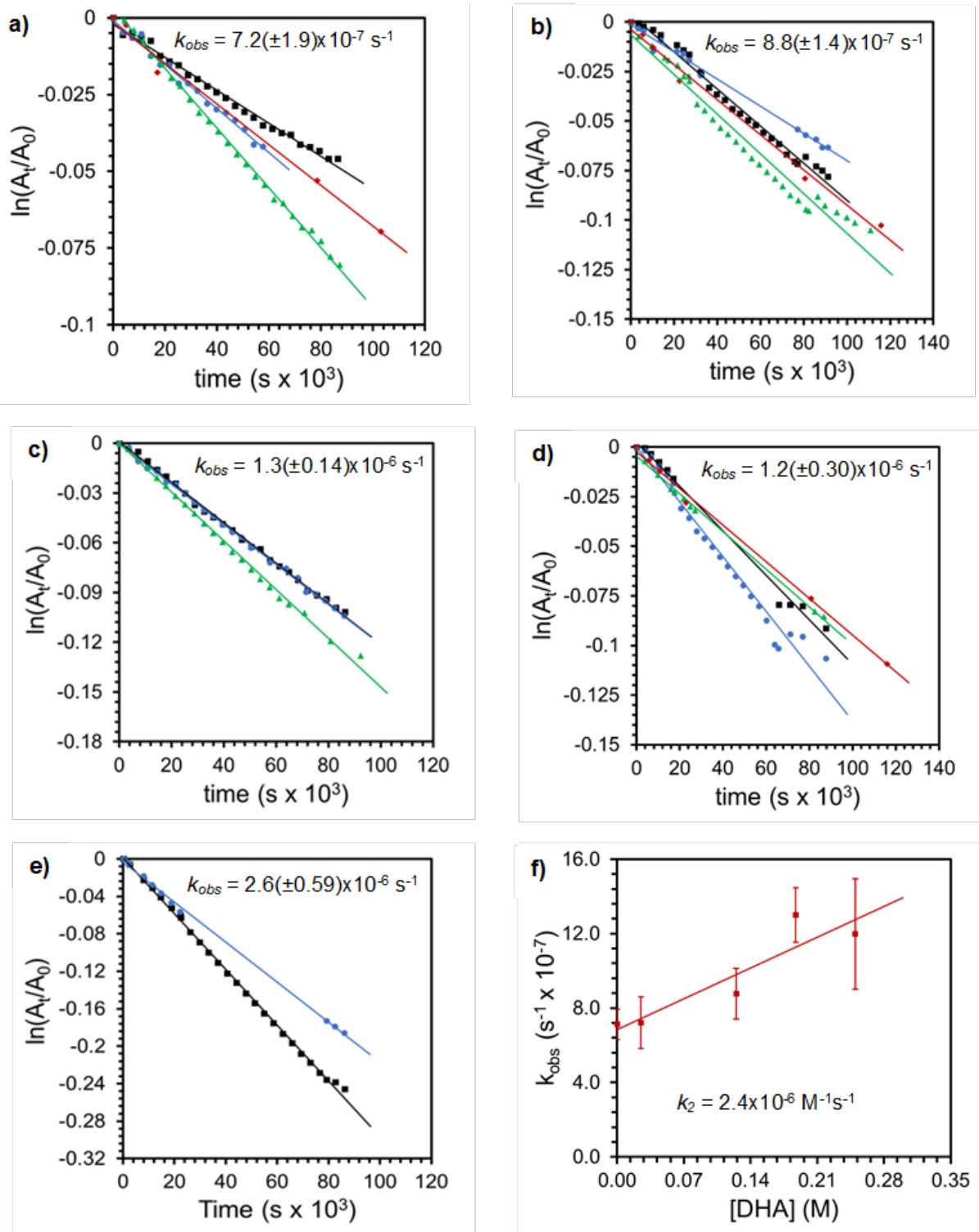


Figure A2.35 Kinetic data obtained for complex 2 (2.5 mM in Et₂O) a) with 10 equiv DHA, b) with 50 equiv DHA, c) with 75 equiv DHA, d) with 100 equiv of DHA, and e) with 50 equiv DHA and 20 equiv of ^sPhI. f) Plot of k_{obs} vs [DHA] to determine the second order rate constant, k_2 .

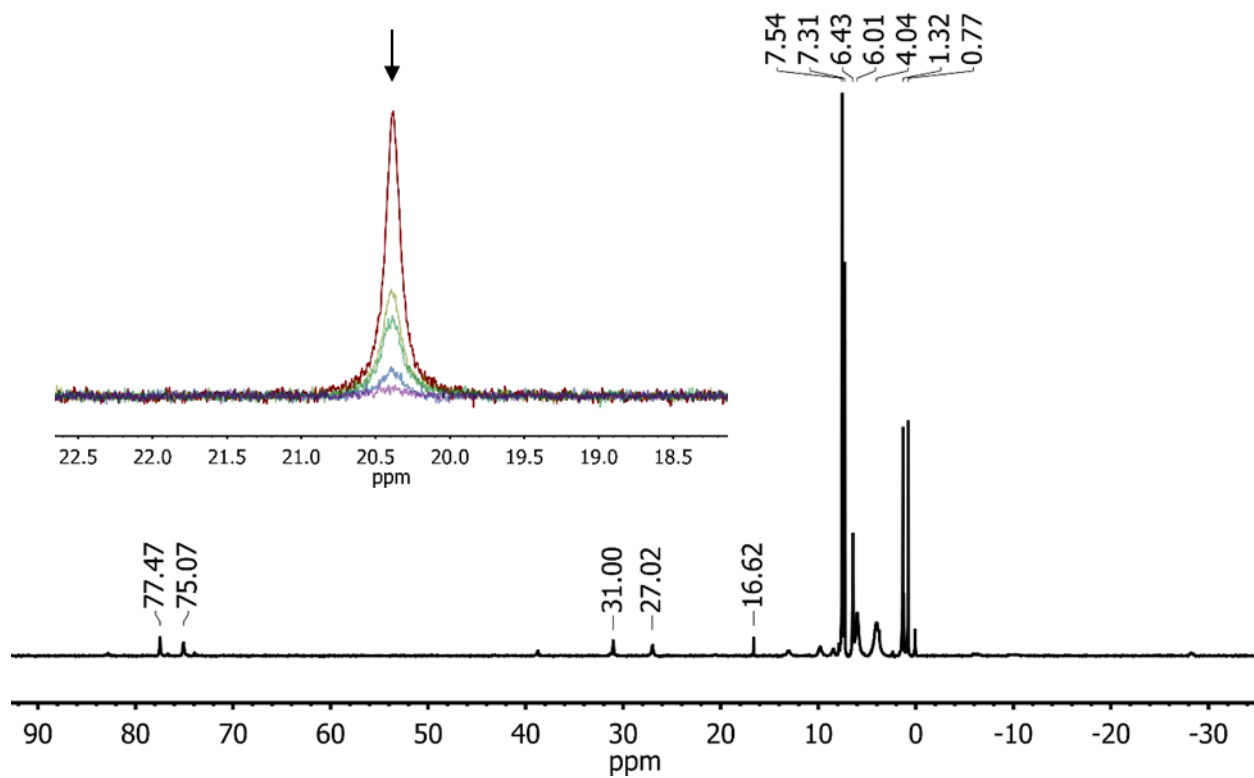


Figure A2.36 The ^1H NMR spectrum of the decay of **3** in CDCl_3 after 32 h at room temperature. Inset: overlay of the change in intensity of the 20.4 ppm resonance over time used to calculate k_{obs} .

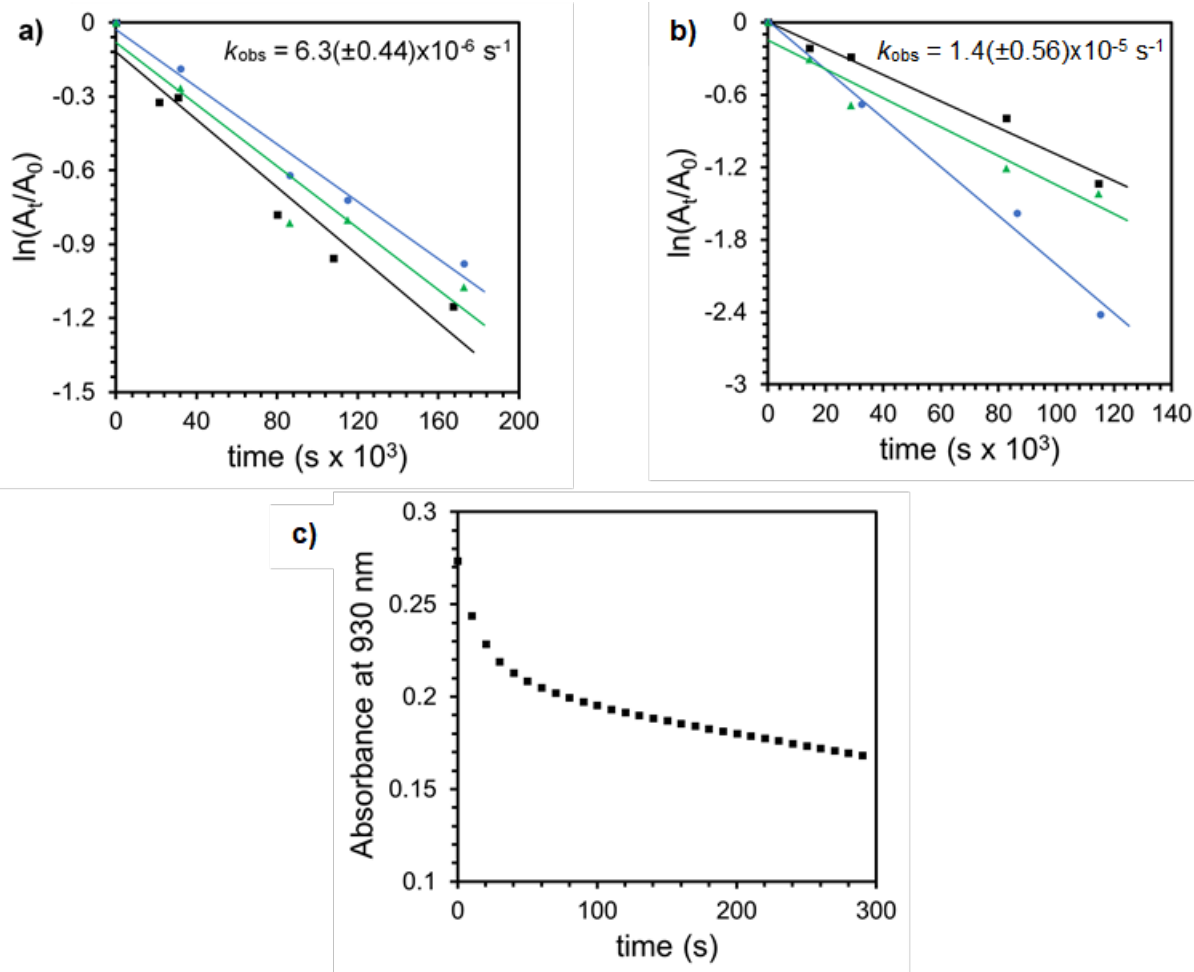


Figure A2.37 Kinetic data obtained for complex **3** (2.5 mM in CDCl₃, monitoring the area of the 20.4 ppm resonance) a) for the self-decay, b) with 10 equiv. thioanisole, and c) with 10 equiv. PPh₃ (2.5 mM Co complex in Et₂O). Plot of the reaction of **3** with 10 equiv. PPh₃ shown as absorbance vs time as it did not fit pseudo-first order kinetics.

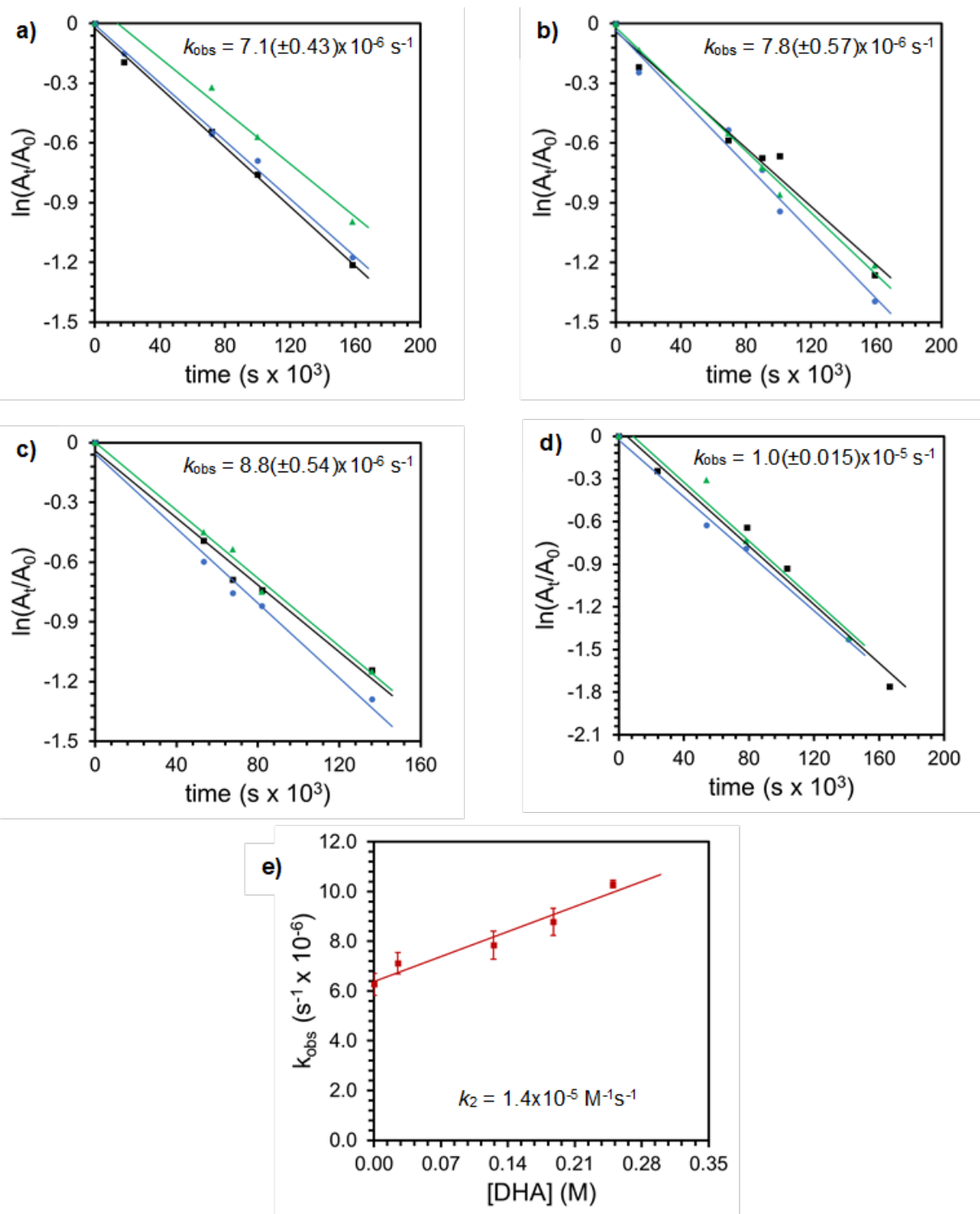


Figure A2.38 Kinetic data obtained for complex 3 (2.5 mM in CDCl_3 , monitoring the area of the 20.4 ppm resonance) a) with 10 equiv DHA, b) with 50 equiv DHA, c) with 75 equiv DHA, and d) with 100 equiv of DHA and e) plot of k_{obs} vs [DHA] to determine the second order rate constant, k_2 .

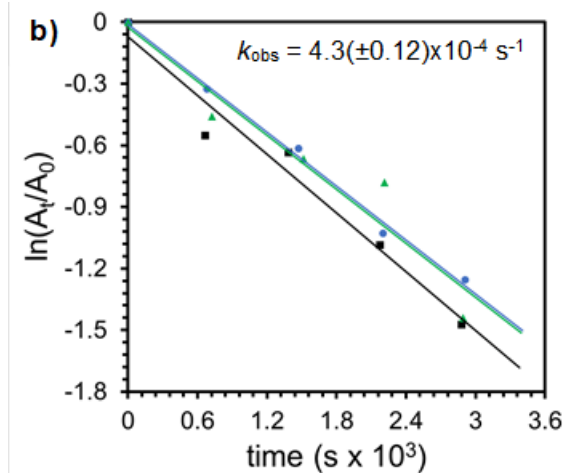
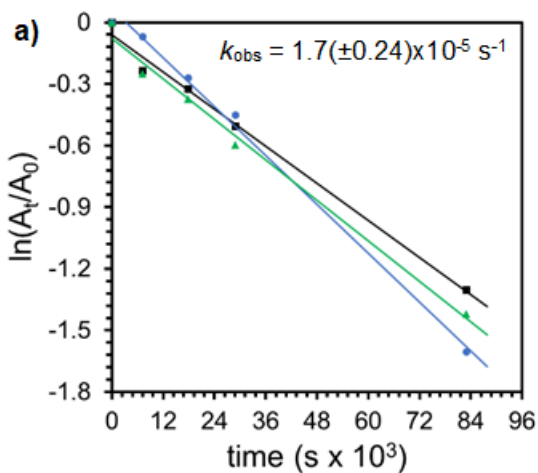


Figure A2.39 Kinetic data obtained for the background reaction of $^s\text{PhIO}$ (2.5 mM in CDCl_3 , monitoring the area of the 8.0 ppm resonance for loss of $^s\text{PhIO}$) a) with 50 equiv DHA and b) with 10 equiv thioanisole.

A2.2.2 Kinetic Isotope Effect

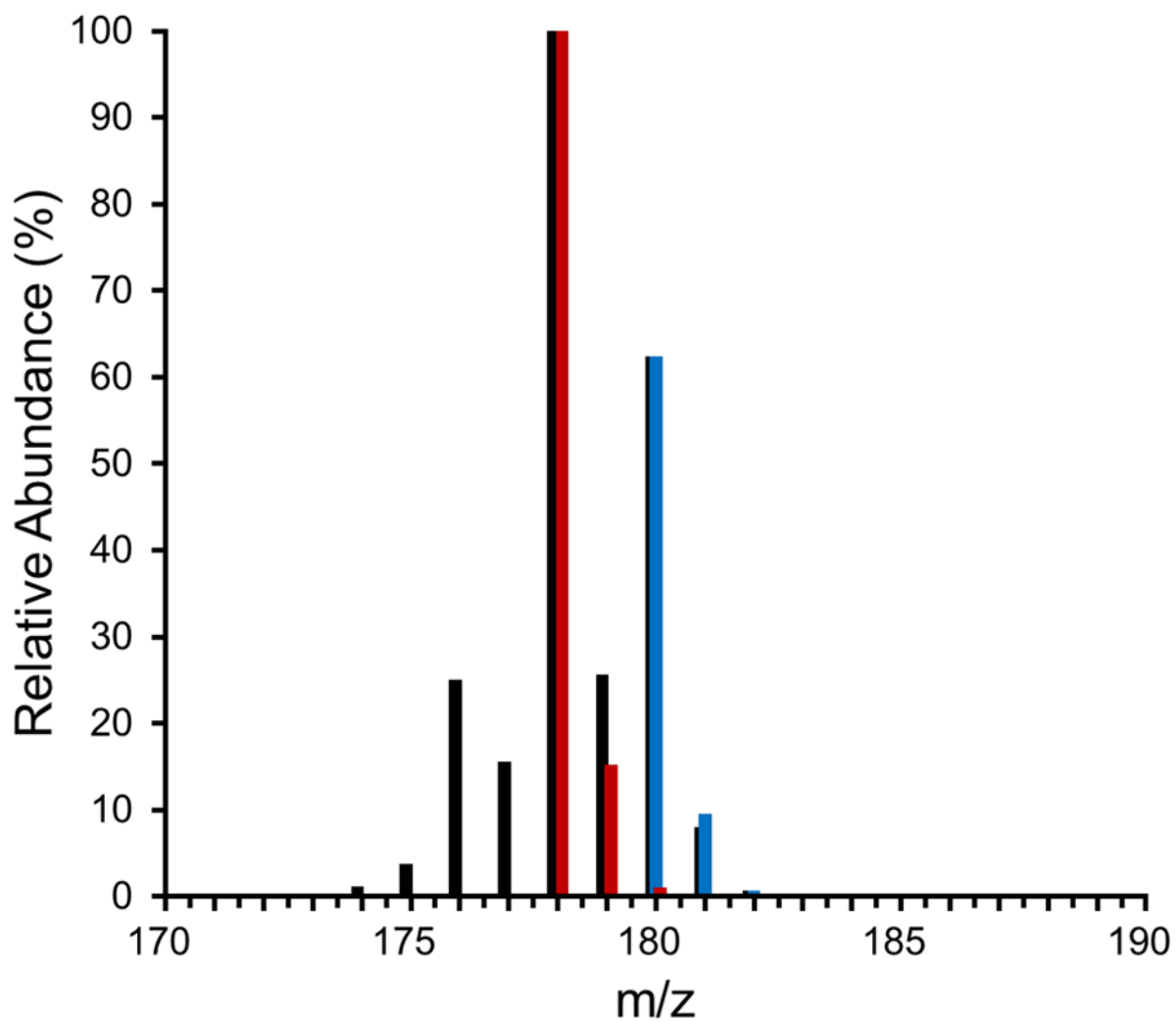


Figure A2.40 A representative MS trace for determination of the KIE from the reaction of **1** with a 1:1 molar ratio of H₄-DHA:D₄-DHA in DCM at 25 °C. Black bars are experimental data, red bars are isotope modeling of anthracene, and blue bars are isotope modeling of D₂-anthracene.

sample	Total [anthracene] mM	[anthracene] detected mM		[anthracene] Increase mM		KIE	average KIE
		proteo	deutero	proteo	deutero		
1:1 mix							
trial 1	0.0087	0.0024	0.0063	N/A	N/A		
trial 2	0.0100	0.0027	0.0073	N/A	N/A		
trial 3	0.0103	0.0029	0.0074	N/A	N/A		
1							
Trial 1	0.0152	0.0094	0.0059	0.0069	-0.0004	-	
Trial 2	0.0164	0.0100	0.0064	0.0074	-0.0009	-	
Trial 3	0.0160	0.0098	0.0062	0.0069	-0.0012	-	-
2							
Trial 1	0.0259	0.0188	0.0071	0.0164	0.0008	20.0	
Trial 2	0.0318	0.0231	0.0088	0.0204	0.0015	13.7	
Trial 3	0.0365	0.0266	0.0099	0.0237	0.0025	9.5	14(±5)
3							
Trial 1	0.0253	0.0174	0.0079	0.0150	0.0016	9.4	
Trial 2	0.0304	0.0213	0.0091	0.0187	0.0018	10.3	
Trial 3	0.0332	0.0231	0.0100	0.0203	0.0026	7.8	9(±1)
^sPhIO							
Trial 1	0.0107	0.0042	0.0066	0.0017	0.0003	5.8	
Trial 2	0.0119	0.0046	0.0073	0.0019	0.0000	-	
Trial 3	0.0122	0.0048	0.0075	0.0019	0.0000	-	-

Table A2.1 Raw data and KIE values determined for the reactions of **1**, **2**, **3**, and ^sPhIO with a 250 mM 1:1 mixture of H₄-DHA:D₄-DHA in DCM.

sample	Total [anthracene] mM	[anthracene] mM		[anthracene] Increase mM		KIE	average KIE
		proteo	deutero	proteo	deutero		
1:1 mix							
trial 1	0.0087	0.0024	0.0063	N/A	N/A		
trial 2	0.0100	0.0027	0.0073	N/A	N/A		
trial 3	0.0103	0.0029	0.0074	N/A	N/A		
1							
Trial 1	0.0152	0.0094	0.0059	0.0069	0.0006	>11.6	
Trial 2	0.0164	0.0100	0.0064	0.0074	0.0006	>12.3	
Trial 3	0.0160	0.0098	0.0062	0.0069	0.0006	>11.5	>12
2							
Trial 1	0.0259	0.0188	0.0071	0.0164	0.0008	20.0	
Trial 2	0.0318	0.0231	0.0088	0.0204	0.0015	13.7	
Trial 3	0.0365	0.0266	0.0099	0.0237	0.0025	9.5	14(±5)
3							
Trial 1	0.0253	0.0174	0.0079	0.0150	0.0016	9.4	
Trial 2	0.0304	0.0213	0.0091	0.0187	0.0018	10.3	
Trial 3	0.0332	0.0231	0.0100	0.0203	0.0026	7.8	9(±1)
^sPhIO							
Trial 1	0.0107	0.0042	0.0066	0.0017	0.0006	>2.9	
Trial 2	0.0119	0.0046	0.0073	0.0019	0.0006	>3.2	
Trial 3	0.0122	0.0048	0.0075	0.0019	0.0006	>3.2	>3

Table A2.2 KIE values determined for the reactions of **1**, **2**, **3**, and ^sPhIO with DHA using a minimum detectable value to replace increases in D₂-anthracene that are smaller than the standard deviation from the 1:1 mix. The average concentration of D₂-anthracene in the 1:1 mix is 0.007(±0.0006) mM. Shown in red are cases where the standard deviation of 0.0006 mM was used as the maximum amount of D₂-anthracene that could be produced but not measured above error. Using this maximum value provides a lower bound for the KIE.

sample	Total [anthracene] mM	[anthracene] mM		[anthracene] Increase mM		KIE	average KIE
		proteo	deutero	proteo	deutero		
1:1 mix		proteo	deutero	proteo	deutero		
trial 1	0.0385	0.0150	0.0236	N/A	N/A		
trial 2	0.0376	0.0140	0.0236	N/A	N/A		
trial 3	0.0415	0.0154	0.0260	N/A	N/A		
^sPhIO + Sc³⁺							
Trial 1	0.142	0.120	.0215	0.106	-0.0021	-	
Trial 2	0.111	0.0942	0.0170	0.0802	-0.0065	-	
Trail 3	0.136	0.115	0.0206	0.0999	-0.0055	-	-
^sPhIO + Na⁺							
Trial 1	0.0505	0.0310	0.0195	0.0160	-0.0041	-	
Trial 2	0.0458	0.0282	0.0175	0.0142	-0.0060	-	
Trial 3	0.0506	0.0313	0.0193	0.0159	-0.0068	-	-

Table A2.3 Raw GCMS data for the reactions of ^sPhIO in the presence of Lewis acids with DHA for KIE calculations. Conditions: 2.5 mM ^sPhIO, 2.5 mM Lewis acid, and 250 mM of 1:1 H₄-DHA:D₄-DHA mixture in DCM, left to stir for 65 h at room temperature.

sample	Total [anthracene] mM	[anthracene] mM		[anthracene] Increase mM		KIE	average KIE
		proteo	deutero	proteo	deutero		
1:1 mix		proteo	deutero	proteo	deutero		
trial 1	0.0385	0.0150	0.0236	N/A	N/A		
trial 2	0.0376	0.0140	0.0236	N/A	N/A		
trial 3	0.0415	0.0154	0.0260	N/A	N/A		
^sPhIO + Sc³⁺							
Trial 1	0.142	0.120	.0215	0.106	0.0014	74	
Trial 2	0.111	0.0942	0.0170	0.0802	0.0014	56	
Trail 3	0.136	0.115	0.0206	0.0999	0.0014	70	>66
^sPhIO + Na⁺							
Trial 1	0.0505	0.0310	0.0195	0.0160	0.0014	11	
Trial 2	0.0458	0.0282	0.0175	0.0142	0.0014	10	
Trial 3	0.0506	0.0313	0.0193	0.0159	0.0014	11	>11

Table A2.4 KIE values determined for the reactions of ^sPhIO with DHA in the presence of Lewis acids using a minimum detectable value to replace increases in D₂-anthracene that are smaller than the standard deviation from the 1:1 mix. The average concentration of D₂-anthracene in the 1:1 mix is 0.024(±0.0014) mM. Shown in red are cases where the standard deviation of 0.0014 mM was used as the maximum amount of D₂-anthracene that could be produced but not measured above error. Using this maximum value provides a lower bound for the KIE.

A2.3 X-Ray Crystallography

A2.3.1 Structures

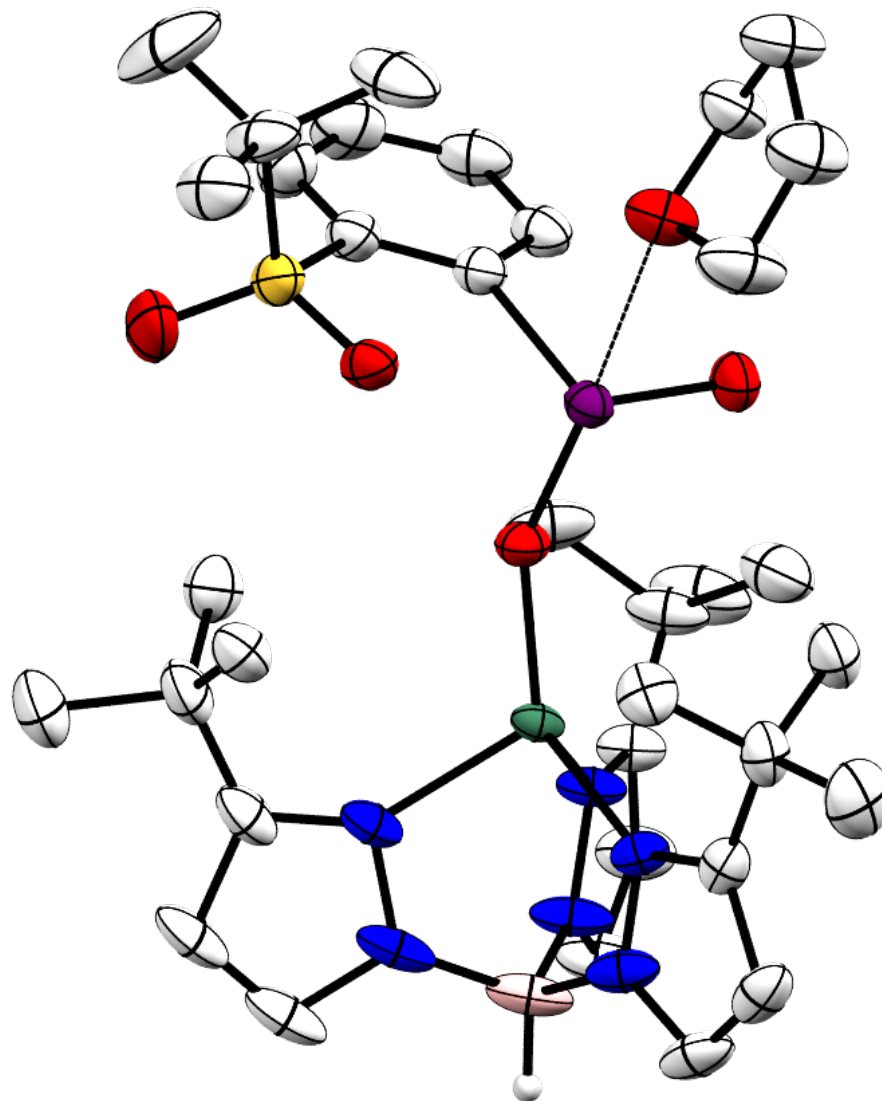


Figure A2.41 Structure of **3** showing the secondary interaction of a THF molecule with the iodine center of the bound ${}^8\text{PhIO}_2$ ligand. The I1-O5 distance is 2.558(4) Å. Thermal ellipsoids shown at 50% probability and counter anion, other solvent, and H-atoms other than B-H omitted for clarity.

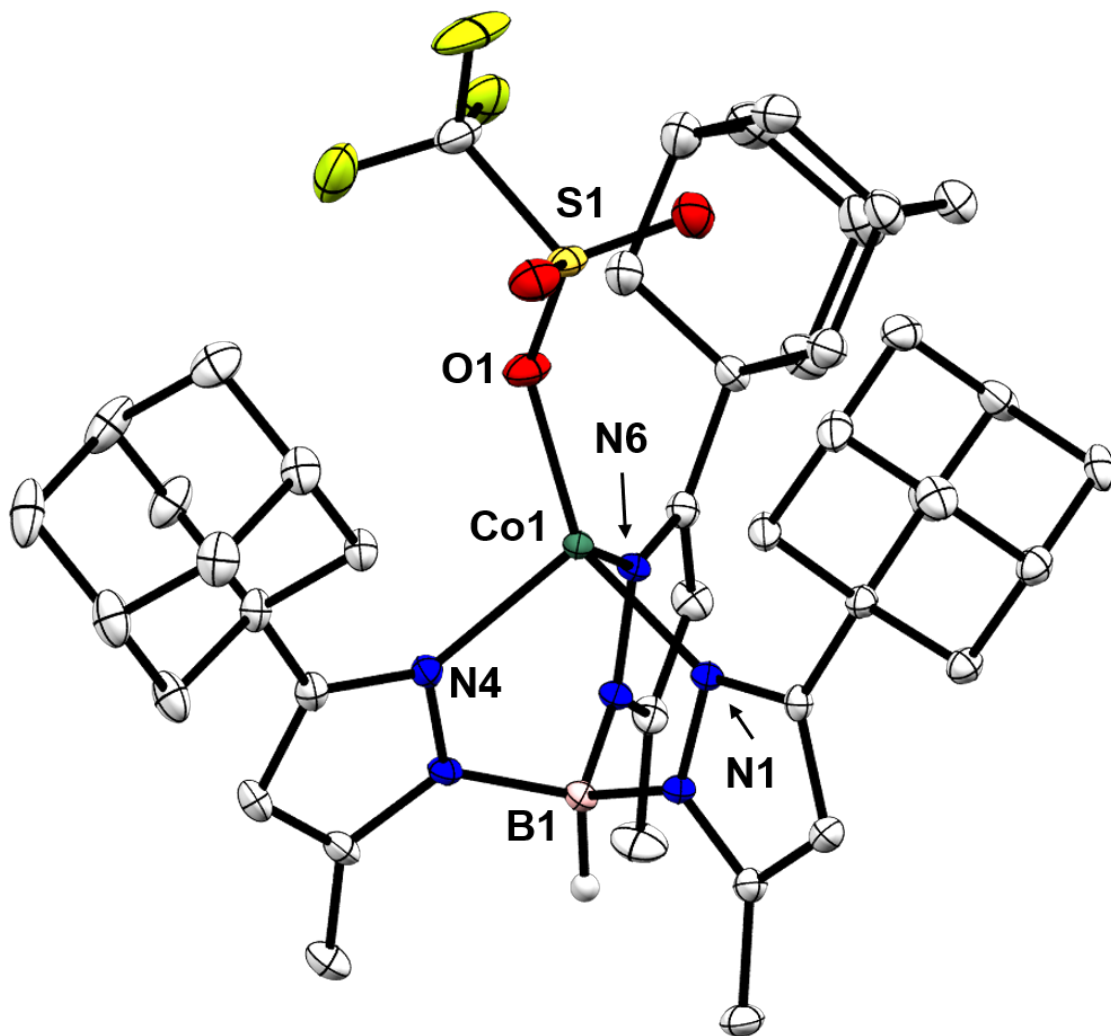


Figure A2.42 Depiction of the molecular structure of **4** determined by X-ray diffraction. Only one of the independent molecules is shown. Thermal ellipsoids shown at 50% probability. H-atoms other than B-H have been omitted for clarity.

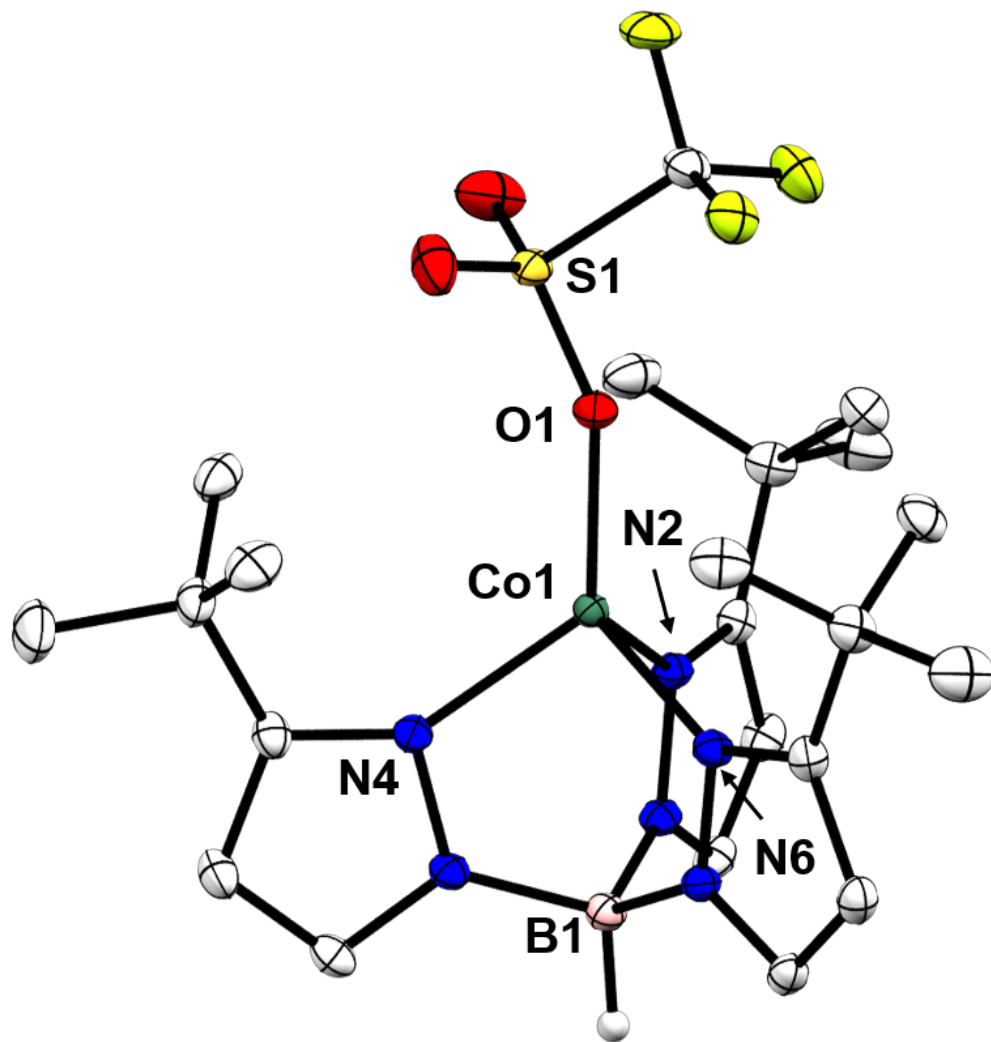


Figure A2.43 Depiction of the molecular structure of **5** determined by X-ray diffraction. Thermal ellipsoids shown at 50% probability. H-atoms other than B-H and a Et₂O molecule have been omitted for clarity.

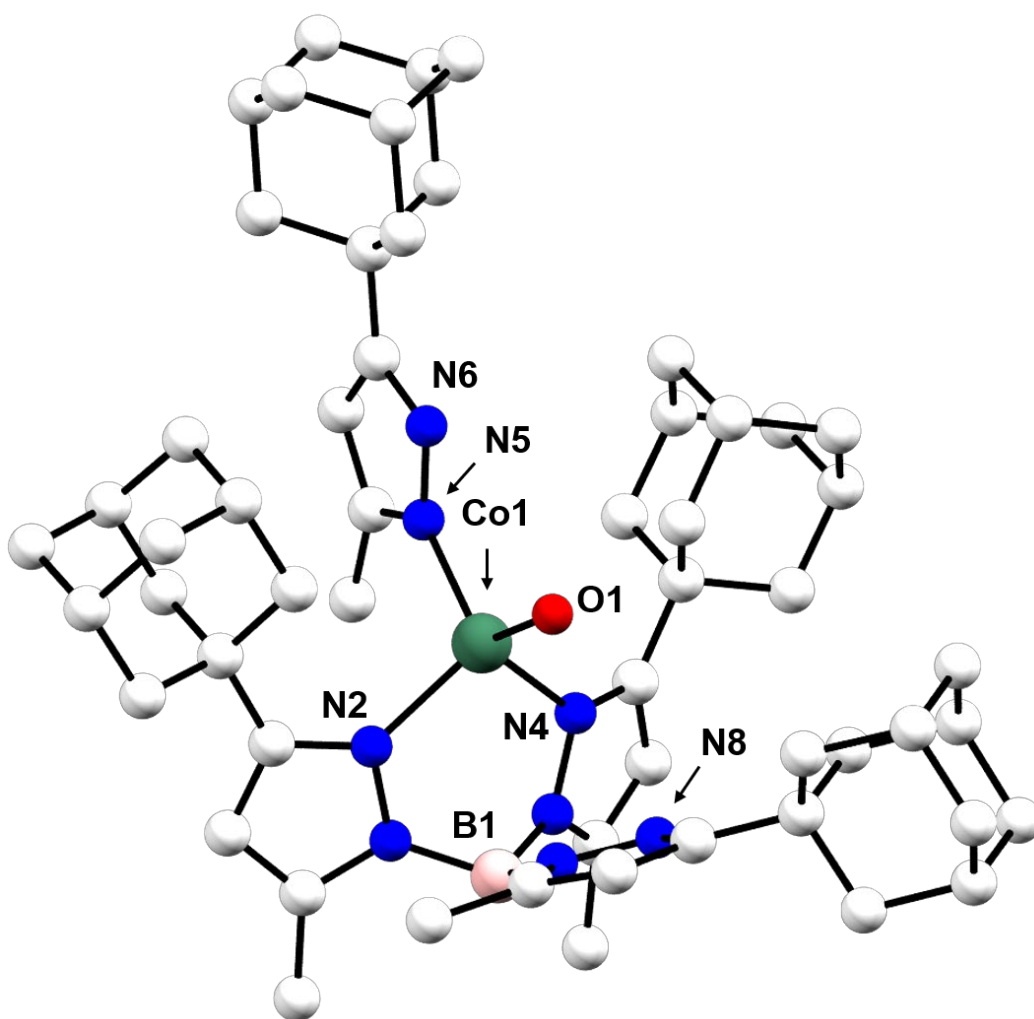


Figure A2.44 Depiction of the molecular structure of **6** determined by X-ray diffraction. Shown as ball and stick model for connectivity only. Atom labeled O1 is from coordinated OTf. The H-atoms, disordered Et₂O solvent molecule, and BAR^F₄ counter ion omitted for clarity.

A2.3.2 Metrical Parameters

Complex:	1	2	3	4	5	6
Bond Length (Å)						
Co1-N _{avg}	2.037	2.032	2.026	2.038	2.016	2.027
Co1-O1	1.920(6)	1.934(3)	1.925(3)	1.955(1)	1.948(1)	1.994(2)
I1-O1	1.878(6)	1.891(3)	1.814(3)	N/A	N/A	N/A
I1-O4	N/A	N/A	1.780(3)	N/A	N/A	N/A
Angle (°)						
B1-Co1-O1	160.4(3)	171.6(1)	173.7(1)	161.11(5)	175.59(4)	107.1(2)

Table A2.5 Selected bond distances and angles for the Co complexes reported.

A2.3.3 Refinement Details

Table S6. Crystal data and structure refinement for 1.

Identification code	1
Empirical formula	C ₁₆₉ H ₁₆₈ B ₄ Cl ₂ Co ₂ F ₄₈ I ₂ N ₁₂ O ₆ S ₂
Formula weight	3925.06
Temperature/K	100(2)
Crystal system	triclinic
Space group	P-1
a/Å	14.2995(9)
b/Å	16.0821(11)
c/Å	38.551(3)
α/°	95.079(2)
β/°	97.357(2)
γ/°	97.863(2)
Volume/Å ³	8658.9(10)
Z	2
ρ _{calc} /cm ³	1.505
μ/mm ⁻¹	0.713
F(000)	3984.0
Crystal size/mm ³	0.33 × 0.24 × 0.12
Radiation	MoKα (λ = 0.71073)
2θ range for data collection/°	4.328 to 50.14
Index ranges	-15 ≤ h ≤ 16, -19 ≤ k ≤ 18, -45 ≤ l ≤ 45
Reflections collected	86794
Independent reflections	29336 [R _{int} = 0.1033, R _{sigma} = 0.1379]
Data/restraints/parameters	29336/363/2310
Goodness-of-fit on F ²	1.068
Final R indexes [I ≥ 2σ (I)]	R ₁ = 0.0887, wR ₂ = 0.1610
Final R indexes [all data]	R ₁ = 0.1561, wR ₂ = 0.1833
Largest diff. peak/hole / e Å ⁻³	1.26/-0.94

Table A2.6 Crystal data and structure refinement for 1.

$$R_{\text{int}} = \frac{\sum |F_o^2 - \langle F_o^2 \rangle|}{\sum |F_o^2|}$$

$$R1 = \frac{\sum ||F_o| - |F_c||}{\sum |F_o|}$$

$$wR2 = \left[\frac{\sum [w (F_o^2 - F_c^2)^2]}{\sum [w (F_o^2)^2]} \right]^{1/2}$$

$$\text{Goodness-of-fit} = \left[\frac{\sum [w (F_o^2 - F_c^2)^2]}{(n-p)} \right]^{1/2}$$

n: number of independent reflections; p: number of refined parameters

Table S7. Crystal data and structure refinement for 2.

Identification code	2
Empirical formula	C ₆₃ H ₅₉ B ₂ CoF ₂₄ IN ₆ O ₃ S
Formula weight	1643.67
Temperature/K	100(2)
Crystal system	triclinic
Space group	P1
a/Å	10.4248(7)
b/Å	12.9027(9)
c/Å	15.4799(11)
α/°	101.302(2)
β/°	105.089(2)
γ/°	113.446(2)
Volume/Å ³	1735.7(2)
Z	1
ρ _{calc} /cm ³	1.572
μ/mm ⁻¹	0.835
F(000)	825.0
Crystal size/mm ³	0.25 × 0.15 × 0.05
Radiation	MoKα (λ = 0.71073)
2θ range for data collection/°	4.308 to 55.12
Index ranges	-13 ≤ h ≤ 13, -16 ≤ k ≤ 16, -20 ≤ l ≤ 20
Reflections collected	49488
Independent reflections	15013 [R _{int} = 0.0272, R _{sigma} = 0.0384]
Data/restraints/parameters	15013/3/926
Goodness-of-fit on F ²	1.036
Final R indexes [I ≥ 2σ (I)]	R ₁ = 0.0256, wR ₂ = 0.0518
Final R indexes [all data]	R ₁ = 0.0290, wR ₂ = 0.0528
Largest diff. peak/hole / e Å ⁻³	0.60/-0.38
Flack parameter	-0.012(3)

Table A2.7 Crystal data and structure refinement for 2.

$$R_{\text{int}} = \frac{\sum |F_o^2 - \langle F_o^2 \rangle|}{\sum |F_o^2|}$$

$$R_1 = \frac{\sum ||F_o| - |F_c||}{\sum |F_o|}$$

$$wR_2 = \left[\frac{\sum [w (F_o^2 - F_c^2)^2]}{\sum [w (F_o^2)^2]} \right]^{1/2}$$

$$\text{Goodness-of-fit} = \left[\frac{\sum [w (F_o^2 - F_c^2)^2]}{(n-p)} \right]^{1/2}$$

n: number of independent reflections; p: number of refined parameters

Table S8. Crystal data and structure refinement for 3.

Identification code	3
Empirical formula	C ₇₁ H ₇₇ B ₂ CoF ₂₄ IN ₆ O ₆ S
Formula weight	1805.89
Temperature/K	100(2)
Crystal system	triclinic
Space group	P-1
a/Å	13.018(3)
b/Å	17.299(4)
c/Å	19.933(4)
α/°	69.338(4)
β/°	77.588(5)
γ/°	78.279(5)
Volume/Å ³	4062.0(14)
Z	2
ρ _{calc} /cm ³	1.477
μ/mm ⁻¹	0.178
F(000)	1830.0
Crystal size/mm ³	0.004 × 0.003 × 0.003
Radiation	synchrotron (λ = 0.41328)
2θ range for data collection/°	1.478 to 32.428
Index ranges	-17 ≤ h ≤ 17, -23 ≤ k ≤ 23, -26 ≤ l ≤ 26
Reflections collected	114410
Independent reflections	19783 [R _{int} = 0.0498, R _{sigma} = 0.0327]
Data/restraints/parameters	19783/136/1055
Goodness-of-fit on F ²	1.022
Final R indexes [I ≥ 2σ (I)]	R ₁ = 0.0624, wR ₂ = 0.1946
Final R indexes [all data]	R ₁ = 0.0670, wR ₂ = 0.1990
Largest diff. peak/hole / e Å ⁻³	2.23/-2.11

Table A2.8 Crystal data and structure refinement for 3.

$$R_{\text{int}} = \frac{\sum |F_o^2 - \langle F_o^2 \rangle|}{\sum |F_o^2|}$$

$$R_1 = \frac{\sum ||F_o| - |F_c||}{\sum |F_o|}$$

$$wR_2 = \left[\frac{\sum [w (F_o^2 - F_c^2)^2]}{\sum [w (F_o^2)^2]} \right]^{1/2}$$

$$\text{Goodness-of-fit} = \left[\frac{\sum [w (F_o^2 - F_c^2)^2]}{(n-p)} \right]^{1/2}$$

n: number of independent reflections; p: number of refined parameters

Table S9. Crystal data and structure refinement for 4.

Identification code	4
Empirical formula	C ₄₃ H ₅₈ BCoF ₃ N ₆ O ₃ S
Formula weight	865.75
Temperature/K	100(2)
Crystal system	triclinic
Space group	P-1
a/Å	11.3925(6)
b/Å	16.9868(8)
c/Å	21.7195(11)
α/°	94.871(2)
β/°	98.674(2)
γ/°	92.305(2)
Volume/Å ³	4134.1(4)
Z	4
ρ _{calc} /cm ³	1.391
μ/mm ⁻¹	0.527
F(000)	1828.0
Crystal size/mm ³	0.36 × 0.22 × 0.15
Radiation	MoKα (λ = 0.71073)
2θ range for data collection/°	4.242 to 56.798
Index ranges	-15 ≤ h ≤ 15, -22 ≤ k ≤ 22, -29 ≤ l ≤ 29
Reflections collected	183013
Independent reflections	20681 [R _{int} = 0.0466, R _{sigma} = 0.0279]
Data/restraints/parameters	20681/0/1057
Goodness-of-fit on F ²	1.030
Final R indexes [I ≥ 2σ (I)]	R ₁ = 0.0411, wR ₂ = 0.0979
Final R indexes [all data]	R ₁ = 0.0646, wR ₂ = 0.1106
Largest diff. peak/hole / e Å ⁻³	0.77/-0.43

Table A2.9 Crystal data and structure refinement for 4.

$$R_{\text{int}} = \frac{\sum |F_o^2 - \langle F_o^2 \rangle|}{\sum |F_o^2|}$$

$$R_1 = \frac{\sum ||F_o| - |F_c||}{\sum |F_o|}$$

$$wR_2 = \left[\frac{\sum [w (F_o^2 - F_c^2)^2]}{\sum [w (F_o^2)^2]} \right]^{1/2}$$

$$\text{Goodness-of-fit} = \left[\frac{\sum [w (F_o^2 - F_c^2)^2]}{(n-p)} \right]^{1/2}$$

n: number of independent reflections; p: number of refined parameters

Table S10. Crystal data and structure refinement for 5.

Identification code	5
Empirical formula	C ₂₆ H ₄₄ BCoF ₃ N ₆ O ₄ S
Formula weight	663.47
Temperature/K	100(2)
Crystal system	monoclinic
Space group	P2 ₁ /n
a/Å	10.4361(10)
b/Å	20.2414(18)
c/Å	15.3862(14)
α/°	90
β/°	91.209(3)
γ/°	90
Volume/Å ³	3249.5(5)
Z	4
ρ _{calc} /cm ³	1.356
μ/mm ⁻¹	0.650
F(000)	1396.0
Crystal size/mm ³	0.45 × 0.3 × 0.1
Radiation	MoKα (λ = 0.71073)
2θ range for data collection/°	4.392 to 55.17
Index ranges	-11 ≤ h ≤ 13, -26 ≤ k ≤ 26, -20 ≤ l ≤ 20
Reflections collected	100848
Independent reflections	7508 [R _{int} = 0.0403, R _{sigma} = 0.0171]
Data/restraints/parameters	7508/0/394
Goodness-of-fit on F ²	1.045
Final R indexes [I ≥ 2σ (I)]	R ₁ = 0.0277, wR ₂ = 0.0648
Final R indexes [all data]	R ₁ = 0.0337, wR ₂ = 0.0673
Largest diff. peak/hole / e Å ⁻³	0.44/-0.32

Table A2.10 Crystal data and structure refinement for 5.

$$R_{\text{int}} = \frac{\sum |F_o^2 - \langle F_o^2 \rangle|}{\sum |F_o^2|}$$

$$R_1 = \frac{\sum ||F_o| - |F_c||}{\sum |F_o|}$$

$$wR_2 = \left[\frac{\sum [w (F_o^2 - F_c^2)^2]}{\sum [w (F_o^2)^2]} \right]^{1/2}$$

$$\text{Goodness-of-fit} = \left[\frac{\sum [w (F_o^2 - F_c^2)^2]}{(n-p)} \right]^{1/2}$$

n: number of independent reflections; p: number of refined parameters

Table S11. Crystal data and structure refinement for 6.

Identification code	6
Empirical formula	C ₉₃ H ₁₀₀ B ₂ CoF ₂₇ N ₈ O ₄ S
Formula weight	2019.41
Temperature/K	100(2)
Crystal system	orthorhombic
Space group	Pbca
a/Å	21.4930(17)
b/Å	22.3378(19)
c/Å	38.715(3)
α/°	90
β/°	90
γ/°	90
Volume/Å ³	18587(3)
Z	8
ρ _{calc} /cm ³	1.443
μ/mm ⁻¹	0.317
F(000)	8336.0
Crystal size/mm ³	0.35 × 0.15 × 0.1
Radiation	MoKα (λ = 0.71073)
2θ range for data collection/°	4.206 to 49.632
Index ranges	-25 ≤ h ≤ 25, -26 ≤ k ≤ 26, -45 ≤ l ≤ 45
Reflections collected	251224
Independent reflections	16006 [R _{int} = 0.1273, R _{sigma} = 0.0598]
Data/restraints/parameters	16006/58/1213
Goodness-of-fit on F ²	1.023
Final R indexes [I ≥ 2σ (I)]	R ₁ = 0.1073, wR ₂ = 0.2609
Final R indexes [all data]	R ₁ = 0.1568, wR ₂ = 0.2964
Largest diff. peak/hole / e Å ⁻³	2.92/-2.37

Table A2.11 Crystal data and structure refinement for 6.

$$R_{\text{int}} = \frac{\sum |F_o^2 - \langle F_o^2 \rangle|}{\sum |F_o^2|}$$

$$R_1 = \frac{\sum ||F_o| - |F_c||}{\sum |F_o|}$$

$$wR_2 = \left[\frac{\sum [w (F_o^2 - F_c^2)^2]}{\sum [w (F_o^2)^2]} \right]^{1/2}$$

$$\text{Goodness-of-fit} = \left[\frac{\sum [w (F_o^2 - F_c^2)^2]}{(n-p)} \right]^{1/2}$$

n: number of independent reflections; p: number of refined parameters

Appendix 3: Supporting Data for Chapter 3

A3.1 NMR Characterization Data

A3.1.1 PPh₂CH₂BF₃K (K1)

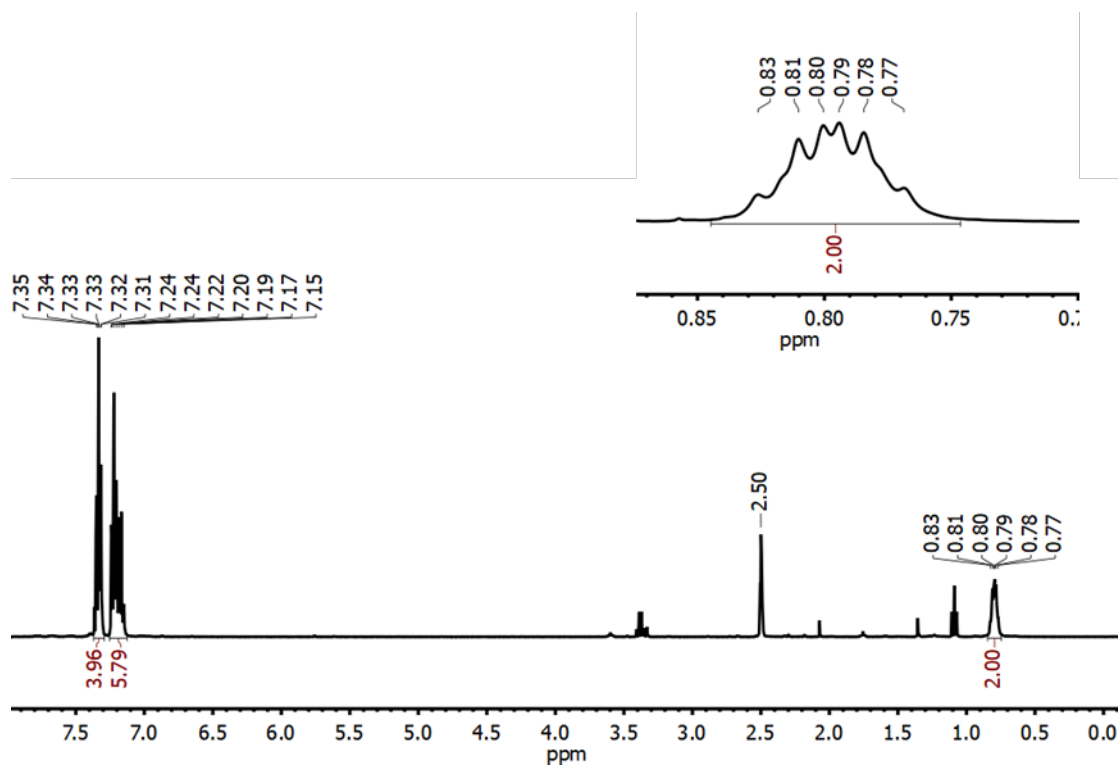


Figure A3.1 ¹H NMR spectrum of K1 in DMSO-*d*₆ with inset showing CH₂ peak.

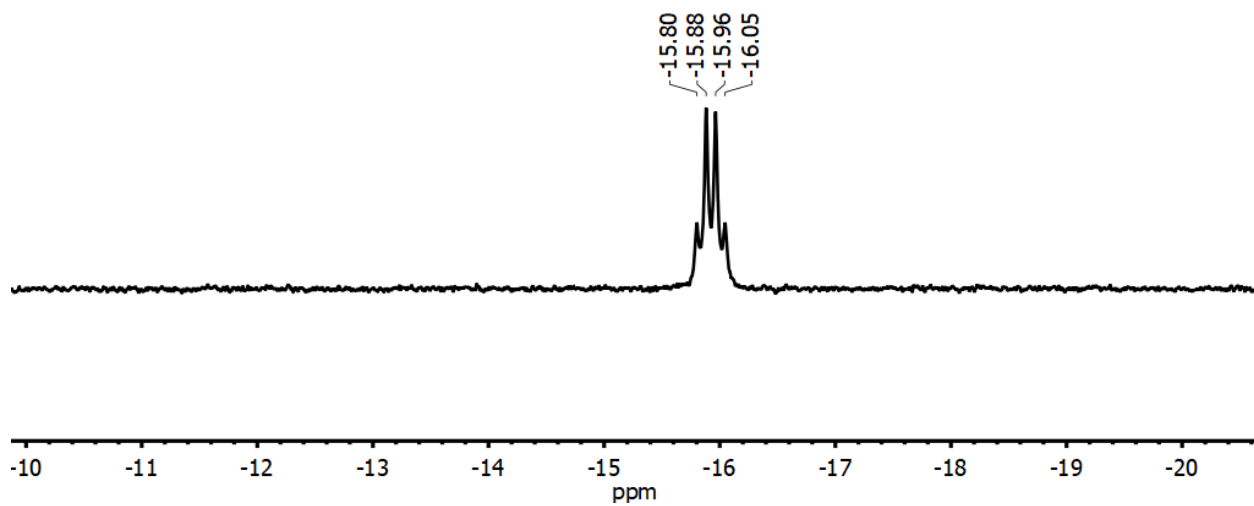


Figure A3.2 $^{31}\text{P}\{^1\text{H}\}$ NMR spectrum of K1 in DMSO- d_6 .

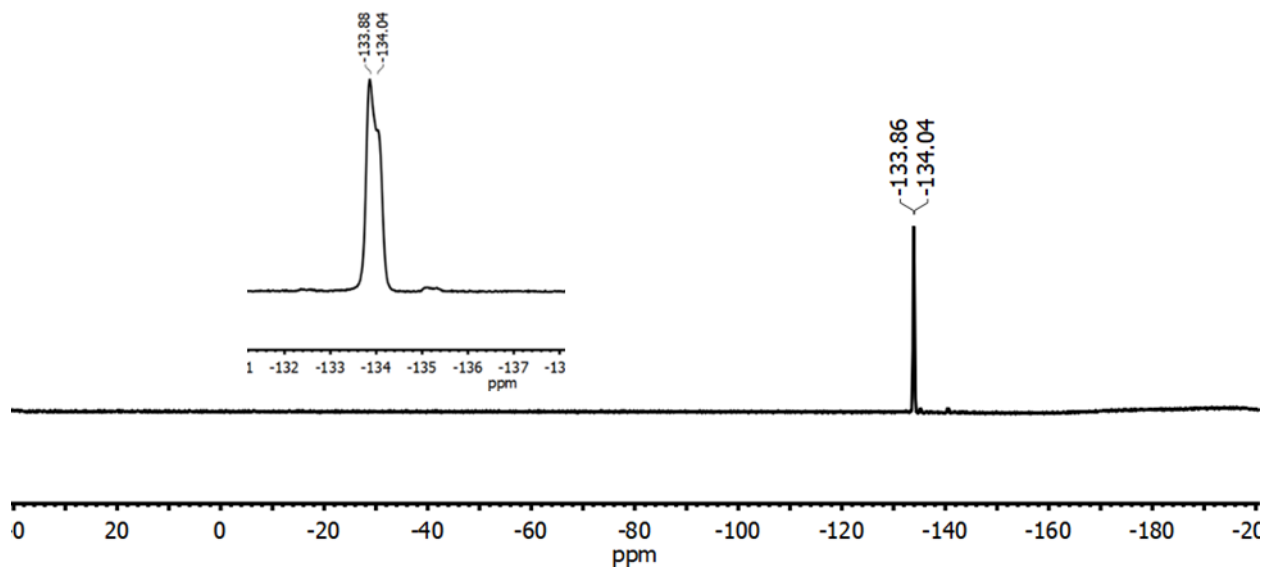


Figure A3.3 $^{19}\text{F}\{^1\text{H}\}$ NMR spectrum of K1 in DMSO- d_6 . Broad feature around -190 ppm is a result of Teflon within the probe.

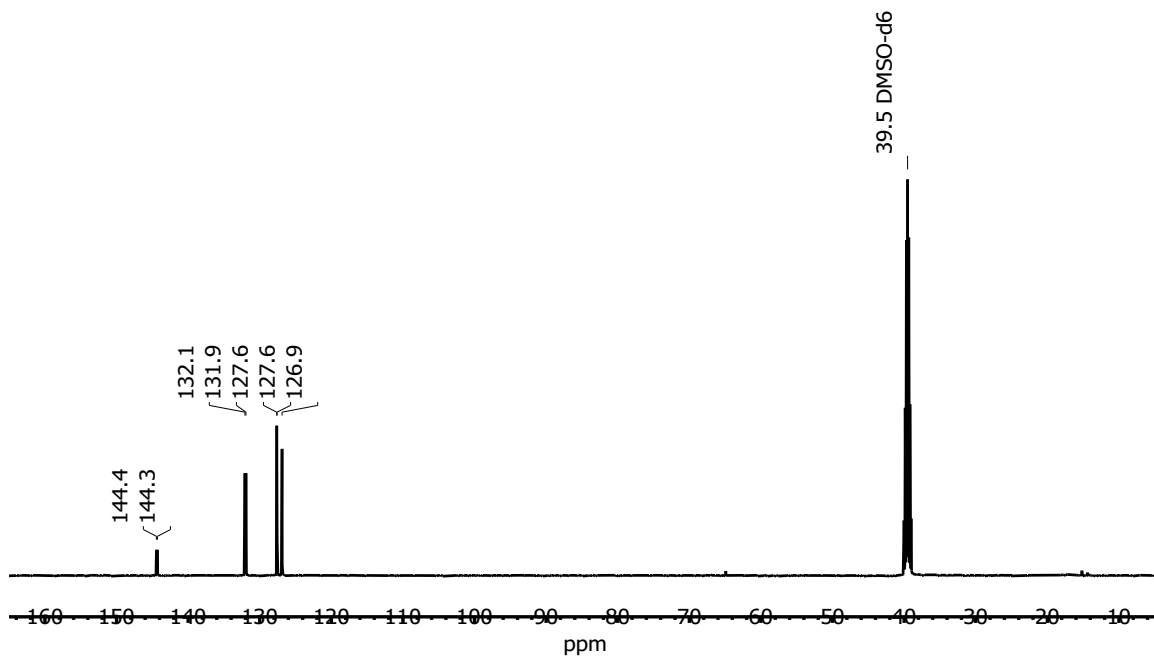


Figure A3.4 $^{13}\text{C}\{^1\text{H}\}$ NMR spectrum of K1 collected in DMSO- d_6 .

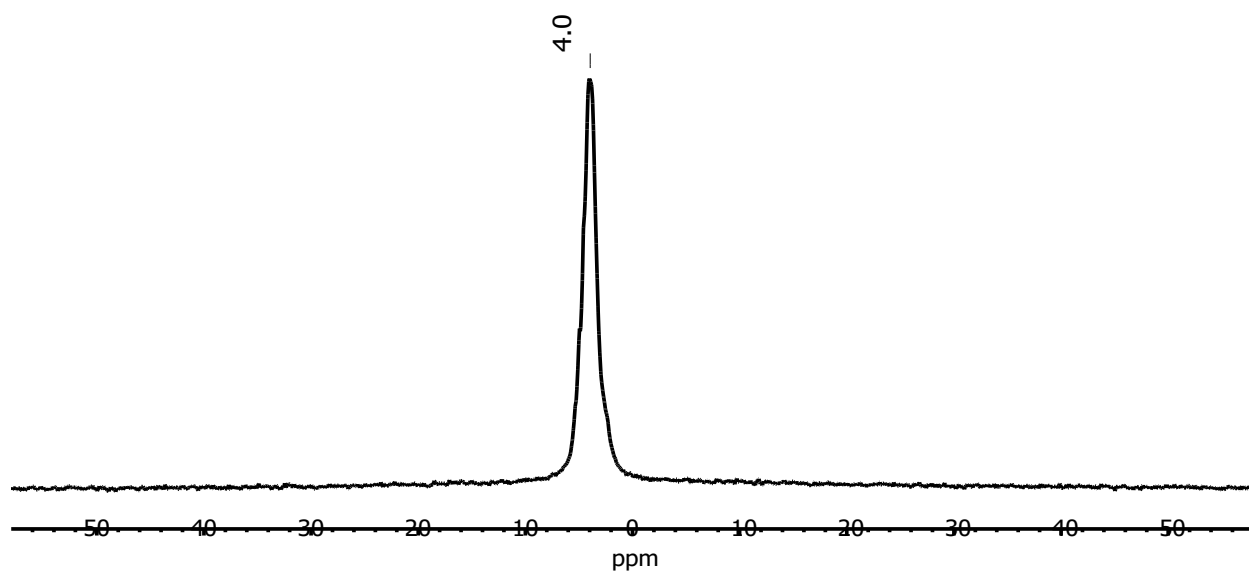


Figure A3.5 $^{11}\text{B}\{^1\text{H}\}$ NMR spectrum of K1 in DMSO- d_6 collected in a quartz NMR tube.

A3.1.2 [PPh₄][Rh(acac)(CO)(PPh₂(CH₂BF₃))] (**2**)

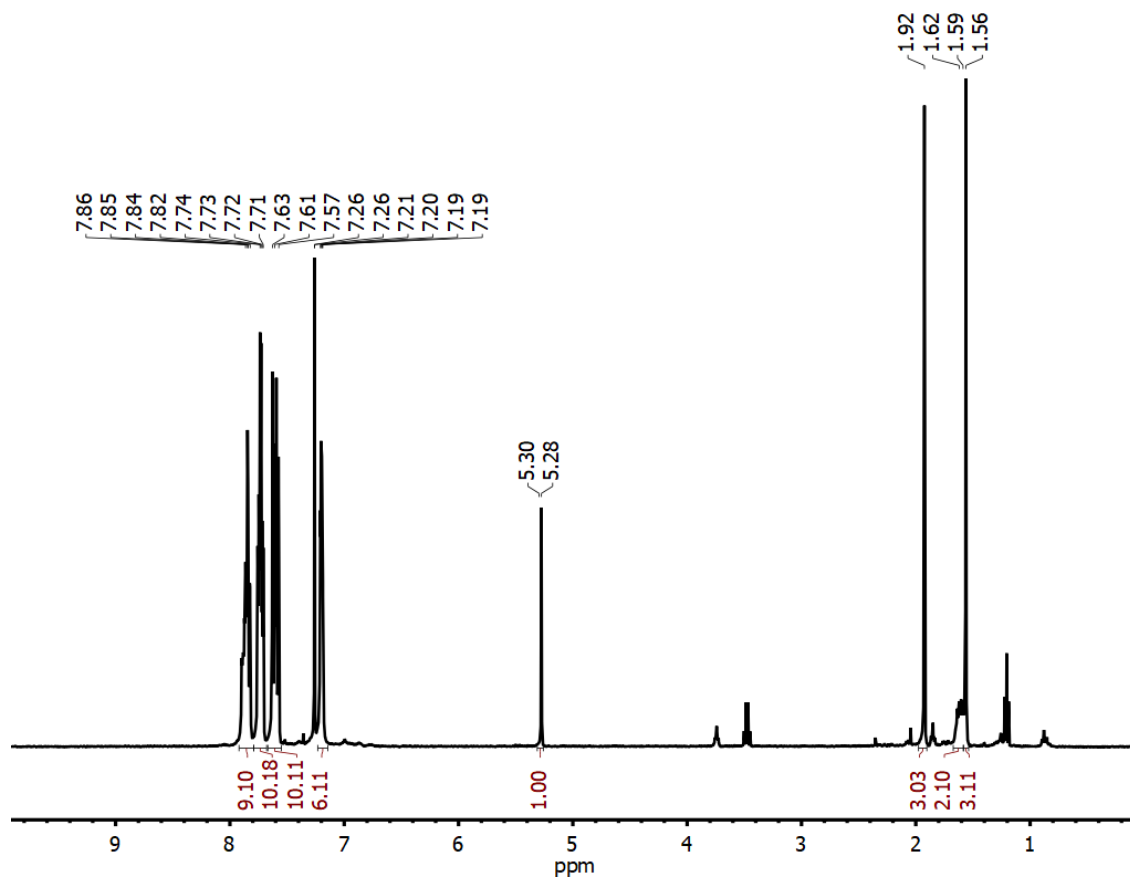


Figure A3.6 ¹H NMR spectrum of **2** collected in CDCl₃.

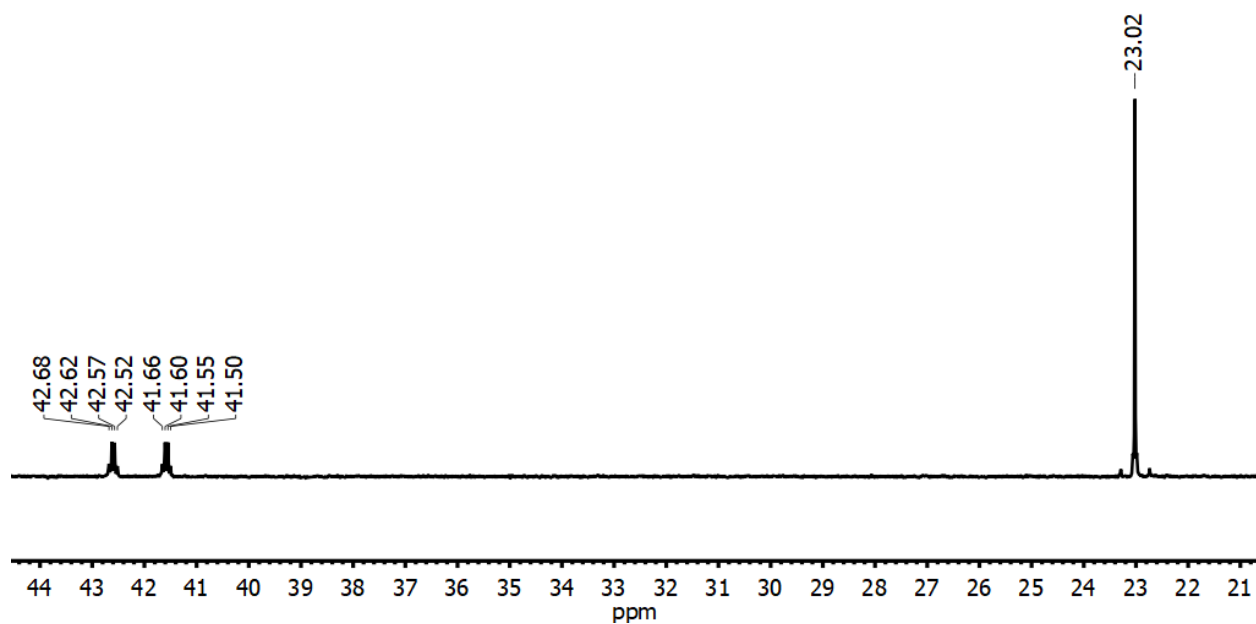


Figure A3.7 $^{31}\text{P}\{^1\text{H}\}$ NMR spectrum of **2** collected in CDCl_3 .

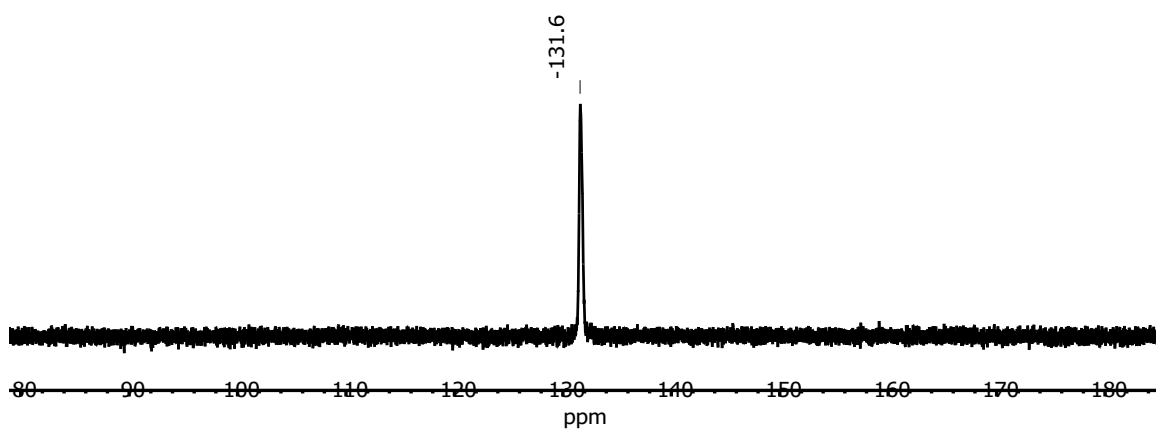


Figure A3.8 $^{19}\text{F}\{^1\text{H}\}$ NMR spectrum of **2** collected in CDCl_3 .

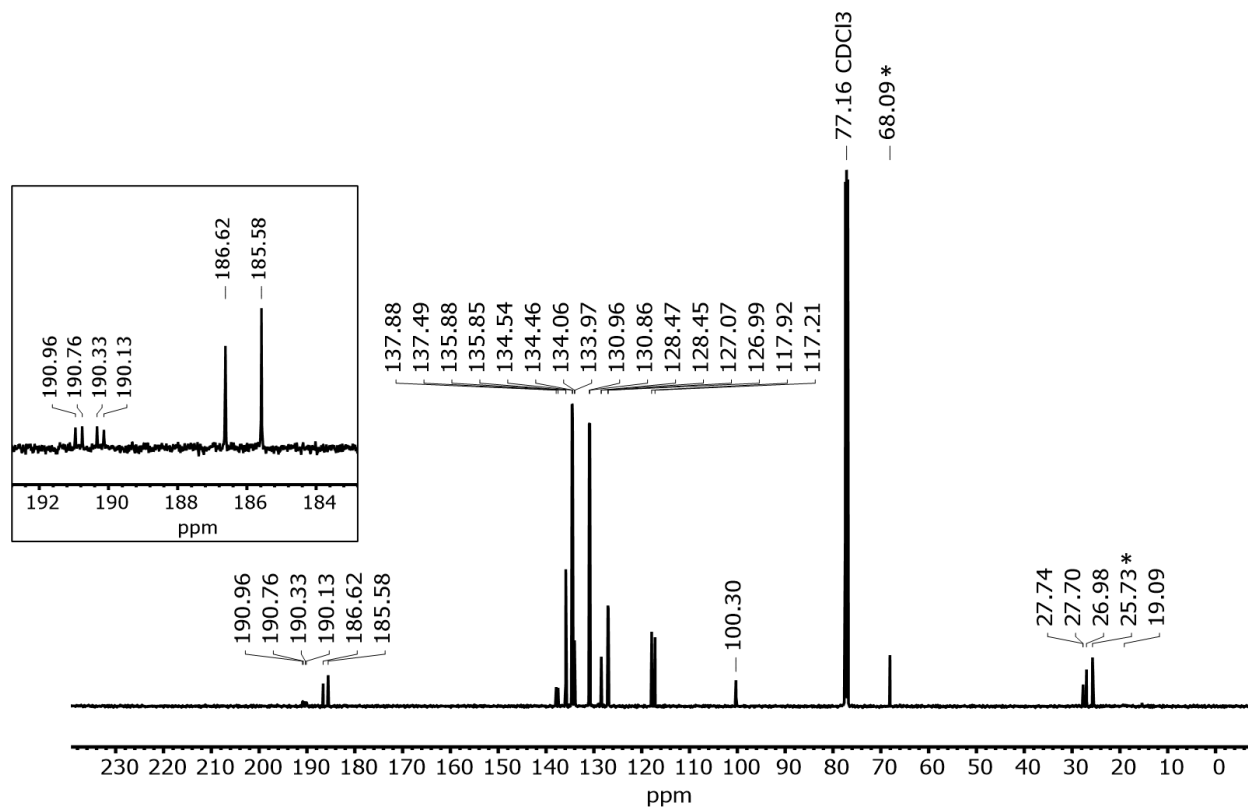


Figure A3.9 $^{13}\text{C}\{^1\text{H}\}$ NMR spectrum of **2** collected in CDCl_3 . Inset depicts doublet of doublets corresponding to the Rh-CO carbon. Asterisks indicate THF impurity.

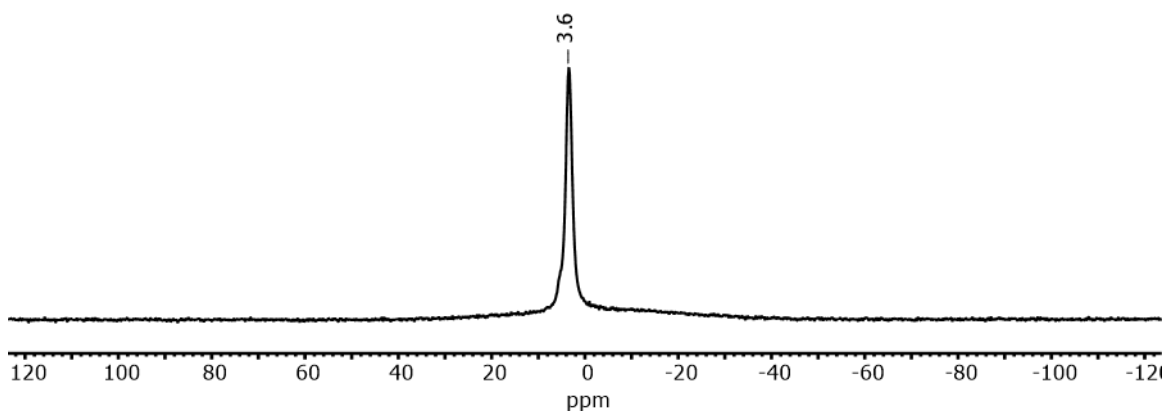


Figure A3.10 $^{11}\text{B}\{^1\text{H}\}$ NMR spectrum of **2** in CDCl_3 collected in a quartz NMR tube, the broad peak centered at 0 in the baseline is a result of borosilicate in the NMR probe.

A3.1.3 [PPh₄][SePPh₂(CH₂BF₃)] ([PPh₄][1^{Se}])

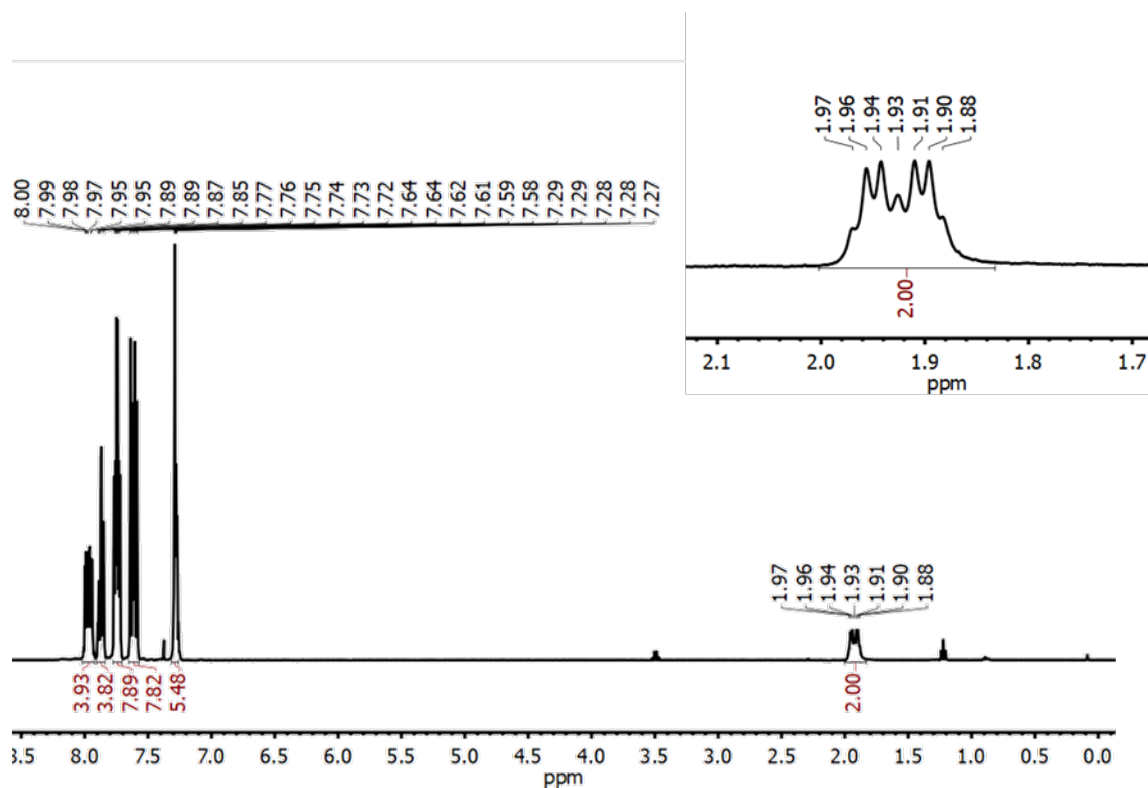


Figure A3.11 ¹H NMR spectrum of [PPh₄][1^{Se}] in CDCl₃, with inset showing splitting on the CH₂ group.

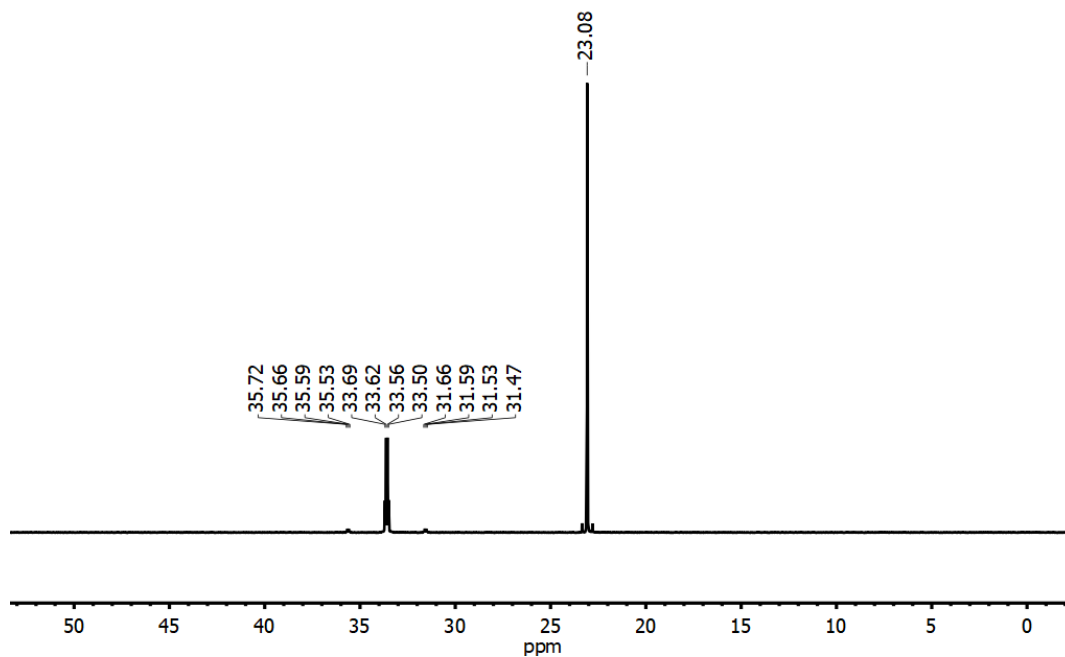


Figure A3.12 ³¹P{¹H} NMR spectrum of [PPh₄][¹Se] in CDCl₃.

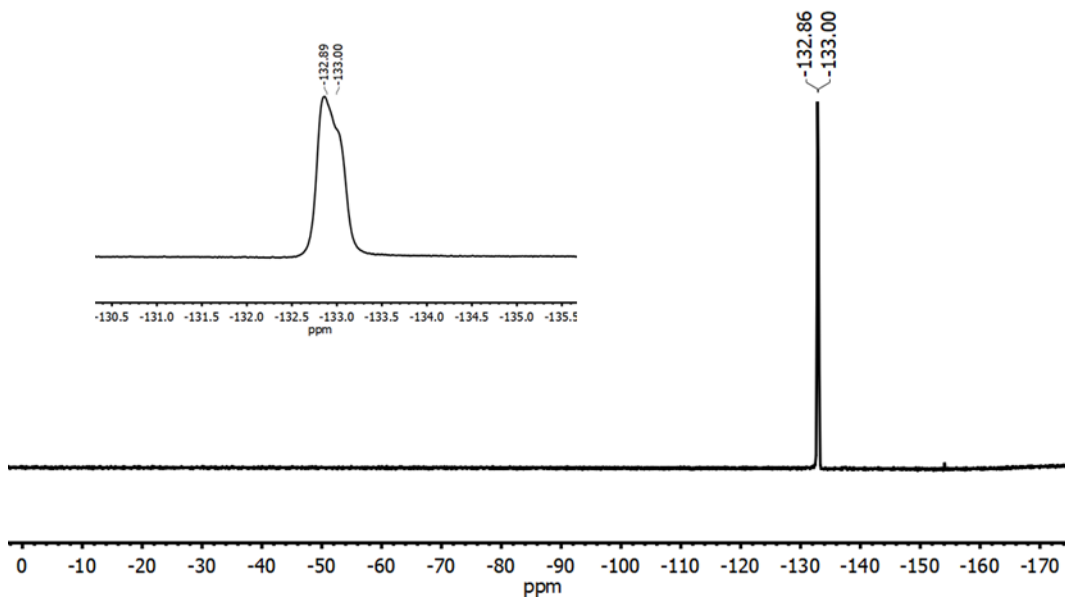


Figure A3.13 ¹⁹F{¹H} NMR spectrum of [PPh₄][¹Se] in CDCl₃.

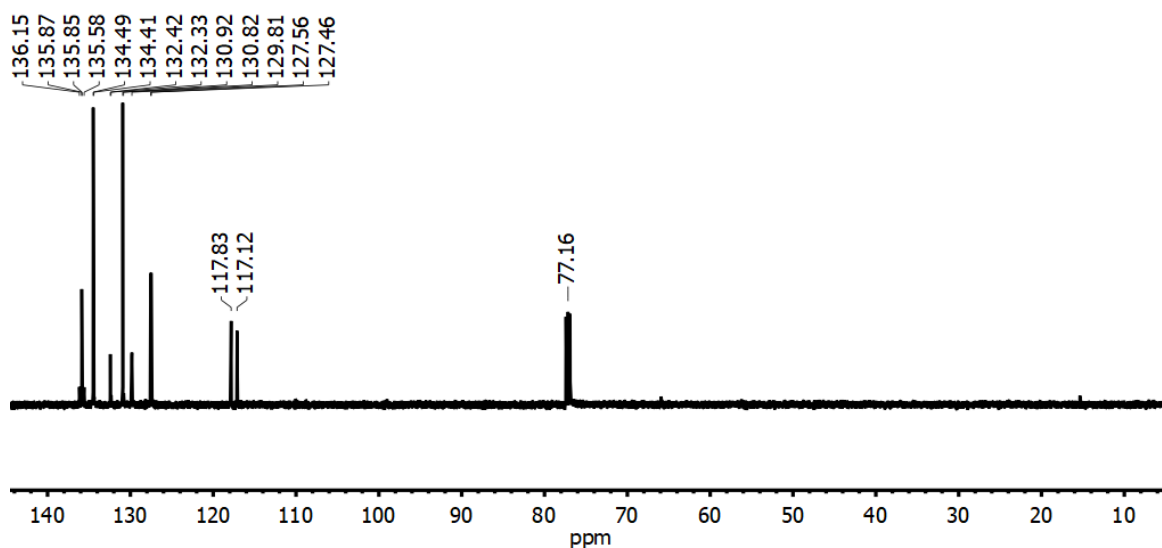


Figure A3.14 $^{13}\text{C}\{^1\text{H}\}$ NMR spectrum of $[\text{PPh}_4][^1\text{Sc}]$ in CDCl_3 .

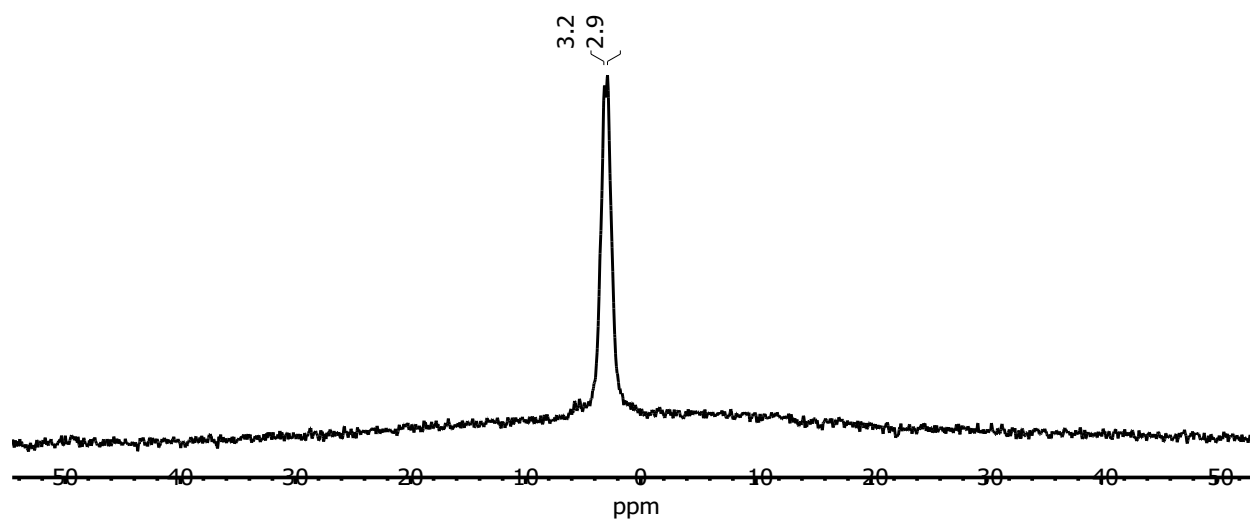


Figure A3.15 $^{11}\text{B}\{^1\text{H}\}$ NMR spectrum of $[\text{PPh}_4][^1\text{Sc}]$ in CDCl_3 collected in a quartz NMR tube.

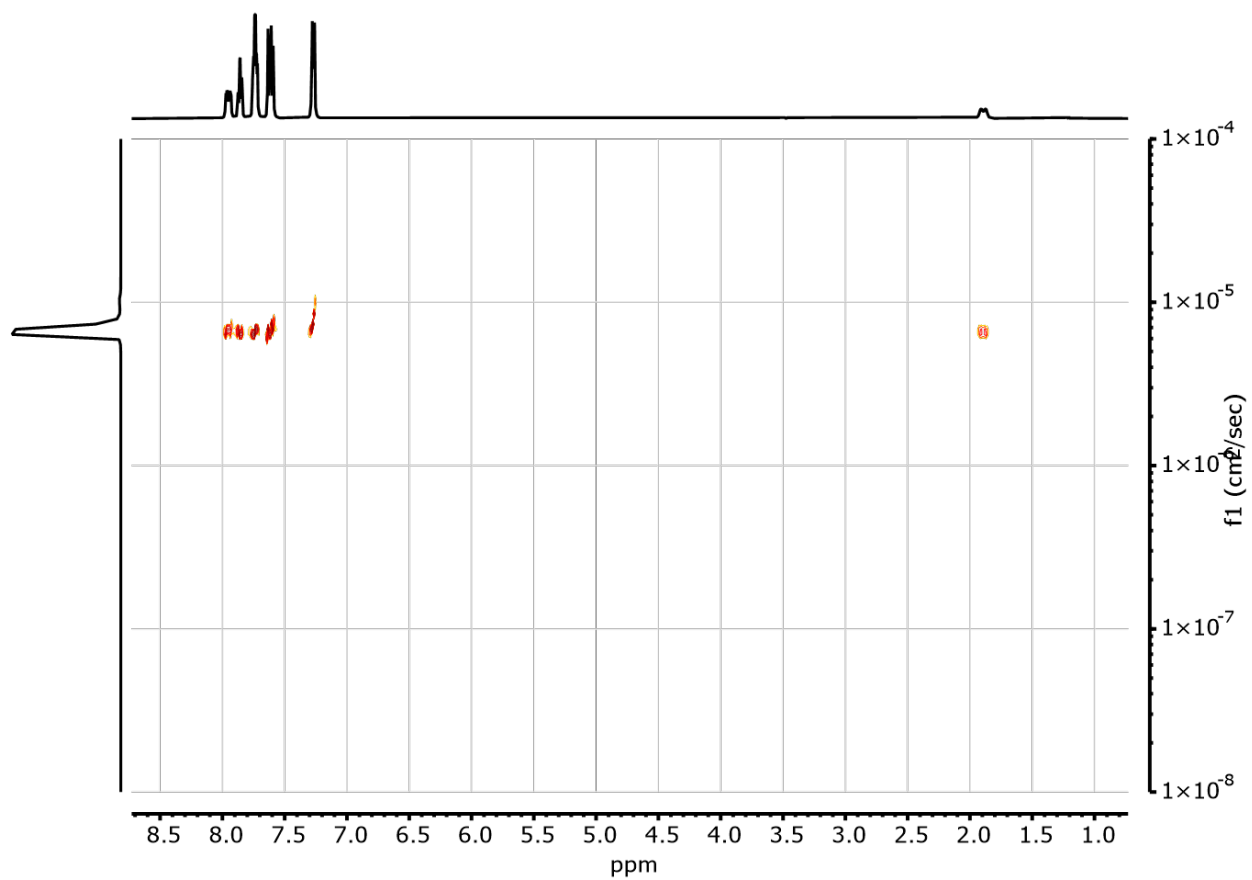


Figure A3.16 DOSY NMR spectrum of [PPh₄][¹Se] in CDCl₃. The diffusion value is 6.64 cm²/sec. Smearing is observed at 7.26 ppm due to the solvent peak.

A3.1.4 [NEt₄][SePPh₂(CH₂BF₃)] ([TEA][1^{Se}])

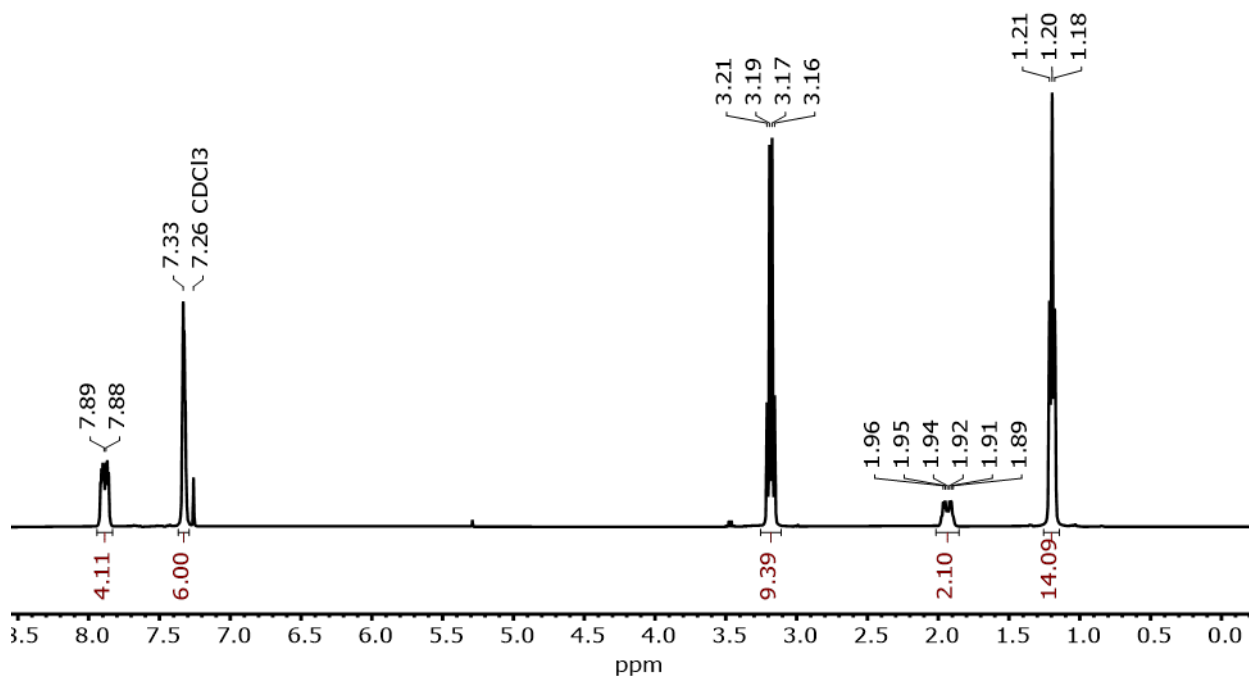


Figure A3.17 ¹H NMR spectrum of [TEA][1^{Se}] in CDCl₃, with inset showing splitting on the CH₂ group.

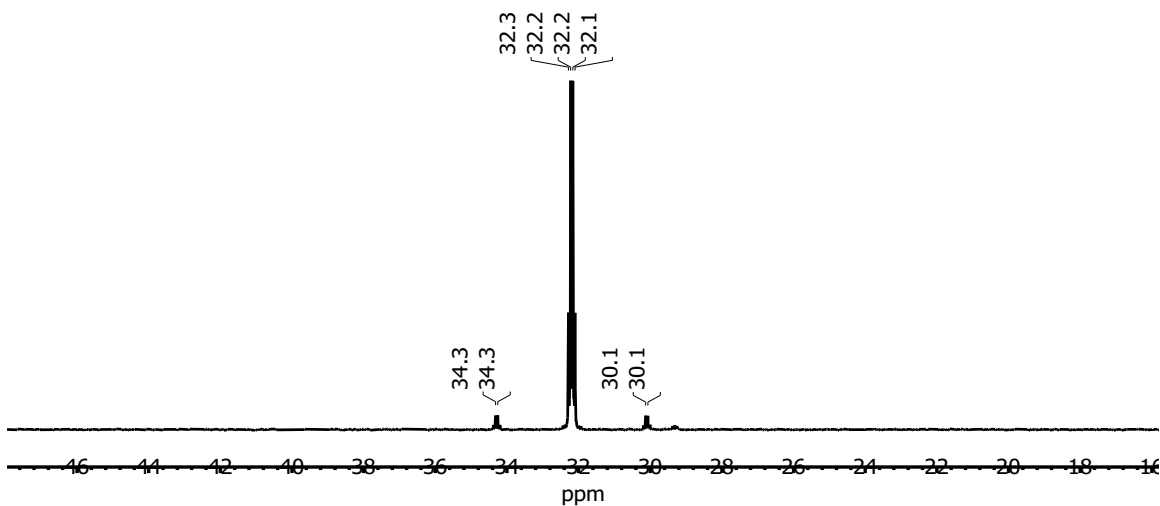


Figure A3.18 ³¹P{¹H} NMR spectrum of [TEA][1^{Se}] in CDCl₃.

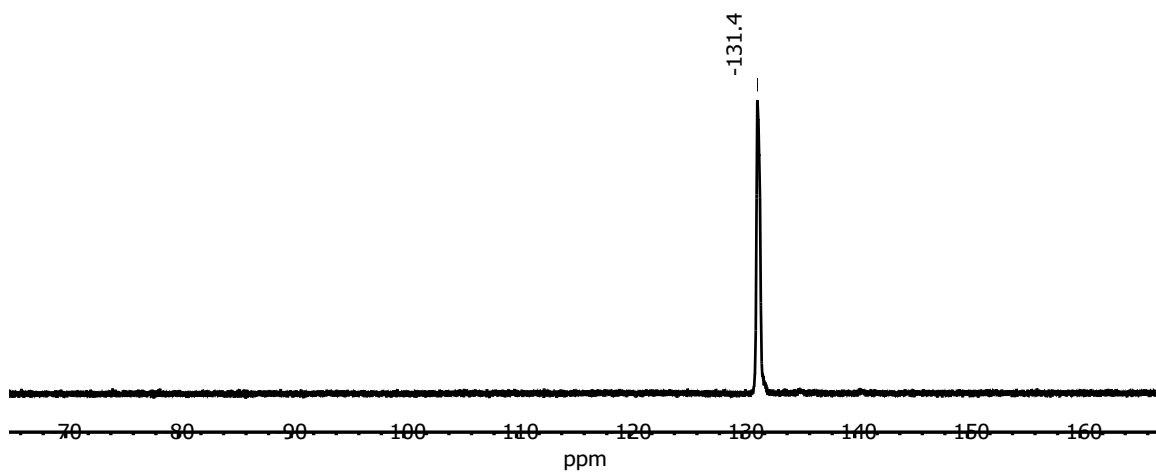


Figure A3.19 $^{19}\text{F}\{^1\text{H}\}$ NMR spectrum of $[\text{TEA}][\mathbf{1}^{\text{Se}}]$ in CDCl_3 .

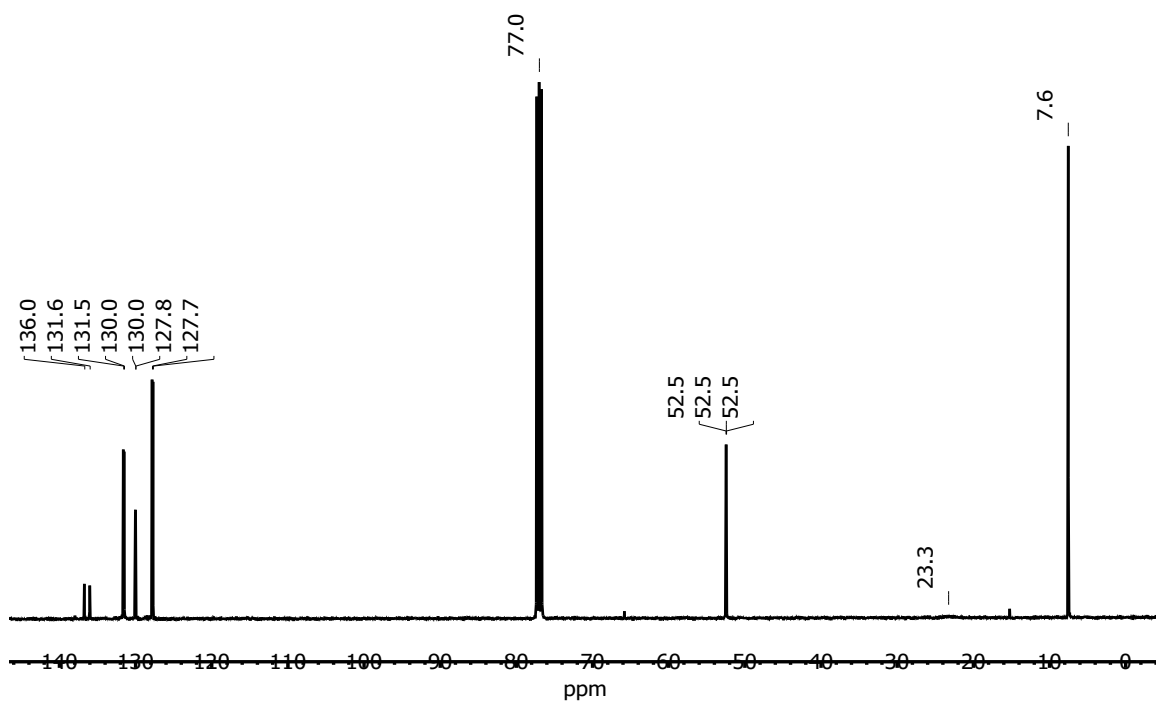


Figure A3.20 $^{13}\text{C}\{^1\text{H}\}$ NMR spectrum of $[\text{TEA}][\mathbf{1}^{\text{Se}}]$ in CDCl_3 .

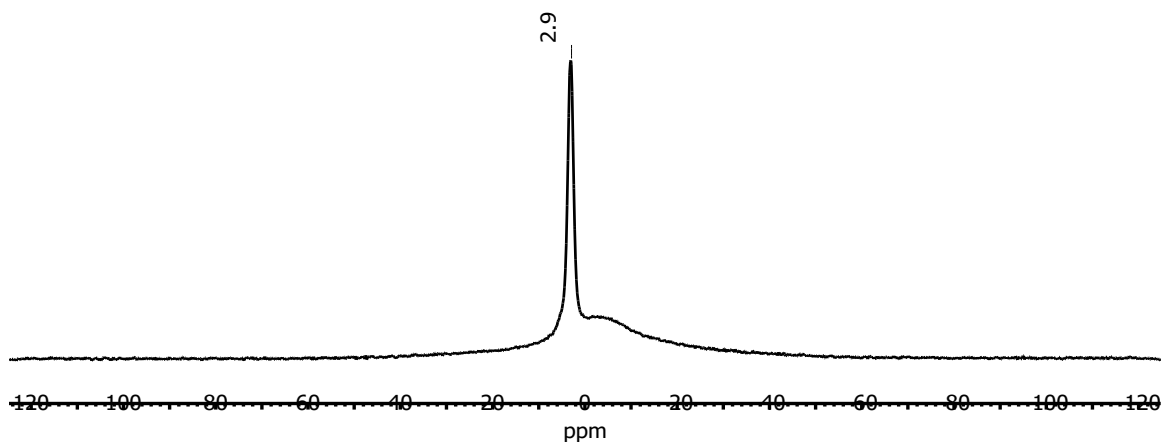


Figure A3.21 $^{11}\text{B}\{^1\text{H}\}$ NMR spectrum of $[\text{TEA}][\mathbf{1}^{\text{Se}}]$ collected in CDCl_3 ; the broad peak centered around 0 ppm is a result of borosilicate in the NMR tube and the NMR probe.

A3.1.5 Comparison between $[\text{TEA}][\mathbf{1}^{\text{Se}}]$ and $[\text{PPh}_4][\mathbf{1}^{\text{Se}}]$

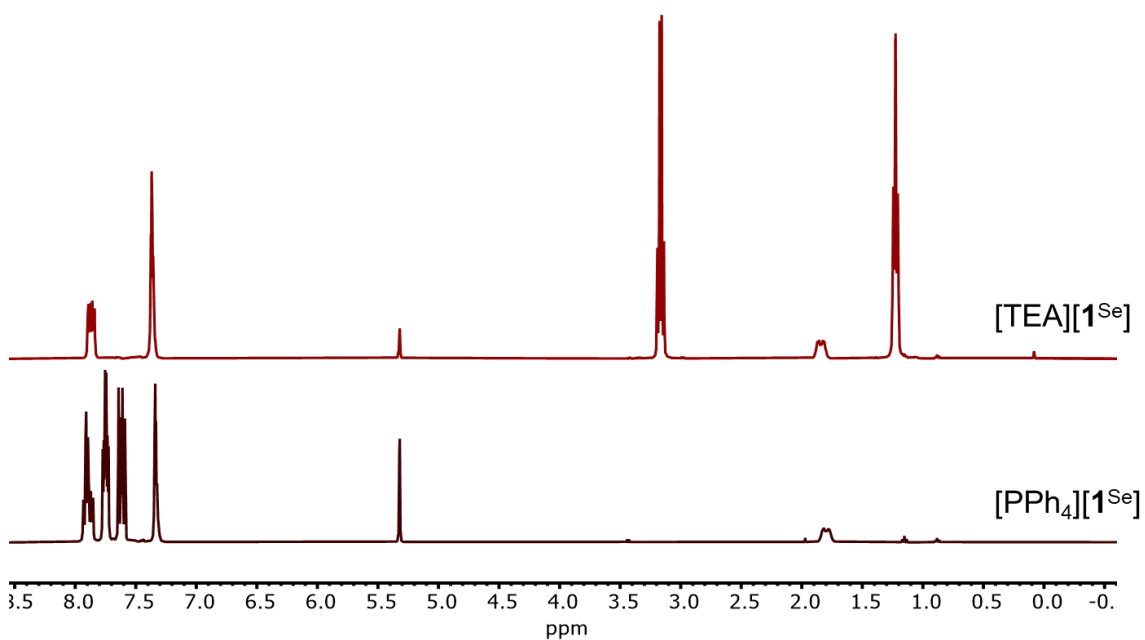


Figure A3.22 ^1H NMR spectra of $[\text{TEA}][\mathbf{1}^{\text{Se}}]$ and $[\text{PPh}_4][\mathbf{1}^{\text{Se}}]$ in CD_2Cl_2 .

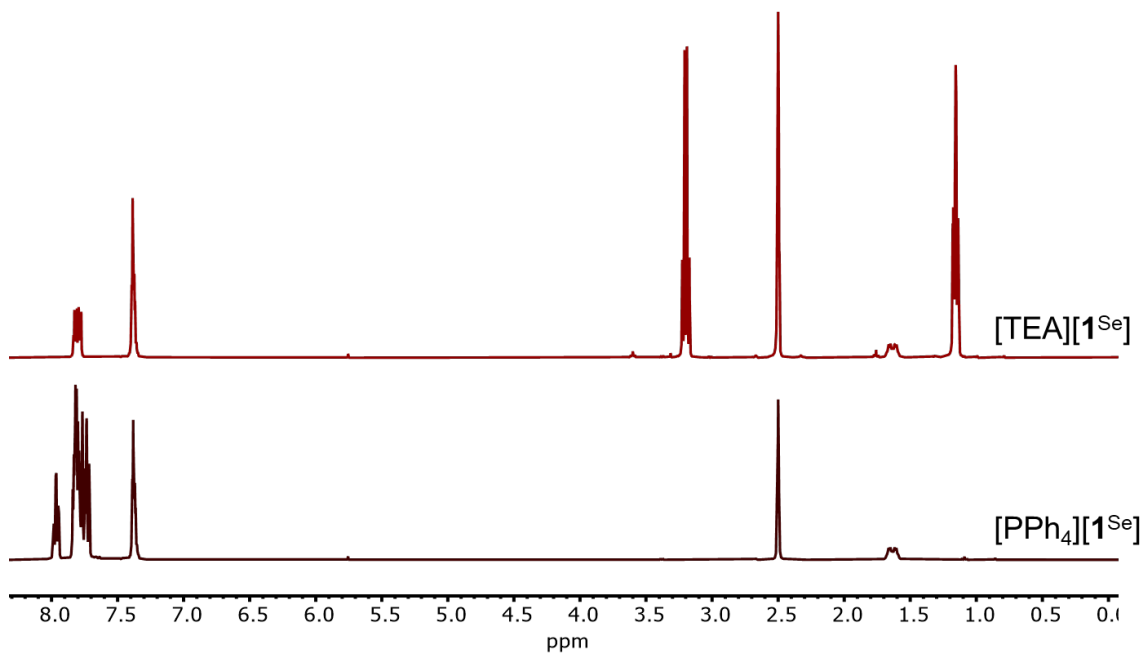


Figure A3.23 ^1H NMR spectra of $[\text{TEA}][\mathbf{1}^{\text{Se}}]$ and $[\text{PPh}_4][\mathbf{1}^{\text{Se}}]$ in $\text{DMSO-}d_6$.

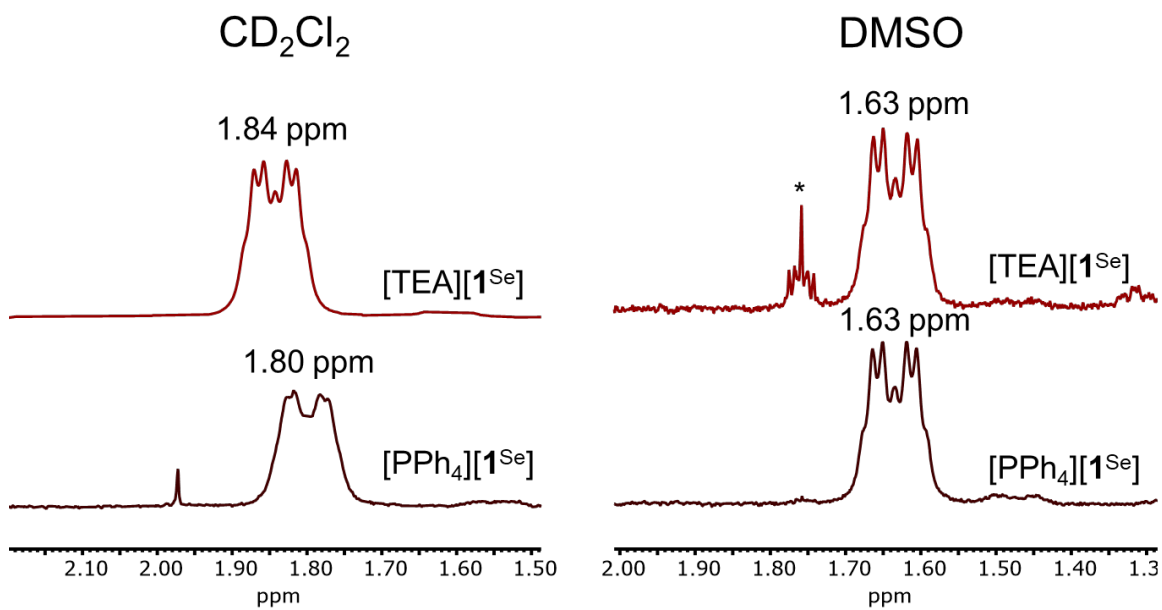


Figure A3.24 ^1H NMR spectra showing methylene resonance of $[\text{TEA}][\mathbf{1}^{\text{Se}}]$ and $[\text{PPh}_4][\mathbf{1}^{\text{Se}}]$ in CD_2Cl_2 and $\text{DMSO-}d_6$. The * indicates a small THF impurity.

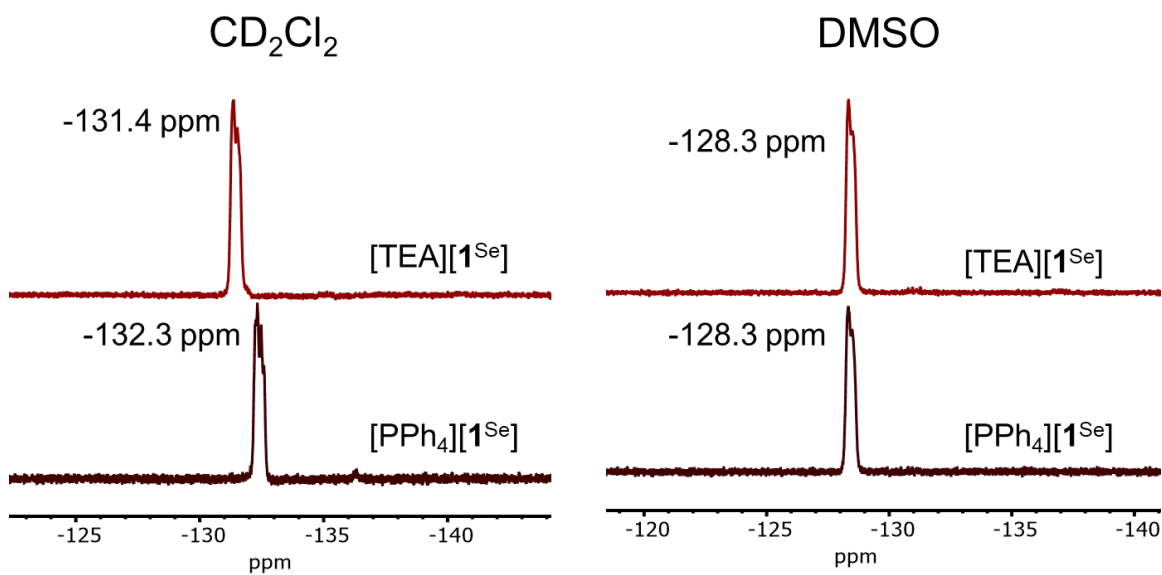


Figure A3.25 ^{19}F NMR spectra showing the BF_3 resonance of $[\text{TEA}][\text{1Se}]$ and $[\text{PPh}_4][\text{1Se}]$ in CD_2Cl_2 and $\text{DMSO}-d_6$.

A3.1.6 [PPh₄][SePPh₂(2-BF₃Ph)] ([PPh₄][**3**^{Se}])

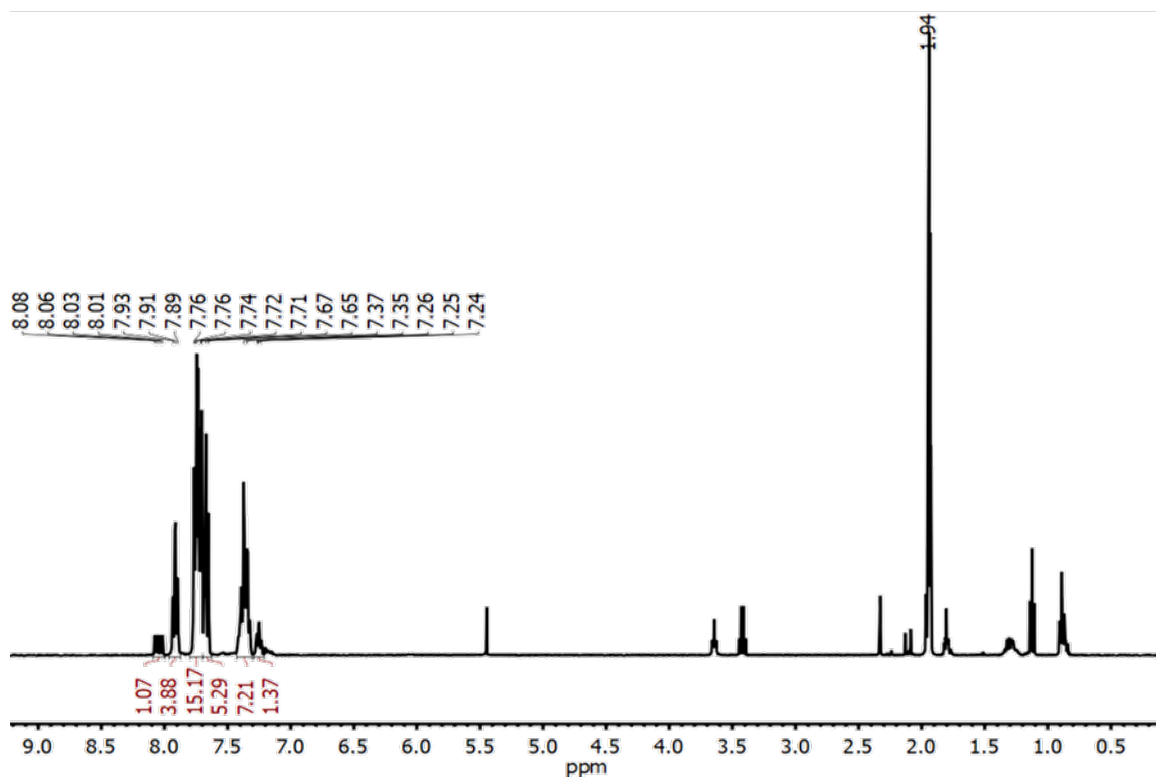


Figure A3.26 ¹H NMR spectrum of [PPh₄][**3**^{Se}] in CD₃CN; observed solvent impurities include DCM, THF and Et₂O.

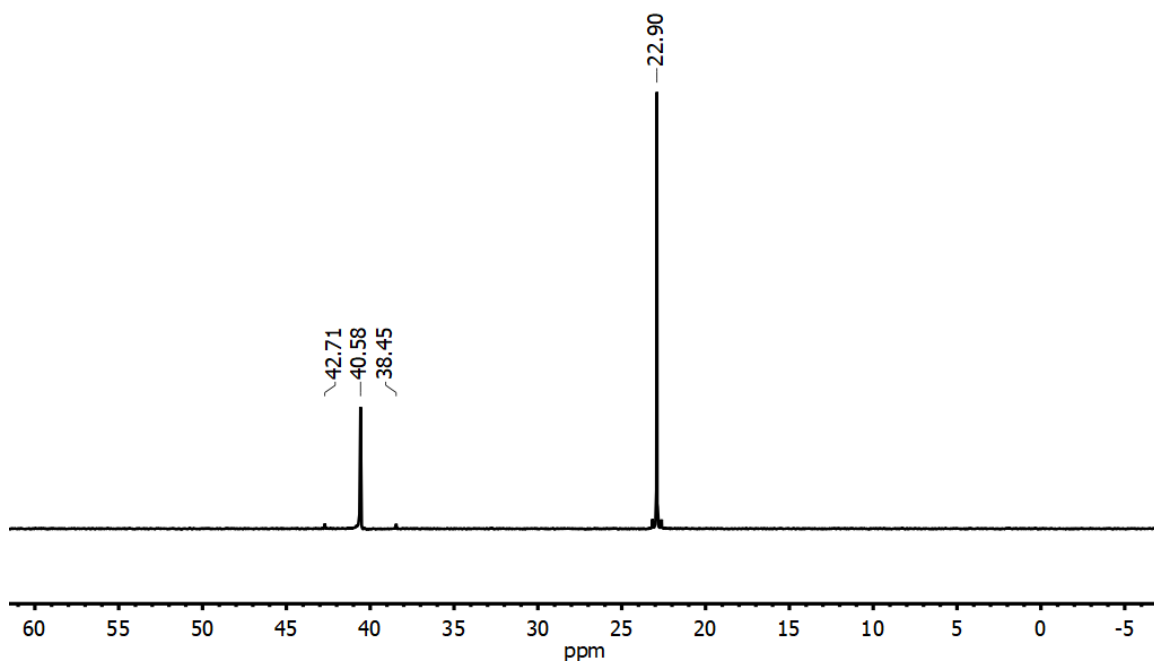


Figure A3.27 ^{31}P $\{^1\text{H}\}$ NMR spectrum of $[\text{PPh}_4][\text{3}^{\text{Se}}]$ in CD_2Cl_2 .

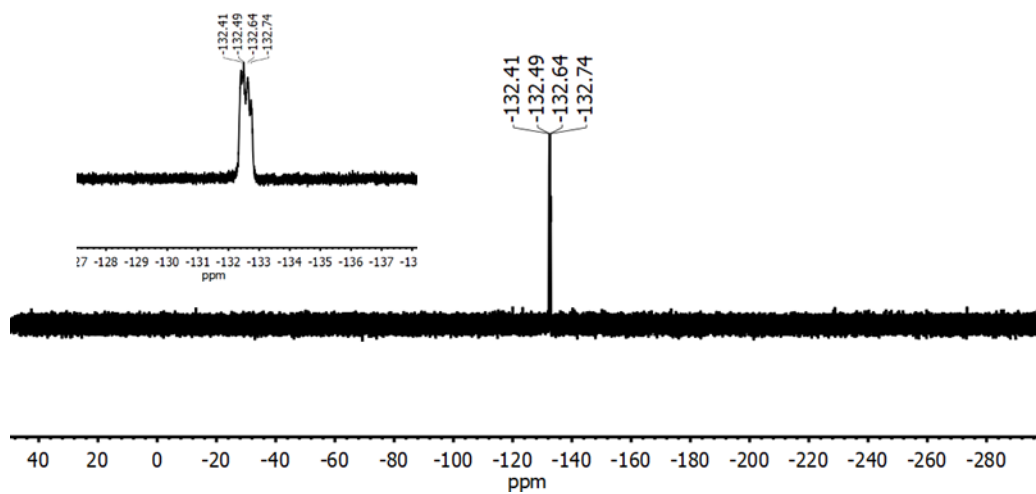


Figure A3.28 ^{19}F $\{^1\text{H}\}$ NMR spectrum of $[\text{PPh}_4][\text{3}^{\text{Se}}]$ in CD_3CN .

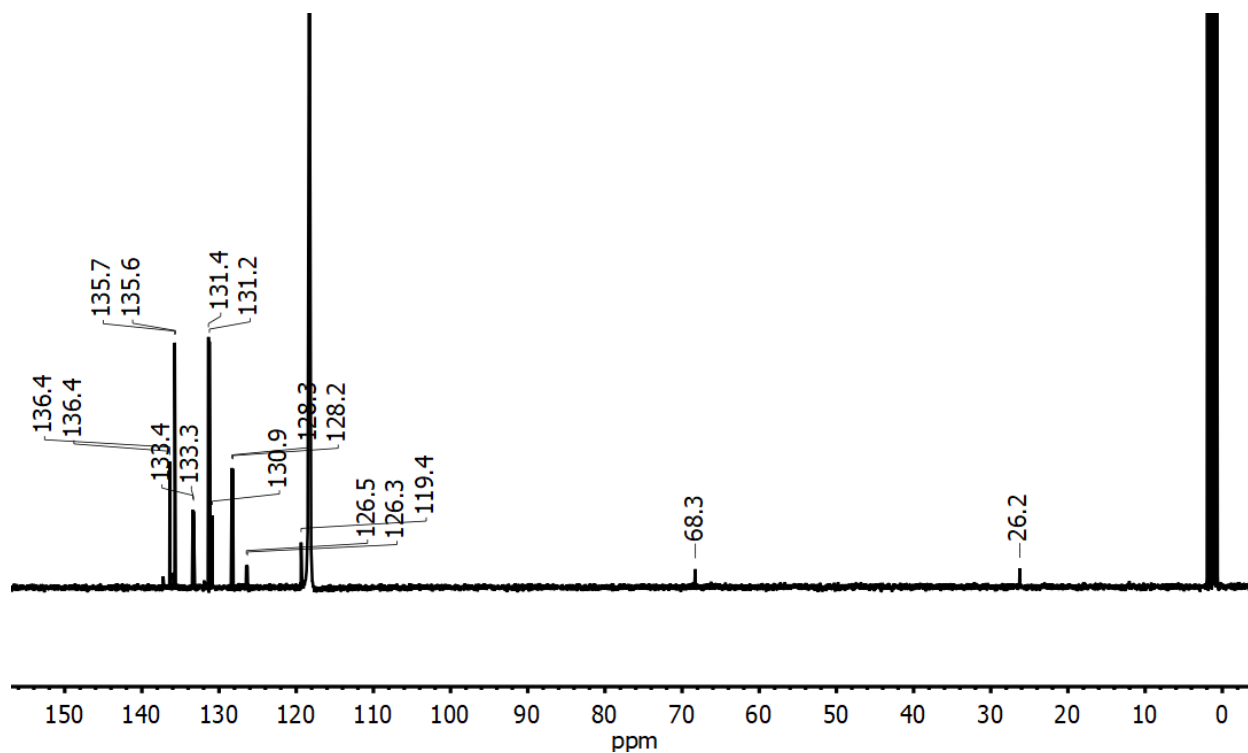


Figure A3.29 $^{13}\text{C}\{^1\text{H}\}$ NMR spectrum of $[\text{PPh}_4][^3\text{Se}]$ in CD_3CN .

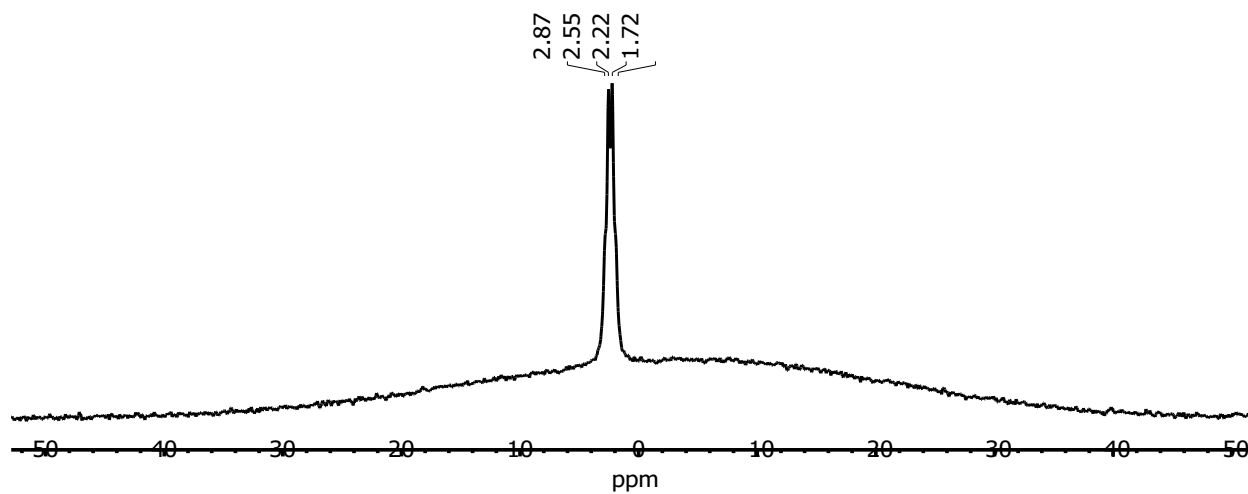


Figure A3.30 $^{11}\text{B}\{^1\text{H}\}$ NMR spectrum of $[\text{PPh}_4][^3\text{Se}]$ in CD_3CN collected in a quartz NMR tube; the broad peak in the baseline around 0 is a result of borosilicate in the NMR probe.

A3.2 Infrared Spectra

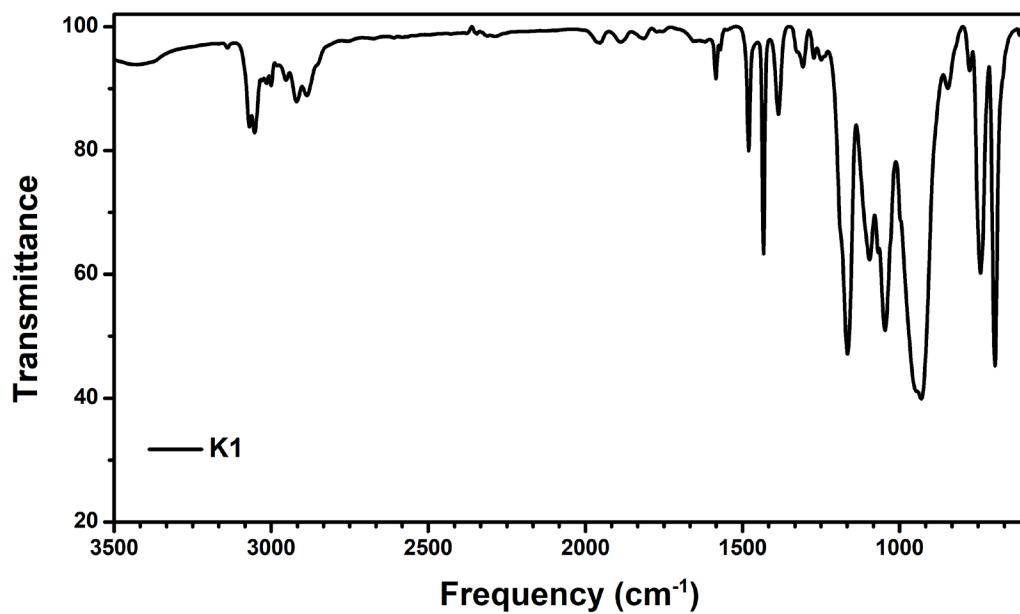


Figure A3.31 IR spectrum (KBr Pellet) of K1.

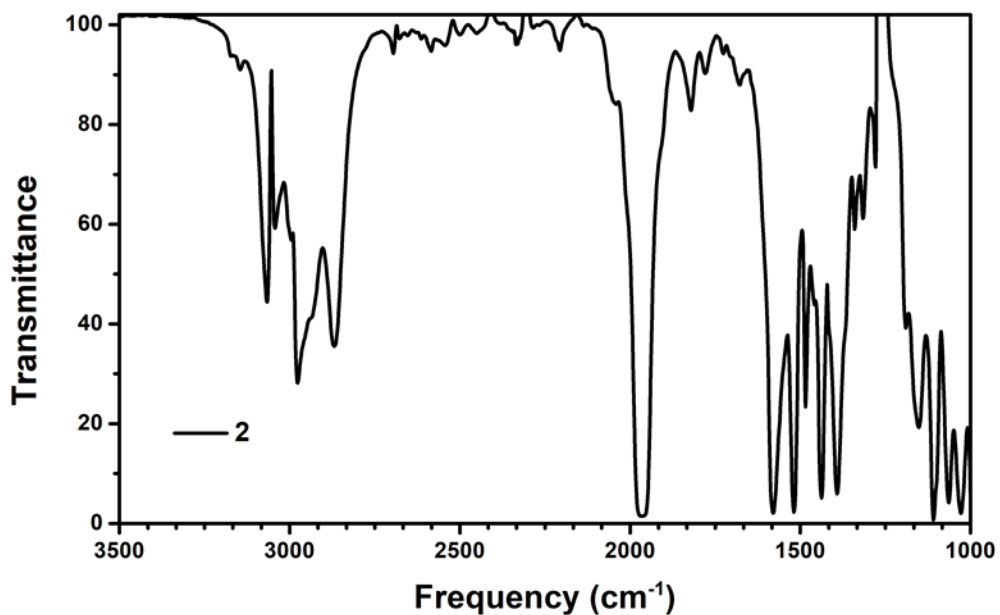


Figure A3.32 IR spectrum (DCM Solution) of 2. The equation correlating the stretching frequency in $\text{Rh}(\text{CO})(\text{acac})\text{L}$ compounds and TEP from $\text{Ni}(\text{CO})_3\text{L}$ is $y = 0.5716x + 938.47$, where y is TEP and x is $\nu_{(\text{CO})\text{Rh}}$ (reference 108 in Chapter 3).

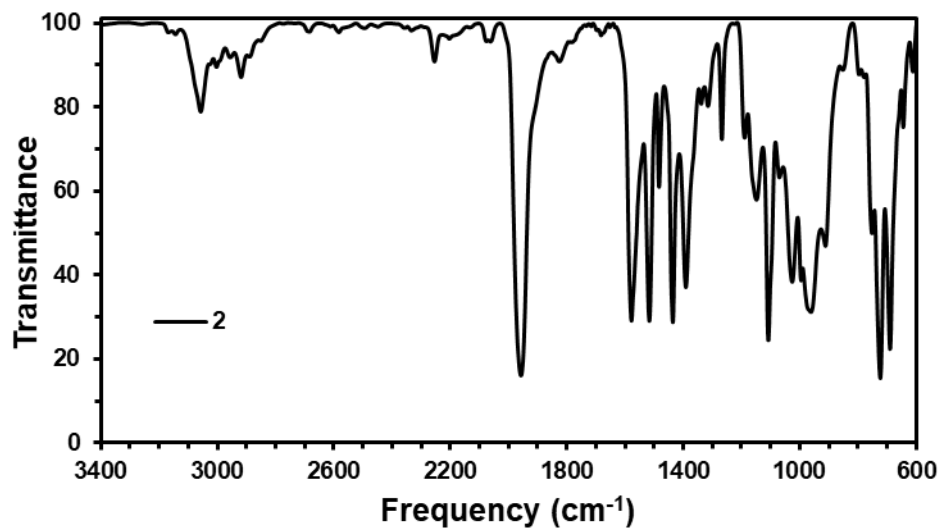


Figure A3.33 IR spectrum (KBr pellet) of 2.

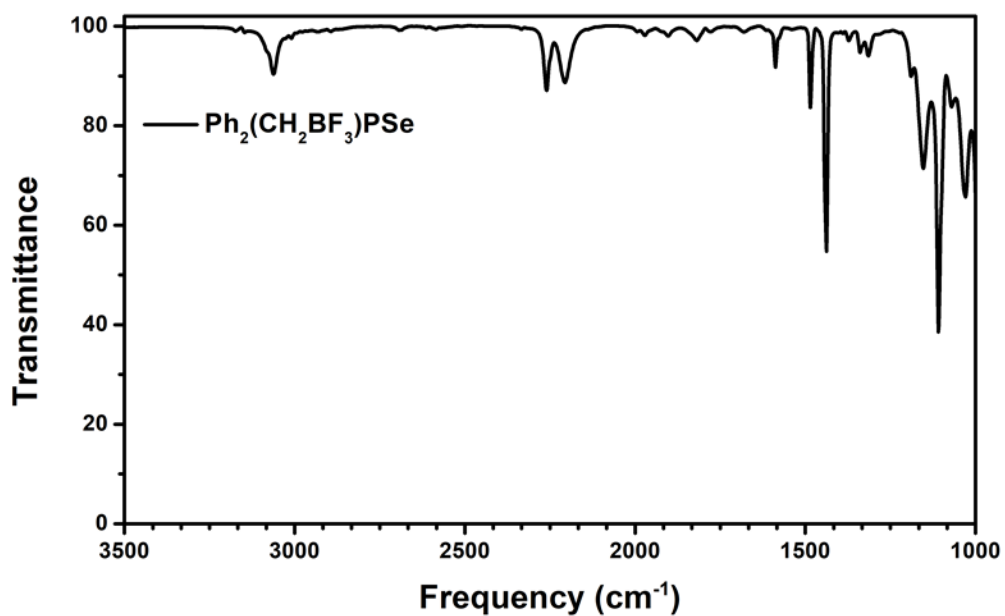


Figure A3.34 IR spectrum (CDCl_3 solution) of $[\text{PPh}_4][1^{\text{Se}}]$. Note that the features around 2250 cm^{-1} are a combination of CO_2 and solvent stretches.

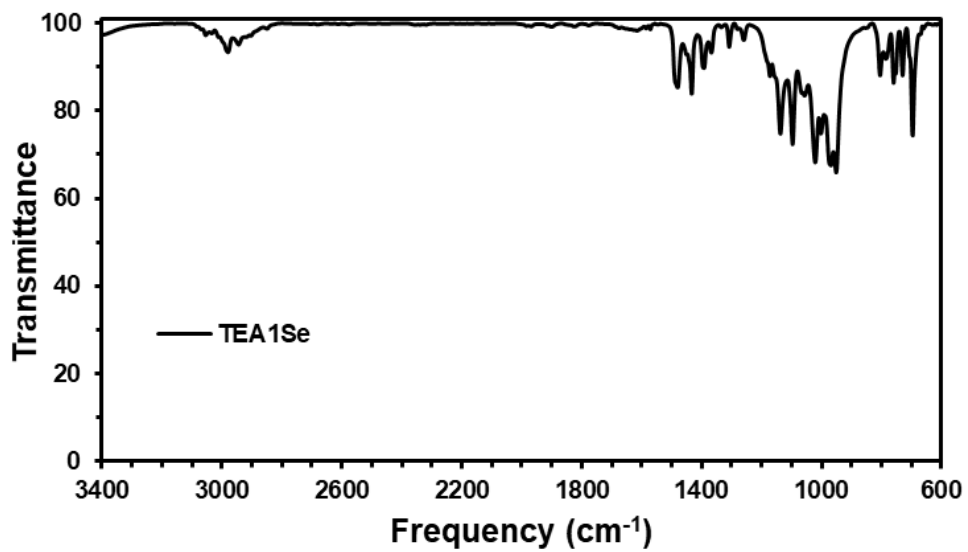


Figure A3.35 IR spectrum (KBr pellet) of [TEA][1^{Se}].

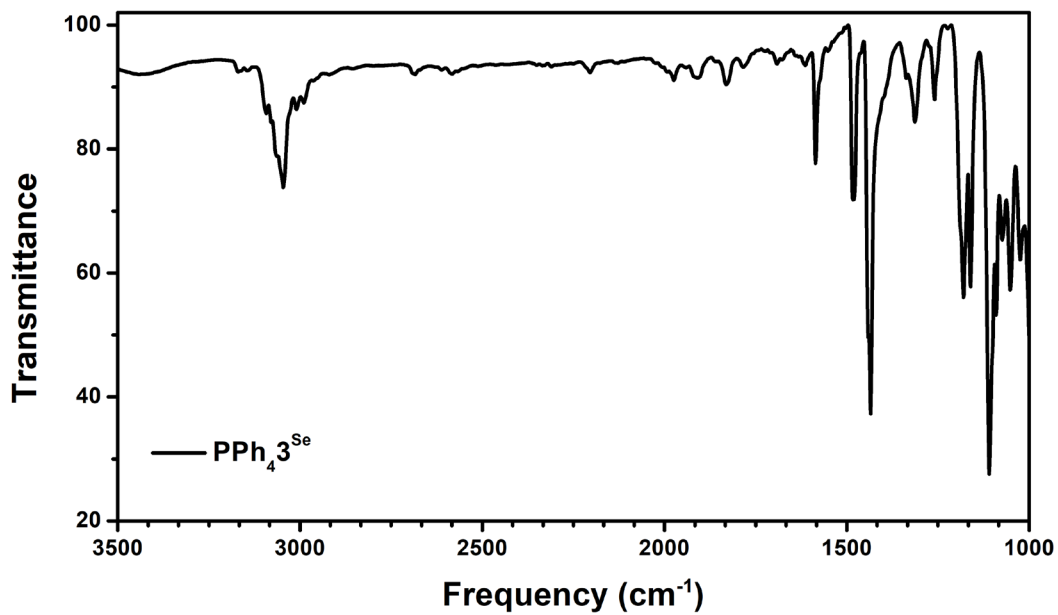


Figure A3.36 IR spectrum (KBr pellet) of [PPh₄][3^{Se}].

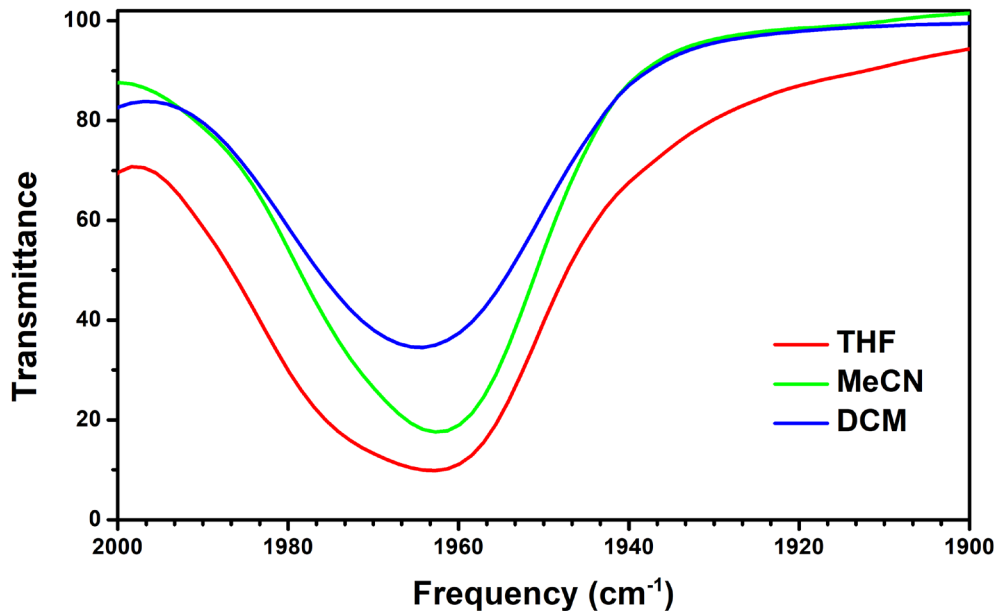


Figure A3.37 IR spectra of **2** in different solvents. ν_{CO} shifts by $\sim 3 \text{ cm}^{-1}$, which is within the instrument error (4 cm^{-1}).

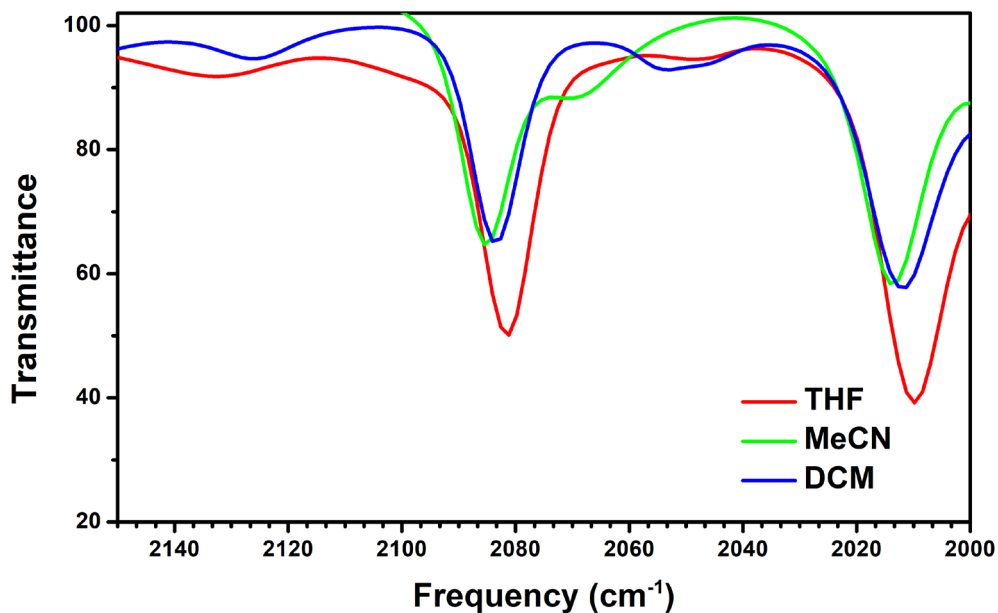


Figure A3.38 IR spectra of $\text{Rh}(\text{CO})_2\text{acac}$ in different solvents.

A3.3 UV-visible spectra

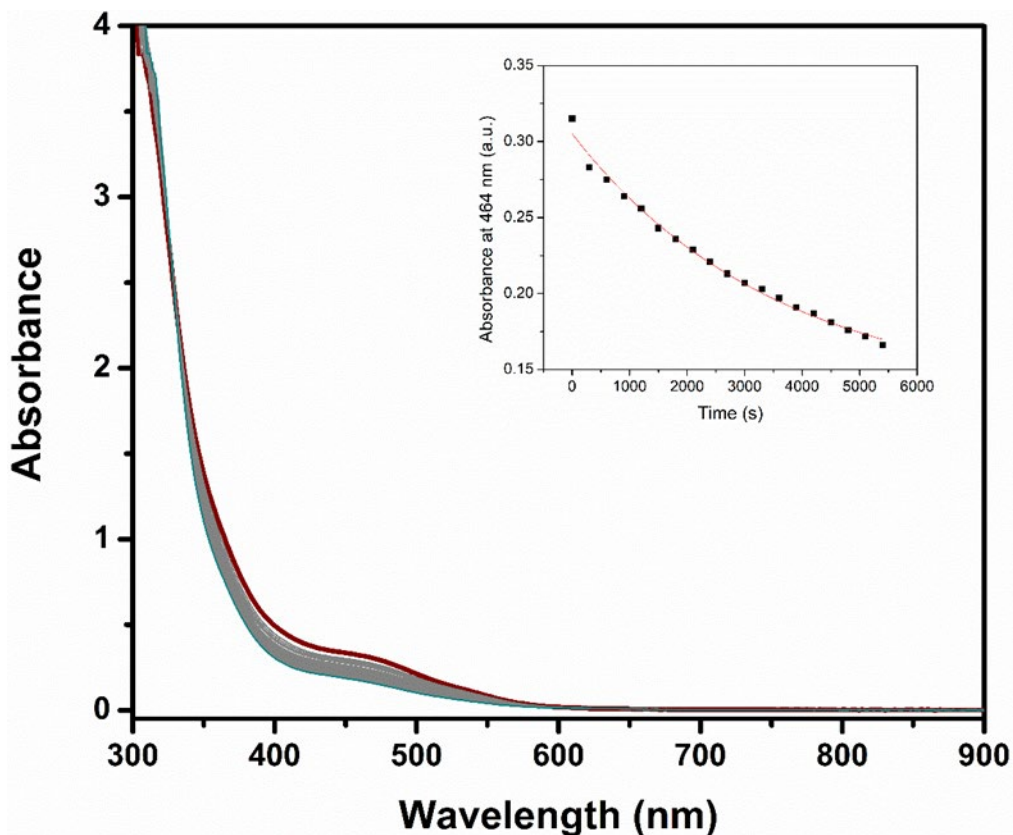


Figure A3.39 UV-vis traces of the reaction between $\text{Ni}(\text{COD})_2$ (0.36 mM), 1 equivalent of **K1**, and 21 equivalents of C_6F_6 in THF at RT, with scans taken every 5 minutes for a total of 70 minutes; the spectrum for the first scan is maroon and the spectrum for the last scan is teal. Inset: Exponential fit to the decay of the absorbance at 464 nm with the equation $y=y_0+A*\exp(R_0*x)$. The fit values are $y_0 = 0.132(9)$, $A=0.173(8)$, and $R_0 = -2.81\text{E-}4(3.05\text{E-}5)$. The k_{obs} determined from this fit is $-2.8\text{E-}4 \text{ s}^{-1}$.

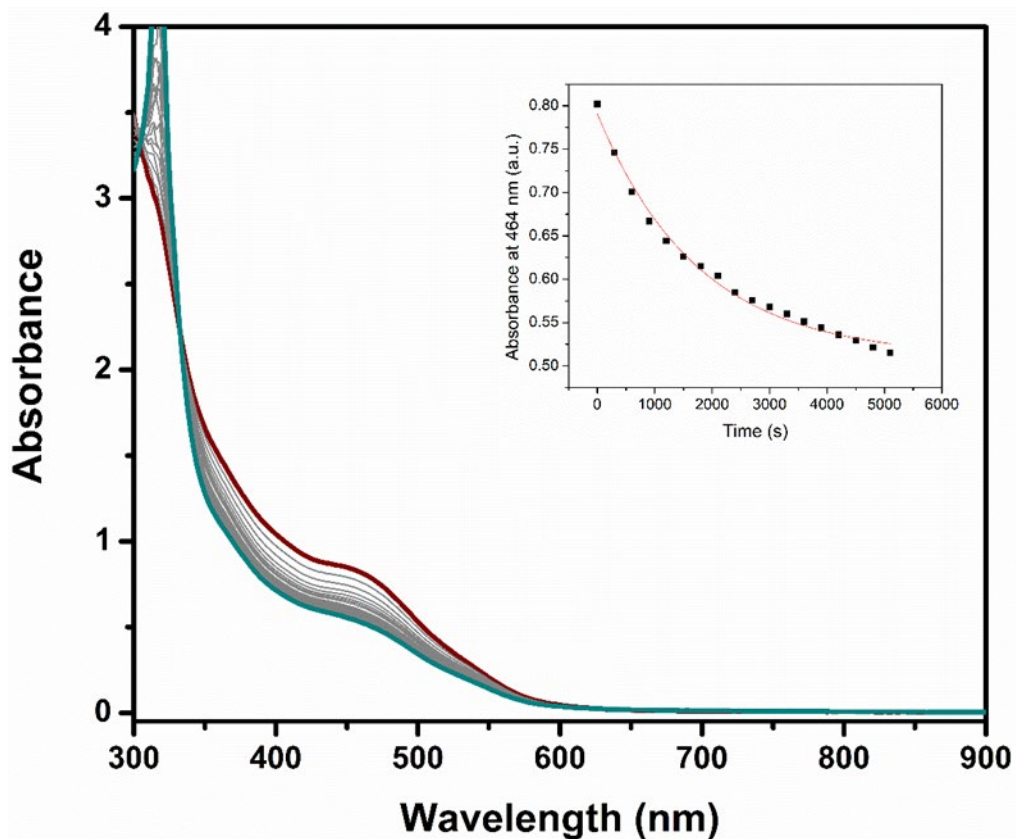


Figure A3.40 UV-vis traces of the reaction between $\text{Ni}(\text{COD})_2$ (0.36 mM), 2 equivalents of K1, and 21 equivalents of C_6F_6 in THF at RT, with scans taken every 5 minutes for a total of 90 minutes; the spectrum for the first scan is maroon and the spectrum for the last scan is teal. Inset: Exponential fit to the decay of the absorbance at 464 nm with the equation $y=y_0+A*\exp(R_0*x)$. The fit values are $y_0 = 0.510(6)$, $A=0.280(6)$, and $R_0 = -5.68\text{E-}4(3.98\text{E-}5)$. The k_{obs} determined from this fit is $-5.6\text{E-}4 \text{ s}^{-1}$.

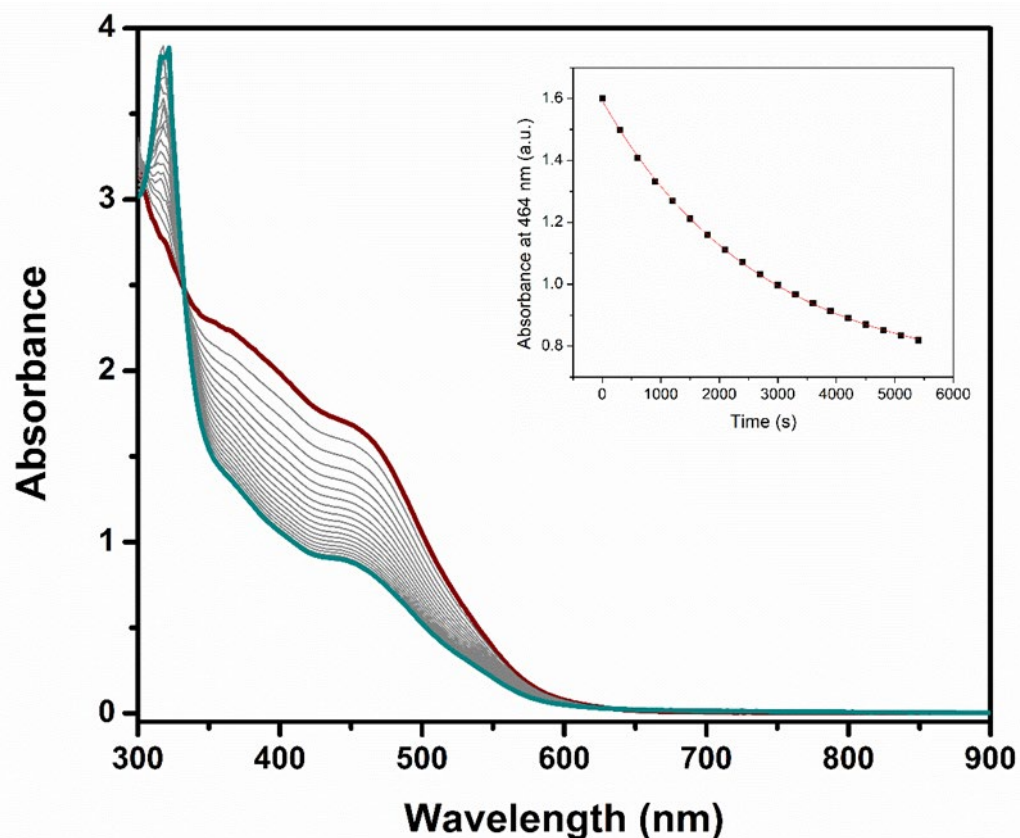


Figure A3.41 UV-vis traces of the reaction between $\text{Ni}(\text{COD})_2$ (0.36 mM), 3 equivalents of K1, and 21 equivalents of C_6F_6 in THF at RT, with scans taken every 5 minutes for a total of 90 minutes; the spectrum for the first scan is maroon and the spectrum for the last scan is teal. Inset: Exponential fit to the decay of the absorbance at 464 nm with the equation $y=y_0+A*\exp(R_0*x)$. The fit values are $y_0 = 0.703(6)$, $A=0.890(5)$, and $R_0 = -3.71\text{E-}4(6.03\text{E-}6)$. The k_{obs} determined from this fit is $-3.7\text{E-}4 \text{ s}^{-1}$.

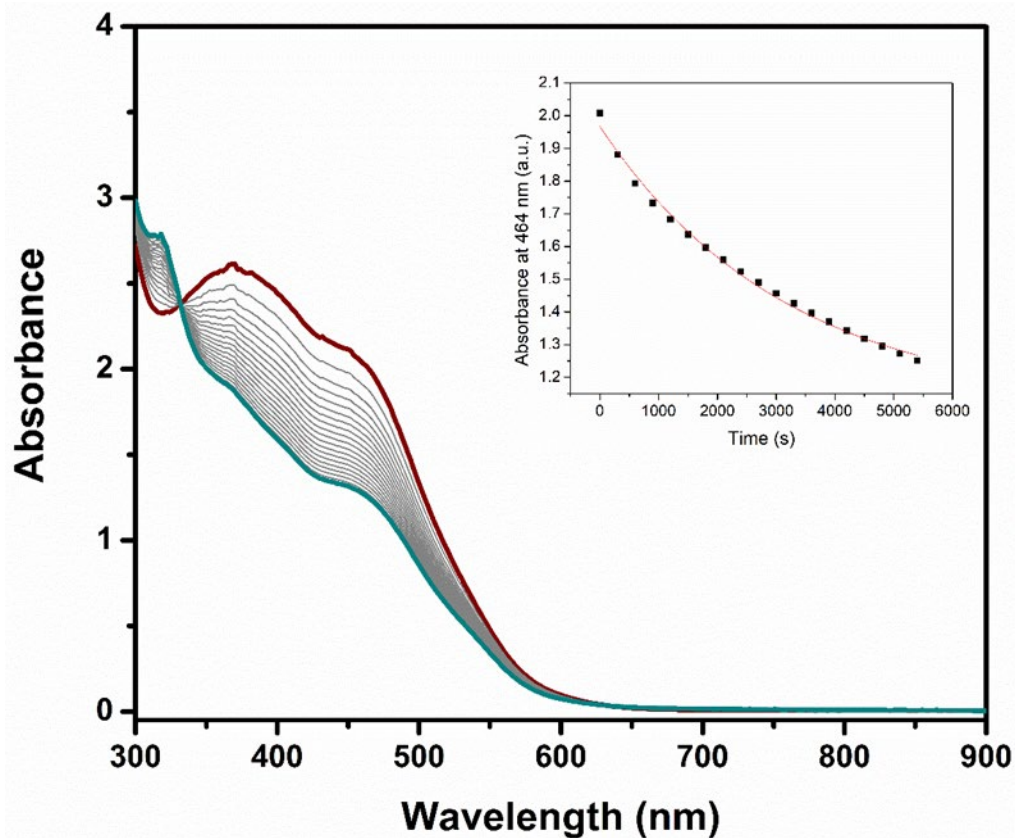


Figure A3.42 UV-vis traces of the reaction between $\text{Ni}(\text{COD})_2$ (0.36 mM), 4 equivalents of **K1**, and 21 equivalents of C_6F_6 in THF at RT, with scans taken every 5 minutes for a total of 90 minutes; the spectrum for the first scan is maroon and the spectrum for the last scan is teal. Inset: Exponential fit to the decay of the absorbance at 464 nm with the equation $y=y_0+A*\exp(R_0*x)$. The fit values are $y_0 = 1.110(35)$, $A=0.857(30)$, and $R_0 = -3.14\text{E-}4(2.69\text{E-}5)$. The k_{obs} determined from this fit is $-3.1\text{E-}4 \text{ s}^{-1}$.

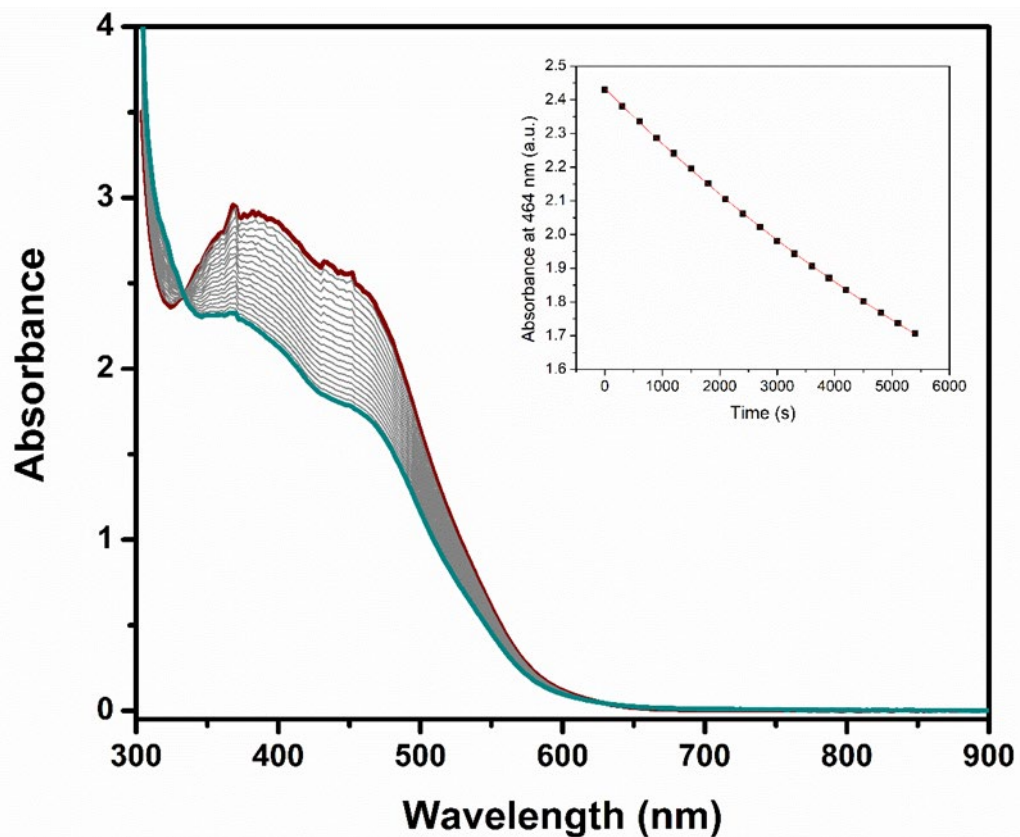


Figure A3.43 UV-vis traces of the reaction between $\text{Ni}(\text{COD})_2$ (0.36 mM), 8 equivalents of K1 , and 21 equivalents of C_6F_6 in THF at RT, with scans taken every 5 minutes for a total of 90 minutes; the spectrum for the first scan is maroon and the spectrum for the last scan is teal. Inset: Exponential fit to the decay of the absorbance at 464 nm with the equation $y=y_0+A*\exp(R_0*x)$. The fit values are $y_0 = 0.609(48)$, $A=1.825(47)$, and $R_0 = -9.44\text{E}-5(3.20\text{E}-6)$. The k_{obs} determined from this fit is $-9.4\text{E}-5 \text{ s}^{-1}$.

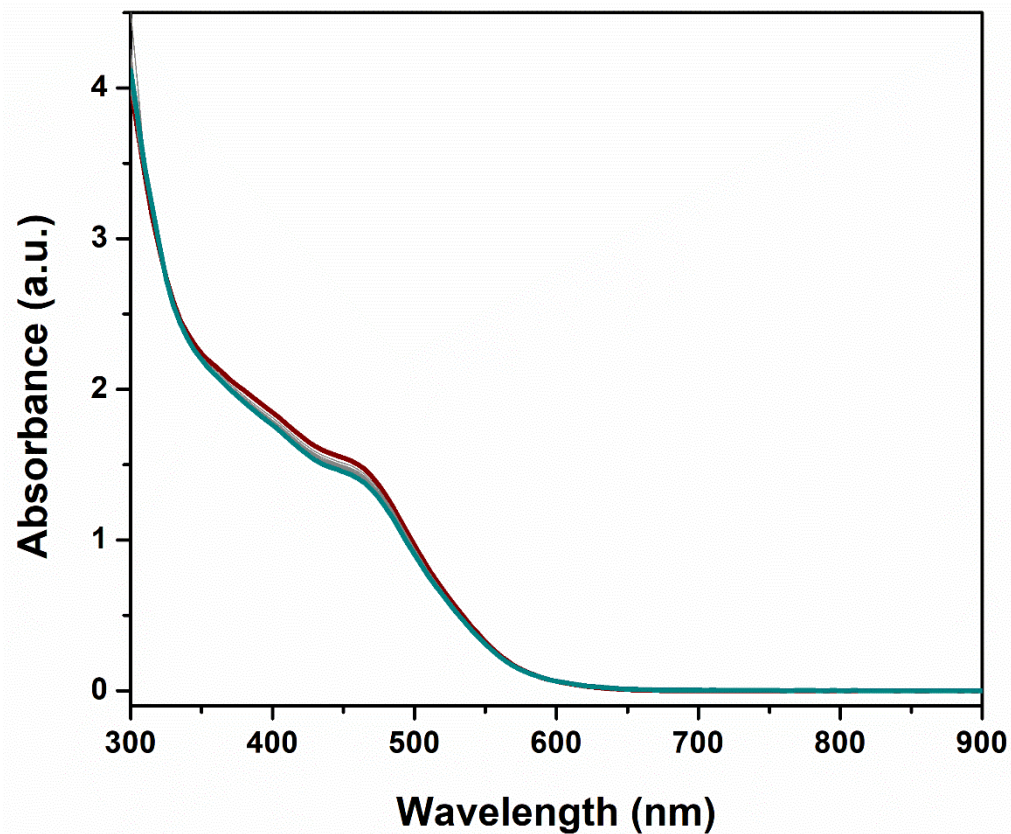


Figure A3.44 UV-vis traces of the reaction of Ni(COD)₂ and K1 without C₆F₆ in THF at RT, with scans taken every 5 minutes for a total of 70 minutes; the spectrum for the first scan is maroon and the spectrum for the last scan is teal.

A3.4 X-Ray Crystallography

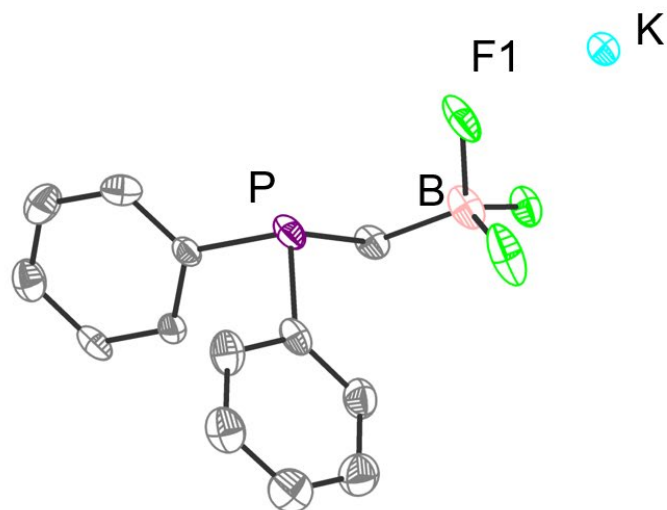


Figure A3.45 SXR structure of K1 with K^+ counterion shown.

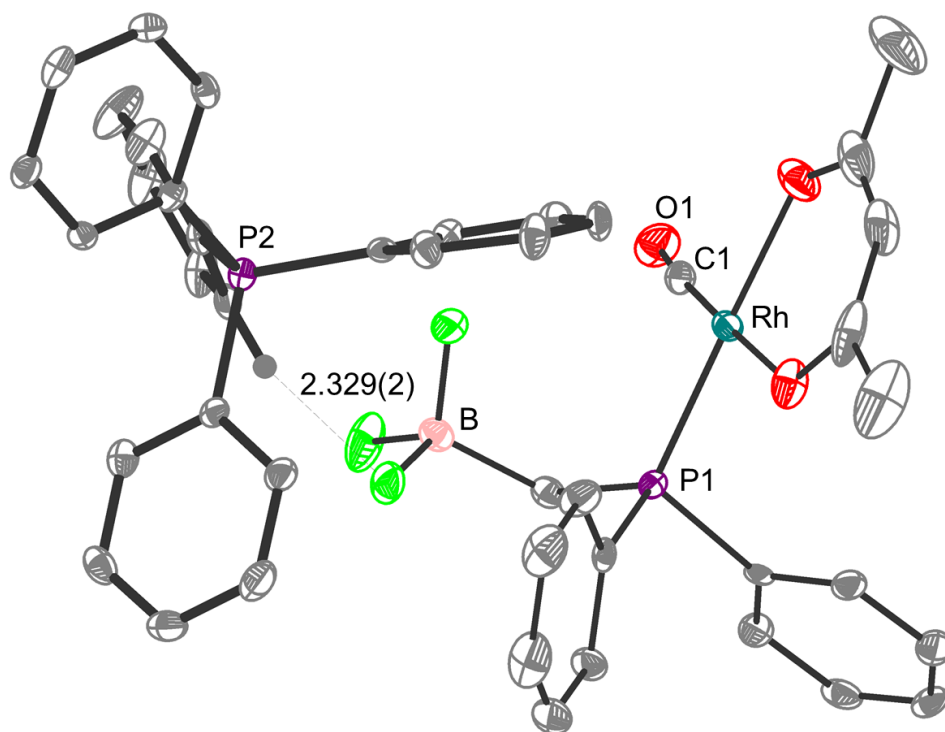


Figure A3.46 SXR structure of **2** with PPh_4^+ counterion shown. H-bonding interaction between BF_3 and PPh_4 indicated by a dashed line. Two independent molecules of $Rh(acac)(CO)(PPh_2(CH_2BF_3))$ are present in the asymmetric unit. The closest H-bonding interaction between the second molecule and PPh_4 is 2.303(2) Å.

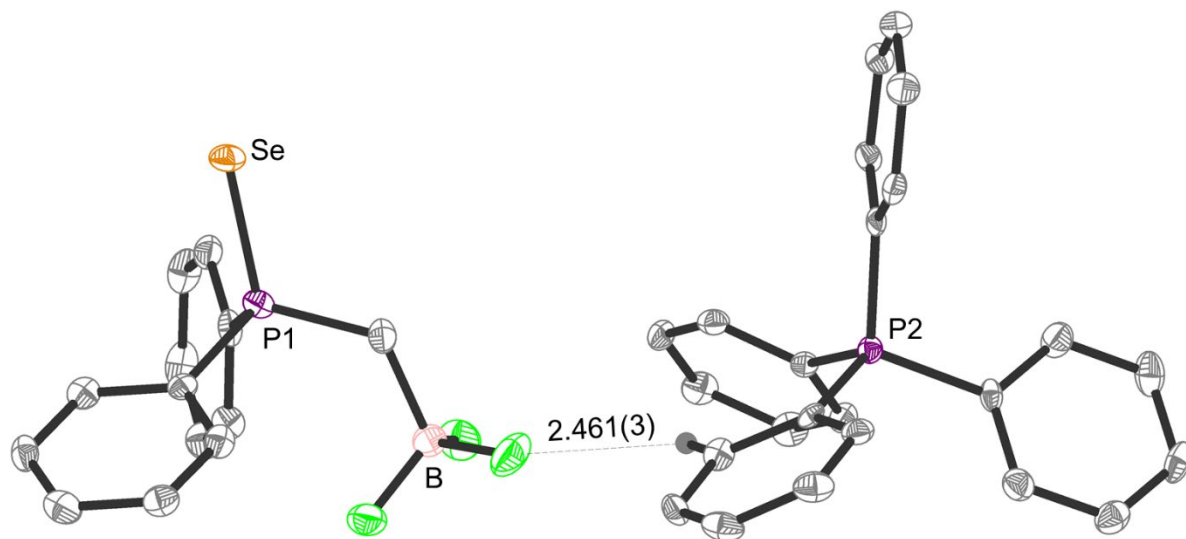


Figure A3.47 SXR structure of $[\text{PPh}_4][\mathbf{1}^{\text{Se}}]$ with PPh_4^+ counterion shown. H-bonding interaction between BF_3 and PPh_4 indicated by a dashed line.

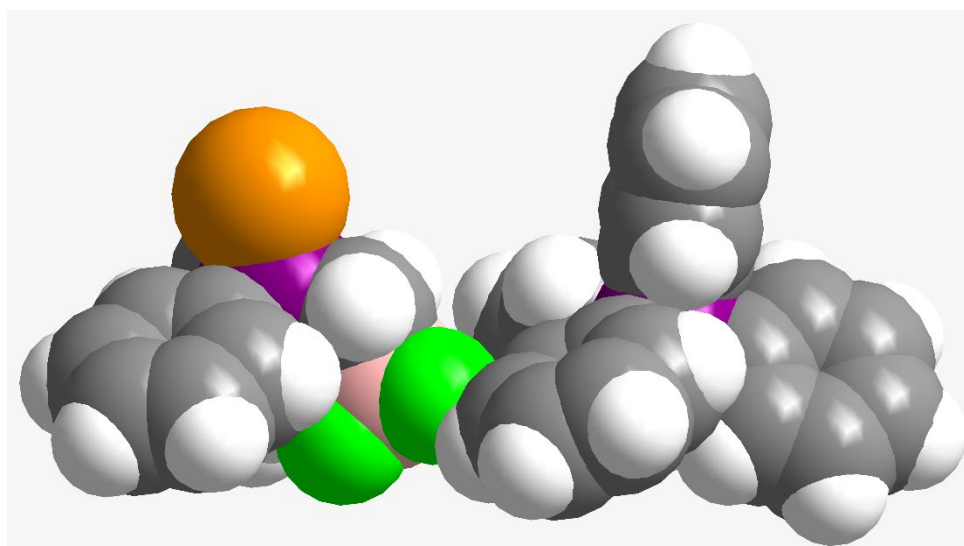


Figure A3.48 Space filling model of the SXR structure of $[\text{PPh}_4][\mathbf{1}^{\text{Se}}]$ with PPh_4^+ counterion shown.

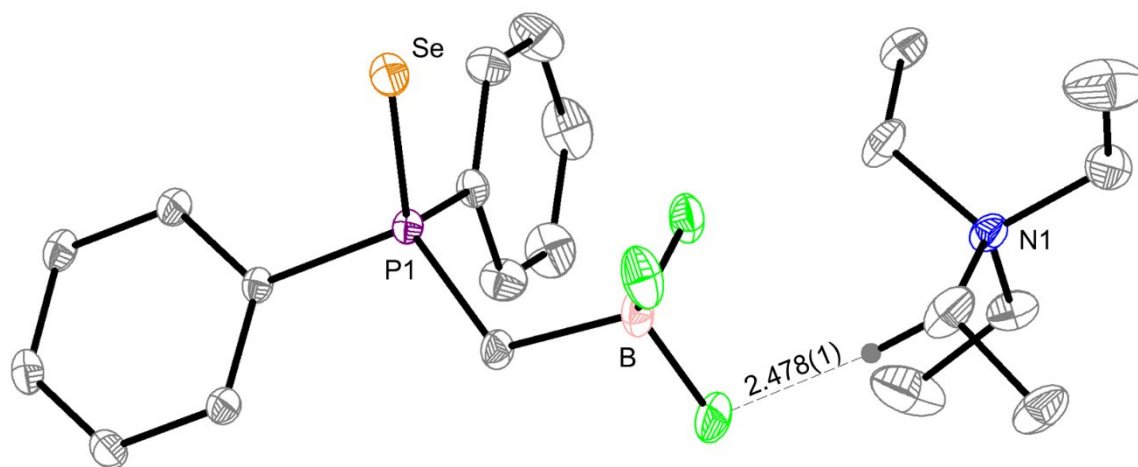


Figure A3.49 SXR structure of $[\text{TEA}][1^{\text{Se}}]$ with TEA^+ counterion shown. H-bonding interaction between BF_3 and TEA indicated by a dashed line.

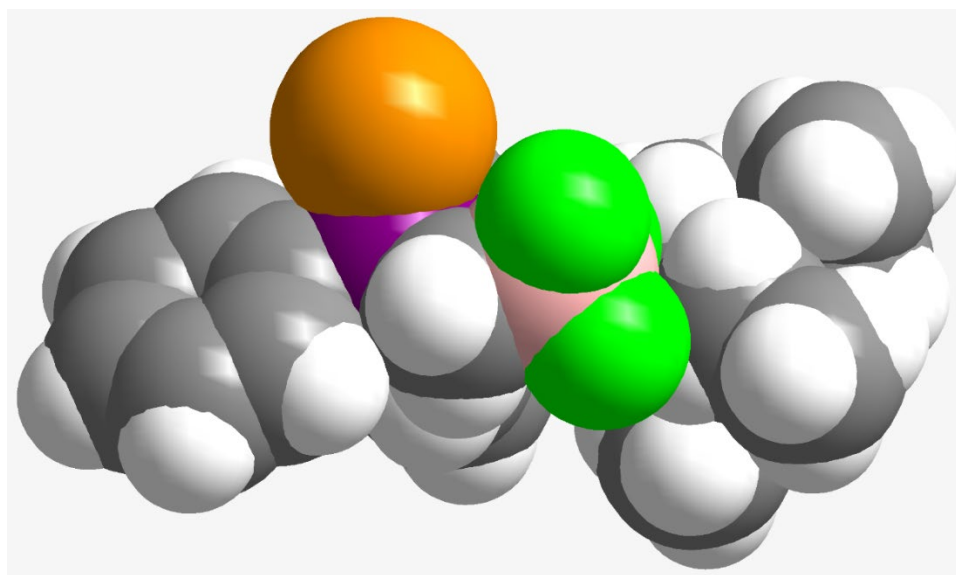


Figure A3.50 Space filling model of the SXR structure of $[\text{TEA}][1^{\text{Se}}]$ with TEA^+ counterion shown.

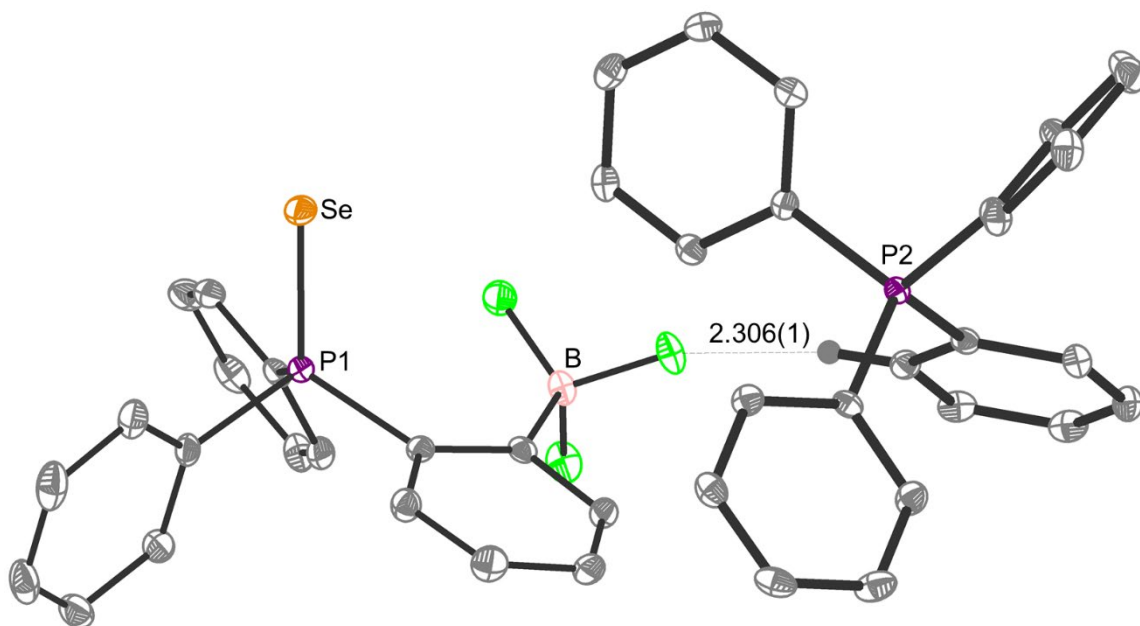


Figure A3.51 SXR structure of $[\text{PPh}_4][3^{\text{Se}}]$ with PPh_4^+ counterion shown. H-bonding interaction between BF_3 and PPh_4 indicated by a dashed line.

	K1	2	$[\text{PPh}_4][1^{\text{Se}}]$	$[\text{TEA}][1^{\text{Se}}]$	$[\text{PPh}_4][3^{\text{Se}}]$
B-P2	2.858(3)	5.685(3)	6.283(6)	-	5.895(2)
B-N1				4.766(2)	
Se-P1	-	-	2.129(1)	2.1124(4)	2.112(5)
P1-B	-	3.006(4)	3.029(6)	2.894(2)	3.562(2)
Se-B			4.848(6)	3.758(2)	4.530(2)
B-K	3.272(3)	-	-	-	-
Rh-C1	-	1.797(3)	-	-	-
B-C1	-	3.719(5)	-	-	-
B-Rh	-	4.150(4)	-	-	-
B-O	-	3.955(4)	-	-	-

Table A3.1 Selected average bond lengths for SXR structures.

Identification code	K1	2	[PPh ₄][1 ^{Se}]
Empirical formula	C ₁₅ H ₁₆ BF ₃ KO _{0.5} P	C ₄₃ H ₃₉ BF ₃ O ₃ P ₂ Rh	C _{36.96} H _{31.91} B _{0.95} F _{2.87} I _{0.05} P ₂ Se _{0.95}
Formula weight	342.21	836.40	683.86
Temperature/K	100(2)	100(2)	100(2)
Crystal system	triclinic	Triclinic	Orthorhombic
Space group	P-1	P-1	Pna2 ₁
a/Å	5.6907(4)	9.1533(6)	14.5444(7)
b/Å	21.5917(16)	13.0253(9)	19.8328(10)
c/Å	26.847(2)	33.273(2)	11.0256(6)
α/°	78.847(2)	83.172(2)	90
β/°	89.976(2)	88.634(2)	90
γ/°	89.948(2)	79.181(2)	90
Volume/Å ³	3231.9(4)	3868.8(4)	3180.4(3)
Z	8	4	4
ρ _{calc} /cm ³	1.407	1.436	1.428
μ/mm ⁻¹	0.450	0.578	1.316
F(000)	1408.0	1712.0	1396
Crystal size/mm ³	0.35 × 0.25 × 0.09	0.47 × 0.26 × 0.17	0.42 × 0.14 × 0.138
Radiation	MoKα (λ = 0.71073)	MoKα (λ = 0.71073)	MoKα (λ = 0.71073)
2θ range for data collection/°	3.96 to 46.752	4.53 to 48.298	4.226 to 52.934
Index ranges	-6 ≤ h ≤ 6, -24 ≤ k ≤ 24, -29 ≤ l ≤ 29	-10 ≤ h ≤ 9, -14 ≤ k ≤ 14, -37 ≤ l ≤ 38	-18 ≤ h ≤ 18, -24 ≤ k ≤ 24, -13 ≤ l ≤ 13
Reflections collected	54508	43102	82448
Independent reflections	9397 [R _{int} = 0.0722, R _{sigma} = 0.0549]	12044 [R _{int} = 0.0802, R _{sigma} = 0.0838]	6480 [R _{int} = 0.0748, R _{sigma} = 0.0434]
Data/restraints/parameters	9397/2441/1070	12044/0/959	6480/13/407
Goodness-of-fit on F ²	1.016	1.014	1.071
Final R indexes [I ≥ 2σ (I)]	R ₁ = 0.0430, wR ₂ = 0.0798	R ₁ = 0.0424, wR ₂ = 0.0703	R ₁ = 0.0401, wR ₂ = 0.0744
Final R indexes [all data]	R ₁ = 0.0748, wR ₂ = 0.0897	R ₁ = 0.0840, wR ₂ = 0.0802	R ₁ = 0.0545, wR ₂ = 0.0788
Largest diff. peak/hole / e Å ⁻³	0..0/-0.26	0.72/-0.53	1.13/-0.32
Flack parameter	-	-	0.015(4)

Identification code	[TEA][1 ^{Se}]	[PPh ₄][3 ^{Se}]
Empirical formula	C ₂₁ H ₃₂ BF ₃ NPSe	C ₄₂ H ₃₄ BF ₃ P ₂ Se
Formula weight	476.2	747.40
Temperature/K	100(2)	100(2)
Crystal system	orthorhombic	triclinic
Space group	Pca21	P-1
a/Å	18.1513(9)	9.6724(5)
b/Å	10.6673(5)	12.8821(6)
c/Å	11.7071(6)	14.5407(7)
α/°	90	84.9610(10)
β/°	90	77.687(2)
γ/°	90	74.085(2)
Volume/Å ³	2266.8(2)	1701.43(15)
Z	4	2
ρ _{calc} /cm ³	1.390	1.459
μ/mm ⁻¹	1.722	1.245
F(000)	981	764.0
Crystal size/mm ³	0.433 × 0.259 × 0.165	0.303 × 0.218 × 0.13
Radiation	MoKα (λ = 0.71073)	MoKα (λ = 0.71073)
2θ range for data collection/°	4.428-62.256	4.466 to 56.758
Index ranges	-26 ≤ h ≤ 26, -15 ≤ k ≤ 15, -16 ≤ l ≤ 17	-12 ≤ h ≤ 12, -17 ≤ k ≤ 17, -19 ≤ l ≤ 19
Reflections collected	59551	62543
Independent reflections	7176 [R _{int} = 0.0245, R _{sigma} = 0.026]	8501 [R _{int} = 0.0322, R _{sigma} = 0.0207]
Data/restraints/parameters	7176/1/258	8501/0/442
Goodness-of-fit on F ²	1.082	1.074
Final R indexes [I ≥ 2σ (I)]	R ₁ = 0.0204, wR ₂ = 0.0518	R ₁ = 0.0293, wR ₂ = 0.0701
Final R indexes [all data]	R ₁ = 0.0219, wR ₂ = 0.0523	R ₁ = 0.0353, wR ₂ = 0.0727
Largest diff. peak/hole / e Å ⁻³	0.64/-0.15	0.55/-0.32
Flack parameter		

Table A3.2 Refinement data for crystal structures of K1, 2, [PPh₄][1^{Se}], [TEA][1^{Se}], and [PPh₄][3^{Se}].

A3.5 Calculations

A3.5.1 Matlab Code for Estimating Electric Field Using Coulombs Law

```
%Electric field at P - defining coordinates - transoid
Px = 0;
Py = 0;
Pz = 0;
Bx = 1.07559/10^10; %enter position in Å, converts to m
By = 1.88457/10^10;
Bz = -2.23090/10^10;
CP = 9E9; %constant of proportionality, units in Vm/C
elec = -1.60218E-19; %electron charge in C

%defining distances
PB = (Px-Bx)^2 + (Py-By)^2 + (Pz-Bz)^2;
rPB = PB^(3/2);

%electric field at P from transoid B1 in V/m
EBx = CP*elec*(Px-Bx)/rPB;
EBy = CP*elec*(Py-By)/rPB;
EBz = CP*elec*(Pz-Bz)/rPB;

%electric field from far B1 in V/Å
EVAx = EBx/10^10;
EVAy = EBy/10^10;
EVAz = EBz/10^10;

%electric field from far B1 in atomic units
Eaux = EVAx/51.4;
Eauy = EVAy/51.4;
Eauz = EVAz/51.4;

%summary/output
EVm = [EBx, EBy, EBz] %x,y,z components of electric field in V/m
EVA = [EVAx, EVAy, EVAz] %x,y,z components of electric field in V/Å
Eau = [Eaux, Eauy, Eauz] %x,y,z components of electric field in atomic
units
```

A3.5.2 Optimized Structures

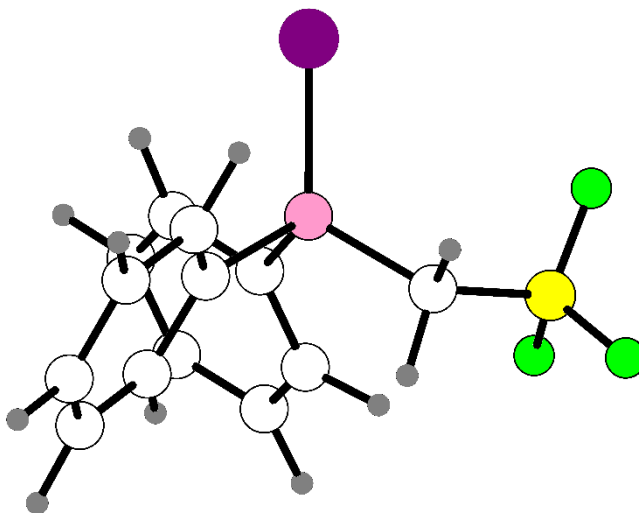


Figure A3.52 Calculated structure of 1^{Sc} (cisoid structure).

P	0.00000	0.00000	-0.00000
C	0.79176	-1.51897	-0.68167
C	-1.68430	-0.09969	-0.70597
C	0.95751	1.26436	-0.84601
C	-2.03216	0.57473	-1.87230
C	-3.30535	0.44636	-2.40740
C	-4.24520	-0.36639	-1.78539
C	-3.90466	-1.03762	-0.61612
C	-2.63696	-0.90181	-0.07134
C	0.34564	-2.11211	-1.86055
C	1.04760	-3.15788	-2.44199
C	2.20703	-3.64068	-1.84793
C	2.64957	-3.06779	-0.65874
C	1.94911	-2.01469	-0.08495
H	-0.54693	-1.73898	-2.35402
H	0.69672	-3.58365	-3.37695
H	2.76413	-4.44933	-2.31062
H	3.55125	-3.43509	-0.17762
H	2.29796	-1.55965	0.83836
H	-1.32880	1.27805	-2.30439
H	-3.56414	0.99679	-3.30539
H	-5.24242	-0.46288	-2.20361
H	-4.64233	-1.66290	-0.11985

H	-2.37684	-1.39091	0.86300
B	0.52958	2.85487	-0.94860
H	1.08297	0.90777	-1.87581
H	1.93004	1.18075	-0.34921
F	-0.65839	3.01138	-1.70523
F	1.56441	3.48557	-1.66849
F	0.38517	3.40672	0.32000
Se	0.00000	0.00000	2.11743

Table A3.3 Coordinates of optimized structure of 1^{Se} (cisoid structure)

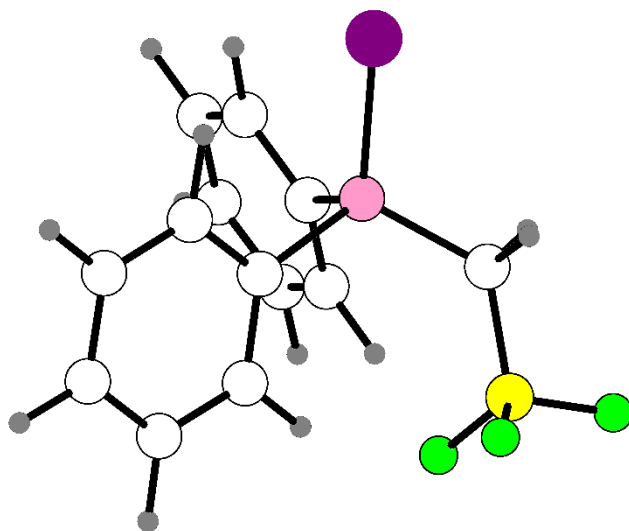


Figure A3.53 Calculated structure of 1^{Se} with the BF_3 group rotated down (transoid structure).

P	0.00000	0.00000	-0.00000
C	0.99330	-1.39843	-0.66597
C	-1.67140	-0.40144	-0.64511
C	0.47747	1.57885	-0.70985
C	-2.05904	-0.01528	-1.93709
C	-3.32542	-0.36388	-2.41501
C	-4.20617	-1.10123	-1.62104
C	-3.82135	-1.48343	-0.33348
C	-2.56304	-1.12866	0.15402
C	1.22296	-1.52383	-2.04616
C	1.83822	-2.67280	-2.54698
C	2.23379	-3.69978	-1.68536
C	2.03814	-3.56165	-0.30944

C	1.42154	-2.41535	0.19733
H	0.92192	-0.72323	-2.72719
H	2.00752	-2.76313	-3.62528
H	2.69143	-4.61047	-2.08801
H	2.36104	-4.35360	0.37473
H	1.24876	-2.29177	1.27209
H	-1.36256	0.54441	-2.57044
H	-3.62385	-0.04992	-3.42069
H	-5.20049	-1.36658	-1.99654
H	-4.51353	-2.04700	0.30141
H	-2.25464	-1.39203	1.17180
B	1.07559	1.88457	-2.23090
H	1.24869	1.94613	-0.01093
H	-0.41508	2.20718	-0.53519
F	2.43491	1.57068	-2.27037
F	0.88434	3.24873	-2.48413
F	0.40887	1.14985	-3.26352
Se	0.00000	0.00000	2.14028

Table A3.4 Coordinates of calculated structure of edited 1^{Se} (transoid structure).

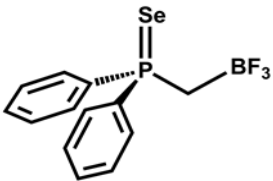
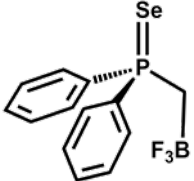
Structure	Electric Field at P from Coulomb's Law (x,y,z) (V/Å)	Electric Field at Se from Coulomb's Law (x,y,z) (V/Å)	Calculated J_{P-Se} (Hz)
 <p>Cisoid</p>	(0.2679, 1.4444, -0.4799)	(0.1014, 0.5467, -0.5872)	849
 <p>Transoid</p>	(0.5145, 0.9015, -1.0672)	(0.1334, 0.2338, -0.5423)	792

Table A3.5 Calculated electric field and J_{P-Se} for calculated structures of 1^{Se} .

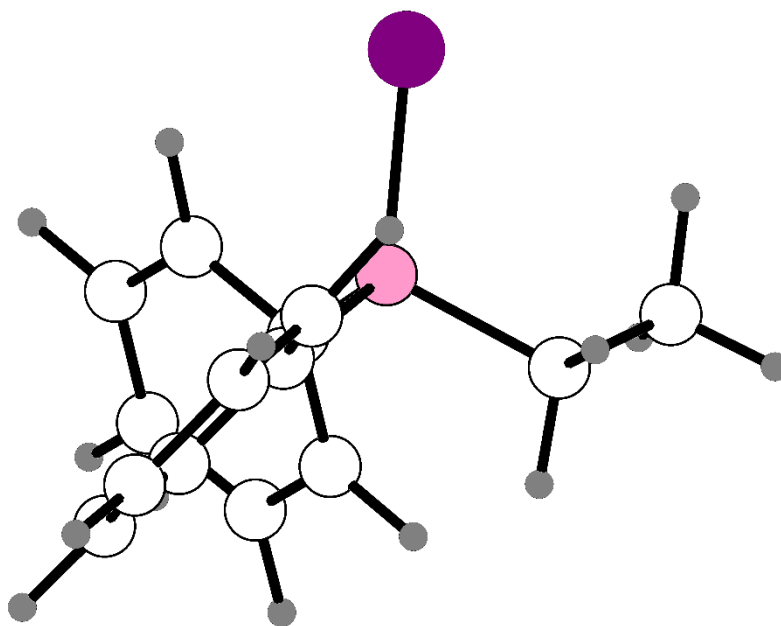


Figure A3.54 Optimized structure of SePPh₂Et.

P	-1.35788240879875	-0.13006160366219	0.01411152467337
C	0.46035043089732	-0.00894111268972	-0.11297709391472
C	-1.94517319766249	1.58601434389281	-0.16172337078438
C	-1.61801775841252	-0.61050169284086	1.76310436384687
C	-2.01014632290093	2.47292110281823	0.92410985893433
C	-2.41206155900290	3.79576392924933	0.72657268228532
C	-2.74084901275680	4.24437941334151	-0.55433651062815
C	-2.68265886616421	3.36481109808462	-1.63800769868336
C	-2.29720178239310	2.03882087923351	-1.44152423911476
C	1.13167743910790	1.22211021431696	-0.09833764454327
C	2.52599984121426	1.26309941428321	-0.17498367322925
C	3.25881284879158	0.07870400585500	-0.25496759670394
C	2.59497006687365	-1.15128021566608	-0.27269699876603
C	1.20289958940165	-1.19608897060009	-0.21338937206687
H	0.56785142998232	2.15646750575397	-0.03584727525056
H	3.04127036520655	2.22861672964623	-0.17613907033801
H	4.35118313528202	0.11411607368298	-0.31698548311317
H	3.16578660570770	-2.08138803595474	-0.34956853358883
H	0.67898692040419	-2.15558358314002	-0.27123364941962
H	-1.74109270514662	2.14154866229593	1.93092698724380
H	-2.47180495620726	4.47777195354649	1.57995780443591

H	-3.05874211021555	5.28023958410241	-0.70753760639855
H	-2.95473464600281	3.71205680917404	-2.63940545838434
H	-2.27331831816806	1.33201706440374	-2.27737773784354
C	-3.07492682591919	-0.83763875445270	2.14339590507861
H	-1.12647794003861	0.14336875047400	2.40307130334858
H	-1.02905993305891	-1.53660194524061	1.87501787192442
H	-3.65864309342022	0.09485089645599	2.08972538205654
H	-3.14747222882146	-1.22835025412969	3.17174579213329
H	-3.54324381001111	-1.56577579313832	1.46318209837571
Se	-2.23970119776762	-1.48167646909590	-1.34535256156543

Table A3.6 Coordinates of calculated structure of SePPh₂Et

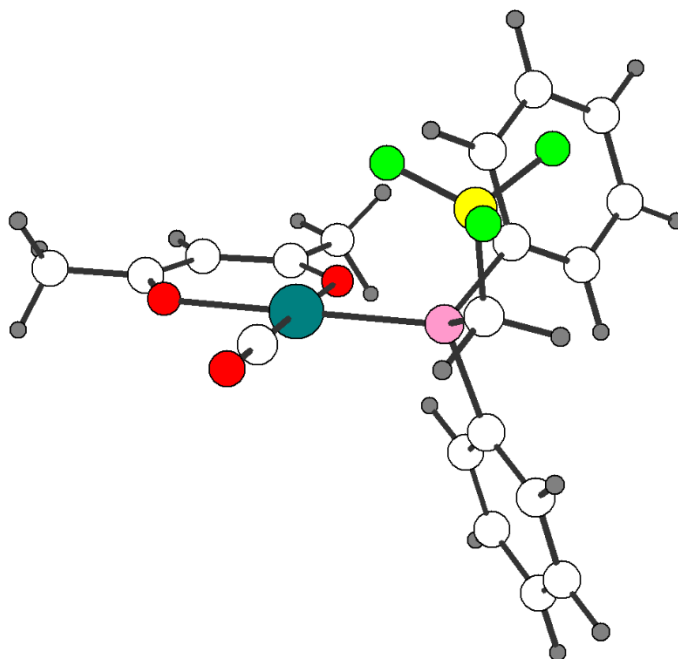


Figure A3.55 Optimized structure of **2**.

C	8.403788	17.368792	2.615641
P	9.705222	18.509041	3.115911
Rh	10.136258	18.933402	5.313363
C	11.221557	17.926186	2.268307
C	9.347099	20.115557	2.288545
O	12.057864	19.603935	4.821644
O	10.615003	19.337603	7.337524
C	8.446174	18.381288	5.731046

C	11.755851	18.531018	1.132847
C	10.200942	21.200914	2.513834
C	8.220460	20.311465	1.492247
C	12.970067	19.954472	5.623701
C	11.726087	19.727819	7.776966
O	7.383820	18.076726	6.041198
C	9.941245	22.438077	1.944732
C	7.951510	21.556867	0.932416
C	14.277143	20.329974	4.968282
C	12.872159	20.025527	7.017917
C	11.802153	19.879283	9.279178
C	8.811293	22.622504	1.153446
B	8.595388	15.744242	2.943153
F	7.324750	15.146053	2.848943
F	9.450987	15.161508	1.986774
F	9.128192	15.529631	4.230298
C	11.858493	16.802787	2.800076
C	12.910173	18.028815	0.541690
C	13.006304	16.301171	2.206666
C	13.539880	16.915029	1.079053
H	8.265032	17.454439	1.531862
H	7.484652	17.707179	3.107181
H	11.272738	19.401040	0.701904
H	11.071467	21.061570	3.147696
H	7.540607	19.486130	1.312565
H	10.616970	23.267955	2.129427
H	7.063383	21.690232	0.321928
H	14.120589	21.199587	4.322298
H	14.601816	19.508033	4.324507
H	15.059281	20.560440	5.693265
H	13.754680	20.343503	7.559616
H	11.578020	18.916231	9.746747
H	11.033490	20.584266	9.608231
H	12.779454	20.225718	9.619559
H	8.602193	23.593992	0.716399
H	11.432442	16.310556	3.667469
H	13.313992	18.511300	-0.343251
H	13.482115	15.419730	2.624111
H	14.440215	16.521415	0.617090

Table A3.7 Coordinates of calculated structure of **2**.

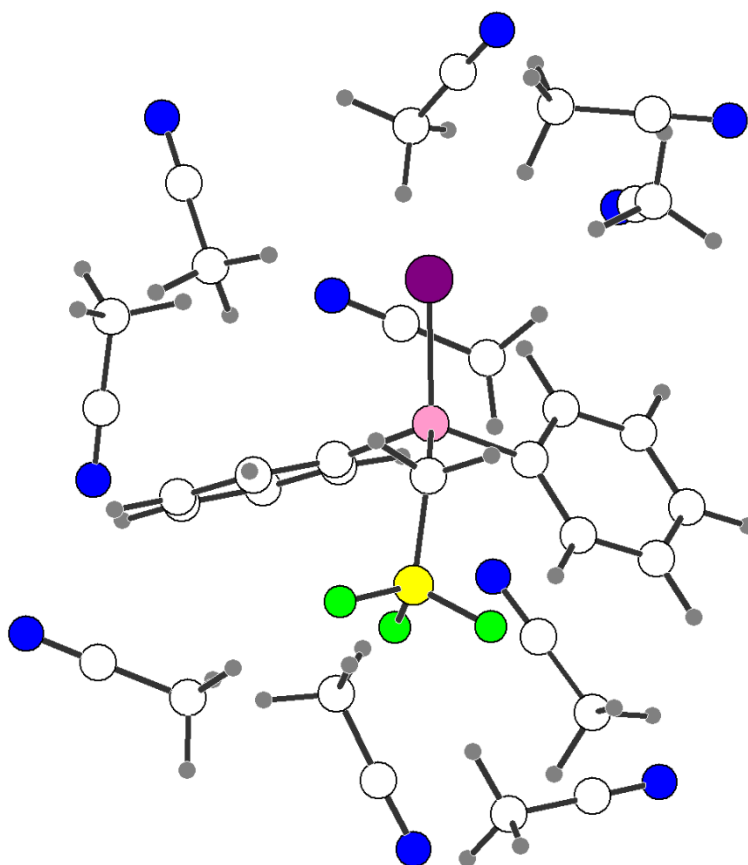


Figure A3.56 Optimized structure of 1^{Se} with explicit MeCN solvation.

P	-1.215603	-0.313816	-0.472603
Se	-0.452603	0.248122	-2.411729
C	-1.721581	-2.066081	-0.495162
C	-1.493133	-2.908706	0.602266
C	-1.822447	-4.263899	0.517415
C	-2.396733	-4.778258	-0.646201
C	-2.638699	-3.938294	-1.735938
C	-2.293813	-2.591119	-1.663500
C	-2.707716	0.674159	-0.128220
C	-3.966208	0.239733	-0.561081
C	-5.087875	1.052126	-0.388416
C	-4.962674	2.299978	0.226319
C	-3.708347	2.734752	0.667955
C	-2.584152	1.927887	0.490717
C	-0.040690	-0.059408	0.866975
B	-0.510147	-0.196130	2.450299

F	-0.170423	0.992445	3.149852
F	0.129594	-1.303411	3.063515
F	-1.933628	-0.398601	2.594030
H	-1.042836	-2.524385	1.514471
H	-1.633018	-4.910069	1.373390
H	-2.649734	-5.836958	-0.706282
H	-3.078320	-4.330834	-2.651482
H	-2.432730	-1.938092	-2.524644
H	-4.078742	-0.742407	-1.013860
H	-6.062973	0.708223	-0.728742
H	-5.843932	2.925502	0.362265
H	-3.604260	3.701942	1.158719
H	-1.613228	2.268975	0.846775
H	0.364301	0.946397	0.685159
H	0.783835	-0.753565	0.647108
C	-5.442646	-2.227617	-3.477505
C	-5.336566	-0.791763	-3.639717
N	-5.237553	0.358162	-3.768755
H	-5.378838	-2.489664	-2.411015
H	-4.631030	-2.716633	-4.035989
H	-6.407195	-2.575770	-3.868225
C	-2.440901	0.309633	-5.580876
C	-1.092308	0.070320	-6.055856
N	-0.006545	-0.133433	-6.416793
H	-3.113227	-0.472801	-5.950284
H	-2.802497	1.293150	-5.904573
H	-2.436771	0.277555	-4.481624
C	2.646389	-0.449481	-4.347672
C	3.094388	-1.828017	-4.419539
N	3.431963	-2.938858	-4.480810
H	1.996284	-0.223324	-5.205310
H	3.505315	0.232815	-4.348115
H	2.058545	-0.289982	-3.429966
C	-5.153169	-4.562444	1.811660
C	-5.385003	-3.618940	0.734791
N	-5.586309	-2.856525	-0.118124
H	-5.729211	-4.268714	2.697871
H	-4.091691	-4.581615	2.088111
H	-5.451597	-5.570295	1.497872
C	-2.835791	2.383102	4.145979
C	-2.954180	3.808661	3.899754
N	-3.052301	4.947176	3.686635
H	-3.520366	1.836220	3.487325
H	-3.082280	2.154222	5.190130

H	-1.819008	2.027970	3.925770
C	-2.999744	2.934914	-2.821018
C	-3.321985	3.440134	-4.139771
N	-3.590052	3.834529	-5.200567
H	-2.853144	3.760663	-2.115272
H	-2.083266	2.320936	-2.842279
H	-3.812313	2.293239	-2.459085
C	-2.203664	-2.654008	4.974889
C	-2.314015	-3.939191	4.313247
N	-2.413328	-4.964999	3.775761
H	-1.923030	-1.883856	4.243357
H	-1.428567	-2.694293	5.749690
H	-3.169898	-2.394630	5.425166
C	-0.182729	-2.966933	-4.418177
C	-1.554122	-3.073047	-4.870747
N	-2.663566	-3.140890	-5.211907
H	0.122377	-3.883151	-3.899510
H	-0.102686	-2.114996	-3.720387
H	0.485249	-2.791158	-5.268621
C	-6.671189	3.308174	-3.147741
C	-7.588852	3.012575	-2.061968
N	-8.314697	2.767618	-1.187945
H	-6.141664	2.393897	-3.452956
H	-5.933715	4.053741	-2.827386
H	-7.214467	3.707480	-4.012696
C	-5.084714	-0.537145	2.567380
C	-5.391995	-1.470471	3.632964
N	-5.627071	-2.236146	4.475949
H	-5.420149	-0.942859	1.606192
H	-3.999278	-0.375841	2.508936
H	-5.590123	0.421405	2.734982

Table A3.8 Coordinates of calculated structure of 1^{Sc} with explicit MeCN solvation.

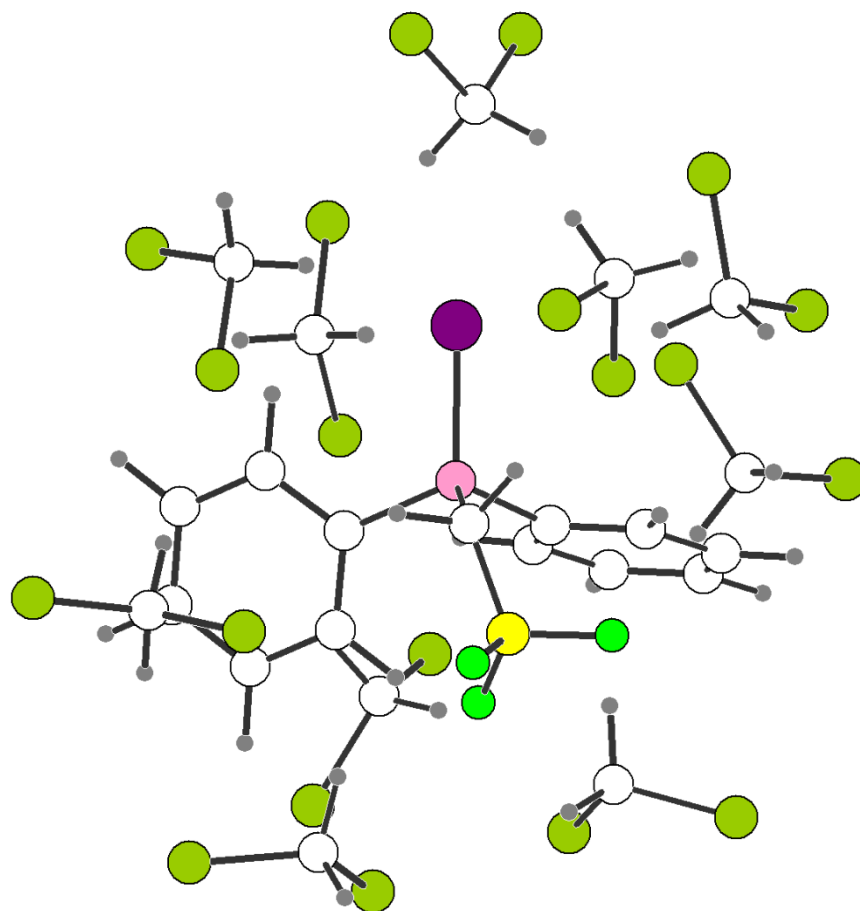


Figure A3.57 Optimized structure of 1^{Se} with explicit DCM solvation.

P	-2.116135	0.987532	0.229504
Se	-2.954463	1.797678	-1.590603
C	-2.211619	-0.819228	0.097613
C	-1.199681	-1.512743	-0.583168
C	-1.327655	-2.880182	-0.817747
C	-2.460240	-3.566243	-0.371599
C	-3.471556	-2.879047	0.301118
C	-3.353379	-1.508392	0.528257
C	-3.142849	1.423475	1.683769
C	-2.962926	0.773611	2.914702
C	-3.764508	1.112543	4.005726
C	-4.750135	2.096078	3.879420
C	-4.918992	2.755379	2.660553
C	-4.118243	2.418084	1.568166
C	-0.429676	1.536481	0.540890
B	0.601136	0.682627	1.516994
F	1.558246	1.567516	2.053702

F	1.277625	-0.331570	0.766092
F	-0.079381	0.026111	2.595216
H	-0.306879	-0.990106	-0.912205
H	-0.532284	-3.407411	-1.340748
H	-2.554500	-4.636278	-0.549579
H	-4.363747	-3.402020	0.639362
H	-4.166033	-0.967010	1.007772
H	-2.196765	0.009247	3.017397
H	-3.618122	0.597313	4.953447
H	-5.377294	2.350763	4.733140
H	-5.669714	3.538224	2.554478
H	-4.251388	2.915878	0.609153
H	-0.562279	2.552734	0.940396
H	0.019468	1.657384	-0.454670
C	-5.969608	-2.017039	-3.073064
Cl	-4.867755	-0.797309	-2.383457
Cl	-6.509231	-3.229418	-1.870345
H	-5.428153	-2.541982	-3.861552
H	-6.852393	-1.495185	-3.445252
C	-1.776886	-1.011407	-3.917404
Cl	-2.429335	-2.640982	-4.256854
H	-0.693943	-1.096877	-3.829627
Cl	-2.131210	0.151098	-5.227299
H	-2.243408	-0.627752	-3.006934
C	-0.674152	-2.993900	2.658287
H	-1.110806	-2.532898	1.774329
Cl	0.480158	-4.239721	2.117588
H	-0.147032	-2.266031	3.273509
Cl	-2.010733	-3.687959	3.632914
C	-2.002481	4.215974	3.938690
Cl	-2.123232	5.875905	4.605239
H	-2.294820	3.520950	4.725543
Cl	-0.359674	3.787055	3.417884
H	-2.657517	4.161415	3.069320
C	-5.220897	1.983551	-4.222838
Cl	-6.401445	1.189694	-5.309250
Cl	-4.958771	3.705000	-4.621753
H	-4.269922	1.459317	-4.325257
H	-5.618409	1.927105	-3.210437
C	-3.285165	5.288915	-0.760646
Cl	-2.103211	5.341202	0.572442
H	-3.066858	6.111391	-1.442497
Cl	-4.978068	5.488211	-0.201112

H	-3.202567	4.298299	-1.227013
C	2.116176	-0.180504	-2.177546
Cl	1.838264	-1.846233	-2.786698
H	3.132958	0.102526	-2.451499
Cl	0.994007	0.996050	-2.915390
H	1.946062	-0.185241	-1.095661
C	-5.163820	-1.906251	3.544488
Cl	-5.223204	-1.991502	5.326420
H	-5.416969	-0.888916	3.244560
Cl	-6.323073	-3.016733	2.760089
H	-4.157872	-2.193600	3.233289
C	-6.564644	1.303696	-0.250783
Cl	-7.724446	1.354494	-1.613141
H	-6.718805	2.199660	0.349914
Cl	-6.811969	-0.116883	0.797554
H	-5.554132	1.253672	-0.671819
C	-0.401302	0.743559	5.533800
Cl	-1.148778	-0.870641	5.670191
H	0.644896	0.662864	5.828554
Cl	-1.181494	1.938817	6.620227
H	-0.504369	1.081119	4.501752

Table A3.9 Coordinates of calculated structure of **1^{Se}** with explicit DCM solvation

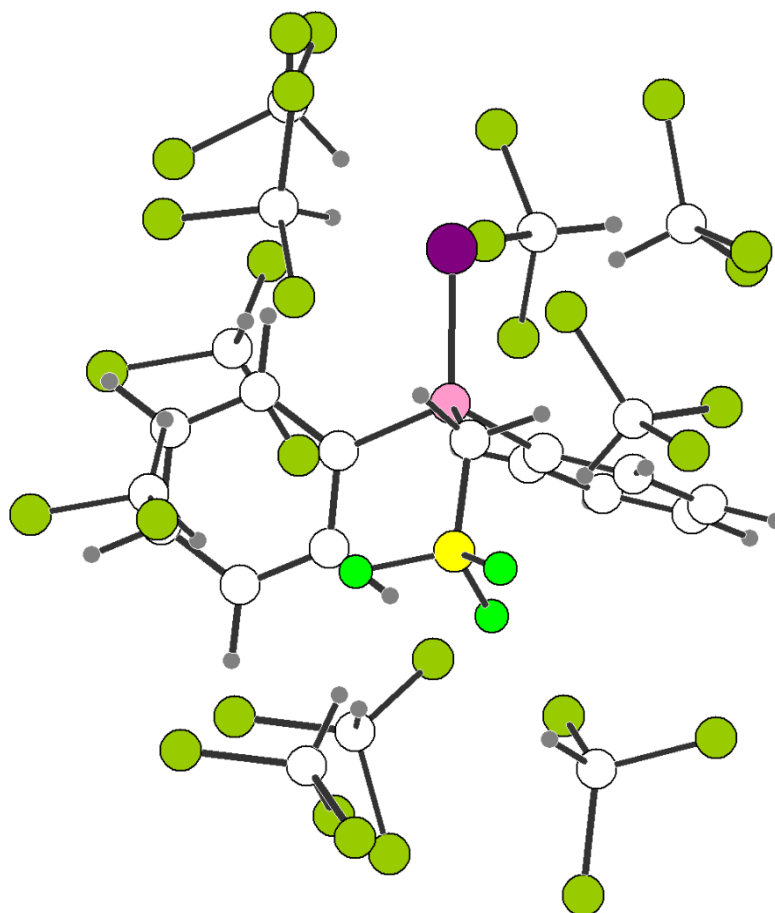


Figure A3.58 Optimized structure of 1^{Se} with explicit CHCl_3 solvation.

P	-2.134019	0.681238	-0.248353
Se	-2.814572	1.554850	-2.112141
C	-2.188081	-1.128495	-0.354260
C	-1.043674	-1.846713	-0.729424
C	-1.122565	-3.222700	-0.933965
C	-2.335810	-3.889513	-0.763018
C	-3.472790	-3.179021	-0.375973
C	-3.403720	-1.802579	-0.170604
C	-3.221703	1.159688	1.130046
C	-3.146912	0.493779	2.363223
C	-3.927119	0.937330	3.429986
C	-4.778828	2.033082	3.279469
C	-4.851725	2.694992	2.054560
C	-4.079132	2.254822	0.980534
C	-0.453351	1.191386	0.118386
B	0.197734	0.865369	1.589279
F	-0.287471	1.790162	2.558936
F	1.611634	0.978494	1.513798

F	-0.125592	-0.449842	2.058268
H	-0.091052	-1.338552	-0.857215
H	-0.229145	-3.773211	-1.222296
H	-2.393730	-4.965345	-0.923716
H	-4.422327	-3.693280	-0.242051
H	-4.293626	-1.253005	0.129152
H	-2.469349	-0.350867	2.484464
H	-3.859349	0.440735	4.395198
H	-5.377578	2.374401	4.121522
H	-5.505006	3.556699	1.931689
H	-4.132532	2.757930	0.015723
H	-0.465635	2.279180	-0.034577
H	0.142362	0.775196	-0.706034
C	-6.339653	-1.842635	-3.113674
Cl	-5.313514	-0.488811	-2.563738
Cl	-6.892051	-2.852374	-1.748532
H	-5.716602	-2.467821	-3.753964
Cl	-7.724154	-1.274897	-4.088006
C	-2.328466	-1.264991	-4.156277
Cl	-2.985679	-2.931279	-4.149064
Cl	-0.555143	-1.279999	-4.239926
Cl	-3.028756	-0.321761	-5.492509
H	-2.616468	-0.765964	-3.223374
C	0.010889	-3.197076	3.079611
Cl	0.326055	-3.892480	4.692052
Cl	1.078086	-3.938600	1.856622
Cl	-1.697584	-3.385802	2.621544
H	0.229050	-2.128625	3.099328
C	-1.938819	4.351160	3.135991
Cl	-0.338063	5.063819	3.443305
Cl	-3.197716	5.032447	4.217264
H	-1.873757	3.278007	3.313988
H	-2.224834	4.582792	2.109328
C	-5.937370	3.146280	-2.733193
Cl	-7.187171	2.527185	-3.831792
Cl	-4.918970	4.366598	-3.526750
H	-5.278578	2.320006	-2.438195
Cl	-6.669463	3.805247	-1.237050
C	-1.978869	4.970948	-1.241594
Cl	-0.510767	4.928049	-0.239278
Cl	-1.718897	5.938131	-2.716411
Cl	-3.362281	5.598708	-0.299382

H	-2.220991	3.940223	-1.545776
C	2.884976	1.225234	-1.218915
Cl	2.361311	-0.275269	-2.043871
Cl	4.666396	1.330431	-1.180932
Cl	2.174394	2.653910	-2.003281
H	2.518728	1.178121	-0.187717
C	-4.706603	-2.498081	4.264596
Cl	-6.035536	-1.523564	4.932598
Cl	-5.216461	-3.342919	2.780700
Cl	-4.080618	-3.643816	5.472684
H	-3.891716	-1.824938	3.994636
C	-7.352896	0.855192	0.532008
Cl	-8.409996	0.409612	-0.822728
Cl	-8.231549	1.880809	1.704523
Cl	-6.668396	-0.575215	1.330325
H	-6.525656	1.448142	0.140035
C	-0.772219	0.489478	5.208282
Cl	-1.738479	-0.980737	5.554662
Cl	0.899158	0.267979	5.765478
Cl	-1.522395	1.927819	5.942119
H	-0.745242	0.646119	4.127642

Table A3.10 Coordinates of calculated structure of **1^{Se}** with explicit CHCl₃ solvation

A3.6 Variable Solvent $^{31}\text{P}\{^1\text{H}\}$ NMR

A3.6.1 $[\text{PPh}_4][\text{I}^{\text{Se}}]$

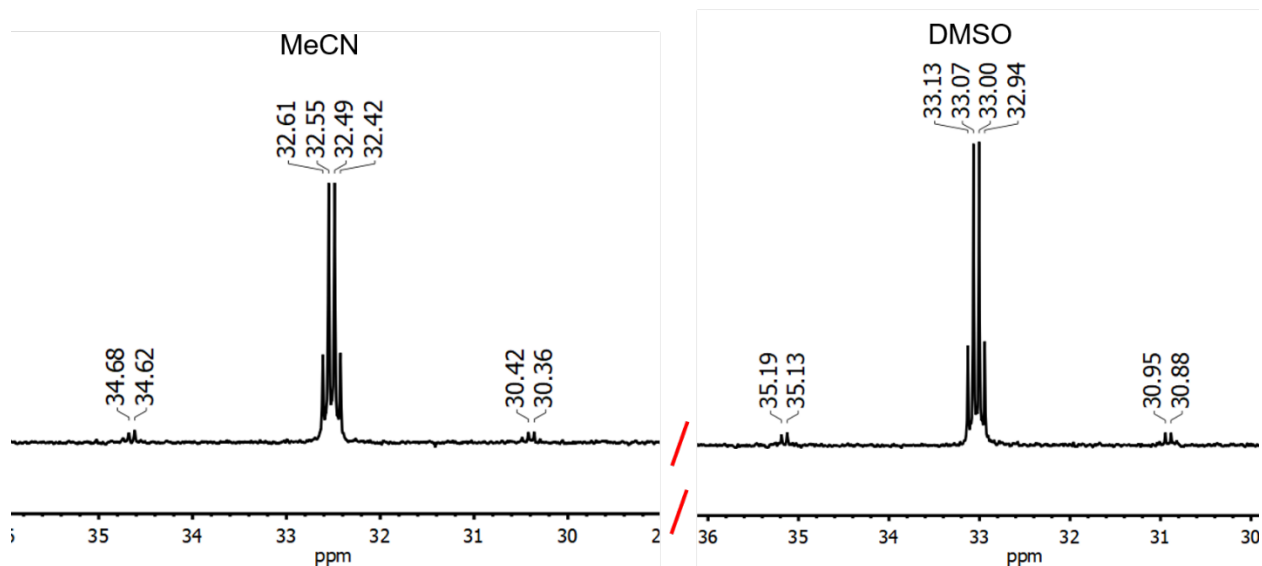


Figure A3.59 $^{31}\text{P}\{^1\text{H}\}$ NMR spectra of $[\text{PPh}_4][\text{I}^{\text{Se}}]$ in CD_3CN (left) and $\text{DMSO}-d_6$ (right) showing the P-Se phosphorus resonance.

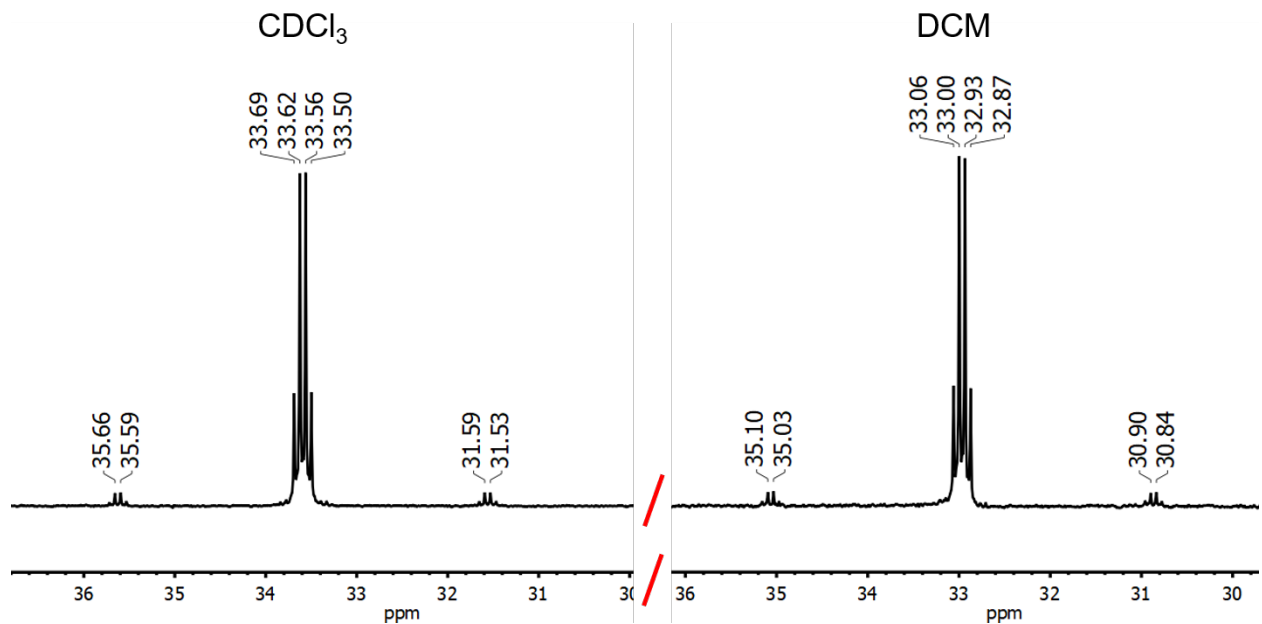


Figure A3.60 $^{31}\text{P}\{^1\text{H}\}$ NMR spectra of $[\text{PPh}_4][\text{I}^{\text{Se}}]$ in CDCl_3 (left) and CD_2Cl_2 (right) showing the P-Se phosphorus resonance.

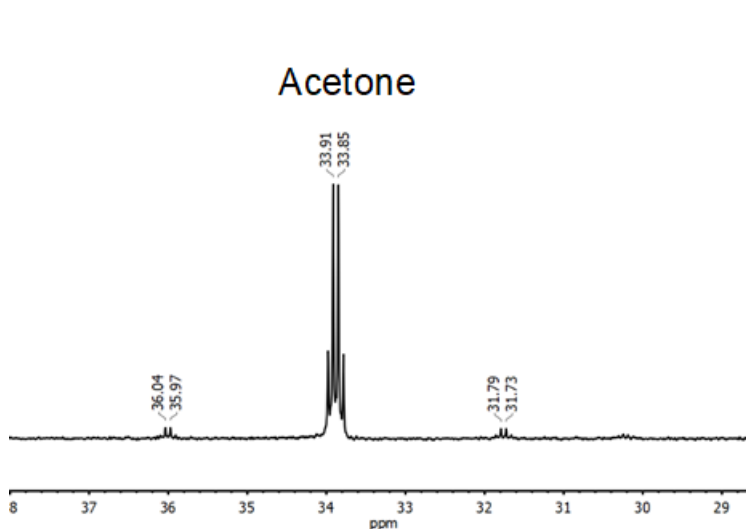


Figure A3.61 $^{31}\text{P}\{^1\text{H}\}$ NMR spectrum of $[\text{PPh}_4][\mathbf{1}^{\text{Se}}]$ in $(\text{CD}_3)_2\text{CO}$ showing the P–Se phosphorus resonance.

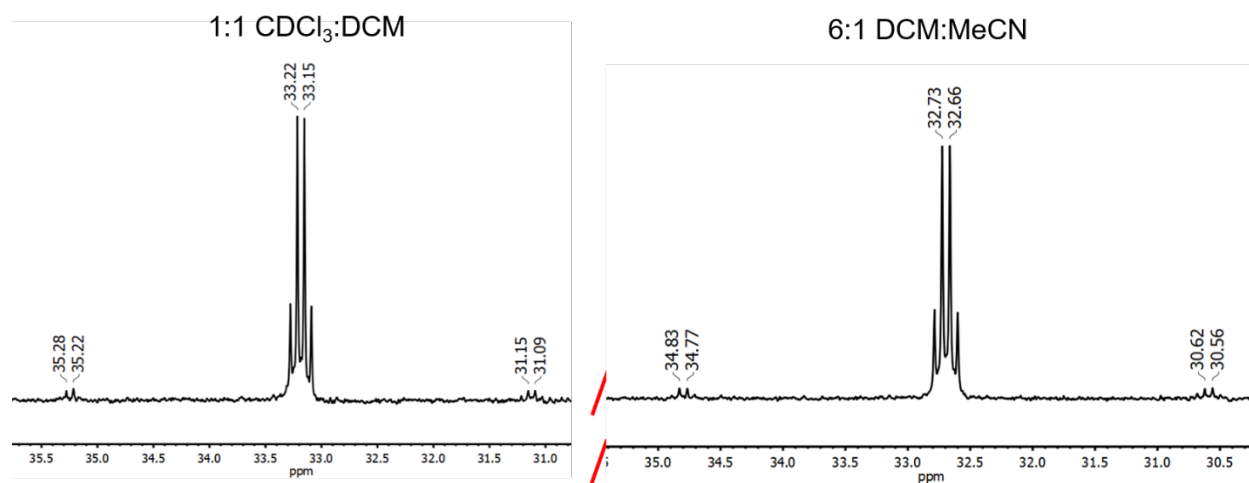


Figure A3.62 $^{31}\text{P}\{^1\text{H}\}$ NMR spectra of $[\text{PPh}_4][\mathbf{1}^{\text{Se}}]$ in the indicated solvent mixtures showing the P–Se phosphorus resonance.

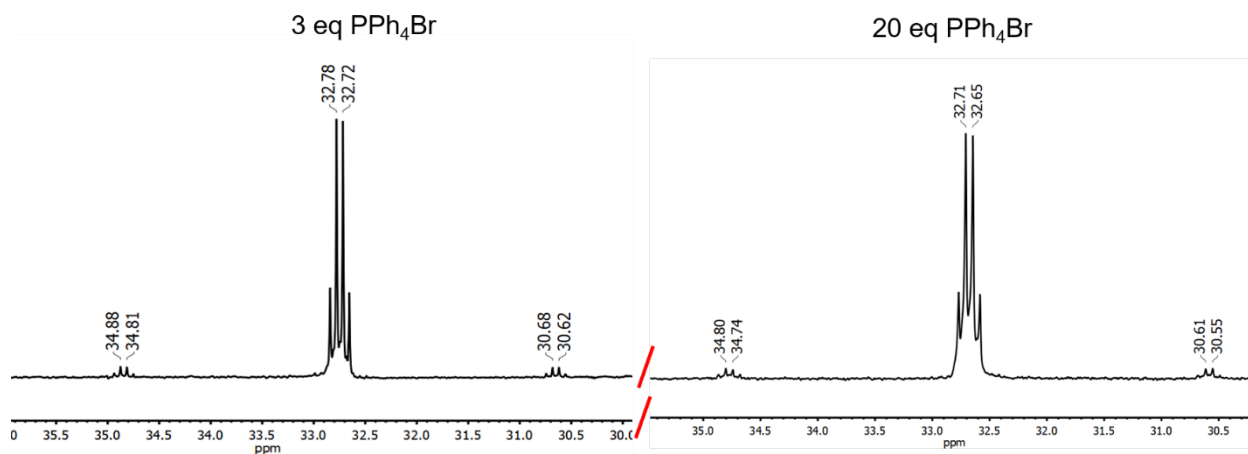


Figure A3.63 $^{31}\text{P}\{^1\text{H}\}$ NMR spectra of $[\text{PPh}_4][^1\text{Se}]$ in CH_2Cl_2 with addition of different equivalents of PPh_4Br . While the changing electrolyte concentration could influence the solvent dielectric, and hence the coupling constant, literature examples with tetra-alkyl ammonium salts suggest that very little change is expected for changing electrolyte concentration over this concentration range (~ 1 M) (ref 156, Chapter 3).

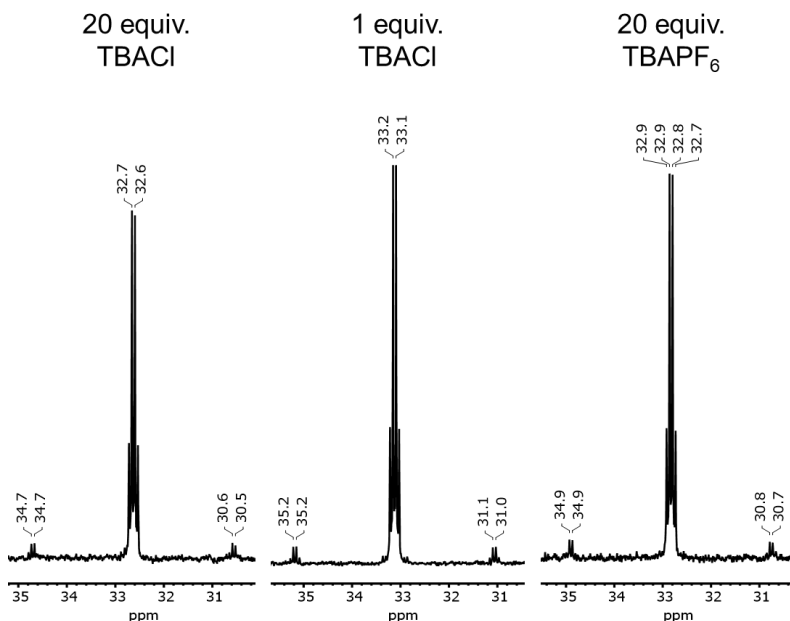


Figure A3.64 $^{31}\text{P}\{^1\text{H}\}$ NMR spectra of $[\text{PPh}_4][^1\text{Se}]$ in CDCl_3 with addition of tetrabutylammonium (TBA) salts.

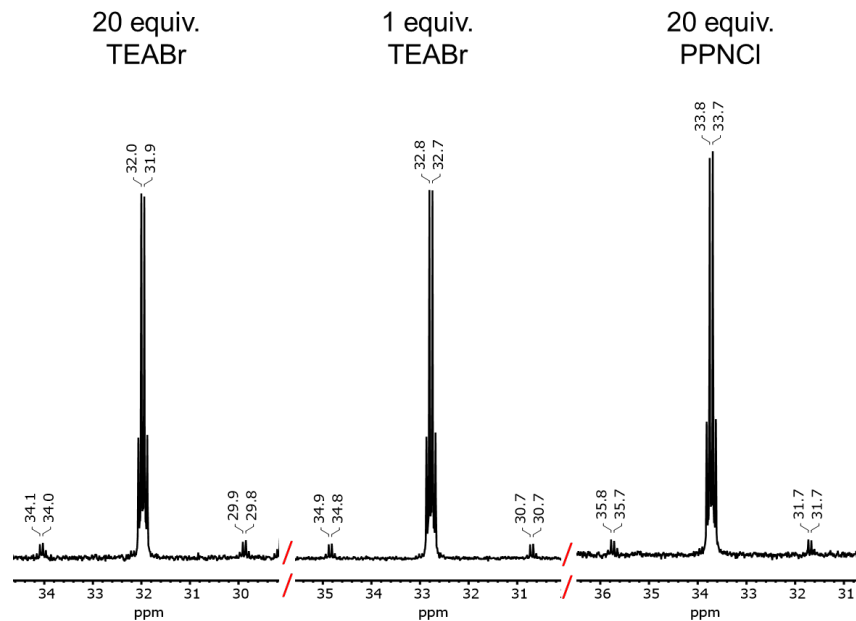


Figure A3.65 $^{31}\text{P}\{^1\text{H}\}$ NMR spectra of $[\text{PPh}_4][\mathbf{1}^{\text{Se}}]$ in CDCl_3 with addition of tetraethylammonium (TEA) and bis(triphenylphosphine)iminium (PPN) salts.

A3.6.2 $[\text{TEA}][\mathbf{1}^{\text{Se}}]$

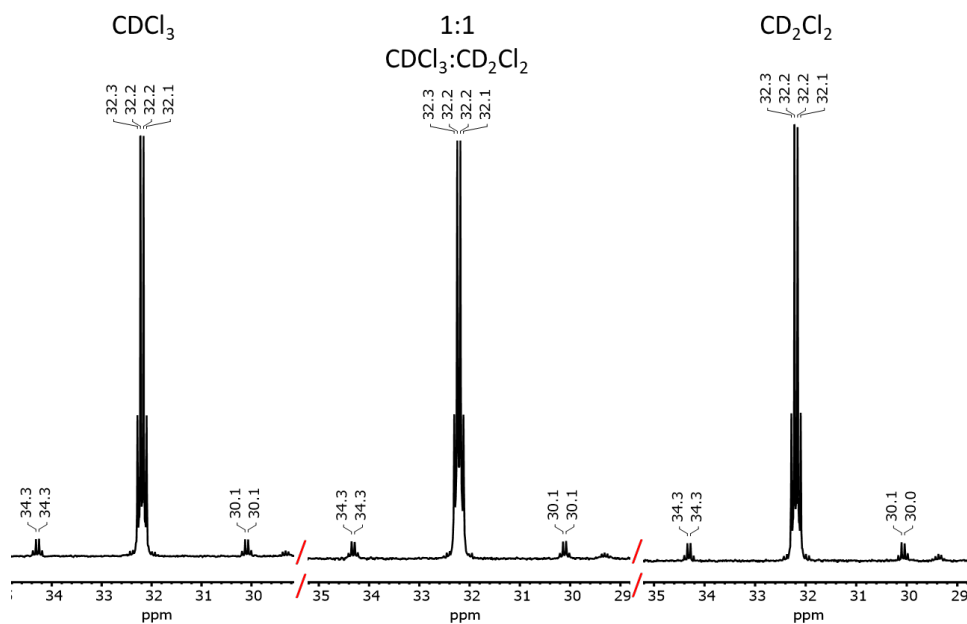


Figure A3.66 $^{31}\text{P}\{^1\text{H}\}$ NMR spectrum of $[\text{TEA}][\mathbf{1}^{\text{Se}}]$ in the indicated solvents showing the P-Se phosphorus resonance.

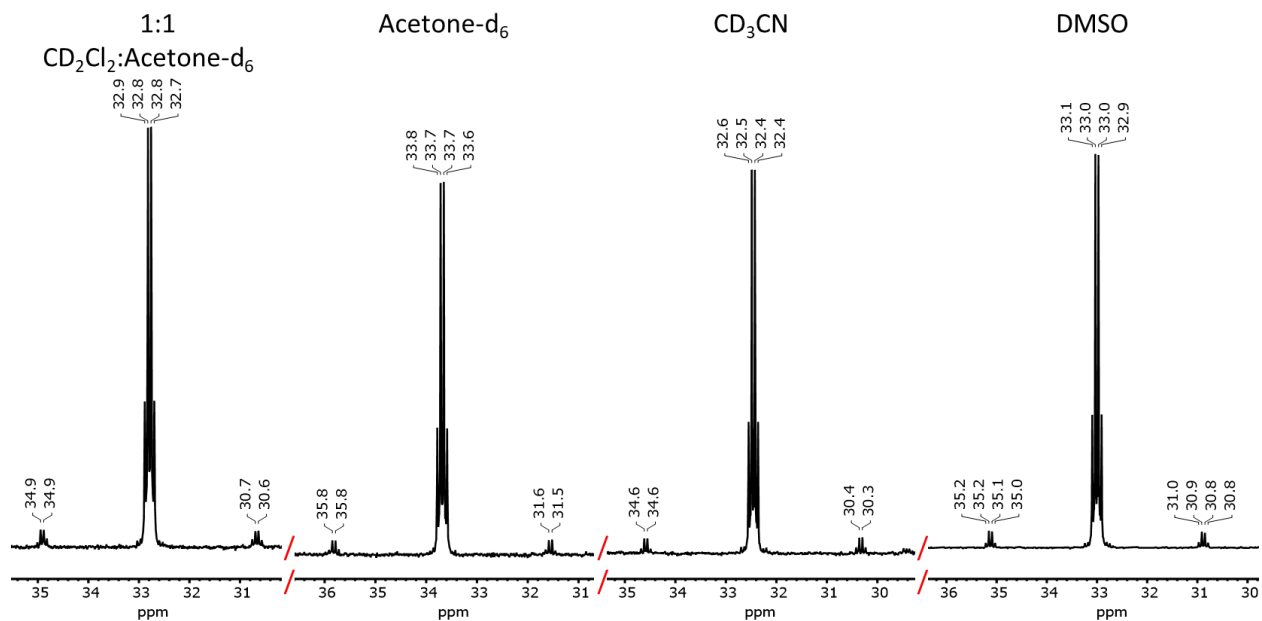


Figure A3.67 $^{31}\text{P}\{^1\text{H}\}$ NMR spectrum of $[\text{TEA}][^1\text{Se}]$ in the indicated solvents showing the P-Se phosphorus resonance.

A3.6.3 $[\text{PPh}_4][^3\text{Se}]$

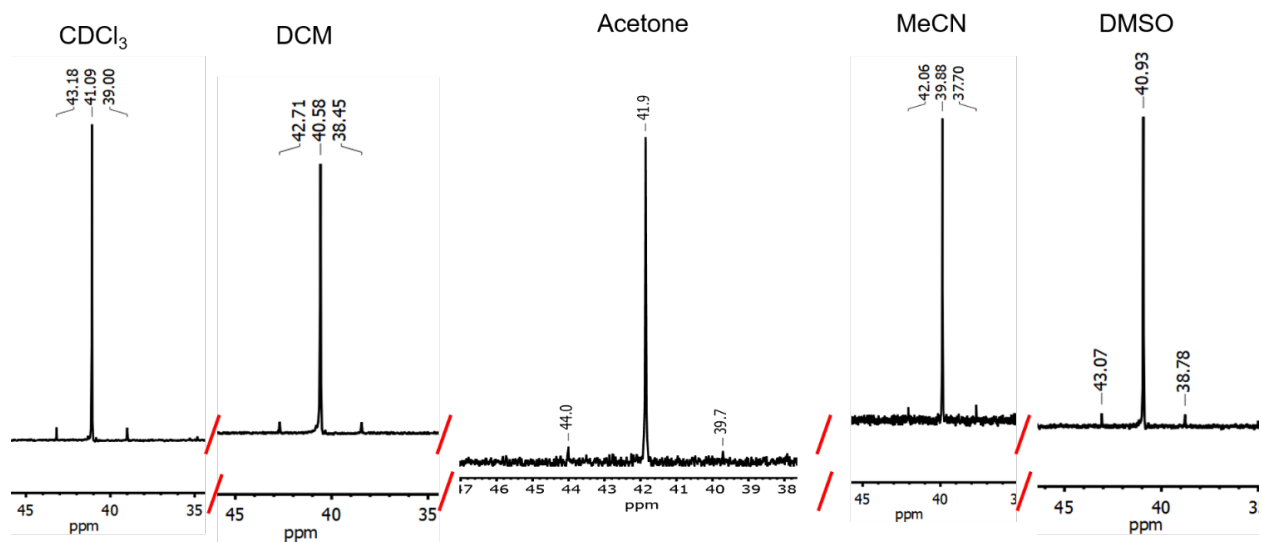


Figure A3.68 $^{31}\text{P}\{^1\text{H}\}$ NMR spectra of $[\text{PPh}_4][^3\text{Se}]$ in different solvents, showing change in $J_{\text{P-Se}}$.

A3.6.4 Neutral Congeners

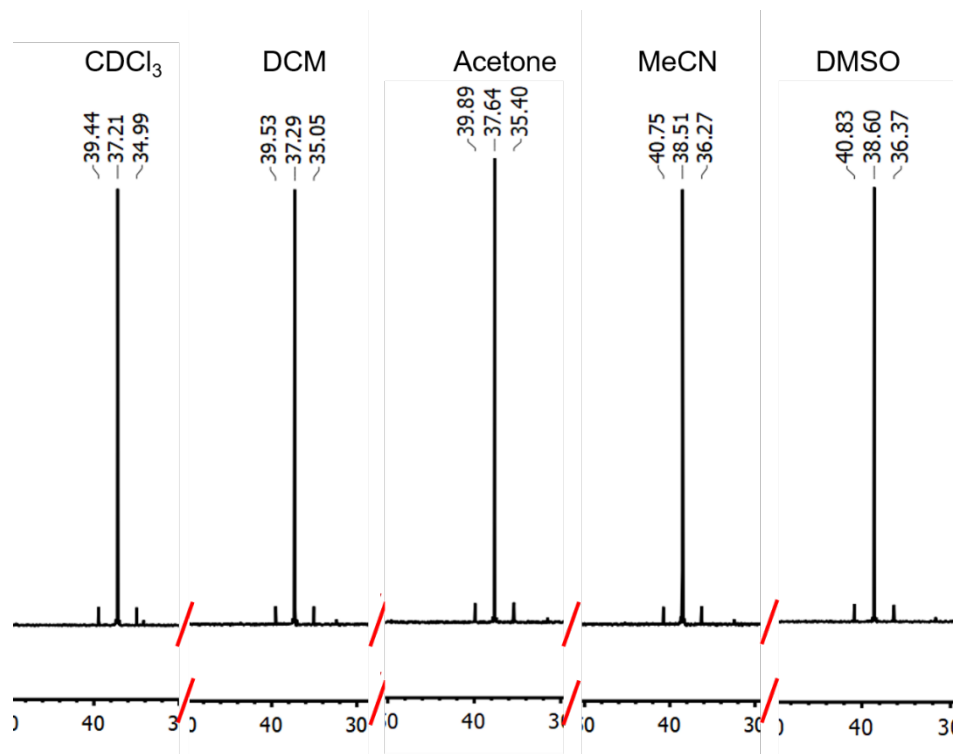


Figure A3.69 $^{31}\text{P}\{^1\text{H}\}$ NMR spectra of SePPh₂Et in the indicated solvents.

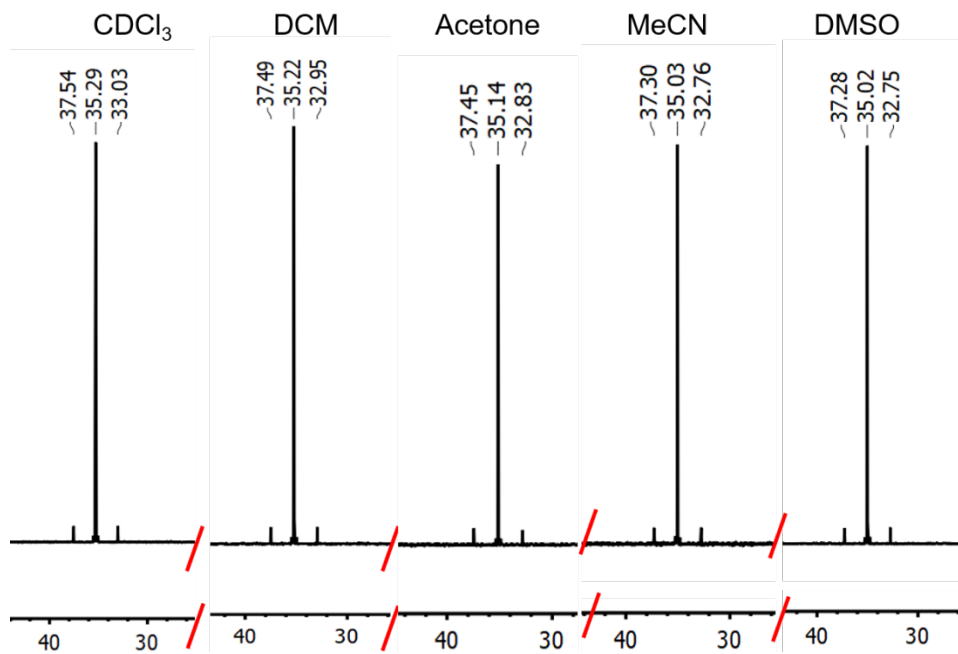


Figure A3.70 $^{31}\text{P}\{^1\text{H}\}$ NMR spectra of SePPh₃ in the indicated solvents.

A3.7 Correlation between J_{P-Se} and TEP

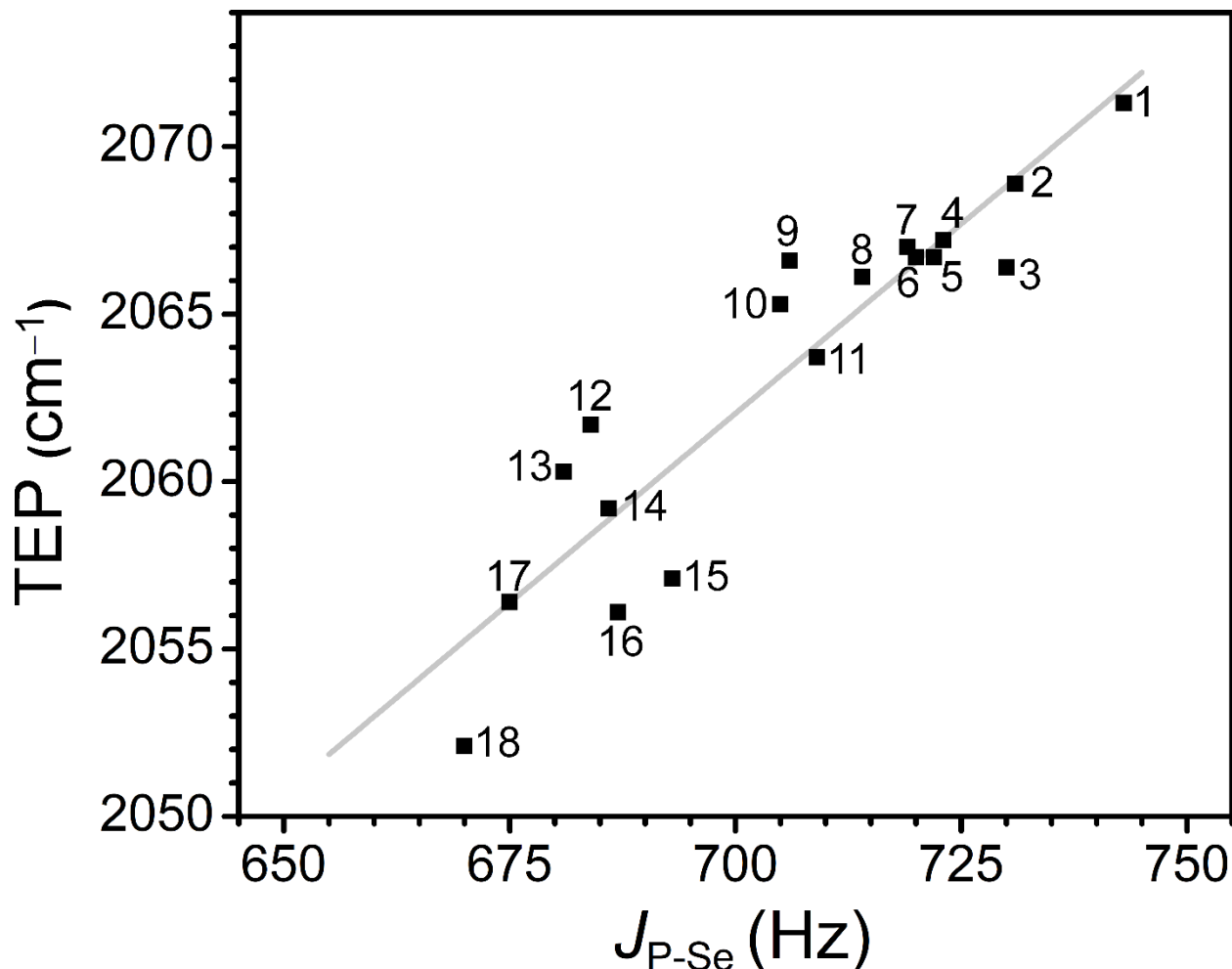


Figure A3.71 Plot of experimental J_{P-Se} reported in $CDCl_3$ vs. TEP determined using $Ni(CO)_3L$ in DCM or $Rh(CO)(acac)L$. Data was fit linearly using $y = mx + b$ with $m = 0.23(2)$ and $b = 1904(17)$ with $R^2 = 0.84$. Phosphines corresponding to each point are listed in the next table.

Compound	Experimental TEP	Experimental J_{P-Se}	Calculated TEP	Calculated J_{P-Se}
2	2061.7 cm^{-1}	-	-	698 Hz
$[PPh_4][1^{Se}] CDCl_3$		657	2052.3	
$[PPh_4][1^{Se}] DMSO$		687	2059.1	
$[PPh_4][3^{Se}] CDCl_3$		677	2056.8	
$[PPh_4][3^{Se}] DMSO$		695	2060.9	

Table A3.11 Additional data points added to Figure 3.2. The linear fit was used to calculate the corresponding TEP or J_{P-Se} from the experimental value. Experimental TEP was determined via the linear correlation between ν_{CO} $Rh(CO)(acac)L$ and TEP.

Number	Phosphine	J_{P-Se} (Hz)	TEP (cm^{-1})
1	P(<i>p</i> -FPh) ₃	743	2071.3
2	PPh ₃	731	2068.9
3	P(Bn) ₃	730	2066.4
4	P(<i>m</i> -Tol) ₃	723	2067.2
5	PPh ₂ Et	722	2066.7
6	P(<i>p</i> -Tol) ₃	720	2066.7
7	P(MePh ₂) ₃	719	2067.0
8	P(<i>p</i> -OMeC ₆ H ₄) ₃	714	2066.1
9	P(<i>o</i> -Tol) ₃	706	2066.6
10	PMe ₂ Ph	705	2065.3
11	PEt ₂ Ph	709	2063.7
12	PEt ₃	684	2061.7
13	P(nBu) ₃	681	2060.3
14	P(^{<i>i</i>} Pr) ₃	686	2059.2
15	PAd ₂ (nBu)	693	[2057.1]
16	P(^{<i>t</i>} Bu) ₃	687	2056.1
17	PCy ₃	675	2056.4
18	PAd ₃	670	[2052.1]

Table A3.12 Phosphines used in the J_{P-Se} vs. TEP fit. Data in brackets were determined using Rh(CO)(acac)L. All other TEP values were determined using Ni(CO)₃L, and all J_{P-Se} values were measured in CDCl₃. Data was collected from references 77, 108 and 122 in Chapter 3.

A3.8 Analysis of J_{P-Se} Solvent Dependence

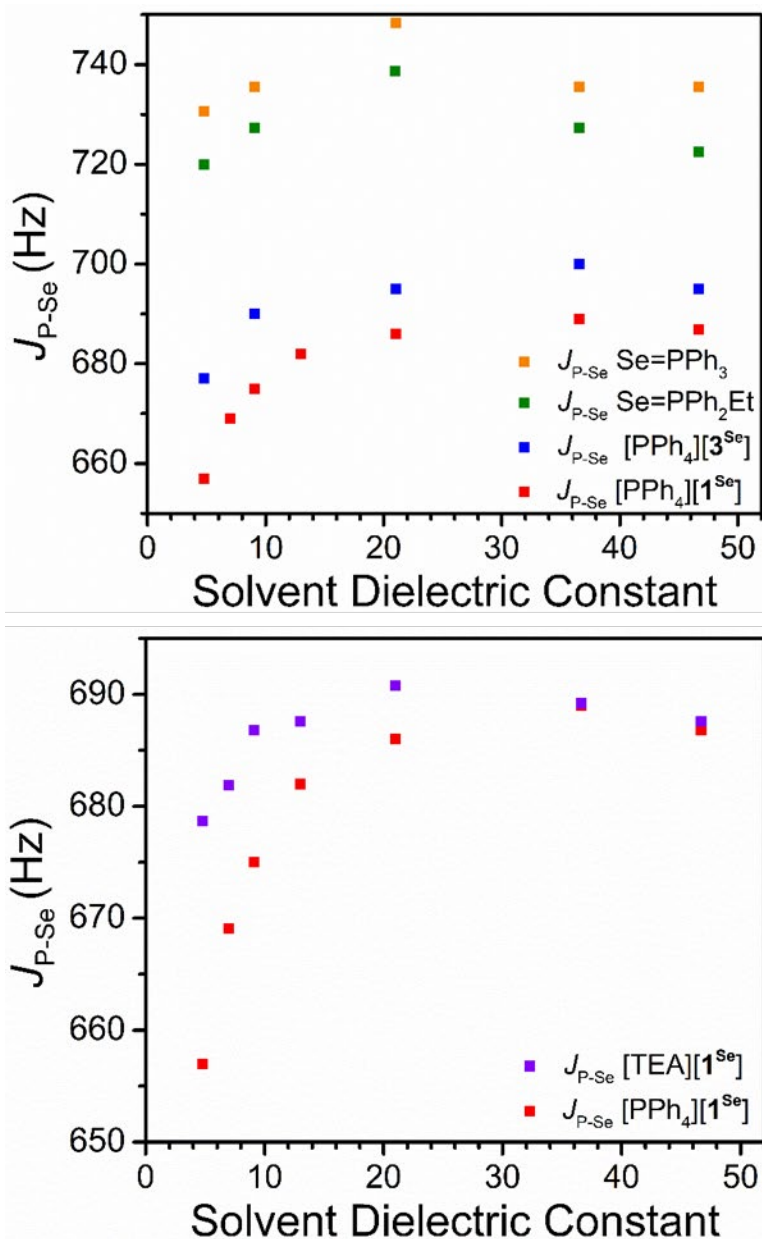


Figure A3.72 Plots of J_{P-Se} as a function of solvent dielectric – the PPh₄ Se compounds are compared to their neutral congeners in the top plot and the coupling of 1^{Se} with two different counterions is compared in the bottom plot. Solvent dielectric for mixtures was estimated using a volume weighted average of the pure solvent dielectrics. We have been unable to find detailed studies of the dielectrics of these binary mixtures, but literature reports suggest that solvent mixtures of low polarity solvents scale approximately linearly with concentration and that using a volume or mole fraction weighted average of the pure solvent dielectric provides a reasonable estimate of the mixture dielectric.* We have chosen to use volume fraction for ease but use of mole fractions results in negligible changes to the values and fits.

* (a) See Figure 2 in Wang, P. Anderko, A. Computation of dielectric constants of solvent mixtures and electrolyte solutions. *Fluid Phase Equilib.* **2001**, *186* (1-2), 103-122. (b) Jouyban, A.; Soltanpour, S.; Chan, H.-K. A Simple Relationship between Dielectric Constant of Mixed Solvents with Solvent Composition and Temperature *Int. J. Pharm.* **2004**, *269*, 353-360. (c) Jouyban, A.; Soltanpour, S. Prediction of Dielectric Constants of Binary Solvents at Various Temperatures *J. Chem. Eng. Data* **2010**, *55*, 2951-2963.

Solvent	Dielectric	[PPh ₄] [1 ^{Se}]	[TEA] [1 ^{Se}]	[PPh ₄] [3 ^{Se}]	SePPh ₂ Et	SePPh ₃	1 ^{Se} DFT explicit solvent
CDCl ₃	4.8	657	679	677	720	731	-648
1:1 CDCl ₃ : CD ₂ Cl ₂	7	669	682	-	-	-	-
CD ₂ Cl ₂	9.1	675	687	690	727	735	-675
1:1 acetone- <i>d</i> ₆ :CD ₂ Cl ₂	13	682	688	-	-	-	-
acetone- <i>d</i> ₆	21	686	691	695	739	748	-
CD ₃ CN	36.6	689	689	700	727	735	-684
DMSO- <i>d</i> ₆	46.7	687	688	695	722	735	-

Table A3.13 J_{P-Se} (Hz) for [PPh₄][1^{Se}], [TEA][1^{Se}], [PPh₄][3^{Se}], SePPh₂Et, SePPh₃ at different dielectrics. To estimate the experimentally accessible electrostatic contribution to donor strength for [PPh₄][1^{Se}], the following calculation was performed: $(687-657)/(722-657)*100 = 46\%$. The experimentally accessible electrostatic contribution for [PPh₄][3^{Se}] is $(695-677)/(735-677)*100 = 31\%$. The coupling predicted by DFT including explicit solvent (Figures A3.56-A3.58) is included in the last column.

Phosphine	[PPh ₄][1 ^{Se}]	[TEA][1 ^{Se}]	[PPh ₄][3 ^{Se}]	SePPh ₂ Et	SePPh ₃
a	693(1)	691(2)	700(2)	731(5)	741(5)
b	$-2.12(12)*10^3$	$-7(2)*10^2$	$-1.4(2)*10^3$	$-5(6)*10^2$	$-5(5)*10^2$
R ²	0.98	0.77	0.92	0.06	0.02

Table A3.14 Fit parameters for the linear fits of J_{P-Se} to $1/(4\pi\epsilon)$ of the form $J_{P-Se} = a + b*(1/(4\pi\epsilon))$.

Salt added	Solvent	Equivalents	J_{P-Se} (Hz)	Difference relative to [PPh ₄][1 ^{Se}]
PPh ₄ Br	CD ₂ Cl ₂	3	679	4
PPh ₄ Br	CD ₂ Cl ₂	20	679	4
Tetrabutylammonium chloride	CDCl ₃	20	671	14
Tetrabutylammonium chloride	CDCl ₃	1	667	9
Tetrabutylammonium PF ₆	CDCl ₃	20	671	14
Tetraethylammonium bromide	CDCl ₃	20	677	19
Tetraethylammonium bromide	CDCl ₃	1	672	14
Bis(triphenylphosphine)iminium chloride	CDCl ₃	20	656	-2

Table A3.15 J_{P-Se} (Hz) for [PPh₄][**1**^{Se}] with the addition of various additional salts, the difference is relative to the coupling value for [PPh₄][**1**^{Se}] in the appropriate solvent. NMR spectra are shown in the NMR section.

A3.9 NMR Spectra of C₆F₆ Oxidative Addition

A3.9.1 K1 with Ni(COD)₂

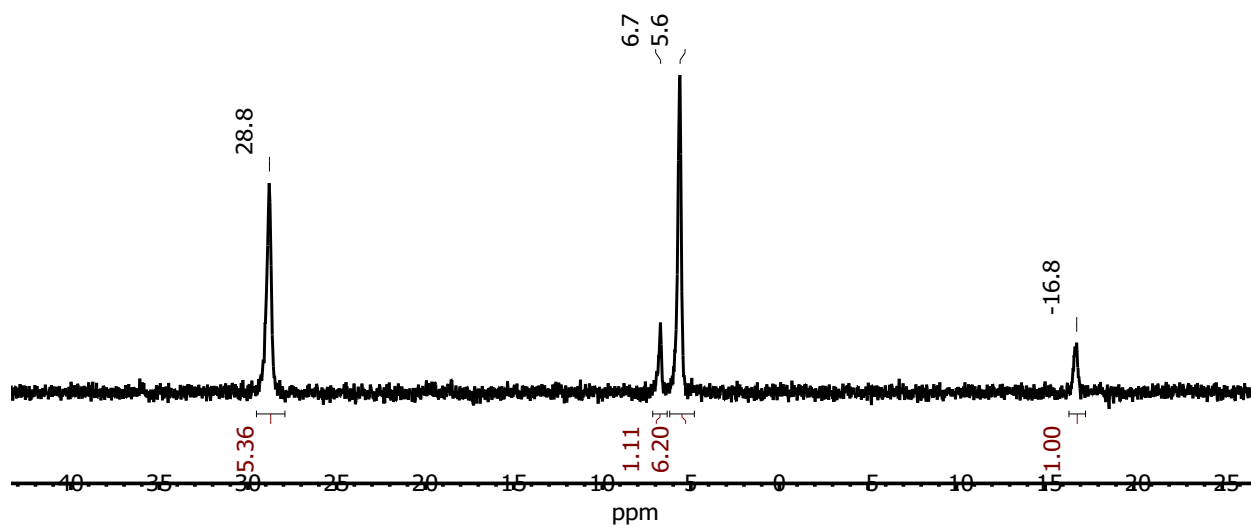


Figure A3.73 ³¹P{¹H} NMR spectrum of the reaction of K1 and Ni(COD)₂ in THF.

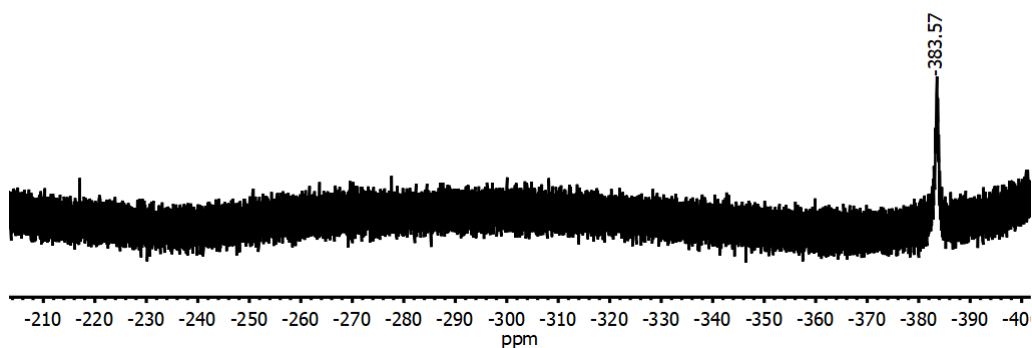


Figure A3.74 $^{19}\text{F}\{^1\text{H}\}$ NMR spectrum of the reaction of K1, Ni(COD) $_2$, and C $_6$ F $_6$ after 1 hr at RT. This upfield region shows the characteristic Ni–F peak.

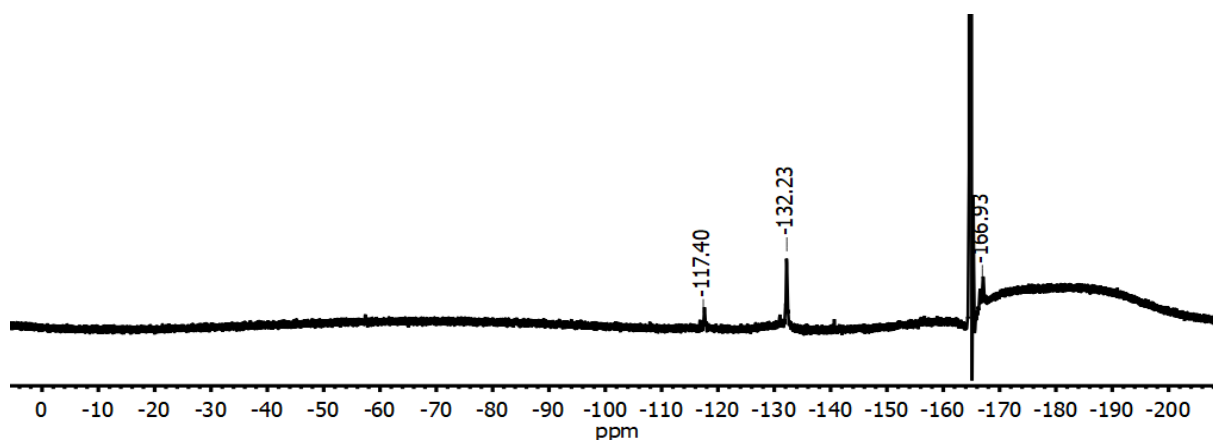


Figure A3.75 $^{19}\text{F}\{^1\text{H}\}$ NMR spectrum of the reaction of K1, Ni(COD) $_2$, and C $_6$ F $_6$ after 1 hr at RT. The broad peak centered around -180 ppm is Teflon within the NMR probe. The peak at -164.6 ppm that is cut off is excess C $_6$ F $_6$.

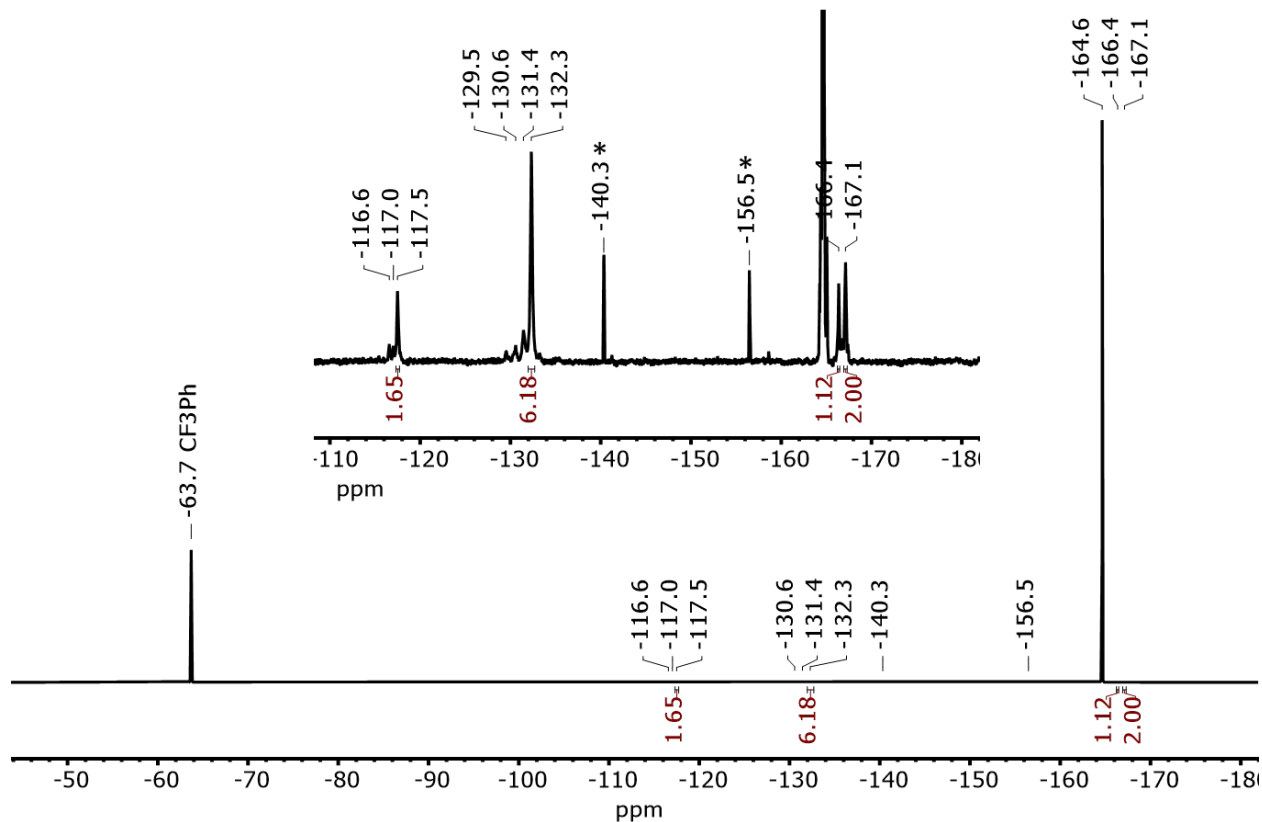


Figure A3.76 ^{19}F NMR spectrum of the reaction between K1 (24 mM), Ni(COD)₂ (12 mM) and C₆F₆ (120 mM) in THF with CF₃Ph (60 mM) and PPh₃O (12 mM) as internal integral standards after 20 h at RT. Oxidative addition product peaks assigned: -117.5 (2F, F_{ortho}), -132.3 (6F, BF₃), -166.4 (1F, F_{para}) -167.1 (2F, F_{meta}) based on comparison to reference 154. Peaks at -140.3 and -156.5 ppm are not always observed and are assigned as unknown impurities. The peak at -164.6 ppm is unreacted C₆F₆.

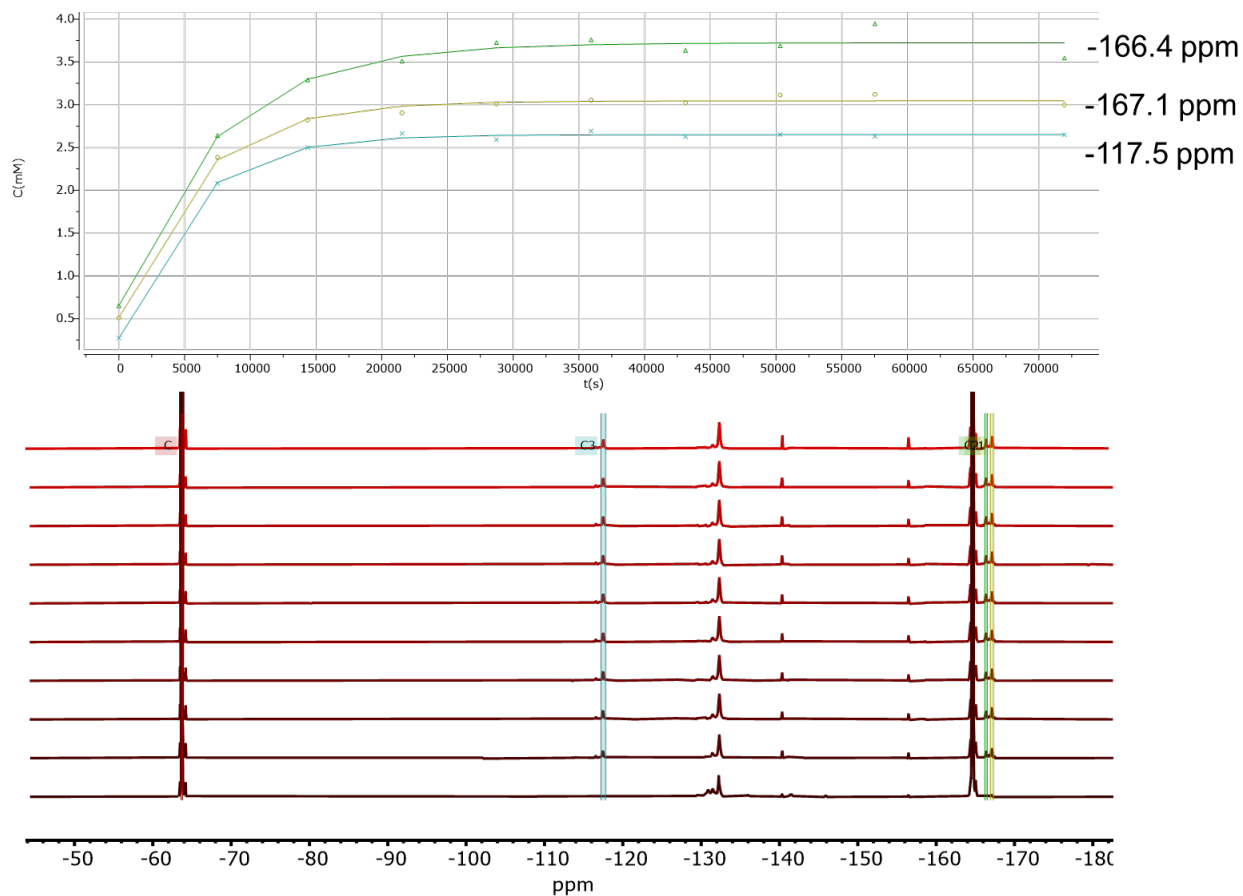


Figure A3.77 Time course monitoring of the ^{19}F NMR spectrum of the reaction between K1 (24 mM), $\text{Ni}(\text{COD})_2$ (12 mM) and C_6F_6 (120 mM) in THF with CF_3Ph (60 mM) and OPPh_3 (12 mM) as internal integral standards over the course of 20 h at RT. The observed rate of formation and % completion for the oxidative addition product for the following peaks are: -166.4 ppm ($1.4\text{E}-4 \text{ s}^{-1}$, 3.5 mM, 30%), -167.1 ppm ($1.7\text{E}-4 \text{ s}^{-1}$, 3.0 mM, 25%), -117.5 ppm ($1.9\text{E}-4 \text{ s}^{-1}$, 2.6 mM, 22%). The average observed rate of formation and % yield are $1.7(3)\text{E}-4 \text{ s}^{-1}$ and 25(4)%.

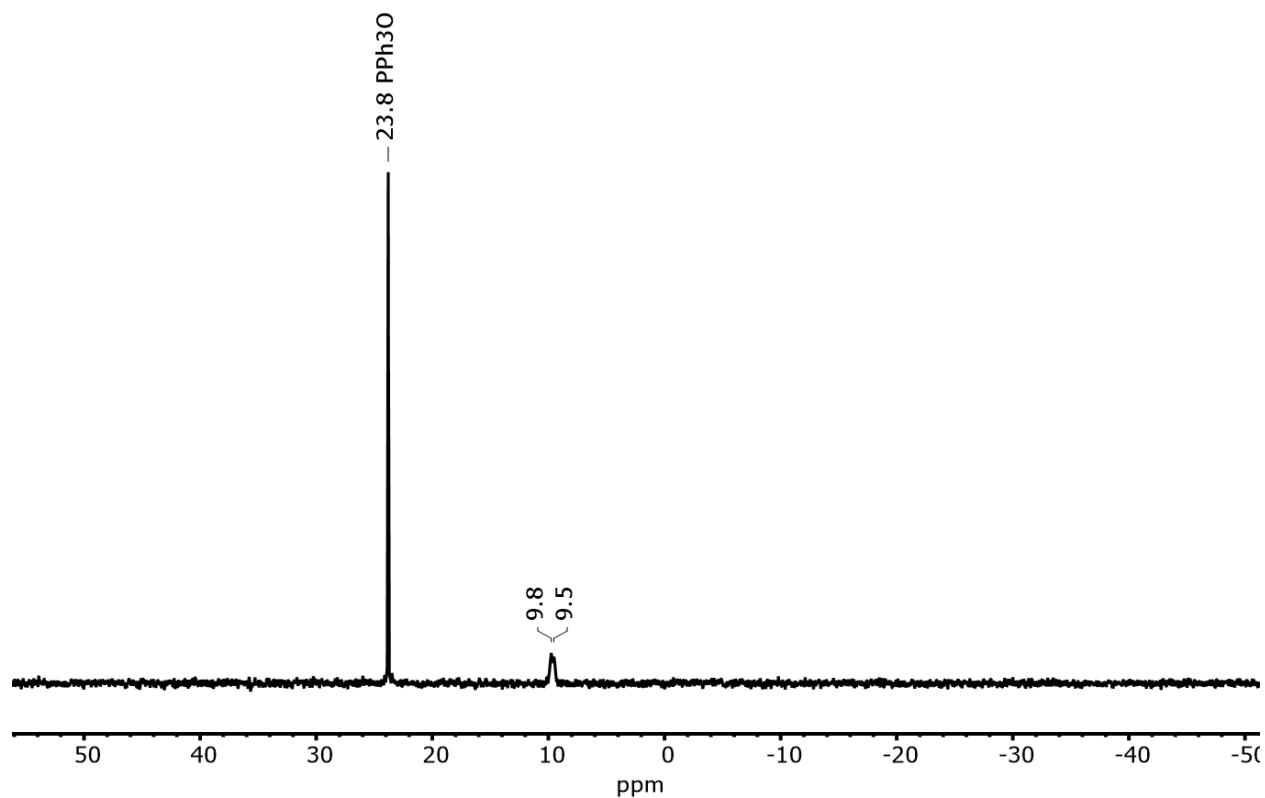


Figure A3.78 $^{31}\text{P}\{^1\text{H}\}$ NMR spectrum of the reaction between K1 (24 mM), Ni(COD) $_2$ (12 mM) and C $_6\text{F}_6$ (120 mM) in THF with CF $_3$ Ph (60 mM) and OPPh $_3$ (12 mM) as internal integral standards after 16 h at RT. The phosphorus resonance for the oxidative addition product is assigned as the doublet at 9.6 ppm on the basis of coupling to ^{19}F on the Ni-F.

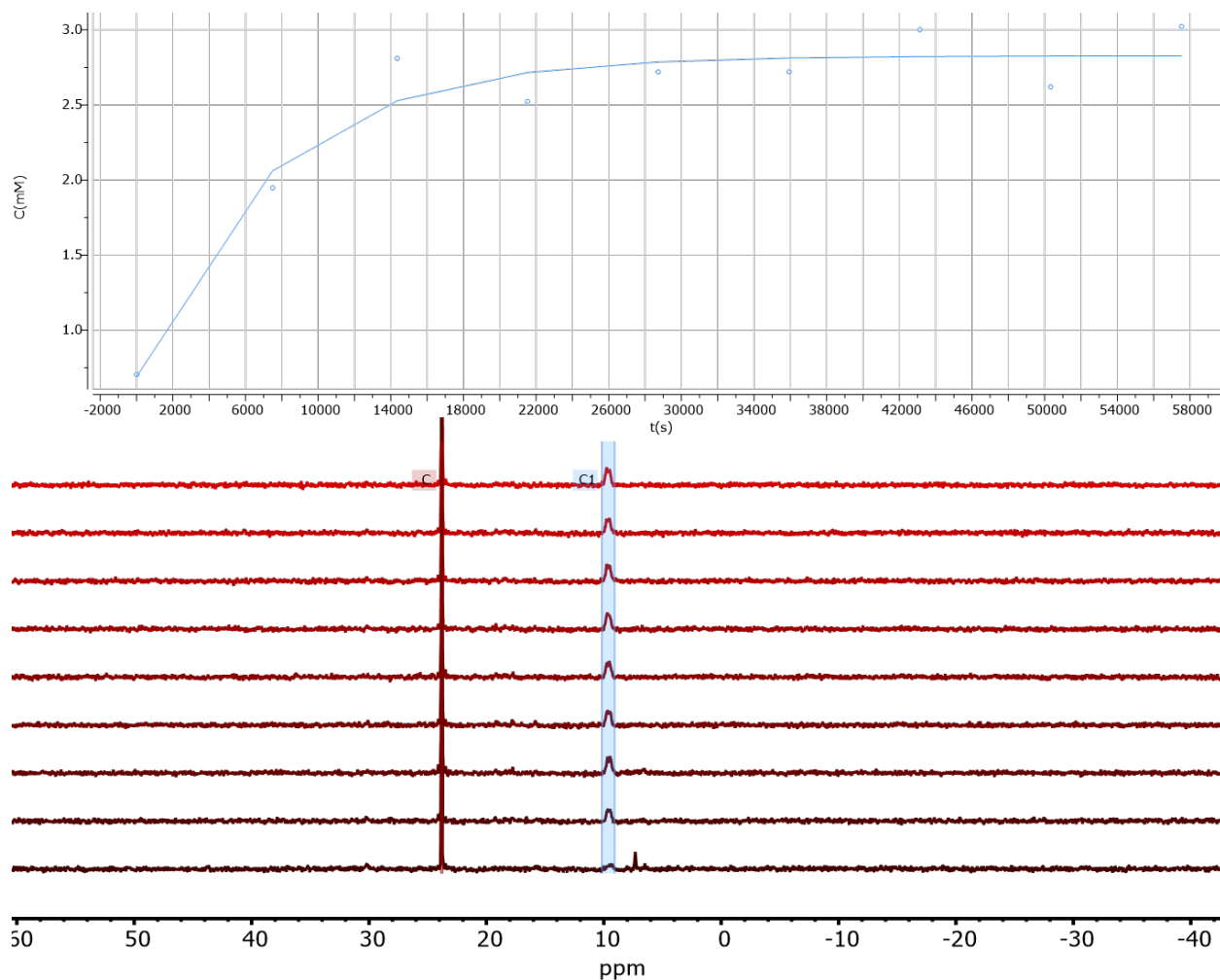


Figure A3.79 Time course monitoring of the $^{31}\text{P}\{^1\text{H}\}$ NMR spectrum of the reaction between **K1** (24 mM), $\text{Ni}(\text{COD})_2$ (12 mM) and C_6F_6 (120 mM) in THF with CF_3Ph (60 mM) and OPPh_3 (12 mM) as internal integral standards over the course of 16 h at RT. The observed rate of formation and % completion for the oxidative addition peak at 9.6 ppm is $1.4\text{E}-4 \text{ s}^{-1}$ and 3.0 mM (25%).

A3.9.2 PCy₃ with Ni(COD)₂

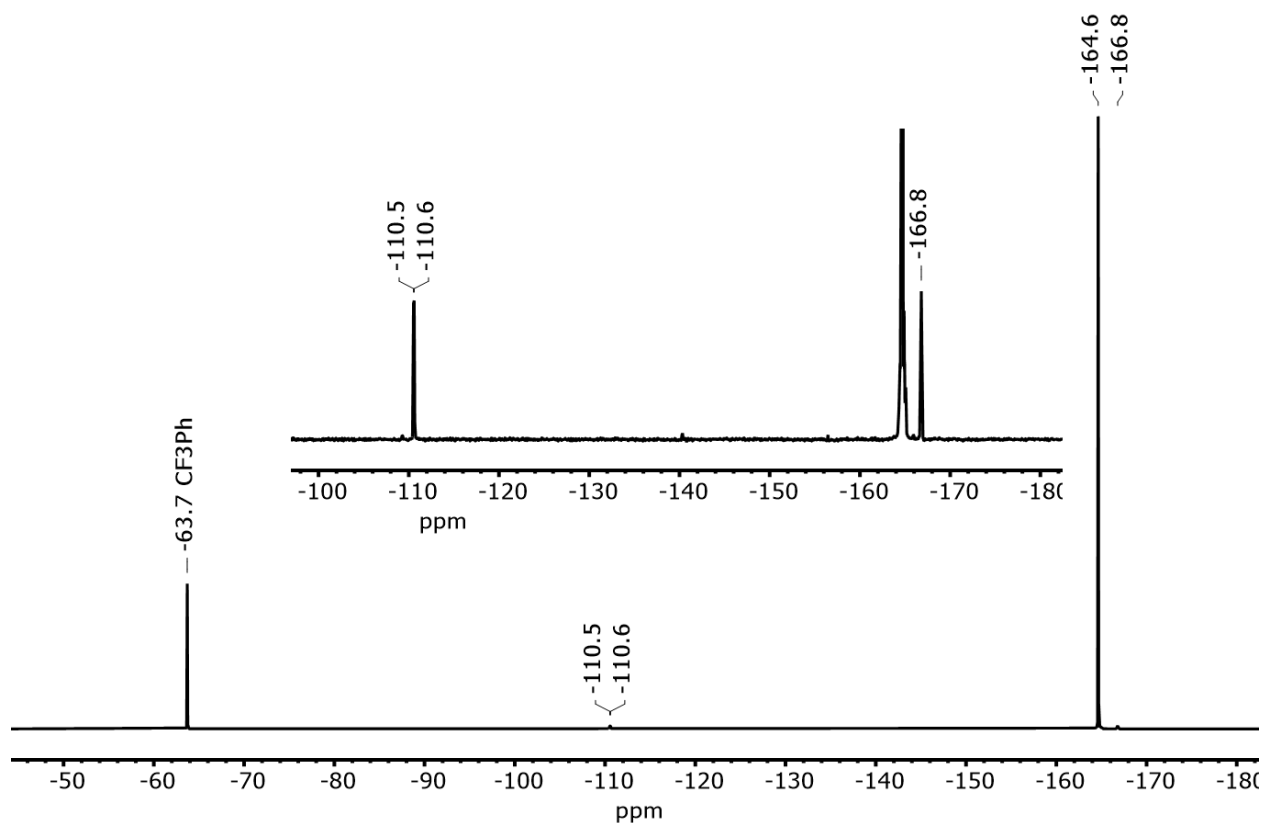


Figure A3.80 ¹⁹F NMR spectrum of the reaction between PCy₃ (24 mM), Ni(COD)₂ (12 mM) and C₆F₆ (120 mM) in THF with CF₃Ph (60 mM) and OPPh₃ (12 mM) as internal integral standards after 53 h at RT. Oxidative addition product peaks assigned: -110.6 (2F, F_{ortho}), -166.8 (2F, F_{meta}) based on comparison to reference 154. The F_{para} peak is hidden under the C₆F₆ peak, but can be observed in the ¹⁹F{¹H} NMR spectrum. The peak at -164.6 ppm is the unreacted C₆F₆.

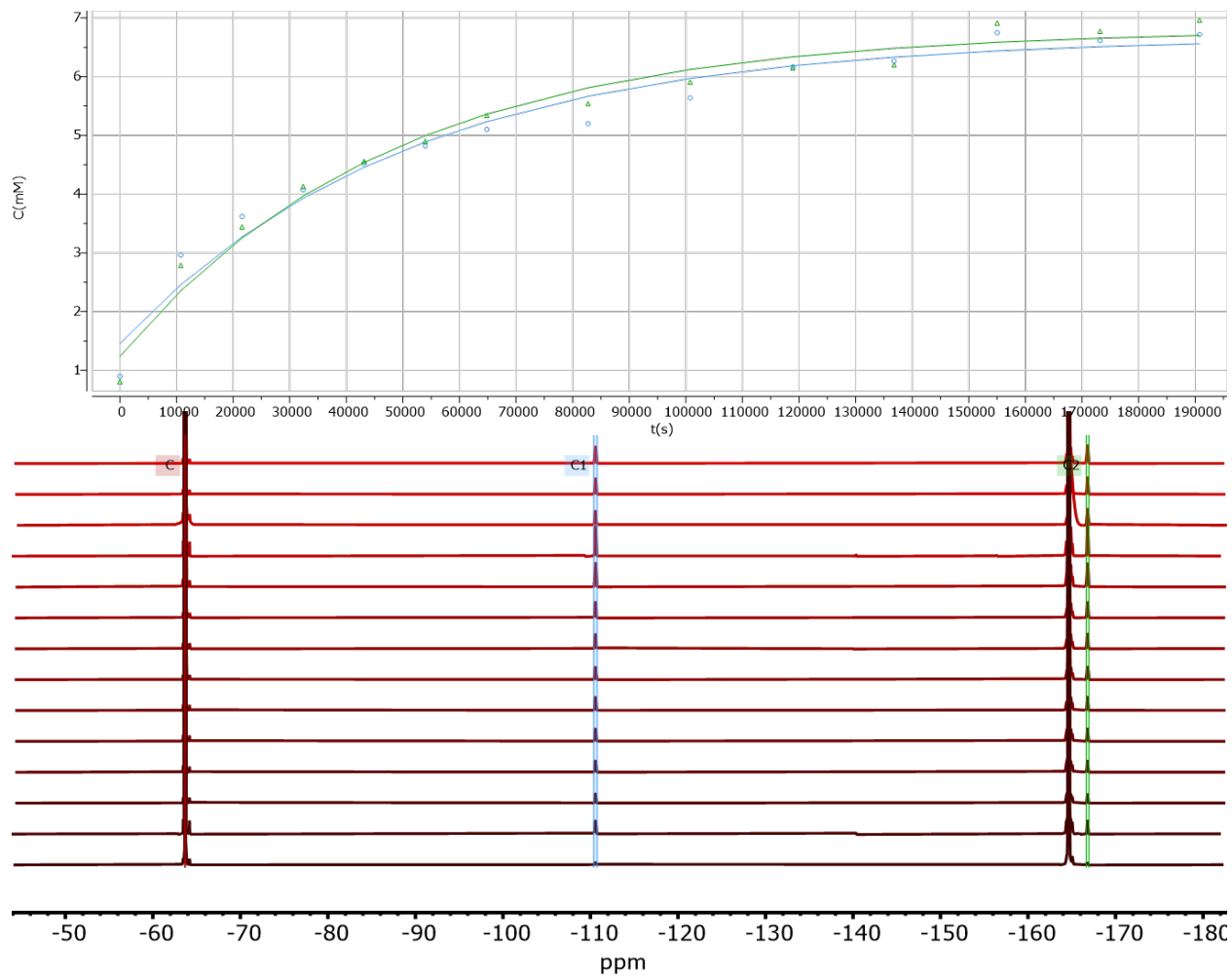


Figure A3.81 Time course monitoring of the ^{19}F NMR spectrum of the reaction between PCy_3 (24 mM), $\text{Ni}(\text{COD})_2$ (12 mM) and C_6F_6 (120 mM) in THF with CF_3Ph (60 mM) and OPPh_3 (12 mM) as internal integral standards over the course of 52 h at RT. The observed rate of formation and % completion for the oxidative addition product for the following peaks are: -110.6 ppm ($2.0\text{E}-5 \text{ s}^{-1}$, 6.7 mM, 56%), -166.8 ppm ($2.1\text{E}-5 \text{ s}^{-1}$, 7.0 mM, 58%). The average observed rate of formation and % yield are $2.10(7)\text{E}-5 \text{ s}^{-1}$ and 57(2)%.

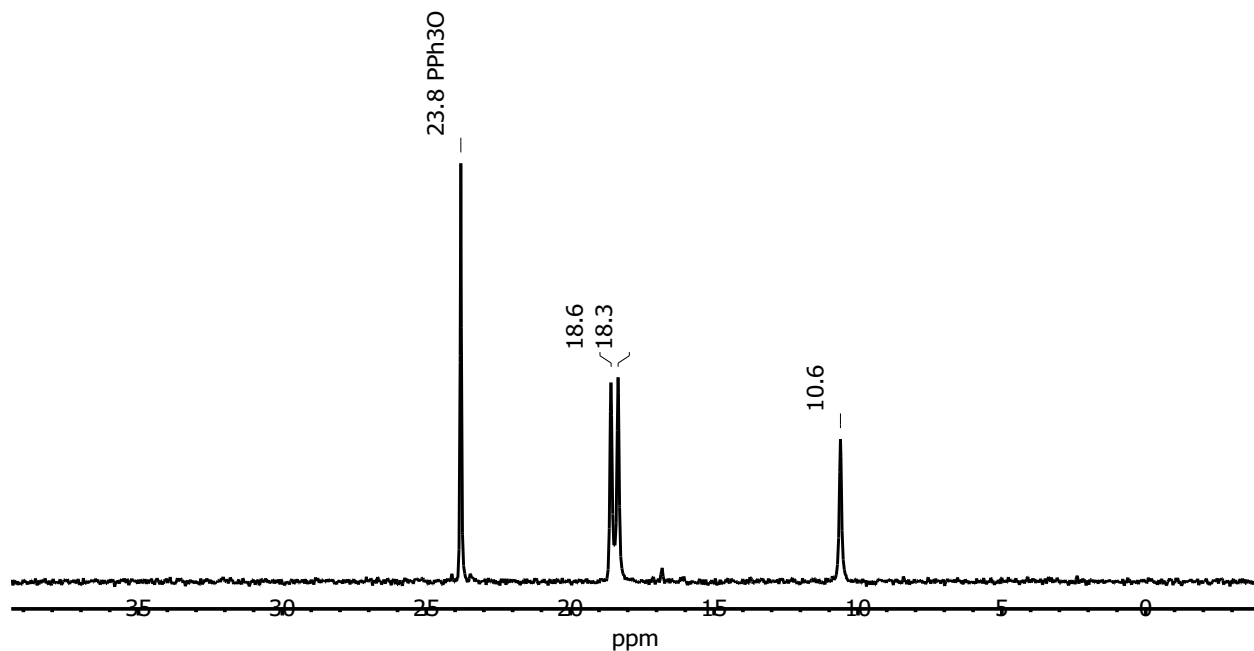


Figure A3.82 $^{31}\text{P}\{^1\text{H}\}$ NMR spectrum of the reaction between PCy_3 (24 mM), $\text{Ni}(\text{COD})_2$ (12 mM) and C_6F_6 (120 mM) in THF with CF_3Ph (60 mM) and OPPh_3 (12 mM) as internal integral standards after 53 h at RT. The phosphorus resonance for the oxidative addition product is assigned as the doublet at 18.5 ppm on the basis of coupling to ^{19}F in the Ni-F. The starting phosphine is assigned as the peak at 10.6 ppm.

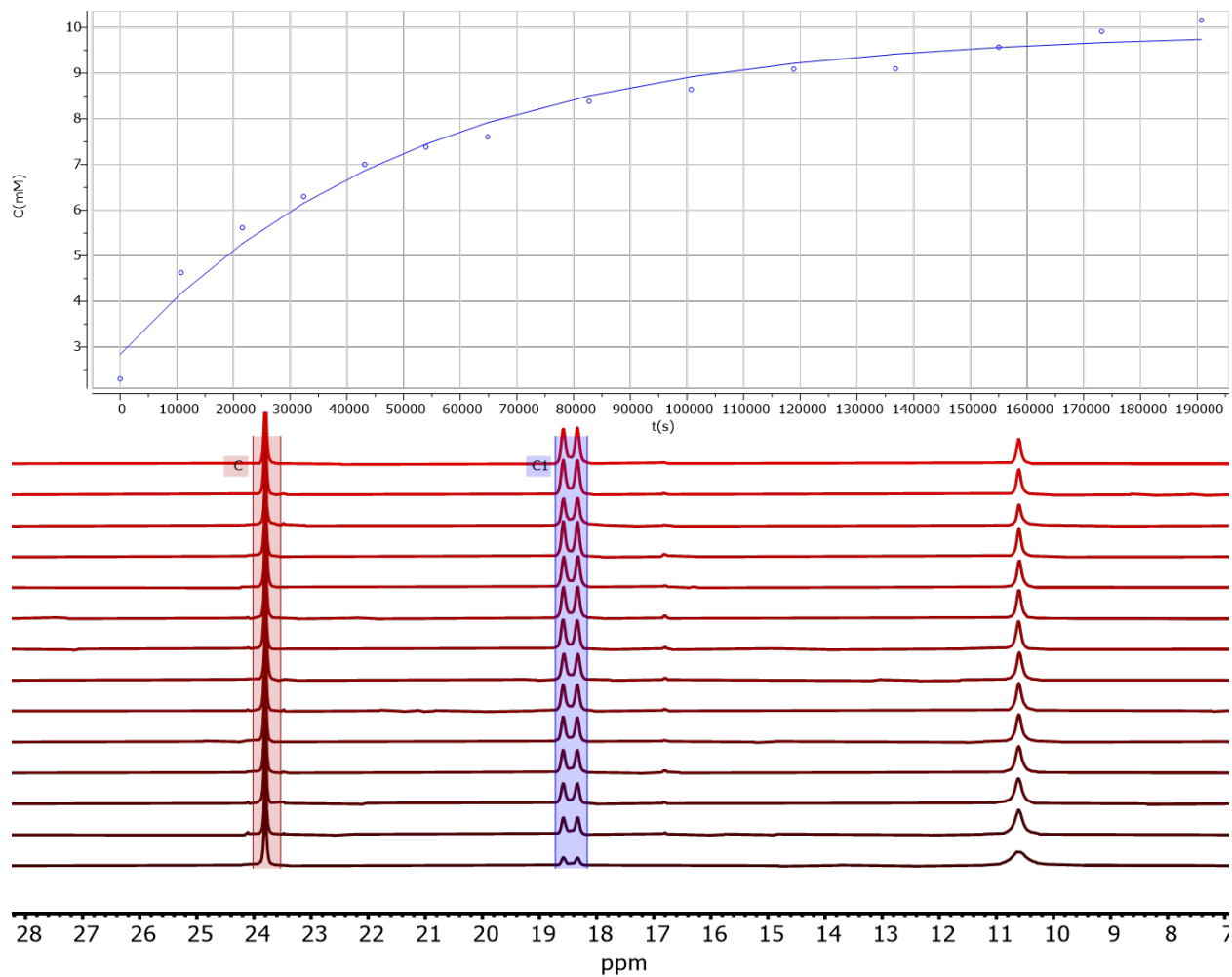


Figure A3.83 Time course monitoring of the $^{31}\text{P}\{^1\text{H}\}$ NMR spectrum of the reaction between PCy_3 (24 mM), $\text{Ni}(\text{COD})_2$ (12 mM) and C_6F_6 (120 mM) in THF with CF_3Ph (60 mM) and OPPh_3 (12 mM) as internal integral standards over the course of 53 h at RT. The observed rate of formation and % completion for the oxidative addition peak at 18.5 ppm is $2.0\text{E}-5 \text{ s}^{-1}$ and 10.0 mM (83%).

A3.9.3 PEt_3 with $\text{Ni}(\text{COD})_2$

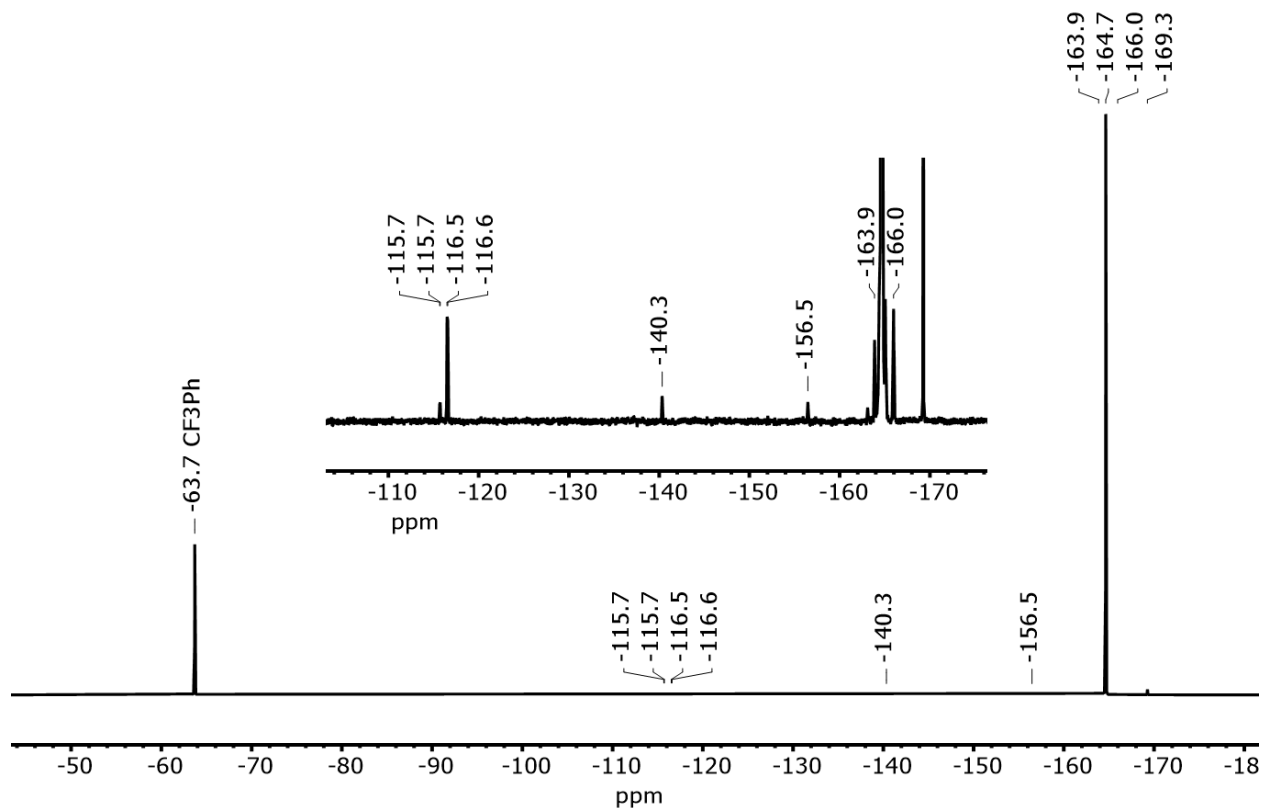


Figure A3.84 ^{19}F NMR spectrum of the reaction between PEt_3 (24 mM), $\text{Ni}(\text{COD})_2$ (12 mM) and C_6F_6 (120 mM) in THF with CF_3Ph (60 mM) and OPPh_3 (12 mM) as internal integral standards after 114 h at RT. Oxidative addition product peaks assigned: -116.6 (2F, F_{ortho}), -163.9 (1F, F_{para}), and -166.0 (2F, F_{meta}) based on comparison to reference 154. Peaks at -140.3 and -156.5, and -169.3 ppm are not always observed and are assigned as unknown impurities. The peak at -164.6 ppm is unreacted C_6F_6 .

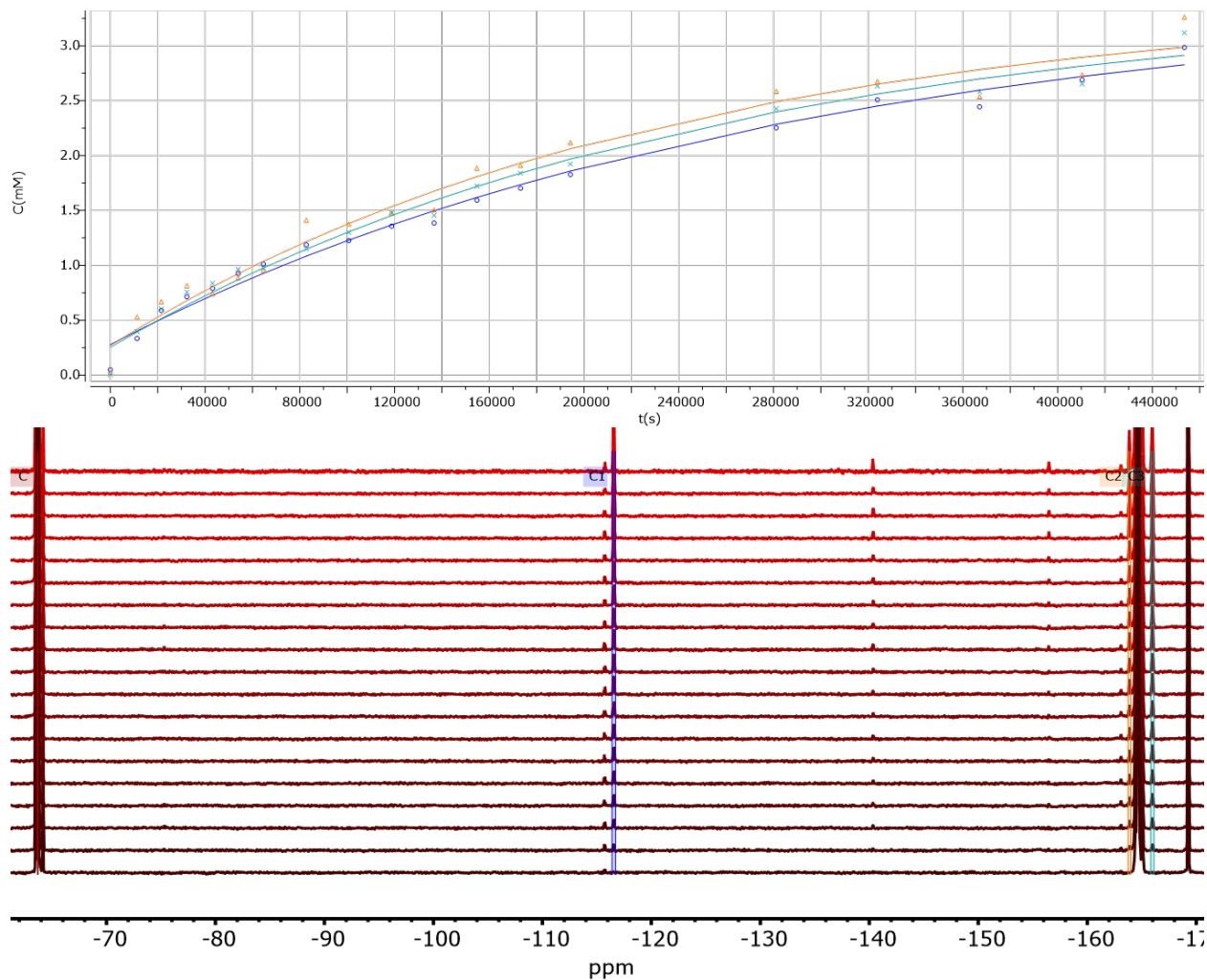


Figure A3.85 Time course monitoring of the ^{19}F NMR spectrum of the reaction between PEt_3 (24 mM), $\text{Ni}(\text{COD})_2$ (12 mM) and C_6F_6 (120 mM) in THF with CF_3Ph (60 mM) and OPPh_3 (12 mM) as internal integral standards over the course of 114 h at RT. The observed rate of formation and % completion for the oxidative addition product for the following peaks are: -116.6 ppm ($3.5\text{E}-6 \text{ s}^{-1}$, 2.7 mM, 23%), -163.9 ppm ($4.3\text{E}-6 \text{ s}^{-1}$, 2.7 mM, 23%), and 166.0 ($4.0\text{E}-6 \text{ s}^{-1}$, 2.7 mM, 23%). The average observed rate of formation and % yield are $4.0(4)\text{E}-6 \text{ s}^{-1}$ and 23%.

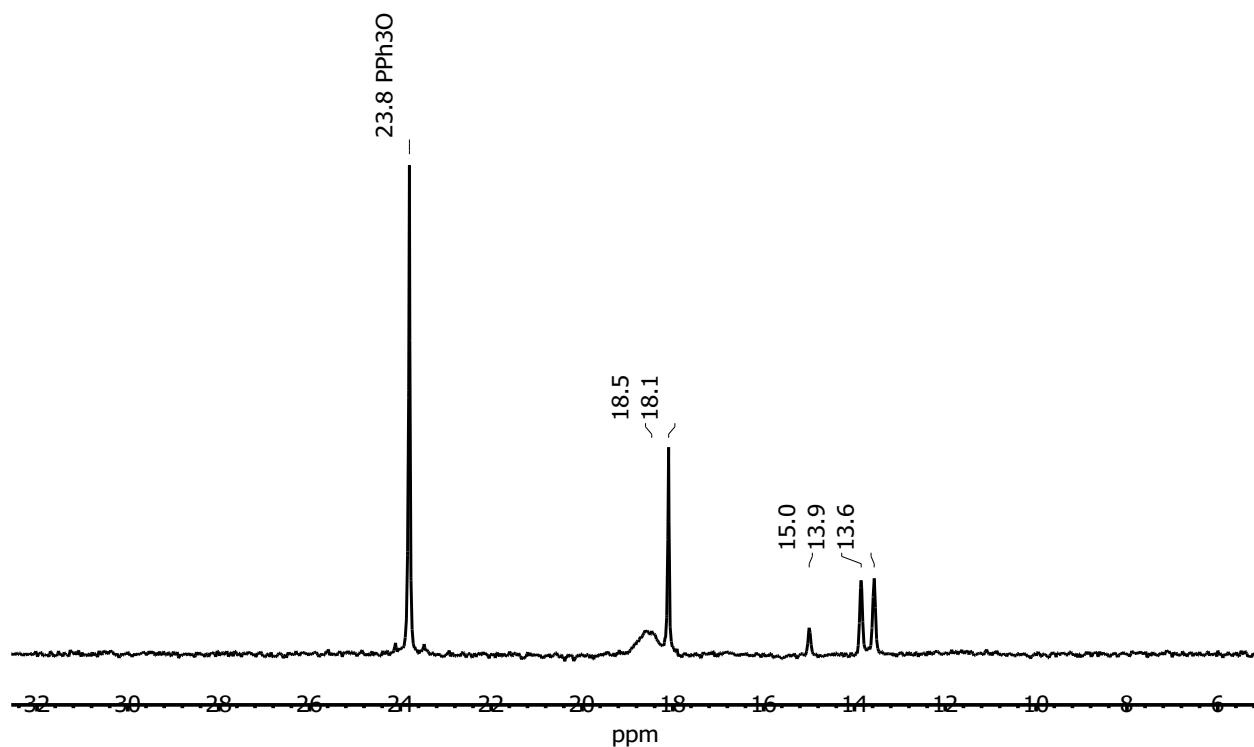


Figure A3.86 $^{31}\text{P}\{^1\text{H}\}$ NMR spectrum of the reaction between PEt_3 (24 mM), $\text{Ni}(\text{COD})_2$ (12 mM) and C_6F_6 (120 mM) in THF with CF_3Ph (60 mM) and OPPh_3 (12 mM) as internal integral standards after 114 h at RT. The phosphorus resonance for the oxidative addition product is assigned as the doublet at 13.8 ppm on the basis of coupling to ^{19}F in the Ni-F. The starting phosphine is assigned as the resonance at 18.1 ppm.

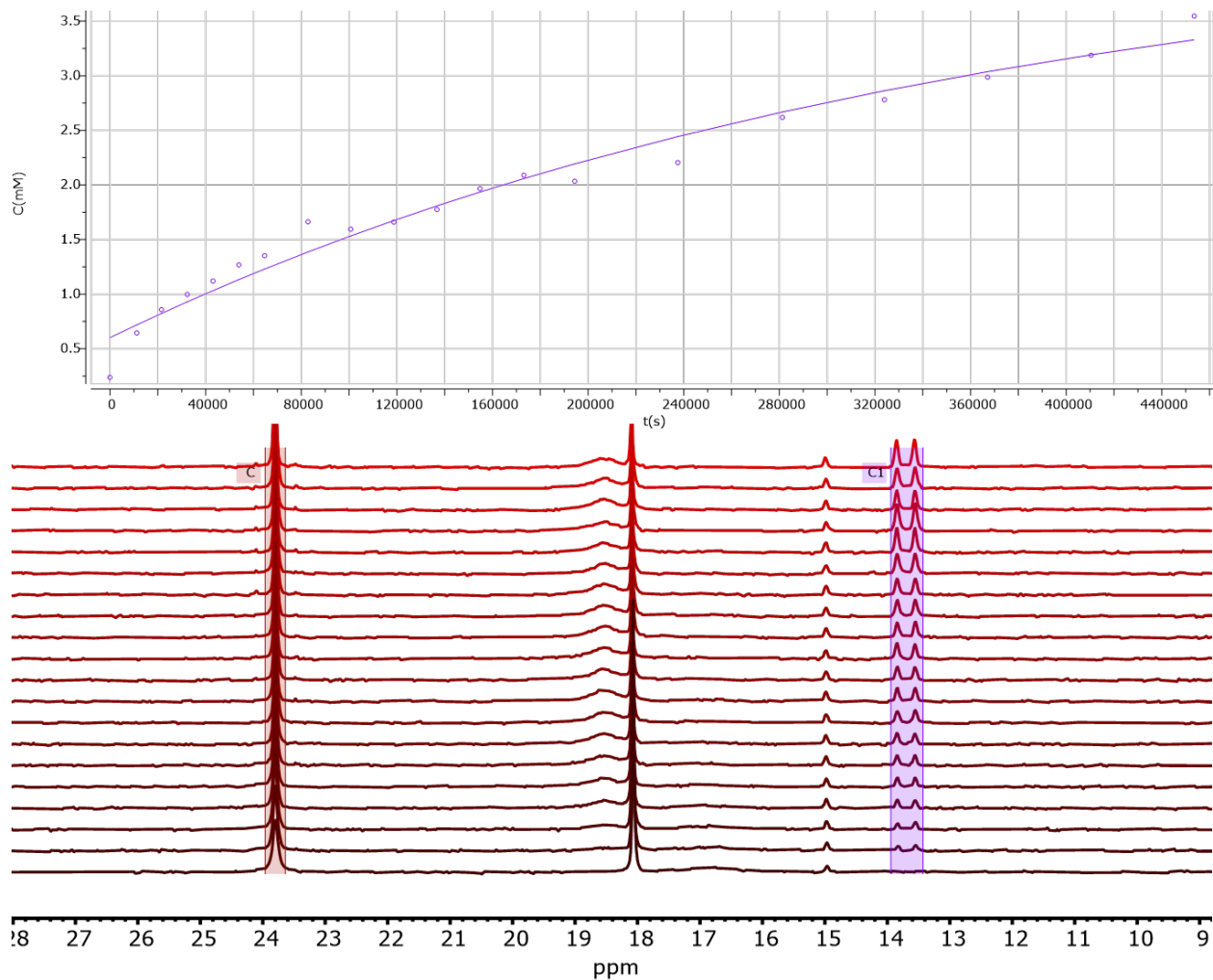


Figure A3.87 Time course monitoring of the $^{31}\text{P}\{^1\text{H}\}$ NMR spectrum of the reaction between PEt_3 (24 mM), $\text{Ni}(\text{COD})_2$ (12 mM) and C_6F_6 (120 mM) in THF with CF_3Ph (60 mM) and OPPh_3 (12 mM) as internal integral standards over the course of 114 h at RT. The observed rate of formation and % completion for the oxidative addition peak at 13.8 ppm is $2.8\text{E}-6 \text{ s}^{-1}$ and 3.2 mM (27%).

Phosphine	Average k_{obs}	Average yield	k_{obs} from ^{19}F NMR	yields from ^{19}F NMR	k_{obs} from ^{31}P NMR	yield from ^{31}P NMR
K1	$1.6(2)\text{E-}4 \text{ s}^{-1}$	25(3)% at 20h	$1.4\text{E-}4 \text{ s}^{-1}$ $1.7\text{E-}4 \text{ s}^{-1}$ $1.9\text{E-}4 \text{ s}^{-1}$	30% 25% 22%	$1.4\text{E-}4 \text{ s}^{-1}$	25%
PCy ₃	$2.0(1)\text{E-}5 \text{ s}^{-1}$	66(15)% at 53 h	$2.0\text{E-}5 \text{ s}^{-1}$ $2.1\text{E-}5 \text{ s}^{-1}$	56% 58%	$2.0\text{E-}5 \text{ s}^{-1}$	83%
PEt ₃	$3.7(7)\text{E-}6 \text{ s}^{-1}$	24(2)% at 114h	$3.5\text{E-}6 \text{ s}^{-1}$ $4.3\text{E-}6 \text{ s}^{-1}$ $4.0\text{E-}6 \text{ s}^{-1}$	23% 23% 23%	$2.8\text{E-}6 \text{ s}^{-1}$	27%

Table A3.16 Summary of observed rates from NMR monitoring experiments

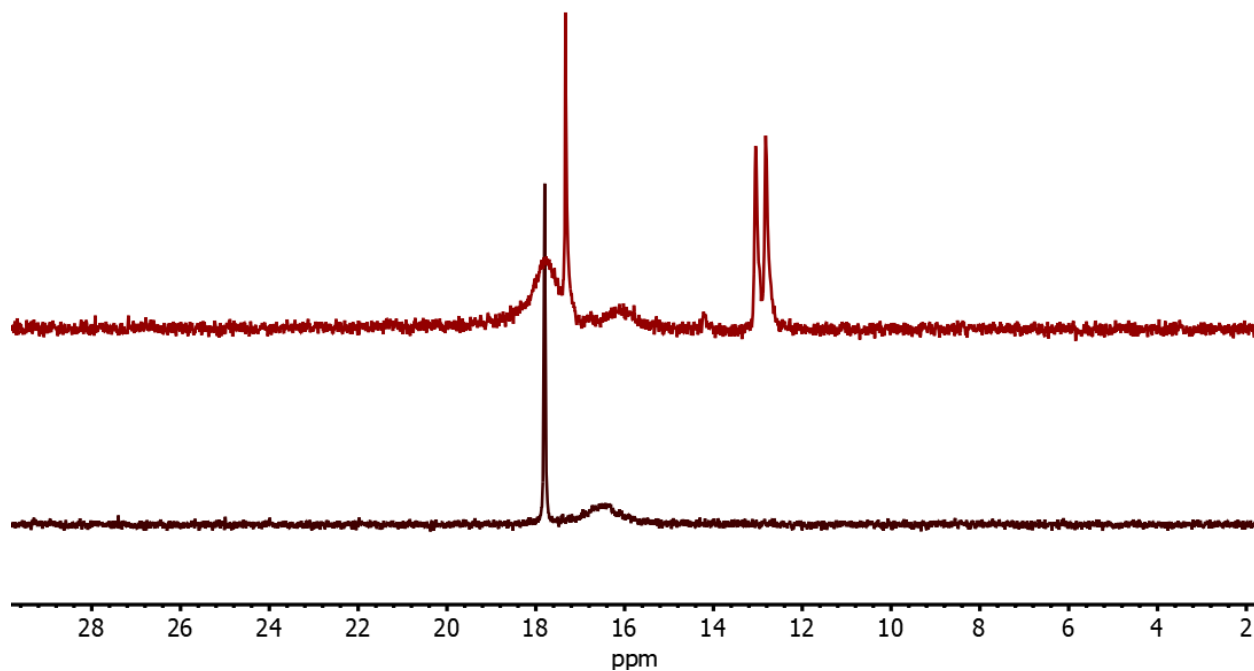


Figure A3.88 $^{31}\text{P}\{^1\text{H}\}$ NMR spectrum of the reaction of PEt₃, Ni(COD)₂, and C₆F₆ in THF after 1 hour (bottom, black) and 1 week (top, red) at RT. The features around 17 ppm are unreacted Ni(COD)₂ PEt₃ adducts and the doublet at 13 ppm is the oxidative addition product with $^1J_{\text{P-F}}$ coupling.

A3.10 Characterization of Products in Defluoroborylation Reactions

A3.10.1 NMR Spectra

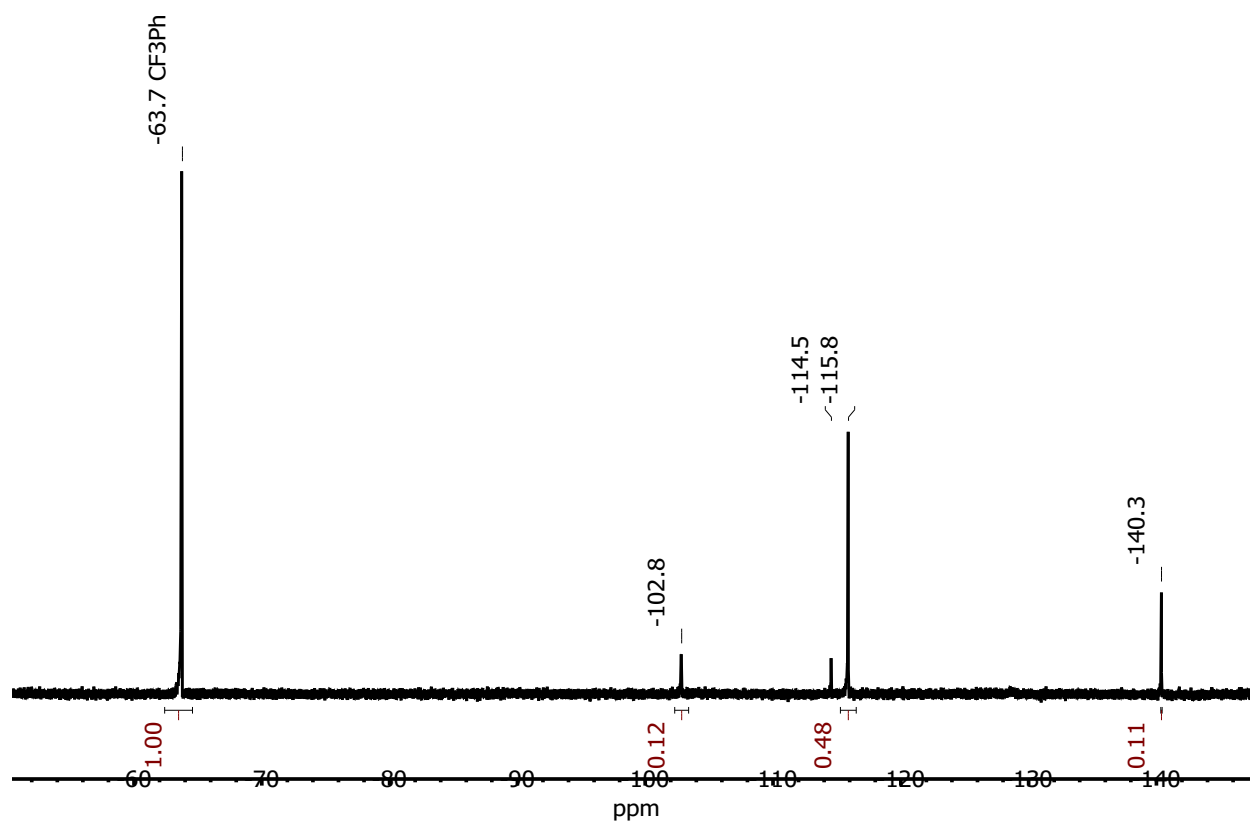


Figure A3.89 $^{19}\text{F}\{^1\text{H}\}$ NMR spectrum of the reaction mixture from one of the catalytic borylation reactions of 1,2-difluorobenzene in THF following standard catalytic conditions detailed in methods section. The peaks at -102.8, -115.8, and -140.3 ppm are assigned as 1-Bpin-2-C₆FH₄, 2,2'-F₂-1,1'-Ph₂, and 1,2-difluorobenzene, respectively.

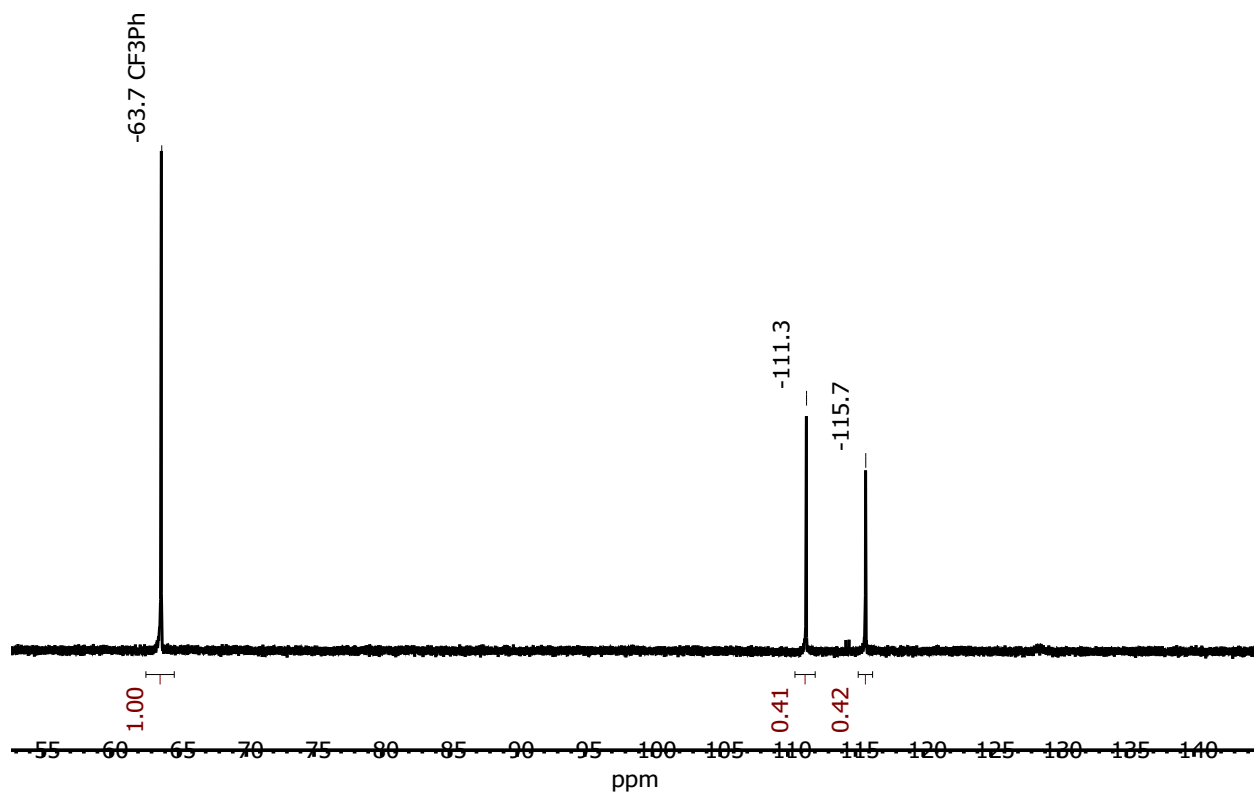


Figure A3.90 $^{19}\text{F}\{^1\text{H}\}$ NMR spectrum of the reaction mixture from one of the catalytic borylation reactions of 1,3-difluorobenzene in THF following standard catalytic conditions detailed in methods section. The peaks at -111.3 and -115.7 ppm are assigned as 1,3-difluorobenzene and 1-Bpin-3- C_6FH_4 , respectively.

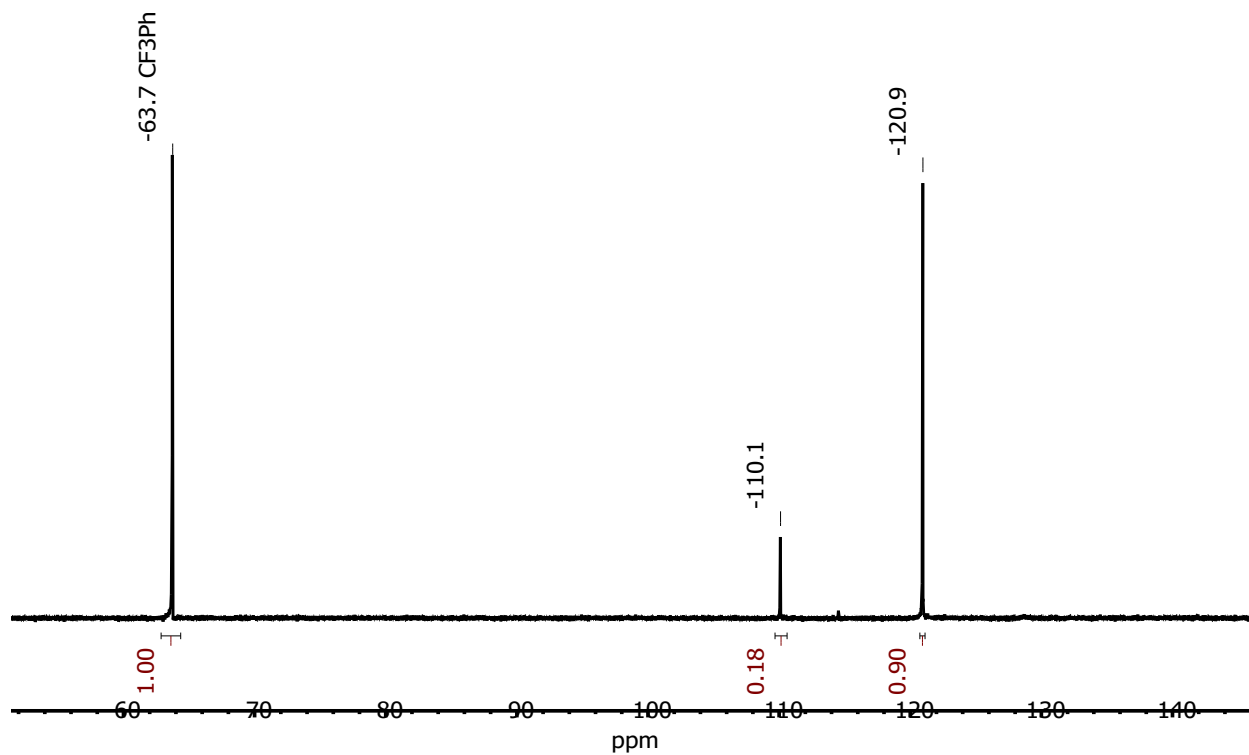


Figure A3.91 $^{19}\text{F}\{^1\text{H}\}$ NMR spectrum of the reaction mixture from one of the catalytic borylation reactions of 1,4-difluorobenzene in THF following standard catalytic conditions detailed in methods section. The peaks at -110.1 and -120.9 ppm are assigned as 1-Bpin-4- C_6FH_4 and 1,4-difluorobenzene, respectively.

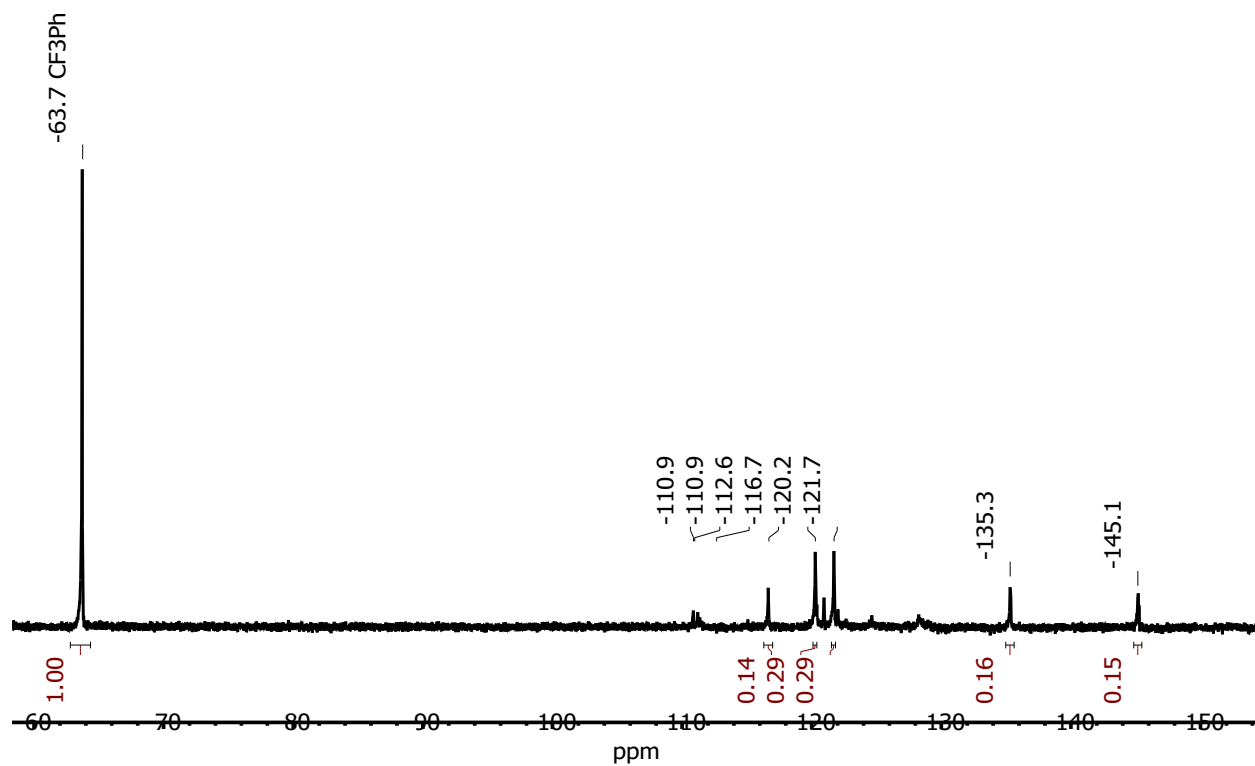


Figure A3.92 $^{19}\text{F}\{^1\text{H}\}$ NMR spectrum of the reaction mixture from one of the catalytic borylation reactions of 1,2,4-trifluorobenzene in THF following standard catalytic conditions detailed in methods section. The peaks at -116.7, -135.3 and -145.1 ppm are assigned to 1,2,4-trifluorobenzene and the peaks at -120.2 and -121.7 ppm are assigned to 2,2',5,5'-F₄-1,1'-Ph₂.

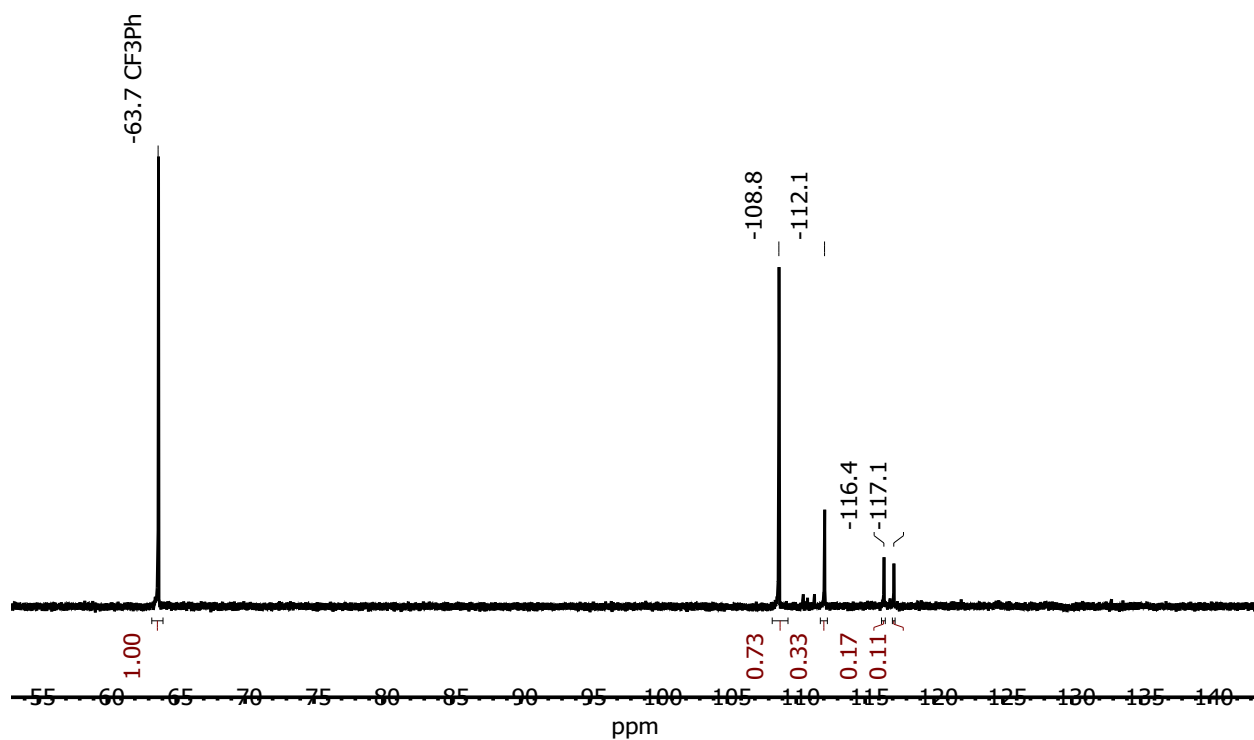


Figure A3.93 $^{19}\text{F}\{^1\text{H}\}$ NMR spectrum of the reaction mixture from one of the catalytic borylation reactions of 1,3,5-trifluorobenzene in THF following standard catalytic conditions detailed in methods section. The peaks at -108.8, -112.1, and -116.4 ppm are assigned as 1,3,5-trifluorobenzene, 1-Bpin-3,5- $\text{C}_6\text{F}_2\text{H}_3$, and 1,3-Bpin-5- C_6FH_3 , respectively.

A3.10.2 GC/MS Characterization

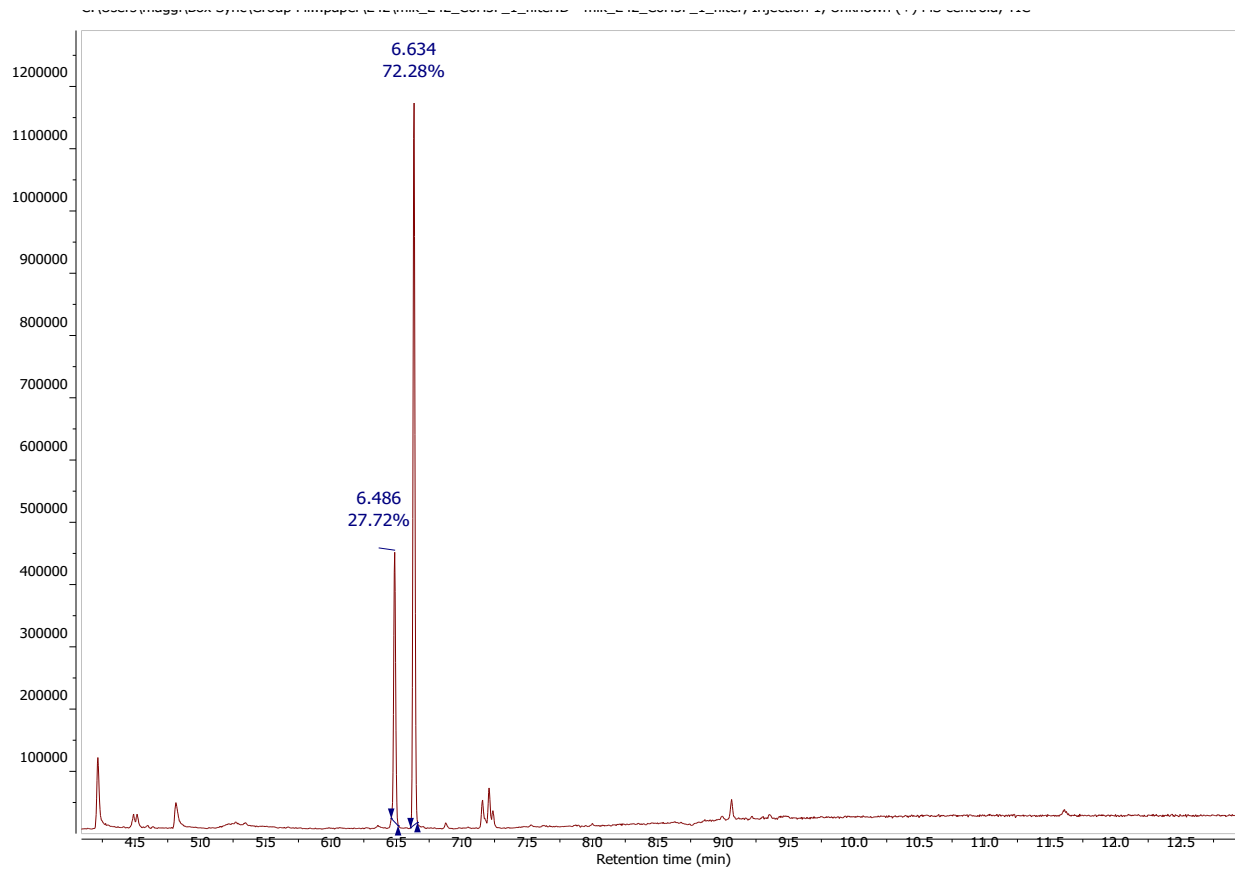


Figure A3.94 GC trace of the reaction mixture resulting from one of the catalytic borylation reactions of C_6H_5F . The peak at a retention time of 6.486 minutes corresponds to C_6H_5Bpin (see MS below) and the peak at 6.634 minutes corresponds to B_2pin_2 .

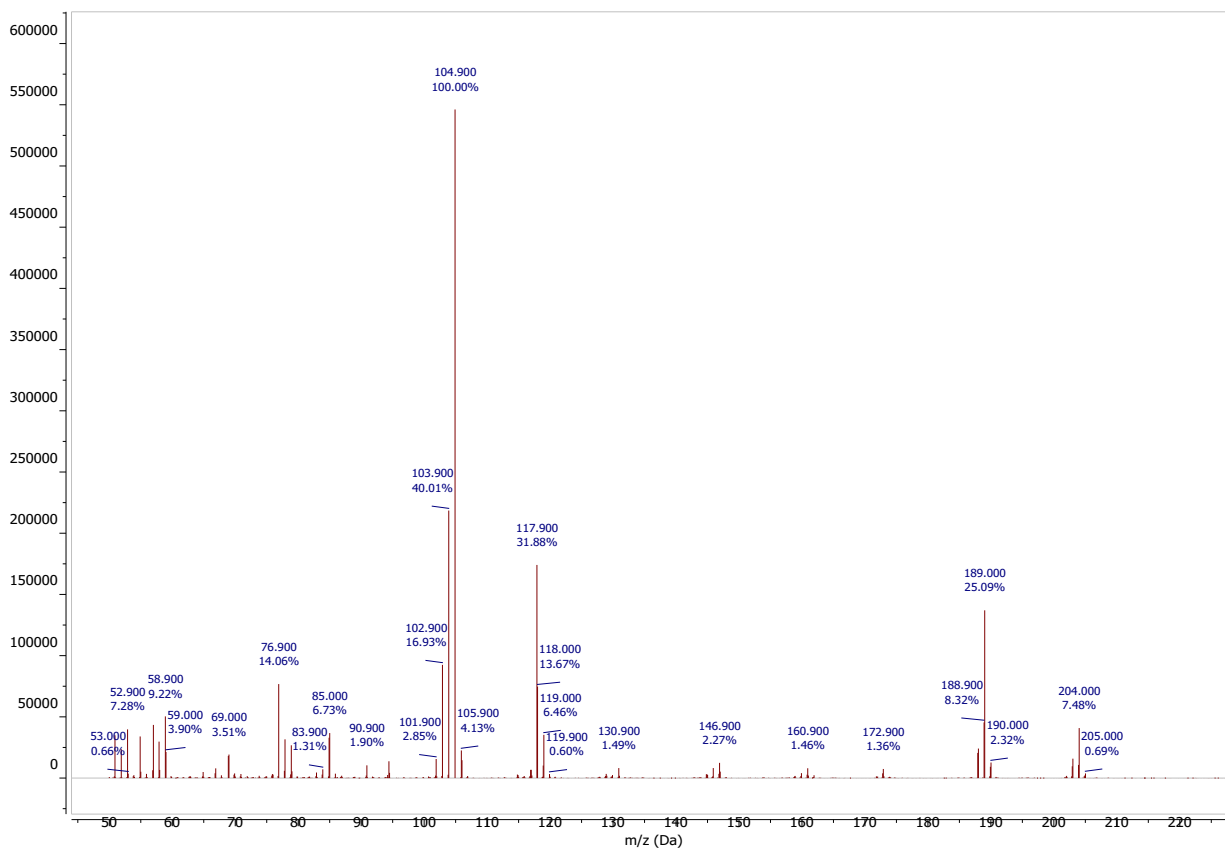
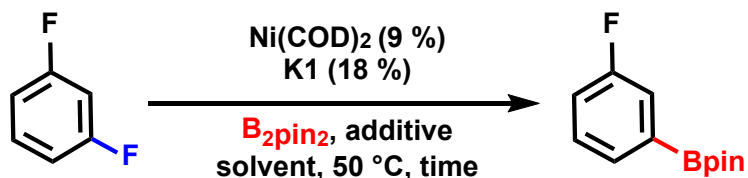


Figure A3.95 Mass spectrum of the C₆H₅Bpin peak from the reaction mixture GC resulting from one of the catalytic borylation reactions of C₆H₅F.

A3.11 Catalytic C-F Borylation Trial Reactions



Other Conditions explored		
Variation	Time (h)	Yield borylated product
CsOH·xH ₂ O (15-20% H ₂ O) (8-8.5 equiv.) + MeOH (20 equiv.) in 2 mL THF	6	53%
CsOH·xH ₂ O (15-20% H ₂ O) (8-8.5 equiv.) + H ₂ O (20 equiv.) + Zn dust (1 equiv.)	16	29%
Ba(OH) ₂	13	17%
CsOH·xH ₂ O (15-20% H ₂ O) (16-17 equiv.)	7	0%
CsOH·xH ₂ O (15-20% H ₂ O) (8-8.5 equiv.)	24	32%
CsOH·xH ₂ O (15-20% H ₂ O) (2-2.1 equiv.)	7	29%
CsOH·xH ₂ O (15-20% H ₂ O) (4-4.3 equiv.) + CsF (5 equiv.)	24	35%
TMSOAc	7	0%
TMAF + LiOH	24	6%
LiOH	24	17%

Reaction conditions unless otherwise stated – 1,3 C₆F₂H₄ (40 μL, 0.4 mmol, 11 equiv.), Ni(COD)₂ (10 mg, 0.036 mmol), K1 (22 mg, 0.072 mmol), B₂pin₂ (92 mg, 0.36 mmol, 10 equiv.), additive (0.36 mmol, 10 equiv.) and CF₃Ph (20 μL, 0.16 mmol, 4.5 equiv) were dissolved in 1 mL of THF and heated with stirring at 50 °C for the specified time. Yields determined by integration of ¹⁹F NMR peak of 1-Bpin-3-C₆FH₄ and comparison to the internal standard CF₃Ph. Yields are relative to the theoretical yield (0.4 mmol) determined using 1,3 C₆F₂H₄.

Table A3.17 Initial scan of additives for C-F borylation of 1,3 difluorobenzene.

Variation of reaction conditions with H ₂ O		
Additive/Variation	Time (h)	Yield borylated product
No additive	7	11%
TMAF • 4H ₂ O	7	0%
TMAOH • 5H ₂ O	7	0%
Ba(OH) ₂	16	42%
Ca(OH) ₂	16	25%
LiOH	13	20%
CsF	7	20%
CsOH•xH ₂ O (15-20% H ₂ O) (8-8.5 equiv.)	7	36%
CsOH•xH ₂ O (15-20% H ₂ O) (4-4.25 equiv.)	13	34%
CsOH•xH ₂ O (15-20% H ₂ O) (8-8.5 equiv.) + H ₂ O (40 equiv.)	13	36%
CsOH•xH ₂ O (15-20% H ₂ O) (8-8.5 equiv.) + H ₂ O (10 equiv.)	13	34%
Reaction conditions unless otherwise stated – 1,3 C ₆ F ₂ H ₄ (40 μL, 0.4 mmol, 11 equiv.), Ni(COD) ₂ (10 mg, 0.036 mmol), K1 (22 mg, 0.072 mmol), B ₂ pin ₂ (92 mg, 0.36 mmol, 10 equiv.), additive (0.36 mmol, 10 equiv.), CF ₃ Ph (20 μL, 0.16 mmol, 4.5 equiv) and H ₂ O (10 μL, 0.72 mmol, 20 equiv.) were dissolved in 1 mL of THF and heated with stirring at 50 °C for the specified time. Yields determined by integration of ¹⁹ F NMR peak of 1-Bpin-3-C ₆ FH ₄ and comparison to the internal standard CF ₃ Ph. Yields are relative to the theoretical yield (0.4 mmol) determined using 1,3 C ₆ F ₂ H ₄ .		

Table A3.18 Variation of reaction conditions with H₂O as an additive.

Variation of reaction conditions with alcohols		
Alcohol	Time (h)	Yield borylated product
MeOH (50 equiv.)	16	36%
<i>i</i> PrOH	16	31%
<i>t</i> BuOH	16	34%
PhOH	16	0
C ₆ F ₅ OH	16	0
EtOH	16	35%
Et(CH ₂ OH) ₃	16	25%

Reaction conditions unless otherwise stated – 1,3 C₆F₂H₄ (40 μL, 0.4 mmol, 11 equiv.), Ni(COD)₂ (10 mg, 0.036 mmol), K1 (22 mg, 0.072 mmol), B₂pin₂ (92 mg, 0.36 mmol, 10 equiv.), CsOH·xH₂O (15-20% H₂O) (54 mg, 0.29-0.31 mmol, 8-8.5 equiv.), CF₃Ph (20 μL, 0.16 mmol, 4.5 equiv.) and alcohol (0.72 mmol, 20 equiv.) were dissolved in 1 mL of THF and heated with stirring at 50 °C for the specified time. Yields determined by integration of ¹⁹F NMR peak of 1-Bpin-3-C₆FH₄ and comparison to the internal standard CF₃Ph. Yields are relative to the theoretical yield (0.4 mmol) determined using 1,3 C₆F₂H₄.

Table A3.19 Variation of reaction conditions with alcohols as additives.

Variation of reaction conditions with MeOH		
Additive/Variation	Time (h)	Yield borylated product
Ba(OH) ₂	16	23%
CsOH·xH ₂ O (15-20% H ₂ O) (8-8.5 equiv.)	13	43%
CsOH·xH ₂ O (15-20% H ₂ O) (8-8.5 equiv.) + B ₂ pin ₂ (20 equiv.)	16	59%
CsOH·xH ₂ O (15-20% H ₂ O) (8-8.5 equiv.) + CsF (2 equiv.) + B ₂ pin ₂ (20 equiv.)	16	53%
CsOH·xH ₂ O (15-20% H ₂ O) (8-8.5 equiv.) + B ₂ pin ₂ (30 equiv.)	16	63%
Reaction conditions unless otherwise stated – 1,3 C ₆ F ₂ H ₄ (40 μL, 0.4 mmol, 11 equiv.), Ni(COD) ₂ (10 mg, 0.036 mmol), K1 (22 mg, 0.072 mmol), B ₂ pin ₂ (92 mg, 0.36 mmol, 10 equiv.), additive (0.36 mmol, 10 equiv.), CF ₃ Ph (20 μL, 0.16 mmol, 4.5 equiv) and MeOH (30 μL, 0.72 mmol, 20 equiv.) were dissolved in 1 mL of THF and heated with stirring at 50 °C for the specified time. Yields determined by integration of ¹⁹ F NMR peak of 1-Bpin-3-C ₆ FH ₄ and comparison to the internal standard CF ₃ Ph. Yields are relative to the theoretical yield (0.4 mmol) determined using 1,3 C ₆ F ₂ H ₄ .		

Table A3.20 Variation of reaction conditions with MeOH as an additive

Variable times and controls		
Variation	Time (h)	Yield borylated product
None	1	47%
None	2	55%
None	4	54%
None	6	55%
PEt ₃ (2 equiv.) no K1	4	0%
PPh ₂ Et (2 equiv.) no K1	4	0%
PCy ₃ (2 equiv.), no K1	4	0%
Reaction conditions unless otherwise stated– 1,3 C ₆ F ₂ H ₄ (40 μL, 0.4 mmol, 11 equiv.), Ni(COD) ₂ (10 mg, 0.036 mmol), K1 (22 mg, 0.072 mmol), B ₂ pin ₂ (184 mg, 0.72 mmol, 20 equiv.), CsOH·xH ₂ O (15-20% H ₂ O) (54 mg, 0.29-0.31 mmol, 8-8.5 equiv.), CF ₃ Ph (20 μL, 0.16 mmol, 4.5 equiv) and MeOH (30 μL, 0.72 mmol, 20 equiv.) were dissolved in 1 mL of THF and heated with stirring at 50 °C for the specified time. Yields determined by integration of ¹⁹ F NMR peak of 1-Bpin-3-C ₆ FH ₄ and comparison to the internal standard CF ₃ Ph. Yields are relative to the theoretical yield (0.4 mmol) determined using 1,3 C ₆ F ₂ H ₄ .		

Table A3.21 Variation of reaction time with MeOH and CsOH additives and control reactions

Other Conditions explored		
Variation	Time (h)	Yield borylated product
None	4	55
LiOH (10 equiv.), no CsOH·xH ₂ O (15-20% H ₂ O)	4	35
Addition order*: combine MeOH and CsOH·xH ₂ O (15-20% H ₂ O) in THF, add B ₂ pin ₂ , fluoroarenes, then Ni complex	4	56
Addition order*: combine MeOH and CsOH·xH ₂ O (15-20% H ₂ O) in THF, then add Ni complex, then B ₂ Pin ₂ and fluoroarenes	4	53
Addition order*: combine MeOH and LiOH (20 equiv.) in THF, add B ₂ pin ₂ , fluoroarenes, then Ni complex, no CsOH·xH ₂ O	4	34
B ₂ neop ₂ (20 equiv.), no B ₂ pin ₂	4	32
B ₂ cat ₂ (20 equiv.), no B ₂ pin ₂	2	0
LiOMe (10 equiv.), no CsOH·xH ₂ O	4	29
LiOMe (10 equiv.), no CsOH·xH ₂ O, no MeOH	4	10
No CsOH·xH ₂ O	2	8
No CsOH·xH ₂ O, no MeOH	2	6
RT	22	44
100 °C	2	48
<p>Reaction conditions unless otherwise stated – 1,3 C₆F₂H₄ (40 μL, 0.4 mmol, 11 equiv.), Ni(COD)₂ (10 mg, 0.036 mmol), K1 (22 mg, 0.072 mmol), B₂pin₂ (184 mg, 0.72 mmol, 20 equiv.), CsOH·xH₂O (15-20% H₂O) (54 mg, 0.29-0.31 mmol, 8-8.5 equiv.), CF₃Ph (20 μL, 0.16 mmol, 4.5 equiv) and MeOH (30 μL, 0.72 mmol, 20 equiv.) were dissolved in 1 mL of THF and heated with stirring at 50 °C for the specified time. Yields determined by integration of ¹⁹F NMR peak of 1-Bpin-3-C₆FH₄ and comparison to the internal standard CF₃Ph. Yields are relative to the theoretical yield (0.4 mmol) determined using 1,3 C₆F₂H₄.</p> <p>*Standard order of addition: combine Ni(COD)₂, K1, and B₂pin₂ in 1 mL THF. Add CF₃Ph, then 1,3 C₆F₂H₄, then CsOH·xH₂O (15-20% H₂O) and finally MeOH before placing on hot plate.</p>		

Table A3.22 Variation of addition order and additives.

Alternative cations		
Variation	Time (h)	Yield borylated product
Combine K1 and PPh ₄ Br (2 equiv.) in THF, filter and dry to isolate crude PPh ₄ 1, use instead of K1	2	8
Combine K1 and TBACl (2 equiv.) in THF, filter and dry to isolate crude TBA1, use instead of K1	2	46
Combine K1 and TEABr (2 equiv.) in THF, filter and dry to isolate crude TEA1, use instead of K1	2	35
Add 18-crown-6 (2 equiv.)	2	43
<p>Reaction conditions unless otherwise stated – 1,3 C₆F₂H₄ (40 μL, 0.4 mmol, 11 equiv.), Ni(COD)₂ (10 mg, 0.036 mmol), K1 (22 mg, 0.072 mmol), B₂pin₂ (184 mg, 0.72 mmol, 20 equiv.), CsOH·xH₂O (15-20% H₂O) (54 mg, 0.29-0.31 mmol, 8-8.5 equiv.), CF₃Ph (20 μL, 0.16 mmol, 4.5 equiv.) and MeOH (30 μL, 0.72 mmol, 20 equiv.) were dissolved in 1 mL of THF and heated with stirring at 50 °C for the specified time. Yields determined by integration of ¹⁹F NMR peak of 1-Bpin-3-C₆FH₄ and comparison to the internal standard CF₃Ph. Yields are relative to the theoretical yield (0.4 mmol) determined using 1,3 C₆F₂H₄.</p> <p>*Standard order of addition: combine Ni(COD)₂, K1, and B₂pin₂ in 1 mL THF. Add CF₃Ph, then 1,3 C₆F₂H₄, then CsOH·xH₂O (15-20% H₂O) and finally MeOH before placing on hot plate.</p>		

Table A3.23 Variation of cations.

Solvent variation		
Variation	Time (h)	Yield borylated product
Dioxane ($\epsilon = 2.25$) instead of THF ($\epsilon = 7.58$)	2	43
Toluene ($\epsilon = 2.38$) instead of THF ($\epsilon = 7.58$)	2	20
Diethyl ether ($\epsilon = 4.33$) instead of THF ($\epsilon = 7.58$)	2	10
Methyl tert-butyl ether ($\epsilon = 4.5$) instead of THF ($\epsilon = 7.58$)	2	13
Cyclopentyl methyl ether ($\epsilon = 4.76$) instead of THF ($\epsilon = 7.58$)	2	24
4-Methyl tetrahydropyran ($\epsilon = 4.8$) instead of THF ($\epsilon = 7.58$)	2	49
Tetrahydropyran ($\epsilon = 5.7$) instead of THF ($\epsilon = 7.58$)	2	59
MeTHF ($\epsilon = 6.97$) instead of THF ($\epsilon = 7.58$)	2	52
Dimethoxyethane ($\epsilon = 7.2$) instead of THF ($\epsilon = 7.58$)	2	47
1,4 C ₆ F ₂ H ₄ instead of 1,3 C ₆ F ₂ H ₄ Tetrahydropyran ($\epsilon = 5.7$) instead of THF ($\epsilon = 7.58$)	2	26

Reaction conditions unless otherwise stated – 1,3 C₆F₂H₄ (40 μ L, 0.4 mmol, 11 equiv.), Ni(COD)₂ (10 mg, 0.036 mmol), K1 (22 mg, 0.072 mmol), B₂pin₂ (184 mg, 0.72 mmol, 20 equiv.), CsOH·xH₂O (15-20% H₂O) (54 mg, 0.29-0.31 mmol, 8-8.5 equiv.), CF₃Ph (20 μ L, 0.16 mmol, 4.5 equiv.) and MeOH (30 μ L, 0.72 mmol, 20 equiv.) were dissolved in 1 mL of THF and heated with stirring at 50 °C for the specified time. Yields determined by integration of ¹⁹F NMR peak of 1-Bpin-3-C₆FH₄ and comparison to the internal standard CF₃Ph. Yields are relative to the theoretical yield (0.4 mmol) determined using 1,3 C₆F₂H₄.

Table A3.24 Variation of reaction solvent.

Appendix 4: Supporting Data for Chapter 4

A4.1 Characterization data

A4.1.1 PPh(6-BF₃-2-pyH)₂

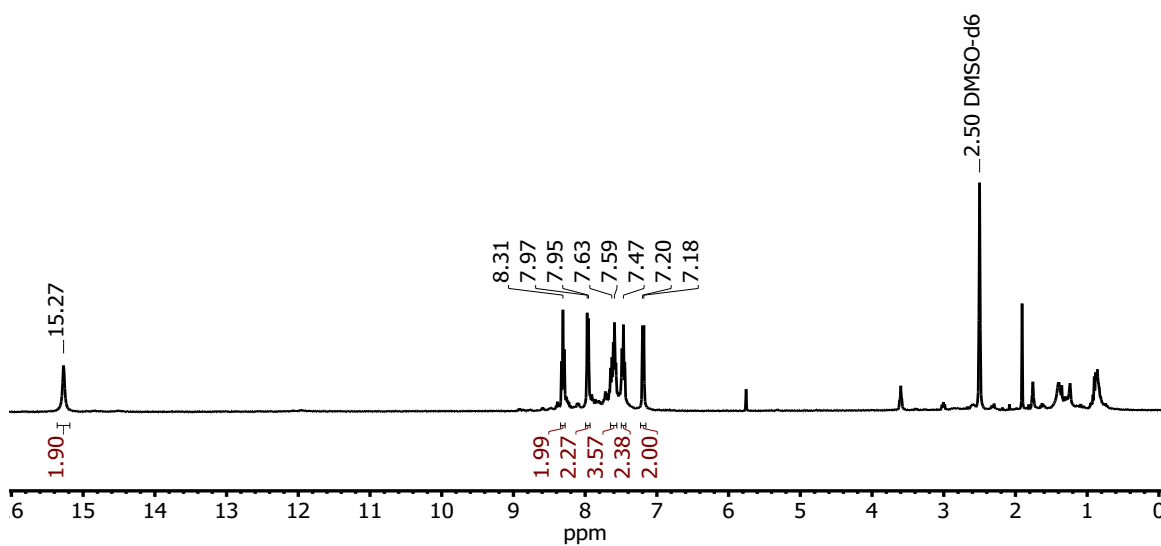


Figure A4.1 ¹H NMR spectrum of PPh(6-BF₃-2-pyH)₂ in DMSO-*d*₆.

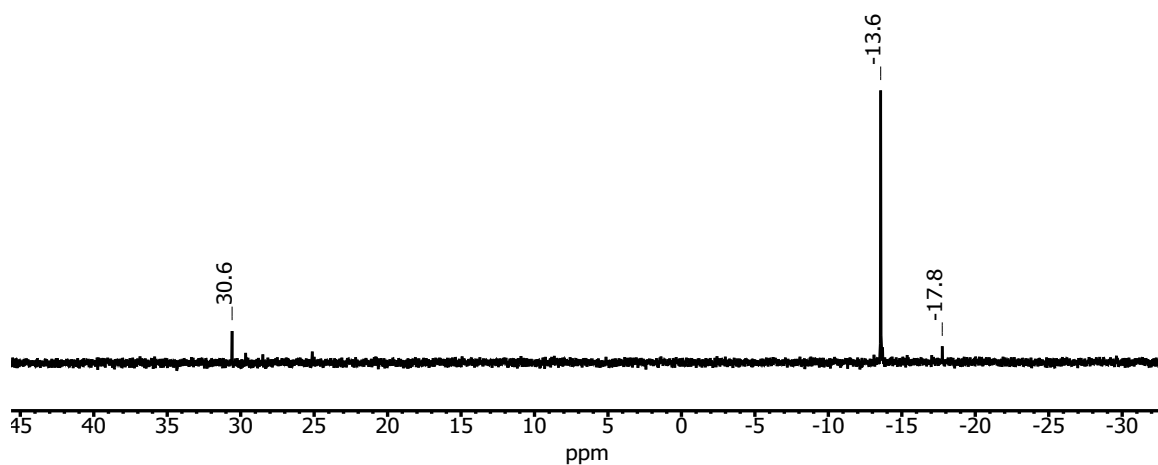


Figure A4.2 $^{31}\text{P}\{^1\text{H}\}$ NMR spectrum of $\text{PPh}(\text{6-BF}_3\text{-2-pyH})_2$ in $\text{DMSO-}d_6$.

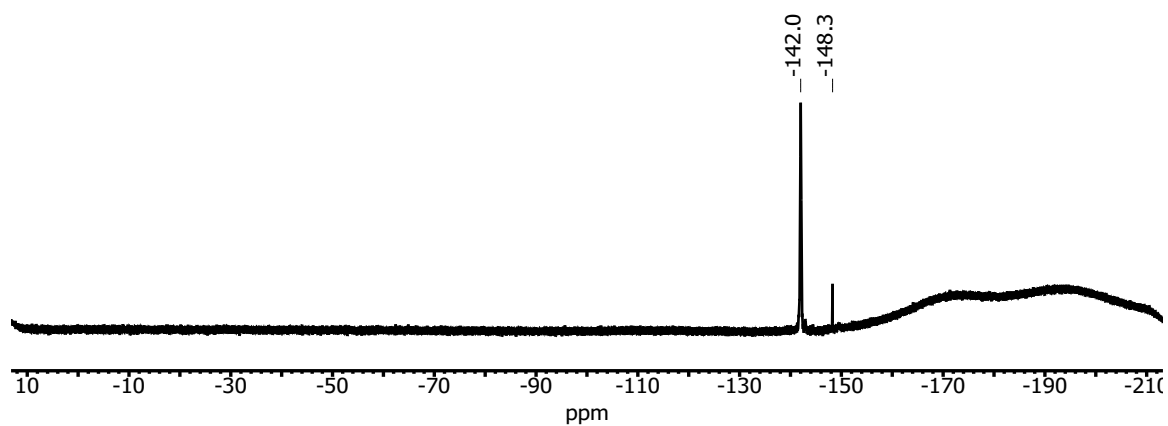


Figure A4.3 $^{19}\text{F}\{^1\text{H}\}$ NMR spectrum of $\text{PPh}(\text{6-BF}_3\text{-2-pyH})_2$ in $\text{DMSO-}d_6$. The broad peaks in the baseline around 150 – 220 ppm result from Teflon within the probe.

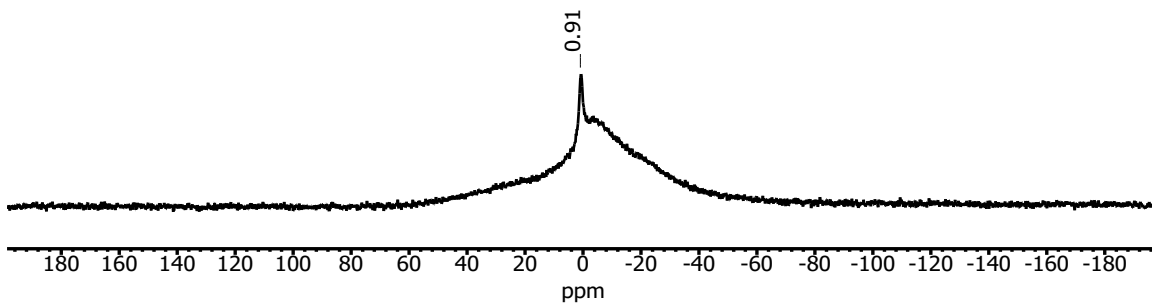


Figure A4.4 $^{11}\text{B}\{^1\text{H}\}$ spectrum of $\text{PPh}(6\text{-BF}_3\text{-2-pyH})_2$ in $\text{DMSO-}d_6$. The broad peak in the baseline is a result of borosilicate in the NMR tube.

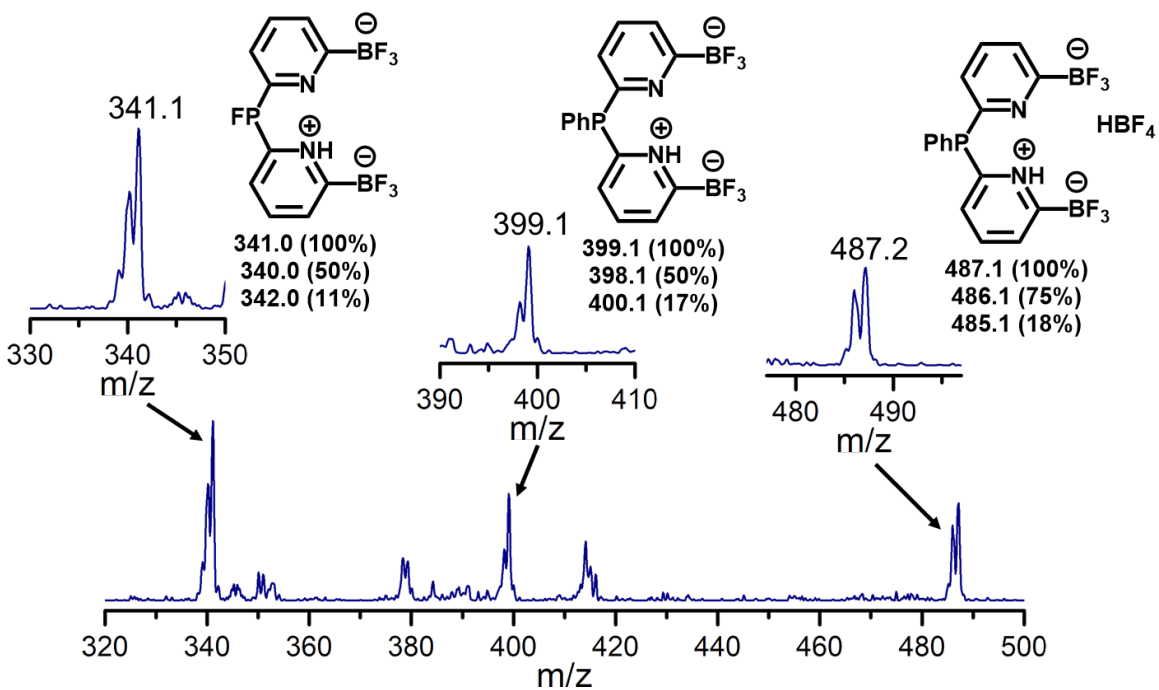


Figure A4.5 Negative mode ESI-MS of $\text{PPh}(6\text{-BF}_3\text{-2-pyH})_2$ in MeCN . Isotope patterns are observed as a result of ^{11}B having 80% abundance and ^{10}B having 20% abundance, but the peak intensity for ^{10}B is increased due to the presence of 2 B atoms. The expected isotope patterns shown written below each assignment were predicted using chemdraw.

A4.1.2 P(6-BF₃-2-pyH)₃

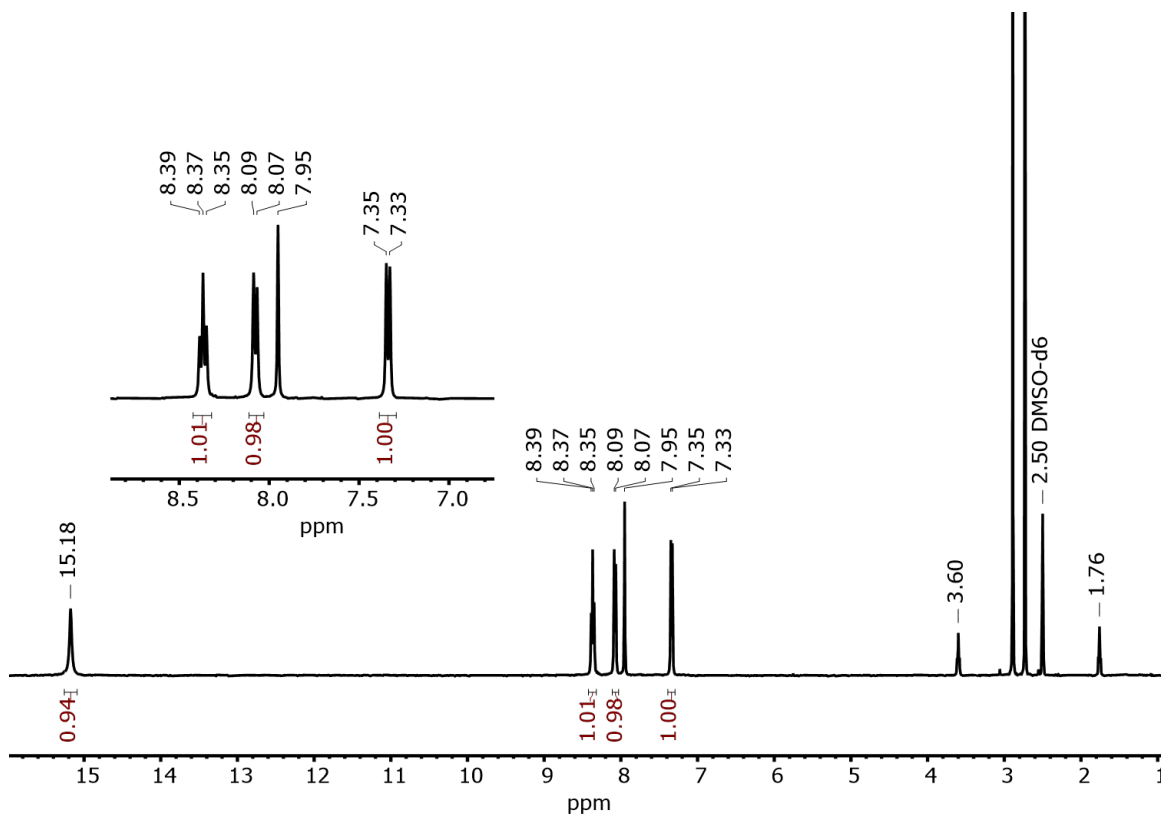


Figure A4.6 ¹H NMR spectrum of P(6-BF₃-2-pyH)₃ in DMSO-*d*₆ with DMF and THF impurities present from the crystallization conditions.

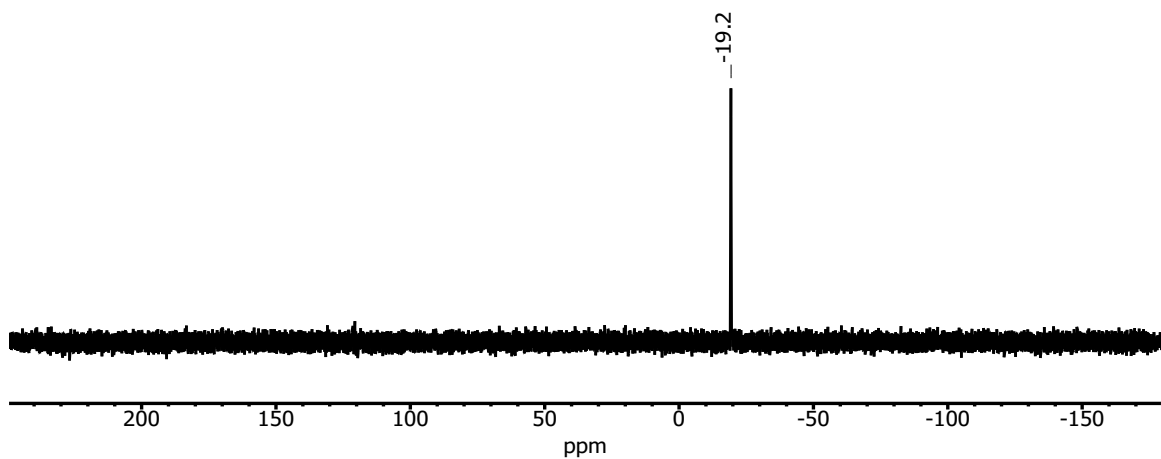


Figure A4.7 ³¹P{¹H} NMR spectrum of P(6-BF₃-2-pyH)₃ in DMSO-*d*₆.

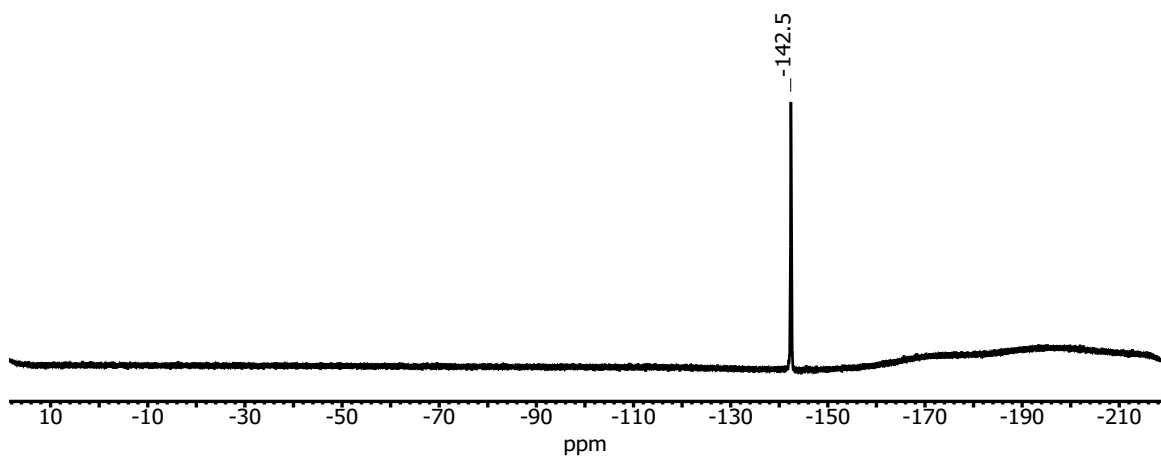


Figure A4.8 $^{19}\text{F}\{^1\text{H}\}$ NMR spectrum of $\text{P}(\text{6-BF}_3\text{-2-pyH})_3$ in $\text{DMSO-}d_6$. The broad peaks in the baseline around 150 – 220 ppm result from Teflon within the probe

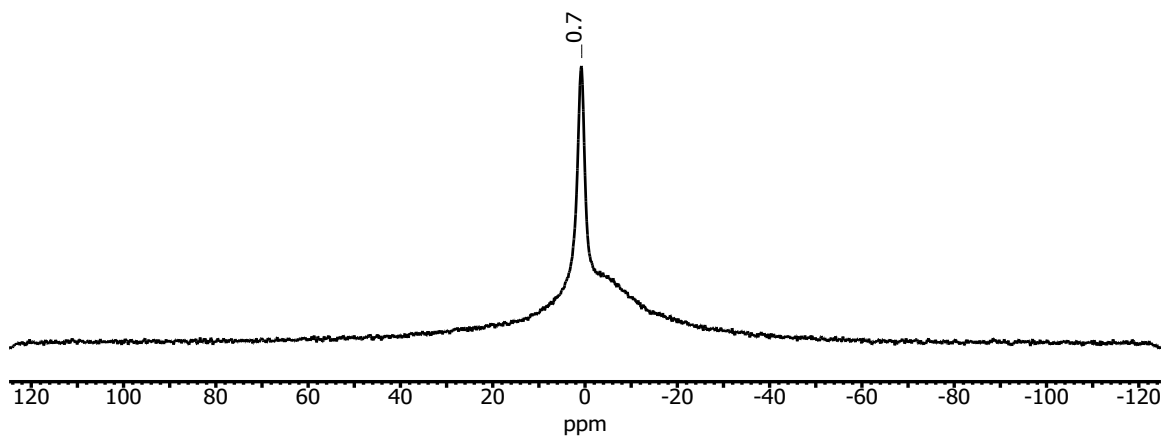


Figure A4.9 $^{11}\text{B}\{^1\text{H}\}$ NMR of $\text{P}(\text{6-BF}_3\text{-2-pyH})_3$ in $\text{DMSO-}d_6$. The broad peak observed in the baseline is a result of borosilicate in the NMR tube.

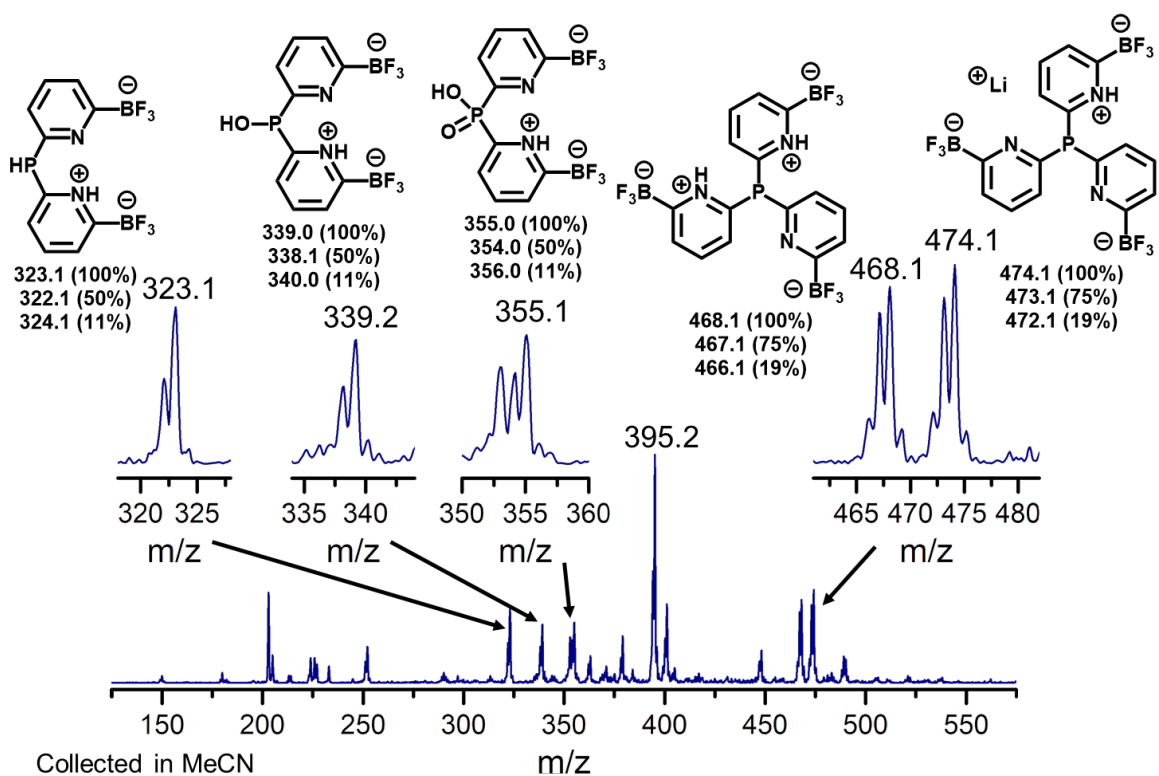


Figure A4.10 Negative mode ESI-MS of $P(6-BF_3-2-pyH)_3$ in MeCN. Isotope patterns are observed as a result of ^{11}B having 80% abundance and ^{10}B having 20% abundance, but the peak intensity for ^{10}B is increased due to the presence of 3 B atoms. The expected isotope patterns shown written below each assignment were predicted using chemdraw.

A4.1.3 [P(2-py)₃NiNO][BPh₄]

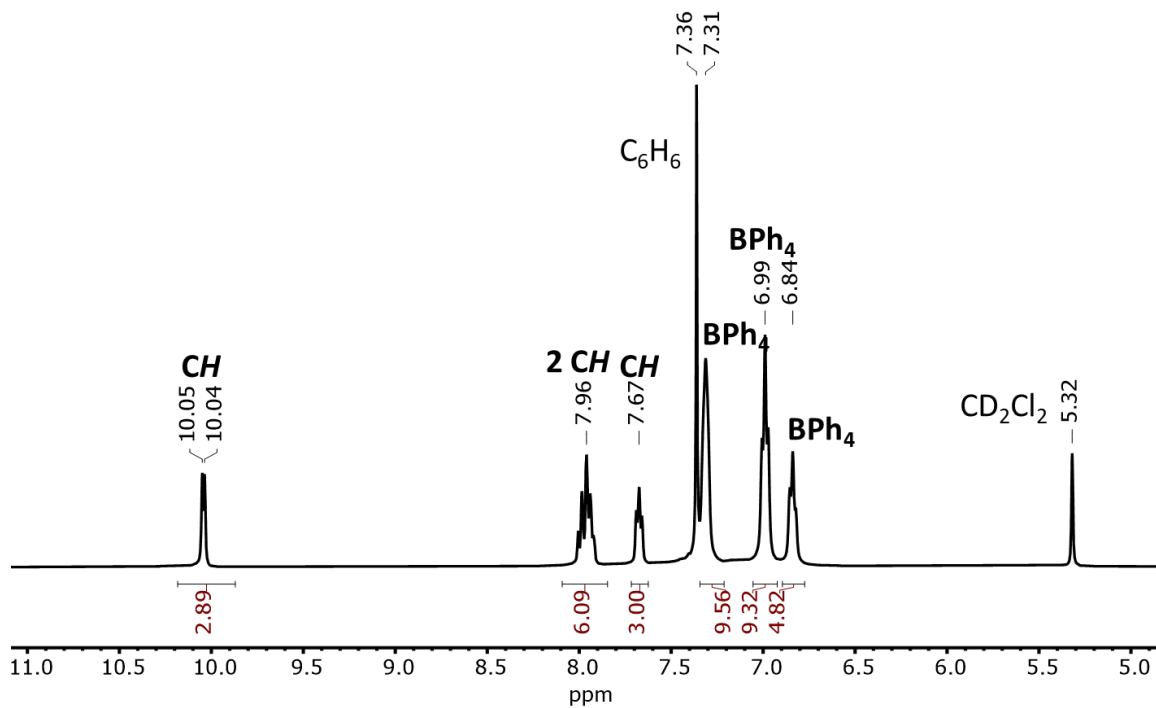


Figure A4.11 Aromatic region of the ¹H NMR spectrum of [P(2-py)₃NiNO][BPh₄] in CD₂Cl₂ with assignments for the resonances. Minor additional impurity peaks are observed outside of this region around 1.3 ppm.

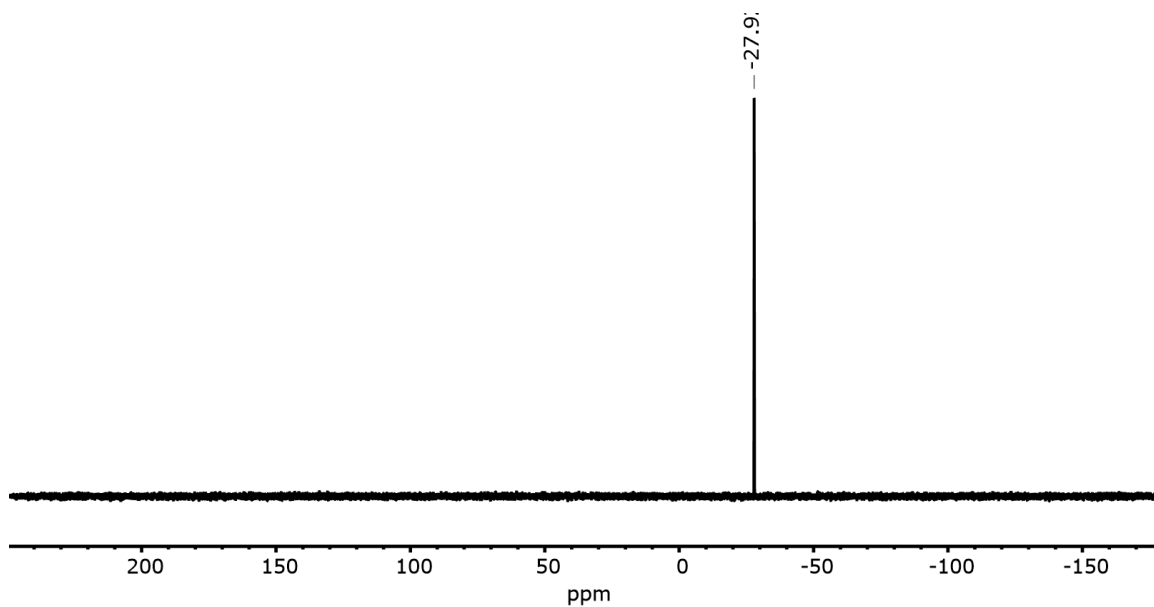


Figure A4.12 $^{31}\text{P}\{^1\text{H}\}$ NMR spectrum of $[\text{P}(2\text{-py})_3\text{NiNO}][\text{BPh}_4]$ in CD_2Cl_2 .

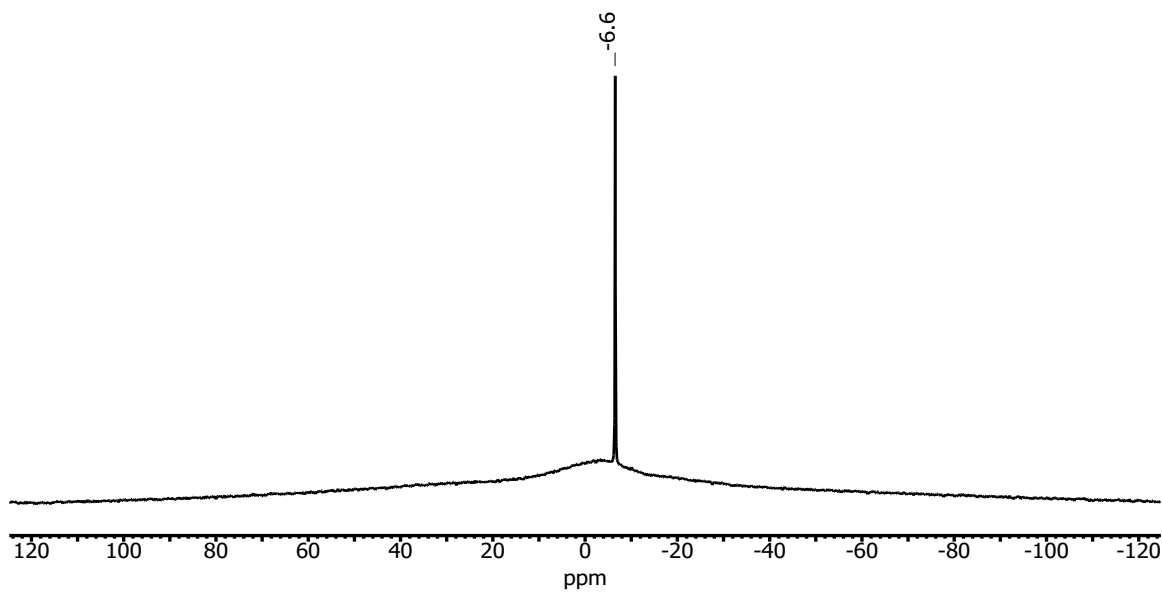


Figure A4.13 $^{11}\text{B}\{^1\text{H}\}$ NMR spectrum of $[\text{P}(2\text{-py})_3\text{NiNO}][\text{BPh}_4]$ in CD_2Cl_2 . The broad peak around 0 is a result of borosilicate in the NMR tube.

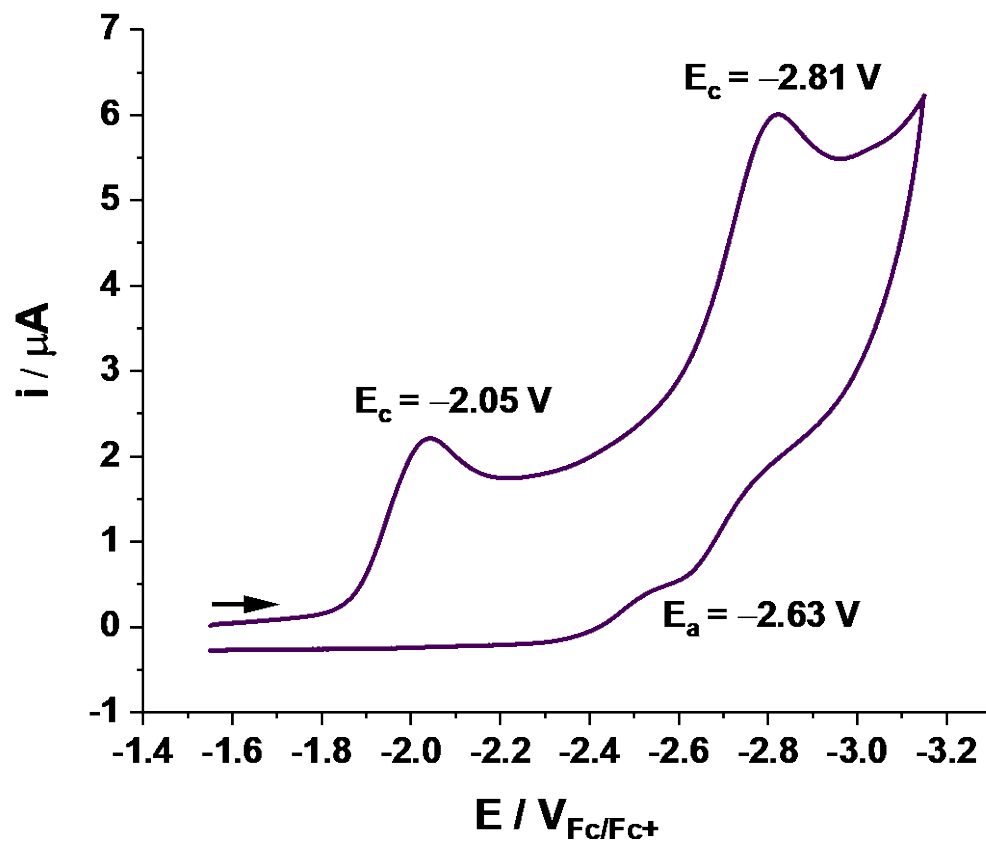


Figure A4.14 Cyclic voltammogram of [P(2-py)₃NiNO][BPh₄] collected in a 0.1 M NaBPh₄ THF solution and referenced to external ferrocenium.

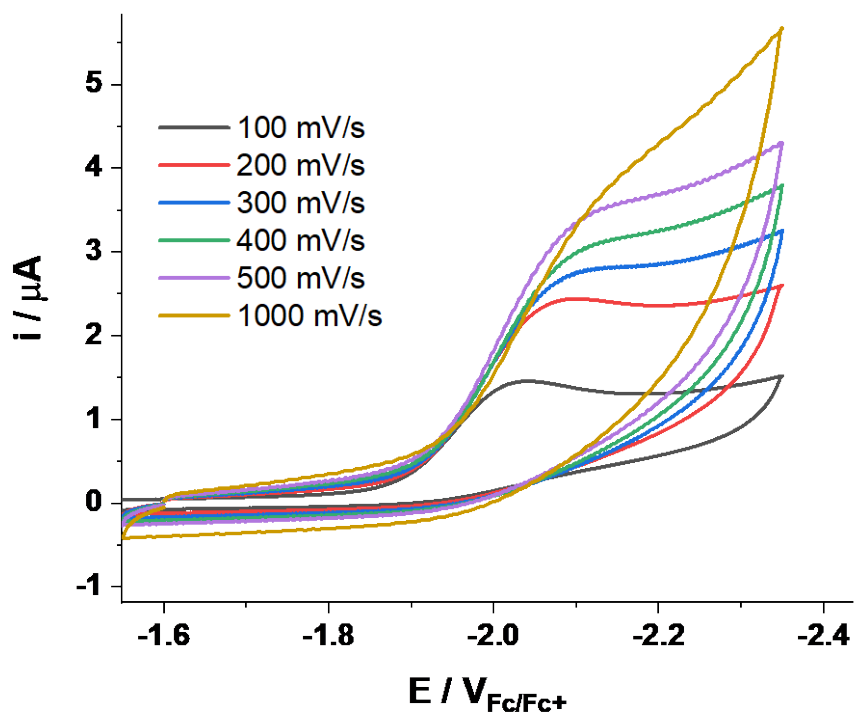


Figure A4.15 Cyclic voltammogram of first reduction of $[P(2\text{-py})_3\text{NiNO}][\text{BPh}_4]$ collected at variable scan rates.

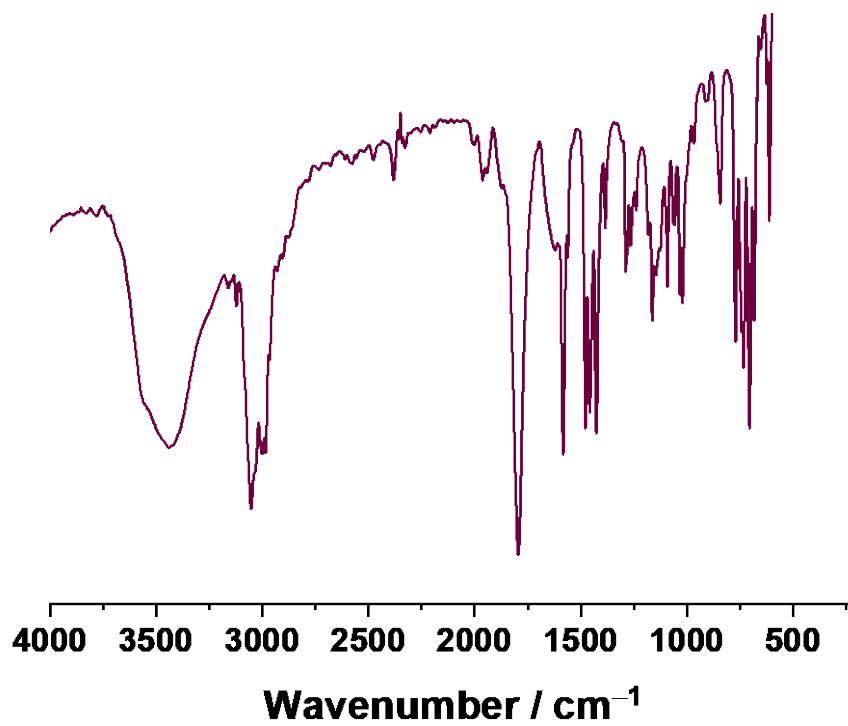


Figure A4.16 IR spectrum of $[P(2\text{-py})_3\text{NiNO}][\text{BPh}_4]$ collected in a KBr pellet.

A4.1.4 K[2-Br-4-BF₂CF₃-py]

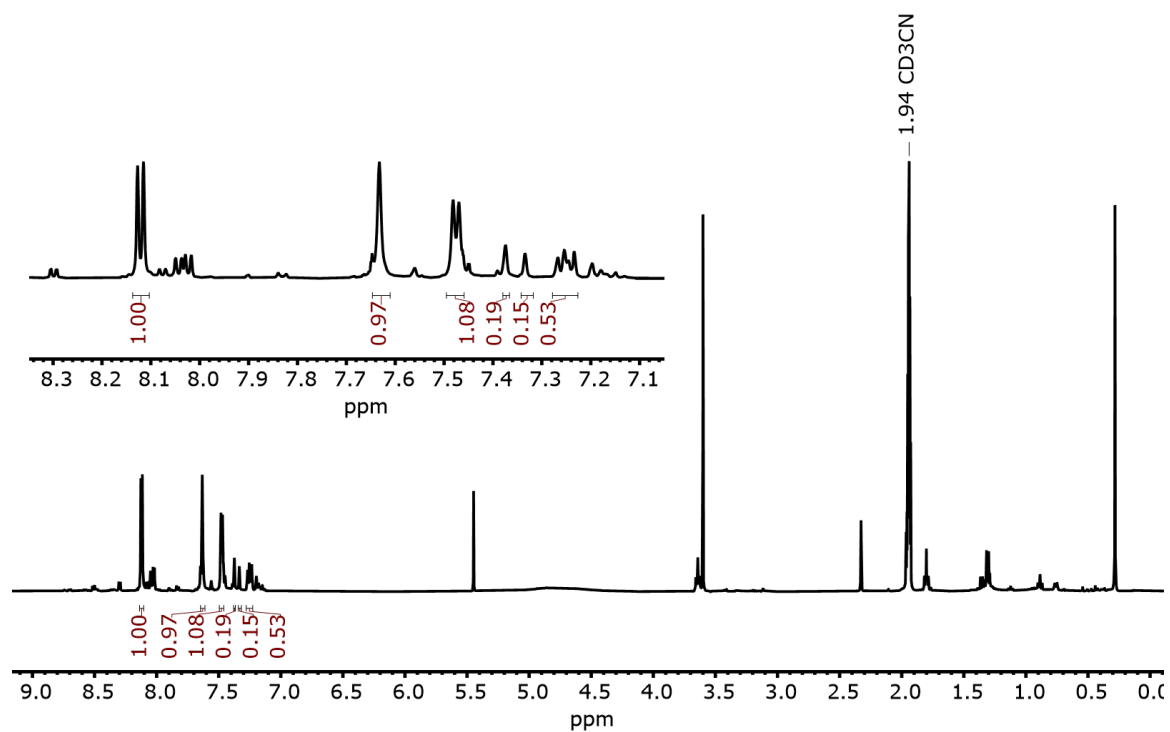


Figure A4.17 ¹H NMR spectrum in CD₃CN of crude product from synthesis of K[2-Br-4-BF₂CF₃-py] after washing with DCM/hexane at -78 °C.

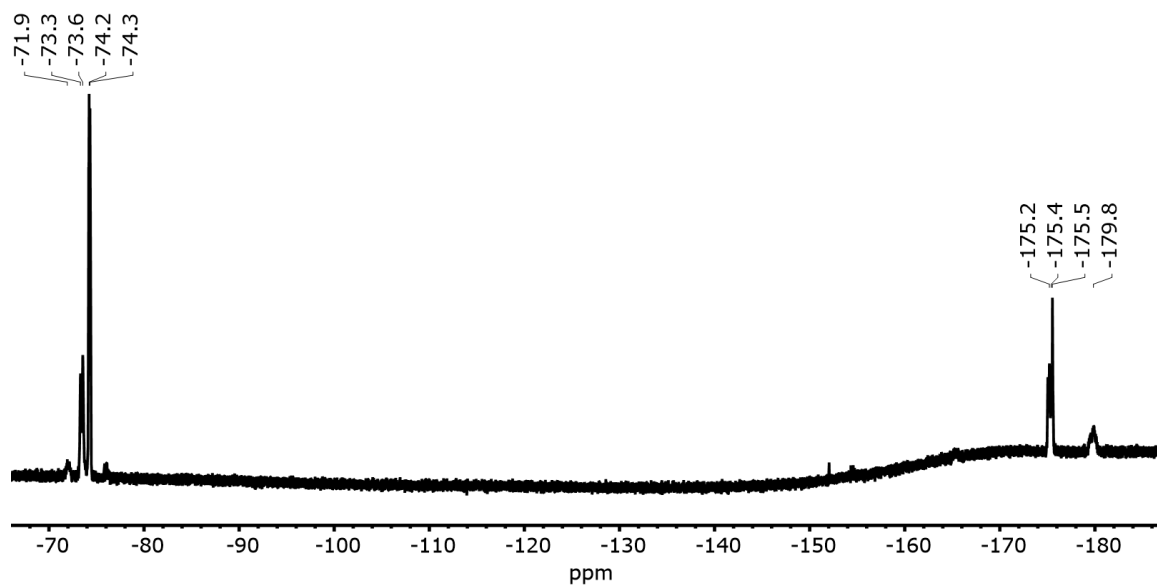


Figure A4.18 $^{19}\text{F}\{^1\text{H}\}$ NMR spectrum in CD_3CN of crude product from synthesis of $\text{K}[2\text{-Br-4-BF}_2\text{CF}_3\text{-py}]$ after washing with DCM/hexane at $-78\text{ }^\circ\text{C}$. The broad peaks in the baseline around 150 – 220 ppm result from Teflon within the probe

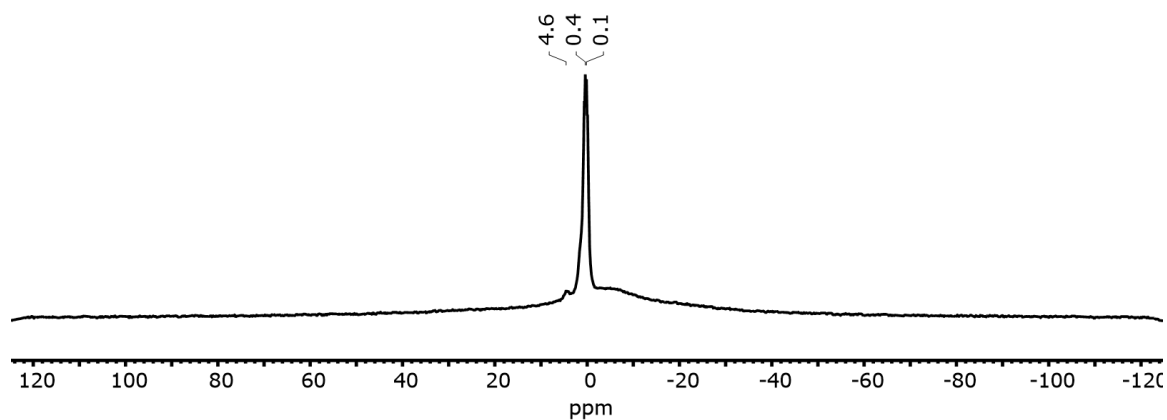


Figure A4.19 $^{11}\text{B}\{^1\text{H}\}$ NMR spectrum in CD_3CN of crude product from synthesis of $\text{K}[2\text{-Br-4-BF}_2\text{CF}_3\text{-py}]$ after washing with DCM/hexane at $-78\text{ }^\circ\text{C}$. The broad peak around 0 is a result of borosilicate in the NMR tube.

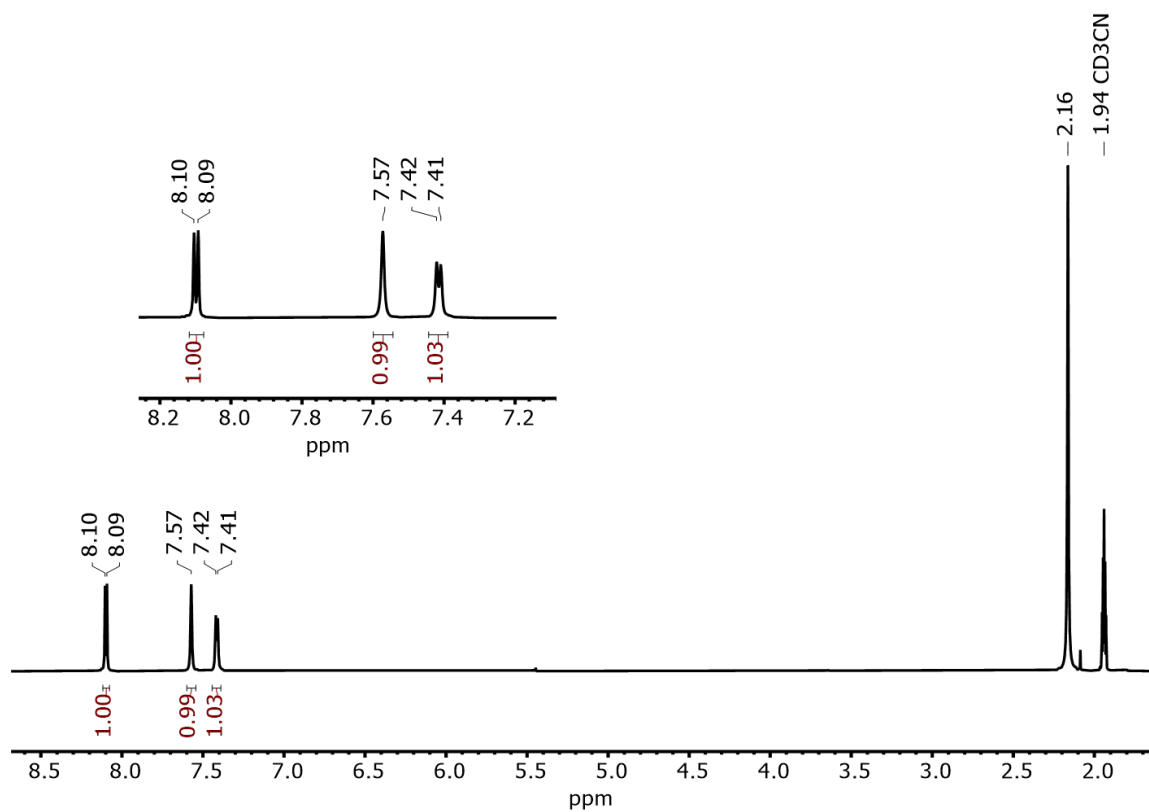


Figure A4.20 ^1H NMR spectrum in CD_3CN of crystalline $\text{K}[2\text{-Br-4-BF}_2\text{CF}_3\text{-py}]$ from a concentrated THF/DCM solution. Deuteriosolvent was stored outside of the glovebox, accounting for the water impurity at 2.16 ppm.

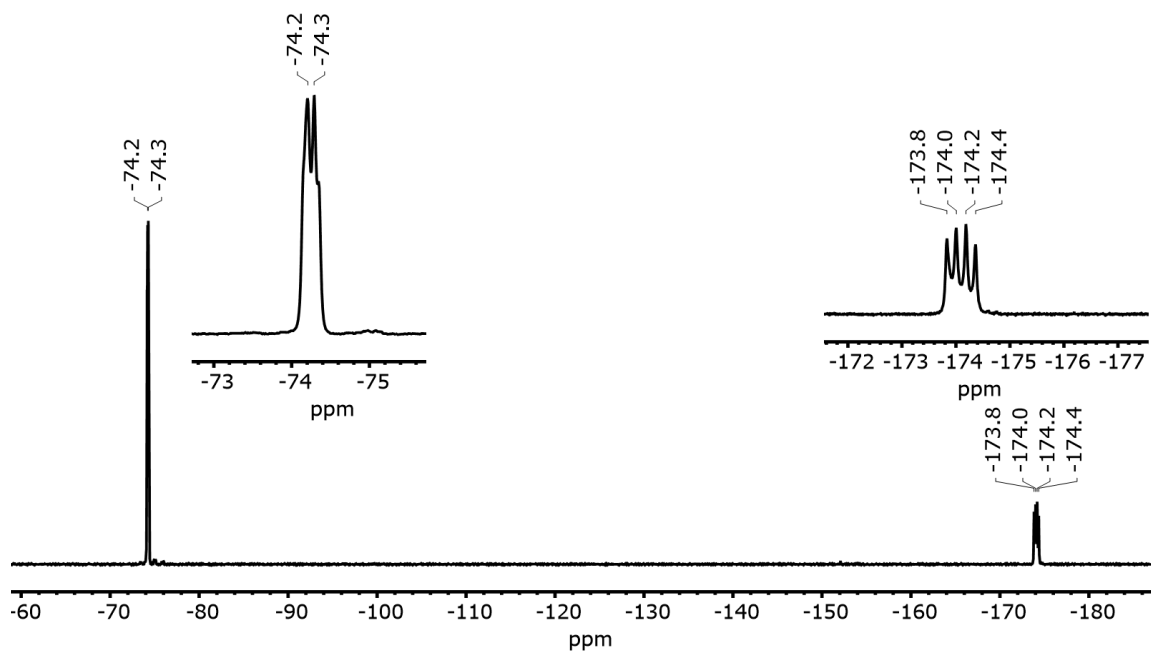


Figure A4.21 $^{19}\text{F}\{^1\text{H}\}$ NMR spectrum in CD_3CN of crystalline $\text{K}[2\text{-Br-4-BF}_2\text{CF}_3\text{-py}]$ from a concentrated THF/DCM solution.

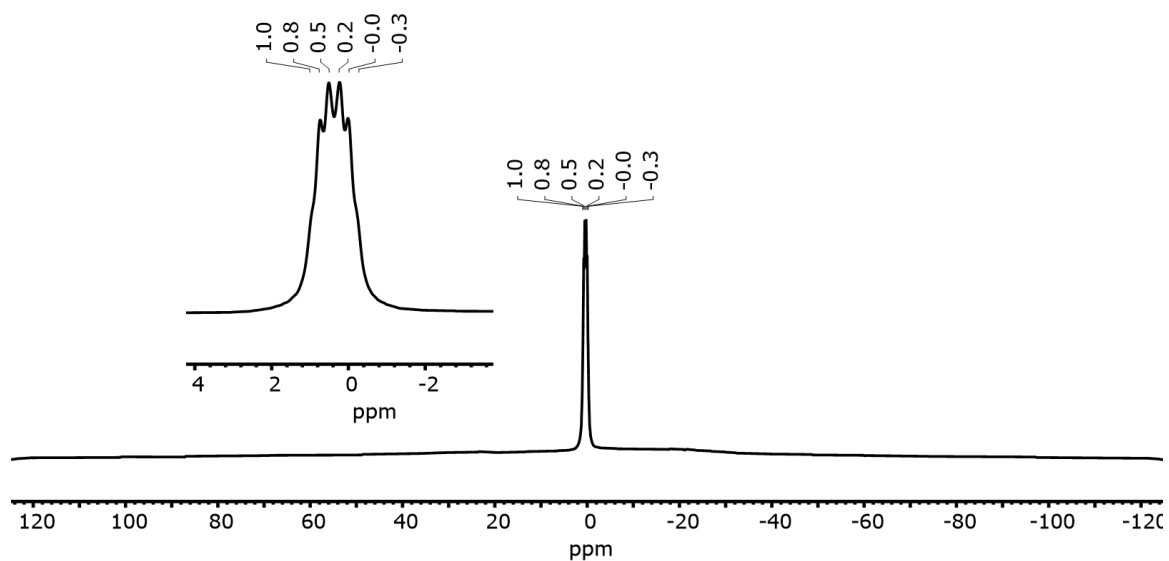


Figure A4.22 $^{11}\text{B}\{^1\text{H}\}$ NMR spectrum in CD_3CN of crystalline $\text{K}[2\text{-Br-4-BF}_2\text{CF}_3\text{-py}]$ from a concentrated THF/DCM solution.

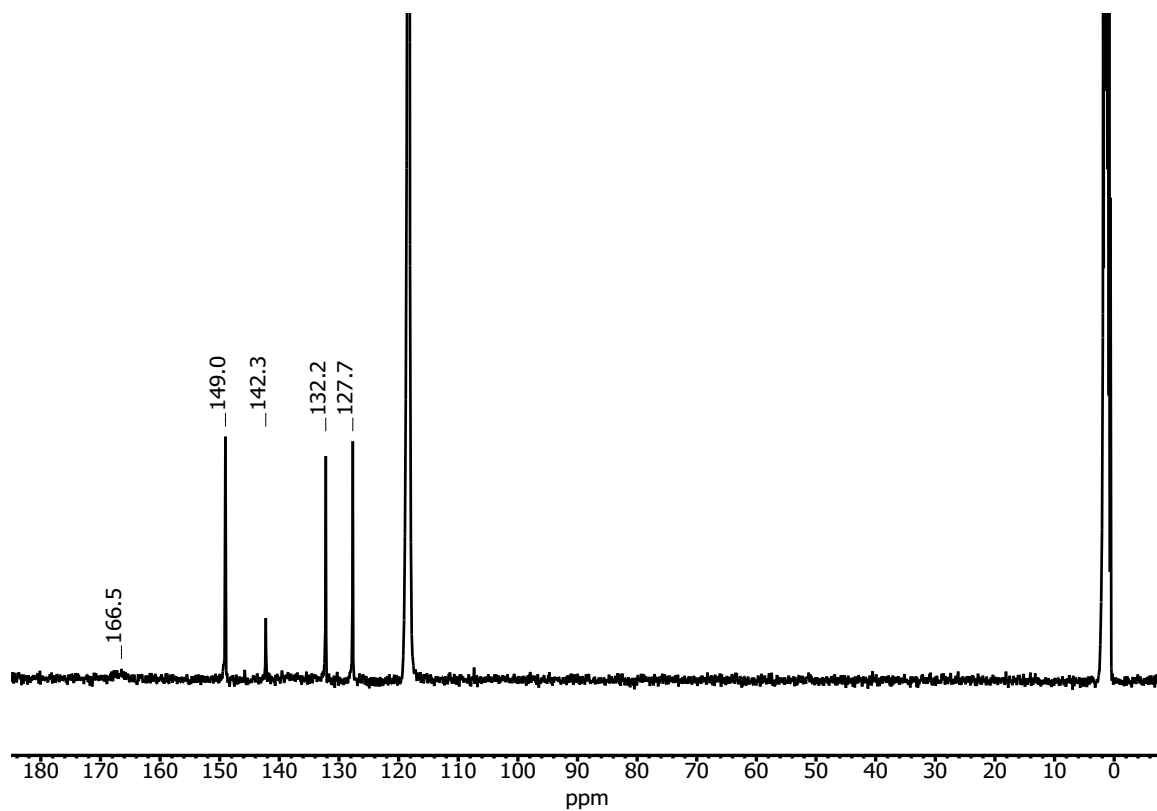


Figure A4.23 $^{13}\text{C}\{^1\text{H}\}$ NMR spectrum in CD_3CN of crystalline $\text{K}[2\text{-Br-4-BF}_2\text{CF}_3\text{-py}]$ from a concentrated THF/DCM solution.

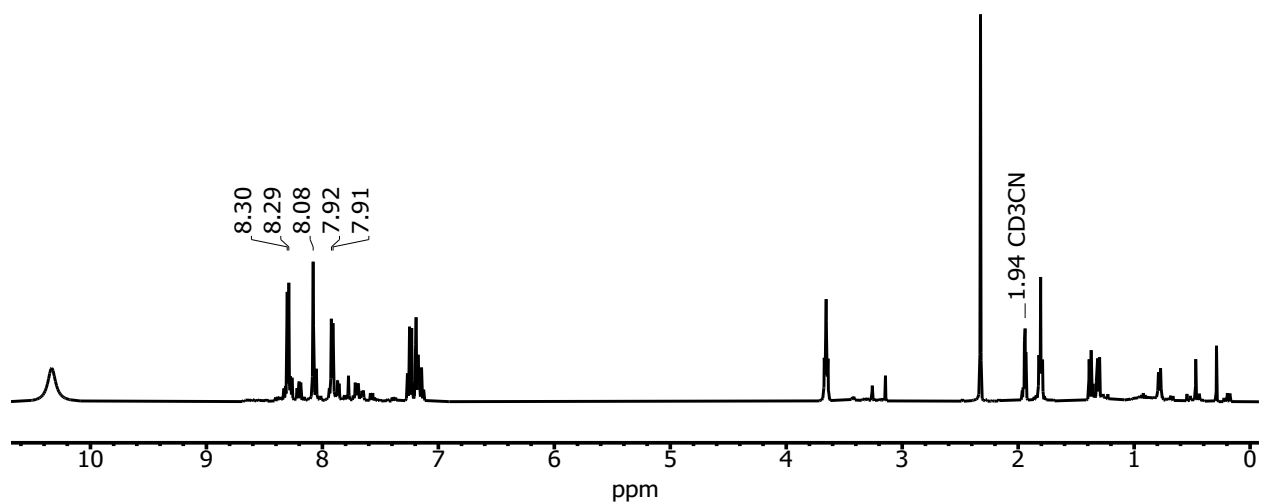


Figure A4.24 ^1H NMR spectrum of crude product of reaction with $\text{B}(\text{OMe})_2\text{CF}_3$ without the use of dioxane.

A4.1.5 K[2-Br-3-BF₂CF₃-py]

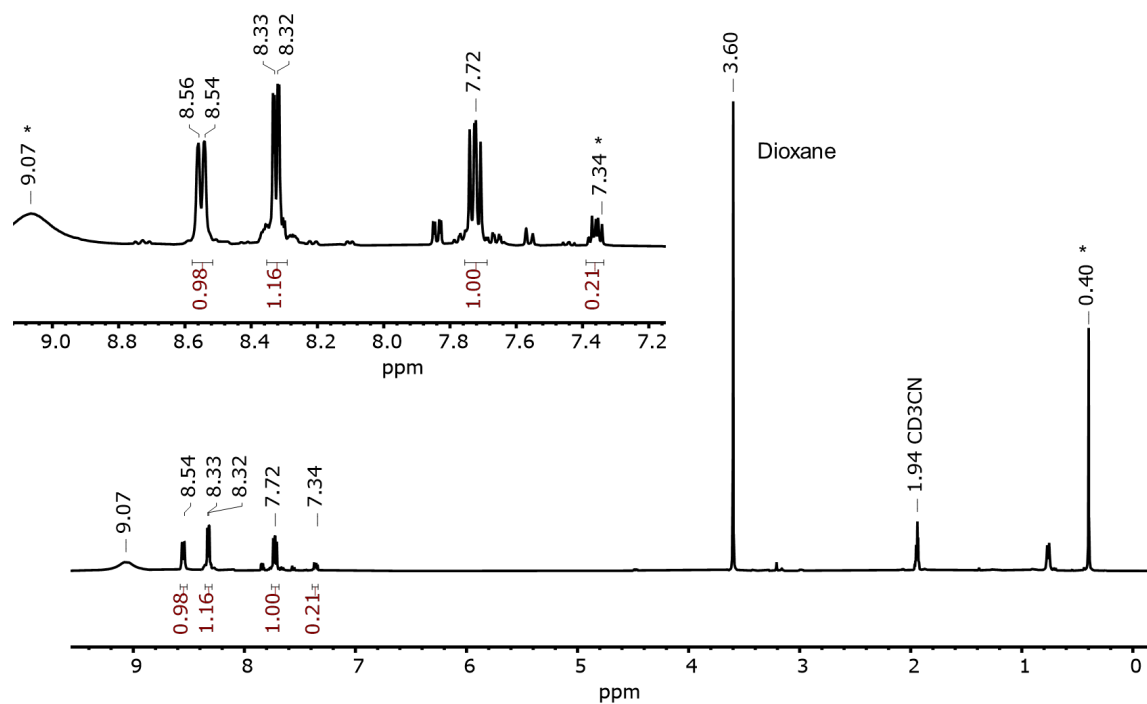


Figure A4.25 ¹H NMR spectrum in CD₃CN of the crude brown oil from the synthesis of K[2-Br-3-BF₂CF₃-py]. Asterisks indicate unknown impurities.

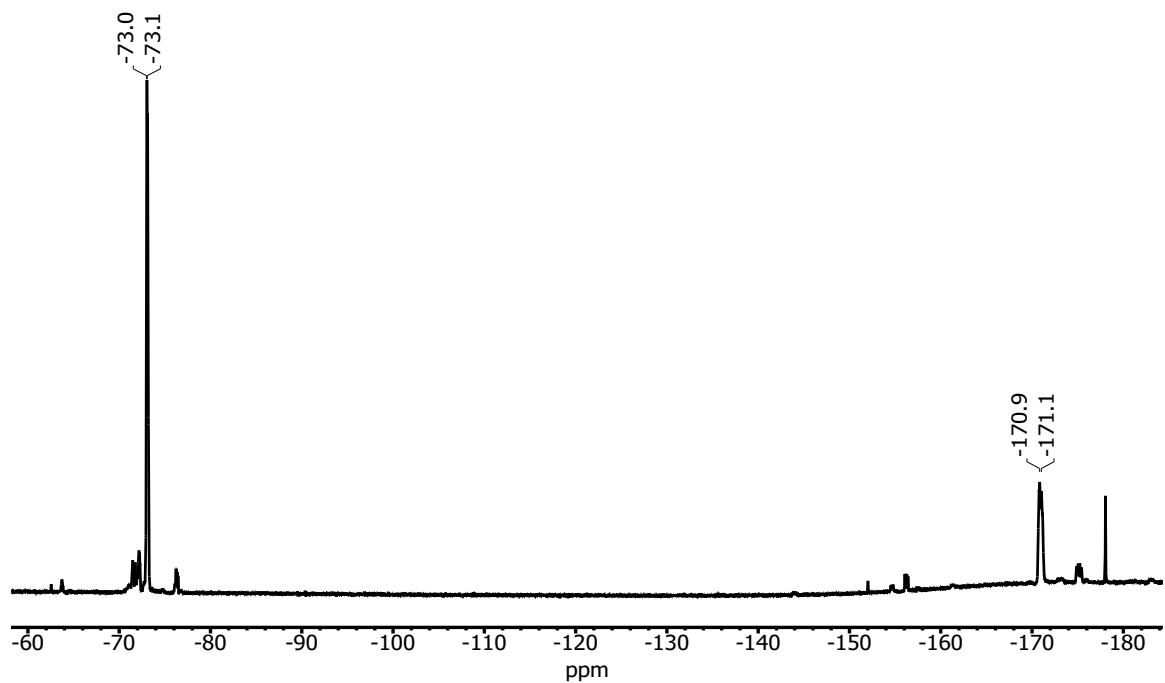


Figure A4.26 $^{19}\text{F}\{^1\text{H}\}$ NMR spectrum collected in CD_3CN of the crude brown oil from the synthesis of $\text{K}[2\text{-Br-3-BF}_2\text{CF}_3\text{-py}]$. The broad peaks in the baseline around 150 – 220 ppm result from Teflon within the probe

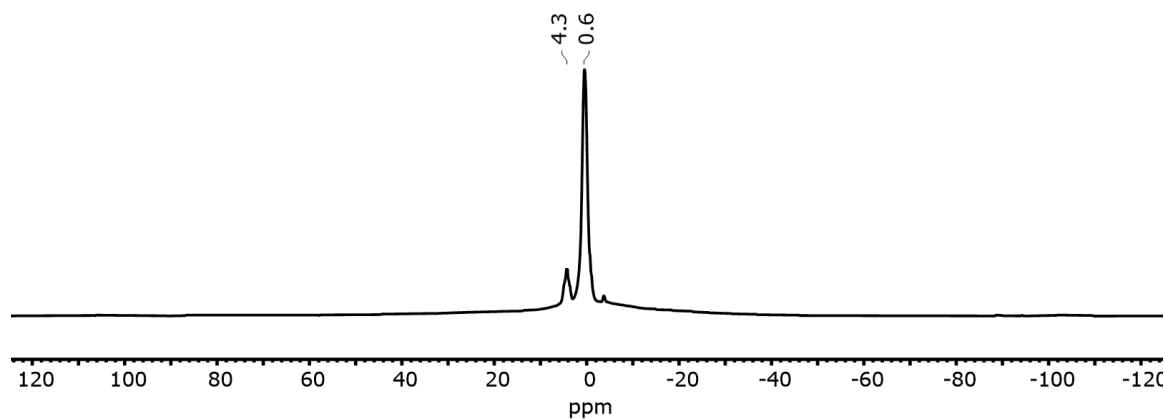


Figure A4.27 $^{11}\text{B}\{^1\text{H}\}$ NMR spectrum collected in CD_3CN of the crude brown oil from the synthesis of $\text{K}[2\text{-Br-3-BF}_2\text{CF}_3\text{-py}]$. The broad peak in the baseline around 0 is a result of borosilicate in the NMR tube.

A4.1.6 K[2-Br-5-BF₂CF₃-py]

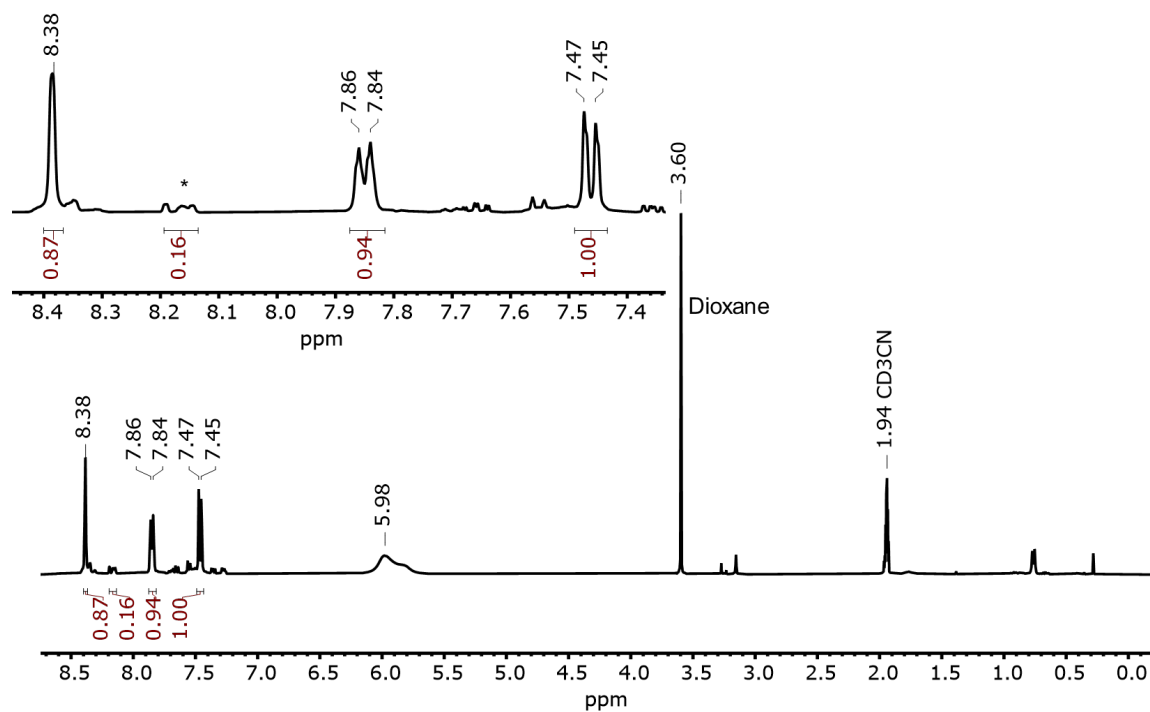


Figure A4.28 ¹H NMR spectrum in CD₃CN of the crude brown oil from the synthesis of K[2-Br-5-BF₂CF₃-py]. Asterisks indicate unknown impurities.

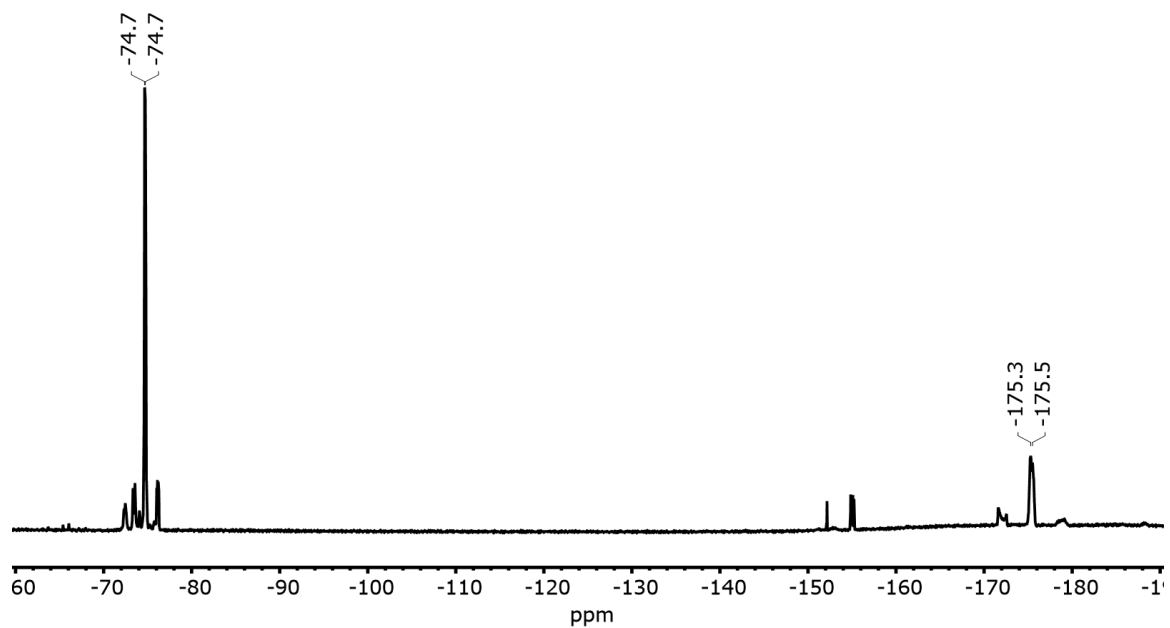


Figure A4.29 $^{19}\text{F}\{^1\text{H}\}$ NMR spectrum collected in CD_3CN of the crude brown oil from the synthesis of $\text{K}[2\text{-Br-5-BF}_2\text{CF}_3\text{-py}]$.

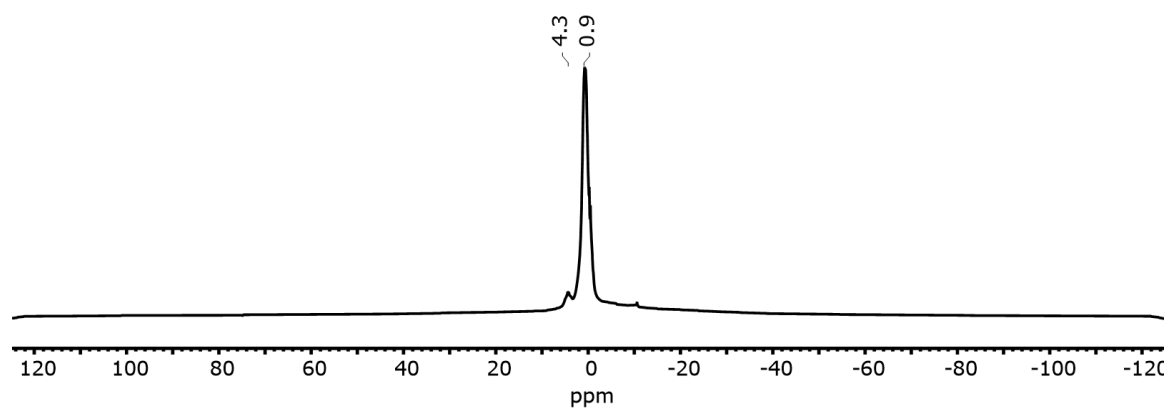


Figure A4.30 $^{11}\text{B}\{^1\text{H}\}$ NMR spectrum collected in CD_3CN of the crude brown oil from the synthesis of $\text{K}[2\text{-Br-5-BF}_2\text{CF}_3\text{-py}]$. The broad peak in the baseline around 0 is a result of borosilicate in the NMR tube.

A4.1.7 K[2-Br-6-BF₂CF₃-py]

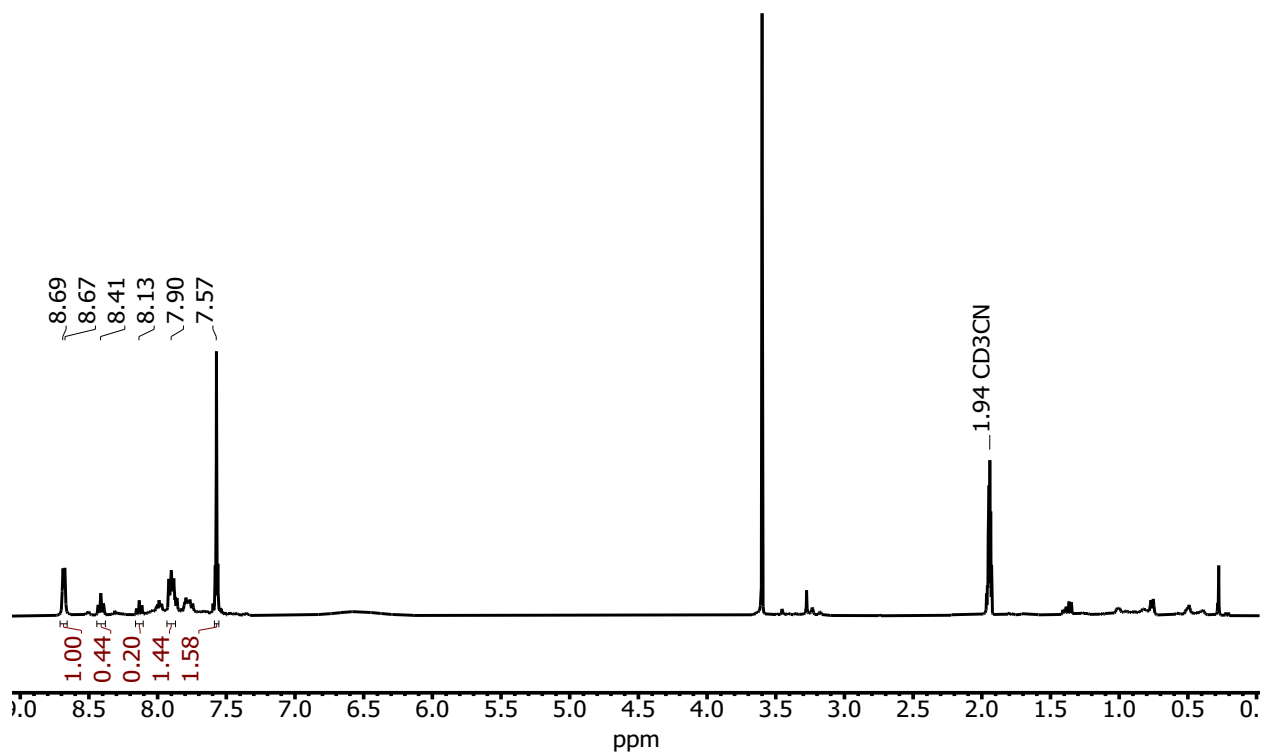


Figure A4.31 ¹H NMR spectrum in CD₃CN of the crude brown oil from the synthesis of K[2-Br-6-BF₂CF₃-py]. Integration and splitting patterns of the resonances are not consistent with the desired product.

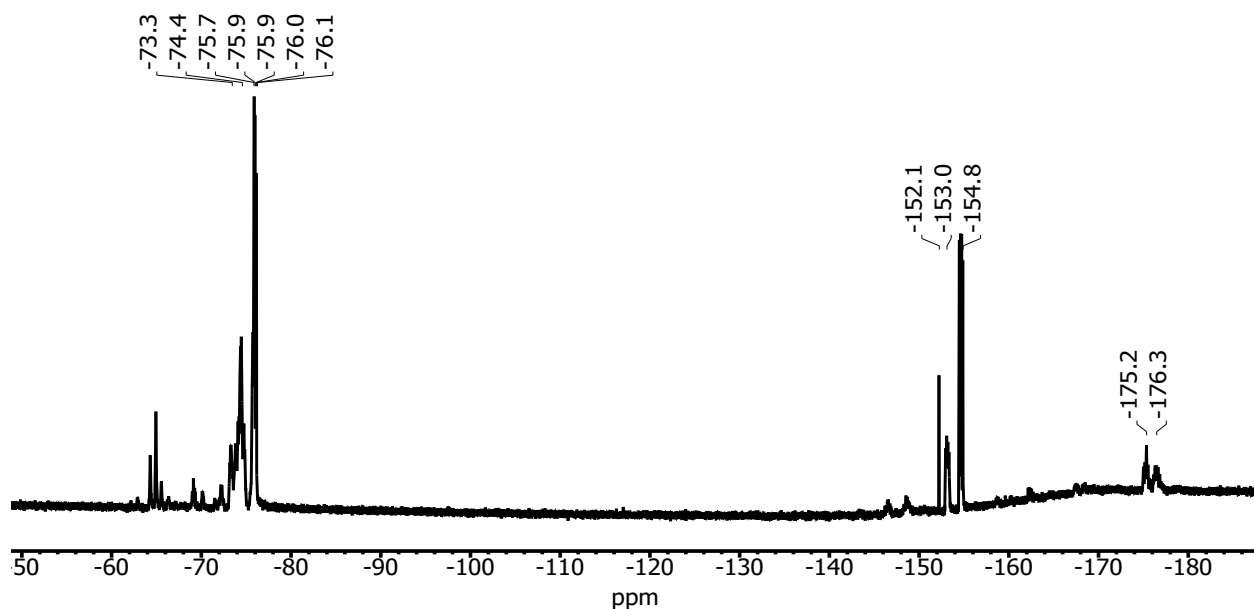


Figure A4.32 $^{19}\text{F}\{^1\text{H}\}$ NMR spectrum collected in CD_3CN of the crude brown oil from the synthesis of $\text{K}[2\text{-Br-6-BF}_2\text{CF}_3\text{-py}]$. The BF_3 resonances in the -150 ppm range are consistent with the reported spectra for $\text{BF}_3\text{CF}_3\text{K}$.

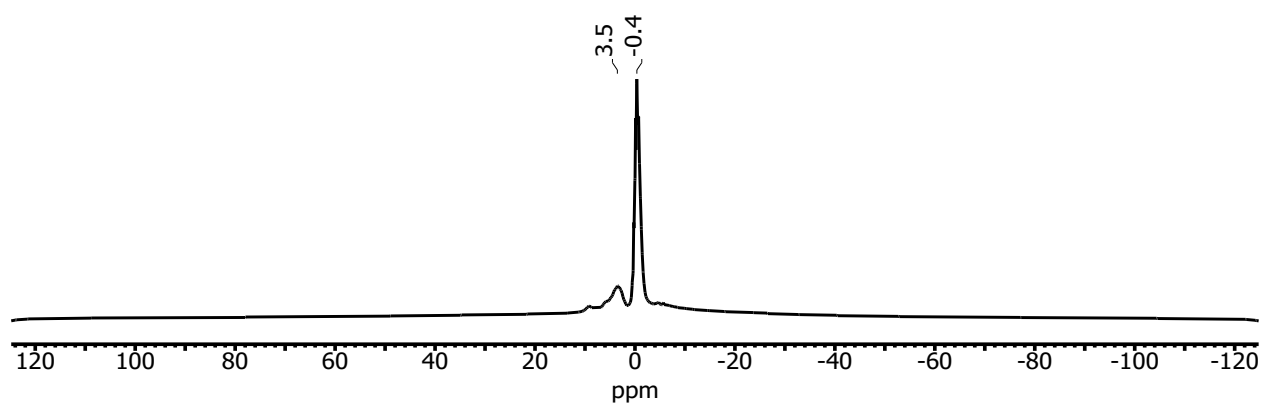


Figure A4.33 $^{11}\text{B}\{^1\text{H}\}$ NMR spectrum collected in CD_3CN of the crude brown oil from the synthesis of $\text{K}[2\text{-Br-6-BF}_2\text{CF}_3\text{-py}]$. The broad peak in the baseline around 0 is a result of borosilicate in the NMR tube.

A4.2 SXR D Tables

Identification code	K[2-Br-4-BF ₂ CF ₃ -py]	[P(2-py) ₃ NiNO][BPh ₄] + 1 benzene molecule
Empirical formula	C ₆ H ₃ BBrF ₅ KN	C ₄₅ H ₃₈ BN ₄ NiOP
Formula weight	313.9	751.3
Temperature/K	100(2)	100 (2)
Crystal system	Monoclinic	Triclinic
Space group	P2 ₁ /c	P-1
a/Å	10.3345(18)	14.2448(8)
b/Å	9.9733(19)	23.4288(14)
c/Å	9.3245(17)	23.4288(14)
α/°	90	73.04
β/°	98.043(5)	85.774(1)
γ/°	90	85.774 (1)
Volume/Å ³	951.6(3)	7447.5(8)
Z	4	8
ρ _{calc} /g/cm ³	2.191	1.340
μ/mm ⁻¹	4.794	0.606
F(000)	600	3136
Crystal size/mm ³	0.093 x 0.099 x 0.274	0.19 x 0.19 x 0.17
Radiation	MoKα (λ = 0.71073)	MoKα (λ = 0.71073)
2Θ range for data collection/°	53.7	49.6
Index ranges	-13 ≤ h ≤ 13, -12 ≤ k ≤ 12, -11 ≤ l ≤ 11	-16 ≤ h ≤ 16, -27 ≤ k ≤ 27, -27 ≤ l ≤ 27
Reflections collected	15935	131642
Independent reflections	2048 [R _{int} = 0.1353, R _{sigma} = 0.0594]	25446 [R _{int} = 0.0921, R _{sigma} = 0.0888]
Data/restraints/parameters	2048/0/136	25446/328/1913
Goodness-of-fit on F ²	1.137	1.011
Final R indexes [I >= 2σ (I)]	R ₁ = 0.0663, wR ₂ = 0.1669	R ₁ = 0.0559, wR ₂ = 0.1068
Final R indexes [all data]	R ₁ = 0.0851, wR ₂ = 0.1777	R ₁ = 0.1029, wR ₂ = 0.1234
Largest diff. peak/hole / e Å ⁻³	1.52/-1.02	0.939/-0.385
Flack parameter	-	-

Table A4.1 Refinement data for crystal structures of K[2-Br-4-BF₂CF₃-py] and [P(2-py)₃NiNO][BPh₄].

A4.3 Calculations

A4.3.1 Coordinates of Optimized Structures

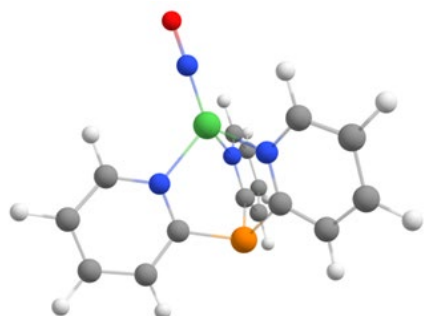


Figure A4.34 Coordinates of optimized geometry for PPy₃NiNO aligned in Avogadro with the Z axis along the NO bond.

N	1.66837	-0.73232	-2.57838
C	1.76805	-0.60029	-3.90775
C	2.62031	-1.39817	-1.91652
P	0.47737	0.31049	-4.86556
C	0.40382	1.87060	-3.87917
C	-1.03382	-0.53194	-4.22097
N	-1.23231	-0.66163	-2.90247
C	0.19120	2.98164	-1.86737
N	0.24503	1.83328	-2.54958
C	-2.33473	-1.27996	-2.46703
Ni	0.11322	0.07218	-1.60812
N	0.00000	0.00000	-0.00000
C	0.29636	4.22009	-2.48276
C	0.46379	4.27169	-3.86063
C	0.51705	3.07684	-4.56833
H	0.55163	5.22888	-4.37895

H	0.64618	3.06808	-5.65195
H	0.24633	5.12822	-1.87936
C	-3.29011	-1.79623	-3.32992
C	-1.94904	-1.02372	-5.15017
C	-3.09602	-1.66616	-4.69916
H	-1.75507	-0.89950	-6.21705
H	-3.82718	-2.06016	-5.40852
H	-4.17181	-2.29371	-2.92345
C	3.71589	-1.96175	-2.55333
C	2.83966	-1.13915	-4.61751
C	3.83065	-1.83070	-3.93119
H	2.88681	-1.01221	-5.70014
H	4.68012	-2.26051	-4.46609
H	4.46521	-2.49542	-1.96650
O	0.00000	-0.00000	1.14499
H	0.05782	2.90246	-0.78769
H	2.49730	-1.48073	-0.83593
H	-2.45152	-1.36355	-1.38569

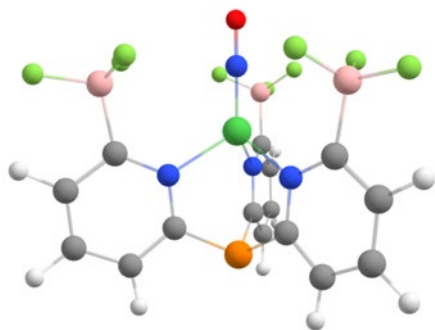


Figure A4.35 Coordinates of optimized geometry for $P(6-BF_3-2-py)_3NiNO$ aligned in Avogadro with the Z axis along the NO bond.

N	1.57862	-0.79004	-2.68357
---	---------	----------	----------

C	1.46253	-0.75892	-4.02017
C	2.68533	-1.34072	-2.12196
P	0.00182	-0.01063	-4.84360
C	-0.07984	1.63160	-4.02727
C	-1.37953	-0.89733	-4.02035
N	-1.45912	-0.98864	-2.68419
C	-0.19278	2.98386	-2.13184
N	-0.11130	1.74963	-2.69129
C	-2.48265	-1.68019	-2.12173
B	-2.66873	-1.89765	-0.49502
B	2.95541	-1.41990	-0.49417
Ni	0.00350	-0.00554	-1.62493
N	0.00000	0.00000	-0.00000
F	-1.55603	-2.54691	0.02895
F	-3.80748	-2.71972	-0.31066
F	-2.88876	-0.67653	0.13518
F	3.03136	-0.13560	0.03717
F	1.96306	-2.17115	0.12581
F	4.20168	-2.06793	-0.30842
B	-0.25706	3.26126	-0.50410
F	-0.35886	4.66300	-0.32422
F	-1.38383	2.65418	0.04093
F	0.90996	2.81234	0.10540
C	-0.23122	4.10856	-2.97005
C	-0.18917	3.99687	-4.34905
C	-0.11448	2.72317	-4.89333
H	-0.21599	4.88235	-4.99265
H	-0.08254	2.54950	-5.97073
H	-0.29609	5.07756	-2.47316
C	-3.44636	-2.26740	-2.95566

C	-2.31537	-1.46616	-4.88250
C	-3.38085	-2.16524	-4.33446
H	-2.18718	-1.34986	-5.96073
H	-4.14019	-2.62503	-4.97611
H	-4.24668	-2.81301	-2.45535
C	3.67952	-1.87195	-2.95784
C	2.42708	-1.27581	-4.88367
C	3.56566	-1.84936	-4.33696
H	2.26367	-1.21711	-5.96134
H	4.34791	-2.26655	-4.97957
H	4.54787	-2.30258	-2.45815
O	0.00000	-0.00000	1.13180

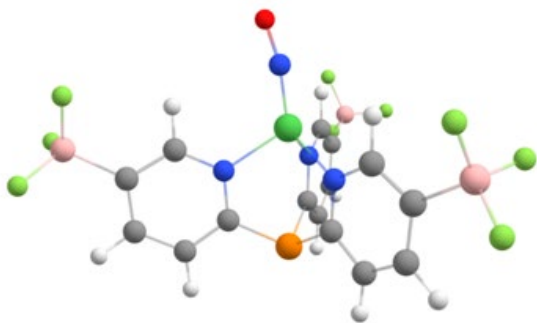


Figure A4.36 Coordinates of optimized geometry for $P(5-BF_3-2-py)_3NiNO$ aligned in Avogadro with the Z axis along the NO bond.

N	1.59368	-0.53693	-2.70770
C	1.75578	-0.11142	-3.96753
C	2.41806	-1.47950	-2.22701
P	0.64251	1.17276	-4.67173
C	0.76846	2.46649	-3.36862
C	-0.99031	0.44140	-4.24954
N	-1.24816	0.04230	-2.99735

C	0.68921	3.13028	-1.15672
N	0.57857	2.16242	-2.07812
C	-2.44406	-0.49674	-2.71907
Ni	0.15088	0.27696	-1.57960
N	0.00000	0.00000	0.00000
C	0.99534	4.46035	-1.44154
C	1.16956	4.76309	-2.79222
C	1.06338	3.77098	-3.75894
H	1.38659	5.79578	-3.08108
H	1.20191	3.98550	-4.82125
B	1.16113	5.58385	-0.25838
C	-3.46123	-0.68685	-3.65433
C	-1.94634	0.31321	-5.25425
C	-3.18025	-0.24841	-4.94837
H	-1.70575	0.66052	-6.26191
H	-3.95398	-0.34880	-5.71505
B	-4.88127	-1.40715	-3.26358
C	3.45122	-2.06956	-2.95461
C	2.76990	-0.62560	-4.77216
C	3.61672	-1.59975	-4.25777
H	2.87936	-0.24786	-5.79127
H	4.43180	-2.00462	-4.86416
B	4.39470	-3.25435	-2.32580
H	2.25246	-1.77561	-1.18967
H	0.51316	2.83319	-0.12121
H	-2.60358	-0.78741	-1.67893
O	0.00000	0.00000	1.15659
F	4.47631	-3.09980	-0.93735
F	5.67172	-3.16710	-2.90151
F	3.83363	-4.50102	-2.63098

F	0.52430	5.13190	0.90365
F	0.58742	6.78828	-0.69059
F	2.52467	5.78446	-0.00563
F	-5.23960	-1.05850	-1.95593
F	-4.73348	-2.79656	-3.35663
F	-5.87018	-0.98392	-4.16620

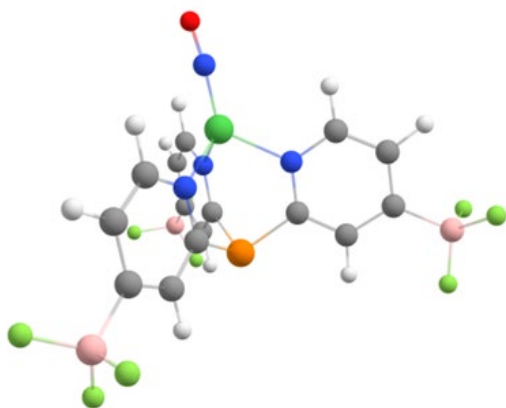


Figure A4.37 Coordinates of optimized geometry for P(4-BF₃-2-py)₃NiNO aligned in Avogadro with the Z axis along the NO bond.

N	2.29731	-0.02575	-1.96639
C	2.72672	-0.01250	-3.23720
C	3.20481	-0.06293	-0.98407
P	1.51575	0.01624	-4.63543
C	0.45007	1.43141	-4.10699
C	0.42243	-1.38568	-4.12929
N	-0.09746	-1.41030	-2.89409
C	-0.80812	2.50399	-2.50516
N	-0.04568	1.46360	-2.86156
C	-0.90569	-2.42487	-2.56266
Ni	0.35584	0.00539	-1.56810

N	0.00000	0.00000	-0.00000
C	-1.11258	3.53700	-3.37307
C	-0.63669	3.53353	-4.68753
C	0.17446	2.44411	-5.02448
B	-1.04959	4.71355	-5.74904
H	0.60495	2.38548	-6.02681
H	-1.72979	4.36924	-3.02578
C	-1.21727	-3.44706	-3.44063
C	0.14924	-2.39375	-5.05318
C	-0.68086	-3.47268	-4.73185
H	0.58712	-2.33781	-6.05239
B	-1.00553	-4.70017	-5.77027
H	-1.89546	-4.24057	-3.11787
C	4.56591	-0.08567	-1.22917
C	4.08781	-0.02926	-3.54022
C	5.06119	-0.05844	-2.53596
H	4.40004	-0.02997	-4.58691
B	6.67305	-0.05133	-2.84106
H	5.26102	-0.13424	-0.38710
H	2.81112	-0.07912	0.03485
H	-1.18057	2.49233	-1.47834
H	-1.31255	-2.39898	-1.54926
O	0.00000	0.00000	1.16398
F	7.29989	-0.92601	-1.94038
F	7.16880	1.24478	-2.64778
F	6.90535	-0.45943	-4.15718
F	-1.19852	5.92126	-5.04916
F	-2.27040	4.37101	-6.34539
F	-0.06078	4.83917	-6.72843
F	-2.38502	-4.95278	-5.74942

F	-0.31900	-5.84477	-5.34341
F	-0.59460	-4.34954	-7.05951

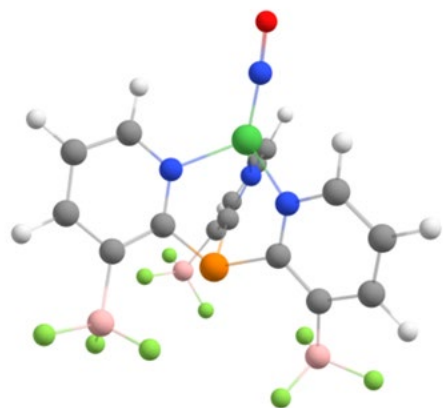


Figure A4.38 Coordinates of optimized geometry for P(3-BF₃-2-py)₃NiNO aligned in Avogadro with the Z axis along the NO bond.

N	1.57327	-0.66628	-2.65086
C	1.51741	-0.64734	-3.99437
C	2.74721	-0.72238	-2.01491
P	-0.14841	-0.84384	-4.84168
C	-0.94902	0.72192	-4.18406
C	-0.92157	-2.04812	-3.62397
N	-1.12754	-1.64982	-2.35613
C	-1.01757	2.32715	-2.49663
N	-0.63691	1.12603	-2.93999
C	-1.84679	-2.39481	-1.51163
Ni	-0.02827	-0.19742	-1.59517
N	0.00000	0.00000	-0.00000
C	-1.78712	3.17388	-3.27178
C	-2.21911	2.70913	-4.50717
C	-1.81781	1.46626	-5.00524
H	-2.90809	3.29559	-5.12055

B	-2.51592	0.95858	-6.41547
H	-2.07135	4.15731	-2.88713
C	-2.36432	-3.61872	-1.88943
C	-1.32099	-3.32470	-4.06768
C	-2.05609	-4.09036	-3.15890
B	-0.87576	-4.04709	-5.48768
H	-2.36438	-5.08739	-3.48309
H	-2.96115	-4.19935	-1.18105
C	3.94406	-0.71165	-2.70484
C	2.68317	-0.52930	-4.77725
C	3.89660	-0.56970	-4.08576
B	2.74096	-0.20311	-6.39752
H	4.81074	-0.46620	-4.67531
H	4.88894	-0.77496	-2.15794
H	2.70948	-0.76291	-0.92453
H	-0.70290	2.59469	-1.48586
H	-1.99147	-1.99297	-0.50680
F	-1.18475	-5.42512	-5.36053
F	0.50696	-3.90061	-5.61384
F	-1.55251	-3.53027	-6.57580
F	-3.70472	1.71805	-6.56196
F	-2.84524	-0.38825	-6.28106
F	-1.70176	1.18760	-7.51264
F	1.81970	0.81149	-6.65817
F	4.04763	0.27549	-6.66920
F	2.50366	-1.32722	-7.16818
O	0.00000	-0.00000	1.16981

A4.3.2 Matlab Code Used to Predict Fz at the Midpoint of the NO Bond for the 3 Isomer

Field predicted for each isomer along the nitrosyl axis:

	Fieldz in V/Å
6-BF ₃	1.127
5-BF ₃	0.4538
4-BF ₃	0.4791
3-BF ₃	0.6981

```
%Charge density in the 3 isomer, NO the z axis
```

```
%Midpoint between N and O in meters
```

```
Nx = 0;
```

```
Ny = 0;
```

```
Nz = 0;
```

```
Ox = 0;
```

```
Oy = 0;
```

```
Oz = 1.16981/10^10;
```

```
NO_x = 0;
```

```
NO_y = 0;
```

```
NO_z = (Oz - Nz) / 2;
```

```
%Location of Boron atoms in meters
```

```
B1x = -2.51592/10^10;
```

```
B1y = 0.95858/10^10;
```

```
B1z = -6.41547/10^10;
```

```
B2x = -0.87576/10^10;
```

```
B2y = -4.04709/10^10;
```

```
B2z = -5.48768/10^10;
```

```
B3x = 2.74096/10^10;
```

```
B3y = -0.20311/10^10;
```

```
B3z = -6.39752/10^10;
```

```
%distance between points
```

```
NB1x = NO_x - B1x;
```

```
NB1y = NO_y - B1y;
```

```
NB1z = NO_z - B1z;
```

```
dNB1 = NB1x^2 + NB1y^2 + NB1z^2;
```

```
NB2x = NO_x - B2x;
```

```
NB2y = NO_y - B2y;
```

```
NB2z = NO_z - B2z;
```

```
dNB2 = NB2x^2 + NB2y^2 + NB2z^2;
```



```

NB3x = NO_x-B3x;
NB3y = NO_y-B3y;
NB3z = NO_z-B3z;
dNB3 = NB3x^2 + NB3y^2 + NB3z^2;
davg = (dNB1^(1/2) + dNB2^(1/2) + dNB3^(1/2))/3;

```

```

%Field direction along NO bond

```

```

CP = 9E9;
elec = -1.60218E-19;
rNB1 = dNB1^(3/2);
rNB2 = dNB2^(3/2);
rNB3 = dNB3^(3/2);

```

```

%Boron 1

```

```

EB1x = CP*elec*-1*(NO_x-B1x)/rNB1;
EB1y = CP*elec*-1*(NO_y-B1y)/rNB1;
EB1z = CP*elec*-1*(NO_z-B1z)/rNB1;

```

```

EVA1x = EB1x/10^10;
EVA1y = EB1y/10^10;
EVA1z = EB1z/10^10;

```

```

Eau1x = EVA1x/51.4;
Eau1y = EVA1y/51.4;
Eau1z = EVA1z/51.4;

```

```

%Boron2

```

```

EB2x = CP*elec*-1*(NO_x-B2x)/rNB2;
EB2y = CP*elec*-1*(NO_y-B2y)/rNB2;
EB2z = CP*elec*-1*(NO_z-B2z)/rNB2;

```

```

EVA2x = EB2x/10^10;
EVA2y = EB2y/10^10;
EVA2z = EB2z/10^10;

```

```

Eau2x = EVA2x/51.4;
Eau2y = EVA2y/51.4;
Eau2z = EVA2z/51.4;

```

```

%Boron 3

```

```

EB3x = CP*elec*-1*(NO_x-B3x)/rNB3;
EB3y = CP*elec*-1*(NO_y-B3y)/rNB3;
EB3z = CP*elec*-1*(NO_z-B3z)/rNB3;

```

```
EVA3x = EB3x/10^10;  
EVA3y = EB3y/10^10;  
EVA3z = EB3z/10^10;
```

```
Eau3x = EVA3x/51.4;  
Eau3y = EVA3y/51.4;  
Eau3z = EVA3z/51.4;
```

```
% Total field in volts per Angstrom along z axis  
EVAz = EVA1z + EVA2z + EVA3z
```